Highlights in Theoretical Chemistry 6

Series Editors: Christopher J. Cramer · Donald G. Truhlar

Benoît Champagne
Michael S. Deleuze
Frank De Proft
Tom Leyssens *Editors*

Theoretical Chemistry in Belgium

A Topical Collection from Theoretical Chemistry Accounts

Springer

Highlights in Theoretical Chemistry

Vol. 6
Series Editors: Ch.J. Cramer • D.G. Truhlar

For further volumes:
http://www.springer.com/series/11166

Benoît Champagne • Michael S. Deleuze
Frank De Proft • Tom Leyssens
Volume Editors

Theoretical Chemistry in Belgium

A Topical Collection from Theoretical Chemistry Accounts

With contributions from

Jean-Marie André • Guillermo Avendaño-Franco • David Beljonne
Frank Blockhuys • Annemie Bogaerts • Jean-Luc Brédas • Patrick Bultinck
Thomas Carette • Emilie Cauët • Andrés Cedillo • Arnout Ceulemans
Benoît Champagne • Aurélie Chenel • Jérôme Cornil • Frank De Proft
Freija De Vleeschouwer • Dirk E. De Vos • Annelies Delabie
Michael S. Deleuze • Maxime Delsaut • Michèle Desouter-Lecomte
Georges Dive • Adri C. T. van Duin • Joseph G. Fripiat • Uma R. Fogueri
Patrick W. Fowler • Renuka Ganesan • Thomas Gathy • Paul Geerlings
Davy Geldof • Victor Geskin • An Ghysels • Michel Godefroid
Xavier Gonze • Myrta Grüning • Maxime Guillaume • Balázs Hajgató
Frank E. Harris • Pierre O. Hubin • Denis Jacquemin • Amir Karton
Sebastian Kozuch • Alisa Krishtal • Clément Lauzin • Laurence Leherte
Tom Leyssens • Jiguang Li • Vincent Liégeois • Jacques Liévin
Erwin Lijnen • Jérôme Loreau • Roger B. Mallion • Jan M. L. Martin
Christoph Meier • Filippo Morini • Fady Nahra • Cédric Nazé
Mamadou Ndong • Erik C. Neyts • Minh Tho Nguyen • Daniel Peeters
Quan Manh Phung • Kristine Pierloot • Bernard Piraux • Tomaz Pisanski
Geoffrey Pourtois • Françoise Remacle • Olivier Riant • Raphaël Robiette
John S. Sears • Gjergji Sini • Brian Sutcliffe • Truong Ba Tai
Nguyen Minh Tam • Nathalie S. Vaeck • Christian Van Alsenoy
Dimitri Van Neck • Tanguy Van Regemorter • Veronique Van Speybroeck
Steven Vancoillie • Matthias Vandichel • Monique A. van der Veen
Daniel P. Vercauteren • Simon Verdebout • Thomas Vergote
Toon Verstraelen • Stéphane Vranckx • Michel Waroquier • Giuseppe Zanti

Springer

Volume Editors
Benoît Champagne
Laboratory of Theoretical Chemisty
Unit of Physical Chemistry
Chemistry Department
University of Namur
Namur, Belgium

Frank De Proft
Faculteit Wetenschappen
Eenheid Algemene Chemie (ALGC)
Free University of Brussels
Brussels, Belgium

Michael S. Deleuze
Research Group of Theoretical Chemistry
and Molecular Modeling
Hasselt University
Diepenbeek, Belgium

Tom Leyssens
Laboratory of Crystal Engineering
Institute of Condensed Matter and Nanosciences
Catholic University of Louvain
Louvain-La-Neuve, Belgium

Originally Published in Theor Chem Acc, Volume 131 (2012) and Volume 132 (2013)
© Springer-Verlag Berlin Heidelberg 2012, 2013

ISSN 2194-8666 ISSN 2194-8674 (electronic)
ISBN 978-3-642-41314-8 ISBN 978-3-642-41315-5 (eBook)
DOI 10.1007/978-3-642-41315-5
Springer Heidelberg New York Dordrecht London

© Springer-Verlag Berlin Heidelberg 2014
This work is subject to copyright. All rights are reserved by the Publisher, whether the whole or part of the material is concerned, specifically the rights of translation, reprinting, reuse of illustrations, recitation, broadcasting, reproduction on microfilms or in any other physical way, and transmission or information storage and retrieval, electronic adaptation, computer software, or by similar or dissimilar methodology now known or hereafter developed. Exempted from this legal reservation are brief excerpts in connection with reviews or scholarly analysis or material supplied specifically for the purpose of being entered and executed on a computer system, for exclusive use by the purchaser of the work. Duplication of this publication or parts thereof is permitted only under the provisions of the Copyright Law of the Publisher's location, in its current version, and permission for use must always be obtained from Springer. Permissions for use may be obtained through RightsLink at the Copyright Clearance Center. Violations are liable to prosecution under the respective Copyright Law.
The use of general descriptive names, registered names, trademarks, service marks, etc. in this publication does not imply, even in the absence of a specific statement, that such names are exempt from the relevant protective laws and regulations and therefore free for general use.
While the advice and information in this book are believed to be true and accurate at the date of publication, neither the authors nor the editors nor the publisher can accept any legal responsibility for any errors or omissions that may be made. The publisher makes no warranty, express or implied, with respect to the material contained herein.

Printed on acid-free paper

Springer is part of Springer Science+Business Media (www.springer.com)

Contents

Theor Chem Acc (2013) 132:1372
DOI 10.1007/s00214-013-1372-6

EDITORIAL

Preface

Benoît Champagne · Michael S. Deleuze ·
Frank De Proft · Tom Leyssens

In Belgium, theoretical chemistry began more than 50 years ago, with an initial focus on quantum chemistry, which gradually developed into a general interest in different domains of theoretical chemistry. In the *Florilège des Sciences en Belgique* [1], Louis d'Or cites as founding members of quantum chemistry in Belgium: Jean-Claude Lorquet at the Université de Liège, Georges Leroy at the Université catholique de Louvain (UCL), Georges Verhaegen at Université libre de Bruxelles (ULB), Luc Vanquickenborne at Katholieke Universiteit Leuven (KUL), and Piet van Leuven at Antwerpen (RUCA).

Nowadays, Belgium counts around 200 theoretical chemists, spread over 10 universities (Fig. 1). This special issue includes contributions from the different theoretical chemistry groups, illustrating the diversity and richness of the field whereas this Editorial is the occasion to sketch some aspects of the evolution of quantum chemistry and theoretical chemistry in our country.

Key elements in the developments of the field have also been the collaborations, the creation of working groups, and the organization of conferences, of which the two-yearly meeting *Quantum Chemistry in Belgium*, that was the stimulus for preparing this special issue. The first issue of the meeting took place in 1995 at the University of Namur, and during the last 17 years (1996 in Leuven, 1997 in ULB, 1999 in Antwerpen, 2001 in Liège, 2003 in Ghent, 2006 in Mons, 2008 in Hasselt, 2010 in Louvain-la-Neuve, 2012 in VUB), it has been organized in all the universities. The second round will start in 2014 in Namur.

Progresses in theoretical chemistry have always been associated with the development of computational resources, from more local architectures to the larger centers recently installed in the two regions of the country, the Vlaams Supercomputer Center and the Consortium des Équipements de Calcul Intensif (CÉCI). Theoretical chemistry in Belgium has over the years largely benefited from funding by scientific agencies such as the *Fonds voor Wetenschappelijk Onderzoek* (FWO-Vlaanderen) and the Instituut voor Wetenschap en Technologie on the Flemish side, the Fonds de la Recherche Scientifique (F.R.S.–FNRS) and the Fonds de la Recherche pour la Formation dans l'Industrie et dans l'Agriculture on the French speaking side, as well as the Belgium Science Policy Office at the national level.

Published as part of the special collection of articles celebrating theoretical and computational chemistry in Belgium.

B. Champagne (✉)
Laboratory of Theoretical Chemistry, Unit of Physical Chemistry, Chemistry Department, University of Namur, Rue de Bruxelles, 61, 5000 Namur, Belgium
e-mail: benoit.champagne@unamur.be

M. S. Deleuze
Research Group of Theoretical Chemistry and Molecular Modeling, Hasselt University, Agoralaan Gebouw D, 3590 Diepenbeek, Belgium
e-mail: michael.deleuze@uhasselt.be

F. De Proft
Faculteit Wetenschappen, Eenheid Algemene Chemie (ALGC), Vrije Universiteit Brussel (VUB), Pleinlaan 2, 1050 Brussels, Belgium
e-mail: fdeproft@vub.ac.be

T. Leyssens
Laboratory of Crystal Engineering, Institute of Condensed Matter and Nanosciences, Université Catholique de Louvain, Place Louis Pasteur 1, bte L4.01.03, 1348 Louvain-La-Neuve, Belgium
e-mail: tom.leyssens@uclouvain.be

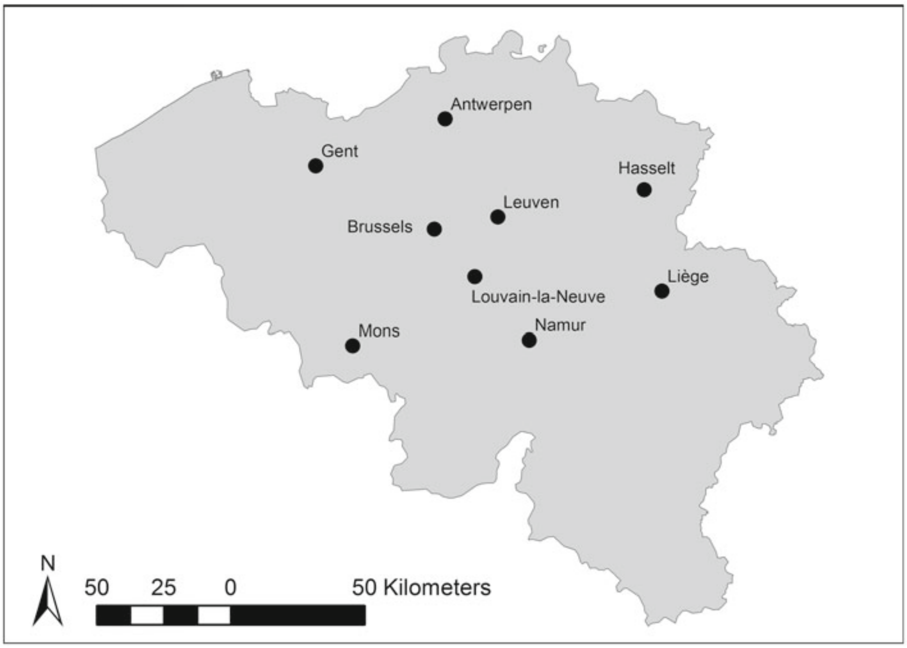

Fig. 1 Map of Belgium representing the cities where the different universities discussed below are located

1 University of Antwerp

The *Universitaire Instelling Antwerpen* (UIA) was founded in 1971. On October 1, 2003, it became part of the University of Antwerp (UA) which united RUCA (State University Centre Antwerp), UFSIA (University Faculties Saint Ignatius Antwerp) and UIA (University Institution Antwerp). Since the foundation of the UIA, research using quantum chemical methods has been performed in the "Structural Chemistry" group led by H.J. Geise working on electron diffraction (ED) and by A.T.H. Lenstra working on X-ray diffraction. At that time, mainly semi-empirical calculations such as MINDO/3 were performed to assist in the interpretation of the experimental data with these techniques. C. Van Alsenoy joined this group in 1978. During this period, structural chemists became aware of the enormous potential of P. Pulay's force method in their research field. With this in mind, C. Van Alsenoy went to the USA for two postdoctoral stays, the first one with L. Schäfer at the University of Arkansas and the second one with J. Boggs at the University of Texas (at Austin) where he worked under the guidance of P. Pulay for a period of 6 months. During this period, the basis for the Multiplicative Integral Approximation (MIA) was established, which later evolved into the Multiplicative Integral Approach.

When C. Van Alsenoy returned to the University of Antwerp, research in the group of quantum chemistry was directed mainly along two lines. A first purpose was to make the Molecular Orbital Constrained Electron Diffraction (MOCED) approach routinely available to people doing Electron Diffraction in the group. In the MOCED approach, differences in bond lengths and vibrational amplitudes from ab initio (HF) gradient calculations were used as constraints in the refinement of ED-experimental data. A code was thereby set up to do geometry refinements, force field, and vibrational frequency calculations, along with normal-mode fitting. The second line of research involved the further development and implementation of the MIA into Pulay's TEXAS quantum chemical package. This code, after further refinement and optimization, evolved into the program BRABO, a package which besides enabling SCF (HF and DFT) calculations in parallel also contains software to relax the molecular structure in geometry optimization, to construct clusters based on fractional coordinates and space group symmetry, to calculate and plot molecular density (-difference) maps, and to partition molecular quantities using the Hirshfeld approach.

To date, the MIA approach can be applied routinely in HF and DFT calculations as well as CPHF and CPKS calculations of polarizabilities and NMR chemical shifts. These developments were used in numerous studies, among others for unraveling the structure of the crambin peptide. At the time, this achievement was recognized by I. Levine in his book "quantum chemistry" as the largest ever performed quantum chemical calculation. Other studies involved cluster calculations in order to explain structural differences and vibrational frequency shifts in molecules between the gas-phase and the crystal-phase structures, depending on the space group. Another important and more recent line of research in C. Van Alsenoy's research group is devoted to the study and use of the Hirshfeld approach for partitioning molecular properties such as total charge distributions, molecular polarizabilities as well as the total molecular energy into atomic contributions, at various levels of theory (HF, DFT, and MP2). A very promising extension along these lines of research is the use of Hirshfeld partitioned quantities of multipole polarizabilities in the study of dispersion effects complementing DFT calculations.

In parallel to the work by C. van Alsenoy, research by Renaat Gijbels and Annemie Bogaerts in Antwerp led over the years to the foundation of an interdisciplinary research group “PLASMANT” (Plasma, Laser Ablation and Surface Modeling—ANTwerp) where theoretical chemistry also forms an important line of research. R. Gijbels started his PhD work at Ghent University in 1961, in the research group of J. Hoste, which later evolved to the Institute of Nuclear Sciences. His topic was the determination of traces of noble metals in other, high-purity noble metals, via neutron activation analysis (NAA). After a few years, D. Desoete and R. Gijbels, together with J. Hoste, embarked on the preparation of a monograph on Neutron Activation Analysis. R. Gijbels took care of the more “fundamental” chapters and realized that NAA practitioners were not enough aware of a number of basic concepts, elastic and inelastic scatterings, excited states and metastable states, among others. So, he started to study and to clarify these concepts in the book. As a consequence, a number of PhD works started in the group, for example, for the determination of average cross-sections of so-called threshold reactions induced by fission neutrons, by J.P. François (see his contribution at the University of Hasselt).

R. Gijbels continued to follow this double track: theory and different practical applications by NAA in a variety of nuclear reactors. Modeling received again a boost with the arrival of a postdoc from the Hungarian Academy of Sciences, A. Vertes who started a 1-D model for laser-solid interaction. Another even more fruitful line of research started with the arrival, in 1986, of Jan M. L. Martin for his master thesis in Antwerp. R. Gijbels had seen a large variety of carbon cluster ions in spark source and laser induced mass spectra, and wondered what their structure could be. J. Martin performed quantum chemical calculations to model these clusters, in close collaboration with J.-P. François, at the University of Hasselt.

In 1993, A. Bogaerts joined the group as a PhD student, and she developed a computer model for a glow discharge plasma, used as an ion source for glow discharge mass spectrometry. After finishing her PhD thesis in 1996, she became an FWO postdoc in the group and started a subgroup on plasma modeling, also for other applications than analytical spectrometry (see below). This group was gradually growing, and new activities started, that is, on classical molecular dynamics simulations for plasma–surface interactions (in 2001) and on modeling for laser ablation (i.e., laser–solid interaction, plume expansion, and plasma formation) (in 2002). In 2001, A. Bogaerts was prize winner of the Royal Flemish Academy of Belgium for Sciences and Arts. In 2003, she was appointed as a professor. After the retirement of R. Gijbels in 2004, the group was renamed as “PLASMANT”. In 2011, E. Neyts, who made his PhD and postdoctoral work in the group on molecular dynamics (MD) simulations for plasma deposition of coatings and carbon nanotube growth, respectively, started in the group as a tenure track professor.

Currently, the group consists of about 20 people (PhD students and postdoctoral researchers; under the supervision of A. Bogaerts and E. Neyts, and one technical-administrative coworker). As the name says, the group is mainly performing computer modeling for (i) plasmas, (ii) laser ablation (laser–surface interactions), and (iii) plasma–surface interactions. The first two fields are under the supervision of A. Bogaerts, whereas the third topic is under the supervision of E. Neyts, especially the combination of modeling both the plasma itself and its interaction with surfaces gives the group a unique expertise.

Theoretical chemistry activities in the University of Antwerp are discussed in the papers by Geldolf et al. [2] and by Neyts and Bogaerts [3] of the present issue.

2 Free University of Brussels

2.1 Université Libre de Bruxelles (ULB)

Quantum chemical research at the Université Libre de Bruxelles started in the mid-sixties. In 1965, Reginald Colin (RC) and Georges Verhaegen (GV) completed their PhD theses in high-temperature chemistry in the Laboratory of P. Goldfinger. The main characteristic of these studies was the discovery of numerous new molecules by mass spectrometry. It was the urge to learn more about the structure of these new species that determined the fields of postdoctoral studies they both chose: RC went to the Herzberg Institute in Ottawa to work with A.E. Douglas in Molecular Spectroscopy; GV went to the “Centre de Mécanique Ondulatoire Appliquée” (CMOA) of R. Daudel in Paris to work with C. Moser in quantum chemistry. The first publications of GV in this emerging field concerned the molecules BeO and MgO, both treated in his thesis.

Ab initio calculations have always demanded, and still demand, the largest possible computing possibilities, both in terms of speed and capacity. Back from the CMOA, the available computer in the ULB-VUB Center was then an IBM 650, much too small to accomplish anything, but a moderate LCAO-SCF calculation on very small atoms. Therefore, after discussions with the FNRS, GV was able to set up the then well-known SCF diatomic molecular program of Nesbet on the large computer of the Darmstadt Center. At the time, a quantum chemistry calculation meant sending by post perforated cards and waiting around a week to receive the listings of results back—converged or not! Fortunately, things improved rapidly, and calculations could then be carried out on the CDC computer mainframes newly installed at ULB. Nevertheless, in order to predict theoretically meaningful results, the Hartree–Fock results are insufficient, and for most properties, correlation effects need to be considered. Since the ab initio calculations involved were much too extensive for the available computers of the time, GV and his students developed an original atom-in-molecule approach to insert correlation effects in the results. Indirectly, this prompted the beginning of studies in theoretical atomic physics in the laboratory. G. Verhaegen was continuously deeply involved in getting the adequate computer resources to perform state-of-the-art calculations. Rector of ULB (1986–1990), he looked for partners interested in using or promoting the access to the first supercomputer of the country. The FNRS launched a stimulus program, leading to the inauguration of the CRAY X-MP/14 installation at the VUB/ULB Computing Center in 1989.

From the early start, G. Verhaegen's successors Jacques Liévin (JL) and Michel Godefroid (MG) and their students have greatly developed both the quantum chemistry (JL) and atomic physics (MG) fields of research in the laboratory. Later on (1990), Nathalie Vaeck (NV) also contributed to the atomic physics field before opening an original research line in quantum dynamics. The three permanent members (JL, MG, and NV) of the "Quantum Chemistry and Atomic Physics" theoretical group of the "Chimie Quantique et Photophysique" Laboratory developed numerous fruitful international collaborations and networks. Their various research activities are illustrated in Cauët et al.'s [4] contribution to the present issue. The contribution of Brian Sutcliffe, who has been a visiting professor in the group since 1998, focuses on formal aspects related to the concept of rovibrational hamiltonians and potential energy surfaces [5].

2.2 Vrije Universiteit Brussel (VUB)

The VUB offered a compulsory course on basic quantum mechanics and an introduction to quantum chemistry from the start of the chemistry curriculum in the early sixties. These lectures were given by André Bellemans, a former student of Nobel Laureate Ilya Prigogine at the ULB and still one of his collaborators at that time, specialist in statistical mechanics. In 1974 when Bellemans resigned from his VUB charge, Henk Lekkerkerker was appointed for teaching the complete range of theoretical physical chemistry courses (including thermodynamics and quantum mechanics). His teaching was as excellent as that of his predecessor, but just like André Bellemans the main part of his research was not devoted to quantum chemistry. In 1985, he changed his Full Professorship at the VUB for the position of head of the prestigious Van't Hoff Institute in Utrecht (where he previously obtained his master degree). Since the late sixties, Hubert Figeys, a pupil of the famous ULB organic chemistry Professor Richard Martin, gave a small elective course on Theoretical Organic Chemistry, followed among others by Paul Geerlings and Christian Van Alsenoy during their Master studies. Both of them graduated with him and finished their PhD in 1976 and 1977, respectively, on theoretical aspects of IR and NMR spectroscopy. Whereas C. Van Alsenoy left the VUB soon after to join Herman Geise's structural chemistry group in Antwerp, P. Geerlings stayed at the VUB and was appointed for the Quantum Mechanics and Theoretical Organic Chemistry Courses in 1985. He started a research group, which at the end of the eighties fully concentrated on theoretical and applied aspects of Density Functional Theory, with particular attention to conceptual or "Chemical Reactivity" DFT. Once appointed as full-time professor in 1990, as successor of Louis Van Hove as director of the General Chemistry Laboratory, his group grew quickly, also under the impetus of two young PhD students, Wilfried Langenaeker and Frank De Proft. For more than 20 years, now his group is responsible for all teaching activities around quantum chemistry, molecular modeling … (besides the basic course in General Chemistry for the Faculty of Science and, until 1997, the Faculty of Medicine). Meanwhile, F. De Proft became professor and codirector of the group, whereas W. Langenaeker left the group for a position in industry. In 2007, F. De Proft was Laureate of the Royal Flemish Academy of Belgium for Sciences and Arts in the division of natural sciences.

The group attracted many pre- and postdoctoral fellows and has collaborated with numerous research groups all over the world. It took care of 30 promotions (six being in progress) and published around 450 papers in international journals or as book chapters. In 2003, the group published an influential review on the field of conceptual DFT (*Chemical Reviews* 2003, *103*, 1793–1873), which, at the present moment, has been cited more than 1,050 times. The group has been the nucleus group for more than 15 years of the FWO Research Network "Quantum chemistry: fundamental and applied aspects of density functional theory", and has been active in the organization of several international meetings around DFT, from which DFT 2003, the Xth International Conference on Applications of Density Functional Theory in Chemistry and Physics, Brussels, Belgium, September 7–12, 2003, is best known.

The present composition of the group varies between 20 and 25 members with various backgrounds (chemistry, biology, physics, chemical, and bio-engineering), often enabling interdisciplinary research. Research activities are varying from fundamental aspects of DFT to applications in organic chemistry, catalysis, bio systems, and "nano" technology such as fullerenes, nanotubes, and graphene for which G. Van Lier was recently offered a part-time professorship. The contribution of the group in this special issue by De Vleeschouwer et al. [6] focuses on the computation of one of these chemical concepts, the electrophilicity, for radicals and the scrutiny of the effect of the solvent on this quantity.

3 Ghent University

3.1 Ghent quantum chemistry group (GQCG)

The department of chemistry at Ghent University, more specifically the then Laboratory of General and Inorganic Chemistry, already started to use quantum chemical calculations in 1970s mainly to assist in interpreting spectroscopic data although a dedicated quantum chemistry group did not exist. Only limited courses were taught by local spectroscopists. In 2000 Professors A. Goeminne and D. Van de Vondel, respectively, head of department and the spectroscopist lecturing quantum chemistry decided that a dedicated quantum chemistry group that bases its lecturing tasks on research expertise was due. Thanks to their initiative and insight, such a group was eventually founded in 2001 and has become known as the Ghent Quantum Chemistry Group (GQCG).

The group started with one professor (Patrick Bultinck) appointed in October 2001 and one Ph.D. student and started activities over a widespread range of areas including computational medicinal chemistry and chiroptical vibrational spectroscopy. At the beginning, the research was rather application directed with emphasis on conformational analysis, QSAR, and electronegativity equalization in medicinal chemistry and combined experimental/computational studies in Vibrational Circular Dichroism (VCD).

Nowadays, the group, varying in number between 8 and 12, concentrates on two themes, broadly categorized as "Electron density (matrices)" and "chiroptical spectroscopies." The first category contains both the fundamental study of density matrices, including their (wavefunction free) variational optimization and especially their use and meaning for studying chemical concepts through analysis of their properties. Examples are the study of Domain Averaged Fermi Holes from the study of the exchange–correlation density, delocalization indices and especially Aromaticity. The interest in the last being an obvious consequence of the fact that F.A. Kekulé published his famous papers on the tetravalence of carbon and the cyclic structure of benzene while being professor at Ghent University. The group introduced the popular density matrix based multicenter indices for aromaticity and scrutinized the meaning of this chemical concept. The meaning and the relevance of the many indices available were critically investigated. A second example of work along these lines is the Hirshfeld-I atom in the molecule, which corrects some issues with the traditional Hirshfeld atom in the molecule. The second line of research concentrates on Chiroptical spectroscopies like VCD and Raman Optical Activity (ROA) where we carry out both experimental studies using own infrastructure and quantum chemical calculations and implement new algorithms with emphasis on using both techniques to establish absolute configurations of molecules and higher-order structures of biomolecules.

3.2 Center for Molecular Modeling (CMM)

Since the end of the eighties, there was a worldwide tendency to break off research activities in low-energy and even intermediate-energy nuclear physics, and policy makers started with emphasizing the necessity of the presence of applied, economical, and utility finalities in the funded research activities. In 1997, Michel Waroquier decided to switch his research field from nuclear many-body problems to ab initio methods for tackling molecular systems. He started the new research area with a PhD student, Veronique Van Speybroeck. The first paper in the new field appeared 3 years later in 2000. It was a subject in the Chemical Technology with focus on model development and application to an industrially important chemical reaction. The strategy was the development of new models, new methodologies going beyond state of the art, implementation in computational codes, and application to important processes to validate the model. It was a success, the first and also the only paper in 2000 is currently still the most cited paper of the CMM in the new field. Gradually, the team grew with special attention in maintaining a good balance between physicists, chemists, and engineers with the principal aim to stimulate a strong synergy between the various research cells, encouraging interdisciplinary research that goes beyond the state of the art, and with a special focus to application driven areas.

The current research of the CMM is focused along six major areas. The core activities are situated in the research domains "Nanoporous materials-catalysis," "Organic Chemistry and Biochemistry," "Spectroscopy," "Computational Material Research," "Model development," and a more fundamental area "Many Particle Physics." The six areas define the core business of the main activities, and research in each of them is performed within the frame of a strong network with partners at the UGent, in Flanders and at an international level. There is a strong synergy between the various research cells, stimulating interdisciplinary research.

Nowadays, the research center has grown to a population of 35 researchers with more than 50 publications per year. The first PhD student in the new field of molecular modeling, V. Van Speybroeck, has become now full professor at the UGent and leads currently the computational division of the CMM. Dimitri Van Neck is head of the more fundamentally oriented area. The other research domains of the CMM are headed by a part-time professor. Currently, the CMM members are author of about 437 papers in ISI journals, among which Nature Materials, Angewandte Chemie, Journal of the American Chemical Society, Physical Review Letters, Journal of Catalysis, etc., with more than 6,600 citations. The paper by A. Ghysels et al. [7] and A. Cedillo et al. [8] in the present issue gives illustrations of the research carried out in the CMM and the GQCG.

4 University of Hasselt

Research in quantum chemistry at the Limburgs University Center (Now: University of Hasselt) started in 1978 under the motivation of Jean-Pierre François (Professor of Chemistry in the period 1975–2008 (JPF)). JPF obtained his PhD in 1971 at the State University of Ghent (Now : Ghent University) in the field of nuclear chemistry under the supervision of the late Prof. J. Hoste. In 1973, J.-P. François left Ghent University and became Chief Assistant at the University of Hasselt (UHasselt). He was promoted Professor of Chemistry in 1975 and switched to quantum chemistry in 1978. The first study that has been undertaken was the computation of an extensive series of monosubstituted pyridines and phenolates in the gas phase using semi-empirical (MINDO/3, MNDO, and AM1) and ab initio methods using a program vectorized in the group for the Cyber 205 vector processor.

In 1987, Jan M.L. Martin (JM) joined the group of quantum chemistry in Hasselt as PhD student. He obtained his PhD degree in Sciences in February 1991 (supervisor: J.-P. François, cosupervisor: R. Gijbels). The main purpose of his research activities was to study extensively neutral and charged carbon and boron-nitride cluster species of relevance in materials science and astrophysics. Combined bond-polarization basis sets were developed for accurate calculations of dissociation energies. In 1991–1995, J. Martin became Postdoctoral Fellow ("Postdoctoraal Onderzoeker") at the Belgian National Science Foundation (NFWO/FNRS). In this period, anharmonic force fields and thermochemical quantities of a variety of molecular species (including clusters) were computed, starting from ab initio potential energy surfaces. The methods used were rovibrational perturbation theory and vibrational CI. In 1995, J. Martin became Senior Research Associate ("Onderzoeksleider") at the NFWO/FNRS. He left the research group in 1996, to become Assistant Professor at the Weizmann Institute of Science, Rehovot, Israel. He has been awarded the Dirac medal at the 7th congress of the *"World Association of Theoretically Oriented Chemists"* (WATOC05, President Henry F. Schaefer III—University of Georgia, USA) in Cape Town, South Africa (January 15–21, 2005). The paper by U. R. Fogueri et al. [9] of the present issue illustrates recent research activities by J. Martin and his coworkers in Rehovot and at the University of North Texas in Denton.

In the period 1988–2001, extensive work was done by J.-P. François and his coworkers on the structure and IR spectra of carbon clusters ranging from C_3 and C_3^+ to C_{24} and on a number of boron-nitrogen B_mN_n clusters. Further theoreticians involved in that work were P.R. Taylor (NASA Ames Research Center, Moffett Field, CA), the late Prof. J. Almlöf (University of Minnesota, Minneapolis, MN), Z. Slanina (Heyrovsky Institute of Physical Chemistry and Electrochemistry, Prague), Zhengli Cai (Nanjing University of Science and Technology, China), M.S. Deleuze (MD), and several PhD students. A main purpose of the work on the larger carbon clusters (C_{20}, …) was to find which species exhibits first a fullerene structure. Results obtained for the vibrational spectra of the lower C_n clusters were of great value for the IR spectroscopic work with Doppler limited resolution of J.R. Heath (University of California, Berkeley, CA), who performed later the historical experiments leading to the discovery of C_{60} with Sir H.W. Kroto, R.E. Smalley, and R.F. Curl as well as S.C. O'Brien. The complex IR spectra of C_n species trapped in noble gas matrices could be analyzed quantitatively with the aid of quantum chemical data obtained using a computer program developed in the group.

The successor of J. Martin, Michael S. Deleuze, obtained his PhD in 1993 at the Facultés Universitaires Notre-Dame de la Paix de Namur in the field of ionization spectroscopy using propagator theory (Supervisor J. Delhalle), prior to undertaking three postdocs on behalf of the FNRS and of the Training and Mobility Research program of the EU, in the groups of Barry T. Pickup (Sheffield University, UK, 1994), Lorenz S. Cederbaum (Heidelberg University, Germany, 1995), and F. Zerbetto (University of Bologna, Italy, 1996). In 1997, Dr. M.S. Deleuze went back to Belgium to join the group of theoretical chemistry at the UHasselt as Postdoctoral Fellow (FWO Vlaanderen). In 1999, he was promoted Senior Research Associate and in 2000 Research Professor. He introduced one-electron Green's function theory and the interpretation of advanced orbital imaging experiments employing Electron

Momentum Spectroscopy or Penning Ionization Electron Spectroscopy into the research activities of the UHasselt. Further research topics developed under his supervision on local ES40, ES45, and ES47 workstations comprise: material sciences and polymer physics (long-range and delocalization effects, hyperconjugation …); electronic excited states; shake-up and correlation bands in valence ionization spectra, linear response properties; molecular dynamics of supramolecular systems (e.g., catenanes) and clusters of buckminsterfullerenes; conformational analysis, with emphasis on the relationships prevailing between the molecular and electronic structures; electronic and structural properties of carbon and boron-nitrogen clusters, or boranes and carboranes; reaction mechanisms of the conversion of sulfoxide, sulfonyl and xanthate precursors of conjugated polymers; thermal effects on the structural, electronic and optical properties of conjugated chains; nucleation of organic half-conductors on inert surfaces; photochemistry under far-UV-radiation; ring currents and magnetic responses in polycyclic aromatic hydrocarbons; symmetry-breakings and correlation effects in *n*-acenes, graphene nanoislands and nanoribbons. In 2006, M. S. Deleuze was prize winner of the Royal Flemisch Academy of Belgium for Sciences and Arts. The paper by B. Hajgató et al. of the present issue [10] gives an illustration of recent research activities of the group of theoretical chemistry at the University of Hasselt on complications inherent to the interpretation of orbital imaging experiments.

5 University of Leuven

Quantum chemistry was introduced at the University of Leuven (KU Leuven) in 1967 by Luc Vanquickenborne, who had obtained a PhD in combustion chemistry in 1964 at that same University. His passion for quantum chemistry was kindled during his 2-year postdoctoral research stay in the US, where he worked in the Laboratory of Sean McGlynn on the theory of molecular spectroscopy. Upon his return to Belgium in 1967, he obtained a FWO postdoctoral fellowship, and he developed a research group focused on theoretical aspects of inorganic chemistry, in close collaboration with the experimental inorganic chemistry groups. Even up to now, the study of inorganic systems remains a major focus of the theoretical chemistry group in Leuven. In the years following his arrival at the KU Leuven, L. Vanquickenborne guided a multitude of PhD students, among which Arnout Ceulemans, Marc Hendrickx, and Kristine Pierloot.

Arnout Ceulemans obtained his PhD working on a ligand field and group theoretical analysis of photochemical reactions of transition metal compounds. Following his PhD, A. Ceulemans obtained a permanent position at the FWO, becoming the second permanent staff member focusing on quantum chemistry. In 1995, A. Ceulemans switched from the FWO to a permanent position as a full professor at KU Leuven. Although his initial research focused on inorganic compounds, his current interest has shifted to research on clusters, fullerenes, and bioorganic systems.

After having received his PhD in 1985 at KU Leuven, Marc F. A. Hendrickx was the second researcher to join the theoretical chemistry group of this university as a permanent member of the academic staff. Since then, the main focus of his research activities has been on the study of properties of a wide variety of transition metal compounds. His recent research activity is mainly directed toward applying quantum chemical methods on small transition metal-containing clusters. Their frequently complicated open-shell electronic structures are studied in relation to their magnetic and spectroscopic properties.

The theoretical chemistry group at Leuven was expanded further with Kristine Pierloot, who like A. Ceulemans obtained a permanent research (FWO) position prior to joining the KU Leuven academic staff in 2000. The current research area of her group primarily concerns the investigation of the electronic structure of transition metals in a variety of coordination environments, with a special focus on bioinorganic and biomimetic systems, as well as on electronic spectroscopy. For this purpose, she is strongly involved in the development and application of multiconfigurational wave function methods, in collaboration with the MOLCAS developer's team, which has its origin in Lund (Sweden), but has by now spread its wings all over the world.

The fourth member, Minh Tho Nguyen, followed a different path. After surviving the difficult years of the Vietnam war, he obtained, in 1971, a scholarship to study chemistry at UCL. In 1980, he completed his doctoral thesis in Louvain-la-Neuve under G. Leroy, focusing on mechanisms of organic reactions. Subsequently, he did several postdocs (Universität Zürich, ETH Zürich, KU Leuven, University College Dublin, Australian National University Canberra) before joining the University of Groningen, Nederland, in 1988 as an associate professor. In 1985, he was awarded a D. Sc. degree by the National University of Ireland. He then received a phone call from L. Vanquickenborne. Ardently attracted by the charm of the Brabant region he returned to Leuven in 1990, definitively and for good, becoming first a research director of the FWO and later a full professor at KU Leuven. Nguyen was/is visiting scientist and professor at different institutions in France, USA (in particular University of Alabama), Taiwan, Japan, and Vietnam. His study focuses on the discovery of novel chemical phenomena and concepts by use of quantum chemical computations.

The last member of the group, Liviu Chibotaru, has obtained his Ph.D degree in 1985 in Chişinău (Moldova, that time in the USSR) under the supervision of Isaac Bersuker. After the collapse of Soviet Union he, like many of his colleagues, drifted West to pursue scientific research. In 1995, he became a postdoctoral fellow in the quantum chemistry group at KU Leuven. He joined the permanent staff in 2004 soon after L. Vanquickenborne became professor emeritus in 2003. His research combines expertise from chemical and condensed matter physics and is currently focused on the investigation of novel nanomagnets, mesoscopic superconductors, and carbon materials.

Together, the theoretical chemistry group that was initiated by L. Vanquickenborne has by now published over 1200 articles in international journals or as book chapters. A total number of 66 students have finished their doctoral studies in this group, and 10 are currently working on a PhD. The group has also attracted many pre- and postdoctoral fellows, and research is most often performed in concert with other, often experimental partners. Together, the staff members take care of a vast number of introductory and advanced theoretical courses in the bachelor and master programs offered by KU Leuven (quantum- and computational chemistry, group theory, molecular spectroscopy, reaction kinetics, solid-state methods). These courses also form the core of the KU Leuven contribution to the European master in theoretical chemistry and computational modeling, an Erasmus Mundus master course offered jointly by six European universities, introduced at KU Leuven in 2010 with A. Ceulemans as the local coordinator.

The theoretical chemistry research activities from the KULeuven are illustrated in the contributions by Ceulemans et al. [11], Phung et al. [12], and Tai et al. [13].

6 University of Liège

The story of quantum chemistry at the university of Liège started in November 1956 when, 2 days after receiving his B. Sc. degree, a young researcher knocked at the door of the Centre de Chimie Théorique in Paris, headed by Raymond Daudel. Jean-Claude Lorquet had received permission from his suspicious adviser to start a thesis in quantum chemistry, and he later on was allowed to develop a research group under the strict condition that “useful results” should be derived. In practice, this meant maintaining close cooperation with an experimental team working by mass spectrometric techniques on the chemistry in ion beams. The way to proceed was not at all obvious. For example, methods to perform calculations on open-shell molecules were largely a matter of debate in the fifties, and each group had to develop techniques of its own. But, even worse, it soon appeared that it also required tackling problems that are not commonly part of the chemist’s stock in trade. As a result, in its efforts to study reaction dynamics in electronically excited states, the group specialized in such problems as nonstationary states, time-dependent wave functions, breakdown of the Born–Oppenheimer approximation, potential energy surface crossings, nonadiabatic transitions, and spin–orbit couplings. Among the persons who were most instrumental in developing proper methods is Michèle Desouter who, in her Ph.D. thesis, established symmetry relations between the diabatic and adiabatic representations and showed their complete equivalence. Much later on, she moved to the university of Paris-Sud. But before leaving Liège, she had supervised the thesis of Françoise Remacle (FR), who has since renewed the impetus and who is currently heading the group.

The group of theoretical physical chemistry (TPC) is led by F. Remacle since 2001, after the retirement of J. C. Lorquet. After her PhD in Liège on the role of resonances in unimolecular reactions, F. Remacle made a postdoc with R. D. Levine at the Hebrew University of Jerusalem and maintains a close collaboration with the Jerusalem group since then. The TPC group focuses on controlling the dynamics of the responses of molecular systems to perturbations, mainly pulses of photon and voltage. Early work includes the study of reactivity in a dense set of excited states in polyatomic molecules, the dynamics of high molecular Rydberg states, and transport properties of nanostructures. More recently, the TPC group showed how to use the specificity of molecular responses to selective excitations viewed as inputs to build complex logic circuits at the molecular scale. Molecular states being discrete, they can be used for implementing memory units, which opens the way to realizing finite state machines: at each cycle, the next state and outputs are functions of both the inputs and the present state. This work was supported by several EC FET grants that involved theorists and experimental groups and provided physical realizations of the designed logic schemes by electrical, optical, and chemical addressing. A new EC collaborative project on unconventional multivalued parallel computing called MULTI, coordinated by F. Remacle, is just starting. The project aims at fully harvesting molecular complexity by going beyond two-valued Boolean logic and implementing logic operations in parallel exploring alternative avenues to quantum computing.

The highest speed for logic operations will ultimately be reached by providing inputs with ultrashort atto (1 as $= 10^{-18}$ s) photon pulses. These will allow addressing electrons directly and reach petaHz cycling frequencies.

The TPC group has a strong research activity in attochemistry and investigates the responses of molecular systems to strong ultrashort, subfemtosecond, photon pulses. The aim is to control chemical reactivity on an ultrashort timescale by directly manipulating electrons before subsequent nuclear dynamics has set in. This is also a challenge since it requires describing the coupled electron-nuclear dynamics beyond the realm of validity of the Born–Oppenheimer approximation. Investigating dynamics implies having good knowledge of electronic structure and the TPC group maintained a strong activity in this field. Special emphasis is given on the properties of gold and metallic nanoclusters and their tuning by the chemical nature of the ligand shell.

Another impulse to the development of quantum chemistry in Liège came from Georges Dive, Pharmacist, who started to work in the medicinal chemistry department of Charles Lapière in 1973. The subject of his PhD thesis was the study of anti-inflammatory drugs by quantum chemistry and multivariate statistical analysis. To analyze the conformations of more than 40 atoms molecules, he worked in Georges Leroy's laboratory at Louvain-La-Neuve (LLN) with the CNDO/2 method. It was the starting point of an efficient collaboration between several researchers, particularly with Daniel Peeters. In the eighties, G. Dive joined the microbiological laboratory of Jean-Marie Ghuysen which was devoted to the study of the activity of penicillin-like molecules on isolated enzymes involved in the synthesis of the external membrane of bacteria. Dominique Dehareng, who performed her chemistry thesis in the field of quantum dynamics with J.C. Lorquet at Liège and Xavier Chapuisat at Orsay, joined the group of J.M. Ghuysen in 1987. At that stage, the main research objective was the study of enzymatic reactions pathways, with a particular attention devoted to the electrostatic potential and its usefullness in providing a fast computable value of the electrostatic energy term in small- and medium-sized molecular complexes. Another research interest of the group is the description of the potential energy surfaces, and the location of its critical points and several PhD theses focused on that point. A special interest has been dedicated to valley-ridge inflexion points. A significant work was also devoted to the study of Hartree–Fock instabilities.

In 1990, with the first financial support of IAP (Inter-university Attraction Poles) program, the microbiological laboratory became the «Centre d'ingénierie des protéines» (CIP). It was organized as a consortium between several internal and external laboratories. A significant contribution has been the collaboration between the theoretical group and the organic laboratory of Léon Ghosez and Jacqueline Marchand (LLN) in the design of novel antibiotic molecules. Apart from pure quantum chemistry, the group extended its research domain to classical molecular modeling based on molecular mechanics force fields and molecular dynamics as well as mixed approaches using both molecular mechanics and quantum chemistry to describe reactions occurring in a large protein-solvent environment. For the study of large molecular systems, the computer power has been very often the rate limiting step. During more than 10 years, powerful computational facilities have been installed at the CIP mainly to run Gaussian program in vectorial/parallel mode. It has been an opportunity to welcome in Liège the Gaussian workshop in December 1996.

The articles by Dive et al. [14] and by Ganesan and Remacle [15] of the present issue describe the theoretical and modeling activities of the theoretical chemistry groups in the University of Liège.

7 University of Louvain-la-Neuve

Georges Leroy (†) can be seen as one of the founders of quantum chemistry research in Belgium. After a PhD in physical chemistry (1959) focusing on crystallization, organic synthesis and UV Spectrometry G. Leroy joined the laboratory of R. Daudel at the CMOA in Paris for a postdoctoral research stay. It was during this period that he developed his passion for quantum chemistry. Upon his return in 1965, he created a physical chemistry research group interested mainly in theoretical chemistry even though experimental chemistry was still going on. The main focus of his research lays on the study of π-electrons systems such as aromatic species, graphite, …, trying to improve semi-empirical methods such as modified Hückel theory, Pariser Parr Pople approaches, and so on. His research was internationally recognized as illustrated by a contribution to the very first issue of the International Journal of Quantum Chemistry. Among his PhD students was J.M. André, who later on founded a laboratory of quantum chemistry at the University of Namur. Physically located in Leuven, the laboratory of G. Leroy moved to Louvain-la-Neuve in 1973.

In 1974, Daniel Peeters obtained his PhD under the guidance of G. Leroy. The purpose of his thesis was to describe the chemical bond using a depiction of the wave function in terms of localized orbitals. At that time, the Centre Européen de Calcul Atomique et Moléculaire directed by C. Moser was the place to be as it provided the computational facilities unavailable elsewhere. D. Peeters, along with M. Sana (†), spent some time at Orsay (France) working on the description of potential hypersurfaces to understand chemical reactivity. In 1981, M. Sana was promoted to a permanent position as research leader of the FNRS, while D. Peeters obtained a permanent position at the UCL, and both joined the quantum chemistry group as full members. At this stage of their career, their research was mainly focused on the investigation of the electronic structure of chemical species, with particular emphasis on their thermodynamic stability, or the description of chemical bonds with regard to reactivity issues. M. Sana, D. Peeters, and G. Leroy continued the development of the quantum chemistry group at the UCL by intensifying their collaborations with the organic chemistry groups and in the later stages with the inorganic chemistry groups. R. Robiette, part of the organic medicinal chemistry group, performed part of his PhD under the coguidance of D. Peeters. Currently, holder of a permanent FNRS research position, R. Robiette, still continues to investigate organic reactions using quantum chemistry. After G. Leroy retired in 2000, T. Leyssens performed his PhD under the guidance of D. Peeters. He then moved to UCB Pharma, and after a short postdoctoral research stay in the group of W. Thiel (Max-Planck-Institut für Kohlenforschung, Mülheim, Germany), finally returned to the UCL in 2009. He focuses on the mechanistic understanding of chemical reactions, using experimental as well as theoretical techniques, in collaboration with D. Peeters.

In parallel, in 1992, X. Gonze joined the UCL as a permanent FNRS researcher, in the engineering faculty. He switched from the FNRS to an UCL academic position in 2004. His research focuses on first principles studies of high-technology material properties at the nanoscale (electronic, optical, dynamical properties). Some fundamental aspects of Density Functional Theory have also been central to his activities over the years. At the end of the nineties, he started to develop ABINIT, to which several dozen scientists have since contributed, and which is now used worldwide for calculations on periodic solids.

The contributions by Zanti et al. [16], Vergote et al. [17], and Dive et al. [14] focus on chemical reactivity of inorganic, organometallic, and organic systems, whereas the contribution of Avendaño-Franco et al. [18] illustrates the research currently going on in the group of X. Gonze.

8 University of Mons

The laboratory for Chemistry of Novel Materials at the University of Mons was founded in 1988 by Jean-Luc Brédas. In the early days, the research activities mostly focused on the understanding of the structural and electronic properties of conducting polymers with the help of (correlated) ab initio and semi-empirical Hartree–Fock calculations and models such as the Valence Effective Hamiltonian. Another center of interest that rapidly grew up was the theoretical modeling of the nonlinear optical properties (i.e., hyperpolarizabilities) of π-conjugated molecules. Experimental activities based on scanning probe microscopies to unravel the solid-state properties of organic materials were grafted on the core research of the laboratory with the arrival of Roberto Lazzaroni in 1990. Over the years, the field of organic electronics blossomed with the exploitation of undoped conjugated molecules and polymers in devices such as light-emitting diodes, solar cells, field-effect transistors, and sensors. Many theoretical studies were then performed to design the best materials for those applications and to understand all key electronic processes (such as energy and charge transport, charge injection, charge recombination, or exciton dissociation). These developments led to the progressive use of Density Functional Theory methods and force-field-based calculations in the research in Mons. J.L. Brédas crossed the Atlantic in 2000 to join first the University of Arizona, then his current position at the Georgia Institute of Technology in Atlanta.

Over the past few years, the theoretical activities have further diversified, with projects revolving around metal/organic interfaces, oxide/organic interfaces, hybrid biomaterials, polymer/nanotube composites, ionic liquids, graphene, and molecular electronics. These research activities are mostly carried out in the framework of national and European projects, allowing the laboratory to establish a wide network of collaborations in Belgium and at the European level. Among the European networks, of particular importance are the STEPLED project, for which the group was awarded the Descartes Prize of the European Commission in 2003, and the FP7 MINOTOR project, which centered on the modeling of interfaces for organic electronics and was coordinated by the University of Mons. A new extension of the research activities took place in 2008 with the opening of electronic device fabrication facilities at the Materia Nova R&D center in Mons; this gives the ability to study materials from the design and modeling to their incorporation in devices, often in joint projects with industrial partners.

Nowadays, the laboratory headed by R. Lazzaroni comprises around 30 researchers, including four permanent FNRS research fellows (David Beljonne, Jérôme Cornil, Philippe Leclère and Mathieu Surin). This laboratory is a founding member of the Interuniversity Scientific Computing Facility located in Namur, the Materia Nova Research Center in Mons, and the Institute for Materials Research recently established at the University of Mons. The article by Van Regemorter et al. in the present issue [19] illustrates the theoretical chemistry activities of the Laboratory for Chemistry of Novel Materials at the University of Mons.

9 University of Namur

In the *Florilège des Sciences en Belgique*, Louis d'Or writes that in 1971, a spreading occurs in the Quantum

Chemistry Laboratory of the Catholic University of Louvain-la-Neuve. Professor J.-M. André, surrounded by several researchers, starts a new laboratory at the Facultés Universitaires Notre-Dame de la Paix de Namur. In agreement with G. Leroy, it is in Namur that from then the research on the quantum chemistry of polymers will take place [20]. The *Laboratoire de Chimie Théorique Appliquée* (CTA) was developed with the help of Marie-Claude Roeland-André, Joseph Fripiat, and Joseph Delhalle. The first doctorate was delivered in 1975 to Simone Vercruyssen-Delhalle. International cooperations were extended making profit of the contacts with Per-Olov Löwdin's group and Enrico Clementi's network (J.-M. André having been postdoc at IBM Research San Jose in 1968 and 1969). To improve visibility in the field of quantum chemistry of polymers, a series of NATO summer schools was organized with Janos Ladik: in 1974 (*Electronic Structure of Polymers and Molecular Crystals*), in 1977 (*Quantum Theory of Polymers*) in Namur, and in 1983 (*Quantum chemistry of polymers, solid-state aspects*) in Braunlage (Germany). In the late 1980s, these summer schools were then followed by the annual SCF (Scientific Computing Facility) meetings.

The research on quantum chemistry of polymers has dealt with conceptual aspects, that is, development of specific codes—Polymol, PLH, DJMol, solving difficult technical questions: long-range Coulomb and exchange contributions, band indexing, as well as specific applications to the interpretation of XPS spectra, the (semi)conductivity in conjugated polymers, studies in linear and nonlinear optical properties of polymers …. In this very quickly evolving period of quantum chemistry, the laboratory has been pioneering new ways of computing starting with the PDP 11/45, followed by the Digital DEC20 to the SCF initiative developed in cooperation between the FNRS, IBM, and FPS.

Several members of the laboratory have now academic or permanent research (FNRS) positions in Belgium or outside: Daniel Vercauteren at the University of Namur, J.-L. Brédas at the Georgia Technical Institute of Technology, M.S. Deleuze at the Hasselt University, Benoît Champagne and Eric Perpète at the University of Namur, and Denis Jacquemin at the University of Nantes. Two personalities issued from the CTA Lab have been awarded the Francqui Prize, the highest Belgian scientific award: Jean-Marie André in 1991 and Jean-Luc Brédas in 1997.

In 1991, the Administration Board of the University of Namur asked for the opening of a second laboratory specialized in theoretical chemistry with the principal aim to foster on the increasingly important aspects of molecular modeling that complemented the already well-established quantum mechanical approaches. A new laboratory, called "Laboratoire de Physico-Chimie Informatique" (PCI for *Computational Physico-Chemistry*), was thus started by D. Vercauteren, former Ph.D. student with J.-M. André and PostDoctoral Fellow with E. Clementi at IBM Poughkeepsie in 1982–1983, with the help of Laurence Leherte, also former Ph.D. student with J.-M. André and PostDoctoral Fellow with Suzanne Fortier and Janice Glasgow in the School of Computing at Queen's University in 1992–1993.

Since then, the PCI Laboratory has developed its research activities in the domain of molecular engineering on computers. Over the years, the research work concerned the study of molecular conformations, similarities, interactions, and recognition in mixed environments (supramolecular systems, adsorbed phases, microporous materials, membranes, …) by molecular modeling (graphics, molecular mechanics, hybrid QM/MM methods, coarse-graining, and multiscaling approaches) and statistical mechanics (Monte Carlo, molecular dynamics, …) methods, as well as by knowledge-based approaches (databases, logic and functional programming, fuzzy logic, expert systems, neural networks, genetic algorithms, hidden-Markov models, …). Shortly, those analyses have been applied to the characterization and manipulation of "molecular images", like the electron density or the electrostatic potential at different levels of resolution, to zeolites, aluminophosphate frameworks, heterogeneous and homogeneous polymerization catalysts, cyclodextrins and their tubular complexes, proteins, drug-DNA, protein-DNA, protein-lipid domains. Researchers in the laboratory also tackled original aspects in computer-assisted organic chemistry and very recently in the development of reactive force-field approaches in the study of organocatalysis. Several members of the PCI Laboratory now occupy leading positions in academic or research institutions outside Belgium. Let us cite, Andy Becue at the University of Lausanne, Nathalie Meurice and Joachim Petit at Mayo Clinic in Scottsdale, and Thibaud Latour at the Tudor Research Institute in Luxembourg.

After 20 years as FNRS researcher, Benoît Champagne took over the position of J.-M. André when he retired in 2009. After defending his PhD Thesis in 1992 on the elaboration of *polymer band structure methods for evaluating the polarizabilities of polymers*, for which he received in 1994 the IBM Belgium Award of Computer Science, B. Champagne accomplished a postdoctoral stay at the Quantum Theory Project (Gainesville, Florida) with Yngve Öhrn and visited frequently Bernard Kirtman at the University of California in Santa Barbara. In 1995, he obtained a permanent position as Research Associate of the FNRS. In 2001, he presented his Habilitation thesis on the *development of methods for evaluating and interpreting vibrational hyperpolarizabilities*. In 2009, he founded the Laboratoire de Chimie Théorique (LCT). The LCT develops an expertise in theoretical and quantum chemistry. Its research focuses on the elaboration and application of methods for predicting and interpreting properties responsible for optical and electrical effects in molecules, supramolecules, polymers, and molecular crystals. The main research axes are the development and application of quantum chemistry methods (i) to predict and interpret the linear and nonlinear optical properties of molecules, polymers, and supramolecular systems, (ii) to study the properties of open-shell systems (radicals, diradicals, multiradicals) and in particular the optical properties, (iii) to simulate and interpret vibrational spectra (VROA, SFG, hyper-Raman, resonant Raman, Raman, VCD, IETS), (iv) to calculate the linear and nonlinear optical properties of molecular crystals using methods combining ab initio calculations and electrostatic interactions, (v) to unravel the structural, reactive, optical, electronic, and magnetic properties of polymer chains, and (vi) to predict and understand the molecular properties associated with chirality.

Several of these investigations are carried out within an interdisciplinary environment where the theoretical work is intertwined with synthesis and experimental characterizations. Over the years, the group has fostered intensive collaborations with B. Kirtman (University of California in Santa Barbara), D.M. Bishop (†) (University in Ottawa), F. Castet (Institut des Sciences Moléculaires de l'Université de Bordeaux), and M. Nakano (Department of Materials Engineering Science of Osaka University). Moreover, the LCT carries on the tradition of participating to the development of high performance computing facilities, via the initiative of the CÉCI of the Fédération Wallonie Bruxelles, a distributed computer architecture for about 400 users, financed by the F.R.S.-FNRS and the Universities.

The theoretical chemistry research activities from the UNamur are illustrated in the contributions by Fripiat and Harris [21], Hubin et al. [22], Leherte and Vercauteren [23], as well as Liégeois and Champagne [24].

Acknowledgments Discussions with many colleagues are acknowledged, in particular with J.-M. André, D. Beljonne, A. Bogaerts, P. Bultinck, J. Cornil, G. Dive, J.-P. François, P. Geerlings, R. Gijbels, M. Godefroid, J. Liévin, J.-C. Lorquet, D. Peeters, K. Pierloot, F. Remacle, C. Van Alsenoy, L. Vanquickenborne, D.P. Vercauteren, G. Verhaegen, M. Waroquier. The authors would also like to thank S. Vanwambeke for the graphical map of Belgium.

References

1. Florilège des Sciences en Belgique, II, p 133 (1980). Available for free downloading at http://www2.academieroyale.be/academie/documents/FLORILEGE_VOL0214276.pdf
2. Geldof D, Krishtal A, Blockhuys F, Van Alsenoy C (2012) Quantum chemical study of self-doping PPV oligomers: spin distribution of the radical form. Theor Chem Acc 131:1243
3. Neyts EC, Bogaerts A (2013) Combining molecular dynamics with Monte Carlo simulations: implementations and applications. Theor Chem Acc 132:1320
4. Cauët E, Carette T, Lauzin C, Li JG, Loreau J, Delsaut M, Nazé C, Verdebout S, Vranckx S, Godefroid M, Liévin J, Vaeck N (2012) From atoms to biomolecules: a fruitful perspective. Theor Chem Acc 132:1254
5. Sutcliffe B (2012) Is there an exact potential energy surface? Theor Chem Acc 131:1215
6. De Vleeschouwer F, Geerlings P, De Proft P (2012) Radical electrophilicities in solvent. Theor Chem Acc 131:1245
7. Ghysels A, Vandichel M, Verstraeken T, van der Veen MA, De Vos DE, Waroquier M, Van Speybroeck V (2012) Host-guest and guest–guest interactions between xylene isomers confined in the MIL-47(V) pore system. Theor Chem Acc 131:1324
8. Cedillo A, Van Neck D, Bultinck P (2012) Self-consistent methods constrained to a fixed number of particles in a given fragment and its relation to the electronegativity equalization method. Theor Chem Acc 131:1227
9. Fogueri UR, Kozuch S, Karton A, Martin JML (2013) A simple DFT-based diagnostic for nondynamical correlation. Theor Chem Acc 132:1291
10. Hajgató B, Morini F, Deleuze MS (2012) Electron Momentum Spectroscopy of metal carbonyls: a reinvestigation of the role of nuclear dynamics. Theor Chem Acc 131:1244
11. Ceulemans A, Lijnen E, Fowler PW, Mallion RB, Pisanski T (2012) S5 graphs as model systems for icosahedral Jahn-Teller problems. Theor Chem Acc 131:1246
12. Phung QM, Vancoillie S, Delabie A, Pourtois G, Pierloot K (2012) Ruthenocene and cyclopentadienyl pyrrolyl ruthenium as precursors for ruthenium atomic layer deposition: a comparative study of dissociation enthalpies. Theor Chem Acc 131:1238
13. Truong BT, Nguyen MT, Nguyen MT (2012) The boron conundrum: the case of cationic clusters B + n with n = 2–20. Theor Chem Acc 131:1241
14. Dive G, Robiette R, Chenel A, Ndong M, Meier C, Desouter-Lecomte M (2012) Laser control in open quantum systems: preliminary analysis toward the Cope rearrangement control in methyl-cyclopentadienylcarboxylate dimer. Theor Chem Acc 131:1236
15. Ganesan R, Remacle F (2012) Stabilization of merocyanine by protonation, charge, and external electric fields and effects on the isomerization of spiropyran: a computational study. Theor Chem Acc 131:1255
16. Zanti G, Peeters D (2013) Electronic structure analysis of small gold clusters Aum ($m \leq 16$) by density functional theory. Theor Chem Acc 132:1300
17. Vergote T, Gathy T, Nahra F, Riant O, Peeters D, Leyssens T (2012) Mechanism of ketone hydrosilylation using NHC-Cu(I) catalysts: a computational study. Theor Chem Acc 131:1253
18. Avendaño-Franco G, Piraux B, Grüning M, Gonze X (2012) Time-dependent density functional theory study of charge transfer in collisions. Theor Chem Acc 131:1289
19. Van Regenmorter T, Guillaume M, Sini G, Sears JS, Geskin V, Brédas JL, Beljonne D, Cornil D (2012) Density functional theory for the description of charge-transfer processes at TTF/TCNQ interfaces. Theor Chem Acc 131:1273
20. Original French text: En 1971, un essaimage se produit dans le Laboratoire de Chimie quantique de l'Université catholique de Louvain-la-Neuve. Le professeur J.M. André, entouré de plusieurs chercheurs, fonde aux Facultés universitaires de Namur un nouveau laboratoire. En accord avec le professeur Leroy, c'est à Namur qu'auront lieu désormais les recherches sur la chimie quantique des polymères

21. Fripiat JG, Harris F (2012) Ewald-type formulas for Gaussian-basis studies of one-dimensionally periodic systems. Theor Chem Acc 131:1257
22. Hubin PO, Jacquemin D, Leherte L, André JM, van Duin ACT, Vercauteren DP (2012) Ab initio quantum chemical and ReaxFF-based study of the intramolecular iminium-enamine conversion in a proline-catalyzed reaction. Theor Chem Acc 131:1261
23. Leherte L, Vercauteren DP (2012) Smoothed Gaussian molecular fields: an evaluation of molecular alignment problems. Theor Chem Acc 131:1259
24. Liégeois V, Champagne B (2012) Implementation in the Pyvib2 program of the localized mode method and application to a helicene. Theor Chem Acc 131:1284

Theor Chem Acc (2012) 131:1215
DOI 10.1007/s00214-012-1215-x

REGULAR ARTICLE

Is there an exact potential energy surface?

Brian Sutcliffe

Received: 15 February 2012 / Accepted: 25 March 2012 / Published online: 15 April 2012

Abstract Transition state theory was introduced in the 1930s to account for chemical reactions. Central to this theory is the idea of a potential energy surface (PES). It was assumed that quantum mechanical computation, when it became possible, would yield such surfaces, but for the time being they would have to be constructed empirically. The approach was very successful. Nowadays, quantum mechanical ab initio electronic structure calculations are possible and from their results PESs can be constructed. Such surfaces are now widely used in the explanation of chemical reactions in place of the traditional empirical ones. It is argued here that theoretical basis of such PESs is not quite as clear as is usually assumed and that, from a quantum mechanical perspective, certain puzzles remain.

Keywords Potential energy surface · Schrödinger Coulomb Hamiltonian · Permutational symmetry

1 Introduction

From the standpoint of quantum mechanics, the potential energy surface (PES) arises from treating the nuclear variables of a collection of electrons and nuclei, formally described by the Schrödinger Coulomb Hamiltonian, as parameters rather than variables. The basis for this approach is nowadays taken to be the work of Born, which is most conveniently found in [1] but is often referred to as "making the Born–Oppenheimer approximation". In order to introduce notation, a brief resume of this well-known approach will be given here.

Born's approach begins from Schrödinger's Hamiltonian for a system of N variables, $\mathbf{x}_i^{\mathrm{e}}$, describing the electrons and another set of A variables, $\mathbf{x}_i^{\mathrm{n}}$, describing the nuclei and $N_T = N + A$.

When the nuclei are clamped at a particular fixed geometry specified by the constant vectors $\mathbf{a}_i, i = 1, 2, \ldots, A$, these constant vectors can be regarded as arising by assigning the values $\mathbf{a}_i$ to the nuclear variables $\mathbf{x}_i^{\mathrm{n}}$, in the full Schrödinger Hamiltonian.

$$\mathsf{H}^{\mathrm{cn}}(\mathbf{a}, \mathbf{x}^{\mathrm{e}}) = -\frac{\hbar^2}{2m}\sum_{i=1}^{N}\nabla^2(\mathbf{x}_i^{\mathrm{e}}) - \frac{e^2}{4\pi\epsilon_0}\sum_{i=1}^{A}\sum_{j=1}^{N}\frac{Z_i}{|\mathbf{x}_j^{\mathrm{e}} - \mathbf{a}_i|} + \frac{e^2}{8\pi\epsilon_0}{\sum_{i,j=1}^{L}}' \frac{1}{|\mathbf{x}_i^{\mathrm{e}} - \mathbf{x}_j^{\mathrm{e}}|} \tag{1}$$

The clamped nucleus problem has solutions of the form

$$\mathsf{H}^{\mathrm{cn}}(\mathbf{a}, \mathbf{x}^{\mathrm{e}})\psi_p^{\mathrm{cn}}(\mathbf{a}, \mathbf{x}^{\mathrm{e}}) = E_p^{\mathrm{cn}}(\mathbf{a})\psi_p^{\mathrm{cn}}(\mathbf{a}, \mathbf{x}^{\mathrm{e}}) \tag{2}$$

In the present context, it is customary to incorporate the nuclear repulsion energy into the clamped nuclei problem and to use the Hamiltonian

$$\mathsf{H}^{bo} = \mathsf{H}^{\mathrm{cn}}(\mathbf{a}, \mathbf{x}^{\mathrm{e}}) + \frac{e^2}{8\pi\epsilon_0}{\sum_{i,j=1}^{A}}' \frac{Z_i Z_j}{|\mathbf{a}_i - \mathbf{a}_j|} \equiv \mathsf{H} + \mathsf{V}^{\mathrm{n}}(\mathbf{a}) \tag{3}$$

The extra term here is merely an additive constant and so does not affect the form of the electronic wavefunction. It affects the spectrum of the clamped nucleus Hamiltonian only trivially by changing the origin of the clamped nucleus electronic energy so that,

---

Published as part of the special collection of articles celebrating theoretical and computational chemistry in Belgium.

B. Sutcliffe (✉)
Service de Chimie quantique et Photophysique,
Université Libre de Bruxelles, 1050 Brussels, Belgium
e-mail: bsutclif@ulb.ac.be

$$E_p^{\mathrm{cn}}(\mathbf{a}) \rightarrow E_p^{\mathrm{cn}}(\mathbf{a}) + \mathsf{V}^{\mathrm{n}}(\mathbf{a}) = \mathsf{V}_p^{\mathrm{cn}}(\mathbf{a}) \qquad (4)$$

If the clamped nuclei solutions were known for all values that could be taken by **a**, they would constitute the solution set $\psi_p^{\mathrm{cn}}(\mathbf{x}^{\mathrm{n}}, \mathbf{x}^{\mathrm{e}})$.

The full Hamiltonian may be written as

$$\mathsf{H}(\mathbf{x}^{\mathrm{n}}, \mathbf{x}^{\mathrm{e}}) = \mathsf{K}^{\mathrm{n}}(\mathbf{x}^{\mathrm{n}}) + \mathsf{H}^{\mathrm{bom}}(\mathbf{x}^{\mathrm{n}}, \mathbf{x}^{\mathrm{e}}) \qquad (5)$$

where K^{n} is the kinetic energy operator for the nuclei, which can be written symbolically as

$$\sum_{k=1}^{A} \frac{\mathsf{p}_k^{\mathrm{n}2}}{2m_k}$$

and, although Born does not explicitly require it, the Hamiltonian H^{bo} is implicitly generalised to allow for nuclear motion as

$$\mathsf{H}^{\mathrm{bom}}(\mathbf{x}^{n}, \mathbf{x}) = \mathsf{H}^{\mathrm{cn}}(\mathbf{x}^{\mathrm{n}}, \mathbf{x}^{\mathrm{e}}) + \frac{e^2}{8\pi\epsilon_0} \sum_{i,j=1}^{A}{}' \frac{Z_i Z_j}{|\mathbf{x}_i^{\mathrm{n}} - \mathbf{x}_j^{\mathrm{n}}|} \qquad (6)$$

The eigenfunctions of this Hamiltonian are assumed to be of the form $\psi_i^{\mathrm{n}}(\mathbf{x}^{\mathrm{n}}, \mathbf{x}^{\mathrm{e}})$ generalising those of (2) and to lead to a potential $\mathsf{V}_p^{\mathrm{bom}}(\mathbf{x}^{\mathrm{n}})$ generalising that of (4). It is this Hamiltonian which is often referred to as the *electronic Hamiltonian*.

Assuming that full problem had eigenstates such that

$$\mathsf{H}(\mathbf{x}^{\mathrm{n}}, \mathbf{x}^{\mathrm{e}})\psi(\mathbf{x}^{\mathrm{n}}, \mathbf{x}^{\mathrm{e}}) = E\psi(\mathbf{x}^{\mathrm{n}}, \mathbf{x}^{\mathrm{e}}), \qquad (7)$$

then the solutions could be expanded as a sum of products of the form

$$\psi(\mathbf{x}^{\mathrm{n}}, \mathbf{x}^{\mathrm{e}}) = \sum_p \Phi_p(\mathbf{x}^{\mathrm{n}})\psi_p^{\mathrm{bom}}(\mathbf{x}^{\mathrm{n}}, \mathbf{x}^{\mathrm{e}}) \qquad (8)$$

where $\Phi_p(\mathbf{x}^{\mathrm{n}})$ describes the nuclear motion and $\psi_i^{\mathrm{n}}(\mathbf{x}^{\mathrm{n}}, \mathbf{x}^{\mathrm{e}})$ is an eigenfunction of the electronic Hamiltonian (6). However, the status of the electronic function is not entirely clear as will be seen shortly.

2 The mathematics of the Born approach

In 1951, Kato [2] established that the full (Coulomb) Hamiltonian, H, is essentially self-adjoint.[1] This property, which is stronger than Hermiticity, guarantees that the time evolution

$$\Psi(t) = \exp(-i\mathsf{H}t/\hbar)\Psi(0)$$

of a Schrödinger wavefunction is unitary and so conserves probability [3]. This is not true for operators that are Hermitian but not self-adjoint. It is easy enough to construct examples of such operators; an example given by Thirring [4] is of the radial momentum operator $-i\hbar\partial/\partial r$ acting on functions $\phi(r)$, $\phi(0) = 0$ with $0 \le r < \infty$.

What Kato showed in Lemma 4 of his paper was that for a Coulomb potential V and for any function f in the domain $\mathcal{D}_0$ of the full kinetic energy operator T_0, the domain of full problem $\mathcal{D}_V$ contains $\mathcal{D}_0$ and there are two constants a, b such that

$$||\mathsf{V}f|| \le a||\mathsf{T}_0 f|| + b||f||$$

and that a can be taken as small as is liked. Thus, the potential energy is bounded relatively to the kinetic energy.

Given this result, he proved in Lemma 5 that the usual operator has a unique self-adjoint extension and thus is indeed, for all practical purposes, self-adjoint and is bounded from below. The sort of problems that can arise if an operator is not self-adjoint or does not have a unique self-adjoint extension are discussed in an accessible way in [5].

In the present context, the important point to note is that the Coulomb term is small only in comparison with the kinetic energy term involving the same set of variables. So the absence of one or more kinetic energy terms from the Hamiltonian means that the Coulomb potential term cannot be treated as small and the Hamiltonian will no longer be self-adjoint in the way demonstrated by Kato. This is not because it ceases to be intrinsically self-adjoint but because the Hamiltonian ceases to be self-adjoint on the domain of the complete kinetic energy operator. It is thus a problem of the extension. This is not to say that there is anything wrong with solutions to the clamped nuclei problem (3). Here the nuclei are fixed and the potential involves only the electronic variables, and the only requirement for self-adjointness is that there be an electronic kinetic energy term for each potential term. It does however mean the Hamiltonian (6) (the *soi-disant* electronic Hamiltonian) is *not* self-adjoint in the Kato sense. The problem is essentially one of domain and to deal with that, the differential equation approach to the electronic problem must be replaced with an approach that starts from the clamped nuclei Hamiltonian.

3 Defining an electronic Hamiltonian

The full Hamiltonian is invariant under all uniform translations of the variables, under all orthogonal transformations of the variables and under the permutation of all variables that correspond to particles of equal charge and mass. It is the first of these invariances that has the most immediate consequences. It implies that the full Hamiltonian has a completely continuous spectrum arising from the free motion of the whole system (atom, molecule, ion or whatever) through space. Any bound-states corresponding

---

[1] The work was completed in 1944 and was actually received by the journal in October 1948.

to discrete values in the spectrum will be clouded by this continuum, which must be removed before attention can be focused on square integrable eigenfunctions. This can be done easily by separating the centre-of-mass motion by choosing the centre-of-mass coordinate and $N_T - 1$ translationally invariant coordinates and transforming the Hamiltonian to have a part corresponding to the free motion of the centre-of-mass and a part H' composed from the translationally invariant coordinates. Although it was not mentioned earlier, this is actually what Kato did and it was the translationally invariant Hamiltonian that he showed to be essentially self-adjoint. He also pointed out that his proof permitted a trivial extension to cover the full Hamiltonian, so what has been said about self-adjointness previously needs no modification. The use of a translationally invariant form poses a problem, however, because one variable has been lost when translational motion has been removed and the translationally invariant coordinates can consist of linear combinations of all the laboratory coordinates. The spectrum of H' is independent of linear combination choice but rather special choices must be made in order to obtain a set of coordinates in which the electronic and nuclear parts can be recognised and the permutational invariances retained. The general problem is discussed in [6]. However, for present purposes in order to identify the electrons let the translationally invariant electronic coordinates be chosen with respect to the centre-of-nuclear mass.

$$\mathbf{t}_i^{\mathrm{e}} = \mathbf{x}_i^{\mathrm{e}} - \mathbf{X}, \quad \mathbf{X} = M^{-1}\sum_{i=1}^{A} m_i \mathbf{x}_i^{\mathrm{n}}, \quad M = \sum_{i=1}^{A} m_i$$

in the case of the atom $A = 1$ and the origin is the nucleus. There is no need to specify the proposed $A - 1$ translationally invariant nuclear variables $\mathbf{t}^{\mathrm{n}}$ other than to say that are expressed entirely in terms of the laboratory nuclear coordinates by means of a A by $A - 1$ matrix $\mathbf{V}^{\mathrm{n}}$ in which the elements of each column sum to zero.

The electronic Hamiltonian now becomes

$$\begin{aligned}\mathsf{H}'^{\mathrm{e}}(\mathbf{x}^{\mathrm{n}}, \mathbf{t}^{\mathrm{e}}) = &-\frac{\hbar^2}{2m}\sum_{i=1}^{N}\nabla^2(\mathbf{t}_i^{\mathrm{e}}) - \frac{\hbar^2}{2M}\sum_{i,j=1}^{N}\vec{\nabla}(\mathbf{t}_i^{\mathrm{e}})\cdot\vec{\nabla}(\mathbf{t}_j^{\mathrm{e}}) \\ &-\frac{e^2}{4\pi\epsilon_0}\sum_{i=1}^{A}\sum_{j=1}^{N}\frac{Z_i}{|\mathbf{t}_j^{\mathrm{e}} - \mathbf{x}_i^{\mathrm{n}}|} \\ &+\frac{e^2}{8\pi\epsilon_0}\left(\sum_{i,j=1}^{N}{}'\frac{1}{|\mathbf{t}_i^{\mathrm{e}} - \mathbf{t}_j^{\mathrm{e}}|} + \sum_{i,j=1}^{A}{}'\frac{Z_i Z_j}{|\mathbf{x}_i^{\mathrm{n}} - \mathbf{x}_j^{\mathrm{n}}|}\right)\end{aligned} \tag{9}$$

where it is understood that the $\mathbf{x}_i^{\mathrm{n}}$ are to be realised by a suitable linear combination of the $\mathbf{t}_i^{\mathrm{n}}$. The electronic Hamiltonian is properly translationally invariant and would yield the usual form were the nuclear masses to increase without limit. Were the nuclear positions to be chosen directly as a translationally invariant set, it would be those values that would appear in the place of the nuclear variables.

The nuclear part involves only kinetic energy operators and has the form:

$$\mathsf{K}^{\mathrm{n}}(\mathbf{t}^{\mathrm{n}}) = -\frac{\hbar^2}{2}\sum_{i,j=1}^{A-1}\frac{1}{\mu_{ij}}\vec{\nabla}(\mathbf{t}_i^{\mathrm{n}}).\vec{\nabla}(\mathbf{t}_j^{\mathrm{n}}) \tag{10}$$

with the inverse mass matrix $\boldsymbol{\mu}$ defined in terms of the inverse nuclear masses and the elements of $\mathbf{V}^{\mathrm{n}}$.

The self-adjointness of (9) requires consideration according to the number of nuclei. For an atom, there is no nuclear kinetic energy part and, denoting the nuclear mass by m_{n}, the full Hamiltonian is simply the electronic Hamiltonian.

$$\begin{aligned}\mathsf{H}'^{\mathrm{e}}(\mathbf{t}^{\mathrm{e}}) = &-\frac{\hbar^2}{2m}\sum_{i=1}^{N}\nabla^2(\mathbf{t}_i^{\mathrm{e}}) - \frac{\hbar^2}{2m_{\mathrm{n}}}\sum_{i,j=1}^{N}\vec{\nabla}(\mathbf{t}_i^{\mathrm{e}})\cdot\vec{\nabla}(\mathbf{t}_j^{\mathrm{e}}) \\ &-\frac{e^2}{4\pi\epsilon_0}\sum_{j=1}^{N}\frac{Z_i}{|\mathbf{t}_j^{\mathrm{e}}|} + \frac{e^2}{8\pi\epsilon_0}\sum_{i,j=1}^{N}{}'\frac{1}{|\mathbf{t}_i^{\mathrm{e}} - \mathbf{t}_j^{\mathrm{e}}|}\end{aligned} \tag{11}$$

The electronic problem for the atom (11) has exactly the same form as the full problem and as required by the Kato self-adjointness conditions, for there is a kinetic energy operator in all of the variables that are used to specify the potential terms. This would continue to be the case were the nuclear mass to increase without limit. The atom is sometimes used as an illustration when considering the original form of the Born–Oppenheimer approximation but the only aspect of the approximation that can be thus illustrated is the translational motion part and that is easily considered in first order by treating the second term in (11) as a perturbation to the solution obtained using an infinite nuclear mass. The inclusion of this term in this way is analogous to making the *diagonal Born–Oppenheimer* correction and it can be made exactly in the case of any one-electron atom. The Born–Oppenheimer approach therefore plays no important part in the consideration of the eigenfunctions of an atomic problem. For systems containing more than a single nucleus, (9) can never be properly self-adjoint even if the nuclear masses increase without limit and so it cannot be used directly in attempting solutions to the full problem.

To turn now to how an electronic Hamiltonian might be defined properly for a system with more than a single nucleus, let it be assumed that a chosen set of $\mathbf{A}$ nuclear positions generate a set $\mathbf{b}$ of $A - 1$ translationally invariant nuclear coordinates. It can be seen that the electronic Hamiltonian (9) commutes with each of the $A - 1$ nuclear position variables. Think now of the molecular bound state space $\mathfrak{H}$ as the square integrable sections in the trivial fibre bundle $\mathbf{R}^{3(A-1)} \otimes \mathcal{L}^2(\mathbf{R}^{3N})$. A fibre bundle is trivial if the two spaces have an associated Cartesian product space. If the base space is a manifold that is only locally a coordinate space, the bundle would be only locally trivial. Here, however, the bundle is globally trivial since the base space is a global coordinate space [7].

The nuclear operator (which is the bare kinetic energy operator) acts in the base space, that is upon functions defined on $\mathbf{R}^{3(A-1)}$ and the electronic Hamiltonian acts only upon the fibre defined by the choice of **b**. (In this case the fibre is a vector space $\mathcal{L}^2(\mathbf{R}^{3N};\mathbf{b})$ and so the fibre bundle in this context is often called a vector bundle. The spaces for different **b** values, are distinct.)

Now write the full electronic Hamiltonian as a direct integral over the fibres.

$$\mathsf{H}'^{\mathrm{e}}(\mathbf{t}^{\mathrm{e}}) = \int^{\oplus} \mathsf{H}'^{\mathrm{e}}(\mathbf{b},\mathbf{t}^{\mathrm{e}})\mathrm{d}\mathbf{b} \tag{12}$$

where the $\mathbf{t}^n$ have been replaced by **b** within the integral, to emphasise that it is over fixed points that the “sum” is occurring.

Modern mathematically secure accounts of the Born–Oppenheimer approximation are given in terms of the electronic Hamiltonian defined as a direct sum and as such do not explicitly consider the requirement that the solutions provide basis functions for the orthogonal group in three dimensions nor is spin symmetry considered. They do not either consider the permutational invariance of the full problem. The arguments can however easily be extended to cover spin and permutational symmetry in the electronic part of the problem. They cannot however be easily extended to cover the full angular momentum symmetry and the nuclear permutation symmetry, except for diatomic molecules. The arguments are based on the idea of a potential provided by the electrons, just as are the traditional arguments, but not directly upon the idea of PES everywhere defined. The arguments require only that it is possible to define a potential sufficiently close to a particular nuclear configuration. Making such assumptions, it is possible to estimate how closely a solution constructed from these forms approximates an exact solution in the region of interest. Serious difficulties arise in such approaches when a unique potential cannot be defined, the situation usually called *surface crossing*. But even where there is a unique potential, it is not possible to use perturbation theory, as is traditionally done, to make the estimation. The best that can be done is by means of an asymptotic expansion of the WKB type.

The original Born–Oppenheimer argument has been reconsidered in a mathematically rigorous way by Klein et al. [8] assuming the potential consists of a single isolated potential well such that the electronic wavefunction effectively vanishes outside it. This assumption corresponds exactly to the original assumption of Born and Oppenheimer. It is not at present clear how these arguments could be extended to deal with multiple minima resulting from permutational invariance. Since no explicit consideration of rotational motion has been attempted, nothing can be said about the rotational motion of the system, though the effects of inversion symmetry are considered. This work is perhaps most usefully seen as a justification of the original Born–Oppenheimer conclusions for a system in which the nuclei are treated as identifiable particles in which electronic motion is unaffected by the rotational motion of the whole system.

It is perfectly proper to perform clamped nuclei electronic structure calculations to obtain electronic energies and wavefunctions, and if it were possible to construct from these a set of electronic wave functions $\psi_n^{\mathrm{e}}(\mathbf{t}^{\mathrm{n}}, \mathbf{t}^{\mathrm{e}})$ covering the whole translationally invariant space, then it would be perfectly proper to attempt a variational solution of the full problem (8) using nuclear-motion wave functions obtained using potentials constructed from the electronic energies. But it would simply be a variational solution valid in the energy region relevant to the potential. Such a solution would not have any particular symmetry under the permutation of identical nuclei nor would it show any particular rotational symmetry were the potential to be treated as rotationally invariant thus making it simply a function of nuclear geometry. Its status as an approximation to an exact solution would thus be somewhat uncertain.

For the present, let this uncertainty be ignored, to consider what might be inferred about a PES were an exact solution to the translationally invariant form of the Schrödinger Coulomb Hamiltonian actually known.

4 The PES from an exact solution?

The presentation of a presumed exact bound state solution of the Schrödinger Coulomb Hamiltonian as a product of an electronic and a nuclear-motion part has been considered both by Hunter [9] and, more recently, by Gross [10]. For the present purposes, the Hunter approach will be employed on the translationally invariant form of the Hamiltonian, given earlier. Were the exact solution known, Hunter argues that it could be written in the form

$$\psi(\mathbf{t}^{\mathrm{n}},\mathbf{t}^{\mathrm{e}}) = \chi(\mathbf{t}^{\mathrm{n}})\phi(\mathbf{t}^{\mathrm{n}},\mathbf{t}^{\mathrm{e}}) \tag{13}$$

defining a nuclear wave function by means of

$$|\chi(\mathbf{t}^{\mathrm{n}})|^2 = \int \psi(\mathbf{t}^{\mathrm{n}},\mathbf{t}^{\mathrm{e}})^*\psi(\mathbf{t}^{\mathrm{n}},\mathbf{t}^{\mathrm{e}})\mathrm{d}\mathbf{t}^{\mathrm{e}} \tag{14}$$

then, providing this function has no nodes,[2] an “exact” electronic wavefunction could be constructed as

---

[2] A similar requirement must be placed on the denominator in equation (12) of [11] for the equation to provide a secure definition.

$$\phi(\mathbf{t}^{\mathrm{n}}, \mathbf{t}^{\mathrm{e}}) = \frac{\psi(\mathbf{t}^{\mathrm{n}}, \mathbf{t}^{\mathrm{e}})}{\chi(\mathbf{t}^{\mathrm{n}})} \tag{15}$$

if the normalisation choice

$$\int \phi(\mathbf{t}^{\mathrm{n}}, \mathbf{t}^{\mathrm{e}})^{*} \phi(\mathbf{t}^{\mathrm{n}}, \mathbf{t}^{\mathrm{e}}) \mathrm{d}\mathbf{t}^{\mathrm{e}} = 1$$

is made. In fact it is possible [12] to show that χ must be nodeless even though the usual approximate nuclear wavefunctions for vibrationally excited states do have nodes. The electronic wavefunction (15) is therefore properly defined and a potential energy surface could be defined in terms of it as

$$\mathsf{U}(\mathbf{t}^{\mathrm{n}}) = \int \phi(\mathbf{t}^{\mathrm{n}}, \mathbf{t}^{\mathrm{e}})^{*} \mathsf{H}'(\mathbf{t}^{\mathrm{n}}, \mathbf{t}^{\mathrm{e}}) \phi(\mathbf{t}^{\mathrm{n}}, \mathbf{t}^{\mathrm{e}}) \mathrm{d}\mathbf{t}^{\mathrm{e}} \tag{16}$$

with H' defined as the sum of (9) and (10) Although no exact solutions to the full problem are known for a molecule, some extremely good approximate solutions are known for excited vibrational states of H_2 and Czub and Wolniewicz [13] took such an accurate approximation for an excited vibrational state in the $J = 0$ rotational state of H_2 and computed $\mathsf{U}(R)$. They found strong spikes in the potential close to two positions at which the usual wave function would have nodes. To quote [13]

> This destroys completely the concept of a single internuclear potential in diatomic molecules because it is not possible to introduce on the basis of non-adiabatic potentials a single, approximate, mean potential that would describe well more than one vibrational level.
>
> It is obvious that in the case of rotations the situation is even more complex.

Bright Wilson suggested [14] that using the clamped nucleus Hamiltonian instead of the full one in (16) to define the potential might avoid the spikes but Hunter in [12] showed why this was unlikely to be the case and Cassam-Chenai [15] repeated the work of Czub and Wolniewicz using an electronic Hamiltonian and showed that exactly the same spiky behaviour occurred. However, Cassam-Chenai showed, as Hunter had anticipated, that if one simply ignored the spikes, the potential was almost exactly the same as would be obtained by deploying the electronic Hamiltonian in the usual way. This would seem to be consistent too with the earlier work of Pack and Hirschfelder [16].

Although Gross [10] does not approach the problem in quite this way, there is reason to believe that this sort of problem is bound to arise whatever the approach. To see this simply rewrite (13) to recognise that the exact states will actually have definite quantum numbers according to their orthogonal symmetry O, the electronic permutational symmetry l, the nuclear permutational symmetry j and the energy n so that it would be more realistic to write

$$\psi_{Oljn}(\mathbf{t}^{\mathrm{n}}, \mathbf{t}^{\mathrm{e}}) = \chi_{Oljn}(\mathbf{t}^{\mathrm{n}}) \phi_{Oljn}(\mathbf{t}^{\mathrm{n}}, \mathbf{t}^{\mathrm{e}}) \tag{17}$$

In the H_2 study cited, the first three quantum numbers are of no relevance, only n remains and here n labels the vibrational states. There is thus every reason to expect that the best that can be done from this approach is a distinct PES for each nuclear-motion state.

At this level, then it cannot be assumed that the potential surface calculated in the usual way is an approximation to anything exact but it remains open to see whether it is possible to associate it with the exact solution when rotational motion is taken into account.

5 Rotational motion in a polyatomic molecule

A transformation to internal coordinates and Eulerian angles can be made to produce a Hamiltonian in which the rotational motion is explicit. The cases of two and of three nuclei present particular and non-general features and so will not be considered here. For details of the transformation see [6] but it is sufficient to notice here that the Eulerian angles are to be chosen as defined by the nuclear variables alone. Such a transformation yields an electronic Hamiltonian whose potential terms depend only upon $3A - 6$ nuclear internal coordinates q_k which are invariant under all rotation-reflections of the translationally invariant coordinates. The electronic variables are simply transformed variables $\mathbf{r}$ where the transformation is an orthogonal one defined by the three angles ϕ_k, $k = 1, 2, 3$. The angular and internal motion parts of the Hamiltonian do not separate, and the electronic angular motion is coupled to the angular motion of the nuclei.

The complete Hamiltonian operator may be written as

$$\mathsf{H}(\mathbf{r}) + \mathsf{K}(\mathbf{q}, \mathbf{r}) + \mathsf{K}(\boldsymbol{\phi}, \mathbf{q}, \mathbf{r}) \tag{18}$$

The first term in (18) arises trivially from (9) simply by replacing the $\mathbf{t}^{\mathrm{e}}$ by the $\mathbf{r}$ and so is

$$\begin{aligned} \mathsf{H}(\mathbf{r}) = & -\frac{\hbar^2}{2m} \sum_{i=1}^{N} \nabla^2(\mathbf{r}_i) - \frac{\hbar^2}{2M} \sum_{i,j=1}^{N} \vec{\nabla}(\mathbf{r}_i) \cdot \vec{\nabla}(\mathbf{r}_j) \\ & - \frac{e^2}{4\pi\epsilon_0} \sum_{i=1}^{A} \sum_{j=1}^{N} \frac{Z_i}{|\mathbf{r}_j - \bar{\mathbf{x}}_i^{\mathrm{n}}|} \\ & + \frac{e^2}{8\pi\epsilon_0} {\sum_{i,j=1}^{N}}' \frac{1}{|\mathbf{r}_i - \mathbf{r}_j|} + {\sum_{i,j=1}^{A}}' \frac{Z_i Z_j}{|\mathbf{x}_i^{\mathrm{n}} - \mathbf{x}_j^{\mathrm{n}}|} \end{aligned} \tag{19}$$

and

$$\mathsf{K}(\boldsymbol{\phi}, \mathbf{q}, \mathbf{r}) = \frac{1}{2} \left(\sum_{\alpha\beta} \kappa_{\alpha\beta} \mathsf{L}_{\alpha} \mathsf{L}_{\beta} + \hbar \sum_{\alpha} \bar{\lambda}_{\alpha} \mathsf{L}_{\alpha} \right) \tag{20}$$

and

$$\mathsf{K}(\mathbf{q},\mathbf{r}) = -\frac{\hbar^2}{2}\left(\sum_{k,l=1}^{3A-6} g_{kl}\frac{\partial^2}{\partial q_k \partial q_l} + \sum_{k=1}^{3A-6} h_k \frac{\partial}{\partial q_k}\right) + \frac{\hbar^2}{2}\left(\sum_{\alpha\beta}\kappa_{\alpha\beta}\mathsf{l}_\alpha \mathsf{l}_\beta + \sum_\alpha \lambda_\alpha \mathsf{l}_\alpha\right) \tag{21}$$

L , the total angular momentum operator, involves only the angular variables, and the angular variables are defined in terms of the translationally invariant nuclear variables only. $\boldsymbol{\kappa}$ is an inverse generalised inertia tensor and, though expressible fully in terms of the q_k, is formally dependent upon the definition of the Eulerian angles. l is the electronic angular momentum operator divided by $\hbar$. The matrix $\mathbf{g}$ has elements that depend on the product of terms arising from the expression of $\frac{\partial q_k}{\partial t^{n}_{\alpha i}}$ while $\mathbf{h}$ has elements that depend on the derivatives with respect to the q_k of these partial derivatives. The λ_α involves the operators $\frac{\partial}{\partial q_k}$ with coefficients which are elements of a matrix $\boldsymbol{\tau}$ which involves products of the first derivatives that form $\mathbf{g}$ and those arising as the same kind of derivative but with respect to the angular variables. $\overline{\lambda}_\alpha$ also contains the electronic angular momentum operator with coefficients that are elements of $\boldsymbol{\kappa}$. This term couples the electronic and angular motions.

The Jacobian for the transformation is

$$|\mathbf{D}|^{-1}|\boldsymbol{\kappa}|^{-\frac{1}{2}}|\mathbf{g}-\boldsymbol{\tau}\boldsymbol{\kappa}^{-1}\boldsymbol{\tau}^{T}|^{-\frac{1}{2}} \tag{22}$$

The factor $|\mathbf{D}|^{-1}$ is the angular part of the Jacobian and in the standard parameterisation $|\mathbf{D}|^{-1} = \sin\phi_2$ as required for the usual interpretation of the matrix elements.

Again the transformed space is a manifold and not a vector space. There will always be a region in which the Jacobian for the transformation vanishes for such difficulties will arise somewhere in any transformed coordinate set that involves angular coordinates to separate off the non-Cartesian rotational space S^3. Difficulties also arise in a suitable choice of internal coordinates. The interparticle distances constitute a properly invariant set from which to construct internal coordinates and a geometrical figure formed by a choice of clamped nuclei can be specified uniquely by specifying all the interparticle distances. However, for[3] $A > 4$ there are more interparticle distances than the $3A - 6$ internal coordinates allowed following the construction of the 3 angular coordinates. Thus, if 9 of the 10 possible interparticle distances are chosen as internal coordinates for the 5-nuclei problem, it is possible to construct two distinct geometrical figures which generate the same values of the chosen internal coordinates. To see this, imagine the nuclei of NH_3 clamped with the protons, numbered 1–3, in a plane and the nitrogen nucleus, numbered 4, on the z-axis. Let a fifth nucleus be placed equivalently either above or below the plane of the protons so that the value of its z-coordinate is either $\pm a$. If we choose nine interparticle coordinates r_{12}, r_{13}, r_{14}, r_{15}, r_{23}, r_{24}, r_{25}, r_{34} and r_{35} as the independent internal coordinates, it is seen that the two possible positions of the fifth nucleus lead to exactly the same values of the chosen internal coordinates. Standard clamped nuclei electronic structure calculations, which can be performed at any geometry would, at each of the geometries, yield different electronic energies. If these energies were assumed to be achievable as a result of assigning coordinate values in a function of the internal coordinates, two energies would arise for a single set of coordinate values and the "function" would not really be a function since a function must be single valued. It is not that such geometries are not possible, it is just that with a particular choice of internal coordinates, they are not distinguishable. Of course if r_{45} was considered, then the two geometries would be distinguishable and other choices of internal coordinates are possible in which this problem can be avoided. But the problem is quite general, see [6] or [18]. If the number of nuclei is five or more, there are always two or more geometries which are distinct but have the same internal coordinate specification, whatever the choice of internal coordinates made.

6 Removing rotational motion in the frame fixed in the body

One can eliminate angular motion from the problem by allowing the operator to work on the function and multiplying from the left by its complex conjugate and integrating out over the angular variables. This yields an effective operator within any (J, M, k) rotation-reflection manifold that depends only on the internal coordinates.

To remove the rotational motion, we write (18) as

$$\mathsf{H}_I(\mathbf{q},\mathbf{z}) + \mathsf{K}_R(\boldsymbol{\phi},\mathbf{q},\mathbf{z}) \tag{23}$$

in which the first term, H_I, consists of the first two terms in (18). The matrix elements with respect to the angular variables of the operators that depend only on the q_k and the $\mathbf{z}_i$ are trivial. Thus

$$\langle J'M'k' \mid \mathsf{H}_I \mid JMk\rangle = \delta_{J'J}\delta_{M'M}\delta_{k'k}\mathsf{H}_I \tag{24}$$

In what follows, explicit allowance for the diagonal requirement on J and M will be assumed and the indices suppressed to save writing. Similarly, the fact that the integration implied is over $\boldsymbol{\phi}$ only will be left implicit.

---

[3] For $A = 4$ the internal coordinate part of the Jacobian becomes ferociously complicated [17] with singularities when $r_{12} = r_{34}$, $r_{13} = r_{24}$ and $r_{14} = r_{23}$. The Jacobian for the interparticle distances in the five particle case is probably even more complicated.

The second term in (23) becomes

$$
\begin{aligned}
&\langle JMk' \mid \mathsf{K}_R \mid JMk\rangle \\
&\quad= \frac{\hbar^2}{4}\left(b_{+2}C^{+}_{Jk+1}C^{+}_{Jk}\delta_{k'k+2} + b_{-2}C^{-}_{Jk-1}C^{-}_{Jk}\delta_{k'k-2}\right) \\
&\quad+ \frac{\hbar^2}{4}\left(C^{+}_{Jk}(b_{+1}(2k+1) + \overline{\lambda}_{+})\delta_{k'k+1}\right. \\
&\quad\left.+ C^{-}_{Jk}(b_{-1}(2k-1) + \overline{\lambda}_{-})\delta_{k'k-1}\right) \\
&\quad+ \frac{\hbar^2}{2}\left((J(J+1) - k^2)b + b_0k^2 + \overline{\lambda}_0 k\right)\delta_{k'k} \qquad (25)
\end{aligned}
$$

In this expression

$$
\begin{aligned}
&b_{\pm 2} = (\kappa_{xx} - \kappa_{yy})/2 \pm \kappa_{xy}/i \\
&b_{\pm 1} = \kappa_{xz} \pm \kappa_{yz}/i \qquad (26)\\
&b = (\kappa_{xx} + \kappa_{yy})/2 \quad b_0 = \kappa_{zz}
\end{aligned}
$$

and in terms of the $\overline{\lambda}_\alpha$ $\overline{\lambda}_0$ is $\overline{\lambda}_z$ and the $\overline{\lambda}_\pm$ are

$$\overline{\lambda}_{\pm} = (\overline{\lambda}_x \pm \overline{\lambda}_y/i) \qquad (27)$$

The apparently odd positioning of the complex unit as $1/i$ when i might have been expected is because the standard commutation conditions have been chosen for the internal angular momentum components.

Thus, within any rotational manifold, it is the eigensolutions of the effective Hamiltonian given by (24) and (25) which are invariant to orthogonal transformations and it is these functions that will be used to consider the separation of electronic and nuclear motion.

7 The separation of electronic and nuclear motion in an embedded frame

The base manifold $R^{3A-6} \otimes S^3$ is clearly coordinatisable in the region in which the Jacobian (22) does not vanish. Over that region, it is, in principle, possible to construct fibre bundles, so it is, in principle, possible to extend mathematically rigorous arguments to the separation of electronic from nuclear motion even when rotational motion is explicitly considered. For any given J state, the Schrödinger Coulomb Hamiltonian is, however, now composed of $2J+1$ coupled differential equations. It should be remembered that the label k does not designate a good quantum number and that states of different k for a given J may couple extensively or not at all. Unfortunately, however, any coupling that there might be, involves the electronic motion because each of the $\overline{\lambda}_\alpha$ contain a term $(\boldsymbol{\kappa}\mathbf{l})_\alpha$. Although the form of $\boldsymbol{\kappa}$ depends upon the choice of embedding, for the Eckart embedding [19], which is the one usually chosen,

$$\boldsymbol{\kappa} = \mathbf{I}''^{-1}\mathbf{I}^0\mathbf{I}''^{-1}$$

where $\mathbf{I}^0$ is the inertia tensor for the molecule at the reference geometry and $\mathbf{I}''$ is of inertia tensor form and becomes the equilibrium inertia tensor when the nuclear variables take their equilibrium values. At the equilibrium values of the nuclear variables, $\boldsymbol{\kappa}$ becomes the inverse of the equilibrium inertia tensor. The notation is that of Watson [20]. Thus, with this embedding this part of coupling matrix will be small only if the matrix elements of the components of the electronic angular momentum between the different k labelled states are small.

There has been no detailed mathematical consideration of this matter but the most useful way to proceed would seem to be to assume that this part of the coupling is of small effect. It is natural then to think of the electronic part of the Hamiltonian as given by (19). This is however to ignore the last term in (21). It would be easy to imagine this term included in the electronic part of the Hamiltonian but for the fact that λ_α contains a term in the nuclear variable derivatives. If such a term is included, it is not the case that this part of the Hamiltonian commutes with the nuclear variables and so appropriate fibre bundles cannot be constructed over a base space defined by fixed values of the nuclear variables. In order to offer an account of the separation of motions analogous to that offered in the translationally invariant case, the second part of the last term in (21) cannot be included in the electronic part of the problem. Consistency would seem to require that the whole term be ignored for the purposes of an initial discussion. It might be argued too that the expectation values of the components of electronic angular momentum would be small is an assumption consistent with the neglect of their matrix elements discussed above. Whether or not all these reservations are valid, a potential can be calculated using the direct integral form with the part (19) of the Hamiltonian and it will be properly defined wherever the domain of the Hamiltonian is restricted to the region in which Jacobian is non-vanishing. Since this space is a manifold, care must be taken to make sure that it remains a proper coordinate space and that the potential is everywhere an analytic function of the chosen coordinates. A mathematical discussion in these sort of terms has been attempted only for a diatomic system in which the internal coordinates are just the internuclear variable R. In this case, two possible fibre bundles are constructible on this manifold and it is this possibility that gives rise to the Berry phase change which can arise when the internal coordinate R is transported around a circle of constant latitude. This is discussed in a mathematically sophisticated way for a rather simplified model of the diatomic molecule in [21]. The authors refer to their results as either "straight up" or "with a twist". If it can be safely assumed that a "straight up" choice has been made, then it can be assumed that at least locally, a potential $\mathsf{V}^{\mathrm{e}}(\mathbf{q})$ can be properly defined.

Assuming that a potential can be calculated from this part of the rotationally invariant Hamiltonian, then the nuclear-motion problem involves the Hamiltonian composed of the first part of (21) added to (25) and to the potential. The terms in (25) other than those involving $\overline{\lambda}_\alpha$ are simply multiplicative in the variables $\mathbf{q}$ and so it is natural to consider these as to be evaluated at fixed values of the nuclear variables and to be dealt with along with the potential. If it can be assumed that it is possible to choose the embedding so that for the energy range of interest k is almost a good quantum number, then the effective potential imagined in these terms would be

$$\mathsf{V}(\mathbf{q}) = \mathsf{V}^{\mathrm{e}}(\mathbf{q}) + \frac{\hbar^2}{2}((J(J+1) - k^2)b + b_0 k^2) \tag{28}$$

For fixed J and k, this extended potential is rotationally invariant so that the fibre bundle arguments used for the translationally invariant approach may simply be carried over. Even with the simplifying assumptions made here, in principle the potential should be affected by the rotational motion of the system, and for any given k, the higher the J value, the shallower the effective potential will become. This is exactly the behaviour observed in the case of H_2 [22] for the electronic Σ ground state of the molecule assumed to dissociate into two hydrogen atoms in their ground states. That work shows that, for example, the $J = 0$ state supports just 14 vibrational states while the $J = 15$ state supports 10 while the $J = 31$ supports only 1 state. Of course in a diatomic molecule, states of different k are states with differ in the electronic angular momentum and these results cannot be regarded as typifying the results for a polyatomic system. However, work on H_3^+ shows that in the case of $J = 0$ there are 1,280 vibrational states below dissociation [23] and that 46 is the highest value of J for which at least one vibrational state exists [24]. These figures should be taken as indicative rather than definitive, for the electronic structure calculations from which they result, though among the best available, do not have quite the accuracy that the calculations on H_2 cited above do. Nevertheless, it is clear that rotational dependence is not just relevant for diatomic molecules. However, in general the importance of the rotational terms will depend on the values of b and b_0. Both of these depend on the reciprocals of the nuclear masses and thus it is reasonable to expect their importance to become less as the constituent atomic masses increase for any given electronic potential. It is clear that a mathematically sound scheme could be developed for the separation of electronic and nuclear motion even when rotational motion is considered though it might be necessary to recognise rotational dependencies. However, it now becomes a much more difficult problem to consider permutational invariance.

8 The permutational invariance of the PES

For the purposes of this discussion, it is convenient to think of the translation-free nuclear cartesian coordinates $\mathbf{t}^{\mathrm{n}}$ as being related to a body-fixed set $\mathbf{z}^{\mathrm{n}}$ by

$$\mathbf{t}^{\mathrm{n}} = \mathbf{C}\mathbf{z}^{\mathrm{n}} \tag{29}$$

The body-fixed electronic variables can now be defined in terms of the transformation defined above by:

$$\mathbf{r}_i = \mathbf{C}^T \mathbf{t}_i^{\mathrm{e}} \quad i = 1, 2, \ldots .N \tag{30}$$

The three orientation variables are specified by means of an orthogonal matrix $\mathbf{C}$, parameterised by the three Euler angles ϕ_m, $m = 1, 2, 3$ as orientation variables. In the present case, the matrix $\mathbf{C}$ is specified entirely in terms of the A translation-free nuclear variables and so there will be just $3A - 6$ internal variables for the nuclei and so three relations among the $\mathbf{z}_i^{\mathrm{n}}$.

It is necessary to consider the behaviour of both the internal coordinates and the Euler angles under the permutation of identical nuclei. Because of the choices made in deriving equation (30), the permutation of electrons is standard and need not be explicitly considered. However, the effect on the nuclear variables of a permutation P with representative $\mathbf{P}$ in the laboratory coordinates induces in the translationally invariant space the $A \times A$ representative matrix

$$\mathbf{H} = \mathbf{V}^{\mathrm{n}-1}\mathbf{P}\mathbf{V}^{\mathrm{n}} \tag{31}$$

The matrix $\mathbf{H}$ is not in general in standard permutational form neither is it orthogonal even though it has determinant ± 1 according to the sign of $\det\mathbf{P}$.

Let the (redundant) set of $(A - 1)^2$ scalar products of the $\mathbf{t}_i$ be denoted by the square matrix $\mathbf{S}$, of dimension $A - 1$. Then, using (31), it is seen that a permutation

$$\mathcal{P}\mathbf{t}^{\mathrm{n}} = \mathbf{t}^{\mathrm{n}}\mathbf{H} = \mathbf{t}'^{\mathrm{n}} \tag{32}$$

so that

$$\mathbf{S}' = \mathbf{H}^T\mathbf{S}\mathbf{H} \tag{33}$$

Making explicit the functional dependencies, (29) may be written as

$$\mathbf{t}^{\mathrm{n}} = \mathbf{C}(\boldsymbol{\phi})\mathbf{z}^{\mathrm{n}}(\mathbf{q}) \tag{34}$$

and using (32) and (33) two different expressions for the permuted translation-free coordinates may be obtained. The first follows at once from (34) and (32):

$$\mathbf{t}'^{\mathrm{n}} = \mathbf{t}^{\mathrm{n}}\mathbf{H} = \mathbf{C}(\boldsymbol{\phi})\mathbf{z}^{\mathrm{n}}(\mathbf{q})\mathbf{H} \tag{35}$$

and this gives the $\mathbf{t}'^{\mathrm{n}}_i$ as functions of ϕ and $\mathbf{q}$.

Alternatively, the Euler angles and the internal coordinates can be expressed directly as functions of the $\mathbf{t}^{\mathrm{n}}$ and hence of the $\mathbf{t}'^{\mathrm{n}}$ according to:

$$\phi_m(\mathbf{t}^{\mathrm{n}}) = \phi_m(\mathbf{t}'^{\mathrm{n}}\mathbf{H}^{-1}) = \phi'_m(\mathbf{t}'^{\mathrm{n}}) = \overline{\phi}_m(\boldsymbol{\phi}, \mathbf{q}) \tag{36}$$

and

$$q_k(\mathbf{S}) = q_k(\mathbf{H}^{-T}\mathbf{S}'\mathbf{H}^{-1}) = q'_k(\mathbf{S}') = \overline{q}_k(\mathbf{q}) \tag{37}$$

Notice that while the effect of the permutation on q_k can at most produce a function of the q_k, the effect of the permutation on ϕ_m can produce a function of both the ϕ_m and the q_k. If the permuted internal coordinates and Euler angles are used in (34), the resulting expression will be for the permuted translation- free variables thus:

$$\mathbf{t}'^{\mathrm{n}} = \mathbf{C}(\overline{\boldsymbol{\phi}}(\boldsymbol{\phi}, \mathbf{q}))\mathbf{z}^{\mathrm{n}}(\overline{\mathbf{q}}(\mathbf{q})) \tag{38}$$

so that:

$$\mathbf{t}'^{\mathrm{n}} = \overline{\mathbf{C}}(\boldsymbol{\phi}, \mathbf{q})\overline{\mathbf{z}}^{\mathrm{n}}(\mathbf{q}) \tag{39}$$

Equating (35) and (39) it follows that

$$\overline{\mathbf{z}}^{\mathrm{n}} = \overline{\mathbf{C}}^T\mathbf{C}\mathbf{z}^{\mathrm{n}}\mathbf{H} \tag{40}$$

and since this expression can be at most a function of the internal coordinates, it follows that the orthogonal matrix $\overline{\mathbf{C}}^T\mathbf{C}$ must have elements which are, at most, functions of the internal coordinates. Denoting this matrix by $\mathbf{U}$ (and from now on, since they will always be the original body-fixed ones, the variables will not be explicitly given), it follows that

$$\overline{\mathbf{z}}^{\mathrm{n}} = \mathbf{U}\mathbf{z}^{\mathrm{n}}\mathbf{H} \tag{41}$$

and

$$\overline{\mathbf{C}} = \mathbf{C}\mathbf{U}^T \tag{42}$$

giving a relationship (albeit implicit) between the permuted and unpermuted body-fixed variables. It is as well to state explicitly that there will be such a relationship for every distinct permutation, and so strictly the matrices should carry a designation to indicate which of the permutations is being considered. But that would be to overload the notation in a way that is not necessary here and so it will not be done.

Now that these relationships have been established, the effects of a permutation on the various parts of the wavefunction must now be worked out. To avoid overloading the notation again, the usual convention will be adopted in which the change (41) is written:

$$\mathbf{z}^{\mathrm{n}} \to \mathbf{U}^T\mathbf{z}^{\mathrm{n}}\mathbf{H}^{-1} \tag{43}$$

while (42) is written:

$$\mathbf{C} \to \mathbf{C}\mathbf{U} \tag{44}$$

when considering the change in a function upon the change of variables.

The angular momentum eigenfunction $|1Mk\rangle$ can be shown [25] to be writable as

$$|1Mk\rangle = \left(\frac{3}{8\pi^2}\right)^{\frac{1}{2}}(\mathbf{X}^T\mathbf{C}\mathbf{X})_{Mk} \tag{45}$$

Since the elements of $|JMk\rangle$ can be obtained by repeated vector coupling of the elements of $|1Mk\rangle$ it is sufficient to know how $|1Mk\rangle$ transforms in order to know the general result. Using (44) for the change in $\mathbf{C}$ it follows from (45) that:

$$\begin{aligned} |1Mk\rangle &\to \left(\frac{3}{8\pi^2}\right)^{\frac{1}{2}}(\mathbf{X}^T\mathbf{C}\mathbf{U}\mathbf{X})_{Mk} \\ &= \left(\frac{3}{8\pi^2}\right)^{\frac{1}{2}}(\mathbf{X}^T\mathbf{C}\mathbf{X}\mathbf{X}^{\dagger}\mathbf{U}\mathbf{X})_{Mk} \\ &= \sum_{n=-1}^{+1}|1Mn\rangle\mathcal{D}^1_{nk}(\mathbf{U}) \end{aligned} \tag{46}$$

so that the change induced in the general symmetric-top function under $\mathcal{P}$ is:

$$|JMk\rangle \to \sum_{n=-J}^{+J}|JMn\rangle\mathcal{D}^J_{nk}(\mathbf{U}) \tag{47}$$

In this equation, $\mathcal{D}^J(\mathbf{U})$ is the matrix made up from the elements of $\mathbf{U}$ in exactly the same way that $\mathcal{D}^J$ is made up from the elements of $\mathbf{C}$. A precise account of how this is to be done is given in Section 6.9 of [26]. Should it turn out that $\mathbf{U}$ is a constant matrix, then $\mathcal{D}^J(\mathbf{U})$ is a constant matrix and (47) simply represents a linear combination. If $\mathbf{U}$ is a unit matrix, then $|JMk\rangle$ is invariant. It should be noted here that this coupling of rotations by the permutations can mean that certain rotational states are not allowed by the Pauli principle and this is important in assigning statistical weights to rotational states.

It is rather difficult to say anything precise about the change induced in the q_k under the permutation. Of course since the internal coordinates are expressible entirely in terms of scalar products[4] and the scalar products of the $\mathbf{t}^{\mathrm{n}}_i$ are identical to the scalar products of the $\mathbf{z}^{\mathrm{n}}_i$, the change is that given in (37) namely

$$\mathbf{q}(\mathbf{S}) \to \mathbf{q}(\mathbf{H}^{-T}\mathbf{S}\mathbf{H}^{-1}) \tag{48}$$

where the notation of (43) has been used and where $\mathbf{S}$ is regarded as a function of the q_k. However, the result has no general form and so the best that can be said is that a permutation of nuclei induces a general function change

$$\Phi^J_k(\mathbf{q}, \mathbf{z}) \to \Phi'^J_k(\mathbf{q}, \mathbf{z}) \tag{49}$$

where the precise nature of the function change depends on the permutation, the chosen form of the internal

---

[4] Because of this, the internal coordinates are invariant under inversion, which simply causes the $\mathbf{t}_i^{\mathrm{n}}$ to change sign. Thus, it is only the nuclear permutation group and not the permutation-inversion group which is relevant here.

coordinates and on the chosen functional form. Thus, the general change in the wavefunction induced by $\mathcal{P}$ can be written

$$\Psi^{J,M}(\boldsymbol{\phi},\mathbf{q},\mathbf{z}) \rightarrow \sum_{k=-J}^{+J}\sum_{n=-J}^{+J}\mathcal{D}^{J}_{nk}(\mathbf{U})\Phi'^{J}_{k}(\mathbf{q},\mathbf{z})|JMn\rangle = \sum_{n=-J}^{+J}\overline{\Phi}^{J}_{n}(\mathbf{q},\mathbf{z})|JMn\rangle \tag{50}$$

This expression will clearly be very difficult to handle for not only will a $\mathbf{U}$ be difficult to determine, but one must be found for each distinct permutation of the identical nuclei and in a problem of any size there will be a very large number of such permutations. It would obviously be desirable to choose a body-fixing matrix, $\mathbf{C}$, that was invariant under all permutations of identical particles. This can be done by choosing $\mathbf{C}$ to be the matrix that diagonalises the translation-free instantaneous inertia tensor and this is how it was chosen in the two very first attempts to body-fix for molecules, [27] and [28], and it has been a choice made subsequently on many occasions, see for example, [29]. However, if this choice is made, then the resulting Hamiltonian is quite inappropriate for the study of molecules because the Jacobian for the transformation vanishes in regions of physical interest. Thus, for a molecule like ammonia, this happens at what is usually thought of as its equilibrium geometry. This was among the reasons that led Eckart to develop his body-fixing prescription, [19], which is the one that is generally taken as the basis for the interpretation of molecular spectra. The embedding defined in this approach is generally invariant only under the subset of permutations of the identical nuclei which correspond to point group operations on the equilibrium geometry figure (for more discussion of this, see [25] and [30]). Thus, it is clear that it is not always possible to avoid these difficulties and the fact that they can arise in the Eckart approach obviously poses some problems for the standard view of the separation of rotational and vibrational motion. These matters are discussed a little more in [31] and [32].

Why these broken symmetry solutions to the clamped nucleus problem turn out to be so effective in practice has been a vexing puzzle since the very beginning of molecular quantum mechanics. It has occasioned an enormous amount of work, particularly since the publication in 1963 of a paper by H. C. Longuet-Higgins [33] in which permutations were divided into *feasible* and *unfeasible* types and in which it was argued that it was necessary to consider only the (often rather small) set of feasible permutations in a given problem. A summary of much of the relevant work in the area of molecular spectroscopy is reviewed in the monographs by Ezra [25] and by Bunker [34] and in a more general context in [35] and [36].

The idea of unfeasibility seems to rest on the notion that the permutation is a real motion of particles in the potential computed from a clamped nucleus calculation. If between the typical geometry and the permuted geometry there is a high potential barrier, then the permutation is unfeasible. The idea that a permutation is a real motion of particles is an incongruous one, from a mathematical point of view, as is the idea of unfeasibility, outside the single product approximation for the wave function and hence a single uncoupled potential function. It might however be speculated, within the present context, that if the usual orbital electronic wavefunction for a typical geometry is projected so that it has the proper permutational invariance, then the elements in the projected function that are small and make only a small contribution to the electronic energy can be neglected without great loss in energy. It would be the permutations that produce these negligible terms that can perhaps properly be called unfeasible. Although calculations could not quite settle this matter, it would be very interesting to attempt some and to see what emerged. To do so however would necessitate a proper consideration of the permutation upon the internal and angular coordinates and it would not be sufficient simply to assume as is usually done, that the permutations can be realised in terms of the nuclear cartesian variables nor should inversion be invoked as relevant to internal motion.

9 Conclusions

This paper has been devoted to trying to "place" the potential energy function in the context of solutions to the full problem. As has been shown, this placing is more problematic than is commonly thought. It cannot therefore be said, with any confidence at present, to what question the potential energy function arising from a clamped nucleus calculation is the answer.

Acknowledgments I am grateful to Guy Woolley for reading some earlier drafts of this contribution. Some of the work reported here developed as part of ESA contract 21790/08/NL/HE and was carried out at the Universite Libre de Bruxelles. I thank the Fonds National de la Recherche Scientifique (F.R.S.-FNRS, contracts FRFC and IISN), the Universite libre de Bruxelles and the "Action de Recherches Concertees de la Communaute francaise de Belgique" for accommodation and the provision of library and computing facilities.

References

1. Born M, Huang K (1955) Dynamical theory of crystal lattices. Oxford University Press, Oxford
2. Kato T (1951) Trans Am Math Soc 70:195
3. Stone MH (1932) Proc Natl Acad Sci 16:172
4. Thirring W (1981) Quantum mechanics of atoms and molecules, vol 3 of A course in mathematical physics (trans: Harrell EM). Springer, Berlin

5. Perez JF, Arajuo VA, Coutinho FAB (2004) Am J Phys 72:203
6. Sutcliffe B (2000) Adv Chem Phys 114:97
7. Schutz B (1980) Geometrical methods of mathematical physics. Cambridge University Press, Cambridge
8. Klein M, Martinez A, Seiler R, Wang XP (1992) Commun Math Phys 143:607
9. Hunter G (1975) Int J Quantum Chem 9:237
10. Abedi A, Maitra NT, Gross EKU (2010) Phys Rev Lett 105:123002
11. Kutzelnigg W (2007) Mol Phys 105:2627
12. Hunter G (1981) Int J Quantum Chem 19:755
13. Czub J, Wolniewicz L (1978) Mol Phys 36:1301
14. Wilson E Bright (1979) Int J Quant Chem Symp 13:5
15. Cassam-Chenai P (2006) Chem Phys Lett 420:354
16. Pack RT, Hirschfelder JO (1970) J Chem Phys 52:521
17. Harris F (2004) Adv Quantum Chem 47:130
18. Collins MA, Parsons DF (1993) J Chem Phys 99:6756
19. Eckart C (1935) Phys Rev 47:552
20. Watson JKG (1968) Mol Phys 15:479
21. Herrin J, Howland JS (1997) Reviews in mathematical physics 9:467
22. Pachucki K, Komasa J (2009) J Chem Phys 130:164113
23. Henderson JR, Tennyson J, Sutcliffe BT (1993) J Chem Phys 98:7191
24. Miller S, Tennyson J (1988) Chem Phys Lett 145:117
25. Ezra G (1982) Symmetry properties of molecules, vol 28 of lecture notes in chemistry. Springer, Berlin
26. Biedenharn LC, Louck JC (1982) Angular momentum in quantum physics. Addison-Wesley, Reading, MA
27. Eckart C (1934) Phys Rev 46:384
28. Hirschfelder JO, Wigner E (1935) Proc Natl Acad Sci 21:113
29. Buck B, Biedenharn LC, Cusson RY (1979) Nucl Phys A 317:215
30. Louck JD, Galbraith HW (1976) Rev Mod Phys 48:69
31. Sutcliffe BT (1994) In: Kryachko ES, Calais JL (eds) Conceptual trends in quantum chemistry. Kluwer, Dordrecht, p 53
32. Sutcliffe BT (1991) In: Wilson S (ed) Methods of computational chemistry, vol 4. Plenum, New York and London, p 33
33. Longuet-Higgins HC (1963) Mol Phys 6:445
34. Bunker PR, Jensen P (1998) Molecular symmetry and spectroscopy, 2nd edn. NRC Research Press, Ottawa
35. Kaplan IG (1975) Symmetry of many-electron systems. Academic, London
36. Maruani J, Serre J (eds) (1983) Symmetries and properties of non-rigid molecules. Elsevier, Amsterdam

Theor Chem Acc (2012) 131:1227
DOI 10.1007/s00214-012-1227-6

REGULAR ARTICLE

Self-consistent methods constrained to a fixed number of particles in a given fragment and its relation to the electronegativity equalization method

Andrés Cedillo · Dimitri Van Neck ·
Patrick Bultinck

Received: 6 March 2012 / Accepted: 21 April 2012 / Published online: 3 June 2012

Abstract The variational procedure of the Hartree–Fock and Kohn–Sham methods can be modified by adding one or more constraints that fix the number of electrons in a given number of molecular fragments. The corresponding Euler–Lagrange equations lead to a modified Fock matrix, where the contribution from the constraints only depends on the overlap matrix, when using the Mulliken or Hirshfeld atoms-in-molecules method. For all compounds in the test set, the energy shows a quadratic dependence on the fixed charges. This behavior provides a procedure to obtain the atomic electronegativity and hardness parameters in the electronegativity equalization method.

Keywords Hartree–Fock method · Kohn–Sham method · Mulliken population analysis · Electronegativity equalization method · Atomic charges

1 Introduction

The way the electrons distribute in a molecule reflects its physical and chemical properties. For example, dipole moments and electron deficient sites are relevant properties in a molecule that affect the way it interacts with the reaction partners, and these properties are determined by the molecular charge distribution. Quantum mechanics allows the computation of the electron density, which tells the way electrons distribute in the molecule. However, the electron density can only be obtained from an electronic structure computation, and simpler methods are also required to estimate the atomic charges in complex systems.

The electronegativity equalization method (EEM) [1] has been successfully used to estimate atomic charges in a wide variety of electronic systems, from simple molecules to inorganic materials [2, 3]. In EEM, a molecule is described in terms of its atoms, and the molecular energy is approximated as a quadratic function of the atomic charges. One can rationalize the EEM approach by partitioning the expectation value of the Hamiltonian operator into intra- and interatomic regions [1, 4–6]:

$$\begin{aligned}\langle\hat{H}\rangle = {} & \sum_{A}\int\limits_{\Omega_A}\left(\left[-\frac{1}{2}\nabla^2+v(\vec{r})\right]\gamma_1(\vec{r};\vec{r}\,')\right)\Bigg|_{\vec{r}\,'=\vec{r}}\mathrm{d}\vec{r}\\ & +\sum_{A,B}\int\limits_{\Omega_A}\int\limits_{\Omega_B}\frac{\gamma_2(\vec{r}_1,\vec{r}_2;\vec{r}_1,\vec{r}_2)}{r_{12}}\mathrm{d}\vec{r}_1\mathrm{d}\vec{r}_2\\ & +\frac{1}{2}\sum_{\substack{A,B\\(A\neq B)}}\frac{Z_AZ_B}{R_{AB}}. \end{aligned} \qquad (1)$$

Here, γ_1 and γ_2 are the one- and two-body density matrices, Ω_A represents the region of space that is allocated to atom A, and v corresponds to the electric potential from the nuclei,

---

Published as part of the special collection of articles celebrating theoretical and computational chemistry in Belgium.

A. Cedillo
Departamento de Química, Universidad Autónoma
Metropolitana-Iztapalapa, San Rafael Atlixco 186,
09340 Mexico, DF, Mexico

A. Cedillo · P. Bultinck (✉)
Department of Inorganic and Physical Chemistry, Ghent
University, Krijgslaan 281 (S3), 9000 Ghent, Belgium
e-mail: Patrick.Bultinck@Ugent.be

D. Van Neck
Center for Molecular Modeling, Ghent University,
Technologiepark 903, 9052 Zwijnaarde, Belgium

$$v(\vec{r}) = \sum_A v_A(\vec{r}) = -\sum_A \frac{Z_A}{\left|\vec{r} - \vec{R}_A\right|}. \tag{2}$$

Then, one can collect the one- and two-region terms:

$$\langle \hat{H} \rangle = \sum_A E_A^* + \sum_{\substack{A,B \\ (A \neq B)}} V_{AB}^*. \tag{3}$$

where the quasi-atomic energies, E_A^*, are one-region contributions,

$$E_A^* = \int_{\Omega_A} \left\{ -\frac{1}{2}\left[\nabla^2 \gamma_1(\vec{r};\vec{r}')\right]\Big|_{\vec{r}'=\vec{r}} + v_A(\vec{r})\rho(\vec{r}) \right\} \mathrm{d}\vec{r} + \int_{\Omega_A}\int_{\Omega_A} \frac{\gamma_2(\vec{r}_1,\vec{r}_2;\vec{r}_1,\vec{r}_2)}{r_{12}} \mathrm{d}\vec{r}_1 \mathrm{d}\vec{r}_2 \tag{4}$$

while the interatomic terms, V_{AB}^*, are two-region ones,

$$V_{AB}^* = \int_{\Omega_B} v_A(\vec{r})\rho(\vec{r})\mathrm{d}\vec{r} + \int_{\Omega_A}\int_{\Omega_B} \frac{\gamma_2(\vec{r}_1,\vec{r}_2;\vec{r}_1,\vec{r}_2)}{r_{12}} \mathrm{d}\vec{r}_1 \mathrm{d}\vec{r}_2 + \frac{1}{2}\frac{Z_A Z_B}{R_{AB}}. \tag{5}$$

Note that a quasi-atomic energy is different from a free-atom energy, since it depends on the molecular density matrices. The two-body density matrix can be written in terms of the density and the pair-correlation function (h):

$$\gamma_2(\vec{r}_1,\vec{r}_2;\vec{r}_1,\vec{r}_2) = \frac{1}{2}\rho(\vec{r}_1)\rho(\vec{r}_2)[1 + h(\vec{r}_1,\vec{r}_2)], \tag{6}$$

where the pair-correlation function leads to the exchange and correlation energy contributions. From the use of a continuous representation of the nuclear density, one has that

$$\begin{aligned} V_{AB}^* + V_{BA}^* &= \int_{\Omega_A}\int_{\Omega_B} \frac{\left[Z_A\delta(\vec{r}_1 - \vec{R}_A) - \rho(\vec{r}_1)\right]\left[Z_B\delta(\vec{r}_2 - \vec{R}_B) - \rho(\vec{r}_2)\right]}{r_{12}} \mathrm{d}\vec{r}_1 \mathrm{d}\vec{r}_2 \\ &+ \int_{\Omega_A}\int_{\Omega_B} \frac{\rho(\vec{r}_1)\rho(\vec{r}_2)h(\vec{r}_1,\vec{r}_2)}{r_{12}} \mathrm{d}\vec{r}_1 \mathrm{d}\vec{r}_2, \end{aligned} \tag{7}$$

where the factors inside the square brackets represent the total molecular density at a given point in space, and the first term is the Coulomb interaction between two charge densities from different regions. The Coulomb term can be computed using the multipole expansion. If one neglects the contribution of the pair-correlation function, by assuming that its effects can be partially included in the parametrization of the quasi-atomic energies, and truncates the multipole expansion up to the monopole term, then one gets a simple expression for the sum of the two-region terms:

$$\sum_{\substack{A,B \\ (A \neq B)}} V_{AB}^* \approx \frac{1}{2} \sum_{\substack{A,B \\ (A \neq B)}} \frac{q_A q_B}{R_{AB}}. \tag{8}$$

Here, q_A represents the charge of atom A.

Since, in general, the atomic charges are not an integer, a second-order Taylor expansion of the energy, around the neutral state, is usually used for the quasi-atomic energies:

$$E_A^* \approx E_A^{o*} + \chi_A^* q_A + \frac{1}{2}\eta_A^* q_A^2 \tag{9}$$

where χ_A^* and η_A^* are the quasi-atomic electronegativity and hardness. From density functional chemical reactivity theory, the electronegativity is identified as the negative of the electronic chemical potential, while the hardness represents the response of the chemical potential to the change in the number of electrons (See for example [7]). In some special cases, it could be important to change the reference point for the Taylor expansion. Such a change slightly alters the form of the quadratic expression by replacing the terms q_A by $\left(q_A - q_A^0\right)$, where, as described below, q_A^0 is the charge on atom A using the unconstrained molecular wave function.

The combination of Eqs. (3) and (8, 9) leads to the EEM master equation:

$$\begin{aligned} E_{mol} = \langle \hat{H} \rangle &\approx E^{EEM} \\ &= \sum_A \left(E_A^{o*} + \chi_A^* q_A + \frac{1}{2}\eta_A^* q_A^2 \right) + \frac{1}{2} \sum_{\substack{A,B \\ (A \neq B)}} \frac{q_A q_B}{R_{AB}}. \end{aligned} \tag{10}$$

Note that the molecular energy is approximated by a quadratic function of the atomic charges. Atomic charges come from the minimization of Eq. (10), subject to the restriction

$$0 = \sum_A q_A - Q \tag{11}$$

where Q is the charge of the molecule, which leads to the following set of equations,

$$\frac{\partial E^{EEM}}{\partial q_A} = \chi_A^* + q_A \eta_A^* + \sum_{B \neq A} \frac{q_B}{R_{AB}} = \alpha, \quad A = 1, \ldots, M. \tag{12}$$

Here, α is the Lagrange multiplier associated with the constraint, and it can be shown that it is equal to the molecular electronegativity:

$$\alpha = \frac{\partial E^{EEM}}{\partial Q} = \chi_{mol}. \tag{13}$$

One can identify the derivative in Eq. (12) with the Politzer–Weinstein [8] definition of the electronegativity of an atom-in-a-molecule, and this equation corresponds to the electronegativity equalization condition. The principle of electronegativity equalization states[9, 10] that the molecular electronegativity, Eq. (13), equals the derivative of the energy with respect to the charge on an atom A and that for all atoms A [8]. The resulting expressions for EEM are usually written in a matrix form as

$$\begin{bmatrix} \eta_1^* & 1/R_{12} & \cdots & 1/R_{1M} & 1 \\ 1/R_{12} & \eta_2^* & \cdots & 1/R_{2M} & 1 \\ \vdots & \vdots & \ddots & \vdots & \vdots \\ 1/R_{1M} & 1/R_{2M} & \cdots & \eta_M^* & 1 \\ 1 & 1 & \cdots & 1 & 0 \end{bmatrix} \begin{bmatrix} q_1 \\ q_2 \\ \vdots \\ q_M \\ -\chi_{mol} \end{bmatrix} = \begin{bmatrix} -\chi_1^* \\ -\chi_2^* \\ \vdots \\ -\chi_M^* \\ Q \end{bmatrix}. \tag{14}$$

The values of the quasi-atomic electronegativity and hardness are obtained from a fitting procedure involving a training set of molecules. This fitting is mostly done in a least squares sense by finding the parameters that minimize the quadratic error between the ab initio computed charges and the ones obtained using a set of systematically improved parameters; see, for example, Refs. [11–18]. In practice, such fitting is far from trivial. Moreover, the parameters significantly depend on the definition used to define an atom in the molecule. There also remains one degree of freedom, that is, one can freely choose one electronegativity parameter and only optimize the others with respect to this chosen value. Besides this trivial degree of freedom, it has been observed by Bultinck et al. [14] that other sources of ambiguity in the parameters remain. Verstraelen et al. [18] recently performed an in-depth analysis of the ambiguity in the parameters, revealing that no unique set of parameters can be obtained. Nevertheless, it has been shown that the parameters derived in such a way are useful to predict atomic charges and different other properties [19, 20] of high quality in molecules not used in the training set for the regression. Moreover, EEM is a key ingredient of many new developments in polarizable force fields and reactive force fields [21–24].

In this work, we follow a different path to EEM parametrization by directly using Eq. (10). Instead of going through the atomic charges, we present an algorithm for the direct calculation of the energy for a given set of atomic charges (populations) and examine how good a sum of quadratic quasi-atom energies is. The parameters are obtained from simple molecules, usually diatomic ones although examples are given also for larger molecules. Once the parameters are known, it is also possible to test their quality by applying them in Eq. (14) to compute atomic charges, which, in turn, are compared to the ab initio charges.

2 Model

The use of the orbital concept in the Hartree–Fock (HF) and Kohn–Sham (KS) methods leads to similar variational equations: a coupled set of eigenvalue equations with a hermitian operator (See for example [7, 25]). This system of integro-differential equations is transformed into a matrix problem when we use a basis set. In both methods, one has to solve a generalized eigenvalue equation:

$$\mathbf{FC} = \varepsilon\mathbf{SC}. \tag{15}$$

When atom-centered basis sets are used, a very simple procedure to assign the electrons among the atoms of the molecule comes from Mulliken's approach [26]. Within this method, the number of electrons assigned to the atom A is given by

$$n_A = \sum_{\mu\in A}\sum_{v} P_{\mu v}S_{\mu v}, \quad P_{\mu v} \equiv \sum_{i=1}^{N} C_{i\mu}C_{iv} \tag{16}$$

where the μ and v indices are used for the basis functions, and the first sum is restricted to only those basis functions centered on atom A, P is the density matrix, and N is the number of electrons in the molecule.

Additional restrictions can be incorporated into the variational problem by making use of the Lagrange multiplier technique [27–31]. For example, if we want to fix the population in the atoms 1, 2, …, r, then for each atom A = 1,...,r the constraint takes the form:

$$\begin{aligned} 0 = n_A - N_A &= \sum_{\mu\in A}\sum_{v} P_{\mu v}S_{\mu v} - N_A, \\ &= \sum_{\mu v} \delta_{A,I_\mu} P_{\mu v}S_{\mu v} - N_A \end{aligned} \tag{17}$$

Here, N_A represents the desired population on atom A, and I_μ represents the atom where the basis function χ_μ is centered. Note that the Kronecker delta is not zero only when the basis function χ_μ is centered in atom A.

The variational solution of the constrained problem comes from minimizing, with respect to the coefficients, the following quantity:

$$\begin{aligned} L = E^{\mathrm{RHF}}\left(\{C_{i\mu}\}\right) &- \sum_{ij}\varepsilon_{ij}\left(\sum_{\mu v} C_{i\mu}S_{\mu v}C_{jv} - \delta_{ij}\right) \\ &- \sum_{A=1}^{r}\lambda_A\left(\sum_{\mu v}\delta_{A,I_\mu}P_{\mu v}S_{\mu v} - N_A\right). \end{aligned} \tag{18}$$

Here, E^{RHF} is the expectation value of the hamiltonian operator with a single-determinant wave function. The second term comes from the orthonormalization condition of the molecular orbitals, while the third one arises from each population restriction. The Euler–Lagrange equations from this problem lead to a matrix problem similar to Eq. (15):

$$\mathbf{F}'\mathbf{C} = \varepsilon'\mathbf{S}\mathbf{C}. \tag{19}$$

The modified Fock matrix, $\mathbf{F}'$, has the form:

$$\mathbf{F}' = \mathbf{F} - \sum_{A=1}^{r} \lambda_A \mathbf{G}^A, \quad G^A_{\mu\nu} \equiv \frac{1}{2}\left(\delta_{A,I_\mu} + \delta_{A,I_\nu}\right) S_{\mu\nu}. \tag{20}$$

Note that the modified Fock matrix is also hermitian.

It is important to note that the eigenvalues from Eq. (19) no longer approximate the ionization energies. However, following Koopmans' idea, we find that the ionization energies can be estimated from

$$IP_k \approx -\varepsilon'_k - \sum_{A=1}^{r} \lambda_A n_{Ak} \tag{21}$$

where n_{Ak} represents the contribution of the k-th orbital to the Mulliken population of the atom A and is given by:

$$n_{Ak} \equiv \sum_{\mu \in A} \sum_{\nu} C_{k\mu} C_{k\nu} S_{\mu\nu}, \quad n_A = \sum_{k=1}^{N} n_{Ak}. \tag{22}$$

For a given set of values of the Lagrange multipliers, $\{\lambda_A\}$, one can solve Eq. (19) and obtain the corresponding energy, the set of the molecular orbital coefficients, and the population on each atom. Since the atomic populations depend on the values of the Lagrange multipliers, one can specify the desired atomic populations and then get the right values of the Lagrange multiplier by solving the constraints,

$$n_A(\{\lambda_B\}) - N_A = 0, \quad A, B = 1, \ldots, r. \tag{23}$$

This set of equations is solved by using a multidimensional Newton–Raphson, or quasi-Newton variant, in a few iterations within any degree of precision. Usually, we take$0 = \lambda_1^{(0)} = \lambda_2^{(0)} = \cdots$ as a starting guess point and displacements below 0.1 to estimate the gradients.

This procedure is implemented in a proof of principle RHF code, and all the results in this paper are computed with the minimal basis set STO-3G.

3 Results and discussion

First, we apply the constrained minimization procedure to diatomic molecules, both homo- and heteronuclear. In this case, there is only one constraint, since the total number of electrons in the molecule is fixed. In every test, we find that the energy shows a quadratic-like dependence on the charge of the atom with the constrained population. The minimum value always corresponds to the Hartree–Fock energy ($\lambda_1 = 0$) because the HF determinant minimizes the expectation value of the Hamiltonian operator. Table 1 shows the energy (E) and charge (q_1) of the first atom for different values of the Lagrange multiplier (λ_1) in some diatomic molecules. The dependence of the energy with the charge can be observed in Fig. 1 for two representative diatomic molecules. It is important to mention that some diatomic charged species (NO^+, O_2^{2+}, HO^-, CN^-) are also included in the test set and their behavior shows no difference with respect to the neutral molecules.

Polyatomic highly symmetric molecules involving only two nonequivalent atoms, such as H_2O, CO_2, CH_4, and CF_4, show the same behavior when one restricts the charge of one atom, see Fig. 2. For other molecules, one can restrict the population on all atoms, but one. It is even possible to fix the population on one or more molecular fragments. The results always show that the energy has a quadratic-like dependence with respect to the fixed charges. It is precisely the quality of this quadratic dependence that underlies EEM. Note that this behavior was previously also observed by Cioslowski et al. [31].

The quadratic-like behavior obtained with the constrained HF method can be used to obtain useful EEM parameters by making use of the quadratic fitting of E^{RHF} as a function of q. For example, for a diatomic molecule, with charge Q, Eq. (10) can be written in the following way:

$$\begin{aligned} E_{mol} = {} & E_1^{o*} + E_2^{o*} + \chi_2^* Q + \frac{1}{2}\eta_2^* Q^2 \\ & + q_1\left(\chi_1^* - \chi_2^* - \eta_2^* Q + \frac{Q}{R}\right) + q_1^2\left(\frac{\eta_1^* + \eta_2^*}{2} - \frac{1}{R}\right). \end{aligned} \tag{24}$$

For a neutral homonuclear molecule, the linear term vanishes and the hardness comes from the quadratic coefficient of the fitting; see, for example, Fig. 1. In contrast, relative electronegativities can be obtained from the linear coefficient of the fitting of the data from the heteronuclear molecules. EEM parameters of some atoms obtained by this procedure are found in Table 2.

The atomic charges and the molecular electronegativity are solved from Eq. (14). Table 3 shows the comparison between the Mulliken charges from a RHF calculation and those from the EEM, using the parameters from Table 2. One can see that the atomic charges from both methods are in fairly good agreement given that they were obtained from only few molecules. In the more traditional EEM approach, parameters are obtained from molecules that mostly contain atoms of (nearly) all elements considered. In the present case, on the other hand, for the hardness only homonuclear diatomics are used.

For larger molecules, we find that the energy of the constrained HF procedure also shows a quadratic dependence with respect to the atomic charges. It is important to remark that the quadratic behavior comes from a truncated Taylor expansion, Eq. (9), and for large charges it may fail. For those cases, there are two alternative options. In the

Table 1 Energy (in Hartree) and Mulliken's atomic charge of the first atom as a function of the Lagrange multiplier, for some diatomic molecules

λ	NN		CO		FF	
	q_N	E	q_C	E	q_F	E
−1.0	2.03	−106.525635	1.73	−110.530475	0.74	−195.651614
−0.9	1.85	−106.692935	1.62	−110.634766	0.69	−195.697961
−0.8	1.67	−106.849769	1.50	−110.737606	0.64	−195.745043
−0.7	1.48	−106.993748	1.37	−110.836596	0.57	−195.791558
−0.6	1.28	−107.122769	1.23	−110.929219	0.50	−195.836022
−0.5	1.07	−107.235017	1.08	−111.012983	0.43	−195.876883
−0.4	0.86	−107.328957	0.91	−111.085538	0.35	−195.912641
−0.3	0.65	−107.403332	0.75	−111.144760	0.27	−195.941953
−0.2	0.44	−107.457163	0.57	−111.188802	0.18	−195.963711
−0.1	0.22	−107.489744	0.39	−111.216114	0.09	−195.977100
0.0	0.00	−107.500651	0.20	−111.225446	0.00	−195.981619
0.1	−0.22	−107.489744	0.01	−111.215842	−0.09	−195.977100
0.2	−0.44	−107.457163	−0.19	−111.186619	−0.18	−195.963711
0.3	−0.65	−107.403332	−0.38	−111.137356	−0.27	−195.941953
0.4	−0.86	−107.328957	−0.58	−111.067872	−0.35	−195.912641
0.5	−1.07	−107.235017	−0.78	−110.978210	−0.43	−195.876883
0.6	−1.28	−107.122769	−0.98	−110.868621	−0.50	−195.836022
0.7	−1.48	−106.993748	−1.18	−110.739544	−0.57	−195.791558
0.8	−1.67	−106.849769	−1.38	−110.591599	−0.64	−195.745043
0.9	−1.85	−106.692935	−1.57	−110.425574	−0.69	−195.697961
1.0	−2.03	−106.525635	−1.77	−110.242423	−0.74	−195.651614

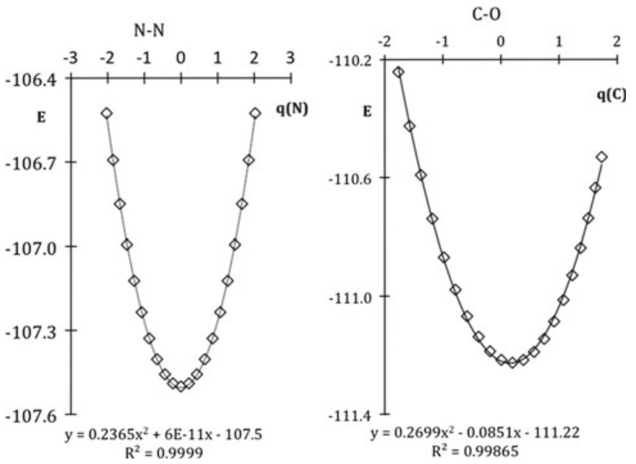

Fig. 1 Atomic charge–energy plots for two representative diatomic molecules. Energy values in Hartree. The *diamonds* are the results of the constrained RHF calculations, while the *curve* is a quadratic fit

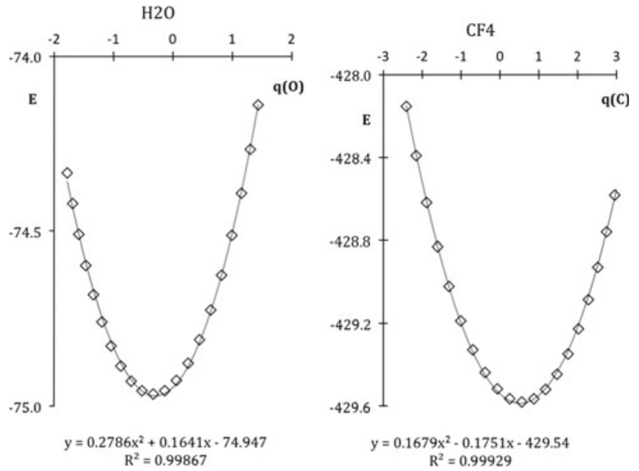

Fig. 2 Atomic charge–energy plots for two binary polyatomic molecules. Energy values in Hartree. The *diamonds* are the results of the constrained RHF calculations, while the *curve* is a quadratic fit

first option, one must add more terms to Eq. (9), which leads to a set of nonlinear equations, in addition to the need of new parameters. The second one consists in a shift of the reference system for the Taylor expansion, which keeps the quadratic form, but one has to take care of the terms from the shift and modify the equations accordingly. As a consequence, it is no longer possible to directly interpret relative values for EEM parameters (such as, e.g., the carbon versus oxygen electronegativity) with respect to expected trends in the periodic system as the latter are based on neutral atoms as reference.

To test whether the quadratic expansion applied to every atom still results in good regressions, some larger

Table 2 EEM parameters from the quadratic fitting of the constrained HF model

A	η_A^*	$\chi_A^* - \chi_H^*$
H	1.108	0.000
C	0.620	0.036
N	0.703	0.097
O	0.789	0.121
F	0.960	0.176

All values are reported in atomic units

The homonuclear diatomic molecules H_2, C_2, N_2, O_2^{2+}, and F_2 are used to obtain the quasi-atomic hardnesses, while CO, CN^-, OH^-, and HF are used for the quasi-atomic electronegativities. The procedure is described in the text

Table 3 EEM charges for some simple molecules computed with the parameters from Table 2

Molecule	Atom	Charge	
		EEM	HF
CO_2	C	0.36	0.44
	O	−0.18	−0.22
H_2O	H	0.14	0.17
	O	−0.27	−0.33
NH_3	N	−0.37	−0.44
	H	0.12	0.15
HCN	H	0.03	0.15
	C	0.11	0.01
	N	−0.14	−0.16
H_2CO	H	0.04	0.06
	C	0.07	0.07
	O	−0.15	−0.19
CH_4	C	−0.25	−0.26
	H	0.06	0.07
CF_4	C	0.53	0.57
	F	−0.13	−0.14

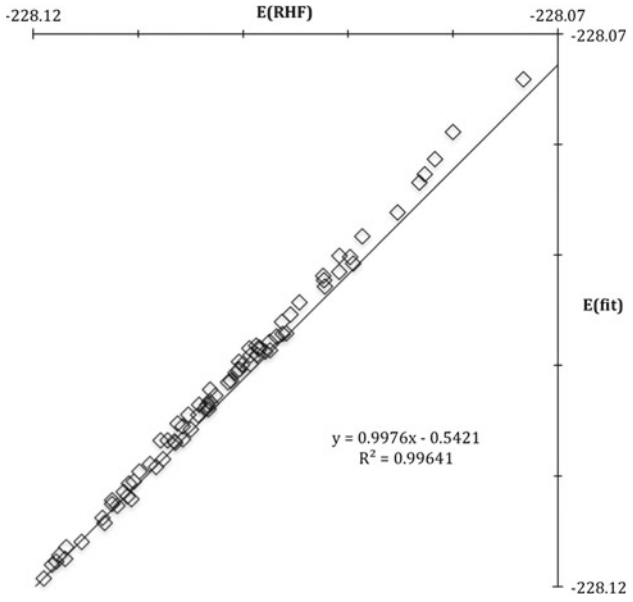

Fig. 3 Comparison between the constrained RHF energy and the quadratic fit for tetrahydrofurane. Energy values in Hartree

molecules were also included in the test set. As an example, we discuss the tetrahydrofurane molecule that contains 13 atoms. The straightforward adaptation of the algorithm developed above resulted in good performance although two further improvements were obtained upon changing two steps. The first is the use of a random assignment of atomic populations among all atoms but limited to within deviations from the reference of maximally 0.3 electrons for each atom. Second, the reference has been changed from neutral atoms to atoms with atomic population as found in the unconstrained Hartree–Fock minimum. Using as input a total of 130 (i.e., 10 times the number of atoms) constrained Hartree–Fock energy evaluations with randomly displaced atomic populations, parameters for the different atoms were fitted in a least square sense to minimize the difference between the constrained Hartree–Fock energy and that based on sums of quadratic atomic approximations. Using singular value decomposition to perform the least squares fit, we find that the summed quadratic model is very good with on average over the 130 points an absolute error in energy of ca. 0.5 milliHartree. Fig. 3 shows the regression quality between both data sets.

As a test of the performance of the optimized parameters in Mulliken charges derived from EEM expressions, we also compared both sets of charges, ab initio and EEM based. As expected on the basis of the excellent regression, the charges are also reproduced very well, see Table 4.

A remarkable feature of these results is that the quadratic form in Eq. (10) produces excellent fits to the constrained RHF data, even though the quadratic form is incomplete. The only off-diagonal quadratic terms are due to the electrostatic interaction between the atoms, Eq. (8).

For a different population analysis model, the constraint takes a different form. For example, in the Hirshfeld method [32], the atomic population takes the form:

$$
\begin{aligned}
n_A^H &= \int w_A^H(\vec{r})\rho(\vec{r})\mathrm{d}\vec{r} = \sum_{\mu\nu} P_{\mu\nu} \int w_A^H(\vec{r})\chi_\mu(\vec{r})\chi_\nu(\vec{r})\mathrm{d}\vec{r} \\
&\equiv \sum_{\mu\nu} P_{\mu\nu} G_{\mu\nu}^A
\end{aligned}
\tag{25}
$$

where w_A^H are the Hirshfeld weight factors, which are independent of the molecular density. The constrained minimization leads to an Euler–Lagrange equation that has

Table 4 Comparison of the atomic charges from the fitting parameters and RHF for tetrahydrofurane

Atom	EEM	Mulliken
O	−0.275	−0.273
C_a	0.009	0.008
$C_{a'}$	0.007	0.008
C_b	−0.115	−0.117
$C_{b'}$	−0.117	−0.117
H_a	0.064	0.064
H_a	0.056	0.055
$H_{a'}$	0.065	0.064
$H_{a'}$	0.058	0.055
H_b	0.061	0.065
H_b	0.061	0.062
$H_{b'}$	0.064	0.065
$H_{b'}$	0.062	0.062

the same form of Eq. (19), but the modified Fock matrix becomes

$$F'_{\mu\nu} \equiv F_{\mu\nu} - \sum_{A} \lambda_A G^{A}_{\mu\nu}. \tag{26}$$

In other cases, a constraint written in terms of the coefficients or the density can be easily incorporated into the constrained procedure.

The implementation of our model in a KS code will be very similar to the procedure described above. A small variation in the parameters is expected due to the inclusion of the correlation effects, but not in the trend along the periodic table.

4 Concluding remarks

The addition of atomic charge constraints to the self-consistent RHF procedure yields a quadratic relationship between the energy and the atomic charges. This behavior provides an alternative way to obtain EEM parameters, which produce atomic charges in good agreement with those from the RHF method. The advantages of the present approach are that one can obtain EEM parameters from one specific molecule instead of requiring several sets of atomic charges for a range of molecules. Second, the performance of the constrained method numerically supports the assumptions from which the EEM is derived.

The use of other kinds of constraints in the electronic structure calculations is currently under exploration.

Acknowledgments A. C. thanks support from CONACYT through the grant 155070 and the sabbatical scholarship. We also thank Laboratorio de Supercómputo y Visualización en Paralelo (UAM-I) for the access to its computing facilities. P. B. Acknowledges the Fund for Scientific Research (FWO Vlaanderen) for continuous support. This work was also carried out using the Stevin Supercomputer Infrastructure at Ghent University, funded by Ghent University, the Hercules Foundation and the Flemish Government—department EWI.

References

1. Mortier WJ, Ghosh SK, Shankar S (1986) J Am Chem Soc 108:4315–4320
2. Mortier WJ (1987) In: Sen KD, Jorgensen CK (eds) Electronegativity. Springer, Berlin
3. Baekelandt BG, Mortier WJ, Schoonheydt RA (1992) In: Sen KD (ed) Chemical hardness. Springer, Berlin
4. Blanco MA, Martín-Pendás A, Francisco E (2005) J Chem Theory Comput 1:1096–1109
5. Vanfleteren D, Ghillemijn D, Van Neck D, Bultinck P, Waroquier M, Ayers PW (2011) J Comput Chem 32:3485–3496
6. Mayer I (2007) Faraday Discuss 135:439–450
7. Parr RG, Yang W (1989) Density functional theory of atoms and molecules. New York, Oxford
8. Politzer P, Weinstein H (1979) J Chem Phys 71:4218–4220
9. Sanderson RT (1951) Science 114:670
10. Sanderson RT (1983) Polar CoValence. Academic Press, New York
11. Baekelandt B, Mortier W, Lievens J, Schoonheydt R (1991) J Am Chem Soc 113:6730–6734
12. Rappe A, Goddard W (1991) J Phys Chem 95:3358–3363
13. Menegon G, Shimizu K, Farah JPS, Dias LG, Chaimovich H (2002) Phys Chem Chem Phys 4:5933–5936
14. Bultinck P, Langenaeker W, Lahorte P, De Proft F, Geerlings P, Waroquier M, Tollenaere JP (2002) J Phys Chem A 106:7887–7894
15. Bultinck P, Langenaeker W, Lahorte P, De Proft F, Geerlings P, Van Alsenoy C, Tollenaere JP (2002) J Phys Chem A 106:7895–7901
16. Bultinck P, Vanholme R, Popelier P, De Proft F, Geerlings P (2004) J Phys Chem A 108:10359–10366
17. Verstraelen T, Van Speybroeck V, Waroquier M (2009) J Chem Phys 131:044127
18. Verstraelen T, Bultinck P, Van Speybroeck V, Ayers PW, Van Neck D, Waroquier M (2011) J Chem Theory Comput 7:1750–1764
19. Bultinck P, Carbó-Dorca R (2002) Chem Phys Lett 364:357–362
20. Bultinck P, Langenaeker W, Carbó-Dorca R, Tollenaere JP (2003) J Chem Inf Comput Sci 43:422–428
21. York DM, Yang W (1996) J Chem Phys 104:159–172
22. Chelli R, Procacci P, Righini R, Califano S (1999) J Chem Phys 111:8569–8575
23. Warshel A, Kato M, Pisliakov AV (2007) J Chem Theory Comput 3:2034–2045
24. van Duin ACT, Strachan A, Stewman S, Zhang Q, Xu X, Goddard WA (2003) J Phys Chem A 107:3803–3811
25. Szabo A, Ostlund NS (1982) Modern quantum chemistry. Macmillan, New York
26. Mulliken RS (1955) J Chem Phys 23:1833–1840
27. Dederichs PH, Blügel S, Zeller R, Akai H (1984) Phys Rev Lett 53:2512–2515
28. Wu Q, Van Voorhis T (2005) Phys Rev A 72:024502
29. Wu Q, Van Voorhis T (2006) J Chem Theory Comput 2:765–774
30. Kaduk B, Kovalczyk T, Van Voorhis T (2012) Chem Rev 112:321–370
31. Cioslowski J, Stefanov BB (1993) J Chem Phys 99:5151–5162
32. Hirshfeld FL (1977) Theor Chim Acta 44:129–138

Theor Chem Acc (2012) 131:1234
DOI 10.1007/s00214-012-1234-7

REGULAR ARTICLE

Host–guest and guest–guest interactions between xylene isomers confined in the MIL-47(V) pore system

**An Ghysels · Matthias Vandichel · Toon Verstraelen ·
Monique A. van der Veen · Dirk E. De Vos ·
Michel Waroquier · Veronique Van Speybroeck**

Received: 1 March 2012 / Accepted: 8 May 2012 / Published online: 21 June 2012

Abstract The porous MIL-47 material shows a selective adsorption behavior for para-, ortho-, and meta-isomers of xylenes, making the material a serious candidate for separation applications. The origin of the selectivity lies in the differences in interactions (energetic) and confining (entropic). This paper investigates the xylene–framework interactions and the xylene–xylene interactions with quantum mechanical calculations, using a dispersion-corrected density functional and periodic boundary conditions to describe the crystal. First, the strength and geometrical characteristics of the optimal xylene–xylene interactions are quantified by studying the pure and mixed pairs in gas phase. An extended set of initial structures is created and optimized to sample as many relative orientations and distances as possible. Next, the pairs are brought in the pores of MIL-47. The interaction with the terephthalic linkers and other xylenes increases the stacking energy in gas phase (−31.7 kJ/mol per pair) by roughly a factor four in the fully loaded state (−58.3 kJ/mol per xylene). Our decomposition of the adsorption energy shows various trends in the contributing xylene–xylene interactions. The absence of a significant difference in energetics between the isomers indicates that entropic effects must be mainly responsible for the separation behavior.

Keywords Adsorption · MIL-47 · DFT-D · Xylenes · Separation

1 Introduction

Since a couple of years, metal organic frameworks (MOFs) are a topical theme; they represent a new class of porous materials with extraordinary physicochemical and mechanical properties due to their hybrid architecture of organic and inorganic building blocks [1–3]. Their applications in the field of gas adsorption, storage, gas separation, and catalysis are almost inexhaustible due to the specificity of the hybrid organic–inorganic composition [4–7]. Examples of their fascinating properties are the flexibility of the framework, the appearance of catalytic sites in the pores, etc. These are a consequence of the unique combination of properties typical for metals and organic species.

In previous work, some of the authors showed that metal organic frameworks could be successfully used as selective adsorbents for the industrially relevant separations of para-xylene (pX) versus meta-xylene (mX) and ortho-xylene (oX) versus ethylbenzene (eB) [8–10]. The separation of mixed C8 alkylaromatic compounds is one of the most challenging issues in the chemical industry, for example because of its direct link with PET production [11]. Among the various types of MOFs that have been tested, the MIL-47 material proved to be very successful. This MOF

Published as part of the special collection of articles celebrating theoretical and computational chemistry in Belgium.

Electronic supplementary material The online version of this article (doi:10.1007/s00214-012-1234-7) contains supplementary material, which is available to authorized users.

A. Ghysels (✉) · M. Vandichel · T. Verstraelen ·
M. Waroquier · V. Van Speybroeck (✉)
Center for Molecular Modeling, Quantum Chemistry-Molecular Modeling Alliance, Ghent University, Technologiepark 903, 9052 Ghent, Belgium
e-mail: an.ghysels@ugent.be

V. Van Speybroeck
e-mail: veronique.vanspeybroeck@ugent.be

M. A. van der Veen · D. E. De Vos
Centre for Surface Chemistry and Catalysis, KU Leuven, Kasteelpark Arenberg 23, 3001 Heverlee, Belgium

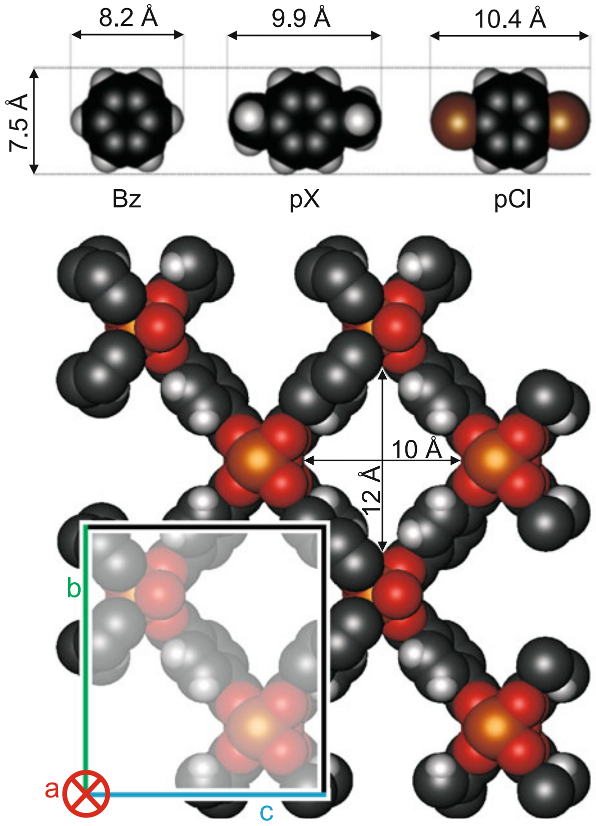

Fig. 1 MIL-47 consists of terephthalic linkers connected by VO^{2+} ions. Xylenes adsorb well in the one-dimensional pore channels. View along the *a* direction; four unit cells are displayed. The pore dimensions of MIL-47 and the characteristic dimensions of the adsorbates are estimated by assigning van der Waals radii to the atoms

consists of one-dimensional pores in which terephthalate ligands are connected by VO^{2+} ions (Fig. 1). MIL-47 is one of an impressive series of MOFs that were synthesized by Férey et al. [12]. It is not completely clear what mechanism is responsible for the preference of adsorption between the three types of xylene isomers and ethylbenzene. In this paper, we try to unravel the molecular interactions between pairs of adsorbed xylenes and between xylenes and organic linkers using in silico experiments. The interactions are studied with quantum mechanical periodic modeling. Once the mechanism of selectivity in adsorption has been understood, the obtained knowledge can be used for designing new materials with tailor-made properties toward gas separation and to possibly modify the organic linkers to control the affinity for specific aromatic adsorbates.

Long-range dispersion interactions and more particularly π–π stacking interactions will manifestly play an important role for the organization of xylenes in the pore. Basically, only very advanced ab initio correlated wave function methods are able to account for these effects, but they are computationally too demanding to apply to our system. Nowadays, density functional theory (DFT) is the most widely used method for electronic structure calculations for extended molecular systems, but without modifications, these methods are not able to account for long-range electrostatic correlations that are responsible for the dispersion forces. Grimme et al. [13–15] proposed the DFT-D method in which an empirical C_6R^{-6} correction is added to the standard density functionals. This method is able to account for the π–π interactions in MOFs [14].

Several molecular modeling studies investigated various adsorbates with grand canonical Monte Carlo techniques (GCMC) on MIL-47: N_2 [16], CO_2 [17], CH_4 [18], H_2 [19], and xylenes [20]. GCMC techniques usually rely on fast classical force field descriptions of the global potential energy of the system. So, GCMC techniques allow a fast computation of thermodynamic quantities and they have been frequently and successfully applied to explain separations over MOFs [16, 20–24]. The force fields required to perform the molecular simulations are taken from the literature. The accuracy of these classical approaches will certainly be improved in the near future when more advanced force fields are available for these particular MOFs that also account for the flexibility of the framework [25]. In the MIL-47 study by Castillo et al. [20], good agreement is found with isotherm experiments using a model with partial atomic charges and the Lennard-Jones potential for the van der Waals interactions. The framework is kept rigid during the simulations. The computed mixture isotherms of the xylene isomers lead to separation factors in MIL-47 predicting a preferential adsorption for ortho-xylene (oX), closely followed by para (pX), and then meta (mX). The adsorption selectivity was found to increase with pressure and the results agree with the experimental findings. The computed adsorption isotherms manifestly overestimate the loading of para- and ortho-xylene at the lowest temperatures. The authors attribute this discrepancy to small changes in the framework structure with temperature. The saturation loading reached in their simulations was about 4 molecules per unit cell, while experimentally the maximum loading was 3.4 molecules per unit cell [8, 9].

The selectivity of xylene isomers in MIL-47 most likely originates from packing effects, as suggested by Alaerts and Finsy et al. [8, 9]. It has been speculated that molecules are adsorbed by pairs at high loadings, their benzene rings facing each other and approximately parallel to the aromatic rings of the terephthalate linkers. Additionally, the spatial arrangement of the methyl groups of each xylene should play a significant role in the determination of the preferential adsorption. It is suspected that the crude force field used in the work of Castillo et al. cannot properly describe these packing effects. With the current lack of suitable more accurate force fields, quantum chemical DFT-D calculations can give some added value in the underlying mechanism for the selective adsorption of xylene isomers. Stacking effects are more accurately described when taking into account the long-range dispersion interactions by using the empirical Grimme corrections [13] complementary to the standard density functionals. A DFT-D approach also has the advantage that the adsorption and stacking energy can be decoupled in various contributions elucidating the interactions responsible for the observed different adsorption behavior. In contrast to the molecular simulations of Castillo et al. [20], we also incorporate in this study the packing of mixed xylene pairs such as pX–oX, pX–mX and oX–mX.

In this work, we first investigate xylene–xylene interactions in the gas phase. The strength of the xylene stacking energy is compared to the stacking energy of benzene pairs and dichlorobenzene pairs. Benzene stacking is well studied [26–28], and dichlorobenzene adsorption shows experimentally a similar selectivity behavior in MIL-47 as xylenes [29]. Next, the pairs are embedded in the MIL-47 framework respecting the maximum loading of two xylene pairs in one unit cell. An extensive set of configurations for the adsorbed xylenes is generated. As such, we are able to validate the effect of the confined environment and interaction with the walls of the material. The adsorption energy of the most stable configuration is studied in detail using an energy decomposition scheme to achieve more insight into the host–guest and guest–guest interactions.

2 Computational methods

2.1 Characterization of a xylene pair

A thorough study on the interaction between xylene pairs will be performed, and thus it is essential to give a good definition of their relative position with respect to each other. The relative position and orientation of a xylene pair is characterized by attaching a Cartesian coordinate frame to each xylene (Fig. 2a) [30] denoted as $(O_1, \boldsymbol{x}_1, \boldsymbol{y}_1, z_1)$ and $(O_2, \boldsymbol{x}_2, \boldsymbol{y}_2, z_2)$ for the two xylenes, X_1 and X_2, respectively. The $\boldsymbol{x}$-axis always coincides with the twofold rotational symmetry axis of each xylene. Note that in the three-dimensional structure, the orientation of the methyl groups may prevent the existence of this C_2 symmetry, but the symmetry axis is always present in the projection on paper (Fig. 2a). The sense of z_2 is chosen such that the angle between z_1 and z_2 is less than 90°. In principle, the relative orientation of two molecules is completely characterized by six parameters. For this work, we only consider the four most important internal coordinate parameters to describe their relative orientation: distance (d), shift (s), tilt (θ), and phase (φ). These are defined below such that an interchange of X_1 and X_2 or a point inversion results in the same values for these four parameters.

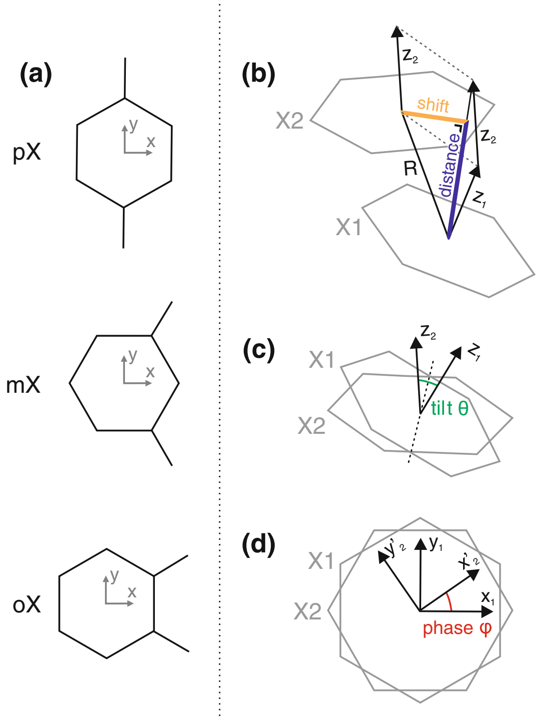

Fig. 2 A coordinate system is attached to each xylene (X_1 and X_2) in a xylene pair. Four parameters are defined to describe their relative position and orientation: shift (s), distance (d), tilt (θ), and phase (φ)

The distance parameter d is the length of the projection of the vector $\boldsymbol{R}$ (connecting the centers of the six-membered rings) on the vector $z_1 + z_2$ (Fig. 2b). The length of the orthogonal complement in this projection is called the shift s. Next, X_2 is translated over the vector $\boldsymbol{R}$ to bring the geometric centers of the six-membered rings on top of each other (Fig. 2c). The tilt θ is defined as the angle between the z_1- and z_2-axis. X_2 is then rotated over θ about the vector $z_1 \times z_2$, such that $(O_2', \boldsymbol{x}_2, \boldsymbol{y}_2, z_2) \rightarrow (O_2', \boldsymbol{x}_2', \boldsymbol{y}_2', z_1)$; the z-axes of the xylenes are now aligned and the $\boldsymbol{x}$-axes and $\boldsymbol{y}$-axes lie in the same plane (Fig. 2d). Finally, the phase φ is determined as the absolute value of the angle between the $\boldsymbol{x}_1$- and $\boldsymbol{x}_2'$-axis.

The above procedure is also applied to a benzene pair and dichlorobenzene pairs.

2.2 Quantumchemical modeling

Density functional theory calculations are carried out using the CPMD code, which allows to simulate systems with periodic boundary conditions [31]. The BP exchange correlation functional [32] is used with ultrasoft Vanderbilt pseudopotentials [33], especially designed to work with a

25 Ry cut off for the auxiliary plane wave grid. To include the possible effects of π–π interactions, the BP functional is combined with the Grimme dispersion correction for van der Waals interactions [13]. Three types of systems are simulated: xylenes in vacuum, the empty MIL-47 framework, and the fully loaded MIL-47 framework with four xylenes per unit cell.

Vacuum calculations of a xylene molecule or a pair of xylenes are performed in a large box of $20 \times 20 \times 20$ Å^3 and are labeled with 'vac'. The investigated molecules are para-xylene (pX), ortho-xylene (oX), and meta-xylene (mX). In addition, benzene (Bz) and dichlorobenzenes in para-, ortho-, and meta-configuration (pCl, oCl, mCl) are simulated in vacuum for comparison.

The initial framework geometry of the empty MIL-47 is taken directly from the refined structure obtained by X-ray diffraction (Supp. Info. of Ref. [12], CCDC-166785, orthorhombic unit cell with $a = 6.8179$ Å, $b = 16.1433$ Å, $c = 13.9392$ Å). In the energy minimization, the internal coordinates are optimized while the unit cell parameters are kept fixed at the experimental values. The metal V^{4+} ions in MIL-47 have each spin ½. The unit cell containing four vanadium centers can have a total spin of 0, 1, or 2. The most stable structure corresponds with $S = 1$, and the gain in energy with respect to the $S = 0$ system amounts to 80 kJ/mol per unit cell. As adsorption energies require the computation of differences in energy, the differences due to the usage of another spin state cancel out if we consistently use the same total spin for the framework. In view of the computational cost, all calculations were performed with $S = 0$.

In the fully loaded state, two xylene pairs are inserted in the pores of MIL-47 with the Zeobuilder package [34], and the geometry is optimized with CPMD [31]. The experimental unit cell parameters are used when MIL-47 is fully loaded with pure pX, oX, or mX (codes CCDC-632101, CCDC-632102, CCDC-632103, respectively [8]). Because of lack of experimental values during multicomponent adsorption experiments, the cell parameters are chosen somewhat arbitrarily when MIL-47 is fully loaded with a mixture of the xylene isomers: the pure oX experimental parameters for the pX–oX mixture (code CCDC-632102 [8]) and the empty framework parameters for pX–mX and oX–mX mixtures (code CCDC-166785 [12]). The variation in cell parameters among the structures is minimal, and keeping them fixed during the geometry optimization is an approximation whose effect is expected to largely cancel when calculating energy differences. The coordinate files of the optimized structures are available in the Supporting Information for the empty framework and the various fully loaded states. The decomposition of adsorption energies in Sect. 3 is derived from static calculations, where xylenes or framework atoms are removed from the fully loaded state and the energy is calculated without prior geometry optimization. These energies are labeled with 'stat'.

3 Results and discussion

3.1 Guest–guest interactions in gas phase

Before tackling the xylenes interactions in the MIL-47 pore system, it is useful to have an understanding of the stacking of xylenes in the gas phase. Therefore, we construct a series of xylene pairs, and the geometry and the stacking energy are investigated for each of them. The geometry is characterized by the four geometry parameters in Fig. 2: shift, distance, tilt, and phase. The stacking energy is calculated from the optimized geometry of the individual xylene molecules X_1 and X_2 and of a xylene pair P_{12}. The *stacking energy* is defined as

$$\Delta E^{\mathrm{vac}}_{\mathrm{stack}}(P_{12}) = E^{\mathrm{vac}}(P_{12}) - E^{\mathrm{vac}}(X_1) - E^{\mathrm{vac}}(X_2) \tag{1}$$

Six pairs are studied: 'pure' pairs (pX–pX, oX–oX, mX–mX) and 'mixed' pairs (oX–mX, oX–pX, pX–mX). An extensive set of initial structures (Fig. 3) is generated by varying the distance d and the phase φ between the pairs: d varies between 2.8 and 4.6 Å with steps of 0.2 Å, while φ is increased with steps of 30° until a symmetrically equivalent structure is met. The initial shift s and tilt θ are set to zero. The geometries of these 330 initial structures are optimized in a large box (vacuum). For each pair, the optimized geometries are ordered according to increasing energy (E_1, E_2,…).

Table 1 presents the geometrical properties and stacking energies for the following two cases. First, the geometrical properties are calculated for the geometry with the lowest energy E_1. Second, in case of thermal equilibrium, the thermal average of a property A is obtained by weighting the contribution of each geometry by its Boltzmann probability $p(E_i)$,

$$p(E_i) = \exp\left(-\frac{E_i}{k_B T}\right) \Bigg/ \sum_j \exp\left(-\frac{E_j}{k_B T}\right) \tag{2}$$

$$\langle A \rangle = \sum_i p(E_i) A(i) \tag{3}$$

with T the temperature and k_B the Boltzmann constant. Due to temperature, not only the lowest energy state E_1 of a pair is populated, but also nearby minima can be reached. It should be noted, however, that our formula only sums over local minima but no nearby non-equilibrium states, which would be required for accurate thermodynamics.

The probability distribution $p(E_i)$ favors the lowest energy geometry E_1 largely at 300 K (highly peaked distribution in Supp. Info. Fig. 1), making this geometry the

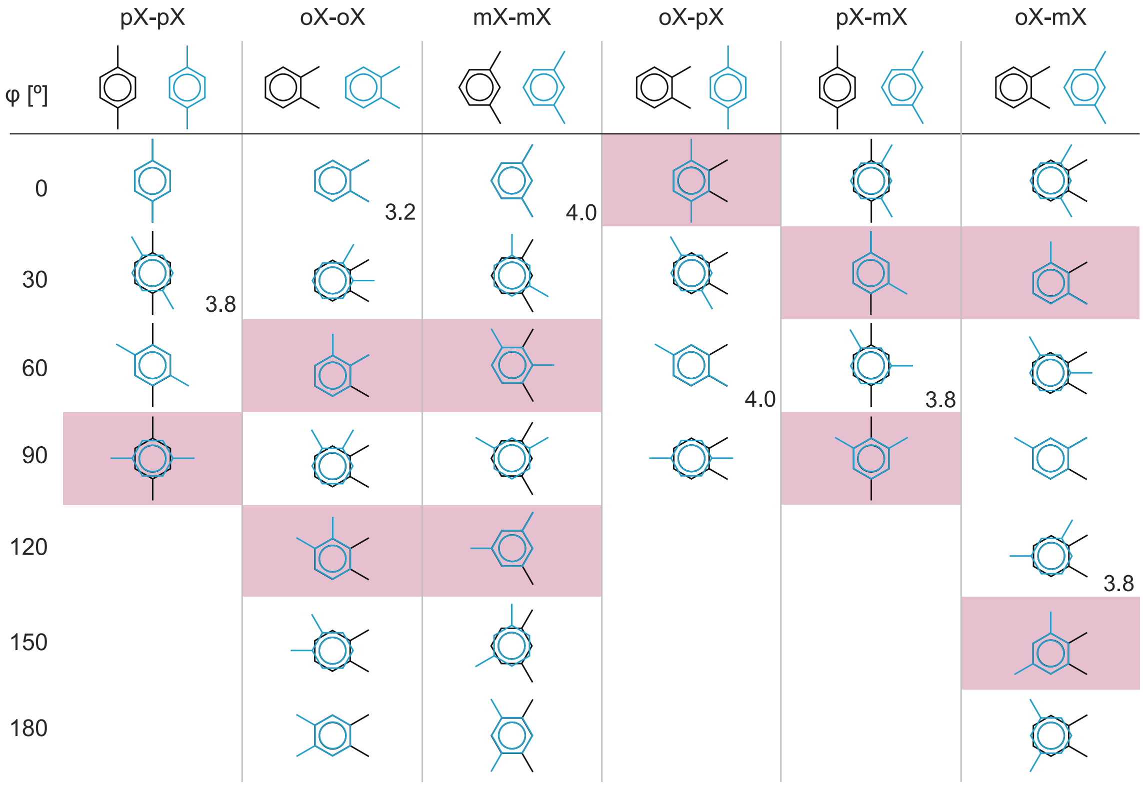

Fig. 3 Initial geometries of six xylene pairs are obtained by varying the phase φ and the distance *d*. A similar study is performed for dichlorobenzene pairs. Orientations that do not fit in the MIL-47 pores are given a *red* background. The initial geometries leading to the most stable structure are labeled with the initial distance

dominant contribution to the sum in Eq. (3). Indeed, the lowest energy properties correlate well with the thermal average properties in Table 1. Figure 4 illustrates the shift and distance parameters in the optimized benzene pair and the most stable pure xylene pairs. Clearly, the pairs take the parallel-displaced configuration.

The stacking energy $\Delta E^{\mathrm{vac}}_{\mathrm{stack}}$ is favorable for benzene, xylenes, and dichlorobenzenes. Xylene pairs are the most stable with an average stacking energy of −31.7 kJ/mol, followed by the dichlorobenzene pairs with −24.3 kJ/mol and benzene pairs with −19.7 kJ/mol. Aromatic π–π stacking has been extensively studied for benzene pairs [35–43], and it was found that T-shaped and parallel-displaced configurations have nearly equal stacking energy, being slightly more stable than the face-to-face sandwich configuration [26–28]. The benzene pair geometry in Table 1 is the parallel-displaced configuration. These studies also indicate that substituents typically make the stacking stronger with respect to benzene stacking, which is confirmed in our results for methyl and chlorine substituents [44–46].

Moreover, Table 1 suggests a relationship between the stacking energy and some of the geometrical parameters. The absolute value of the stacking energy correlates negatively with the distance (Fig. 5) and positively with the shift, whereas it appears to be relatively independent of the tilt and the phase. This means that the most favorable stacking is obtained when the rings lie close to each other and are somewhat shifted. Indeed, perfectly stacked rings with zero shift are less stable than parallel-displaced rings. The xylenes have higher shifts and lower distances than the dichlorobenzenes, thus explaining the systematically stronger stacking energy of the xylenes. The benzene pair is an outlier and does not follow this trend.

3.2 MIL-47 packed with four xylenes: decomposition of the adsorption energy

The stacking of xylenes is a favorable interaction in the gas phase of the order of −31.7 kJ/mol. Since the walls of the MIL-47 pores contain aromatic rings in the terephthalic linkers, it is expected that adsorbed xylenes are stabilized by an additional stacking energy: the interaction between the adsorbed xylenes and the framework, that is, the so-called host–guest interactions. We have investigated the geometrical characteristics and adsorption energy when MIL-47 is loaded with a xylene pair in each of its pores, which amounts to a total of four xylenes (two pairs) per unit cell. The adsorption energy is calculated as the difference in energy between the framework wherein two

Table 1 The geometrical parameters (shift s, distance d, tilt θ, and phase φ) and stacking energy (Eq. 1) calculated for the optimized structure with lowest energy and calculated as a thermal average

	Lowest energy geometry					300 K	Thermal average 300 K				
	Shift (Å)	Distance (Å)	Tilt (°)	Phase (°)	ΔE^{vac}_{stack} (kJ/mol)	$p(E_1)$	⟨Shift⟩ (Å)	⟨Distance⟩ (Å)	⟨Tilt⟩ (°)	⟨Phase⟩ (°)	$\langle \Delta E^{vac}_{stack} \rangle$ (kJ/mol)
Bz–Bz	1.66	3.22	5.5	9.0	−19.7	1.0	1.66	3.22	5.5	9.0	−19.7
pX–pX	0.8	3.27	3.3	38.5	−31.1	0.3	0.6	3.31	4.0	80.3	−28.5
oX–oX	1.3	3.25	2.6	41.9	−32.6	0.8	1.1	3.30	3.3	47.6	−30.3
mX–mX	1.5	3.22	4.7	104.9	−33.0	0.4	1.2	3.28	5.3	75.1	−30.6
pX–oX	1.3	3.34	4.2	102.5	−34.5	0.3	1.3	3.30	3.6	162.7	−32.7
pX–mX	1.4	3.20	8.9	−15.8	−36.3	0.5	1.3	3.23	7.5	29.0	−33.8
oX–mX	1.5	3.28	1.0	−26.9	−37.1	0.5	1.3	3.27	2.4	−25.3	−34.4
Average	*1.3*	*3.26*	*4.1*	*40.8*	*−34.1*	*0.4*	*1.1*	*3.28*	*4.4*	*61.6*	*−31.7*
pCl–pCl	1.1	3.17	4.1	59.4	−28.0	0.3	0.5	3.30	3.2	80.5	−24.1
oCl–oCl	0.9	3.27	2.9	124.6	−27.8	0.2	0.6	3.33	2.4	140.5	−25.2
mCl–mCl	0.4	3.40	9.6	64.0	−24.8	0.1	0.3	3.40	5.0	85.8	−21.6
pCl–oCl	0.9	3.28	1.9	152.5	−25.1	0.1	0.5	3.36	4.9	168.8	−22.5
pCl–mCl	0.9	3.23	5.9	91.7	−28.3	0.2	0.8	3.29	4.2	84.5	−25.3
oCl–mCl	1.0	3.24	2.5	−149.5	−29.9	0.3	0.8	3.29	2.3	−123.1	−27.0
Average	*0.9*	*3.27*	*4.5*	*57.1*	*−27.3*	*0.2*	*0.6*	*3.33*	*3.7*	*72.8*	*−24.3*

The probability $p(E_1)$ to find the structure in the lowest energy state at 300 K is also listed. Averages in the table are taken over the six xylene pairs and over the six dichlorobenzene pairs

pairs (P_{12}, P_{34}) are adsorbed, the empty framework (F), and the individual xylene molecules (X_1, X_2, X_3, X_4),

$$\Delta E_{ads}(P_{12}, P_{34}) = E(F, P_{12}, P_{34}) - E(F) - E^{vac}(X_1) - E^{vac}(X_2) - E^{vac}(X_3) - E^{vac}(X_4) \quad (4)$$

Both guest–guest and guest–host interactions contribute to this adsorption energy.

In order to find the most favorable configurations of xylene pairs in the framework, an extensive set of initial structures is generated in a similar fashion as in the gas phase analysis in Sect 2.1. Each unit cell contains two pores, and each pore is filled with a xylene pair. As in the gas phase, the list of pair geometries is generated systematically by varying the distance d between 2.8 and 4.0 Å in steps of 0.2 Å and by varying the phase φ in steps of 30°. This gives 231 initial pair geometries, as shown in Fig. 3. However, the confinement in the pore prevents some of the proposed pairs to be adsorbed (these orientations are given a red background in Fig. 3), leaving 161 plausible initial pair geometries. We adopt now the following procedure, as depicted in Fig. 6: for each of the plausible pair geometries, a duplicate is placed in the center of the first pore and another in the center of the second pore. This procedure results in 161 initial structures for fully loaded MIL-47.

An extra degree of freedom in the adsorbed state, compared to the gas phase, is the relative orientation of a pair as a whole with respect to the framework. Whereas rotating a pair or applying symmetry operations does not affect the energy in vacuum, this symmetry is broken when a pair is brought in the pores. Our 161 initial structures only represent 23 possible pair orientations. Unfortunately, a full sampling of this orientational degree of freedom is computationally not feasible. Nevertheless, we have added 15 orientations to improve the sampling, mainly for the mixed pairs which have lower symmetry than the pure pairs. In total, 266 initial structures for the fully loaded MIL-47 are created and optimized.

The geometry of each initial structure for the fully loaded state is optimized. Figure 7 shows the resulting geometries of the adsorbed pure pairs, and the mixed pairs are given in Figures 6–8 of the Supp. Info. For a given pore filling, the geometries are ordered according to increasing energy and the probability distribution is calculated (Eq. 2). Since the Boltzmann distribution is peaked (Supp. Info. Fig. 2), only the dominant geometry with the lowest energy is considered in the remainder of this section.

Comparison of the geometrical parameters of the adsorbed pairs (Table 2) with the pairs in vacuum (Table 1) shows that the distance is similar to the values for the adsorbed pairs in vacuum and that the shift has increased. Whereas the tilt takes values up to 34.1° in the adsorbed state, it remains close to zero in vacuum. In gas phase, this could be a consequence of our selection of initial structures where the tilt has been put to zero

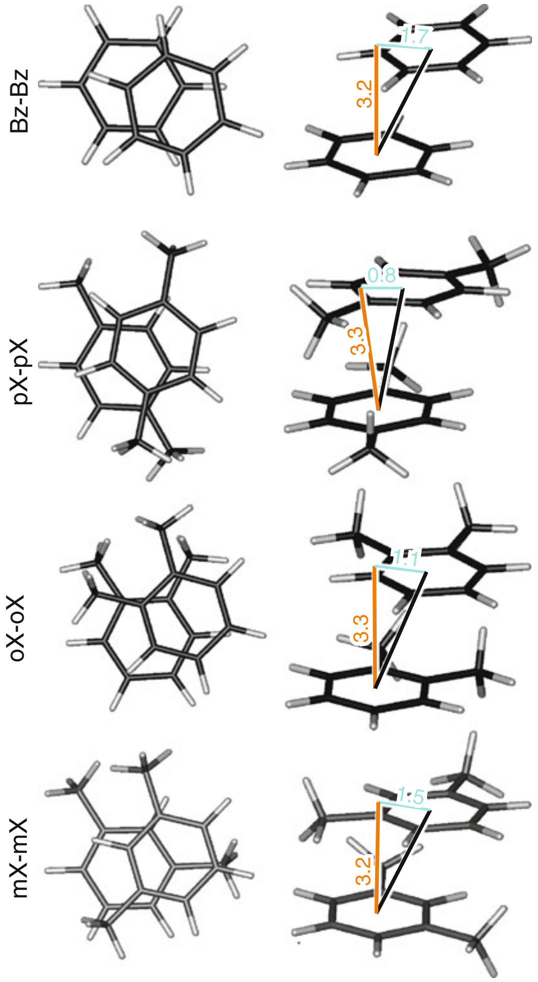

Fig. 4 Some stacked pairs in the gas phase viewed along the z_1 axis and sideways: benzene pair and pure pX, oX, and mX xylene pairs. The *orange* and *blue line* indicate the distance *d* and shift *s* parameters, respectively

systematically. When the pair is brought into the pore, the xylenes have to reorient themselves to attain optimal stacking with the terephthalic framework linkers, thus causing the large rotation.

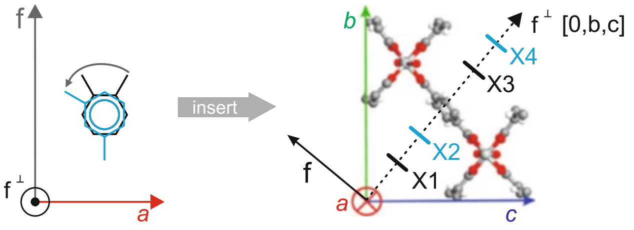

Fig. 6 The initial geometries of the fully loaded framework are created by inserting the xylene pairs of Fig. 3 into the MIL-47 pores. The vectors f and $f^{\perp}$ denote the diagonals in the (b, c) plane, orthogonal to the a direction. The pairs are inserted at the origin and translated over the vector 0.5a. Subsequently, one pair is translated over the vector 0.25$f^{\perp}$ and the other over the vector 0.75$f^{\perp}$

The selectivity of xylene isomers in MIL-47 has earlier been attributed to geometrical packing effects [8, 9]. From X-ray data at high loadings [8, 9], it was suggested that molecules are adsorbed by pairs, with their aromatic rings facing each other. The occurrence of certain geometrical effects for single-component adsorption obtained by Rietveld refinement is as follows [8].

1. pX: The methyl groups within a stacked para-xylene pair are perfectly staggered.
2. oX: Structure refinement of ortho-xylene pairs reveals that the stacking of these isomers is analogous to that of para-xylene, but ring alignment is slightly less effective: the rings are shifted with respect to each other.
3. mX: Within pairs of meta-xylene, a steric interaction arises between an aromatic ring of one molecule and a methyl group of a molecule in the neighboring unit cell in the *a* direction. This interaction causes a tilt and a rotation of the aromatic molecules, preventing the optimal stacking of the rings.

In the three cases, the methyl groups dictate the spatial arrangement of the pairs. However, these experimental geometries differ from our most stable optimized structures (visualized in Fig. 7 and Figures 6–8 of Supp. Info.): the rings of the energetically most stable structures are often

Fig. 5 The stacking energy of the pairs becomes stronger with increasing shift *s* and decreasing distance *d*. The benzene pair is an outlier; the linear fits are based on the thermal average values at 300 K of the xylene and dichlorobenzene pairs

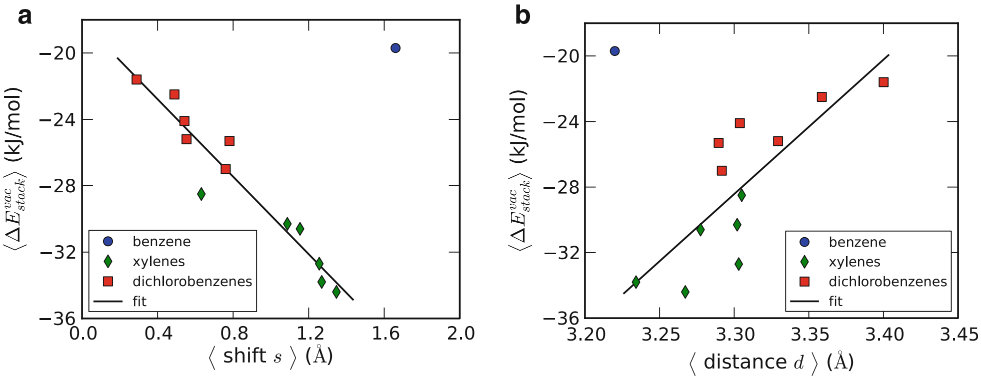

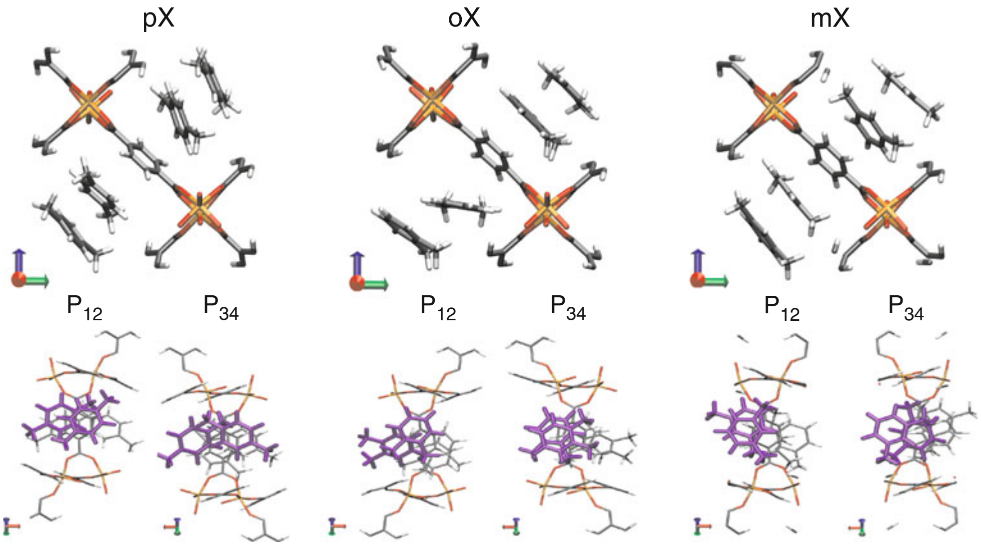

Fig. 7 The most stable geometry of the pure pX, oX, and mX pairs adsorbed in MIL-47. *Top* one unit cell viewed along the one-dimensional channels, in the *a* direction (*red arrow*), loaded with four xylenes. *Bottom* for each adsorbed state, the geometry of the P_{12} and P_{34} pairs is highlighted in purple in a view along the vector $f^{\perp}$, as defined in Fig. 6, for P_{12} and in the opposite sense (vector $-f^{\perp}$) for P_{34}

Table 2 Geometrical parameters of individual xylene pairs P_{12} and P_{34} in their adsorbed state

	Pair P_{12} in first pore				Pair P_{34} in second pore			
	Shift (Å)	Distance (Å)	Tilt (°)	Phase (°)	Shift (Å)	Distance (Å)	Tilt (°)	Phase (°)
pX–pX	3.8	3.17	23.0	246.5	2.1	3.26	24.8	21.1
oX–oX	1.2	3.20	6.3	109.2	3.2	3.03	26.3	69.1
mX–mX	2.8	3.11	23.3	154.3	1.3	3.26	6.5	140.3
pX–oX	1.3	3.27	5.1	216.3	1.8	3.14	5.8	219.9
pX–mX	1.8	3.57	33.3	3.0	1.7	3.24	3.1	−23.0
oX–mX	2.9	3.33	34.1	56.7	1.6	3.21	9.2	49.6
Average	*2.3*	*3.3*	*20.9*	*131.0*	*2.0*	*3.2*	*12.6*	*79.5*

not parallel (tilt θ) and are shifted (shift s). Such a more random ordering was also observed by Castillo et al. [20] in GCMC simulations of a fully packed 4 × 2 × 2 unit cell. Their unordered embedding of the ortho-xylenes in the pores resembles the configuration of our oX pair P_{34} [20]. They only found ordering for the pX pairs, in which all CH_3 groups between neighboring cells have the same orientation, resembling the geometry of our pX pair P_{12}.

3.3 Decomposition of adsorption energy in MIL-47

The adsorption energy is influenced by three effects: framework deformation, interaction of xylenes with the pore walls, and stacking of xylenes. The adsorption energy is thus decomposed into three terms

$$\Delta E_{\mathrm{ads}} = E_{\mathrm{deform}} + E_{\mathrm{inter}} + E_{\mathrm{stack}} \tag{5}$$

The physical interpretation of the terms is visualized in Fig. 8, and the calculated values are reported in Table 3.

A first contribution is the framework deformation. In order to accommodate the xylene pairs in the pores, the structure needs to relax and the linkers may need to reorient. This effect is quantified by the deformation energy E_{deform}, which is defined as the difference in energy between the empty framework with its geometry as in the fully adsorbed state (F, stat) and the empty framework with its geometry relaxed (F),

$$E_{\mathrm{deform}} = E^{\mathrm{stat}}(F) - E(F) \tag{6}$$

The framework deformation due to the loading requires energy ($E_{\mathrm{deform}} > 0$).

A second contribution is the host–guest interactions. The xylenes are physisorbed in the pores due to interactions with the framework. The interaction energy E_{inter} is defined as the energy difference of the fully loaded framework (F, P_{12}, P_{34}) with respect to the energy of the empty host (F, stat) and the energy of the xylenes pairs (P_{12}, P_{34}, stat).

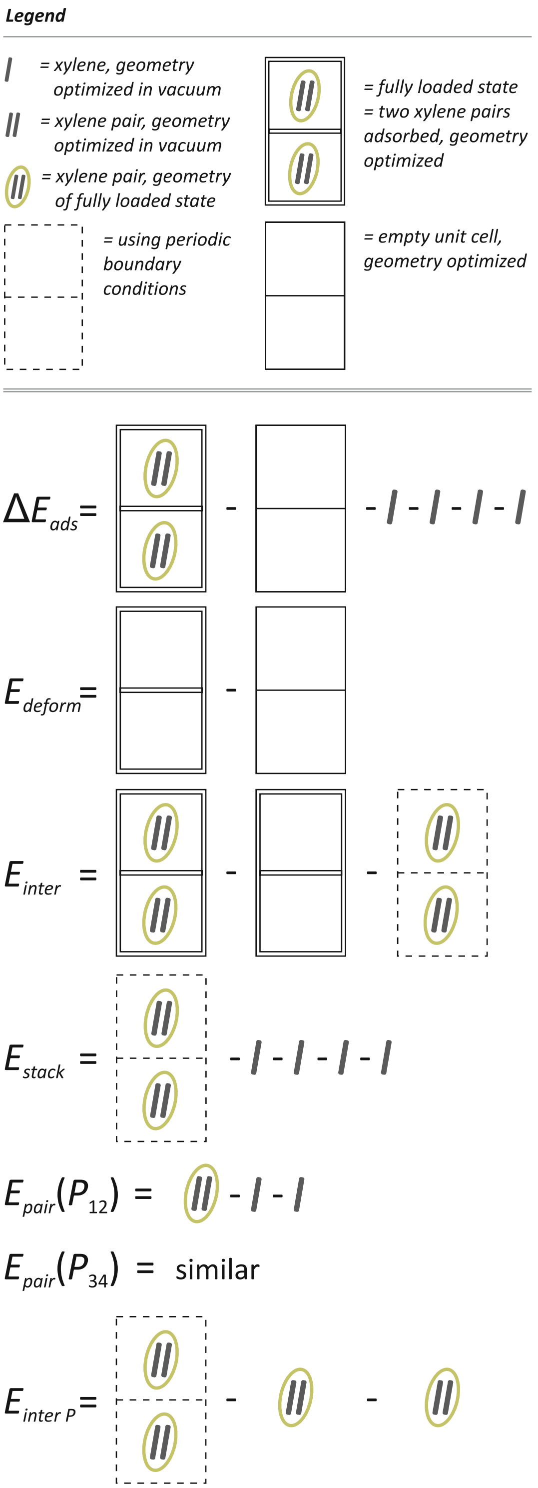

Fig. 8 Visualization of the decomposition of the adsorption energy (Eq. 5): the deformation energy (Eq. 6), the xylene–framework interaction (Eq. 7), and the stacking energy (Eq. 10) are calculated by deleting the xylenes or the framework from the fully loaded framework, and performing static calculations. The stacking energy is further decomposed in pair energies (Eq. 8) and the inter-pair energy (Eq. 9)

$$E_{\text{inter}} = E(F, P_{12}, P_{34}) - E^{\text{stat}}(F) - E^{\text{stat}}(P_{12}, P_{34}) \tag{7}$$

The latter two static calculations are simple single-point energy computations using the same geometry as in the fully loaded host (no geometry optimization is performed) from which the xylenes or the framework are removed (Fig. 8). The interaction of the xylenes with the pore walls, in this case mainly the terephthalic linkers, is attractive ($E_{\text{inter}} < 0$).

The third contribution in Eq. (5) is the interaction E_{stack} between the xylene molecules. As the xylenes appear in pairs in the pores, a large part of these xylene interactions per unit cell is the stacking energy of the first pair E_{pair} (P_{12}) and the stacking energy of the second pair E_{pair} (P_{34}). Due to the interaction with the host, the xylene pairs have different geometries than in vacuum. Instead of using Eq. (1), these pair stacking energies should be calculated by comparing the energy of an isolated pair in vacuum with the energies of two individual xylenes in vacuum. For instance, the geometry of the isolated pair P_{12} is obtained by removing the framework and pair P_{34} from the optimized fully loaded state. The static energy of this P_{12} geometry is then calculated with a single-point computation in a large box (vacuum, P_{12}, stat),

$$E_{\text{pair}}(P_{12}) = E^{\text{stat,vac}}(P_{12}) - E^{\text{vac}}(X_1) - E^{\text{vac}}(X_2) \tag{8}$$

and similarly for pair P_{34}. The pair stacking energy is schematically visualized in Fig. 8.

The remainder of the adsorption energy represents interactions between xylene pairs due to the periodicity of the material and is labeled as the inter-pair interaction $E_{\text{inter}P}$. A xylene pair interacts with other adsorbed xylene pairs in its own channel as well as with xylene pairs in adjacent channels. The interaction is calculated from the static energy of the pairs in the fully loaded geometry, where the framework has been removed, with the periodicity set to the framework lattice parameters (P_{12}, P_{34}, stat). This energy is compared with the static energy of the individual pairs, still in the same geometry, using a large box (vacuum, P_{12}, stat and vacuum, P_{34}, stat).

$$E_{\text{inter}P} = E^{\text{stat}}(P_{12}, P_{34}) - E^{\text{stat,vac}}(P_{12}) - E^{\text{stat,vac}}(P_{34}) \tag{9}$$

This procedure measures the interaction between the two pairs and the interaction with the periodic images of the pairs. Similar to the stacking energy of two molecules, the inter-pair interaction is favorable for the adsorption ($E_{\text{inter}P} < 0$). The total stacking energy in Eq. (5), which is also a negative contribution, can now be calculated as the sum of the pair stacking energies and the inter-pair stacking:

Table 3 Energy contributions to the adsorption energy of the fully loaded framework: deformation energy of the framework (E_{deform}), interaction energy between xylenes and framework (E_{inter}), and xylene stacking energy (E_{stack})

	ΔE_{ads}			E_{stack}			ΔE_{ads}	$\Delta E_{\mathrm{ads}}/4$
	E_{deform}	E_{inter}	E_{stack}	E_{pair} (P_{12})	E_{pair} (P_{34})	$E_{\mathrm{inter}P}$		
MIL-47 + 4pX	19.3	−120.8	−131.2	−29.1	−18.4	−83.7	−232.7	−58.2
MIL-47 + 4oX	29.3	−120.1	−137.4	−26.9	−34.1	−76.5	−228.3	−57.1
MIL-47 + 4mX	18.8	−138.3	−109.2	−31.8	−37.2	−40.3	−228.8	−57.2
MIL-47 + 2pX–oX	15.6	−134.4	−103.9	−30.9	−35.9	−37.2	−222.8	−55.7
MIL-47 + 2pX–mX	8.0	−147.0	−116.0	−28.8	−22.3	−65.0	−255.0	−63.8
MIL-47 + 2oX–mX	5.9	−141.9	−95.0	−27.6	−25.2	−42.2	−231.0	−57.7
Average	16.2	−133.8	−115.5	−29.2	−28.9	−57.5	−233.1	−58.3

The stacking energy consists of the stacking energies of the individual pairs and the inter-pair stacking energy. The adsorption energy per xylene is obtained by division by four. All energies in kJ/mol

$$E_{\mathrm{stack}} = E_{\mathrm{pair}}(P_{12}) + E_{\mathrm{pair}}(P_{34}) + E_{\mathrm{inter}P} \qquad (10)$$

The predicted total adsorption energies are on average −233.1 kJ/mol per unit cell (Table 3), which amounts to −58.3 kJ/mol per adsorbed xylene molecule. On average, the host–xylene interaction E_{inter} and the xylene stacking energy E_{stack} contribute equally. But in individual cases, we notice some significant deviations: the total stacking energy can vary by more than 40 kJ/mol. Nevertheless, this effect is mostly compensated by the interaction energy between the xylenes and the walls of the host. A large stacking energy of the xylenes is accompanied systematically by a higher repulsive deformation energy of the framework. This feature could be understood by assuming that some framework relaxation is required to accommodate the xylene pair in its most favorable stacked conformation.

Within the category of pure pairs, the xylene–framework interaction energy is by far the strongest for the adsorption of pure mX pairs (−138.3 kJ/mol). The trend to favor mX is maintained when using mixed pairs, since the adsorption of mixed pairs oX–mX or pX–mX shows by far the largest interaction energies with the host. However, these favorable interactions are partially cancelled out by the lower stacking energies. Note also that more favorable energies for pure pairs not systematically lead to more favorable energies in the mixed pairs. For instance, mixing with the xylene isomer with the strongest stacking energy (oX) does not result in the strongest stacking energies for the mixed pairs (oX–mX, oX–pX). From Table 3, we conclude that the data for pure pairs are insufficient to predict adsorption energetics for mixed pairs.

The decomposition of the stacking energy in Table 3 shows that the pair stacking energies of the adsorbed pairs are less favorable than those of the pairs in vacuum (average −31.7 kJ/mol). Nevertheless, the pair stacking attains an average stacking efficiency of $(-29.2 - 28.9)/2 = -29.0$ kJ/mol. The inter-pair stacking energy can be very large, up to −83.7 kJ/mol for pX. The variation in the inter-pair stacking is explained by the organization of the xylenes in the pores, which may be derived from the geometrical parameters as follows. It is clear from Fig. 6 that X_1 and X_2 are nearest neighbors in the channel, and X_3 and X_4 are nearest neighbors in the adjacent channel. The interaction of a xylene with its nearest neighbors is included in the pair stacking energies E_{pair} (P_{12}) and E_{pair} (P_{34}). The interaction of xylenes with their next nearest neighbors is then of course included in the $E_{\mathrm{inter}P}$. According to our geometry versus energy analysis in vacuum (Fig. 5), the strength of the xylene–xylene interaction is mainly determined by the distance between the two molecules. To see the effect of the distance on the inter-pair energy, we determined the distance from the xylenes to their second nearest neighbor, which should be the dominant contribution. This distance is calculated as the root of $s^2 + d^2$ (s and d as defined in Fig. 2), which equals the distance between the centers of their rings. For pX, the second neighbors are separated by 4.96 and 5.77 Å, and these relatively short separations result in the strong inter-pair stacking energy of −83.7 kJ/mol. In contrast, the second neighbors for mX are separated by 5.75 and 7.40 Å, resulting in a much weaker inter-pair energy of −40.3 kJ/mol.

The typical stacking energy in vacuum, about −31.7 kJ/mol (Table 1), may be used as a 'unit for energy' to compare the importance of the energy contributions. The interaction energy of two pairs with the framework is worth over four units, the stacking of the pairs is worth one unit each, the inter-pair stacking is worth two units, and the deformation diminishes the total by half a unit. This brings the adsorption energy to nearly eight vacuum stacking energy equivalents (−233.1 kJ/mol). The attractive stacking between xylene molecules is here of the same importance as the attractive interaction energy between xylenes and framework.

Summarizing, the pure pairs deform the framework more (larger positive E_{deform}) and interact more weakly with the framework (weaker E_{inter}) than the mixed pairs. However, the pure xylene pairs stack more efficiently in the pores (stronger E_{stack}). Overall, the values of adsorption energy for the various xylene pairs all have the same order of magnitude and appear not to explain the different adsorption selectivity of the pX, oX, and mX isomers. If the pure adsorption isotherms were to be solely determined by the strength of the adsorption energy, one would need a strong adsorption energy for pX, followed by oX, and a considerably weaker adsorption energy for mX. Since this is not the case, our results indicate that the selective adsorption behavior cannot be explained purely energetically. This means that temperature and entropy are expected to play a determining role for the selectivity.

The entropy arises from the many possible configurations the xylenes can take when adsorbed in the pores. In general, the more configurations the xylenes can take within the pores, the higher the entropy, and the more favorable the adsorption. A first contribution to the entropy is the relative orientation of the molecules in a xylene pair. The presence of the methyl groups can here reduce the number of configurational states. The fewer states are prohibited (because of overlapping methyl groups), the more states are available, and the more entropy is available. A second contribution to the entropy is the positioning of the pair in the channels. Likewise, the pair may take a number of different orientations and positions inside the channels. Bulkier pairs show a more limited number of available configurations, leading to a lower entropy. A third entropic contribution arises in the process of multicomponent adsorption, referred to as mixing entropy. Many ways exist to distribute the xylenes of each kind over the pores. The information about entropy is lacking in adsorption energy calculations, but could be obtained by a vibrational analysis [47, 48], Monte Carlo or Molecular Dynamics simulations. GCMC calculations, as those by Castillo et al. [20], include energetic and entropic effects and agree with experimental single-component isotherms. Our study now shows that the energetics of the pure and mixed xylene adsorption at high loadings are not alone responsible for the selectivities between isomers, such that the separation is also entropically driven.

4 Conclusions

The molecular packing effects of xylene isomers inside the confining environment of the MIL-47 pore system have been studied by quantumchemical calculations. The guest–guest interactions are first quantified in the gas phase. Xylenes show a high stacking energy in vacuum, such that xylenes are expected to stack efficiently with the rings of the MIL-47 linkers. When the xylenes are inserted in the MIL-47 pores, not only guest–guest interactions contribute to the adsorption energy, but also host–guest interactions. The adsorption energy for high loadings of para-, ortho-, and meta-xylene has thus been decomposed in three contributions: the deformation energy of the framework, the framework–xylene interaction, and the stacking energy. The stacking energy has been found to be equally important as the framework–xylene interaction, hence confirming the hypothesis that π–π stacking is responsible for the adsorption. The average stacking energy of xylene pairs in vacuum can be used as a unit for the interactions. The adsorption energy in the fully loaded state amounts to nearly two vacuum stacking equivalents per adsorbed xylene, which explains the efficient adsorption at room temperature.

The energetics could not explain the experimentally observed separation of xylene isomers with a preferential adsorption for ortho-xylene and para-xylene, since all adsorption energies lie in the same range. Therefore, entropic effects are likely the main driving force for the adsorption selectivity. This has two implications. First, sampling of configurational space should be adequately performed to assess the entropic effects, which can only be obtained with molecular dynamics or Monte Carlo simulations. Second, since the accuracy of the energetics is of subordinary importance to the sampling, it is expected that reasonable results can be obtained with classical force fields. Whereas force fields are less accurate than an ab initio treatment, they allow considerably longer sampling times because of the reduced computational cost.

Acknowledgments This work was supported by the Fund for Scientific Research—Flanders (FWO), the research Board of Ghent University, and BELSPO in the frame of IAP 6/27. Funding was also received from the European Research Council under FP7 with ERC grant agreement number 240483. A.G., T.V., and M.A.vdV. are postdoctoral researchers of the Fund for Scientific Research—Flanders (FWO). The computational resources and services used were provided by Ghent University (Stevin Supercomputer Infrastructure).

References

1. Férey G (2008) Hybrid porous solids: past, present, future. Chem Soc Rev 37:191–214
2. Long JR, Yaghi OM (2009) The pervasive chemistry of metal-organic frameworks. Chem Soc Rev 38:1213–1214
3. Perry JJ, Perman JA, Zaworotko MJ (2009) Design and synthesis of metal-organic frameworks using metal-organic polyhedra as supermolecular building blocks. Chem Soc Rev 38:1400–1417
4. Eddaoudi M, Kim J, Rosi N, Vodak D, Wachter J, O'Keeffe M, Yaghi OM (2002) Systematic design of pore size and functionality in isoreticular MOFs and their application in methane storage. Science 295:469–472
5. Férey G, Serre C, Devic T, Maurin G, Jobic H, Llewellyn PL, De Weireld G, Vimont A, Daturi M, Chang JS (2011) Why

hybrid porous solids capture greenhouse gases? Chem Soc Rev 40:550–562

6. Meek ST, Greathouse JA, Allendorf MD (2011) Metal-organic frameworks: a rapidly growing class of versatile nanoporous materials. Adv Mater 23:249–267
7. Tranchemontagne DJ, Mendoza-Cortes JL, O'Keeffe M, Yaghi OM (2009) Secondary building units, nets and bonding in the chemistry of metal-organic frameworks. Chem Soc Rev 38:1257–1283
8. Alaerts L, Kirschhock CEA, Maes M, van der Veen MA, Finsy V, Depla A, Martens JA, Baron GV, Jacobs PA, Denayer JEM, De Vos DE (2007) Selective adsorption and separation of xylene isomers and ethylbenzene with the microporous vanadium(IV) terephthalate MIL-47. Angew Chem Int Edit 46:4293–4297
9. Finsy V, Verelst H, Alaerts L, De Vos D, Jacobs PA, Baron GV, Denayer JFM (2008) Pore-filling-dependent selectivity effects in the vapor-phase separation of xylene isomers on the metal-organic framework MIL-47. J Am Chem Soc 130:7110–7118
10. Vermoortele F, Maes M, Moghadam PZ, Lennox MJ, Ragon F, Boulhout M, Biswas S, Laurier KGM, Beurroies I, Denoyel R, Roeffaers M, Stock N, Düren T, Serre C, De Vos DE (2011) p-xylene-selective metal–organic frameworks: a case of topology-directed selectivity. J Am Chem Soc 133:18526–18529
11. Fritz Ullmann's encyclopedia of industrial chemistry, 6th edn. In: Electronic release, 2000
12. Barthelet K, Marrot J, Riou D, Férey G (2002) A breathing hybrid organic-inorganic solid with very large pores and high magnetic characteristics. Angew Chem Int Edit 41:281
13. Grimme S (2006) Semiempirical GGA-type density functional constructed with a long-range dispersion correction. J Comput Chem 27:1787–1799
14. Grimme S, Antony J, Schwabe T, Muck-Lichtenfeld C (2007) Density functional theory with dispersion corrections for supramolecular structures, aggregates, and complexes of (bio)organic molecules. Org Biomol Chem 5:741–758
15. Schwabe T, Grimme S (2008) Theoretical thermodynamics for large molecules: walking the thin line between accuracy and computational cost. Acc Chem Res 41:569–579
16. Liu B, Smit B (2009) Comparative molecular simulation study of CO_2/N_2 and CH_4/N_2 separation in zeolites and metal—organic frameworks. Langmuir 25:5918–5926
17. Ramsahye NA, Maurin G, Bourrelly S, Llewellyn PL, Devic T, Serre C, Loiseau T, Férey G (2007) Adsorption of CO_2 in metal organic frameworks of different metal centres: grand Canonical Monte Carlo simulations compared to experiments. Adsorpt J Int Adsorpt Soc 13:461–467
18. Rosenbach N, Jobic H, Ghoufi A, Salles F, Maurin G, Bourrelly S, Llewellyn PL, Devic T, Serre C, Férey G (2008) Quasi-elastic neutron scattering and molecular dynamics study of methane diffusion in metal organic frameworks MIL-47(V) and MIL-53(Cr). Angew Chem Int Edit 47:6611–6615
19. Salles F, Jobic H, Maurin G, Koza MM, Llewellyn PL, Devic T, Serre C, Férey G (2008) Experimental evidence supported by simulations of a very high H-2 diffusion in metal organic framework materials. Phys Rev Lett 100(24):245901
20. Castillo JM, Vlugt TJH, Calero S (2009) Molecular simulation study on the separation of xylene isomers in MIL-47 metal—organic frameworks. J Phys Chem C 113:20869–20874
21. Wang S, Yang Q, Zhong C (2008) Adsorption and separation of binary mixtures in a metal-organic framework Cu-BTC: a computational study. Sep Purif Technol 60:30–35
22. Hamon L, Llewellyn PL, Devic T, Ghoufi A, Clet G, Guillerm V, Pirngruber GD, Maurin G, Serre C, Driver G, Beek WV, Jolimaître E, Vimont A, Daturi M, Férey GR (2009) Co-adsorption and separation of CO_2–CH_4 mixtures in the highly flexible MIL-53(Cr) MOF. J Am Chem Soc 131:17490–17499
23. Gallo M, Glossman-Mitnik D (2009) Fuel gas storage and separations by Metal—organic frameworks: simulated adsorption isotherms for H_2 and CH_4 and their equimolar mixture. J Phys Chem C 113:6634–6642
24. Pan L, Olson DH, Ciemnolonski LR, Heddy R, Li J (2006) Separation of hydrocarbons with a microporous metal-organic framework. Angew Chem Int Edit 45:616–619
25. Vanduyfhuys L, Verstraelen T, Vandichel M, Waroquier M, Van Speybroeck V (2012) Ab initio parametrized force field of the metal-organic framework MIL-53(Al) for use in molecular simulations including lattice dynamics. J Chem Theory Comput (submitted)
26. Sinnokrot MO, Sherrill CD (2003) Unexpected substituent effects in face-to-face π-stacking interactions. J Phys Chem A 107:8377–8379
27. Sinnokrot MO, Sherrill CD (2004) Highly accurate coupled cluster potential energy curves for the benzene dimer: sandwich, T-shaped, and parallel-displaced configurations. J Phys Chem A 108:10200–10207
28. Sinnokrot MO, Sherrill CD (2004) Substituent effects in π–π interactions: sandwich and T-shaped configurations. J Am Chem Soc 126:7690–7697
29. Alaerts L, Maes M, Jacobs PA, Denayer JFM, De Vos DE (2008) Activation of the metal-organic framework MIL-47 for selective adsorption of xylenes and other difunctionalized aromatics. Phys Chem Chem Phys 10:2979–2985
30. Cremer D, Pople JA (1975) General definition of ring puckering coordinates. J Am Chem Soc 97:1354–1358
31. Car R, Parrinello M (1985) Unified approach for molecular dynamics and density-functional theory. Phys Rev Lett 55:2471–2474
32. Becke AD (1988) Density-functional exchange-energy approximation with correct asymptotic behavior. Phys Rev A 38:3098
33. Vanderbilt D (1990) Soft self-consistent pseudopotentials in a generalized eigenvalue formalism. Phys Rev B 41:7892
34. Verstraelen T, Van Speybroeck V, Waroquier M (2008) ZEOBUILDER: a GUI toolkit for the construction of complex molecular structures on the nanoscale with building blocks. J Chem Inf Model 48:1530–1541
35. Gu J, Wang J, Leszczynski J, Xie Y, Schaefer HF (2008) Chem Phys Lett 459:164
36. McGaughey GB, Gagne M, Rappe AK (1998) J Biol Chem 273:15458
37. Morgado C, Vincent MA, Hillier IH, Shan X (2007) Phys Chem Chem Phys 9:448
38. Pavone M, Rega N, Barone V (2008) Chem Phys Lett 452:333
39. Piacenza M, Grimme S (2004) J Comput Chem 25:83
40. Podeszwa R, Bukowski R, Szalewicz K (2006) J Phys Chem A 110:10345
41. Waller MP, Robertazzi A, Platts JA, Hibbs DE, Williams PA (2006) J Comput Chem 27:491
42. Zhao Y, Truhlar DG (2005) Phys Chem Chem Phys 7:2701
43. Zhao Y, Truhlar DG (2006) J Chem Theory Comput 2:1009
44. Lee EC, Hong BH, Lee JY, Kim JC, Kim D, Kim Y, Tarakeshwar P, Kim KS (2005) Substituent effects on the edge-to-face aromatic interactions. J Am Chem Soc 127:4530–4537
45. Raju RK, Bloom JWG, An Y, Wheeler SE (2011) Substituent effects on non-covalent interactions with aromatic rings: insights from computational chemistry. ChemPhysChem 12:3116–3130
46. Hohenstein EG, Duan JN, Sherrill CD (2011) Origin of the surprising enhancement of electrostatic energies by electron-donating substituents in substituted sandwich benzene dimers. J Am Chem Soc 133:13244–13247

47. De Moor BA, Ghysels A, Reyniers M-F, Van Speybroeck V, Waroquier M, Marin GB (2011) Normal mode analysis in zeolites: toward an efficient calculation of adsorption entropies. J Chem Theory Comput 7:1090–1101

48. Van der Mynsbrugge J, Hemelsoet K, Vandichel M, Waroquier M, Van Speybroeck V (2012) An efficient approach for the computational study of alcohol and nitrile adsorption in H-ZSM-5. J Phys Chem C 116:5499–5508

Theor Chem Acc (2012) 131:1236
DOI 10.1007/s00214-012-1236-5

REGULAR ARTICLE

Laser control in open quantum systems: preliminary analysis toward the Cope rearrangement control in methyl-cyclopentadienylcarboxylate dimer

G. Dive · R. Robiette · A. Chenel · M. Ndong ·
C. Meier · M. Desouter-Lecomte

Received: 29 February 2012 / Accepted: 10 May 2012 / Published online: 8 June 2012

Abstract We present a preliminary simulation toward the control of the Cope rearrangement of the most stable isomer of methyl-cyclopentadienylcarboxylate dimer. An experimental investigation of the dimerization of methyl-cyclopentadienylcarboxylate has been carried out. It shows that the most stable isomer of the dimer, the Thiele's ester, is the major product of the dimerization. The simulation takes it as the initial state for the further control of the Cope reaction. The aim of the simulation is to examine the possibility of laser control to form the target product, not detected during the dimerization. The relevant stationary states have been characterized at the DFT B3LYP level, particularly the Cope transition state in which the dimer is connected only by a single bond r_1. A minimum energy potential surface has been computed in a two-dimensional subspace of two bounds r_2 and r_3 which achieve the dimerization and have a very high weight in the reaction path from the Cope TS to the two adducts. Quantum wave packet optimal control simulation has been studied in a one-dimensional model using an active coordinate $r_- = r_3 - r_2$ which nearly corresponds to the reaction path. The stability of the optimal field against dissipation is examined by a non-Markovian master equation approach, which is perturbative in the system-bath coupling but without limitation on the strength of the field.

Keywords Cope rearrangement · Diels–Alder reaction · Optimal control · Dissipative dynamics · Non-Markovian quantum master equation

Published as part of the special collection of articles celebrating theoretical and computational chemistry in Belgium.

Electronic supplementary material The online version of this article (doi:10.1007/s00214-012-1236-5) contains supplementary material, which is available to authorized users.

G. Dive
Centre d'Ingéniérie des Protéines, Université de Liège,
Sart Tilman, B6, 4000 Liège, Belgium
e-mail: gdive@ulg.ac.be

R. Robiette
Institute of Condensed Matter and Nanosciences,
Université catholique de Louvain,
1348 Louvain-la-Neuve, Belgium
e-mail: raphael.robiette@uclouvain.be

A. Chenel · M. Ndong · M. Desouter-Lecomte (✉)
Laboratoire de Chimie Physique, UMR 8000,
Université de Paris-Sud, 91405 Orsay, France
e-mail: michele.desouter-lecomte@u-psud.fr

A. Chenel
e-mail: aurelie.chenel@ens-cachan.fr

M. Ndong
e-mail: mamadou.ndong@u-psud.fr

C. Meier
Laboratoire Collisions, Agrégats, Réactivité,
UMR 5589, IRSAMC, Université Paul Sabatier,
31062 Toulouse, France
e-mail: chris@irsamc.ups-tlse.fr

M. Desouter-Lecomte
Département de Chimie, Université de Liège,
Sart Tilman, B6, 4000 Liège, Belgium

1 Introduction

Experimental control in condensed phase by feedback loops is now a very efficient technique to modify reactivity

[1]. As discussed in this recent review [1], numerical simulations in complex systems are usually too simplified to be really predictive in laser design since experiments automatically work with exact systems without any knowledge of the molecular Hamiltonian. However, simulations remain important in this context to explore the feasibility of control in different systems, analyze the mechanism and particularly the role of the surrounding. Therefore, to induce future progress in experiment–theory interplay, it is crucial to develop efficient numerical methods to simulate laser control in complex systems.

In this work, we present a preliminary analysis of a possible interesting candidate for a control of a Cope rearrangement in the framework of the Diels–Alder reaction. We focus here on the Cope rearrangement of the dimer of methyl-cyclopentadienylcarboxylate. The first step is an experimental exploring of the dimerization to identify the major adduct and justify that we can take it as the initial state for a further control of its Cope rearrangement. In a second step, a full determination of all minima and transition states (TS) connecting different isomers has been carried out to characterize the reactant and the target for the isomerization control. Finally, we take this molecular system to calibrate a strategy for simulating control in a surrounding. We present here the first results suggesting the feasibility of the control.

Control of isomerization reaction by designed laser pulses in a thermal environment has been frequently investigated since the early days of laser chemistry [2–21]. Isomerization involves transfer from a potential well to another one and different control strategies have been suggested either in the UV domain via the electronic excited states in the pump and dump scheme [6–11] or in the infrared range in the ground electronic state by overcoming the barrier via the delocalized highly excited vibrational states [2–5, 12–21]. We focus here on a particular isomerization involving a Cope rearrangement inspired by a pioneering theoretical investigation about a Cope rearrangement in substituted semibullvalenes [2]. It is well-known that the surface surrounding the Cope transition state (TS) of a pericyclic rearrangement is very flat leading to a large barrier and well-localized vibrational ground states in each well with negligible tunnel effect. Few years ago, we have studied the dynamics of the dimerization of cyclopentadiene in the bifurcating region connecting the TS1 of C_2 symmetry and the Cope TS and examined the possibility of preparing shaped wave packets in this region by optimal control theory (OCT) [22]. Here, we want to control the Cope rearrangement, and therefore, we choose a situation with a substituted cyclopentadiene so that the two isomers connected by the Cope TS are sufficiently different to be easily detected after control. The dimerization of methyl-cyclopentadienylcarboxylate (**1**) can involve different isomers but the major product is known to be Thiele's ester **2a** (Scheme 1) [23]. This ester is the reactant for the control and the target is the product of the Cope rearrangement of this later. An extensive investigation of all the possible conformers has been carried out by quantum chemistry at the B3LYP level to determine the relevant minima and the Cope TS. A two-dimensional potential energy surface in a selected subspace and the dipole moment surfaces have been calculated.

Quantum control by optimally shaped laser pulses exploits fine quantum interferences in the system and is therefore extremely sensitive to decoherence due to the uncontrolled surrounding. We adopt here the optimal control theory (OCT) in which the laser field is optimized on a temporal grid [24]. It is obvious that simulation of control in a complex system must involve a simplified quantum model and the full dimensional potential energy surface is often approximated by the system-bath model of a molecular subsystem bilinearly coupled to a harmonic bath describing the environment [25]. At this stage, different dynamical strategies can be followed: an extensive quantum computation with the multilayer multi-configuration time-dependent Hartree (MCTDH) up to some hundreds of atoms [26] or dissipative dynamics in which the surrounding is taken into account by a global spectral density [27]. Here, we implement a non-Markovian dissipative dynamics in the density matrix formalism valid at the second order in the system-bath coupling but with no limitation on the strength of the field [28]. Such a time non-local non-Markovian approach with a memory including the whole dynamics from the initial time allows that the surrounding and the system have similar dynamical timescales leading to easy energy exchanges. Following the particular Meier–Tannor parameterization of the spectral density of the bath [28–30], the field-dressed dissipation is treated by a set of auxiliary matrices implicitly containing the memory terms and coupled to the system. This leads to a local dynamics which remains, however, difficult to manage numerically and up to now has been applied on model or small systems. Our aim is to calibrate the auxiliary matrix

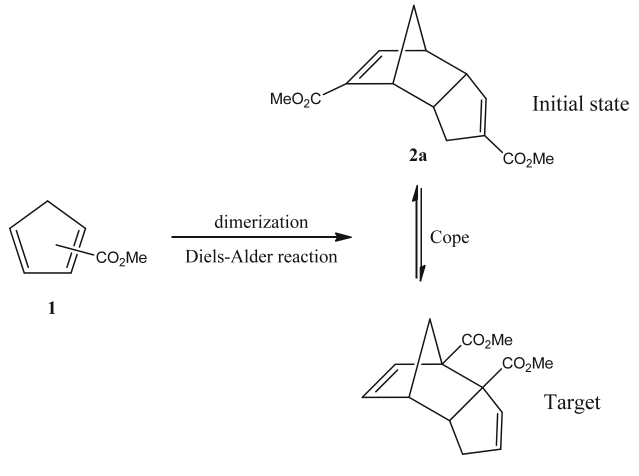

Scheme 1 Formation of dimer **2a** and its Cope rearrangement

Scheme 2 Synthesis and dimerization of methyl-cyclopentadienylcarboxylate

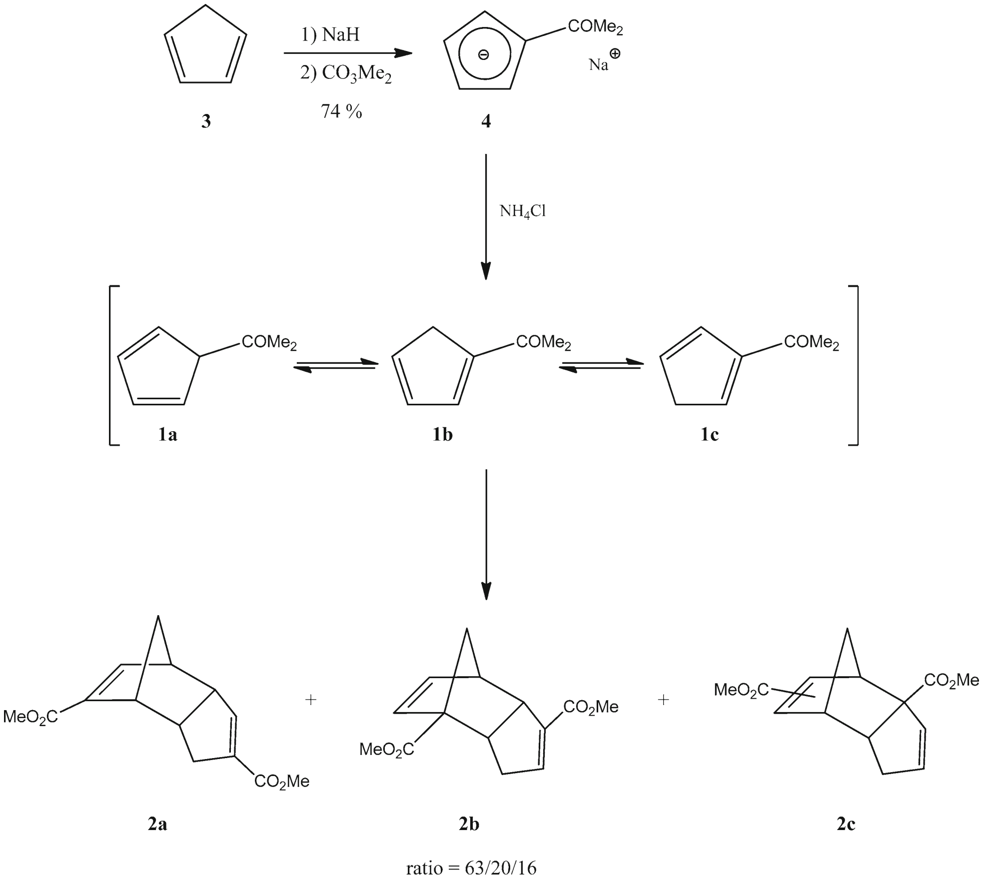

method in a large system. We begin by an analysis of a one-dimensional model along a particular scan connecting the reactant and the target. An optimal field is designed in the system and we analyze the stability of the control in various environments with different frequency cutoffs, coupling strengths and temperatures. In this work, we want to concentrate on the dissipation effects on an optimal control field. To this end, an optimal control field was constructed without the influence of the bath, and subsequently, in a second step used in a dissipative environment. The inclusion of the bath into the control scenario and thus the study to which extent optimal control theory can compensate for dissipative effects is the subject of current studies, which will be presented on the future.

2 Chemistry of dimerization

The aim of this experimental section is (1) to justify that it is realistic to propose Thiele's ester as the initial state of an isomerization laser control because it is the major adduct of the dimerization of methyl-cyclopentadienylcarboxylate, (2) develop reaction conditions and (3) fully characterize all the products of the dimerization. The monomer exists in three tautomeric forms (**1a**, **1b**, and **1c**; Scheme 2) which are in rapid equilibrium [31]. It is well-known that this species is highly reactive and undergoes dimerization (via a Diels–Alder cycloaddition) to yield Thiele's ester (**2a**) [23, 32–34].

Since its high reactivity, methyl-cyclopentadienylcarboxylate (**1**) cannot be isolated and must be synthesized in situ, just prior to its use. We thus have prepared the corresponding anion, lithium carbomethoxycyclopentadienide (**4**), by treatment of cyclopentadiene with sodium hydride in THF, followed by addition of dimethyl carbonate [35]. This procedure gives cyclopentadienide **4**, which is stable and can be stored for months, in 74 % yield. Formation of diene **1** was performed by adding a saturated solution of NH_4Cl to a dichloromethane solution of **4**. Under these conditions, anion **4** undergoes a rapid protonation to yield the desired methyl-cyclopentadienylcarboxylates (**1a**–**c**). As mentioned previously, these later are highly reactive and undergo a rapid dimerization (by Diels–Alder reaction). Previous reports indicate that after purification this experiment affords Thiele's ester [32–34]. However, analysis of the crude mixture revealed that there is not just one product which is formed but three (**2a**, **2b**, and **2c**) in a 63/20/16 ratio. These three adducts could be separated by column chromatography and analyzed by nuclear magnetic resonance (NMR), high resolution mass spectrometry (HRMS) and infrared spectroscopy (see Electronic Supplementary Material).

First, ^{1}H and COSY NMR analysis of the major product showed a perfect concordance with reported data [36] and confirmed that it is Thiele's ester (**2a**). HRMS analysis then confirmed the $C_{14}H_{16}O_4$ molecular formula for the two minor compounds; these later being thus indeed also dimeric forms. A detailed NMR study (^{1}H, ^{13}C, COSY, HMQC, HMBC) of these two compounds allowed identifying **2b** and **2c** as possessing the structure showed in Scheme 2 (the localization of the ester function on the double bond in **2c** could not be determined).

It is important to note that these two isomers (**2b** and **2c**) do not come from the same arrangement of reactants as the one leading to Thiele's ester or the product of its Cope rearrangement. And this later could not be detected in the crude mixture.

3 Quantum chemistry investigation

All the calculations have been performed with the Gaussian suite of programs [37] at the B3LYP level [38] using the double ζ basis set 6-31G(d) [39]. As described by Spino et al. [31], methyl-cyclopentadienylcarboxylate can exist in three equilibrium isomers noted **1a**, **1b**, and **1c** but only a combination of the diene with the ester in the 2-position (**1c**) and 1 position (**1b**) could give rise to the Thiele's ester adduct [23]. **2b** and the two forms of **2c** products are 4.2 and 4.5/4.9 kcal less stable than **2a**. It can be noted that the heat of formation is higher for **2a** (16.6 kcal) than the one for **2b** (12.4 kcal) and **2c** (13.9/13.5 kcal).

This Diels–Alder reaction can be described as a two-step mechanism as previously analyzed in the dimerization of unsubstituted cyclopentadiene [22]. Depending on the conformation of both ester fragments, four geometric arrangements can be obtained as stationary points. All the calculations have retained the most stable one. A first transition state structure (TS1) has been located as for the unsubstituted cyclopentadiene addition with the formation of a single bond between both cycles. This first bond is equal to 2.007 Å and will be noted r_1 It is associated with a imaginary frequency of 369.89 cm^{-1}. Following this coordinate, the Cope TS is reached at $r_1 = 1.644$ Å which is 3.402 kcal more stable than the first transition state (TS1). At that point, the normal mode of the 80.05 cm^{-1} imaginary frequency is associated with the formation the r_2 and r_3 bonds respectively. The adduct with r_1 and r_2 bonds is the Thiele's ester which defines the barrier height of 26.8 kcal (1.16 eV). This minimum is 10.4 kcal (0.45 eV) more stable than the other adduct with r_1 and r_3 bonds. The energy and the values of the three important coordinates r_1 r_2 and r_3 are reported in Table 1. The three equilibrium structures of the Cope TS and the two adducts are depicted in Fig. 1. C_1 and C_2 atoms define the z-axis and the x-axis is in the C_1–C_2–C_3, plane.

Table 1 Energy and geometry of the main stationary points

	TS1	TS cope	Adduct $r_1 - r_2$	Adduct $r_1 - r_3$
E	30.2	26.8	0.0	10.4
r_1	2.0	1.6	1.6	1.6
r_2	3.0	2.7	1.6	3.4
r_3	3.0	2.8	3.5	1.6

E relative energy in kcal with respect to Thiele's ester minimum. Coordinates r_1, r_2, r_3 are in Å

The computed higher stability (by 10.4 kcal/mol) of Thiele's ester as compared to adduct $r_1 - r_3$, and the barrier to isomerization for this latter, suggest that experimentally (at room temperature), among these two adducts, only Thiele's ester should be observed. This in good agreement with our expermiental results which showed the formation of Thiele's ester but did not allow detecting adduct $r_1 - r_3$ in the crude mixture (vide supra).

Starting from the Cope TS structure, IRC has been searched along the forward and reverse directions in mass-weighted cartesian coordinates. The reverse branch could lead to the most stable minimum but stops after six steps. Using the standard Z-matrix, the optimization along all the others coordinates leads to the vicinity of the minimum but stops at r_2 distance equals to 1.693 Å while the adduct distance at equilibrium is 1.57 Å and is 6.0 kcal more stable than this last IRC point. As well in cartesian coordinates or using Z-matrix description, the forward branch comes back and does not go in the hoped direction. In the surrounding of the TS, the surface is particularly flat. To overcome this problem, another starting point has been arbitrarily chosen setting the r_3 distance to 2.6 Å. At that non-equilibrium structure, the Hessian matrix has a negative eigenvalue and the associated eigenvector is mainly defined by r_3. Such a way, the IRC starts in the right direction and stops near the second minimum with $r_2 = 3.43$ Å and $r_3 = 1.63$ Å to be compared to the optimized structure values which are 3.45 and 1.63 Å respectively.

In order to obtain a more complete description of the 1D model, a scan of r_2 and r_3 by steps of 0.5 Å has been performed starting from the TS structure in Z-matrix description without any other constraints up to 1.45 Å for both bonds. This 1D scan well connects the three stationnary points. It can be noted the good agreement between the three bond lengths obtained by the 1D scan and the selected IRC points. The r_1 distance lies in the range of 1.57–1.64 Å at the Cope TS. This scan is the one-dimensional model for the preliminary control of the

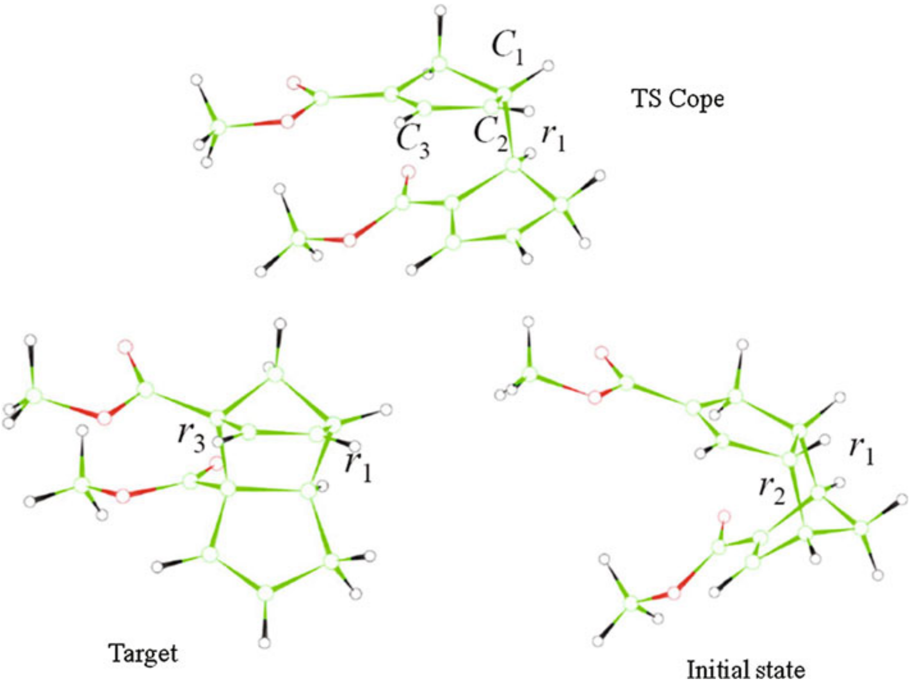

Fig. 1 Equilibrium geometry of the three stationary states involved in the control simulation. *Upper panel*: Cope TS with bond r_1 already formed. *Lower right panel*: Thiele's ester which is the lowest energy adduct obtained by forming the r_2 bond. *Lower left panel*: the target resulting from the formation of the r_3 bond. The atoms noted C_1, C_2 fixes the orientation of the *z*-axis. The *x*-axis is in the plane C_1, C_2, C_3

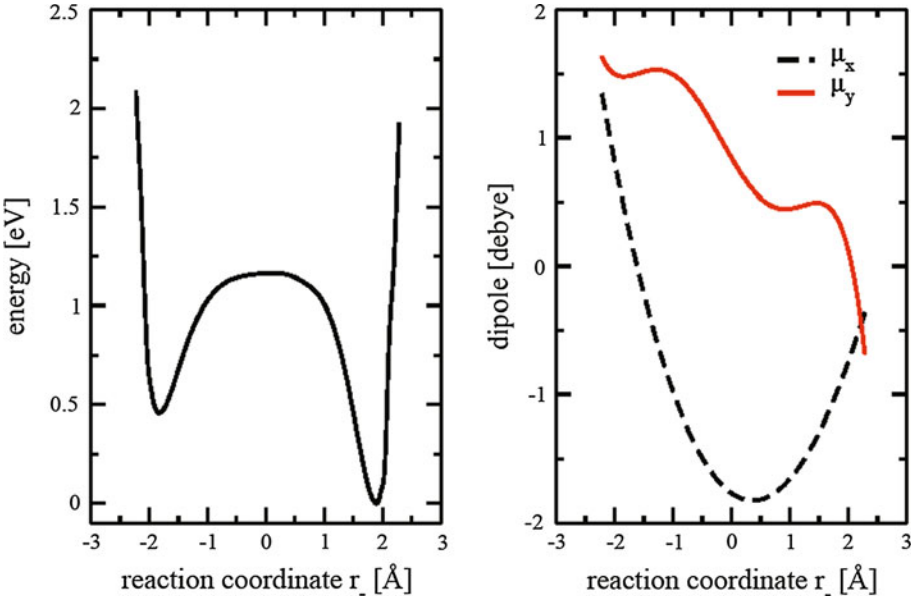

Fig. 2 *Left panel*: one-dimensional minimum potential energy curve along the active coordinate $r_- = r_3 - r_2$, *right panel*: the dipole moment components chosen for the control

rearrangement. The potential energy curve as a function of $r_- = r_3 - r_2$ and two dipole components selected for the control are shown in Fig. 2. Ab initio points are computed in the interval 1.45–3.50 Å and extrapolation is performed in order to get walls for the wave packet dynamics.

Next, a 2D map has been explored in a large range of r_2 and r_3 from 1.2 to 4.6 Å by steps of 0.1 Å by optimization of all the 3 *N*-8 degrees of freedom. This map contains 35 × 35 points. For very short distances, the energy of several points has been extrapolated. For large distances, another problem occurs: r_1 is abruptly broken. Therefore, to obtain a complete map with realistic walls as required for future 2D dynamics which mainly explores the central region of the grid, most of the points of the upper corner have been optimized following r_2 and r_3 with a r_1 distance set just before breaking mainly in the range of 1.7 Å. The map drawn in Fig. 3 have been obtained by the SAS spline fitting procedure [40].

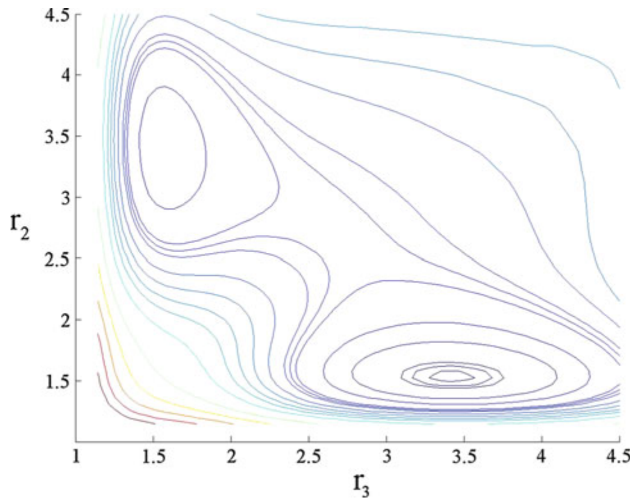

Fig. 3 Minimum energy potential energy surface in the r_2 and r_3 subspace with optimization of all the 3 N-8 degrees of freedom. The energy is given in eV and the successive contours are plot for $E = 0.02, 0.06, 0.1, 0.4, 0.7, 1.0, 1.1, 1.2, 1.6, 1.9, 2.2, 2.5, 3.0, 3.5, 4.0, 4.5, 6.0, 7.0$, and 8.0 eV. Coordinates r_2 and r_3 are in Å

4 Model and methods

4.1 System-bath model

We consider a one-dimensional model with an active coordinate $r_- = r_3 - r_2$. The potential energy $V(r_-)$ curve and the components of the dipole moment are shown in Fig. 2. In the r_2, r_3 subspace, we adopt a Cartesian kinetic energy operator with no cross-term what is justified since both coordinates have no common atom. The corresponding masses are $\mu_2 = \mu_3 = \mu_C/2$ with μ_C being the mass of a C atom. By taking linear combinations $r_- = r_3 - r_2$ and $r_+ = r_3 + r_2$, the kinetic energy remains separable and the part related to the $r_- = r_3 - r_2$ coordinate is $T_{r_-} = -\frac{\hbar^2}{2\mu_-}\frac{\partial^2}{\partial r_-^2}$ with $\mu_- = \mu_2/2 = \mu_C/4$. The model Hamiltonian describing the system and the bath is

$$H(t) = H_S(t) + H_B + H_{\mathrm{SB}} + H_{\mathrm{ren}} \tag{1}$$

with $H_S(t) = T_{r_-} + V(r_-) + W(r_-, E(t))$ where $W(r_-, E(t)) = -\sum_j \mu_j(r_-)E_j(t)$ describes the light-matter interaction at the electric dipolar approximation and j denotes the chosen linear polarizations of the field. In this expression, $H_B = \sum_{i=1}^{N}\left(T_i + m_i\omega_i^2 q_i^2/2\right)$ is a collection of harmonic oscillators which mimic the effects of the remaining modes and the solvent environment. We choose a bilinear coupling $H_{\mathrm{SB}} = -\sum_{i=1}^{N} c_i q_i r_-$ of the system degree of freedom to the modes of the model environment, which leads to a renormalization term $H_{\mathrm{ren}} = Cr_-^2/2$ with $C = \sum_{i=1}^{N} c_i^2/m_i\omega_i^2$. The coupling to the environment is determined by the coupling coefficients c_i, the distribution of which is given by the spectral density defined as

$$J(\omega) = \frac{\pi}{2}\sum_{i=1}^{N}\frac{c_i^2}{m_i\omega_i}\delta(\omega - \omega_i). \tag{2}$$

Within a perturbative approach, which is second order in the system-bath coupling, the entire bath dynamics enters into the system dynamics via the complex bath correlation function, defined by

$$C(t) = \frac{1}{2\pi}\int_{-\infty}^{\infty} \mathrm{d}\omega J(\omega)[\cos(\omega t)\coth(\beta\omega/2) - i\sin(\omega t)] \tag{3}$$

with $\beta = 1/k_B T$.

4.2 Auxiliary density matrix method

Open systems are generally described within the density matrix formalism [27–30, 41, 42]. The reduced density matrix $\rho_S(t)$ associated with the system is obtained by tracing over the bath coordinates. In the Nakajima–Zwanzig formalism [43], $\rho_S(t)$ is solution of a reduced equation containing a memory which depends on the whole history of the global system-bath

$$\dot{\rho}_S(t) = L_{\mathrm{eff}}\rho_S(t) + \int_0^t \mathrm{d}t' K(t,t')\rho_S(t') \tag{4}$$

where we have supposed a factorizing initial condition and where $L_{\mathrm{eff}}\cdot = -i[H_S(t) + H_{\mathrm{ren}}, \cdot]$ with $\hbar = 1$ and $[\cdot,\cdot]$ designates the commutator. Within the weak system-bath coupling (but not the light-matter interaction), the second-order perturbation gives a tractable expression for the memory kernel in which the bath only enters via its correlation function $C(t)$ and its Hermitian conjuguate $\bar{C}(t)$ [28–30, 38, 39]

$$\begin{aligned} K(t,t')\rho_S(t') = &-\left[x, C(t-t')\mathrm{e}^{L_S(t-t')}x\rho_S(t')\right] \\ &+\left[x, \bar{C}(t-t')\mathrm{e}^{L_S(t-t')}\rho_S(t')x\right] \end{aligned} \tag{5}$$

where we have noted x the active coordinate of the system ($x = r_-$ in our case) and $L_S\cdot = -i[H_S(t), \cdot]$. The basic efficient idea of the auxiliary matrix method is to propose a particular parameterization of the spectral density [28] as a combination of Lorentzian functions so that $C(t)$ can be expressed as a sum over the poles in the complex plane and takes a simple expression

$$C(t-t') = \sum_{k=1}^{n} C_k(t-t') = \sum_{k=1}^{n}\alpha_k \mathrm{e}^{i\gamma_k(t-t')} \tag{6}$$

A detailed derivation of these relations is given in Ref. [30]. By inserting this expression for $C(t)$, the integral of the memory term is split into a sum of contributions for each component k of the correlation function and each partial integral is set equal to an auxiliary matrix

$$\rho_k(t) = i\alpha_k \int_0^t \mathrm{d}t' \mathrm{e}^{i\gamma_k(t-t')} \mathrm{e}^{L_S(t-t')} x \rho_S(t') \tag{7}$$

By taking the time derivative of this integral, one obtains a set of coupled equations for the density matrix of the system $\rho_S(t)$ and the n auxiliary matrices $\rho_k(t)$. The main point is that this technique allows us to carry out non-Markovian dynamics by a system of coupled equations local in time.

At this stage, our contribution is an exploration of different numerical methods to get a stable solution in a molecular system involving many states. Different strategies exist to write the coupled system depending on the definition of the auxiliary matrices and the parameterization of $C(t-t')$ and $\bar{C}(t-t')$. Two different matrices can be connected to the real and imaginary part of each contribution $C_k(t-t')$ [29] or, as discussed in Ref. [30], we can attach only one matrix to each contribution $C_k(t-t')$ but still consider two possibilities for $\bar{C}(t-t')$. We present here only the working equations for which we have obtain stable numerical results. We use

$$\bar{C}(t-t') = \sum_{k=1}^{n} \bar{\alpha}_k e^{i\gamma_k(t-t')} \tag{8}$$

with the same γ_k as in Eq. (6). Then the equations take the form

$$\dot{\rho}_S(t) = L_{eff}\rho_S(t) + i\sum_k [x,\ \rho_k(t)] \tag{9}$$

$$\rho_k(t) = i\int_0^t dt' e^{i\gamma_k(t-t')} e^{L_s(t-t')} (\alpha_k \rho_s(t') - \bar{\alpha}_k \rho_s(t')x)$$

$$\dot{\rho}_k(t) = (i\gamma_k + L_S)\rho_k(t) + i[\alpha_k x \rho_S(t) - \bar{\alpha}_k \rho_S(t)x] \tag{10}$$

Finally, we give the operational relations for the α_k and the γ_k. If the spectral density is fitted by m Lorentzian functions

$$J(\omega) = \frac{\pi}{2}\sum_{k=1}^{m} p_k \frac{\omega}{\left[(\omega+\Omega_k)^2 + \Gamma_k^2\right]\left[(\omega-\Omega_k)^2 + \Gamma_k^2\right]} \tag{11}$$

m couples of poles in the evaluation of $C(t-t')$ come from $J(\omega)$. The corresponding coefficients are

$$\begin{aligned} \alpha_{k,1} &= \frac{p_k}{8\Omega_k\Gamma_k}[\coth(\beta(\Omega_k + i\Gamma_k)/2) - 1], \\ \alpha_{k,2} &= \frac{p_k}{8\Omega_k\Gamma_k}[\coth(\beta(\Omega_k - i\Gamma_k)/2) + 1] \\ \gamma_{k,1} &= \Omega_k + i\Gamma_k \text{ and } \gamma_{k,2} = -\Omega_k + i\Gamma_k \end{aligned} \tag{12}$$

Besides, a number of poles in principle infinite but finite in practice for a non-vanishing temperature come from the hyperbolic cotangent function in $C(t-t')$. They are

$$\alpha_k = 2iJ(i\nu_k)/\beta \text{ and } \gamma_k = i\nu_k \tag{13}$$

where $\nu_k = 2\pi(k-m)/\beta$ are the Matsubara frequencies. For $\bar{C}(t-t')$, one must take $\bar{\alpha}_{k,2} = \alpha^*_{k,1}, \bar{\alpha}_{k,1} = \alpha^*_{k,2}$ for $1 < k \leq m$ and $\bar{\alpha}_k = \alpha_k$ for $k > m$ [30].

The coupled equations have been integrated by the split-operator technique [44]. In matrix form, the system reads

$$\begin{pmatrix} \dot{\rho}_S(t) \\ \vdots \\ \dot{\rho}_k(t) \\ \vdots \end{pmatrix} = \begin{pmatrix} L_{eff}(t) & \cdots & L^- & \cdots \\ \vdots & & \vdots & \\ O_k & & L_S(t) + i\gamma_k & \\ \vdots & & \vdots & \end{pmatrix} \begin{pmatrix} \rho_S(t) \\ \vdots \\ \rho_k(t) \\ \vdots \end{pmatrix} \tag{14}$$

where $O_k = \frac{1}{2}[\alpha_k(L^- + L^+) + \bar{\alpha}_k(L^- - L^+)]$ where $O_k = \frac{1}{2}[\alpha_k(L^- + L^+) + \bar{\alpha}_k(L^- - L^+)]$ with $L^- = i[x, .]$ (i.e., a commutator) and $L^+ = i[x, .]_+$ (i.e., an anticommutator). In a more concise form, this can be written as

$$\partial_t \hat{\rho}(t) = \left(L_{\text{diag}} + L_{\text{off}}\right)\hat{\rho}(t)$$

where $\hat{\rho}(t)$ is a vector containing the system $\rho_S(t)$ and auxiliary density matrices $\rho_k(t)$, and L_{diag} and L_{off} are the diagonal and off-diagonal matrix blocks of Eq. (14) containing the operators in Liouville space. By splitting the diagonal and off-diagonal part, one gets $\hat{\rho}(t+\delta t) = e^{L_{\text{off}}\delta t/2} e^{L_{\text{diag}}\delta t} e^{L_{\text{off}}\delta t/2}\hat{\rho}(t)$. The diagonal part is applied on a grid basis set by using the usual fast Fourier transform between the position representation for the potential operator and the impulsion representation for the kinetic operator. The off-diagonal part is treated by a Cayley iteration procedure [29, 45].

4.3 Optimal control

In a preliminary step, the field is designed by optimal control theory without dissipation in the Hilbert space and we examine the stability when dissipative dynamics is used in the Liouville space with different spectral densities and system-bath couplings. Optimizing directly with the auxiliary matrices is in progress for a future work. In the case of the dynamics without dissipation, we can use the standard OCT approach based on the time-dependent Schrödinger equation. The optimal field able to drive the initial wave packet toward the target is determined by variational theory. In reactivity, the functional is usually the probability that the steered wave packet is the target at a given final time $t_{\max}$. The functional is maximized under the constraints that the laser fluence remains acceptable and the Schrödinger equation is satisfied at any time [24]

$$F[E(t)] = \left|\left\langle \psi(t_{\max}) \mid \psi_{\text{target}} \right\rangle\right|^2 - \alpha_0 \int_0^{t_{\max}} dt \sum_j E_j^2(t) - 2\Re e\left[\left\langle \psi(t_{\max}) \mid \psi_{\text{target}} \right\rangle \int_0^{t_{\max}} dt \langle \chi(t) | \partial_t - i\left(H^0 - \sum_j \mu_j E_j(t)\right) | \psi(t) \rangle\right] \tag{15}$$

with a positive Lagrange multiplier α_0. Varying the functional leads to three coupled equations: the Schrödinger equation for $|\psi(t)\rangle$ with an initial condition $|\psi(t=0)\rangle$ (usual forward propagation), the Schrödinger equation for the Lagrange multiplier $|\chi(t)\rangle$ which must be solved with a final condition $|\chi(t_{\max})\rangle = \left|\psi_{\text{target}}\right\rangle$ so that in practice it is solved by a backward propagation and the optimum field for each polarization j.

$$E_j(t) = -(1/\alpha_0)\Im m\left[\left\langle \psi(t) \mid \psi_{\text{target}}(t) \right\rangle \left\langle \psi_{\text{target}}(t) | \mu_j | \psi(t) \right\rangle\right] \tag{16}$$

The equations are solved by the Rabitz iterative monotonous algorithm [24]. We have used the improvement proposed in Ref. [46]. At each iteration k, the field is given by $E_j^{(k)} = E_j^{(k-1)} + \Delta E_j^{(k)}$ where $\Delta E_j^{(k)}$ is calculated by Eq. (16).

5 Results

In this section, we present the results for the laser control of the isomerization of Tiele's ester by a Cope rearrangement. Specifically, the aim is to design laser pulses which, when interacting with the sample, induce an isomerization from the Thiele's ester form (**2a**) to the product of its Cope rearrangement, noted target in Scheme 1, with the corresponding geometries given in Fig. 1. In what follows, we show that the interaction with specifically shaped laser pulses can indeed induce this isomerization reaction (Cope rearrangement), and thus produce a high yield of this molecule. Within this context, the influence of the surrounding bath plays a key role, and its effects are studied in detail in Sect. 5.2.

5.1 Control without dissipation

Only the ground vibrational state of the reactant is populated at room temperature since the energy gap between the two wells is 0.453 eV. One can consider that the initial ensemble is a pure case. The initial state is then this first vibrational eigenvector $|\psi(t=0)\rangle = |\phi_{n=1}\rangle$ where the n labels the eigenvectors. The ground state of the second well is the fifth eigenvector $\left|\psi_{\text{target}}\right\rangle = |\phi_{n=5}\rangle$. We optimize a field with a duration $t_{\max} = 5\,ps$ as short as possible taking into account a limiting value of the field amplitude of about 0.02 a.u. (1.028×10^8 Vcm^{-1}) to avoid strong fields able to ionize the molecule and to justify the neglect of polarization effects. We take two linear polarizations along directions x and y after an analysis of the dipole matrix elements. As usually in control theory the molecules are assumed to be oriented in the laboratory else we must admit that the field acts on the molecules well oriented in the ensemble. The trial field is chosen so that the localized vibrational states in the initial well up to the middle of the barrier are early populated in order to initiate the heating. Then the OCT finds the field able to cool the wave packet in the second well. The trial field is given by $E_j^{(0)}(t) = \varepsilon_0 s(t) \sum_{k=1}^{n_j} \cos(\omega_k t)$ with $j = x, y$. We choose three frequencies for the x polarization, ω_{12} (1,027.0 cm^{-1}), ω_{23} (1,004.6 cm^{-1}), ω_{34} (977.7 cm^{-1}) and two for y, ω_{46} (943.2 cm^{-1}), ω_{68} (892.0 cm^{-1}) with an amplitude $\varepsilon_0 = 10^{-2}$ a.u. (5.142×10^7 Vcm^{-1}). $s(t) = \sin^2(\pi t/t_{\max})$ is a smooth switching function. The fidelity defined by the probability to be in the target state at the end of the pulse $f = \left|\left\langle \psi(t_{\max}) \mid \psi_{\text{target}} \right\rangle\right|^2$ converges at 99.9 % after about 200 iterations. However, to force a limit maximum field amplitude, we divide the amplitude by a factor two and let iterate again for 100 iterations. This process is repeated twice. The final optimal field is drawn in Fig. 4 with its Fourier transform in which we find the zero-order frequencies mainly used for heating and all the other ones obtained by OCT to drive the wave packet in the delocalized states and to cool it toward the target.

Figure 5 gives the evolution of the population in the initial state and in the target as well as in some transitorily populated states during the control. The states belonging to the reactant well are drawn in full lines, those of the target well in dashed lines and the delocalized states in dots. At the beginning, the heating mainly populates the excited states of the reactant well using mainly the transitions proposed by the trial field. Then few highly delocalized states are transitorily populated and the OCT algorithm finds the transitions efficient for the cooling from the delocalized states. Some high frequencies appear in the Fourier transform of the field corresponding to very highly excited states but the probability remains very small and is not drawn in Fig. 5.

5.2 Stability of the control under dissipation

The optimal field is used to propagate the coupled system of auxiliary matrices by varying the spectral density of the

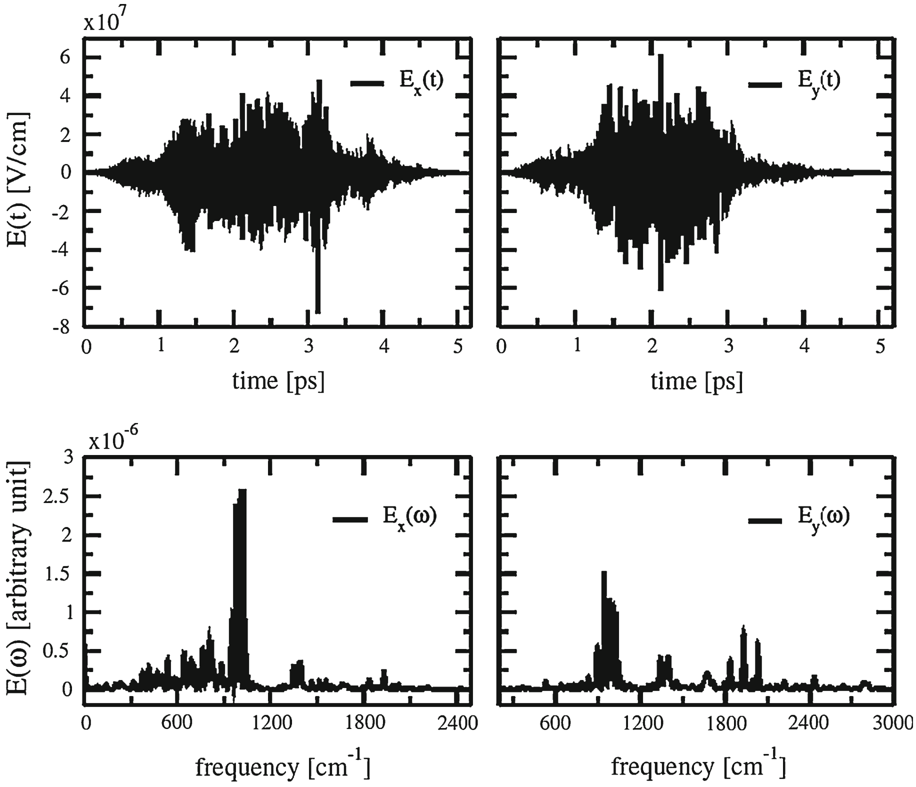

Fig. 4 Optimal field driving the isomerization in the 1D model without dissipation and the corresponding Fourier transforms

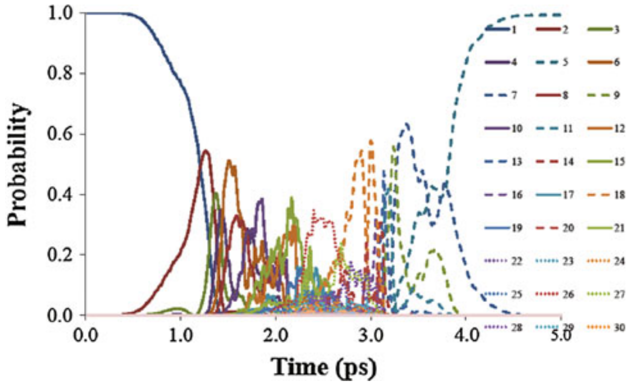

Fig. 5 Probability of populating the eigenstates of the 1D model during the control without dissipation. *Full lines*: states of the reactant well, *dashed lines*: states of the target well, *dots*: delocalized states

bath. The spectral density is taken to be Ohmic with a high-frequency cutoff ω_c

$$J(\omega) = \lambda\omega e^{-\omega/\omega_c} \tag{17}$$

This is fitted to the functional form of Eq. (11) with a single set of parameters k. We examine three cutoff frequencies ($\omega_c = 400$, 900 and 1,700 cm^{-1}), two coupling strengths ($\lambda = 10^{-3}$ and 5×10^{-4}) and three temperatures. The coupled system of auxiliary matrices is solved with 5, 10, and 15 Matsubara frequencies for

Table 2 Fidelity $f = \left|\left\langle \psi(t_{\max}) \mid \psi_{target} \right\rangle\right|^2$ of the control in % for different temperatures, cutoff frequencies ω_c and system-bath couplings λ (Eq. 17)

λ	300 K		200 K		100 K	
	10^{-3}	5×10^{-4}	10^{-3}	5×10^{-4}	10^{-3}	5×10^{-4}
ω_c (cm^{-1})						
400	84.7	91.9	89.1	94.3	93.7	96.7
900	83.3	91.1	87.8	93.6	92.3	96.0
1,700	80.6	89.7	85.9	92.8	88.7	96.3

$T = 300$, 200, and 100 K, respectively. The fidelities of the control are summarized in Table 2. As expected, the control field optimized without surrounding cannot achieve a perfect fidelity when dissipation occurs. However, we have selected examples showing that control is not completely destroyed and that in the context of reactivity an acceptable ratio can be obtained.

Upper left panel of Fig. 6 shows the evolution of the average energy of the field free system $\bar{E} = Tr[(T_{r_-} + V(r_-))\rho_S(t)]$ during the process and the upper right panel gives $Tr\left[\rho_S^2(t)\right]$ which is a measure of the decoherence of the quantum system. Lower panels of Fig. 6 show the Gabor transform of the field indicating when the frequencies appear in time

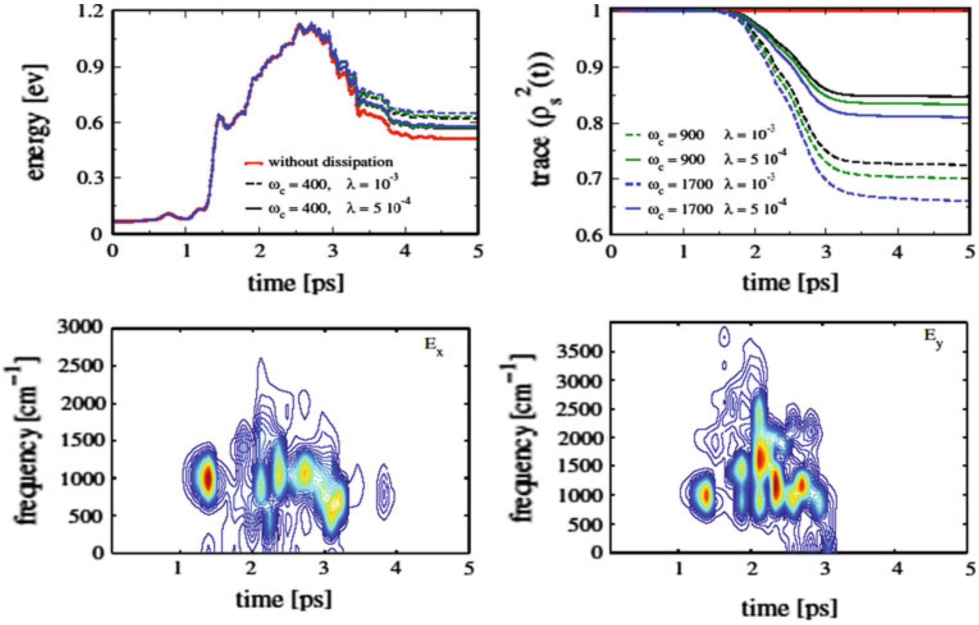

Fig. 6 Dissipative dynamics of the system for different cut-off frequencies ω_c and coupling λ (Eq. 17) at $T = 300$ K. The system is driven by the control field optimized without surrounding. *Left upper panel*: average energy $\bar{E} = Tr[(T_{r_-} + V(r_-))\rho_S(t)]$ of the field free system, *right upper panel*: measure of the purity of the system $Tr\left[\rho_S^2(t)\right]$. *Lower panels*: Gabor transform (Eq. 18) of the field showing when the frequencies operate during the process

$$F(\omega, t) = \left| \int_{-\infty}^{+\infty} H(s-t,\tau)E(s)e^{i\omega s}ds \right|^2 \qquad (18)$$

where $H(s,\tau)$ is the Blackman window [47] $H(s,\tau) = 0.08\cos(4\pi s/\tau) + 0.5\cos(2\pi s/\tau) + 0.42$ if if $|s| \le \tau/2$ and $H(s,\tau) = 0$ elsewhere and τ is the time-resolution chosen to be $\tau = 0.2$ ps. As shown also in Fig. 4, one sees that the process involves frequencies below 3,000 cm^{-1} and mainly frequencies around 1,000 cm^{-1}. They operate principally between 1.5 and 3.5 ps, thus during the crossing of the barrier. As a consequence, for a low value of the cutoff, the main frequencies experience a smaller effect of the surrounding bath, which is clearly confirmed by the results presented on Table 2. As expected, a higher temperature or an increased coupling strength also increases the dissipative effects, with the consequence that fidelity of the control, which was close to 100 % in the dissipative-free case, drops to about 80 % for the values $\omega_c = 1{,}700\ \text{cm}^{-1}$, $T = 300$ K and $\lambda = 10^{-3}$. This increased dissipative effects are also seen as a loss of the purity measured by $Tr\left[\rho_S^2(t)\right]$, given in Fig. 6 (right upper panel). Interestingly, in Fig. 6 (left upper panel), we find that the initial heating process is less affected by the dissipation than the subsequent cooling. Besides, the fact that dissipative effects accumulate in time, one reason could be that the isomerization proceeds via strongly delocalized states (see Fig. 5), which experience a higher degree of dissipation due to the position dependent coupling to the bath. To which extent an approach which includes dissipation at the design stage can compensate for this effect is currently under investigation.

6 Conclusion

We have presented preliminary studies toward the laser control of a Cope rearrangement in a realistic molecular system.

Our experimental study of the dimerization of methylcyclopentadienylcarboxylate (**1**) allowed identifying and characterizing all the products of the reaction. The process predominantly leads to Thiele's ester (**2a**), but the product of its Cope rearrangement could not be detected in the crude mixture.

The control process under study is the further isomerization of Thiele's ester at room temperature. In order to theoretically assess the possibility of laser control of this reaction, we have in a first step analyzed the reaction path and the transition state using high-level quantum chemistry methods. Based on these results, we have constructed a one- and two-dimensional model where the bond lengths r_2 and r_3 which achieve the dimerization after the Cope TS, are chosen as dynamical variables, the most representative ones of the motion along the reaction path. The one-dimensional model was used to theoretically construct a control field using optimal control theory. To assess the effect of a dissipative environment, we have applied the obtained optimal control field within a dissipative quantum propagation using a non-Markovian master equation approach. As expected, the control yield drops for an increasing dissipation. However, the objective chosen in our example retained a high degree of controllability, an encouraging result in view of a possible experimental realization. The next steps in our study consist in extending the control calculation to the proposed two-dimensional model. Furthermore, a very interesting aspect is the inclusion of the dissipation at the design step of the control field, to explore to which extent the external laser field can compensate, at least partially, for the dissipative effects caused by the environment. Studies along this line are currently in progress.

Acknowledgments Dr. G. Dive and Pr. R. Robiette are research fellows of the F.R.S.-FNRS of Belgium. The financial support of the F.R.S for the access to the HPC facilities installed at ULg and UCL is greatly acknowledged. This work was supported by the COST Action CM0708 CUSPFEL.

References

1. Brif C, Chakrabarti R, Rabitz H (2010) New J Phys 12:075008–075068
2. Korolkov MV, Manz J, Paramonov GK (1996) J Chem Phys 105:10874–10889
3. Došlić N, Sundermann K, González L, Mó O, Giraud-Girard J, Kühn O (1999) Phys Chem Chem Phys 1:1247–1257
4. Kühn O (2002) J Phys Chem A 106:7671–7679
5. Hoki K, Ohtsuki Y, Fujimura Y (2001) J Chem Phys 114:1575–1581
6. Vogt G, Krampert G, Niklaus P, Nuemberger P, Gerber G (2005) Phys Rev Lett 94:068305-4
7. Hoki K, Brumer P (2005) Phys Rev Lett 95:168305-4
8. Vogt G, Nuernberger P, Brixner T, Gerger G (2006) Chem Phys Lett 433:211–215
9. Kotur M, Weinacht T, Pearson BJ, Matsika S (2009) J Chem Phys 130:134311-5
10. Mitrić R, Petersen J, Bonačić-Koutecký V (2009) Phys Rev A 79:053416-6
11. Prokhorenko VI, Halpin A, Johnson PJM, Dwayne Miller RJ, Brown LS (2011) J Chem Phys 134:085105-10
12. Sha SP, Rice SA (2000) J Chem Phys 113:6536–6541
13. Gong J, Ma A, Rice SA (2005) J Chem Phys 122:204505-5
14. Zhang M, Gong J, Ma A, Rice SA (2007) J Chem Phys 127:144501-9
15. Artamonov M, Ho T-S, Rabitz H (2006) J Chem Phys 124:064306-10
16. Artamonov M, Ho T-S, Rabitz H (2006) Chem Phys 328:147–155
17. Sugny D, Kontz C, Ndong M, Justum Y, Dive G, Desouter-Lecomte M (2006) Phys Rev A 74:043419-14
18. Gräfe S, Meier C, Engel V (2007) J Chem Phys 122:184103-8
19. Cheng T, Darmawan H, Brown A (2007) Phys Rev A 75:013411-11
20. Kondorskiy A, Nakamura H (2008) Phys Rev A 77:043407-8
21. Kurosaki Y, Artamonov M, Ho T-S, Rabitz H (2009) J Chem Phys 131:044306-8
22. Lasorne B, Dive G, Desouter-Lecomte M (2005) J Chem Phys 122:184304-10
23. Marchand A, Zhao D, Ngooi T, Vidyasagar V (1993) Tetrahedron 49:2613–2620
24. Zhu W, Botina J, Rabitz H (1998) J Chem Phys 108:1953–1963
25. Garg A, Ohnuchic JN, Ambegaokar V (1985) J Chem Phys 83:4491–4503
26. Westermann T, Brodbeck R, Rozhenko AB, Shoeller W, Manthe U (2011) J Chem Phys 135:184102-12
27. Yan Y, Xu R (2005) Annu Rev Phys Chem 56:187–219
28. Meier C, Tannor DJ (1999) J Chem Phys 111:3365–3376
29. Keinekathöfer U (2004) J Chem Phys 121:2505–2514
30. Pomyalov A, Meier C, Tannor DJ (2010) Chem Phys 370:98–108
31. Spino C, Pesant M, Dory Y (1998) Angew Chem Int Ed 37:3262–3265
32. Thiele J (1901) Ber 34:68
33. Peters D (1959) J Chem Soc 1761–1765
34. Dunn GL, Donohue JK (1968) Tet Lett 31:3485–3487
35. Rippert AJ, Hansen H-J (1995) Helv Chem Acta 78:238–241
36. Minter DE, Marchand AP, Lu S (1990) Magn Reson Chem 28:623–627
37. Gaussian 09, Revision A.1, Frisch MJ, Trucks GW, Schlegel HB, Scuseria GE, Robb MA, Cheeseman JR, Scalmani G, Barone V, Mennucci B, Petersson GA, Nakatsuji H, Caricato M, Li X, Hratchian HP, Izmaylov AF, Bloino J, Zheng G, Sonnenberg JL, Hada M, Ehara M, Toyota K, Fukuda R, Hasegawa J, Ishida M, Nakajima T, Honda Y, Kitao O, Nakai H, Vreven T, Montgomery Jr JA, Peralta JE, Ogliaro F, Bearpark M, Heyd JJ, Brothers E, Kudin KN, Staroverov VN, Kobayashi R, Normand J, Raghavachari K, Rendell A, Burant JC, Iyengar SS, Tomasi J, Cossi M, Rega N, Millam JM, Klene M, Knox JE, Cross JB, Bakken V, Adamo C, Jaramillo J, Gomperts R, Stratmann RE, Yazyev O, Austin AJ, Cammi R, Pomelli C, Ochterski JW, Martin RL, Morokuma K, Zakrzewski VG, Voth GA, Salvador P, Dannenberg JJ, Dapprich S, Daniels AD, Farkas Ö, Foresman JB, Ortiz JV, Cioslowski J, Fox DJ, Gaussian, Inc., Wallingford CT (2009)
38. Becke AD (1993) J Chem Phys 98:5648–5652
39. Francl MM, Pietro WJ, Hehre W, Binkley J, DeFrees D, Pople JA, Gordon M (1982) J Chem Phys 77:3654–3665
40. SAS 9.1 licenced to University of Liège; copyright (c) 2002–2003 by SAS Institute Inc., Cary, NC, USA
41. Ohtsuki Y (2001) J Chem Phys 119:661–671
42. Xu R, Yan Y, Ohtsuki Y, Fujimura Y, Rabitz H (2004) J Chem Phys 120:6600–6608
43. Breuer H-P, Petruccione F (2003) The theory of open quantum systems. Wiley, New-York
44. Feit MD, Fleck JA, Steiger A (1982) J Comput Phys 47:412–433
45. Press WH, Flannery BP, Teukolsky SA, Vetterling WT (1989) Numerical Recipes. Cambridge University Press, Cambridge
46. Palao JP, Kosloff R (2002) Phys Rev Lett 89:188301-4
47. Sugawara M, Fujimura Y (1994) J Chem Phys 100:5646–5655

Theor Chem Acc (2012) 131:1238
DOI 10.1007/s00214-012-1238-3

REGULAR ARTICLE

Ruthenocene and cyclopentadienyl pyrrolyl ruthenium as precursors for ruthenium atomic layer deposition: a comparative study of dissociation enthalpies

Quan Manh Phung · Steven Vancoillie ·
Annelies Delabie · Geoffrey Pourtois ·
Kristine Pierloot

Received: 2 March 2012 / Accepted: 14 May 2012 / Published online: 20 June 2012

Abstract $RuCp_2$ (ruthenocene) and RuCpPy (cyclopentadienyl pyrrolyl ruthenium) complexes are used in ruthenium (Ru) atomic layer deposition (ALD) but exhibit a markedly different reactivity with respect to the substrate and co-reactant. In search of an explanation, we report here the results of a comparative study of the heterolytic and homolytic dissociation enthalpy of these two ruthenium complexes, making use of either density functional theory (DFT) or multiconfigurational perturbation theory (CASPT2). While both methods predict distinctly different absolute dissociation enthalpies, they agree on the relative values between both molecules. A reduced heterolytic dissociation enthalpy is obtained for RuCpPy compared to $RuCp_2$, although the difference obtained from CASPT2 (19.9 kcal/mol) is slightly larger than the one obtained with any of the DFT functionals (around 17 kcal/mol). Both methods also agree on the more pronounced stability of the Cp^- ligand in RuCpPy than in $RuCp_2$ (by around 9 kcal/mol with DFT and by 6 kcal/mol with CASPT2).

Keywords Ruthenocene · Dissociation enthalpy · DFT · CASPT2

1 Introduction

Atomic layer deposition (ALD) [1] is an advanced technique to deposit nanometer-thin films on a substrate, starting from gas-phase precursors and making use of a cyclic process of at least two consecutive self-limiting chemisorption reactions, the so-called "reaction cycle". Two important properties, namely (a) conformal deposition on complex nanostructures (i.e., following the shape of the underlying structure) and (b) control of the deposition process at the atomic level, have turned ALD into a powerful technique in nanotechnology [2]. For example, ALD is used in the industrial production of MOSFETs (Metal Oxide Semiconductor Field Effect Transistors) and memories to deposit thin highly insulating dielectric oxide layers [3].

ALD of ruthenium (Ru) is currently under extensive investigation. Ru is a new electrode material for trenched metal–insulator–metal capacitors of dynamic random access memories (DRAM), as well as a possible component of the metal connection between the elements of an integrated circuit. The Ru ALD reaction cycle consists of two reactions: a Ru precursor chemisorption reaction followed by a co-reactant chemisorption reaction. The most suitable precursors for ALD of high-quality Ru thin films have not yet been identified. Ru precursors under investigation are the organometallic Ru compounds with cyclopentadienyl (Cp, C_5H_5) or pyrrolyl (Py, C_4H_4N) ligands,

---

Published as part of the special collection of articles celebrating theoretical and computational chemistry in Belgium.

Electronic supplementary material The online version of this article (doi:10.1007/s00214-012-1238-3) contains supplementary material, which is available to authorized users.

Q. M. Phung · S. Vancoillie (✉) · K. Pierloot
Department of Chemistry, University of Leuven,
Celestijnenlaan 200F, 3001 Leuven, Belgium
e-mail: steven.vancoillie@chem.kuleuven.be

A. Delabie · G. Pourtois
imec, Kapeldreef 75, 3001 Leuven, Belgium

G. Pourtois
Department of Chemistry, PLASMANT research group,
University of Antwerp, Universiteitsplein 1,
2619 Antwerp, Wilrijk, Belgium

β-diketonates, amidinates, and RuO_4 [4, 5]. An ALD precursor should be stable in the gas phase, but reactive on both the initial substrate and the deposited film. $RuCp_2$ and RuCpPy as well as their substituted complexes, for example, $Ru(EtCp)_2$ (Et = ethyl) and Ru(MeCp)Py (Me = methyl), have the advantage to be stable up to high temperatures in the gas phase and may be used in combination with different co-reactants, such as O_2 or a plasma (N_2, H_2, N_2/H_2, or NH_3 plasma). In the latter case, the process is referred to as plasma-enhanced ALD or PEALD (Fig. 1). In a recent comparative study of $Ru(EtCp)_2$ and Ru(MeCp)Py as precursors for PEALD of Ru, the reactivity of these two molecules was found to be quite different [6]. Starting from a TiN surface, a major nucleation delay was observed for the $Ru(EtCp)_2$ precursor, whereas much better nucleation was observed with Ru(MeCp)Py. Moreover, the growth-per-cycle at steady state, that is, the thickness of the deposited Ru layer per reaction cycle, was 0.038 nm/cycle for Ru(MeCp)Py, but only 0.016 nm/cycle for $Ru(EtCp)_2$.

Fundamental understanding of ruthenium ALD chemisorption reaction mechanisms and how the precursor chemistry controls the process (e.g., the specific role of Py versus Cp ligands) is still lacking. Theoretical calculations may play an important role in obtaining such understanding, by providing information concerning the stability of different ALD precursors and by predicting possible chemisorption reaction mechanisms. However, so far, almost no theoretical studies of reaction mechanisms for Ru ALD have been reported in the literature. Only one study reports the reaction mechanisms for homoleptic Ru precursors and oxygen [7]. In this work, we present the results from a computational study of the relative stability of $RuCp_2$ and RuCpPy with respect to ligand dissociation, either heterolytically or homolytically. No substituents on the ligands were included, as experiments have indicated that such substituents only have a minor influence on the ALD process. We have employed both density functional theory (DFT) and multiconfigurational perturbation theory (CASPT2) to obtain the Ru–Cp and Ru–Py binding energies. No experimental data are available for the dissociation enthalpies of the complexes studied. Therefore, to judge the quality of the present calculations, we will rely on the results of our previous computational study [8], using the same approach, of the heterolytic dissociation enthalpy of a number series of first-row metallocenes MCp_2 (M = V, Mn, Fe, Ni) for which experimental data are indeed available. In that study, we showed that with multiconfigurational perturbation theory, CASPT2 or RASPT2 (with "R" denoting that the reference wave function is built from a restricted rather than a complete active space) based on an extended active space (up to 18 active orbitals), the dissociation enthalpy of these first-row metallocenes may be predicted with an accuracy that is close to (or even within) the experimental accuracy for manganocene, ferrocene, and nickelocene (the difference with the experimental values amounting to 0.5, 4.1 and −6.6 kcal/mol, respectively), while a (unexpected) larger error, 9.6 kcal/mol, was obtained for vanadocene. Of course, since we have no experimental values for the dissociation enthalpies of ruthenocene, we can never be completely sure that the CASPT2 errors are similar to those of the first-row metallocenes. Among the DFT functionals used, the hybrid functional B3LYP-D is obviously superior, with an average (absolute) error on the dissociation enthalpy of 4.1 kcal/mol and a maximum error of +8.7 kcal/mol for nickelocene. Importantly, both dispersion interactions and relativistic effects were found to give significant contributions to the binding energies, and should therefore be taken into account. Two other functionals, PBE0 and M06, were also intensively studied, but were both found to overbind, with average errors of +12.4 kcal/mol (PBE0, with dispersion corrections taken from B3LYP) and 11.3 kcal/mol (M06). In this work, we will present the results obtained from DFT with three functionals, that is, the hybrid functionals B3LYP and PBE0 and the GGA PBE. The latter functional is included because it is widely used in solid-state calculations, an alternative approach to study the bonding and reactivity of the present Ru compounds at different surfaces, which we intend to use in a future study. The main goal of the present study therefore is to benchmark the results obtained with different functionals, PBE in particular, against high-level ab initio results.

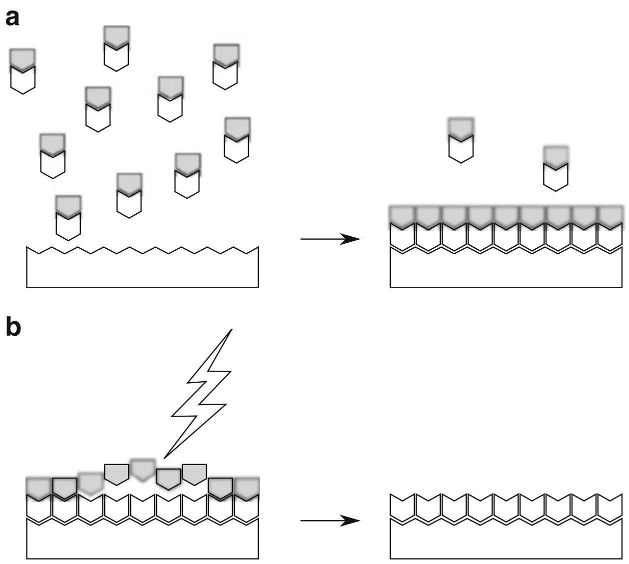

Fig. 1 Schematic representation of the reaction cycle for Ru PEALD. **a** Ru precursor chemisorption reaction, **b** plasma reaction

2 Computational details

Both density functional theory (DFT) and multiconfigurational perturbation theory, that is, complete active space self-consistent field (CASSCF) followed by second-order perturbation theory (CASPT2), were used to investigate the heterolytic and homolytic dissociation enthalpies of $\mathrm{RuCp_2}$ and RuCpPy. The enthalpies of nine possible reaction steps involved in the dissociation (R1–R9, see Figs. 2, 3) were computed. All DFT calculations were performed with TURBOMOLE v. 6.3 [9], while the CASSCF/CASPT2 calculations were performed with MOLCAS 7.6 [10].

Extensive basis sets were used in the DFT calculations: def2-QZVPP for the Ru atom [11] and def2-TZVP for all other atoms [12]. We showed previously that these basis sets yield reliable results with small basis set superposition errors (BSSE) [8]. To describe scalar relativistic effects, an effective core potential was used for ruthenium, describing the behavior of 28 core electrons (ecp-28-mwb) [13]. A dispersion correction to DFT (DFT-D2) [14] was used to cover the attractive dispersion interaction between two cyclopentadienyl rings, which was shown to contribute significantly to the metal–Cp binding energies in our previous study [8]. Since the DFT-D2 parameters are only available for the B3LYP and PBE functionals, dispersion corrections for the PBE0 functional were adopted from B3LYP-D.

For the multiconfigurational perturbation theory (CASPT2) calculations, extended all-electron ANO-RCC basis sets were used with the following contractions: [10s9p8d6f4g2h] for the Ru atom [15], [8s7p4d3f1g] for carbon and nitrogen [16], and [6s4p3d1f] for hydrogen [17]. We showed that such large basis sets are needed to reduce the basis set superposition errors (BSSE) on the heterolytic dissociation enthalpy of first-row metallocenes to an acceptable level of a few kcal/mol [8, 18]. The Cholesky decomposition technique was used to approximate the two-electron integrals, using a threshold of 10^{-6} au [19]. Scalar relativistic effects were included using the standard second-order Douglas–Kroll–Hess Hamiltonian [20–22]. In the perturbation step, the default IPEA shift for the zeroth-order Hamiltonian [23] (0.25 au) was used, and an imaginary level shift [24] of 0.1 au was included to prevent weak intruder states. All valence electrons, including the ruthenium (4s,4p) semi-core electrons, were included in the CASPT2 calculations. Since it is computationally unfeasible to optimize the metallocene structure with CASPT2, single-point calculations were instead performed on the ground state PBE0 structures of all molecules. In previous studies [8, 18, 25] we have already shown that this functional performs best for obtaining accurate structures for transition metal complexes (close to experiment, and, in comparison with other functionals, also providing the lowest CASPT2 energy).

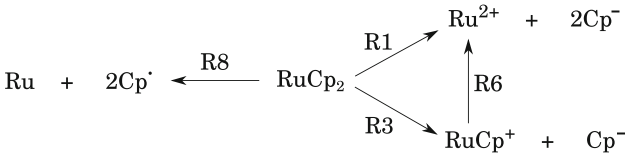

Fig. 2 Dissociation reactions of $\mathrm{RuCp_2}$

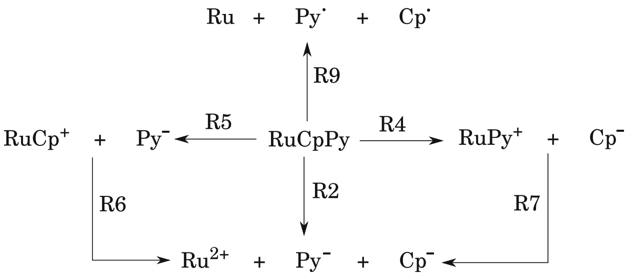

Fig. 3 Dissociation reactions of RuCpPy

Within the $\mathrm{D_{5h}}$ symmetry of ruthenocene, the Ru 4d orbitals belong to the irreducible representations (irreps) $\mathrm{a}_1'(4\mathrm{d}_{z^2}), \mathrm{e}_2'(4\mathrm{d}_{xy}, 4\mathrm{d}_{x^2-y^2})$, and e_1'' ($4\mathrm{d}_{xz}$, $4\mathrm{d}_{yz}$), whereas the cyclopentadienyl carbon $2\mathrm{p}_z$ orbitals form symmetry-adapted combinations giving rise to six occupied π orbitals belonging to the $\mathrm{a}_1', \mathrm{a}_2'', \mathrm{e}_1', \mathrm{e}_1''$ irreps, and four empty π^* orbitals belonging to the e_2' and e_2'' irreps. Only those Cp π and π^* within the same irreps as the metal d orbitals can interact to form covalent metal–ligand combinations, that is, the $\mathrm{a}_1', \mathrm{e}_2'$, and e_1'' irreps. Since the metal $4\mathrm{d}_{z^2}$ and $\mathrm{Cp^-}$ π orbitals in irrep a_1' are energetically well separated, they do not strongly interact. Ru–Cp bonding occurs through charge donation from the Cp e_1'' (π) into the metal e_1'' ($4\mathrm{d}_{xz}$, $4\mathrm{d}_{yz}$) orbitals, counteracted by backdonation from the metal e_2' $(4\mathrm{d}_{xy}, 4\mathrm{d}_{x^2-y^2})$ into the Cp $\mathrm{e}_2'(\pi^*)$ orbitals. The Cp e_1'' (π) and e_2' (π^*) cyclopentadienyl orbitals should therefore be added to the metal d orbitals in the active space, yielding a total of nine active orbitals containing eight electrons. In previous studies [8, 18], we have shown, however, that a more accurate description of the dissociation enthalpy of metallocenes may be obtained from the second-order perturbation treatment after extending the reference active space with (a) four additional cyclopentadienyl orbitals: $\mathrm{e}_1'(\pi)$, $\mathrm{e}_2''(\pi^*)$ and (b) an extra virtual 4d′ shell to describe the double-shell effect. This would then give a total of 14 electrons in 18 active orbitals, CAS(14,18) becoming computationally unaffordable with CASSCF. However, test calculations (making instead use of RASSCF, that is, restricting the excitation level in the active space) made clear that an active space of 14 orbitals, lacking two virtual shells $\mathrm{e}_1'', \mathrm{e}_2'$ would in fact suffice in the present case. The obvious reason is that the nd double-shell effect is much less pronounced for 4d than for 3d transition metals [26]. This being the case, these four orbitals, which were intended to have Ru 4d$'$ character, instead rotated into Ru 4f, while remaining very weakly occupied (<0.01). The 14 orbitals included in the CAS(14,14) active space of ruthenocene are plotted in Fig. 4, with their occupation numbers indicated within brackets. As one can see, the weakly occupied a_1' orbital is almost pure $4d'_{z^2}$, whereas the weakly occupied $e_1''(\pi^*)$ shell also shows significant admixture of $(4d'_{xy}, 4d'_{x^2-y^2})$ character. This suffices to describe the 4d double-shell effect in the present $4d^6$ systems.

Upon heterolytic dissociation, the CAS(14,14) active space gets subdivided in a CAS(4,4) space on each of the ligand anions, leaving CAS(10,10) for $RuCp^+$ and $RuPy^+$ and a CAS(6,6) space for the Ru^{2+} ion. In order to provide a more balanced treatment of symmetry and correlation for the ^5D ground state of this ion, four extra 4d$'$ orbitals were included, giving a CAS(6,10) space (note that a similar procedure was also used previously for ferrocene [18]). Using instead the smaller CAS(6,6) space, however, gives a total CASPT2 energy for Ru^{2+}, which is lower by only 0.4 kcal/mol, and hence would also lower the CASPT2 results for the heterolytic dissociation enthalpies involving Ru^{2+} (Tables 2, 3) by the same amount. This confirms that the 4d double-shell effect is indeed very limited in the present $4d^6$ case. Homolytic dissociation energies (R8, R9 in Figs. 2, 3) were obtained by subtracting from the heterolytic dissociation energy the $Ru \rightarrow Ru^{2+}$ ionization energy and adding the electron affinities of both ligands. In these calculations, the 4s orbital was included in the active space of the Ru atom, giving CAS(8,11), while the ligand radicals were described with a CAS(3,4) space.

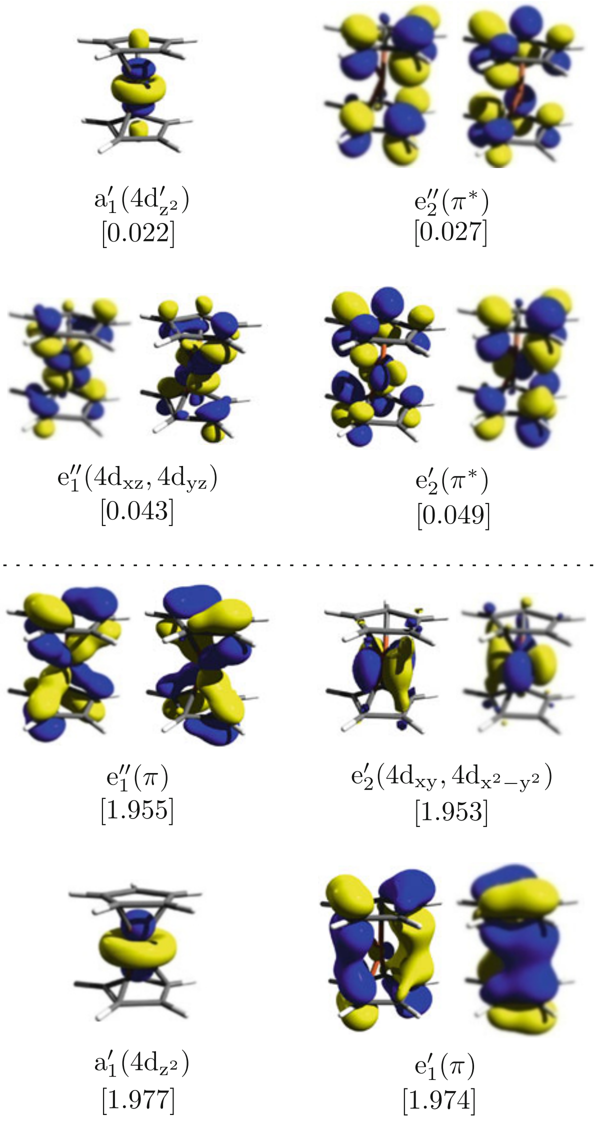
$a_1'(4d'_{z^2})$
[0.022]
$e_2''(\pi^*)$
[0.027]
$e_1''(4d_{xz}, 4d_{yz})$
[0.043]
$e_2'(\pi^*)$
[0.049]
$e_1''(\pi)$
[1.955]
$e_2'(4d_{xy}, 4d_{x^2-y^2})$
[1.953]
$a_1'(4d_{z^2})$
[1.977]
$e_1'(\pi)$
[1.974]

Fig. 4 The active space CAS(14,14)

Dissociation enthalpies at room temperature ΔH°_{298} were obtained by starting from the electronic binding energies (denoted as ΔE_{elec} in Table 2) and including corrections for the zero-point vibrational energy (ΔE_{ZPE}) and thermal energy ($\Delta E_{thermal}$), as obtained from frequency calculations on the molecules involved in the chemical process described. For the CASPT2 data, these values were taken from PBE0. Moreover, a counterpoise correction (ΔE_{CPC}) was added to all binding energies to account for basis set superposition errors. The composition of the dissociation enthalpies ΔH°_{298} with respect to the different terms described here is provided in Table 2, describing the (full) heterolytic dissociation processes of both considered molecules (reactions R1 and R2). For the other reactions, only ΔH°_{298} values are given in Tables 3, 4, while the detailed composition of these data is provided in Online Resource 1.

3 Results and discussion

3.1 Heterolytic dissociation enthalpy of $RuCp_2$ and RuCpPy

Bond distances of the experimental and calculated structures of ruthenocene are shown in Table 1. $RuCp_2$ has an eclipsed structure belonging to the D_{5h} point group, with a $^1A_1'$ electronic ground state. For RuCpPy, the eclipsed geometry (C_s symmetry, $^1A_1'$ electronic state) was also found to be slightly more stable (by 0.3 kcal/mol computed with the B3LYP functional) than the staggered geometry.

GGA functionals are expected to provide reasonably accurate geometries for second-row transition metal complexes [28]. This is true for the PBE functional, giving a Ru–Cp ring distance that is shorter by only 0.013 Å with respect to the experimental value. Corresponding errors of B3LYP and PBE0 are +0.021 Å and −0.021 Å,

Table 1 Experimental and calculated bond lengths (Å) in $RuCp_2$ and RuCpPy

	PBE	B3LYP	PBE0	Exp. [27]
$RuCp_2$				
C–C	1.436(1.437)[a]	1.427(1.428)[a]	1.424	1.430
Ru–Cp[b]	1.803(1.794)[a]	1.837(1.823)[a]	1.795	1.816
RuCpPy				
Ru–Cp[b]	1.797(1.789)[a]	1.829(1.816)[a]	1.788	–
Ru-Py[b]	1.813(1.805)[a]	1.850(1.839)[a]	1.807	–

[a] The values in parentheses correspond to the dispersion corrected geometry

[b] Distance to the center of the ring

respectively. In our previous study on ferrocene [8], the PBE0 geometry of this molecule was found to be in closer agreement with experiment (i.e., shorter by only 0.009 Å). The larger discrepancy observed for the PBE0 functional in case of ruthenocene might arise from the fact that the experimental structure of ruthenocene was measured at 101 K and was not vibrationally corrected [27]. As the values within parentheses in Table 1 indicate, including a dispersion correction leaves the C–C and C–H distances invariant, while shortening the Ru–Cp and Ru–Py ring distances. Obviously, this is related to the attractive dispersion interaction between both ligands, as was also found in first-row metallocenes [8]. All functionals predict a shorter Ru–Cp distance (by about 0.01 Å) in RuCpPy as compared to $RuCp_2$. The Ru–Cp distance is also systematically shorter by 0.02 Å than the Ru–Py distance.

We started by studying the full heterolytic dissociation reactions of both molecules: R1 (Fig. 2) and R2 (Fig. 3). The computed dissociation enthalpies are shown in Table 2. Among the DFT results, we find the following order with respect to the size of the heterolytic dissociation enthalpies: PBE > PBE0 > B3LYP, with differences of around 20 kcal/mol between successive results in this list. The CASPT2 results are in between PBE and PBE0, 9–11 kcal/mol lower than the PBE values, and about 30 kcal/mol higher than the lowest DFT result, obtained from B3LYP. These trends are very similar between both molecules. However, it is already clear from these results that the Ru–Py bond is considerably weaker than the Ru–Cp bond. We can see that the heterolytic dissociation enthalpy of RuCpPy is 17.4, 17.2, and 18.1 kcal/mol smaller than the corresponding value of $RuCp_2$ using PBE, B3LYP, and PBE0 functionals, respectively. Thus, the difference between the data obtained for both molecules remains virtually constant across the different functionals and is also close to the difference obtained with CASPT2, 19.9 kcal/mol.

We note that the DFT results in general show the same general trends as for ferrocene [8], although for the latter molecule, a much larger difference was found between the PBE and PBE0 result of ΔH°_{298} (60 kcal/mol, as compared to 20 kcal/mol here), whereas the results obtained with both hybrid functionals were closer (with a difference of only 10 rather than 20 kcal/mol). More remarkable though are the relative values as compared to CASPT2. Although the ab initio results for ferrocene were obtained with a larger active space of 18 orbitals (and, for that reason, employing RASPT2 rather than CASPT2), we believe that the accuracy of the present CASPT2(14,14) results should be comparable to the RASPT2(14,18) results for ferrocene. This is because the four extra orbitals in the active space of ferrocene are describing the nd double-shell effect, which is pronounced for 3d metals, but much less for the present 4d systems (see also the Sect. 2). The RASPT2(14,18) result for ΔH°_{298} of ferrocene, 639.1 kcal/mol, agrees with the experimental value, 635 ± 6 kcal/mol, to within the experimental uncertainty. As such, a similar accuracy may be expected for the CASPT2 results presented in Table 2. However, when it comes to judging the quality of the DFT results against CASPT2, we find that for $RuCp_2$ and RuCpPy, the results obtained from the PBE functional are closest, that is, higher by 9–12 kcal/mol, whereas for ferrocene, the same functional grossly overestimates the

Table 2 ΔH°_{298} (kcal/mol) of the full heterolytic dissociation reactions of $RuCp_2$ and RuCpPy

	$RuCp_2 \longrightarrow Ru^{2+} + 2Cp^-$ (R1)				$RuCpPy \longrightarrow Ru^{2+} + Cp^- + Py^-$ (R2)			
	PBE	B3LYP	PBE0	CASPT2	PBE	B3LYP	PBE0	CASPT2
ΔE_{elec}	724.6	680.0	700.8	722.8	707.1	662.8	682.8	701.1
ΔE_{disp}	8.1	10.9	10.9[a]	–	7.5	10.1	10.1[a]	–
ΔE_{CPC}	−5.7	−5.2	−4.8	−4.7	−5.7	−5.1	−4.7	−3.5
ΔE_{ZPE}	−7.9	−8.1	−8.1	−8.1[b]	−7.0	−7.3	−7.4	−7.4[b]
$\Delta E_{thermal}$	1.8	1.7	1.8	1.8[b]	1.6	1.6	1.7	1.7[b]
ΔH°_{298}	720.9	679.3	700.6	711.8	703.5	662.1	682.5	691.9

[a] Dispersion correction taken from B3LYP

[b] Taken from PBE0

dissociation enthalpy, by 50 kcal/mol. On the other hand, both hybrid functionals perform considerably worse than for $FeCp_2$. Whereas the PBE0 value of ΔH°_{298}, 639.4 kcal/mol, was in excellent agreement with RASPT2 for ferrocene, it is now about 11 kcal/mol too low. Similarly, the B3LYP value is now 30 kcal/mol below CASPT2 instead of 10 kcal/mol in case of ferrocene. In general, the binding enthalpies predicted from DFT are considerably lowered with respect to CASPT2 when going from ferrocene to the present ruthenium complexes.

As a next step in our study of the stability of $RuCp_2$ and RuCpPy, we also looked at the individual dissociation steps of a single Cp^- and Py^- ligand from either $RuCp_2$ or RuCpPy. The results obtained for the reaction enthalpies of the consecutive single ligand dissociation steps (a first ligand in reactions R3, R4, and R5, and a second ligand in reactions R6 and R7; cf. Figs. 2, 3) are collected in Table 3 and presented graphically in Fig. 5. We first note that both $RuCp^+$ and $RuPy^+$ are characterized by a low-spin S = 0 ground state. The lowest triplet excited state was found at a considerably higher energy relative to the singlet ground state, 24.0–29.0 kcal/mol for $RuCp_2$ and 18.4–24.3 kcal/mol for RuCpPy, with the lowest quintet state at an even higher energy. This then also means that the first ligand dissociation step is spin conserving, whereas the second dissociation step involves a singlet-to-quintet spin flip. This fact may be used to (partially) rationalize the trends observed in the DFT data in Table 3. For the first, spin conserving step, the enthalpies obtained from PBE and PBE0 are close to within 5 kcal/mol, the latter functional systematically giving the highest value. On the other hand, B3LYP predicts significantly (10–15 kcal/mol) weaker Ru–ligand bond strengths. As compared to CASPT2, all three functionals underestimate the dissociation enthalpy, although for PBE0, the difference with CASPT2 is small, between 2 and 5 kcal/mol. As for the second dissociation step, here the difference between PBE and PBE0 is much larger. The pure GGA functional PBE typically considerably overestimates the stability of the low-spin monoligated complex with respect to the high-spin Ru^{2+} ground state, thus giving too large binding enthalpies. Including (25 %) Hartree–Fock exchange in PBE0 remediates for this, but seems to overshoot, as the PBE0 binding enthalpies now become smaller by about 7 kcal/mol than the corresponding CASPT2 data. With 20 % Hartree–Fock exchange, B3LYP should do well for the spin flip contribution, but also here this functional seems to quite strongly underestimate the bond strength, by 12–14 kcal/mol as compared to the CASPT2 results.

Table 3 Heterolytic dissociation enthalpy ΔH°_{298} (kcal/mol) of the first dissociation reactions R3, R4, and R5 and the second dissociation reactions R6 and R7

	PBE	B3LYP	PBE0	CASPT2
$RuCp_2 \longrightarrow RuCp^+ + Cp^-$ (R3)	232.5	221.7	236.6	241.7
$RuCpPy \longrightarrow RuPy^+ + Cp^-$ (R4)	241.6	231.5	245.7	247.3
$RuCpPy \longrightarrow RuCp^+ + Py^-$ (R5)	215.0	204.5	218.4	221.9
$RuCp^+ \longrightarrow Ru^{2+} + Cp^-$ (R6)	488.4	457.6	464.0	470.1
$RuPy^+ \longrightarrow Ru^{2+} + Py^-$ (R7)	461.9	430.6	436.8	444.6

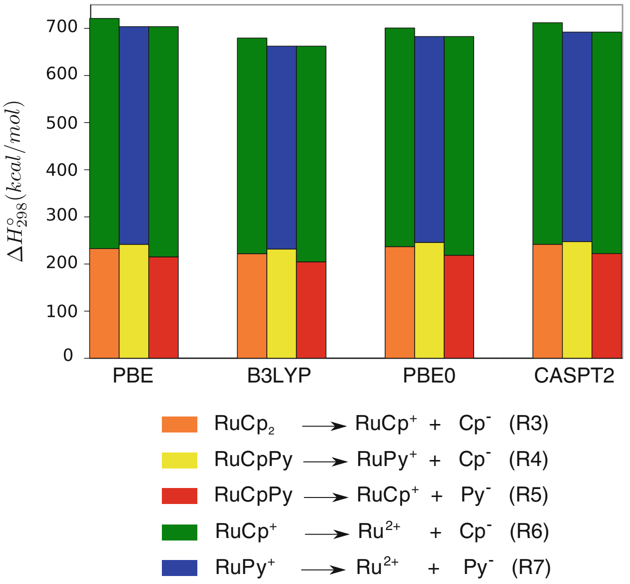

Fig. 5 Heterolytic dissociation enthalpies of the two consecutive reactions leading to full dissociation of $RuCp_2$ and RuCpPy, as computed with different methods

As Table 3 indicates, both DFT and CASPT2 predict easier dissociation of a first ligand from RuPyCp than from $RuCp_2$. The first ligand to dissociate from RuPyCp is Py^- (R5), and this dissociation step requires 17–18 kcal/mol less with DFT and 19.8 kcal/mol less with CASPT2 than the dissociation of the first Cp^- ligand from $RuCp_2$ (R3). As both reactions result in the same monoligated complex, $RuCp^+$, the differences between the first dissociation enthalpies necessarily equal the differences in the total heterolytic dissociation enthalpies of both molecules (Table 2). Reactions R3 and R4 involve the dissociation of a Cp^- ligand from either $RuCp_2$ or RuCpPy. Comparing these two reactions, we note that the presence of a pyrrolyl rather than a cyclopentadienyl as the second ligand in the complex induces a Ru–Cp bond strengthening: Cp^- dissociation from RuCpPy is harder than from $RuCp_2$ at all calculated levels. This is in agreement with the shorter Ru–Cp ring distance found for the former compound (Table 1). The difference between both dissociation enthalpies is similar for the different functionals (9.1–9.8 kcal/mol), whereas from CASPT2, a smaller difference of 5.6 kcal/mol is obtained. Reactions R4 and R5 describe the dissociation of either Cp^- or Py^- from RuCpPy. The latter process is clearly more favorable, with a dissociation enthalpy that is lower by as much as 27 kcal/mol with DFT (again fluctuations between different functionals are minor) and slightly less, 25.4 kcal/mol, with CASPT2.

Another important point to note from Table 3 is that the second dissociation steps, either $RuCp^+ \longrightarrow Ru^{2+} + Cp^-$ (R6) or $RuPy^+ \longrightarrow Ru^{2+} + Py^-$ (R7), require an energy which is about twice as high as any of the first dissociation steps. This is another observation that might be relevant to the course of the chemical reactions occurring during the ruthenium ALD process. Indeed, based on this, one might suspect that perhaps a first but not both ligands could be dissociated from the Ru precursor already during the first chemisorption step of the ALD reaction cycle (Fig. 1), meaning that the co-reactant would have to assist in the removal of the second ligand.

3.2 Homolytic dissociation enthalpy of $RuCp_2$ and RuCpPy

Table 4 shows the homolytic dissociation enthalpies of $RuCp_2$ (R8) and RuCpPy (R9). They were computed starting from the heterolytic dissociation enthalpies (reactions R1 and R2) by subtracting the ionization energy (IE_{Ru}) of ruthenium and adding the electron affinities (EA) of the relevant ligands, Cp or Py radical (including thermal corrections, giving ΔH_{Cp} and ΔH_{Py}), as described by the reaction cycles in Fig. 6. As the IE_{Ru} and ligand EAs are the only quantities calculated in this work for which experimental data are available, it is worthwhile to first take a closer look at these data. Both properties are notoriously difficult to describe accurately by means of traditional wave-function-based methods, requiring extensive basis set to fully capture the difference in dynamical correlation between two systems differing by one or two electrons. As to be expected, CASPT2 overestimates the electron affinities of both radicals, while underestimating the (absolute) value of the Ru ionization energy. The errors are, however, quite acceptable, 3 kcal/mol or less. The CASPT2 error on the Ru ionization energy is the sum of two errors 0.6 and 2.4 kcal/mol for the first and second ionization energies, respectively. On the other hand, less accurate results for both properties are obtained from DFT, with errors in the opposite direction. All functionals overestimate the (absolute) value of IE_{Ru}. The pure PBE functional suffers from an error as large as 17.7 kcal/mol. As indicated by a study of a series of 4d and 5d transition metal atoms [33], errors of this size are typical for pure GGA functionals. The B3LYP and PBE0 functionals perform better, with errors between 5 and 10 kcal/mol. The Cp and Py EAs are fairly accurately described by all considered functionals. B3LYP shows the largest deviation from experiment (around –6 kcal/mol), while PBE gives the best result (around –3 kcal/mol).

Assuming that the values obtained from CASPT2 for the heterolytic dissociation enthalpy of both molecules, 711.8 kcal/mol for $RuCp_2$ and 691.9 kcal/mol for RuCpPy (cfr Table 2), are of a similar accuracy as found in our previous work on ferrocene [8, 18] (i.e., within the experimental uncertainty of ±6 kcal/mol for that molecule), an accurate estimate of the homolytic dissociation enthalpies of both molecules considered here should be obtained by combining those values with the experimental data of IE_{Ru}, ΔH_{Cp}, and ΔH_{Py}. These estimates are 241.0 kcal/mol for $RuCp_2$ and 227.9 kcal/mol for RuCpPy. The difference between both values is reduced by 7.0 kcal/mol with respect to the difference in heterolytic dissociation enthalpies, because of the larger EA of Py as compared to Cp. As can be seen from Table 4, the combined errors on IE_{Ru} and the ligand EAs add up to a total error of around +8 kcal/mol with CASPT2. While CASPT2 thus overestimates the homolytic dissociation enthalpies, the

Table 4 ΔH°_{298} (kcal/mol) of the homolytic dissociation reactions of $RuCp_2$ and RuCpPy

	$RuCp_2 \longrightarrow Ru + 2Cp^{\cdot}$ (R8)				$RuCpPy \longrightarrow Ru + Cp^{\cdot} + Py^{\cdot}$ (R9)				
	PBE	B3LYP	PBE0	CASPT2	PBE	B3LYP	PBE0	CASPT2	Exp.
ΔH_{hetero}	720.9	679.3	700.7	711.9	703.7	662.1	682.5	691.9	
$-IE_{Ru}$	−573.9	−565.9	−561.1	−553.3	−573.9	−565.9	−561.1	−553.3	−556.2[b]
ΔH_{Cp}	39.9	36.9	38.0	45.4[a]	39.9	36.9	38.0	45.4[a]	42.7[a,c]
ΔH_{Py}					46.6	43.9	44.6	51.6[a]	49.6[a,c]
ΔH_{homo}	226.8	187.2	215.5	249.3	216.1	177.0	204.0	235.6	

[a] ZPE and thermal correction to the enthalpy were taken from PBE0 result

[b] Ref. [29, 30]

[c] Electron affinity (*EA*) of the cyclopentadienyl radical (41.69 ± 0.14 kcal/mol) from Ref. [31] and of the pyrrolyl radical (49.47 ± 0.23 kcal/mol) from Ref. [32]. ΔH_{Cp} and ΔH_{Py} are defined as the enthalpy difference for the reactions $Cp^- \longrightarrow Cp^{\cdot} + e^-$ and $Py^- \longrightarrow Py^{\cdot} + e^-$, see Fig. 6

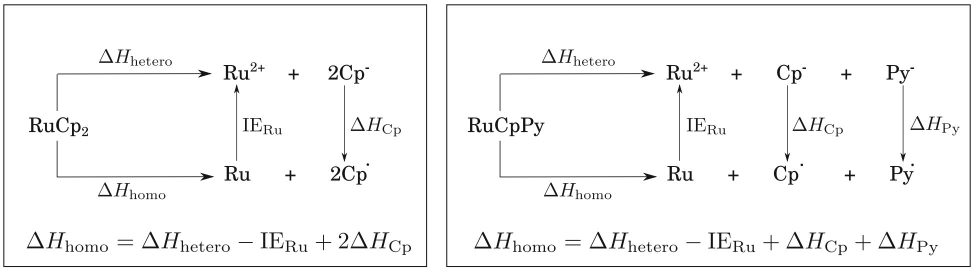

Fig. 6 Reaction cycle for computing the homolytic dissociation enthalpy of $RuCp_2$ and RuCpPy

corresponding DFT errors are negative but more severe. The ordering of the homolytic dissociation energies with respect to the different functionals, PBE > PBE0 > B3LYP, remains the same as for the heterolytic dissociation energies, but all three functionals now underbind. As for the heterolytic dissociation energies, the "best" results are still obtained with PBE, with an error of −12 to −14 kcal/mol, while the largest errors are found with B3LYP, −54 to −58 kcal/mol. However, more importantly, in view of our aim to study the relative performance of these and other Ru compounds in ALD experiments, the difference in the homolytic dissociation enthalpies between both molecules is very similar for the three functionals, 10–11 kcal/mol, and also lies within 3 kcal/mol of the difference 13.1 kcal/mol obtained as our "best estimate" (i.e., making use of experimental data for the IE and EA), while CASPT2 gives 13.7 kcal/mol.

4 Conclusions

The calculated heterolytic dissociation enthalpies of $RuCp_2$ and RuCpPy show that both molecules are very stable, since their binding energies are very high. This is in agreement with the high thermal stability of these precursors, allowing ALD up to temperatures as high as 350–400 °C [4, 5]. RuCpPy is about 20 kcal/mol less stable than ruthenocene with respect to heterolytic dissociation and 13 kcal/mol with respect to homolytic dissociation. This could at least partly explain the higher reactivity of RuCpPy in ALD experiments. However, other factors, such as the adsorption energy at the surface and structural changes during adsorption affecting the possibility of dissociation, may of course play an equally or even more important role. Therefore, we are currently also investigating the chemisorption reactions of $RuCp_2$ and RuCpPy at different surfaces. For this purpose, we make use of DFT with periodic boundary conditions. The present study therefore also serves as a benchmarking study for the quality of different DFT functionals, with PBE in particular, as this functional will be used in the solid-state calculations. To test the quality of the different functionals, high-level CASPT2 calculations with extensive basis sets were employed. From the comparison between the DFT results and CASPT2, we find that, although the absolute dissociation energies obtained from DFT may be afflicted with very large errors (up to more than 50 kcal/mol with B3LYP), the differences between both molecules, both for the heterolytic and homolytic dissociation enthalpies, are well-described. This is of course due to a large cancellation of errors of the absolute dissociation enthalphies of both molecules. The calculations also indicate that, of the three functionals studied, PBE performs best as compared to CASPT2. This is, however, a conclusion that we believe is not extendable to other (e.g., first-row metallocene) systems.

Acknowledgments This investigation has been supported by grants from the Flemish Science Foundation (FWO) and from the Concerted Research Action of the Flemish Government (GOA).

References

1. George SM (2010) Chem Rev 110:111
2. Knez M, Nielsch K, Niinistö L (2007) Adv Mater 19:3425
3. Bohr M, Chau R, Ghani T, Mistry K (2007) Spectrum, IEEE 44:29
4. Aaltonen T, Alén P, Ritala M, Leskelä M (2003) Chem Vap Deposition 9:45
5. Kukli K, Kemell M, Puukilainen E, Aarik J, Aidla A, Sajavaara T, Laitinen M, Tallarida M, Sundqvist J, Ritala M, Leskelä M (2011) J Electrochem Soc 158:D158
6. Swerts J, Salimullah MM, Popovici M, Kim MS, Pawlak MA, Delabie A, Schaekers M, Tomida K, Kaczer B, Opsomer K, Vrancken C, Debusschere I, Altimime L, Kittl JA, Van Elshocht S (2011) ECS Trans 41:41
7. Elliott SD (2010) Langmuir 26:9179
8. Phung QM, Vancoillie S, Pierloot K (2012). J Chem Theory Comput 8:883
9. Ahlrichs R, Bär M, Häser M, Horn H, Kälmel C (1989) Chem Phys Lett 162:165
10. Aquilante F, De Vico L, Ferré N, Ghigo G, Malmqvist PÅ, Neogrády P, Pedersen TB, Pitoňák M, Reiher M, Roos BO, Serrano-Andrés L, Urban M, Veryazov V, Lindh R (2010) J Comput Chem 31:224
11. Weigend F, Furche F, Ahlrichs R (2003) J Chem Phys 119:12753
12. Weigend F, Häser M, Patzelt H, Ahlrichs R (1998) Chem Phys Lett 294:143
13. Andrae D, Häußermann U, Dolg M, Stoll H, Preuß H (1990) Theoretica Chimica Acta 77:123
14. Grimme S (2006) J Comput Chem 27:1787

15. Roos BO, Lindh R, Malmqvist PÅ, Veryazov V, Widmark PO (2005) J Phys Chem A 109:6575
16. Roos BO, Lindh R, Malmqvist PÅ, Veryazov V, Widmark PO (2004) J Phys Chem A 108:2851
17. Widmark PO, Malmqvist PÅ, Roos BO (1990) Theor Chem Acc 77:291
18. Vancoillie S, Zhao H, Tran VT, Hendrickx MFA, Pierloot K (2011) J Chem Theory Comput 7:3961
19. Aquilante F, Malmqvist PÅ, Pedersen TB, Ghosh A, Roos BO (2008) J Chem Theory Comput 4:694
20. Hess BA (1986) Phys Rev A 33:3742
21. Reiher M, Wolf A (2004) J Chem Phys 121:2037
22. Reiher M, Wolf A (2004) J Chem Phys 121:10945
23. Ghigo G, Roos BO, Malmqvist PÅ (2004) Chem Phys Lett 396:142
24. Forsberg N, Malmqvist PÅ (1997) Chem Phys Lett 274:196
25. Pierloot K, Vancoillie S (2006) J Chem Phys 125:124303
26. Pierloot K (2001) In: Cundari TR (ed.) Computational organometallic chemistry, pp 123–158. Marcel Dekker, Inc., New York
27. Seiler P, Dunitz JD (1980) Acta Crystallogr Sect B 36:2946
28. Waller MP, Braun H, Hojdis N, Bühl M (2007) J Chem Theory Comput 3:2234
29. Callender CL, Hackett PA, Rayner DM (1988) J Opt Soc Am B 5:614
30. Shenstone AG, Meggers WF (1958) J Res Natl Bur Stand (US) 61:373
31. Ichino T, Wren SW, Vogelhuber KM, Gianola AJ, Lineberger WC, Stanton JF (2008) J Chem Phys 129:084310
32. Gianola AJ, Ichino T, Hoenigman RL, Kato S, Bierbaum VM, Lineberger WC (2004) J Phys Chem A 108:10326
33. Wu Z, Kawazoe Y (2006) Chem Phys Lett 423:81

Theor Chem Acc (2012) 131:1241
DOI 10.1007/s00214-012-1241-8

REGULAR ARTICLE

The Boron conundrum: the case of cationic clusters B_n^+ with $n = 2$–20

Truong Ba Tai · Nguyen Minh Tam ·
Minh Tho Nguyen

Received: 3 March 2012 / Accepted: 21 May 2012 / Published online: 7 June 2012

Abstract We investigate the molecular and electronic structure and thermochemical properties of the cationic boron clusters B_n^+ with $n = 2$–20, using both MO and DFT methods. Several functionals are used along with the MP2, G3, G3B3, G4, and CCSD(T)/CBS methods. The latter is the high accuracy reference. While the TPSS, TPSSh, PW91, PB86, and PBE functionals show results comparable to high-accuracy MO methods, both BLYP and B3LYP functionals are not accurate enough for three-dimensional (3D) structures. A negligible difference is observed between the B3LYP, MP2, and CCSD(T) geometries. A transition between 2D and 3D structures occurs for this series at the B_{16}^+–B_{19}^+ sizes. While smaller clusters B_n^+ with $n \leq 15$ are planar or quasi-planar, a structural competition takes place in the intermediate sizes of B_{16-19}^+. The B_{20}^+ cation has a 3D tubular shape. The standard heats of formation are determined and used to evaluate the cluster stability. The average binding energy tends to increase with increasing size toward a limit. All closed-shell species B_n^+ has an aromatic character, but an enhanced stability is found for B_5^+ and B_{13}^+ whose aromaticity and electron delocalization are analyzed using the LOL technique.

Keywords Boron clusters · Boron cations · Heats of formation · Thermochemical parameters · Aromaticity · Electron delocalization

1 Introduction

Boron-based clusters continue to be a subject of considerable theoretical and experimental interests. Extensive investigations have been performed on small boron clusters using various theoretical and experimental methods [1–25]. While there is a good agreement for the electronic structure and chemical properties of small boron clusters B_n with $n \leq 13$ in the recent literature [26, 27], those of the larger clusters are still a matter of controversy [11, 19, 28, 29]. Such a discrepancy almost arises from the fact that the computational methods used in previous studies differ much from each other. For instance, most of the recent studies on small boron clusters were performed using the density functional theory (DFT), but with a variety of functionals [27]. Although many theoretical predictions based on the popular hybrid B3LYP functional were found in good agreement with available experimental results [27], it has been claimed in other reports that this functional is not reliable for boron clusters. Based on calculated results for the twenty-atom clusters $B_{20}^{0/-}$, An et al. [30] argued that the PBE0 functional behaves better than the B3LYP, as compared to the perturbation theory (MP4) and coupled-cluster (CCSD(T)) results. Pan et al. [31] also claimed that the B3LYP functional is not reliable for relative energies of three-dimensional structures. The latter authors reported that the PBE, TPSS, and TPSSh functionals provide energetic parameters for B-compounds more comparable to the CCSD(T) counterparts. More recently, Li et al. [32] reexamined the structures of B_{20} using the molecular orbital

---

Published as part of the special collection of articles celebrating theoretical and computational chemistry in Belgium.

T. B. Tai · N. M. Tam · M. T. Nguyen (✉)
Department of Chemistry, University of Leuven,
3001 Leuven, Belgium
e-mail: minh.nguyen@chem.kuleuven.be

N. M. Tam
Institute for Computational Science and Technology (ICST),
HoChiMinh City, Vietnam

(MO) methods at the CCSD(T)/6-311G(d)//MP2/6-311G(d) level along with eight different density functionals, including the BLYP, B3LYP, PBE, PBE0, TPSS, TPSSh, mPW1PW91, and M06-2X. Their calculated results pointed out that the relative energies of B_{20} isomers obtained from PBE and TPSS functionals are closer to the CCSD(T) values than those obtained from other functionals. In this context, a calibration of the accuracy of various computational methods, in particular of the less popular density functionals, needs to be done carefully.

The cationic boron clusters have been the subject of several experimental investigations. For instance, Anderson et al. [1, 2] performed experimental investigations on small cationic boron clusters B_n^+ ($n = 2$–13) using the absolute collision-induced dissociation (CID) technique. Measurements of fragment appearance potentials and fragmentation branching ratios were carried out, and the obtained data were analyzed to interpret the stabilities of the ionic clusters along with the ionization energies (IEs) of the corresponding neutrals. Recently, a combined experimental and theoretical study on larger cationic boron clusters B_n^+ with $n = 12$–25 was also carried out by Oger et al. [28]. In this report, the collision cross sections of the low-lying isomers B_n^+ were obtained by using DFT calculations and compared to the experimental data based on ion mobility spectrometry.

According to our best knowledge, while a number of theoretical studies on small cationic clusters B_n^+ with $n = 2$–14 were carried out [33–47], investigations on the larger clusters are rather limited [28, 29]. Moreover, as stated above, the identity of the global minima of B_n^+ clusters (being the most stable isomeric forms) remains a matter of debate. Let us mention the cationic $B_6{}^+$ cluster as a case in point. At the MP2/6-311G(d) level, Li et al. [43] found that the $B_6{}^+$ ion exhibits a C_{2h} ^2B_g global minimum. Using DFT methods, Ma et al. [44] indicated instead a high symmetry D_{2h} $^2B_{1u}$ structure to be the most stable isomer for $B_6{}^+$. While Ray et al. [33] subsequently claimed that the global minimum $B_6{}^+$ is a square pyramid, a perfect hexagonal structure was reported as its lowest-energy isomer by Niu et al. [35]. Another C_2 structure was also indicated to be the most stable $B_6{}^+$ isomer by Kato et al. [34]. Similar stories can be told for other sizes such as $B_5{}^+$, $B_7{}^+$, $B_8{}^+$, $B_9{}^+$, and $B_{13}{}^+$ [33–35, 38, 39, 45–47]. More interestingly perhaps is the fact that the transition between 2D and 3D structures has been assumed to occur at the cation $B_{16}{}^+$ following a combined experimental and theoretical study by Oger et al. [28]. Accordingly, the cationic clusters B_n^+ with $n = 17$–25 were found to possess tubular structures, similar to the tubular B_{20} [11], while the $B_{16}{}^+$ has a caged form. However, a recent report by Boustani et al. [29] pointed out that the $B_{19}{}^+$ ion has rather a 3D pyramid structure. These discrepancies, typical of the *boron conundrum*, require the identity of the molecular structures of the B_n^+ clusters to be reliably established.

We recently performed the theoretical investigations of thermochemical properties and electronic structures of small boron clusters B_n ($n = 2$–13) in both neutral and anionic states [17, 18, 26], and of the larger neutral clusters B_n with n up to 20 [20] using high-accuracy molecular orbital G3B3 and CCSD(T)/CBS methods. Our theoretical predictions are in good agreement with the available experimental results. In addition, our calculated results allowed different aspects of their bonding and growth pattern to be understood. Some non-classical types of bonding and aromaticity have been discovered [20]. Motivated by the above reasons, we now continue our investigations on the cationic boron clusters B_n^+ with $n = 2$–20. The calibration of computational methods used is done carefully by using various methods, including MP2, G3, G4, CCSD(T), and CBS, and seven different density functionals. Thermochemical properties are determined using the G3B3 and CCSD(T)/CBS methods.

2 Computational methods

All quantum chemical calculations are carried out using the Gaussian 03 [48] and Molpro 2008 [49] suites of programs. The initial search for all possible lower-lying isomers of each of the B_n^+ clusters considered is performed using a stochastic search algorithm that was implemented by us [50]. Firstly, the possible structures of each of the clusters B_n^+ are generated by a random kick method and then rapidly optimized at the B3LYP/6-31G level [51]. In this search procedure, the minimum and maximum distances between atoms are limited to 1.5 and 9 Å, respectively. Geometries of the stationary points located and their harmonic vibrational frequencies are further refined using the B3LYP functional, initial part of the composite G3B3 approach [52], for the series of small clusters B_n^+ with $n = 2$–13. For the series of larger sizes of $n = 14$–20, geometry optimizations and vibrational calculations are performed using the B3LYP [53–55] and PBE [56] functionals in conjugation with the 6-311+G(d) basis set [57]. Their single-point electronic energies are subsequently calculated using the coupled-cluster CCSD(T) theory [58] at their B3LYP optimized geometries.

In order to obtain more accurate energetic values, the electronic energies of the global minima are calculated using the coupled-cluster CCSD(T) theory at the complete basis set limit (CBS) for the small sizes of $n = 2$–8, and the composite G3B3 technique for all B_n^+ clusters considered (with $n = 2\_20$). Geometrical parameters are also fully optimized at the coupled-cluster CCSD(T) theory for the small sizes of $n = 2$–8, in conjunction with the correlation-consistent aug-cc-pVTZ basis set.

A detailed description for the CCSD(T)/CBS approach is found elsewhere [26, 59–61]. Briefly, the single-point electronic energies are calculated by using the restricted/unrestricted coupled-cluster R/UCCSD(T) formalism [62–64] and extrapolated to the complete basis set limit (CBS) based on the correlation-consistent aug-cc-pV*n*Z ($n =$ D, T, and Q) basis sets [65, 66]. The CCSD(T) energies are then extrapolated to the CBS limit energies using expression (1) [67]:

$$E(x) = A_{\mathrm{CBS}} + B\exp[-(x-1)] + C\exp[-(x-1)]^2 \qquad (1)$$

where $x = 2$, 3, and 4 for the aug-cc-pV*n*Z basis sets with $n =$ D, T, and Q, respectively.

The zero-point energies (ZPE) are calculated from harmonic vibrational frequencies at either the CCSD(T)/aug-cc-pVTZ or the MP2/aug-cc-pVTZ level. Additional smaller corrections are included in the evaluation of total atomization energies (TAE). Core-valence corrections (ΔE_{CV}) are obtained at the CCSD(T)/cc-pwCVTZ level [68, 69]. Douglas–Kroll–Hess (DKH) scalar relativistic corrections ($\Delta E_{\mathrm{DKH-SR}}$), which account for changes in the relativistic contributions to the total energies of the molecule and the constituent atoms, are calculated using the spin-free, one-electron DKH Hamiltonian [70–73]. $\Delta \mathrm{E}_{\mathrm{DKH\text{-}SR}}$ is defined as the difference in the atomization energy between the results obtained from basis sets recontracted for DKH calculations and the atomization energy obtained with the normal valence basis set of the same quality. The DKH calculations are obtained as the differences of the results from the CCSD(T)/cc-pVTZ and the CCSD(T)/cc-pVTZ-DK levels of theory. Finally, a spin–orbit (SO) correction of 0.03 kcal/mol for the B-atom obtained from the excitation energies of Moore [74] is used. The total atomization energy (ΣD_0 or TAE) of a compound is given by (2):

$$\Sigma D_0 = \Delta E_{\mathrm{elec}}(\mathrm{CBS}) + \Delta E_{\mathrm{CV}} + \Delta E_{\mathrm{DKH-SR}} + \Delta E_{\mathrm{SO}} - \Delta E_{\mathrm{ZPE}} \qquad (2)$$

By combining our computed ΣD_0 values from either the CBS or G3B3 calculations, with the known heat of formation at 0 K for the element B, we can derive the heats (enthalpies) of formation $\Delta_f H^\circ$ values at 0 K for the molecules in the gas phase. In this work, we use the value of $\Delta_f H^\circ(\mathrm{B}) = 135.1 \pm 0.2$ kcal/mol [75], and the rationale for this selection was discussed in our previous work [26, 76–78]. The heats of formation at 298 K are obtained by following the usual thermochemical procedures [79]. The calculated heats of formation at 0 K are used to evaluate the ionization energies and other energetic quantities.

In a further step to evaluate the accuracy of the computational approaches used, the relative energies of B_6 isomers are calculated using a series of different methods, including the MP2, G3 [80], G3B3 [52], G4 [81], CCSD(T)/CBS, and seven different density functional including BLYP [54, 82], B3LYP [41], TPSS [83], TPSSh [84, 85], PBE [56], BP86 [86], and PW91 [87]. The B_6 is chosen as a sample for calibration because of two reasons: first, there exist several stable isomers B_6, including the planar, quasi-planar, and three-dimensional structures as shown in Fig. 1. Second, it is simply due to the fact that B_6 is small enough to allow the demanding methods such as CCSD(T)/CBS to be performed within our computational resources.

3 Results and discussion

3.1 Evaluation of computational methods

The relative energies of B_6 isomers obtained from various methods are given in Table 1, while the illustrating plots are shown in Fig. 2. There is a consistency between high-accuracy theoretical methods such as G3, G3B3, G4, CCSD(T)/aug-cc-pVTZ, and CCSD(T)/CBS (Fig. 2a). The relative energies obtained from the simpler MP2 method are much different as compared to those obtained from the above methods. The MP2 method tends to favor three-dimensional (3D) caged structures. Figure 2a shows that the MP2 relative energies of 3D structures **II** and **III** are much lower than those obtained from CCSD(T) and other methods, while the MP2 relative energies of two-dimensional (2D) structures **IV**, **V,** and **VI** become considerably higher.

Interestingly, all density functionals considered present the energy values approximately close for planar or quasi-planar closed-shell structures, that are also in good agreement with the relevant CCSD(T)/CBS values. However, for 3D structures, the B3LYP and BLYP results turn out to be less accurate as compared to other functionals, relative to the CBS values. Opposite to the MP2, the two latter

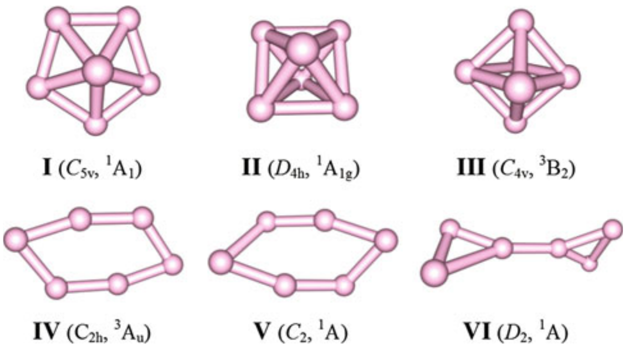
I (C_{5v}, $^1A_1$) **II** (D_{4h}, $^1A_{1g}$) **III** (C_{4v}, $^3B_2$)

IV (C_{2h}, ^3A_u) **V** (C_2, ^1A) **VI** (D_2, ^1A)

Fig. 1 Shapes of the lower-lying isomers of B_6

Table 1 Relative energies (kcal/mol) of the low-lying isomers B_6 obtained at various computational methods

Method	I	II	III	IV	V	VI
CBS[a]	0.0	40.8	37.9	7.7	10.2	56.7
G3	0.0	36.3	36.4	5.8	6.1	50.0
G3B3	0.0	38.0	36.4	6.2	6.4	50.2
G4	0.0	35.9	34.4	8.9	9.0	52.7
MP2/6-311+G(d)	0.0	23.8	18.6	11.6	17.9	57.9
CCSD(T)/aug-cc-pVTZ	0.0	41.2	38.3	5.9	8.2	53.0
CCSD(T)/6-311+G(d)	0.0	41.3	38.5	3.8	5.8	48.5
CCSD(T)/MP2[b]	0.0	36.9	38.5	4.2	6.3	48.5
CCSDT/B3LYP[c]	0.0	41.2	38.6	3.8	6.4	48.4
B3LYP/6-311+G(d)[d]	2.7	59.2	43.3	0.0	9.2	63.2
BLYP/6-311+G(d)	5.2	54.3	41.3	0.0	6.0	55.3
TPSS/6-311+G(d)	2.1	45.1	27.8	0.0	11.3	64.2
TPSSh/6-311+G(d)	1.4	47.7	29.3	0.0	13.1	67.5
PBE/6-311+G(d)	0.0	39.8	24.4	0.7	9.6	62.8
PW91/6-311+G(d)	0.6	42.1	26.7	0.0	9.2	62.5
BP86/6-311+G(d)	1.2	44.2	29.5	0.0	8.3	60.0

[a] CBS energy calculated from the CCSD(T)/aug-cc-pVnZ energies (n = D, T, Q) with the CCSD(T)/aug-cc-pVTZ geometries

[b] CCSD(T) single-point energy calculated at the MP2 geometries with the 6-311+G(d) basis set

[c] CCSD(T) single-point energy calculated at the B3LYP geometries with the 6-311+G(d) basis set

[d] DFT energy values included the zero-point energies (ZPEs)

functionals do not favor 3D structures as shown in Fig. 2b. These observations agree well with the recent reports [30–32]. In addition, the relative energies of open-shell species obtained from DFT methods are smaller than the corresponding CCSD(T)/CBS values.

In order to evaluate further the accuracy of the methods used, electronic energies of the isomers are further calculated using the CCSD(T) method with the B3LYP, MP2, and CCSD(T) optimized geometries. The results plotted in Fig. 2c point out that there is a remarkably good agreement between the CCSD(T) values with three different geometries. Thus, we can conclude that the use of geometries of isomers optimized by different methods induce a negligible difference in their relative energies. The difference in relative energies is mainly due to the electronic energies of the methods used.

3.2 Shape of the low-lying isomers of cationic B_n^+ clusters

Shapes, relative energies, number of imaginary frequencies, symmetry point group, and electronic states of lower-lying isomers B_n^+ are depicted in Figs. 3, 4, and 5.

B_2^+, B_3^+, and B_4^+ Our calculated results agree well with the earlier reports [33–39, 88] that the structures **2.1** ($D_{\infty h}$, $^2\Sigma_g^+$), **3.1** (D_{3h}, $^1A_1'$), and **4.1** (D_{2h}, ^2A_g) are the global minima of B_2^+, B_3^+, and B_4^+, respectively. These structures have almost the same shapes as their neutral counterparts.

B_5^+ As stated above, there is a controversy about the global minimum of B_5^+. Anderson et al. [2] and Ray et al. [33] reported that the most stable isomer of B_5^+ is a trigonal bipyramid structure **5.2**. Subsequent studies are in agreement with each other that the B_5^+ ion possesses a C_{2v} structure **5.1**, being distorted form of high symmetry D_{5h} [27, 34, 40, 42]. Our calculated results concur with the latter results. **5.1** can thus be established as the lowest-energy isomer of B_5^+, while **5.2** is found to be 51.4 kcal/mol less stable than the **5.1**.

B_6^+ As discussed above, due to the use of different theoretical methods, there is also a discrepancy in the results for the global minimum B_6^+ reported in the literature. Let us briefly mention again the reported results. At the MP2/6-311G(d) level, Li et al. [43] showed that the B_6^+ exhibits the C_{2h} ^2B_g global minimum **6.3**. Using DFT calculations, Ma et al. [44] and Rica et al. [40] indicated the high symmetry D_{2h} $^2B_{1u}$ structure **6.1** to be the most stable isomer for B_6^+. While Ray et al. [33] claimed that the B_6^+ global minimum is a square pyramid structure **6.4**, a perfect hexagonal structure was reported by Niu et al. [35] as the most stable isomer. Two other structures, including a capped pentagonal **6.2** and a C_2 structure, were also suggested to be the most stable isomers of B_6^+ by Hanley et al. [2] and Kato et al. [34], respectively.

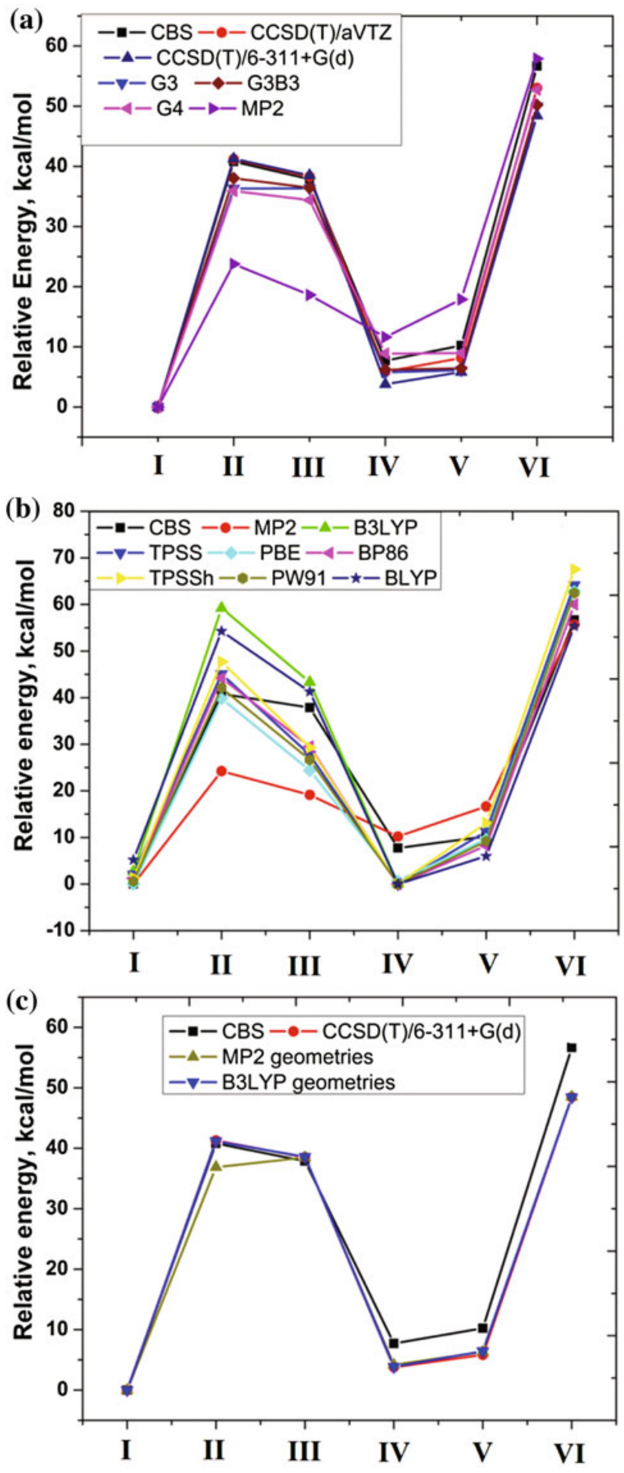

Fig. 2 The curves of relative energies (kcal/mol) of the lower-lying B_6 isomers obtained using various computational methods

To gain additional insights, we reexamine the energies of all above structures using both G3B3 and CCSD(T)/aug-cc-pVTZ methods. Our calculations point out that the two structures **6.1** (D_{2h} $^2B_{1u}$) and **6.2** (C_s $^2A'$), which is a distorted form of the neutral B_6, are almost degenerate in energy (Fig. 3). The energy difference between them amounts to only 0.7 and 1.0 kcal/mol at the G3B3 and CCSD(T) levels of theory, respectively. The C_{2h} ^2B_g structure **6.3** is only a transition state with one imaginary frequency connecting **6.1**, and a relative energy of 7.8 kcal/mol at the CCSD(T) level (5.7 kcal/mol at G3B3). **6.4** that was reported to be the global minimum by Ray et al. [33] was also located, but it is now found to be much less stable with a relative energy of 27.7 kcal/mol.

B_7^+ Our calculations concur with the recent reports [34, 36, 38, 39] that the C_{6v} $^1A_1$ structure **7.1** is the global minimum of B_7^+. Although another structure with bipyramid pentagonal shape was reported as the B_7^+ global minimum, it turns out to be much less stable.

B_8^+ The C_{2v} $^2B_1$ structure **8.1** is indicated to be the most stable isomer for B_8^+ in many previous reports [36, 38–40]. Other electronic state (C_{2v} $^2A_2$) was reported by Kato et al. [34] at the MP4(SDTQ)/3-21G level. Interestingly, our calculations at the full CCSD(T)/aug-cc-pVTZ level showed that both electronic states are located having nearly the same energy content. Consequently, **8.1** is the most stable isomer of B_8^+ in both electronic states $^2B_1$ and $^2A_2$ that are apparently the two stabilized states by a Jahn–Teller distortion of a higher symmetry form.

B_9^+ Two different structures were reported as the global minimum of B_9^+. While Boustani [38] and Ricca and Bauschlicher [39, 40] found that the C_s $^1A'$ structure **9.1** is the most stable B_9^+ isomer, Kato et al. [34] showed another minimum **9.3**. Our G3B3 calculations indicate that the B_9^+ global minimum is actually the C_s $^1A'$ structure **9.1**. While the high-spin D_{8h} $^3A_{1g}$ structure **9.2** is the next isomer, **9.3** is found to be 17.7 kcal/mol less stable than **9.1**.

B_{10}^+, B_{11}^+, and B_{12}^+ Our calculations reveal that **10.1** (C_{2v}, $^2A_1$), **11.1** (C_s $^1A'$), and **12.1** (C_s, $^2A'$) are the global minima of B_{10}^+, B_{11}^+, and B_{12}^+, respectively (Fig. 3). These findings agree well with previous reports [38, 40].

B_{13}^+ The cationic cluster B_{13}^+ has been examined extensively in the literature. Anderson et al. [2]. proposed a filled icosahedron. A three-dimensional C_s structure was reported by Kawai and Weare [45] to be the most stable isomer. A distorted form of the elongated structure B_{13} was reported for B_{13}^+ by Boustani [38]. In another way, Ricca and Bauschlicher [40], Schleyer et al. [46], and Fowler and Ugalde [47] found that the global minimum of B_{13}^+ is a C_{2v} $^1A_1$ structure that is similar to its neutral. Our theoretical predictions lend a support for the assignment that the C_{2v} **13.1** structure is the most stable isomer. The other C_{2v} structure **13.2** is very close in energy to **13.1**, but it is only transition state with one imaginary frequency, whereas the C_s $^1A'$ structure **13.3** is located at 15.8 kcal/mol (Fig. 3).

Fig. 3 Shapes, electronic states, number of imaginary frequencies (NImag), and relative energy (ΔE, kcal/mol) of the low-lying isomers B_n^+ with $n = 2$–13. The ΔE values obtained at the G3B3 approach. The values in square bracket are obtained at the CCSD(T)/aug-cc-pVTZ level

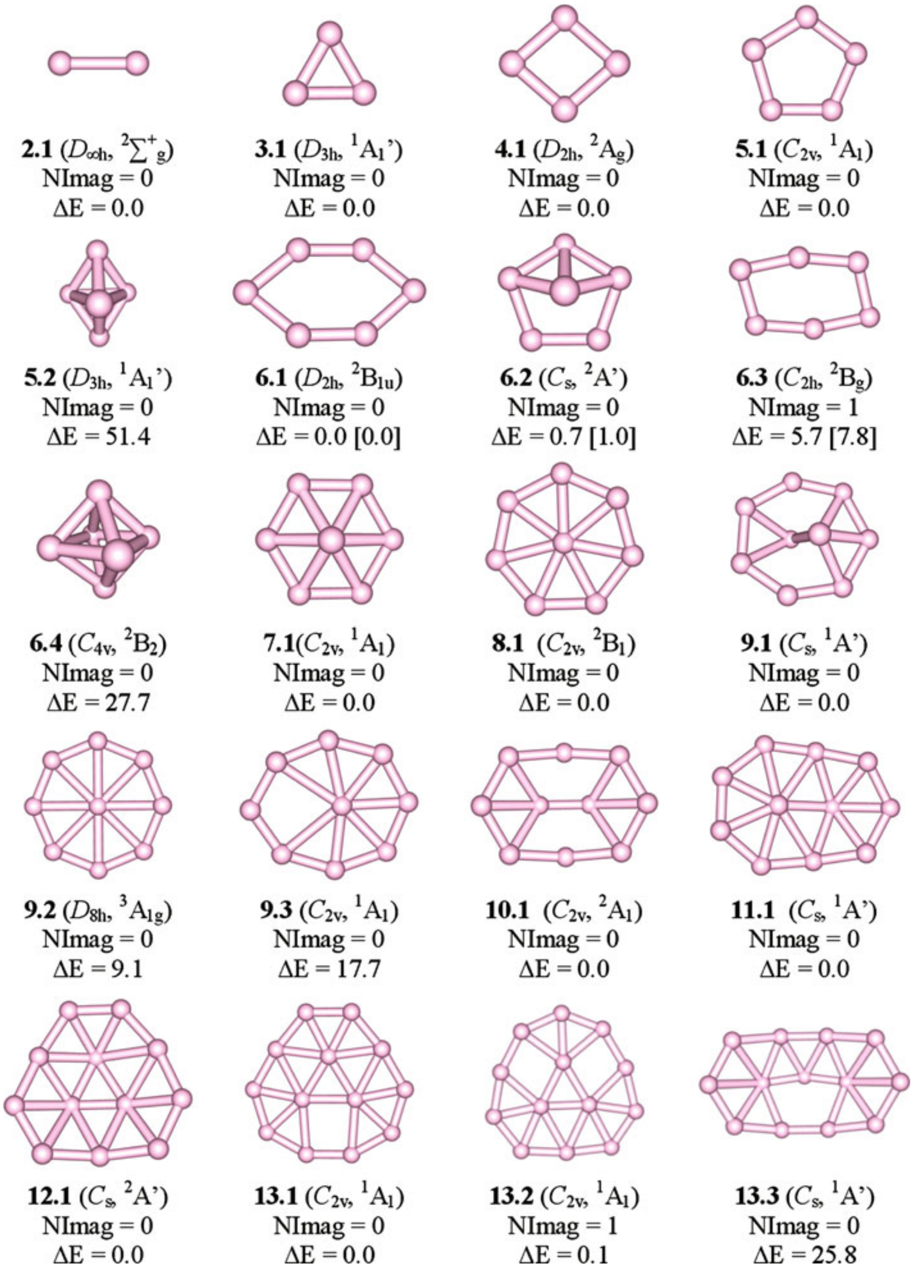

The high stability of $B_{13}{}^+$ was interpreted from a MO correlation diagram [18].

$B_{14}{}^+$ and $B_{15}{}^+$ The B_n^+ systems with $n \geq 14$ have received less attention as compared to the smaller sizes. At all levels considered, our predictions concur to earlier studies [38, 40] that the C_{2v} $^2A_1$ **14.1** and C_s ^1A' **15.1** structures are the most stable forms of $B_{14}{}^+$ and $B_{15}{}^+$, respectively (Fig. 4).

$B_{16}{}^+$ Using the TPSS/def2-TZVPP level, Oger et al. [28] reported that the most stable isomer of $B_{16}{}^+$ is a caged form with C_{2v} symmetry **16.2**. Two structures, including an elongated form **16.1** (C_{2h} ^2A_u) and a tubular form **16.3** (D_4, $^2B_1$), are the next isomers with relative energies of 0.07 and 0.09 eV, respectively. Our BPE/6-311+G(d) results show that **16.3** is the lowest-energy isomer that is 2.3 and 6.9 kcal/mol more stable than **16.1** and **16.2**, respectively. However, B3LYP/6-311+G(d) results point out an opposite trend that **16.1** is the most stable isomer. At this level of theory, **16.2** and **16.3** are found now to be 24.9 and 3.1 kcal/mol less stable than **16.1**, respectively. Due to the difference arising from the methods employed, we further perform CCSD(T) calculations on these structures. Interestingly, our CCSD(T) results show that both structures **16.1** and **16.2** are almost degenerate with the same content in energy and 3.9 kcal/mol more stable than **16.3**. Consequently, we conclude that both structures **16.1** and **16.2** can be regarded as the degenerate lowest-energy isomers of $B_{16}{}^+$ (Fig. 4).

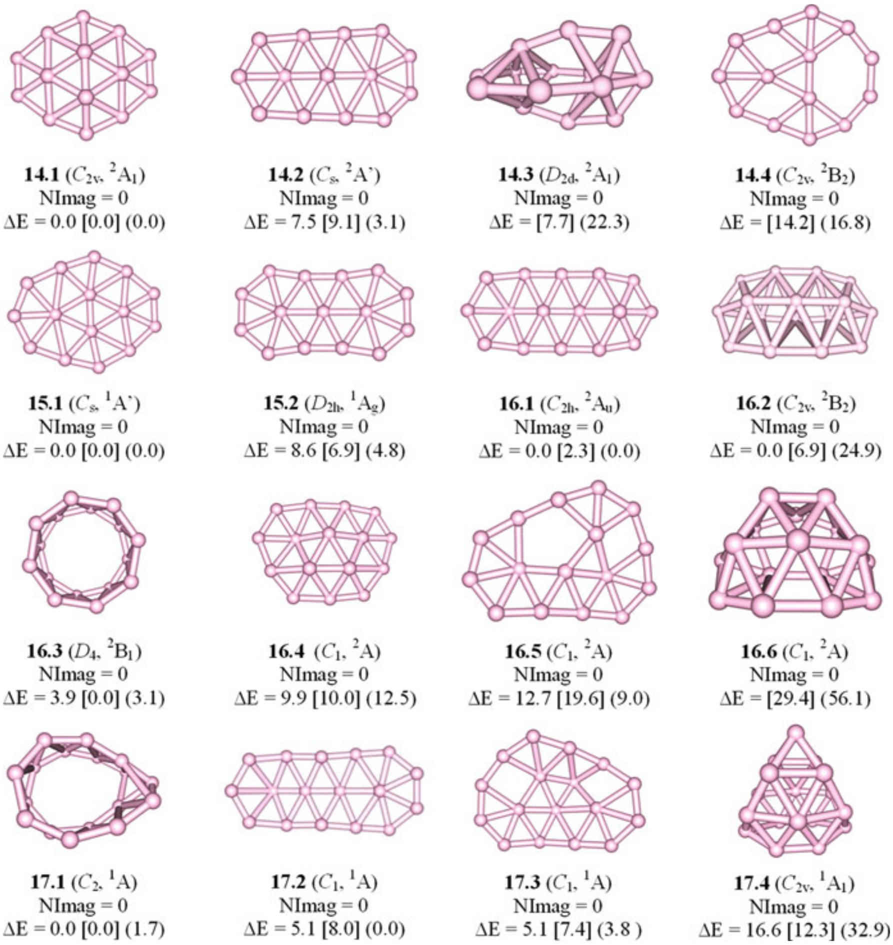

14.1 (C_{2v}, $^2A_1$) NImag = 0 ΔE = 0.0 [0.0] (0.0)

14.2 (C_s, $^2A'$) NImag = 0 ΔE = 7.5 [9.1] (3.1)

14.3 (D_{2d}, $^2A_1$) NImag = 0 ΔE = [7.7] (22.3)

14.4 (C_{2v}, $^2B_2$) NImag = 0 ΔE = [14.2] (16.8)

15.1 (C_s, $^1A'$) NImag = 0 ΔE = 0.0 [0.0] (0.0)

15.2 (D_{2h}, ^1A_g) NImag = 0 ΔE = 8.6 [6.9] (4.8)

16.1 (C_{2h}, ^2A_u) NImag = 0 ΔE = 0.0 [2.3] (0.0)

16.2 (C_{2v}, $^2B_2$) NImag = 0 ΔE = 0.0 [6.9] (24.9)

16.3 (D_4, $^2B_1$) NImag = 0 ΔE = 3.9 [0.0] (3.1)

16.4 (C_1, ^2A) NImag = 0 ΔE = 9.9 [10.0] (12.5)

16.5 (C_1, ^2A) NImag = 0 ΔE = 12.7 [19.6] (9.0)

16.6 (C_1, ^2A) NImag = 0 ΔE = [29.4] (56.1)

17.1 (C_2, ^1A) NImag = 0 ΔE = 0.0 [0.0] (1.7)

17.2 (C_1, ^1A) NImag = 0 ΔE = 5.1 [8.0] (0.0)

17.3 (C_1, ^1A) NImag = 0 ΔE = 5.1 [7.4] (3.8)

17.4 (C_{2v}, $^1A_1$) NImag = 0 ΔE = 16.6 [12.3] (32.9)

Fig. 4 Shapes, electronic states, number of imaginary frequencies (NImag), and relative energy (Δ*E*, kcal/mol) of the low-lying isomers B_n^+ with $n = 14$–17. The ΔE values obtained at the CCSD(T)/6-311G//B3LYP/6-311+G(d) level. The values in square bracket are obtained at the PBE/6-311+G(d) level. The values in parentheses are obtained at the B3LYP/6-311+G(d) level

$B_{17}{}^+$ Our B3LYP/6-311+G(d) results show that two structures, including a tubular form **17.1** and an elongated **17.2**, are almost degenerate with an energy difference of 1.6 kcal/mol in favor of **17.2**. However, PBE/6-311+G(d) calculations show an opposite ordering that **17.1** is the most stable isomer and 8.0 kcal/mol more stable than **17.2**. At the higher G3B3 and CCSD(T)/6-311G(d)//B3LYP/6-311+G(d) levels, **17.1** also turns out to be the most stable isomer as showed in Fig. 4. Thus, we conclude that $B_{17}{}^+$ exhibits a C_2 ^1A global minimum **17.1**. This prediction also agrees with the earlier study by Oger et al. [28]. The C_1 ^1A structure **17.3** is the next isomer with relative energy of 5.1 kcal/mol, while 3D structure **17.4** (C_{2v}, $^1A_1$) is much less stable, as compared to other forms.

$B_{18}{}^+$ There is an interesting competition in energy between 2D and 3D structures for the $B_{18}{}^+$ species. Based on DFT calculations using two functionals B3LYP and PBE, the tubular structure **18.1** is the most stable isomer (Fig. 5). The next isomer is the quasi-planar structure **18.2** with relative energy of 5.6 and 8.7 kcal/mol at the PBE/6-311+G(d) and B3LYP/6-311+G(d) levels, respectively. However, this energy gap is decreased to 1.1 kcal/mol at the CCSD(T)/6-311G(d) level. Accordingly, both structures **18.1** and **18.2** are established as the lowest-energy isomers of $B_{18}{}^+$.

18.3 is a distorted form of the neutral global minimum B_{18} and becomes the next isomer with 7.7 kcal/mol higher than **18.1**. Two other quasi-planar structures **18.4** and **18.5** are also found to be stable with relative energies of 12.0 and 15.6 kcal/mol, respectively.

$B_{19}{}^+$ There is a controversy over the identity of the $B_{19}{}^+$ global minimum. At the TPSSh/def2-TZVPP level, Oger et al. [28] reported that the most stable isomer of $B_{19}{}^+$ is a tubular form **19.2**, but it is only 0.09 eV more stable than **19.1**. Based on LDA results, Boustani et al. [29] recently showed that a 3D pyramid structure **19.8** is rather the most stable isomer for this size. In this context, we reexamine its structures using several computational methods, including three functionals B3LYP, PBE, and TPSS, and both G3B3 and CCSD(T) methods (Fig. 5). While the B3LYP and TPSS functionals provide the same trend that **19.1** is more stable but with a small energy separation of ~2.0 kcal/mol, both structures actually have the same energy content

Fig. 5 Shapes, electronic states, number of imaginary frequencies (NImag), and relative energy (ΔE, kcal/mol) of the low-lying isomers B_n^+ with $n = 18$–20. The ΔE values obtained at the CCSD(T)/6-311G(d)//B3LYP/6-311+G(d) level. The values in square bracket are obtained at the PBE/6-311+G(d) level. The values in parentheses are obtained at the B3LYP/6-311 + G(d) level

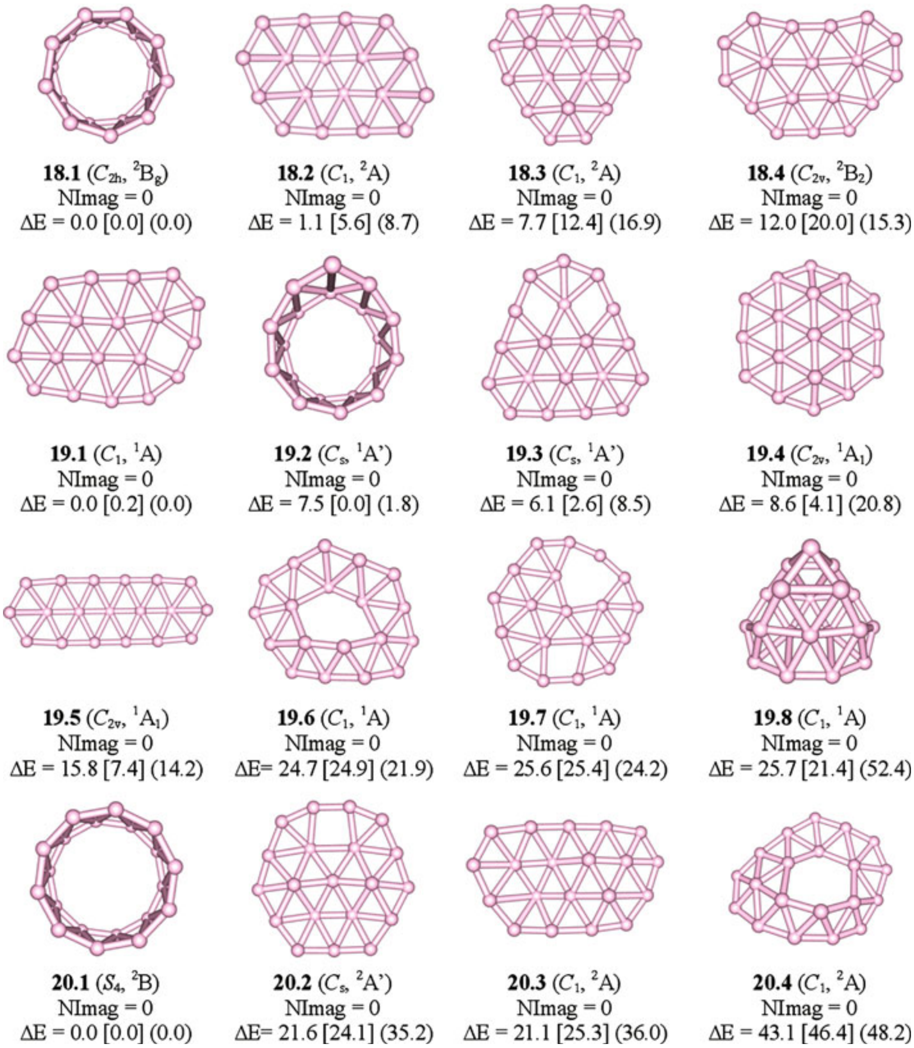

18.1 (C_{2h}, ^2B_g)
NImag = 0
ΔE = 0.0 [0.0] (0.0)

18.2 (C_1, ^2A)
NImag = 0
ΔE = 1.1 [5.6] (8.7)

18.3 (C_1, ^2A)
NImag = 0
ΔE = 7.7 [12.4] (16.9)

18.4 (C_{2v}, $^2B_2$)
NImag = 0
ΔE = 12.0 [20.0] (15.3)

19.1 (C_1, ^1A)
NImag = 0
ΔE = 0.0 [0.2] (0.0)

19.2 (C_s, $^1A'$)
NImag = 0
ΔE = 7.5 [0.0] (1.8)

19.3 (C_s, $^1A'$)
NImag = 0
ΔE = 6.1 [2.6] (8.5)

19.4 (C_{2v}, $^1A_1$)
NImag = 0
ΔE = 8.6 [4.1] (20.8)

19.5 (C_{2v}, $^1A_1$)
NImag = 0
ΔE = 15.8 [7.4] (14.2)

19.6 (C_1, ^1A)
NImag = 0
ΔE= 24.7 [24.9] (21.9)

19.7 (C_1, ^1A)
NImag = 0
ΔE = 25.6 [25.4] (24.2)

19.8 (C_1, ^1A)
NImag = 0
ΔE = 25.7 [21.4] (52.4)

20.1 (S_4, ^2B)
NImag = 0
ΔE = 0.0 [0.0] (0.0)

20.2 (C_s, $^2A'$)
NImag = 0
ΔE= 21.6 [24.1] (35.2)

20.3 (C_1, ^2A)
NImag = 0
ΔE = 21.1 [25.3] (36.0)

20.4 (C_1, ^2A)
NImag = 0
ΔE = 43.1 [46.4] (48.2)

by PBE calculations. At higher levels, CCSD(T) results point out that **19.1** is the global minimum, being 7.5 kcal/mol more stable than **19.2**. G3B3 calculations also provide the same prediction. G3B3 energies indicate a difference of 6.3 kcal/mol in favor of **19.1**. Consequently, we conclude that the planar structure **19.1** is the global minimum of $B_{19}{}^+$.

It is surprising that while some other planar isomers **19.3–19.7** are found to be quite low in energy, the 3D pyramid structure **19.8** is much less stable, in contrast to the recent LDA results. This discrepancy can be understood by the fact that the LDA method is not suitable for treatment of boron clusters.

$B_{20}{}^+$ Our calculations concur with previous report that the 3D tubular structure **20.1** is the most stable isomer for $B_{20}{}^+$. Although some other isomers are also located, they are much less stable, being at least 36.0 kcal/mol higher in energy.

Generally, a structural transition in going from two-dimensional to three-dimensional forms is found to occur for this series at the $B_{16}{}^+$–$B_{19}{}^+$ sizes. While smaller B_n^+ species with $n \leq 15$ are planar or quasi-planar, a structural competition becomes effective within the intermediate sizes of B_{16-19}^+. The $B_{20}{}^+$ is clearly characterized as a 3D tubular structure. Compared to the neutral and anionic counterparts whose shapes were previously reported [27], it seems that while addition of one excess electron tends to extend the planar feature of anionic clusters, detachment of one electron from the neutrals turns out to increase the three-dimensional structural feature of cationic clusters B_n^+.

3.3 Energetic and thermochemical properties

While the different components obtained in the CBS protocol for evaluating total atomization energies (ΣD_0) of the B_n^+ cations are given in Table 2, the corresponding heats of

Table 2 CCSD(T)/CBS total atomization energies (ΣD_0, TAE, kcal/mol) for the cationic B_n^+ clusters ($n = 1$–8) and the different components

Structure	ΔCBS[a]	ΔE_{ZPE}^{b}	ΔE_{CV}^{c}	ΔE_{SR}^{d}	ΔE_{SO}^{e}	ΣD_0 TAE (0 K)
B_2^+ ($^2\Sigma_g^+$)	−146.82	0.62	−0.52	0.03	0.06	−147.88
B_3^+ ($^1A_1'$)	−31.05	4.30	1.51	−0.13	0.09	−33.88
B_4^+ (^2A_g)	90.77	6.98	3.39	−0.26	0.12	87.03
B_5^+ ($^1A_1$)	230.26	9.13	4.10	−0.27	0.15	225.10
B_6^+ ($^2B_{1u}$)	326.39	11.33	5.25	−0.36	0.18	320.13
B_6^+ ($^2A'$)	327.26	12.62	5.89	−0.43	0.18	320.27
B_7^+ ($^1A_1$)	480.34	16.50	7.25	−0.50	0.21	470.80
B_8^+ ($^2A_2$)	600.21	16.87	8.26	−0.55	0.24	591.29

[a] Extrapolated by using Eq. (1) with the aVDZ, aVTZ, and aVQZ basis sets

[b] Zero-point energies taken from the CCSD(T) harmonic frequencies for small clusters B_n^+ ($n = 2$–6) and the MP2 harmonic frequencies for larger clusters B_n^+ ($n = 7$–8)

[c] Core-valence corrections obtained with the aug-cc-pwCVTZ basis sets at the optimized CCSD(T) geometries

[d] Scalar relativistic correction based on a CCSD(T)-DK/cc-pVTZ-DK calculation and is expressed relative to the CCSD(T) result without the DK correction

[e] Correction due to the incorrect treatment of the atomic asymptotes as an average of spin multiplets. Values based on C. Moore's Tables, Ref. [74]

Table 3 Heats of formation at 0 K [$\Delta_f H$ (0 K)] and 298 K [$\Delta_f H$ (298 K)] (kcal/mol) and average binding energies (E_b, eV) of the lowest-lying isomers B_n^+ obtained using G3B3 and CCSD(T)/CBS approaches

Structure	Label	$\Delta_f H$ (0 K)		$\Delta_f H$ (298 K)		E_b
		CBS	G3B3	CBS	G3B3	G3B3
B_2^+ ($^2\Sigma_g^+$)	**2.1**	418.1	421.6	419.8	423.1	0.84
B_3^+ ($^1A_1'$)	**3.2**	439.2	437.6	440.8	439.2	2.28
B_4^+ (^2A_g)	**4.1**	453.4	454.2	455.3	456.1	2.99
B_5^+ ($^1A_1$)	**5.1**	450.4	449.7	452.4	452.4	3.60
B_6^+ ($^2B_{1u}$)	**6.1**	490.5	489.6	492.6	492.2	3.69
B_6^+ ($^2A'$)	**6.2**	490.3	490.3	492.1	492.2	3.69
B_7^+ ($^1A_1$)	**7.1**	474.9	474.0	476.6	475.8	4.10
B_8^+ ($^2A_2$)	**8.1**	489.5	486.4	491.7	489.2	4.25
B_9^+ ($^1A'$)	**9.1**	–	506.9	–	509.4	4.33
B_{10}^+ ($^2B_1$)	**10.1**	–	511.2	–	513.6	4.47
B_{11}^+ ($^1A'$)	**11.1**	–	517.9	–	520.9	4.57
B_{12}^+ (^2A)	**12.1**	–	538.8	–	541.6	4.60
B_{13}^+ ($^1A_1$)	**13.1**	–	535.1	–	538.6	4.71
B_{14}^+ ($^2A_1$)	**14.1**	–	567.6	–	570.6	4.69
B_{15}^+ ($^1A_1$)	**15.1**	–	577.2	–	581.2	4.74
B_{16}^+ (^2A_u)	**16.1**	–	605.9	–	609.8	4.73
B_{17}^+ (^1A)	**17.1**	–	614.2	–	617.5	4.78
B_{17}^+ (^1A)	**17.2**	–	622.4	–	626.7	–
B_{17}^+ (^1A)	**17.3**	–	621.1	–	625.3	–
B_{18}^+ (^2B_g)	**18.1**	–	628.8	–	632.4	4.80
B_{19}^+ ($^1A'$)	**19.1**	–	641.8	–	645.8	4.83
B_{20}^+ (^2B)	**20.1**	–	646.4	–	649.9	4.87

formation at 0 and 298 K calculated from the CBS and G3B3 energies are summarized in Table 3. Adiabatic ionization energies (IEs) of the neutral clusters are calculated as the difference between heats of formation of neutral and cationic clusters at the same computational methods, and the results are shown in Table 4.

The heats of formation of neutral boron clusters B_n are taken from our previous reports [20, 26]. At the first glance, there are small differences between heats of formation obtained from CCSD(T)/CBS and G3B3 energies. The largest difference is found to be 3.5 kcal/mol for diatomic B_2^+, while the others vary in the range of 0.7–3.1 kcal/mol. Similar observations were also found in our earlier reports on the neutral and anionic boron clusters $B_n^{0/-}$. Consequently, the heats of formation of the larger sizes B_n with $n \geq 9$ are only calculated using the composite G3B3 method.

The adiabatic ionization energies (IE) of the clusters B_n are calculated from the heats of formation of neutrals and corresponding cations obtained from both G3B3 and CCSD(T)/CBS approaches. The results are given in Table 4, together with some previous theoretical predictions and available experimental values. Small differences between the G3B3 and CBS values can again be noticed. Compared to the earlier theoretical predictions, the present G3B3 results reveal a better agreement with the available experimental data. While the IE values obtained by Boustani et al. [21] are systematically smaller than our calculated results, the MP4 values reported in Ref. [40] are much different. This discrepancy is due to the fact that the structures located in Ref. [40] differ significantly from our present structures, as discussed in a preceding section.

3.4 Relative stability of clusters

The relative stability of the B_n^+ clusters can be approached by using energetic parameters such as the average binding energy (E_b) and second-order difference in total energies ($\Delta^2 E$). These energetic properties can be defined as follows:

$$E_b\left(B_n^+\right) = \left[(n-1)E(B) + E(B^+) - E\left(B_n^+\right)\right]/n \tag{3}$$

$$\Delta^2 E\left(B_n^+\right) = E\left(B_{n-1}^+\right) + E\left(B_{n+1}^+\right) - 2E\left(B_n^+\right) \tag{4}$$

where $E(B)$, $E(B^+)$ and $E(B_n^+)$ are the total energies of B-atom, cation B^+, and B_n^+ cluster obtained at the G3B3 approach, respectively.

While the plots of these energetic parameters are displayed in Fig. 6, together with those of their corresponding neutrals for the purpose of comparison, the calculated values are given in Table 3. The average binding energy (E_b) of cationic clusters B_n^+ uniformly increases with increasing size of clusters (Fig. 6a). Similar to the trend of neutrals B_n, the highest E_b value is found for the B_{20}^+ cation. The E_b values of smaller cationic clusters B_n^+ ($n \leq 6$) are slightly smaller than those of corresponding neutral B_n. However, at larger sizes in both cationic and neutral states, the E_b values are approximately close to

Table 4 Adiabatic ionization energies (IE$_a$, eV) of boron clusters B_n obtained using G3B3 and CBS approaches

Ion structure	Neutral structure	G3B3	CBS	B3LYP[a]	MP4[b]	Exptl[c]	
B_2^+ ($^2\Sigma_g^+$)	B_2 ($D_{\infty h}$, $^3\Sigma_g^-$)	9.41	9.20	8.734	6.813	10.4	10.3
B_3^+ ($^1A_1'$)	B_3 (D_{3h}, $^2A_1'$)	9.87	9.93	9.199	8.960	9.70	14.0
B_4^+ (^2A_g)	B_4 (D_{2h}, ^1A_g)	9.86	9.92	9.813	14.390	9.80	11.8
B_5^+ ($^1A_1$)	B_5 (C_{2v}, $^2B_2$)	8.45	8.62	9.430	7.240	8.10	7.8
B_6^+ ($^2A'$)	B_6 (C_{5v}, $^1A_1$)	8.89	9.15	8.439	8.841	7.80	9.1
B_6^+ ($^2B_{1u}$)	B_6 (C_{2h}, ^3A_u)	8.59	8.82				
B_7^+ ($^1A_1$)	B_7 (C_{2v}, $^2B_2$)	8.13	8.36	7.955			
B_8^+ ($^2A_2$)	B_8 (D_{7h}, $^3A_2'$)	8.72	8.97	8.625			
B_9^+ ($^1A'$)	B_9 (C_{2v}, $^2A_1$)	8.46		8.112			
B_{10}^+ ($^2B_1$)	B_{10} (C_{2h}, ^1A_g)	8.61		8.685			
B_{11}^+ ($^1A'$)	B_{11} (C_{2v}, $^2B_2$)	8.01		7.993			
B_{12}^+ (^2A)	B_{12} (C_{3v}, $^1A_1$)	8.91		8.684			
B_{13}^+ ($^1A_1$)	B_{13} (C_s, $^2A''$)	7.24		7.941			
B_{14}^+ ($^2A_1$)	B_{14} (C_{2v}, $^1A_1$)	8.11					
B_{15}^+ ($^1A_1$)	B_{15} (C_1, ^2A)	7.39					
B_{16}^+ (^2A_u)	B_{16} (C_{2h}, ^1A_g)	8.07					
B_{17}^+ (^1A)	B_{17} (C_1, ^2A)	7.55					
B_{18}^+ (^2B_g)	B_{18} (C_{3v}, $^1A_1$)	8.05					
B_{19}^+ (^1A)	B_{19} (C_s, $^2A'$)	7.38					
B_{20}^+ (^2B)	B_{20} (D_{10d}, $^1A_{1g}$)	7.53					

[a] Theoretical values at the B3LYP/6-311+G(d) level obtained from Ref. [21]

[b] Theoretical values at the MP4/3-21G(d) level obtained from Ref. [21]

[c] Experimental values obtained from Ref. [2]

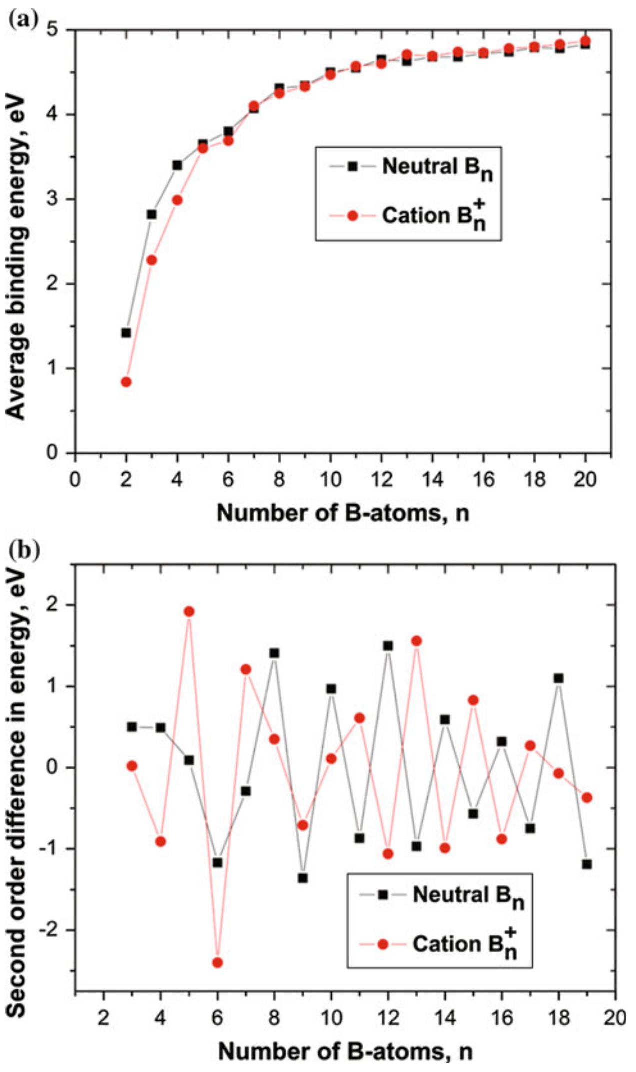

Fig. 6 Average binding energy (E_b, eV) and second-order difference in total energy (Δ^2E, eV) of the B_n^+ clusters using the composite G3B3 method. The E_b and Δ^2E values of neutral boron cluster B_n ($n = 2$–20) obtained from Refs. [20] and [26]

each other. In the cases of $n \geq 13$, the E_b values of cations B_n^+ becomes even larger than those of the neutral B_n.

The second-order difference in total energy (Δ^2E) can be considered as a measure of relative stability of clusters. Accordingly, a high value of Δ^2E indicates a higher stability of the size as compared to its two left and right neighbors. From Fig. 6b, a consistent odd–even oscillation is easily found for the curves of Δ^2E. The closed-shell systems with an odd number of B-atoms for cation B_n^+ (with even number of B-atoms for neutral B_n) reveal local maximum peaks. Interestingly, the Δ^2E plot of cationic clusters B_n^+ shows the enhanced peaks at $n = 5$ and 13, while the closed-shell systems $B_9{}^+$ and $B_{19}{}^+$ correspond to local minimum peaks. These observations are consistent with experimental results of mass spectroscopy previously reported that the $B_5{}^+$ and $B_{13}{}^+$ are enhanced stability systems with high intensity peaks, whereas the low intensity peaks were found at sizes of $n = 9$ and 19 [2].

3.5 Dissociation energies (D_e)

In order to probe further the thermodynamic stability, the dissociation energies (D_e) for various fragmentation channels of the clusters are considered.

The dissociation energies for the channels $B_n^+ \rightarrow B_{n-m}^+ + B_m$ with $1 \leq m \leq n$ is defined in Eq. (3) where $\Delta_f H^0$ (B_n) and $\Delta_f H^0$ (B_n^+) are the heats of formation at 0 K of the B_n and B_n^+ clusters, respectively:

$$D_e\left(B_n^+\right) = \Delta_f H^0\left(B_{n-m}^+\right) + \Delta_f H^0\left(B_m\right) - \Delta_f H^0\left(B_n^+\right) \qquad (5)$$

The smaller D_e values are found for either the fragmentation channel $B_n^+ \rightarrow B_{n-1} + B^+$ or $B_n^+ \rightarrow B_{n-1}^+ + B$ (cf. Table 5). This indicates that a B_n^+ cluster tends to decompose to form either smaller clusters B_{n-1} plus the B^+ radical or smaller cations B_{n-1}^+ plus the B-atom. Both fragmentation channels are competitive. Additionally, an odd–oven oscillation can be found for the plots of two these fragment channels (Fig. 7). The closed-shell systems B_n^+ with odd number of B-atoms reveal maximum local peaks. An exception is also found for $B_9{}^+$ whose D_e value is smaller than that of its two open-shell neighbors. This exception is consistent with the above discussions for the lower stability of $B_9{}^+$.

More interestingly is perhaps the finding that the D_e values for the fragmentation channel $B_n^+ \rightarrow B_{n-1} + B^+$ are smaller than those for the channel $B_n^+ \rightarrow B_{n-1}^+ + B$ in the cases of small clusters B_n^+ with $n \leq 11$ (cf. Fig. 7). However, for larger sizes of $n \geq 14$, an opposite trend can be found that the latter channel is more favored. These observations are consistent with our E_b predictions that the binding energy of large clusters B_n^+ ($n \geq 13$) are higher as compared to those of their corresponding neutral species.

3.6 Electron delocalization and aromaticity of cationic clusters B_n^+

Aromaticity is no doubt one of the most interesting features of small boron clusters. Possessing planar structures, these boron clusters were characterized as highly aromatic systems, on the basis of various indices such as nucleus-independent chemical shift (NICS), electron localization function (ELF), resonance energy (RE), the presence of ring current induced by an external magnetic field, and the classical Hückel rule of ($4\,N + 2$) valence electrons, etc… [8–10, 27]. In recent reports [20, 26], we found that all small boron clusters B_n with $n \leq 20$ have an aromatic character, irrespective of their numbers of valence electrons.

Table 5 Dissociation energies (D_e eV) for various fragmentation channels of cationic boron clusters B_n^+ obtained using G3B3 calculations

n	D_e (1)	D_e (2)	D_e (3)	D_e (4)	D_e (5)	D_e (6)	D_e (7)	D_e (8)	D_e (9)	D_e (10)
2	1.67					1.67				
3	5.16	3.99				3.99	5.16			
4	5.14	7.45	3.50			3.50	7.45	5.14		
5	6.05	8.34	7.88	4.42		4.42	7.88	8.34	6.05	
6	4.13	7.33	6.85	6.88	3.92	3.92	6.88	6.85	7.33	4.13
7	6.53	7.82	8.24	8.26	8.78	5.91	8.78	8.26	8.24	7.82
8	5.32	9.01	7.51	8.44	8.94	5.43	9.56	8.94	8.44	7.51
9	4.97	7.44	8.35	7.35	8.77	4.49	8.72	9.36	8.77	7.35
10	5.67	7.79	7.49	8.90	8.39	5.45	8.49	9.23	9.90	8.39
11	5.57	8.39	7.73	7.93	9.82	5.19	9.34	8.89	9.66	9.41
12	4.95	7.67	7.72	7.56	8.24	5.17	8.48	9.14	8.71	8.56
13	6.02	8.12	8.06	8.61	8.94	5.34	9.52	9.33	10.01	8.67
14	4.45	7.62	6.95	7.39	8.42	5.45	8.12	8.81	8.64	8.41
15	5.44	7.05	7.43	7.26	8.19	5.57	9.21	8.40	9.11	8.03
16	4.61	7.21	6.03	6.92	7.24	5.46	8.51	8.67	7.87	7.67
17	5.50	7.26	7.08	6.40	7.78	5.66	9.28	8.85	9.02	7.32
18	5.23	7.88	6.86	7.18	6.99	5.91	9.21	9.35	8.93	8.20
19	5.29	7.67	7.54	7.03	7.83	5.48	9.53	9.34	9.50	8.17
20	5.66	8.10	7.70	8.07	8.05	6.52	9.46	10.03	9.86	9.11

(1) $B_n^+ \rightarrow B + B_{n-1}^+$; (2) $B_n^+ \rightarrow B_2 + B_{n-2}^+$; (3) $B_n^+ \rightarrow B_3 + B_{n-3}^+$; (4) $B_n^+ \rightarrow B_4 + B_{n-4}^+$; (5) $B_n^+ \rightarrow B_5 + B_{n-5}^+$; (6) $B_n^+ \rightarrow B^+ + B_{n-1}$; (7) $B_n^+ \rightarrow B_2{}^+ + B_{n-2}$; (8) $B_n^+ \rightarrow B_3{}^+ + B_{n-3}$; (9) $B_n^+ \rightarrow B_4{}^+ + B_{n-4}$; (10) $B_n^+ \rightarrow B_5{}^+ + B_{n-5}$

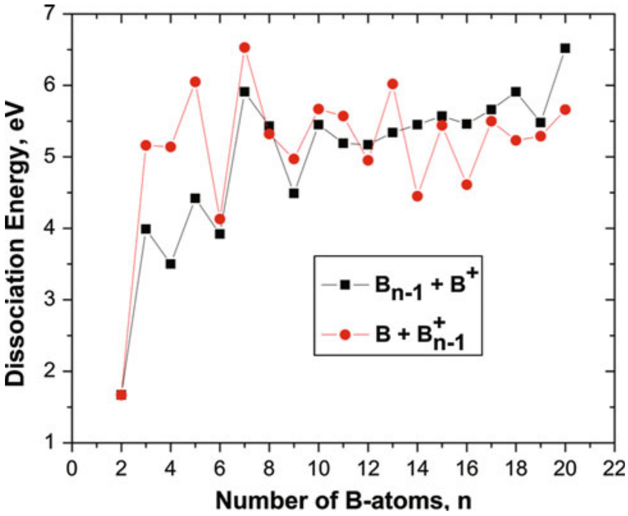

Fig. 7 Dissociation energy (D_e) of the B_n^+ clusters using the G3B3 method

In this present work, we perform an evaluation of aromaticity of closed-shell clusters B_n^+ using the NICS indices [89]. Accordingly, a compound could be regarded as aromatic when it shows negative NICS values at the ghost atoms placed on its structure. In an opposite direction, a compound is anti-aromatic when its related NICS values are positive. The NICS indices are commonly used to evaluate the aromatic features of planar cycles in the literature [8–10, 27]. Recently, it was also found to be effective for evaluating the aromaticity of three-dimensional tubular structure B_{2n} with $n = 8$–12 [90]. In this context, the NICS values of cationic boron clusters are calculated at the central positions of the global minimum structures and also at the positions of 1.0 Å on the out-plane z axis. Table 6 shows that all closed-shell species B_n^+ have an aromatic character with negative NICS values.

The electron localization of B_n^+ clusters can now be probed further by an analysis of the localized orbital locator (LOL) [91] for the enhanced stability clusters $B_5{}^+$

Table 6 NICS values of closed-shell B_n^+ cations obtained at the B3LYP/6-311+G(d) level

Structures	NICS (0,0)	NICS(0,1)
$B_3{}^+$ ($^1A_1{}'$)	−66.3	−17.4
$B_5{}^+$ ($^1A_1$)	−36.2	−18.8
$B_7{}^+$ ($^1A_1$)	−36.7	−23.1
$B_9{}^+$ ($^1A'$)	−23.9	−12.2
$B_{11}{}^+$ ($^1A'$)	−33.2	−20.5
$B_{13}{}^+$ ($^1A_1$)	−17.2	−20.1
$B_{15}{}^+$ ($^1A_1$)	−10.2	−5.9
$B_{17}{}^+$ (^1A)	−34.7	−27.2
$B_{19}{}^+$ (^1A)	−14.6	−12.0

and B_{13}^{+}. The LOL technique was proposed by Schmider and Becke [91] and is defined as follows:

$$\mathrm{LOL} = \frac{1}{1 + \frac{\tau}{D_0}} \qquad (6)$$

where τ is the local kinetic energy, D_0 is the kinetic energy in the uniform electron gas.

Consequently, high LOL values are associated with slow electrons that are characteristic of localized electrons such as electrons located in bonds or lone pairs and vice versa. Recently, the LOL indices have been effectively applied for analysis of electron delocalization of organic compounds [92, 93] and also the B_{20} cluster [20].

Our analysis of canonical molecular orbital (CMO) showed that seven valence MOs of B_5^{+} are divided into two sets. The first set includes five MOs (HOMO-2, HOMO-3, HOMO-4, HOMO-5, and HOMO-6) that are responsible for five two-electron (2e)–two-center (2c) bonds between B-atoms. The two remaining MOs, including π-MO (HOMO-1) and σ-MO (HOMO) (Fig. 8a) are globally delocalized, and thus responsible for aromaticity of the B_5^{+}. The LOL plots for B_5^{+} (Fig. 8b) reveal an internal consistence with our CMO analysis. Green-colored contractors of the first set of MOs are distributed on the B–B bonds and contribute to five 2e-2c bonds. Interestingly, the σ-LOL (in red domains) and π-LOL (in blue domains) show the contractors that are delocalized over the entire system, and thus responsible for aromaticity of B_5^{+}.

Similar observations are found for B_{13}^{+} as shown in Fig. 9. Nineteen valence MOs can be divided into three sets. The first set of three π-MOs (HOMO-2, HOMO-3, and HOMO-8) and the second set of three σ-MOs (HOMO, HOMO-1, and HOMO-4) are globally delocalized, while the third set of remaining MOs are responsible for the B–B bonds of outer rings [18]. The LOL plots in Fig. 9b emphasize that the red-colored contractors of σ-LOL and blue-colored contractors of π-LOL are delocalized globally, and thereby make the B_{13}^{+} cation aromatic.

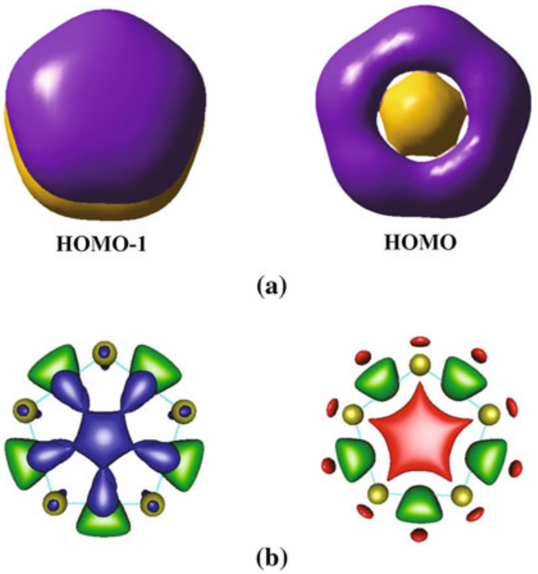

Fig. 8 **a** Selected MOs of the B_5^{+} (C_{2v}) and **b** LOL isosurfaces of the B_5^{+} (C_{2v}) at the LOL values of 0.67 ÷ 0.80

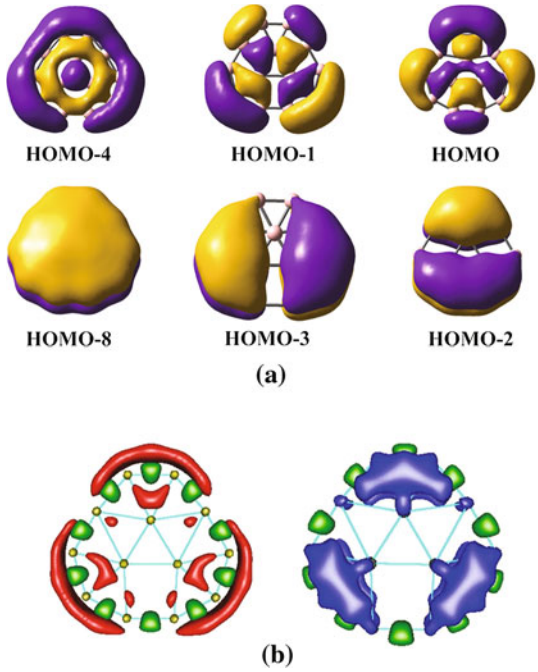

Fig. 9 **a** Selected MOs of the B_{13}^{+} (C_{2v}) and **b** LOL isosurfaces of the B_{13}^{+} (C_{2v}) at the LOL values of 0.67 ÷ 0.80

4 Concluding remarks

In this study, we attempt to approach the boron conundrum in performing theoretical investigations on molecular structures and thermochemical properties of the cationic boron clusters B_n^{+} with $n = 2$–20. Indeed, for these systems, inconsistent results on their structures and energies constitute a typical characteristic of the current literature.

In establishing the global minima, we use a stochastic search method along with high-accuracy quantum chemical calculations. The performance of computational methods is evaluated by using CCSD(T)/CBS energies as standard references. The following important points emerge from the calculated results:

1. There is a consistency between high-accuracy computational methods such as G3, G3B3, G4, and CCSD(T)/CBS.
2. For planar and quasi-planar structures, the relative energies obtained from seven different density functionals including B3LYP, BLYP, TPSS, TPSSh, PW91, PB86, and PBE are close to each other and

can be compared to the CCSD(T)/CBS values. While the BLYP and B3LYP functionals are apparently less accurate for three-dimensional structures, the MP2 method is not reliable for boron clusters.

3. Single-point electronic energies obtained from CCSD(T) calculations with the MP2 and B3LYP geometries agree well with the CCSD(T)/CBS values based on CCSD(T) geometries. Differences in geometries between the B3LYP, MP2, and CCSD(T) methods induce negligible variations in relative energies.
4. A structural transition is found to occur in going from two-dimensional to three-dimensional forms for this series at the B_{16}^+–B_{19}^+ sizes. While smaller B_n^+ clusters with $n \leq 15$ are planar or quasi-planar, a structural competition becomes effective within the intermediate sizes of B_{16-19}^+. The cation B_{20}^+ is clearly characterized as a 3D tubular structure.
5. We determine a reliable and consistent set of standard heats of formation for the cationic boron clusters that are missing up to now. The adiabatic ionization energies can thereby be predicted. The average binding energy tends to increase with increasing size toward a certain limit. Enhanced stability is found for closed-shell systems B_5^+ and B_{13}^+; and
6. Finally, all closed-shell species B_n^+ have an aromatic character with negative NICS values. The electron delocalization of the enhanced stability systems B_5^+ and B_{13}^+ are analyzed by using the LOL index.

Acknowledgments The authors are indebted to the KULeuven Research Council for continuing support (GOA, IUAP, and IDO programs). TBT thanks the Arenberg Doctoral School of the KULeuven for a scholarship. We thank professor Arnout Ceulemans for illuminating discussion on the boron conundrum.

References

1. Hanley L, Anderson SL (1987) J Phys Chem 91:5161
2. Hanley L, Whitten JL, Anderson SL (1988) J Phys Chem 92:5803
3. Zhai HJ, Wang LS, Alexandrova AN, Boldyrev AI (2002) J Chem Phys 117:7917
4. Zhai HJ, Kiran B, Li J, Wang LS (2003) Nat Mat 2:827
5. Zhai HJ, Alexandrova AN, Birch KA, Boldyrev AI, Wang LS (2003) Angew Chem Int Ed 42:6004
6. Sergeeva AP, Zubarev DY, Zhai HJ, Boldyrev AI, Wang LS (2008) J Am Chem Soc 130:7244
7. Sergeeva AP, Averkiev BB, Zhai HJ, Boldyrev AI, Wang LS (2011) J Chem Phys 134:224304
8. Huang W, Sergeeva AP, Zhai HJ, Averkiev BB, Wang LS, Boldyrev AI (2010) Nat Chem 2:202
9. Alexandrova AN, Boldyrev AI (2004) J Phys Chem A 108:3509
10. Zubarev DY, Boldyrev AI (2006) J Comput Chem 28:251
11. Kiran B, Bulusu S, Zhai HJ, Yoo S, Cheng XC, Wang LS (2005) Proc Natl Acad Sci USA 102:961
12. Gopakumar G, Nguyen MT, Ceulemans A (2008) Chem Phys Lett 450:175
13. Ceulemans A, Muya JT, Gopakumar G, Nguyen MT (2008) Chem Phys Lett 461:226
14. Muya JT, Nguyen MT, Ceulemans A (2009) Chem Phys Lett 483:10
15. Muya JT, Gopakumar G, Nguyen MT, Ceulemans A (2011) Chem Phys Phys Chem 13:7524
16. Bean DE, Muya JT, Flower PW, Nguyen MT, Ceulemans A (2011) Chem Phys Phys Chem 13:20855
17. Nguyen MT, Matus MH, Ngan VT, Grant DJ, Dixon DA (2009) J Phys Chem A 113:4895
18. Kiran B, Gopakumar G, Nguyen MT, Kandalam AK, Jena P (2009) Inorg Chem 48:9965
19. Tai TB, Ceulemans A, Nguyen MT (2012) Chem Eur J 18:4510
20. Tai TB, Tam NM, Nguyen MT (2012) Chem Phys Lett 530:71
21. Akman N, Tas M, Ozdogan C, Boustani I (2011) Phys Rev B 84:075463
22. Boustani I (1997) Phys. Rev. B 55:16426
23. Grimes RN (2004) J Chem Edu 81:657 and references therein
24. Bean DE, Fowler PW (2009) J Phys Chem C 113:15569
25. Chacko S, Kanhere DG (2003) Phys Rev B 68:035414
26. Tai TB, Grant DJ, Nguyen MT, Dixon DA (2010) J Phys Chem A 114:994
27. Alexandrova AN, Boldyrev AI, Zhai HJ, Wang LS (2006) Coord Chem Rev 250:2811 and references therein
28. Oger E, Crawford NRM, Kelting R, Weis P, Kappes MM, Ahlrichs R (2007) Angew Chem Int Ed 46:8503
29. Boustani IB, Zhu Z, Tomanek D (2011) Phys Rev B 83:193405
30. An W, Bulusu S, Gao Y, Zeng XC (2006) J Chem Phys 124:154310
31. Pan L, Li J, Wang LS (2008) J Chem Phys 129:024302
32. Li F, Jin P, Jiang D, Wang L, Zhang SB, Zhao J, Chen Z (2012) J Chem Phys 136:074302
33. Ray AK, Howard IA, Kanal KM (1992) Phys Rev B 45:14247
34. Kato H, Yamashita K, Morokuma K (1992) Chem Phys Lett 190:361
35. Niu J, Rao BK, Jena P (1997) J Chem Phys 107:132
36. Bonacic-Koutecky V, Fantucci P, Koutecky J (1991) Chem Rev 91:1035
37. Garcia-Molina R, Heredia-Avalos S, Abril I (2000) J Phys Condens Matter 12:5519
38. Boustani I (1994) Int J Quant Chem 52:1081
39. Ricca A, Bauschlicher CW Jr (1997) J Chem Phys 106:2317
40. Ricca A, Bauschlicher CW Jr (1996) Chem Phys 208:233
41. Gillery C, Linguerri R, Rosmus P, Maier JP (2005) J Phys Chem 219:467
42. Li QS, Jin HW (2002) J Phys Chem A 106:7042
43. Li QS, Jin Q, Luo Q, Tang AC, Yu JK, Zhang HX (2003) Int J Quant Chem 94:269
44. Ma J, Li Z, Fan K, Zhou M (2003) Chem Phys Lett 372:708
45. Kawai R, Weare JH (1992) Chem Phys Lett 191:311
46. Gu FL, Yang X, Tang AC, Jiao HJ, Schleyer PVR (1998) J Comput Chem 19:203
47. Fowler JE, Ugalde JM (2000) J Phys Chem A 104:397
48. Frisch MJ, Trucks GW, Schlegel HB, Scuseria GE, Robb MA, Cheeseman JR, Montgomery JA Jr, Vreven T, Kudin KN, Burant JC, Millam JM, Iyengar SS, Tomasi J, Barone V, Mennucci B, Cossi M, Scalmani G, Rega N, Petersson GA, Nakatsuji H, Hada M, Ehara M, Toyota K, Fukuda R, Hasegawa J, Ishida M, Nakajima T, Honda Y, Kitao O, Nakai H, Klene M, Li X, Knox JE, Hratchian HP, Cross JB, Bakken V, Adamo C, Jaramillo J, Gomperts R, Stratmann RE, Yazyev O, Austin AJ, Cammi R, Pomelli C, Ochterski JW, Ayala PY, Morokuma K, Voth GA, Salvador P, Dannenberg JJ, Zakrzewski VG, Dapprich S, Daniels AD, Strain MC, Farkas O, Malick DK, Rabuck AD, Raghavachari K, Foresman JB, Ortiz JV, Cui Q, Baboul AG, Clifford S, Cioslowski J, Stefanov BB, Liu G, Liashenko A,

Piskorz P, Komaromi I, Martin RL, Fox DJ, Keith T, Al-Laham MA, Peng CY, Nanayakkara A, Challacombe M, Gill PMW, Johnson B, Chen W, Wong MW, Gonzalez C, Pople JA (2004) Gaussian 03, revision C.02, Gaussian Inc., Wallingford

49. Werner H-J, Knowles PJ, Lindh R, Manby FR, Schütz M, Celani P, Korona T, Rauhut G, Amos RD, Bernhardsson A, Berning A, Cooper DL, Deegan MJO, Dobbyn AJ, Eckert F, Hampel C, Hetzer G, Lloyd AW, McNicholas SJ, Meyer W, Mura ME, Nicklass A, Palmieri A, Pitzer R, Schumann U, Stoll H, Stone A J, Tarroni R, Thorsteinsson T (2006) MOLPRO, version 2006.1, a package of ab initio programs
50. Tai TB, Nguyen MT (2011) J Chem Theory Comput 7:1119
51. Stevens WJ, Krauss M, Basch H, Jasien PR (1992) Can J Chem 70:612
52. Baboul AG, Curtiss LA, Redfern PC (1999) J Chem Phys 110:7650
53. Becke AD (1993) J Chem Phys 98:5648
54. Lee C, Yang W, Parr RG (1988) Phys Rev B 37:785
55. Stephens PJ, Devlin FJ, Chabalowski CF, Frisch MJ (1994) J Phys Chem 98:11623
56. Perdew JP, Burke K, Ernzerhof M (1996) Phys Rev Lett 77:3865
57. Pople JA (1980) J. Chem. Phys 72:650
58. Bartlett RJ, Musial M (2007) Rev Mod Phys 79:291 and references therein
59. Tai TB, Kadlubanski P, Roszak S, Majumdar D, Leszkzynski J, Nguyen MT (2011) Chem Phys Chem 12:2948
60. Tai TB, Nguyen MT (2012) J Comput Chem 33:800
61. Tai TB, Nhat PV, Nguyen MT, Li S, Dixon DA (2011) J Phys Chem A 115:7673
62. Rittby M, Bartlett RJ (1988) J Phys Chem 92:3033
63. Knowles PJ, Hampel C, Werner H-J (1994) J Chem Phys 99:5219
64. Deegan MJO, Knowles PJ (1994) Chem Phys Lett 227:321
65. Dunning TH (1989) J Chem Phys 90:1007
66. Kendell RA, Dunning TH, Harrison RJ (1992) J Chem Phys 96:6796
67. Peterson KA, Woon DE, Dunning TH (1994) J Chem Phys 100:7410
68. Helgaker T, Klopper W, Koch H, Nagel J (1997) J Chem Phys 106:9639
69. Halkier A, Helgaker T, Jørgensen P, Klopper W, Koch H, Olsen J, Wilson AK (1998) Chem Phys Lett 286:243
70. Douglas M, Kroll NM (1974) Ann Phys 82:89
71. Hess BA (1985) Phys Rev A 32:756
72. Hess BA (1986) Phys Rev A 33:3742
73. De Jong WA, Harrison RJ, Dixon DA (2001) J Chem Phys 114:48
74. Moore CE (1949) Atomic energy levels as derived from the analysis of optical spectra, Volume 1, H to V; U.S. National Bureau of Standards Circular 467, U.S. Department of Commerce, National Technical Information Service, COM-72-50282: Washington, DC
75. Karton A, Martin JML (2007) J Phys Chem A 111:5936
76. Tai TB, Nguyen MT (2009) Chem Phys Lett 483:35
77. Tai TB, Nguyen MT (2010) Chem Phys 475:35
78. Tai TB, Nguyen MT, Dixon DA (2010) J Phys Chem 114:2893
79. Curtiss LA, Raghavachari K, Redfern PC, Pople JA (1997) J Chem Phys 106:1063
80. Curtiss LA, Raghavachari K, Redfern PC, Rassolov V, Pople JA (1998) J Chem Phys 109:7764
81. Curtiss LA, Redfern PC, Raghavachari K (2007) J Chem Phys 126:084108
82. Becke AD (1988) Phys Rev A 38:3098
83. Tao J, Perdew JP, Staroverov VN, Scuseria GE (2003) Phys Rev Lett 91:146401
84. Perdew JP, Kurth S, Zupan A, Blaha P (1999) Phys Rev Lett 82:2544
85. Perdew JP, Tao J, Staroverov VN, Scuseria GE (2004) J Chem Phys 120:6898
86. Perdew JP (1986) Phys Rev B 33:8822
87. Perdew JP, Burk K, Wang Y (1996) Phys Rev B 54:16533
88. Bruna PJ, Wright JS (1990) J Mol Struct Theochem 210:243
89. PvR Schleyer, Maerker C, Dransfeld A, Jiao H, Hommes NJRE (1996) J Am Chem Soc 118:6317
90. Johansson MP (2009) J Phys Chem C 113:524
91. Schmider HL, Becke AD (2000) Theochem 527:51
92. Jacobsen HJ (2009) J Comput Chem 30:1093
93. Steinmann SN, Mo Y, Corminboeuf C (2011) Phys Chem Chem Phys 13:20584

Theor Chem Acc (2012) 131:1243
DOI 10.1007/s00214-012-1243-6

REGULAR ARTICLE

Quantum chemical study of self-doping PPV oligomers: spin distribution of the radical forms

D. Geldof · A. Krishtal · F. Blockhuys ·
C. Van Alsenoy

Received: 29 February 2012 / Accepted: 22 May 2012 / Published online: 14 June 2012

Abstract A quantum chemical study was performed on ten different self-doping PPV oligomers. The geometry and the different weak intramolecular interactions were studied. The atomic spin populations were calculated using the FOHI method and related to the calculated EPR parameters. The effects of the removal of methoxy groups, the introduction of nitrogen atoms, and the relocation of the self-doping sidechain on the geometry, the spin distribution, and the EPR parameters have been described.

Keywords FOHI partitioning method · Self-doping PPV oligomers · Spin density · EPR parameters

1 Introduction

Within the class of oligomeric or low-molecular-weight organic semiconductors distyrylbenzenes (DSBs)—oligomers of poly(*p*-phenylene vinylene) or PPV and their derivatives enjoy a great deal of interest as new materials for opto-electronic applications such as organic light-emitting diodes (OLEDs) [1–7], gas- and ion-selective sensors [8, 9, 10, 11], organic memories, and nonlinear optics (NLO) [12]. In a number of these applications, the oligomers need to be in their electrically conducting state (the neutral compounds are electrical insulators) and this can be easily achieved by oxidizing or reducing them using either a chemical or an electrochemical procedure; the latter has the advantage that the active material can be electro-deposited from a standard electrochemical cell directly onto a pre-chosen substrate. In order to increase the purity of the deposited material, the necessary background electrolyte can be eliminated from the cell by covalently binding it to the oligomer backbone, giving rise to self-doping oligomers (Fig. 1) [13].

As useful and interesting as these new materials may be, further studies of the properties of this new type of oligomer—in particular, the spin (de)localization in their electrically conducting radical form—are hampered somewhat by the fact that self-doping oligomers in their native, undoped form are difficult to prepare and even more difficult to purify: the simultaneous presence of the polar, ionic, self-doping side chain, and the bulky apolar backbone of the oligomer results in the compounds being equally soluble in both polar (even water) and apolar solvents, and conventional ways of purification such as extraction and recrystallization are useless. Since the ionic side chain is present from the very start of the multi-step synthetic pathway [13], purification of the intermediates is skipped, leading to an accumulation of impurities in the final self-doping oligomer and, in general, a decrease in the yields of the various reactions. Introduction of the self-doping chain at the end is impractical, as the Wittig reaction—traditionally used to prepare DSBs—is incompatible with the free hydroxyl group that would necessarily be present on the oligomer during the entire synthetic

---

Published as part of the special collection of articles celebrating theoretical and computational chemistry in Belgium.

Electronic supplementary material The online version of this article (doi:10.1007/s00214-012-1243-6) contains supplementary material, which is available to authorized users.

D. Geldof · A. Krishtal · F. Blockhuys · C. Van Alsenoy (✉)
Department of Chemistry, University of Antwerp,
Universiteitsplein 1, 2610 Antwerp, Belgium
e-mail: kris.vanalsenoy@ua.ac.be

A. Krishtal
Fachbereich Chemie, Technische Universität Kaiserslautern,
Erwin Schrödinger Straße, 67663 Kaiserslautern, Germany

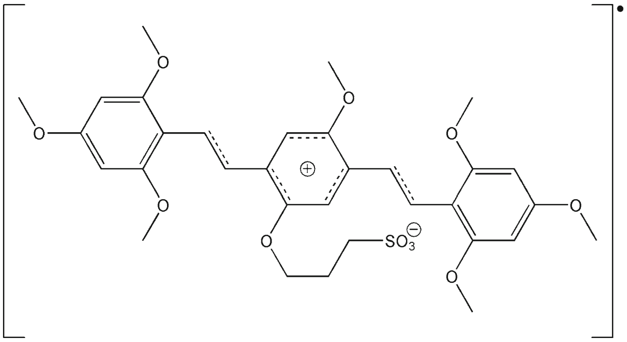

Fig. 1 Schematic representation of the self-doped radical form of *E, E*-2-(3-sulfopropoxy)-5-methoxy-1,4-bis[2-(2,4,6-trimethoxyphenyl) ethenyl]benzene

pathway. The use of protecting groups for this hydroxyl group would make an already lengthy preparative procedure even longer.

Other synthetic procedures, however, do not display this incompatibility with free hydroxyl groups and would allow the preparation and purification of an OH-substituted oligomer, which could then, in the final step, be equipped with a self-doping side chain. The benzylidene-aniline (BA) condensation, used to prepare DSBs in which the spacers are CH=N rather than CH=CH [14, 15], is one such procedure and oligomers such as 5 and 6 (Fig. 2) would become available. Naturally, the introduction of nitrogen atoms in the carbon backbone of the oligomers leads to a rearrangement of the electron density, not only of the native, undoped material but also of the self-doped system, which would result in properties that differ considerably from those of, for instance, the original all-carbon material (1) [13, 16].

The most efficient way to gauge the effects of changes in the molecular structure in terms of the electron distribution is by performing quantum chemical calculations at a suitably reliable level, rather than preparing the compounds and determining their properties experimentally. In this paper, the results of a quantum chemical study on the structure and electronic properties of a series of derivatives of *E, E*-2-(3-sulfopropoxy)-5-methoxy-1,4-bis[2-(2,4,6-trimethoxyphenyl)ethenyl]benzene (1) (Fig. 2) are presented. Apart from the geometries of the non-oxidized, native systems, and those of the self-doped forms in different conformations, the main focus of the paper is on the charge and spin distribution of the self-doped radicals and the influence of the presence and/or position of heteratoms and substituents thereon; compound 1 will be used as a reference structure. Replacement of the ether-oxygen atom of the self-doping chain by nitrogen (1 → 3) as well as the removal of the methoxy group on the central ring (1 → 2 and 3 → 4) will be investigated. Introduction of nitrogen atoms in the vinyl spacer *alpha* to the central (1 → 5) and *alpha* to the peripheral rings (1 → 6) leads to the two BA derivatives. Finally, the self-doping side chain will be moved to one of the peripheral rings (7) and the two methoxy groups on the central one are removed (9). The introduction of one (8) or two nitrogen atoms (10) into the latter structure will also be studied. The paper will be concluded with a short discussion of the hyperfine coupling constants calculated for the different derivatives, in the context of those experimentally determined for the reference structure (1).

2 The FOHI method

In this work, we use the fractional occupation Hirshfeld-I (FOHI) method, which is an extension of the Hirshfeld-I (HI) method to calculate atomic spin populations. In the original Hirshfeld method [17], a weight function is used to partition the molecular density $\rho(\vec{r})$ into atomic densities $\rho_a(\vec{r})$:

$$\rho_a(\vec{r}) = w_a(\vec{r})\rho(\vec{r}). \tag{1}$$

The method is based on the use of diffuse boundaries in which the weight function of an atom a can be in principle nonzero in every point $\vec{r}$ of space. The "share" of each atom at point $\vec{r}$ is calculated using:

$$w_a(\vec{r}) = \frac{\rho_a^{[0]}(\vec{r})}{\sum_b \rho_b^{[0]}(\vec{r})} \tag{2}$$

The promolecular density, the denominator in Eq. (2), is defined as the sum of the densities of the isolated atoms $\rho_b^{[0]}$, positioned at the same coordinates as the atomic nuclei in the real molecule. Integration of the atomic density leads to the population of every atom:

$$N_a = \int \rho_a(\vec{r})\mathrm{d}\vec{r} = \int w_a(\vec{r})\rho(\vec{r})\mathrm{d}\vec{r}. \tag{3}$$

This procedure suffered from a number of shortcomings, the most prominent of them being the arbitrary choice of the free atom densities used to construct the promolecular density [18, 19]. Although some of these were corrected in an iterative version of the procedure (the HI method), change in spin, of importance in open shell systems, was not taken into account. This point was remedied in the fractional occupation Hirshfeld-I method (FOHI) through the use of separate weight functions for α and β spin densities. The weight function for the α electrons is given by

$$w_A^{\alpha}(\vec{r}) = \frac{\rho_A^{\alpha}(\vec{r})}{\sum_B \rho_B^{\alpha}(\vec{r})} \tag{4}$$

Equivalent formulas are used for the β density. The spherical symmetry of the free atom densities was ensured

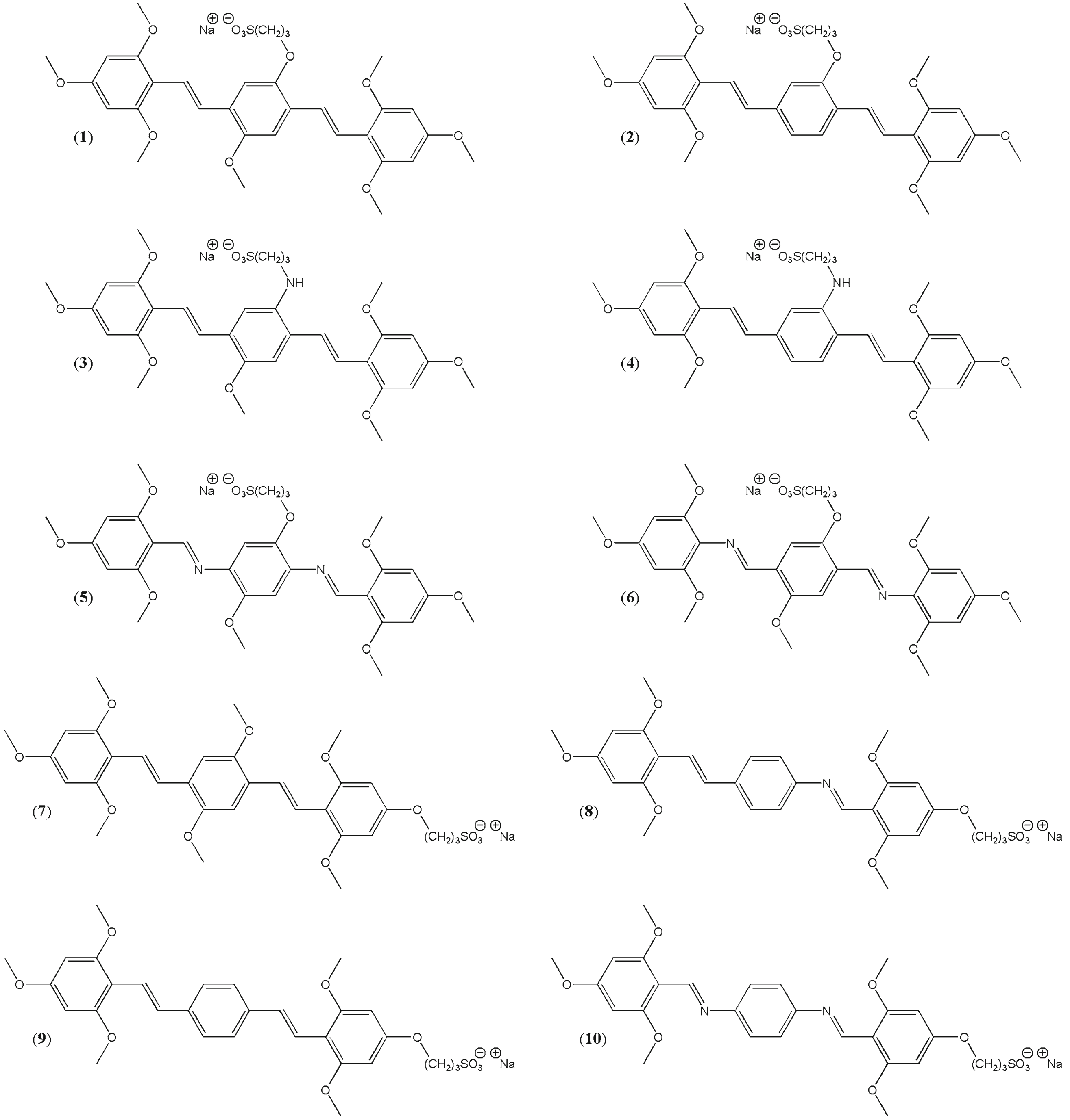

Fig. 2 Structural formulas of the native materials under investigation

through the use of fractional occupations for degenerate atomic orbitals. We refer to the original paper for further details [20].

3 Computational details

For the oligomers depicted in Fig. 2, the geometries were optimized for the neutral, anionic, and radical forms using the B3LYP functional [21–24] and the 6-311+G* basis set [25] with the Gaussian09 program [26]. The EPR parameters were calculated with the ORCA package [27] using the B3LYP functional combined with the EPR-II basis set [28] for the carbon, hydrogen, and nitrogen atoms and the Ahlrichs-SVP basis set [29, 30] for the oxygen and sulfur atoms. Identical basis sets were chosen as used in previous calculations [16]. For the fractional occupation Hirshfeld-I partitioning (FOHI), the atomic densities were calculated at every iteration using the BRABO program [31] with the B3LYP functional and 6-311+G* basis set. The FOHI charge and spin populations were evaluated by making use of the STOCK program [32]. Both programs are part of the BRABO package. The geometries of the neutral and anionic forms can be found in the supplementary material.

4 Results and discussion

4.1 Geometry and atomic charges

For each of the ten oligomers, a number of geometry optimizations were performed: (1) the neutral structure (presented in Fig. 2), (2) the "anionic" structure which is obtained by removing the sodium atom from the neutral structure, and (3) the two conformations of the radical form given in Fig. 3. In the following, only the radical structures will be discussed.

Two different structures can be envisaged for the self-doped systems, that is, the radical form of the oligomers: (1) a structure in which the sulfonated alkyl chain is extended from the conjugated backbone of the oligomer (Fig. 3a), which will be designated "extended structure," and (2) a structure in which the sulfonated alkyl chain is directed toward one of the vinyl spacers of the conjugated backbone (Fig. 3b), which will be designated "folded structure" [13]. The folded structure is found to be more stable, [13] due to the decreased distance between the charge sites and the resulting stabilizing non-bonded intramolecular interactions of the sulfoalkyl sidechain with the conjugated backbone. For oligomers 1, in which the sulfoalkyl sidechain is connected to the central ring, and 7, in which the sulfoalkyl sidechain is connected to the peripheral ring, these interactions have been represented in Fig. 4a, b, respectively. In the folded structure of oligomer 1, four intramolecular CH $\cdots$ O interactions involving the oxygen atoms of the SO_3 group stabilize the folded sulfoalkyl sidechain. These interactions are also found for oligomers 2, 3, 4, and 5. Likewise, when the sulfoalkyl sidechain is positioned on a peripheral ring, two of the oxygen atoms of the SO_3 group are involved in four similar CH $\cdots$ O interactions; this is seen for oligomers 7, 8, 9, and 10. The energy differences ΔE between the extended and folded structure ($E_{\text{extended}} - E_{\text{folded}}$) given in Table 1 (disregarding the value of oligomer 5, see below) indicates that stabilization of the folded structure is greater when the sidechain is connected to the peripheral ring.

Oligomers 5 and 6 represent two exceptions. Due to the presence of the two nitrogen atoms next to the central ring, this ring is twisted out of the plane of the peripheral rings and the CH=N spacers by about 40° [14, 15]. Consequently, the SO_3 group of the sidechain is able to contact two of the *ortho*-methoxy groups on the peripheral rings and forms the stabilized structure presented in Fig. 5a, which means that the extended structure that is found for the nine other oligomers (Fig. 3a) does not exist for oligomer 5. A second, more stable folded structure, similar to the ones found for the other nine oligomers (Fig. 3b), was found by replacing the relevant CH functionalities in oligomer 1 (B2 and D1) by nitrogen atoms and reoptimizing the structure. (For numbering of the atoms, see Fig. 6) This explains the small value of 13.88 kJ mol^{-1} for the energy difference for oligomer 5 in Table 1.

The situation for oligomer 6 is reversed. It presents a regular extended structure in which the peripheral rings are twisted out of the molecular plane due to the presence of the nitrogen atoms by about 40°. However, when the folded structure is generated and optimized, one of the CH=N bonds changes its configuration resulting in weak intramolecular CH $\cdots$ O interactions between the SO_3 group and the methoxy groups in the 4- and 6-positions of the peripheral ring (Fig. 5b). Consequently, the SO_3 group is positioned above one of the peripheral rings; even though the negatively charged SO_3 group is in close proximity to the electron-rich peripheral ring, this folded structure is stabilized to a greater extent than the one of oligomer 1 (Table 1).

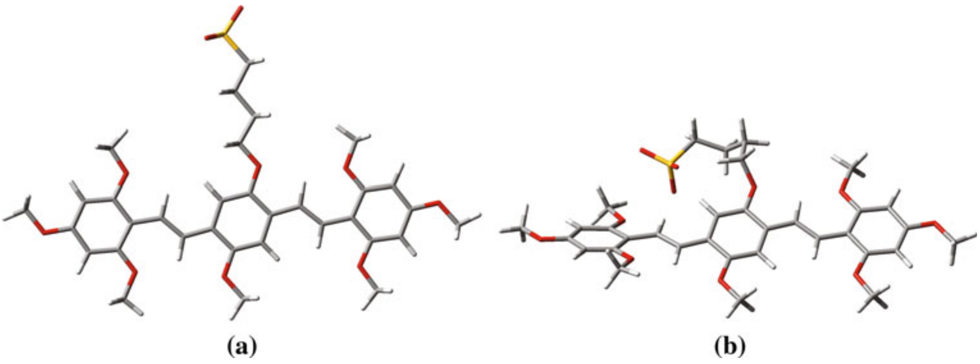

Fig. 3 Different structures of the radical form of the oligomer. **a** Extended structure of the oligomer. **b** Folded structure of the oligomer

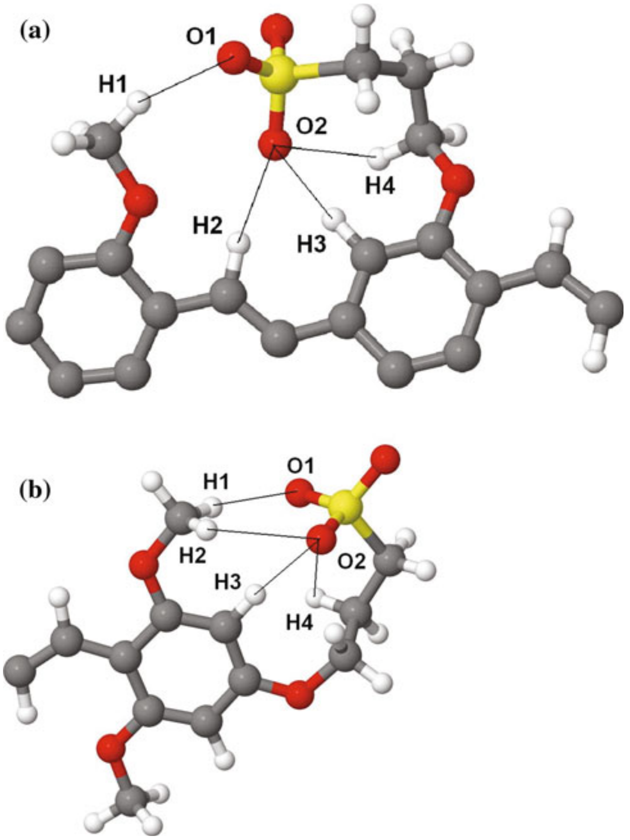

Fig. 4 Intramolecular interactions involving the oxygen atoms of the SO_3 group when the sulfoalkyl sidechain is bonded on the central benzene ring (**a**) or on the outer benzene ring (**b**)

Analysis of the atomic charges using the FOHI method indicates that, regardless of the whereabouts of the SO_3 group and the three-dimensional organization of the folded structure, the SO_3 group always carries a charge of approximately -1. The positive charge is distributed over the entire conjugated backbone, but when nitrogen atoms are present, they carry a significant negative charge and this is linked to a higher spin density.

Table 1 Energy difference ΔE (in $kJ \cdot mol^{-1}$) between the extended and folded radical structures of the ten oligomers

Oligomer	ΔE
1	49.46
2	48.73
3	39.58
4	38.56
5	13.88
6	59.40
7	62.89
8	54.75
9	59.91
10	48.90

($E_{\text{extended}} - E_{\text{folded}}$)

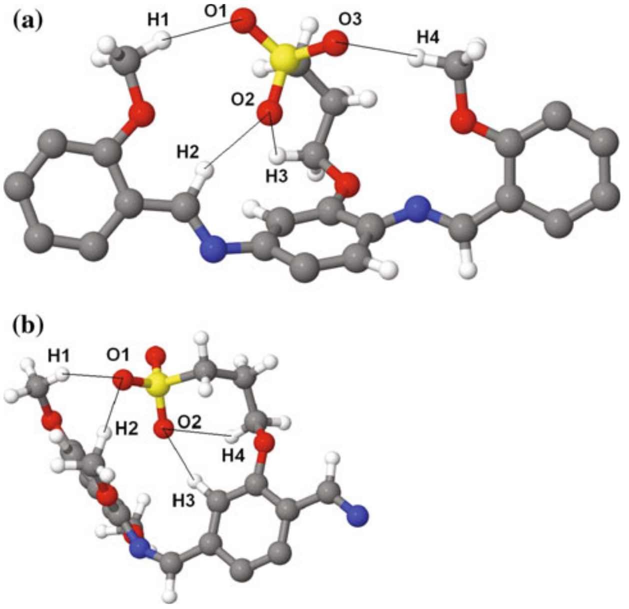

Fig. 5 Intramolecular interactions of the sulfoalkyl sidechain with the conjugated backbone for (**a**) the extended structure of oligomer 5 and (**b**) the folded structure of oligomer 6

4.2 Spin distribution and hyperfine coupling

Based on the FOHI method, atomic spin populations of the ten oligomers were analyzed and compared with the calculated EPR parameters. Because of the large number of atoms for the different oligomers, the changes in the atomic spin populations of the radicals are represented by dividing each oligomer into six fragments. As presented in Fig. 6, these comprise each of the two peripheral rings with substituents (A and E), the central ring (C), the two vinyl spacers (B and D), and the sidechain (S). The results can be found in Table 2. The maximum ^{1}H and ^{14}N hyperfine couplings and the positions of the relevant atoms in the structure can be found in Table 3.

The maximum ^{1}H hyperfine coupling of oligomer 1 has been determined experimentally [16] and has a value of about 10.9 MHz. The absolute value of the calculated hyperfine coupling for hydrogen (D2) is about 11.6 MHz, in good agreement with the experimental value. The absence of the methoxy group on the central benzene ring ($1 \rightarrow 2$) does not seem to have a significant influence. The spin populations in Table 2 suggest that there is only a slight reorganization of the spin and then mostly on the central ring, which is also seen in the results of the EPR calculations. Upon introducing one nitrogen atom into the sulfoalkyl sidechain ($1 \rightarrow 3$), a considerable amount of spin becomes located on the sidechain (Table 2) and then mostly on the nitrogen atom. Therefore, for oligomer 3, the proton *alpha* to the nitrogen atom in the sidechain has the

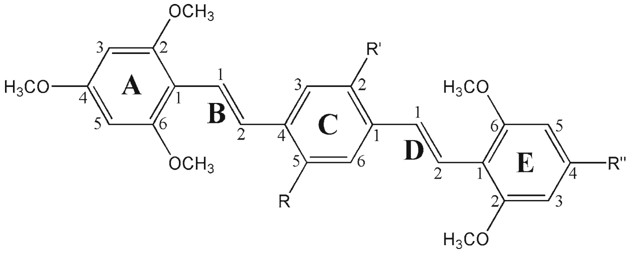

Fig. 6 Labeling of the atoms in the conjugated backbone and schematic representation of the different groups in which the atomic spin has been summed. *R′* and *R″* indicate the sulfoalkyl sidechain or a methoxy group. R is a methoxy group or a hydrogen atom

highest ^{1}H hyperfine coupling. Removing the methoxy group from the central benzene ring (3 → 4) again changes the spin distribution significantly in the central ring (C), but also in the sidechain (S). The difference with respect to the ^{14}N hyperfine coupling is considerable, and this can be explained by the absence of the mesomeric interaction between the methoxy group and the aniline moiety in oligomer 4.

For oligomer 5, the spin is mainly localized on the central ring (C) and the vinyl spacer B, and the maximum ^{1}H hyperfine coupling is found for the hydrogen atom in the CH=N group, which interacts with the sulfoalkyl sidechain. This is reflected in the increased values of both the ^{1}H and ^{14}N hyperfine coupling. As expected, for oligomer 6, the spin shifts almost completely to peripheral benzene ring A and vinyl spacer B, which interact with the sulfoalkyl sidechain. This considerable spin localization is clearly reflected in the large values of the ^{1}H and ^{14}N hyperfine coupling constants.

As expected for oligomer 7, moving the sulfoalkyl sidechain to peripheral ring E leads to a shift of the spin distribution in the conjugated backbone to this ring; the presence or absence of methoxy groups on the central ring (oligomer 9) does not change, and therefore, the ^{1}H hyperfine coupling constants are similar. Introduction of a single nitrogen atom in the conjugated backbone (7 → 8) leads to an increase in the spin delocalization, and again the largest ^{1}H hyperfine coupling is found for the hydrogen atom in the CH=N spacer. Introduction of two nitrogen atoms (7 → 10) leads to a higher spin density in fragments C, D, and E, which results in a higher ^{1}H hyperfine coupling in oligomer 10 than in oligomer 8.

Table 2 Spin population of the different groups in the oligomers as defined in Fig. 6

Oligomer	A	B	C	D	E	S
1	0.22	0.20	0.34	0.11	0.11	0.02
2	0.23	0.20	0.28	0.14	0.13	0.01
3	0.14	0.12	0.45	0.08	0.09	0.13
4	0.18	0.16	0.35	0.12	0.12	0.08
5	0.08	0.18	0.52	0.12	0.03	0.06
6	0.65	0.31	0.03	0.00	0.00	0.01
7	0.09	0.08	0.24	0.21	0.33	0.05
8	0.14	0.14	0.28	0.16	0.23	0.04
9	0.09	0.08	0.18	0.22	0.36	0.06
10	0.05	0.11	0.32	0.20	0.27	0.05

Table 3 Absolute values of the maximum ^{1}H and ^{14}N hyperfine coupling constants (in MHz) of the ten oligomers and the position in the structure

Oligomer	^{1}H Hyperfine coupling	Position	^{14}N Hyperfine coupling	Position
1	11.6	D2		
2	12.2	D2		
3	14.1	Sidechain	6.3	Sidechain
4	13.3	D2	3.6	Sidechain
5	28.2	B1	20.7	B2
6	51.3	B2	39.9	B1
7	12.8	D1		
8	19.9	D2	12.8	D1
9	15.3	D1		
10	25.5	D2	15.7	D1

5 Conclusion

A set of self-doping PPV oligomers has been studied using quantum chemical calculations in order to analyze the effects of different functionalities on the geometry of the self-doped structure, its spin distribution obtained using the FOHI method, and the resulting maximum hyperfine coupling constants. Moving the sidechain from the central ring to the peripheral ring does not significantly change the spin distribution nor the values of the EPR parameters, but it does lead to an increased stability of the self-doped system. Of all the studied structures, oligomer 8 is the best candidate to replace oligomer 1, as it combines a similar spin distribution with an increased ^{1}H hyperfine coupling, an additional ^{14}N hyperfine coupling and a CH=N spacer, which allows the preparation and full purification of an OH-substituted oligomer.

Acknowledgments This work was carried out using the Turing HPC infrastructure at the CalcUA core facility of the University of Antwerp, a division of the Flemish Supercomputer Center VSC, funded by the Hercules Foundation, the Flemish Government (department EWI) and the Universiteit Antwerpen. Financial support by the University of Antwerp under Grant GOA-2404 is gratefully acknowledged. AK is greatful to the Research Foundation—Flanders (FWO) for a postdoctoral position and financial support.

References

1. Tachelet W, Jacobs S, Ndayikengurukiye H, Geise HJ, Grner J (1994) Appl Phys Lett 64:2364–2366
2. Yang JP, Heremans PL, Hoefnagels R, Tachelet W, Dieltiens P, Blockhuys F, Geise HJ, Borghs G (2000) Synth Met 108:95–100
3. Yang JP, Jin YD, Heremans PL, Hoefnagels R, Dieltiens P, Blockhuys F, Geise HJ, Vander Auweraer M, Borghs G (2000) Chem Phys Lett 325:251–256
4. Jin YD, Chen HZ, Heremans PL, Aleksandrzak K, Geise HJ, Borghs G, Vander Auweraer M (2002) Synth Met 127:155–158
5. Chen HZ, Jin YD, Xu RS, Peng BX, Desseyn H, Janssens J, Heremans P, Borghs G, Geise HJ (2003) Synth Met 139:529–534
6. Ding XB, Zheng JG, Jin YD, Heremans PL, Geise HJ, Borghs G (2003) Synth Met 137:1003–1004
7. Ding XB, Zheng JG, Jin YD, Aerts G, Peng BX, Heremans PL, Borghs G, Geise HJ (2004) Synth Met 142:267–273
8. Staes E, Nagels LJ, Verreyt G, Jacobs S, Bao Y, Geise HJ (1997) Electroanalysis 9:1197–1200
9. Poels I, Nagels LJ, Verreyt G, Geise HJ (1998) Anal Chim Acta 370:105–113
10. Szymaska I, Ocicka K, Radecka H, Radecki J, Geise HJ, Dieltiens P, Aleksandrzak K (2001) Mat Sci Eng C 18:171–176
11. Zimkus A, Cretscu I, Grzybowska I, Radecka H, Geise HJ, Dieltiens P, Aleksandrzak K (2003) Pol J Environ Stud 12:773–778
12. Collas A, De Borger R, Amanova T, Vande Velde CML, Baeke JK, Dommisse R, Van Alsenoy C, Blockhuys F (2011) New J Chem 35:649–662
13. Baeke JK, De Borger R, Lemire F, Van Alsenoy C, Blockhuys F (2009) J Phys Org Chem 22:925–932
14. Collas A, De Borger R, Amanova T, Blockhuys F (2011) CrystEngComm 13:702–710
15. Collas A, Zeller M, Blockhuys F (2011) Acta Cryst C 67:o171–o174
16. Ling Y, Kozakiewicz P, Blockhuys F, Biesemans M, Van Alsenoy C, Moons H, Goovaerts E, Willem R, Van Doorslaer S (2011) Phys Chem Chem Phys 13:18516–18522
17. Hirshfeld FL (1977) Theoret Chem Acta 44:129–138
18. Bultinck P, Van Alsenoy C, Ayers PW, Carbo-Dorca R (2007) J Chem Phys 126:144111
19. Bultinck P, Ayers PW, Fias S, Tiels K, Van Alsenoy C (2007) Chem Phys Lett 444:205
20. Geldof D, Krishtal A, Blockhuys F, Van Alsenoy C (2011) J Chem Theory Comput 7:1328–1335
21. Becke AD (1993) J Chem Phys 98:5648–5652
22. Lee C, Yang W, Parr RG (1988) Phys Rev B 37:785–789
23. Vosko SH, Wilk L, Nusair M (1980) Can J Phys 58:1200–1211
24. Stephens PJ, Devlin FJ, Chabalowski CF, Frisch MJ (1994) J Phys Chem 98:11623–11627
25. Krishnan R, Binkley JS, Seeger R, Pople JA (1980) J Chem Phys 72:650–654
26. Gaussian 09, Revision A.02, Frisch MJ, Trucks GW, Schlegel HB, Scuseria GE, Robb MA, Cheeseman JR, Scalmani G, Barone V, Mennucci B, Petersson GA et al (2009) Gaussian, Inc., Wallingford CT
27. Neese F (2008) ORCA an ab initio, density functional and semiempirical program package, Version 2.6. University of Bonn, Bonn
28. Barone V (1996) Recent advances in density functional methods. World Scientific Publ. Co., Singapore
29. Schaefer A, Horn H, Ahlrichs RJ (1992) Chem Phys 97:2571–2577
30. The Ahlrichs (2df,2pd) polarization functions were obtained from the TurboMole basis set library under ftp.chemie.uni-karlsruhe.de/pub/basen, R. Ahlrichs and co-workers (unpublished)
31. Van Alsenoy C, Peeters A (1993) J Mol Struct (Theochem) 286:19
32. Rousseau B, Peeters A, Van Alsenoy C (2000) Chem Phys Lett 324:189

Theor Chem Acc (2012) 131:1244
DOI 10.1007/s00214-012-1244-5

REGULAR ARTICLE

Electron momentum spectroscopy of metal carbonyls: a reinvestigation of the role of nuclear dynamics

Balázs Hajgató · Filippo Morini · Michael S. Deleuze

Received: 14 February 2012 / Accepted: 5 June 2012 / Published online: 22 June 2012

Abstract The main purpose of this work is to reinvestigate the influence of nuclear dynamics in the electronic ground state of group 6 metal hexacarbonyl compounds [$W(CO)_6$, $Cr(CO)_6$, $Mo(CO)_6$] on electron momentum density profiles obtained from experimental orbital reconstructions employing Electron Momentum Spectroscopy. We call into question the view (Liu et al. in Chem Phys Lett 497:229, 2010) that thermally induced nuclear displacements associated with the first three triply degenerate $1T_{2g}$, $1T_{1u}$, and $1T_{2u}$ vibrational eigenmodes can be large enough at or near room temperature (298–310 K) to explain on their own the unexpectedly large electron densities inferred for the frontier orbitals of these compounds at low momenta. In this purpose, we resort to an analysis of populations over these three vibrational eigenmodes, according to a description of vibrational excitations employing Maxwell–Boltzmann statistical thermodynamics. Comparison is made with Born–Oppenheimer Molecular Dynamical (BOMD) simulations over the potential energy surface associated with the electronic ground state. The role of nuclear dynamics in the final ionized state, in the form of Jahn–Teller distortions, is also tentatively investigated.

Keywords Electronic structure theory · Electron Momentum Spectroscopy · Orbital imaging experiments · Electron impact (e, 2e) ionization · Distorted wave effects · Molecular dynamics · Statistical thermodynamics

1 Introduction

Electron Momentum Spectroscopy [1–4] is a powerful orbital imaging technique, which enables straightforward reconstructions of electron momentum distributions associated with specific ionization channels (i.e., of orbital momentum profiles in a one-electron picture of ionization), according to an angular analysis of intensities in electron impact (e, 2e) ionization experiments [$M + e^- \ (E_0 + \varepsilon_b) \rightarrow M^+ + 2e^- \ (E_0/2)$] at high kinetic energies ($E_0 =$ 1.2 keV or more). The analysis of EMS experiments represents one of the main research topics of the theoretical chemistry research group at Hasselt University (Belgium) since 2000 (see e.g. Ref. [5]). Numerous approximations are required in this purpose. The first of these is the *Born–Oppenheimer (BO) approximation*, in which the coordinate-space representations of the initial and final states are products of separate electronic, vibrational and rotational functions. The corresponding (e, 2e) cross-sections are thereby obtained as transition amplitudes in between these states over the electron scattering potential [6, 7], which involves all electrons and nuclei in the molecular target. Upon invoking the *binary encounter approximation*, it is then

---

Published as part of the special collection of articles celebrating theoretical and computational chemistry in Belgium.

B. Hajgató · F. Morini · M. S. Deleuze (✉)
Research Group of Theoretical Chemistry and Molecular Modeling, Hasselt University, Agoralaan Gebouw D,
3590 Diepenbeek, Belgium
e-mail: michael.deleuze@uhasselt.be

B. Hajgató
e-mail: hajgato@vub.ac.be

B. Hajgató
General Chemistry Division, QCMM Research Group,
Alliance Ghent-Brussels, Free University of Brussels,
Pleinlaan 2, 1050 Brussels, Belgium

Present Address:
B. Hajgató
Algemene Chemie, Vrije Universiteit Brussel,
Pleinlaan 2, 1050 Brussels, Belgium

assumed that the momentum lost by the incident electron is entirely transferred to the ejected ones. Under these conditions, the transition operator depends solely upon the coordinates of the impinging electron and of the two ejected electrons. This approximation is designed for the kinematic situation on the Bethe ridge [1–4] where the momentum of the ionized electron is equal in magnitude to the momentum transferred from the incident to the scattered electron, ensuring thereby a clean "knock-out" process, a condition which is best satisfied experimentally by a symmetric non-coplanar set-up. In the framework of the *first Born* (or sudden) *approximation*, the incident electron is assumed to interact with the target *only once*. When the incident electron only interacts with the ejected electrons and neither affects the target nor is affected by the target, the *impulse approximation* is considered, and a simple relationships prevails between the azimuthal angle under which the electrons are collected and the momentum of the ejected electron *prior* to ionization. Modeling the incident and outgoing electrons as plane waves yields ultimately the *Plane Wave Impulse Approximation* (PWIA) [1–4], which implies that the energies of the unbound electrons are so high that their interactions with the residual ion are negligible. Upon the assumption that all these approximations are valid (e, 2e), ionization cross-sections for specific ionization channels in EMS conditions ultimately relate to spherically averaged and resolution folded structure factors that are obtained as the square of the Fourier Transform toward momentum space of the relevant *Dyson orbitals*, defined [8–11] as partial overlaps between the neutral initial ground state and final ionized state. A further and most useful approximation is the *target Kohn–Sham approximation* [12], which consists in substituting Dyson orbitals by the relevant Kohn–Sham orbitals, along with *ad hoc* or calculated spectroscopic pole strengths, in order to account for the flux of ionization intensity toward shake-up [13] and valence correlation bands [14] at higher electron binding energies. In many cases, (rescaled) Kohn–Sham orbitals are empirically known to be excellent approximations to Dyson orbitals [15, 16]. In practice, however, the interpretation of EMS experiments is subject to numerous complications such as: overlap effects in overcrowed ionization bands [17, 18], conformational mobility [19–21] and (thermally induced) nuclear dynamics in the electronic initial (neutral) ground state [22], shake-up processes due to electronic configuration interactions in the final ionized state [23–26], distorted wave and post-collision (e.g., rescattering) effects [27–33], and possibly ultra-fast nuclear dynamics in the final ionized state, in the form of bond breaking [22] or Coulomb explosion processes [34–36], as well as Jahn–Teller distortions [37] in the final ionized state.

Transition metal hexacarbonyls such as $W(CO)_6$, $Mo(CO)_6$, and $Cr(CO)_6$ are important precursors in organometallic chemistry [38–41]. Because of their high volatility and octahedral symmetry, they are also most useful molecular models for studies of bond formation between carbonyl groups and metal surfaces. Investigations of the outermost valence orbitals of these compounds comprise the ultra-violet [He I, He II] and X-ray photoelectron experiments by Higginson et al. [42] and various studies [43–45] employing Electron Momentum Spectroscopy (EMS). In the EMS studies of $Cr(CO)_6$, $Mo(CO)_6$, and $W(CO)_6$ by Chornay et al. [43], and by Rolke et al. [44], the measured (e, 2e) ionization cross-sections for the HOMO were found to be much larger than expected in the low momentum region, according to standard theoretical models of (e, 2e) ionization processes in the high energy limit, and to be largely inconsistent with the nodal characteristics of an uncorrelated (Hartree–Fock) $2t_{2g}$ orbital at $p = 0$. Within the framework of the Plane Wave Impulse Approximation [1–3], and from symmetry considerations, the spherically averaged momentum density of the HOMO of these three compounds is indeed expected to identically vanish at zero electron momentum, outside of a marginal contribution arising from finite angular resolution effects, that is, from experimental limitations in momentum resolution. On the contrary, particularly large "turn-ups" of the frontier electron densities were experimentally observed in the low momentum region [43, 44]. Accounting for electronic correlation in the ground state by means of the target Kohn–Sham approximation did not improve significantly the agreement between theory and experiment. This was expected, since the same symmetry constraints apply in Hartree–Fock and Density Functional Theories. By analogy with EMS experiments on atomic targets and calculations employing the Distorted Wave Impulse Approximation (DWIA [1–3]) of the Xe 4d, Cr 3d, Ti 3d and Mo 4d (e, 2e) ionization cross-sections [46], it was tentatively concluded [43, 44] that these discrepancies between theory and experiment are due to a breakdown of the plane wave impulse approximation and distorted wave effects in the continuum, which are known indeed nowadays [47] to be particularly significant when the ionized molecular orbital has a d-type topology (i.e., two perpendicular nodal planes).

However, the more recent EMS experiments by K. Liu et al. [45] on $W(CO)_6$ at electron impact energies of 1.2 and 2.4 keV gave at first glance quite similar momentum profiles for the HOMO and led thus on the contrary to the conclusion that distorted wave and post-collision effects are too weak to explain the experimentally observed turn-ups at low electron momenta. Since the target compounds contain relatively heavy metal atoms, this discrepancy between theory and experiment was then also thought to be the outcome of the limitations inherent to a non-relativistic depiction. Further investigations of scalar relativistic and spin–orbit coupling effects indicated, however, a very marginal influence of these effects upon the computed momentum distributions [45]. In their ultimate attempt to reconcile theory with experiment, Liu et al. [45] invoked large-amplitude structural distortions in the form of wagging or bending motions associated with the three lowest and triply degenerate vibrational frequencies and the corresponding $1T_{2u}$, $1T_{1u}$, and $1T_{2g}$ eigenmodes (Fig. 1), regardless of anharmonic effects and of excessive energy demands resulting from exacerbated electrostatic repulsions between strongly polarized C=O substituents. In their study, it was simply assumed that thermally induced nuclear dynamics in the electronic ground state can be conveniently described by displacing nuclei away from their equilibrium position, according to so-called normalized vibrational eigenvectors (i.e., to eigenvectors the norm of which amounts to 1 Å^2, according to the ADF output for atomic displacements), and averaging thereby the obtained momentum distributions for the first three $1T_{2u}$, $1T_{1u}$, and $1T_{2g}$ eigenmodes. The main argument by Liu et al. [45] in support to their approach was that the population of the vibrational ground state accounts for less than 10 % of the total vibrational populations of the three lowest eigenmodes, at an estimated experimental temperature of 310 K, according to (Maxwell-) Boltzmann statistics. With this simple depiction of nuclear dynamics in the electronic ground state, Liu et al. [45] managed to obtain a much better match between theory and experiment and claimed therefore the case of the frontier orbital momentum distributions of $W(CO)_6$ to be understandable in terms of low-frequency vibrations. However, the extreme crudeness of their approach makes us believe that it is certainly worth reconsidering in details whether their analysis can resist more thorough analyses of thermally induced vibrational motions in the electronic ground state, and re-evaluate whether the observed discrepancies between the theoretical and experimental orbital momentum densities of group 6 metal hexacarbonyls are not at the end of the day the outcome of still unaccounted physical complications, such as ultra-fast nuclear dynamics in the final ionized state, or distorted wave and post-collision effects in the continuum.

At this stage, we wish to emphasize that so far an exact treatment of distorted wave effects for polyatomic systems remains intractable as it requires a multi-centre expansion of the continuum states in terms of Coulomb waves [48, 49]. Rigorous enough theoretical studies of distorted wave effects are nowadays only tractable for atomic targets [50], diatomic molecules (e.g., H_2 [30]), and small molecules such as H_2O [51]), the electron densities of which approach spherical symmetry, which enables slowly converging but highly accurate expansions of their molecular orbitals in a basis of *s*, *p*, *d*, *f*, *g* … atomic orbitals with varying exponents but with all the same location on the central "heavy" (O) atom. Note that highly qualitative theoretical studies of triple differential cross-sections for electron impact ionization experiments upon larger polyatomic systems (formic acid, methane, tetrahydrofurane, pyrimidine, …) using a three-body distorted wave model have also been reported recently (see [52] and references therein). A most serious drawback of these latter studies is that orientational averages of molecular orbitals (OAMOs) are used to represent the target bound state wave function, which means that the information associated with the nodal structure of the orbitals is almost entirely lost in the modeling of the distorted wave effects. In particular, OAMOs identically vanish at every point in space, except if the target bound state has the full symmetry of the molecular symmetry point group. Clearly, distorted wave effects from large polyatomic systems are still awaiting a satisfactory enough theoretical treatment.

The first purpose of the present work is thus to evaluate whether the structural distortions which were proposed by Liu et al. [45] are compatible with thermal fluctuations at or near standard room temperature, that is, at 298 and 310 K, according to Maxwell–Boltzmann (MB) statistics [53, 54] on vibrational energy levels. The analysis is supplemented by Born–Oppenheimer Molecular Dynamical (BOMD) simulations [55–57] at the same temperatures of momentum profiles inferred from *vertical* (e, 2e) ionization cross-sections. A main advantage of this approach is that, by virtue of ergodicity [58], it enables a complete exploration of phase space which is equivalent to an ensemble

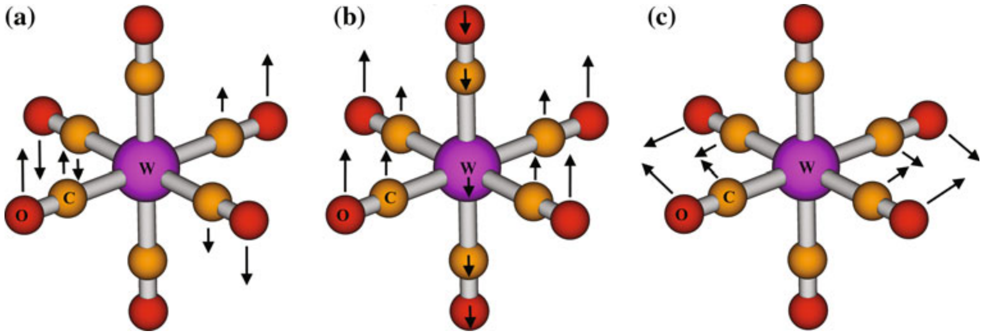

Fig. 1 The three lowest vibrational eigenmodes of $W(CO)_6$ (B3LYP/aug-cc-pVTZ-PP level): **a** 59.5 cm^{-1}, **b** 81.7 cm^{-1}, and **c** 84.3 cm^{-1}

average over all internal degrees of freedom of the system of interest, such as is computed in Monte Carlo simulations. Born–Oppenheimer Molecular Dynamics is therefore the most convenient approach for a realistic description of the intrinsically chaotic nature of nuclear motions in a large polyatomic system, taking into account non-harmonic effects (anharmonicities in the vibrational potentials, couplings between vibrations and rotations, couplings between internal and external rotations due to Coriolis forces, …) in the classical approximation. The interested reader is referred in particular to studies of non-harmonic effects in infra-red vibrational spectra, obtained by Fourier transforming to the energy domain dipole time-dependent autocorrelation functions inferred from BOMD simulations [59–62].

To our knowledge [63], there is no way to precisely control the temperature with the current experimental (e, 2e) setup which Liu et al. [45] used at Tsinghua University (Beijing, China) for their experiments on W(CO)$_6$, a set-up which employs effusive molecular beams. In contrast with experiments based on free expansions in supersonic jets, it is usually assumed that the relatively high pressure in the collision cell ensures a full randomization of molecular motions, and thermal equilibrium therefore with the environment (298 K). Therefore, we wish to consider both the estimated experimental and standard room temperatures in our BOMD analysis. At last, the role played by nuclear dynamics in the final ionized state is also tentatively investigated. In this purpose, we revise before all (theory section) how electron momentum distributions may vary in response to a change in the molecular geometry induced by ionization.

2 Theory

Within the framework of the Born–Oppenheimer, binary encounter, plane wave impulse and target Kohn–Sham [KS] (or target Hartree–Fock [HF]) approximations, and disregarding rotational wave functions, differential (e, 2e) ionization cross-sections are proportional to the square of a structure factor $F_n(\vec{p})$, which is given by [1–3, 64]:

$$F_n(\vec{p}) = \int dQ\ X^*_{\upsilon'}(Q)\ X_\upsilon(Q)\ S_n(Q)\ \varphi_i(\vec{p}, Q). \qquad (1)$$

In the above equation, Q is the set of internal coordinates determining the displacements from equilibrium of atomic nuclei in the molecule, $X_\upsilon(Q)$ and $X_{\upsilon'}(Q)$ are the vibrational wave functions corresponding to the initial (neutral) ground state $[\Psi_0^N(Q)]$ and final ionized state $[\Psi_n^{N-1}(Q)]$ of the molecule, $\varphi_i(\vec{p}, Q)$ is the Fourier transform to momentum space of the target KS or HF orbital $[\varphi_i(\vec{r}, Q)]$ in the initial (neutral) ground state, and $S_n(Q)$ is the overlap integral of the electronic wave functions for the final ionized state and the electronic residue left after annihilating an electron from the target orbital $\varphi_i(\vec{r}, Q)$:

$$S_n(Q) = \left\langle \Psi_n^{N-1} \right| a_i \left| \Psi_0^N \right\rangle, \qquad (2)$$

with a_i the relevant annihilation operator, and where N represents the number of electrons in the target molecule. Upon carrying integrations over vibrational coordinates, Eq. (1) can be further reduced to [1, 3, 64]:

$$F_n(\vec{p}) = g_\upsilon^{\upsilon'}\ S_n(\bar{Q})\ \varphi_i(\vec{p}, \bar{Q}), \qquad (3)$$

where $g_\upsilon^{\upsilon'} = \int dQ\ X^*_{\upsilon'}(Q)\ X_\upsilon(Q)$ is the usual Franck–Condon factor, and $\bar{Q}$ represent *some mean values of nuclear coordinates that are intermediate* between the equilibrium coordinates of nuclei Q_0 and Q'_0 in the initial neutral ground state and final ionized state, respectively. Vibrational states are most commonly unresolved in Electron Momentum Spectroscopy, which enables us to derive the relevant (e, 2e) ionization cross-sections from the spherical average:

$$\sigma^{\mathrm{EMS}} \propto \left|S_n(\bar{Q})\right|^2 \int \mathrm{d}\Omega_{\vec{p}}\ \left|\varphi_i(\vec{p}, \bar{Q})\right|^2, \qquad (4)$$

with $d\Omega_{\vec{p}}$ an infinitesimal element of solid angle associated with the target electron momentum, and where $\left|S_n(\bar{Q})\right|^2$ represents the spectroscopic strength of the electronic transition $[\Psi_0^N(\bar{Q}) + 1e^- \rightarrow \Psi_n^{N-1}(\bar{Q}) + 2e^-]$ of interest.

At high enough impact electron energies, it is most customary to assume a *vertical* ionization process, in which case $\bar{Q} = Q_0$. Due to the long-range character of the Coulomb force and wave packet nature of the impinging electron, deviations from a vertical transition can*not* be systematically ruled out in (e, 2e) ionization experiments. At another extreme, when nuclear dynamics is expected to compete with (i.e., to be faster than) the (e, 2e) ionization process, one may thus empirically resort to an *adiabatic* depiction, in which case $\bar{Q} = Q'_0$. Such rare situations may typically occur with Jahn–Teller distortions associated with conical intersections, which are known to generally yield a non-radiative decay of the upper electronic state within the femtosecond regime [65, 66], that is, within a time scale which is comparable to the effective time scale inferred recently in studies of bond dissociation processes [67] induced by (e, 2e) ionization processes at electron impact energies around 1.2 keV.

3 Methodology

The geometry optimizations as well as the vibrational and dynamical analyses which are reported in the sequel have been performed using Density Functional Theory (DFT)

[68] in conjunction with the standard hybrid Becke-3-parameters-Lee–Yang–Parr [B3LYP] functional [69, 70], or the dispersion-corrected ωB97XD exchange–correlation functional [71]. Our main motivation for using a dispersion-corrected functional is to enable a proper treatment of non-bonded interactions between carbonyls. In all our calculations upon group 6 [W, Mo, Cr] hexacarbonyls, use was made of the aug-cc-pVDZ and aug-cc-pVTZ basis sets [72, 73] for the carbon and oxygen atoms. Chromium was also described using the all-electron aug-cc-pVDZ and aug-cc-pVTZ basis sets. Relativistic effects arising from the chemically inert cores of Mo and W were accounted for through the interplay of accurately designed pseudo-potentials (PPs). Specifically, the Mo atom was described by the ECP28MDF energy-consistent effective pseudopotential, which was constructed from a multi-state fit of a fully relativistic Dirac–Fock calculation for the isolated atom [74], together with the correspondingly adjusted correlation consistent aug-cc-pVDZ-PP and aug-cc-pVTZ-PP basis sets. The energy-consistent effective core potential ECP60MDF [75] has been adopted for the tungsten atom in conjunction with its accompanying correlation consistent aug-cc-pVDZ-PP and aug-cc-pVTZ-PP basis sets. Although this goes much beyond our present purpose, it is worth noting that errors arising from the use of these pseudo-potentials are effectively extremely small and comparable to the accuracies that can be achieved nowadays with modern all-electron ab initio calculations. Comparison to large basis set, all electron, relativistic calculations indicate errors of $\sim$0.002 Å only in equilibrium bond lengths and less than 0.5 kcal/mol in dissociation energies, due to the pseudo-potential approximation [76]. Along with standard gradient-corrected hybrid functionals (e.g., B3LYP), effective relativistic small-core pseudo-potentials are known also to enable insight into vibrational frequencies within a few cm^{-1} accuracy [77]. For our purpose, the main advantage of these pseudo-potentials is mainly to enable the computation of analytic energy gradients and, thus, of molecular dynamical trajectories on accurate enough potential energy surfaces, which are still to date beyond reach in a fully relativistic treatment. All DFT calculations presented in this work were performed by means of the Gaussian09 package of programs [78].

In this work, we simulate the outcome of EMS experiments upon W(CO)$_6$ using a standard (e, 2e) non-coplanar symmetric kinematical setup at an electron impact energy of 2.4 keV above the vertical ionization energy threshold (VIE $\sim$ 8.6 eV). According to the characteristics of the (e, 2e) spectrometer [79] which was employed by Liu et al. at Tsinghua University (Beijing) [45], the relevant parameters for the momenta of the impinging and outgoing electrons amount therefore to $p_0 = 0.271105(2400 + \text{VIE})^{1/2}$ au (1 au = 1 a_0^{-1}, with a_0 as the Bohr radius, that is, 0.5292 Å) and $p_1 = p_2 = 9.39135$ au, respectively ($E_1 = E_2 =$ 1,200 eV). The binary (e, 2e) encounter, plane wave impulse, and target Kohn–Sham approximations are invoked in conjunction with calculations employing DFT and the B3LYP or ωB97XD functionals. Deviations from basis set completeness (BSC) are checked by comparing results employing the aug-cc-pVDZ-PP and aug-cc-pVTZ-PP basis sets. It is worth reminding that Kohn–Sham orbitals and their energies are known to represent valuable approximations to the corresponding Dyson orbitals and (electronically relaxed) ionization energies produced in CI (Configuration Interaction) calculations [80, 81], and that, by virtue of Janak's theorem [82] or the extended Koopmans' theorem [83], the approximation becomes exact when considering specifically the HOMO and an (hypothetical) exact exchange–correlation functional.

Spherically averaged orbital momentum distributions have been generated from the obtained Kohn–Sham orbitals using the MOMAP program by Brion and coworkers [84] and homemade interfaces. In line with the study by Liu et al. [45], and employed (e, 2e) spectrometer therein, resolution folding of the computed momentum distributions was made using a Monte Carlo simulation procedure [85, 86], considering angular resolutions of 0.53° and 0.84° on azimuthal and polar angles, respectively. For the sake of consistency with the EMS experiments by Rolke et al. [44], the following parameters have been retained for the simulation of the outermost (e, 2e) momentum profiles of Mo(CO)$_6$ and Cr(CO)$_6$: $E_0 = 1{,}200$ eV, $\Delta\theta = 0.60°$, and $\Delta\phi = 1.20°$.

In all BOMD simulations, the Bulirsch-Stoer method was used for the integration scheme [87, 88], along with an integration step size of 0.2 fs, and using a fifth-order polynomial fit in the integration correction scheme. The trajectory step size was set to 0.250 a.u, and atomic coordinates were dumped at time intervals of approximately 1 fs. Thermalization to standard room temperature (298 K) was ensured by setting the initial rotational energy from a thermal distribution assuming a symmetric top. The time average was made on momentum densities computed at each point of the calculated BOMD trajectory in the MD run. Runtimes comprised between 1.5 and 1.7 ps, corresponding to time averages over 1,500–1,700 thermally distorted structures.

In line with equation 4, the influence of nuclear dynamics in the final ionized state has been tentatively and phenomenologically investigated upon the assumption of an adiabatic ionization process, by computing (resolution folded and spherically averaged) frontier electron momentum profiles for the target orbitals in the initial neutral ground state upon nuclei configurations corresponding to all possible equilibrium geometries of the final cationic state ($\bar{Q} = Q_0'$). The approach we consider in this purpose is therefore the same as that used recently by Chen XJ and his co-workers [37] for unraveling the outcome of Jahn–Teller distortions in EMS experiments upon cyclopropane, which were found to leave clearly identifiable fingerprints in the frontier (e, 2e) ionization bands and the correspondingly inferred electron momentum distributions. It is worth noting that, by virtue of the equations presented in section II, such an approach will clearly provide *upper estimates* to the changes in momentum profiles due to vibronic coupling interactions induced by the (e, 2e) ionization processes. Molecular structures and orbital contours were drawn using the MOLDEN program [89].

4 Results and discussion

Prior to any further discussion, it is worth considering the integrated (e, 2e) ionization spectrum of $W(CO)_6$ recorded by Liu et al. [45] (Fig. 2). Upon examining this spectrum, it is clear that the momentum distribution characterizing the HOMO ($2t_{2g}$) is free of any unwanted complications related to band overlaps [18] and that individual Jahn–Teller components remain unresolved. Also (Fig. 3), this momentum distribution is almost insensitive to the employed functional. Compared with the aug-cc-pVDZ(-PP) basis set, the aug-cc-pVTZ(-PP) basis set appears to be large enough to ensure the required saturation of results toward the BSC limit. Our momentum profiles are also almost identical to results obtained by Liu et al. [45], according to B3LYP relativistic calculations coping with scalar relativistic and spin–orbit coupling interactions at the level of the zero-order regular approximation (ZORA [90]) using a specifically designed triple-zeta doubly polarized basis set.

All B3LYP calculations (including frequency calculations) by Liu et al. [45] were performed upon the MP2 geometry which was optimized by Ehlers and Frenking [91], using an effective core potential [92] and the (441/2111/2) valence basis set derived from the minimal Hay–Wadt (55/5/3) basis set [93] on the tungsten atom and the 6-31G* basis set [94] on carbon and oxygen atoms. This methodological inconsistency resulted into a rather significant underestimation of the W–C and C–O bond lengths by 0.0125 Å and 0.025 Å, respectively, compared with the methodologically correct B3LYP values. Since the B3LYP vibrational calculations by Liu et al. [45] were performed away from the global energy minimum, they resulted (Table 1) in much too large values (by ~40 % or more) for the frequencies characterizing the three lowest and triply degenerate vibrational eigenmodes ($1T_{2u}$, $1T_{1u}$, $1T_{2g}$), compared with experiment—an overestimation which has in turn most clearly led to further severe errors in the computations of vibrational populations. A further consequence of using a non-stationary point on the potential energy surface is that nuclear displacements characterizing normalized vibrational eigenmodes have also been certainly overestimated. In contrast, our theoretical estimates for vibrational frequencies, in particular, the B3LYP ones, are in remarkable agreement with the available experimental values [95, 96], as well as with the results of quasi-relativistic (QR) DFT calculations [97] employing GGA functionals. Deviations between our results, the QR-GGA results by Bérces and experiment for the three modes of interest does not exceed 6 cm^{-1}.

Although vibrations of the order of 60–80 cm^{-1} are not uncommon at all in organic and inorganic compounds, Liu et al. [45] considered these to be indicative of a very shallow energy minimum on the potential energy surface,

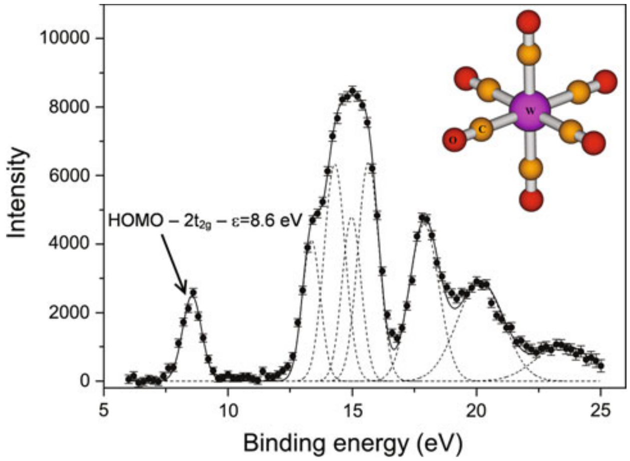

Fig. 2 Experimental electron momentum spectrum [45] of $W(CO)_6$ summed over all angles ($E_0 = 1{,}200$ eV, $\Delta\theta = 0.53°$, $\Delta\phi = 0.84°$)

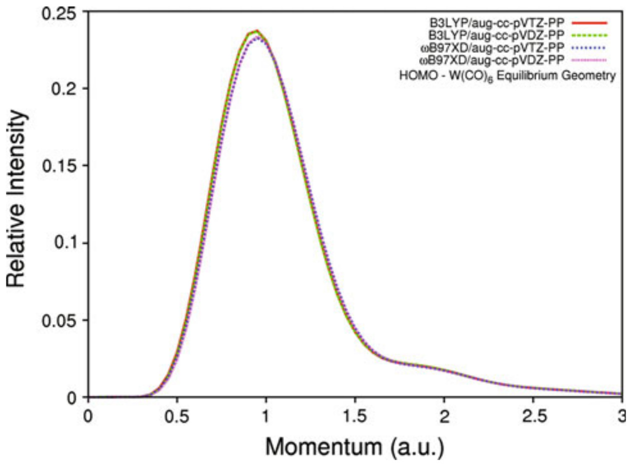

Fig. 3 Spherically averaged theoretical momentum profiles (without resolution folding) of the HOMO of $W(CO)_6$

Table 1 Lowest vibrational frequencies (in cm^{-1}) of W(CO)$_6$

Mode	Liu et al.[a]	B3LYP/aug-cc-pVTZ-PP	ωB97XD/aug-cc-pVTZ-PP	GGA + QR[b]	Experimental[c]
t_{2u}	100.3	59.5	55.8	63.6	61 ± 15[d]
t_{1u}	133.5	81.7	79.3	80.8	82.0 ± 3[e]
t_{2g}	120.8	84.3	81.6	85.9	88.3 ± 6[f]

[a] From Ref. [45]

[b] From Ref. [97]

[c] From Refs. [95] and [96]

[d] Raman, solid phase, from overtone combination

[e] IR, gas phase

[f] Raman, liquid phase

that would therefore permit extremely large atomic displacements, away from the minimum, due to thermal fluctuations and vibrational excitations in the electronic ground state, and would provide a convenient way to describe nuclear dynamics in the electronic neutral ground state. In support to these assertions, Liu et al. calculated relative populations for the ground ($n = 0$) and vibrationally ($n > 0$) excited states, on the ground of (Maxwell-)Boltzmann statistics [98–100]:

$$p_n(i) = \frac{g_n(i)}{\exp(\varepsilon_n/kT)} = \frac{g_n(i)}{\exp([n + 1/2]h\nu_i/kT)}, \tag{5}$$

with n the relevant vibrational quantum number ($n = 0, 1, 2, 3 \ldots$), and $g_n(i)$ the multiplicity factor proposed by Herzberg [101] for triply degenerate vibrations:

$$g_n(i) = \frac{1}{2}(n + 1)(n + 2). \tag{6}$$

Since the vibrational eigenmodes (i) of interest exhibit frequencies in the 60–100 cm^{-1} range, and characteristic temperatures ($\theta_i = h\nu_i/k$) of the order of 86 to 144 K only, the Boltzmann approximation can be regarded as valid at and above room temperature ($T = 298$ K). With this approximation, inversions of relative populations are observed at around $n = 6$, 4 and 3 for the $1T_{2u}$, $1T_{1u}$, and $1T_{2g}$ vibrational modes (Table 2), respectively.

The analysis by Liu et al. [45] simply accounts for thermal distortions of the molecular structure in the electronic ground state by arbitrarily displacing atoms according to so-called *normalized* vibrational displacements for the first three eigenmodes, and averaging the ultimately obtained momentum distributions. We remind that these normalized displacements are nothing else than vibrational eigenmodes taken from the ADF output, the norms of which are equal to 1 Å^2. This approach obviously neglects anharmonic effects and the excessive energy penalties resulting from the imposed structural distortions, because of electrostatic repulsions between strongly polarized CO substituents, due to bond donation to the group 6 metal (the same considerations on charge transfers also prevail for Mo(CO)$_6$ and Cr(CO)$_6$—see natural atomic charges in Table 3). To quantitatively investigate these penalties, we refer the reader to Table 4, in which each listed configuration ($\alpha = 0.0, 0.1, 0.2, 0.3 \ldots 1.0$) is the one obtained by adding to the nuclear coordinates characterizing the O_h energy minimum form nuclear displacements taken to be equal to α times the relevant and so-called "normalized" eigenmode (see above definition, following the conventions used by Liu et al. [45]). Calculations at the B3LYP/aug-cc-pVTZ-PP level (Table 5) of the corresponding anharmonic energy demands and required thermal fluctuations are conclusive enough for refuting the view that normalized vibrational eigenmodes enable a consistent description of thermally induced vibrational motions in the electronic ground state. Indeed, upon considering the obtained energy values, it is clear that thermal fluctuations at or near room temperature are consistent with α factors ranging from $\sim$0.3 to $\sim$0.5, whereas in normal conditions, a full "normalized" displacement ($\alpha = 1$) is thermodynamically unreachable (since the corresponding energy demands would imply thermal fluctuations ranging

Table 2 Relative population occupations [$p_n(i)$] of the three lowest vibrational levels of W(CO)$_6$ at 298.15 K arising from the first three eigenmodes (harmonic approximation, Boltzmann statistics, B3LYP/aug-cc-pVTZ(-PP) results)

Vib. level (n)	t_{2u}	t_{1u}	t_{2g}
0	1.0000	1.0000	1.0000
1	2.2511	2.0222	1.9973
2	3.3783	2.7262	2.6594
3	4.2250	3.0627	2.9508
4	4.7554	3.0966	2.9467
5	4.9957	2.9223	2.7465
6	4.9981	2.6264	2.4380
7	4.8220	2.2762	2.0868
8	4.5228	1.9178	1.7366
9	4.1480	1.5800	1.4131

Table 3 Natural atomic charges

W(CO)$_6$[a]		Mo(CO)$_6$[b]		Cr(CO)$_6$[c]	
Atom	Charge	Atom	Charge	Atom	Charge
W	−2.26677	Mo	−2.12850	Cr	−2.55633
C	0.80226	C	0.79384	C	0.87483
C	0.80226	C	0.79384	C	0.87483
C	0.80226	C	0.79384	C	0.87483
C	0.80226	C	0.79384	C	0.87483
C	0.80226	C	0.79384	C	0.87483
C	0.80226	C	0.79384	C	0.87483
O	−0.42446	O	−0.43909	O	−0.44877
O	−0.42446	O	−0.43909	O	−0.44877
O	−0.42446	O	−0.43909	O	−0.44877
O	−0.42446	O	−0.43909	O	−0.44877
O	−0.42446	O	−0.43909	O	−0.44877
O	−0.42446	O	−0.43909	O	−0.44877

[a] B3LYP/aug-cc-pVTZ(-PP)

[b] B3LYP/aug-cc-pVDZ(-PP)

[c] B3LYP/aug-cc-pVDZ

from 2,500 to 8,000 K). For the 1T$_{2u}$ mode, a temperature of about 450 K is required (Table 5) for increasing the population of the relevant vibrational levels ($n = 31$, 32) relative to the vibrational ground state above a significant enough threshold (100 %). At this temperature, the relative population of the relevant vibrational levels ($n = 70$, 71) or ($n = 37$, 38) for the 1T$_{1u}$ and 1T$_{2g}$ modes are still below 0.005 and 0.5 %, respectively (Table 5). Clearly, at or near room temperature, it makes no sense to simply consider nuclear displacements amounting to a "normalized" vibrational eigenmode for unraveling the outcome in EMS experiments of low-frequency vibrational motions in tungsten hexacarbonyl, especially for the 1T$_{1u}$ and 1T$_{2g}$ modes, because of the high energy demand required by excitations to vibrational quanta that correspond to exceedingly large displacements.

Different theoretical models of nuclear dynamics in the initial state are tested in Figs. 4 and 5 and compared (Fig. 5) against the experimental electron momentum distributions inferred by Liu et al. [45] for the HOMO (2t$_{2g}$ orbital) of tungsten hexacarbonyl. In line with the latter work, molecular vibrations in the ground state are first accounted for by averaging the outcome of normalized ($\alpha = 1$) and rescaled ($\alpha = 0.4$) nuclear displacements. As was noted by Liu et al. [45], whereas vanishing (e, 2e) ionization intensities are expected for the HOMO at $p \rightarrow 0$ for the ground state octahedral energy minimum form of tungsten hexacarbonyls, enforcing normalized nuclear displacements results into a significant enhancement [i.e., a turn-up (using the technical jargon in use for 2–3 decades already in the EMS community)] of frontier momentum densities in the low momentum region. Note nonetheless that in our case, the predicted increase of (e, 2e) ionization intensities at $p \rightarrow 0$ when $\alpha = 1$ is still far from enabling us to fully reproduce the experimentally obtained momentum densities in the low momentum region. Results obtained upon properly rescaled ($\alpha = 0.4$) nuclear displacements for the first three eigenmodes (1T$_{2u}$, 1T$_{1u}$, 1T$_{2g}$) demonstrate that, at room temperature, these molecular vibrations in the electronic ground state can on their own certainly not be at the origin of the experimentally observed turn-up in momentum densities at low momenta. As a matter of fact, there is almost no discernable difference in between these latter results and the momentum profile calculated for the HOMO upon using the equilibrium geometry of W(CO)$_6$.

Table 4 Anharmonic energy demands and thermal fluctuations associated with distortions associated with the first three normal vibrational modes of W(CO)$_6$ (B3LYP/aug-cc-pVTZ-PP results, see text for a definition of the scaling factor α)

α	t$_{2u}$			t$_{1u}$			t$_{2g}$		
	Energy (kcal/mol)	Energy (cm^{-1})	Energy (K)	Energy (kcal/mol)	Energy (cm^{-1})	Energy (K)	Energy (kcal/mol)	Energy (cm^{-1})	Energy (K)
0.0	0.00	0.0	0	0.00	0.0	0	0.00	0.0	0
0.1	0.06	21.0	30	0.06	19.3	28	0.05	16.7	24
0.2	0.13	45.6	66	0.24	82.5	119	0.20	68.7	99
0.3	0.26	91.2	131	0.59	205.4	296	0.46	161.9	233
0.4	0.47	164.6	237	1.18	413.6	595	0.87	305.8	440
0.5	0.79	275.2	396	2.12	741.5	1,067	1.47	513.7	739
0.6	1.24	434.7	625	3.52	1,230.8	1,771	2.29	802.0	1,154
0.7	1.88	657.0	945	5.51	1,928.2	2,774	3.40	1,189.8	1,712
0.8	2.74	957.9	1,378	8.25	2,884.0	4,150	4.86	1,698.6	2,444
0.9	3.87	1,354.3	1,949	11.86	4,149.6	5,971	6.72	2,351.7	3,384
1.0	5.33	1,864.6	2,683	16.51	5,775.9	8,311	9.07	3,173.3	4,566

Table 5 Fractional populations of vibrational levels (n) approaching a normalized vibrational displacement (i.e., $\alpha = 1$), relative to the ground state ($n = 0$)

T (K)	n	t_{2u} E_v (cm^{-1})	Relative fraction	n	t_{1u} E_v (cm^{-1})	Relative fraction	n	t_{2g} E_v (cm^{-1})	Relative fraction
298	31	1,845	7.18×10^{-2}	70	5,721	2.61×10^{-9}	37	3,119	2.15×10^{-4}
	32	1,904	5.72×10^{-2}	71	5,803	1.81×10^{-9}	38	3,204	1.51×10^{-4}
310	31	1,845	1.01×10^{-1}	70	5,721	7.51×10^{-9}	37	3,119	3.82×10^{-4}
	32	1,904	8.14×10^{-2}	71	5,803	5.28×10^{-9}	38	3,204	2.72×10^{-4}
320	31	1,845	1.32×10^{-1}	70	5,721	1.72×10^{-8}	37	3,119	6.01×10^{-4}
	32	1,904	1.07×10^{-1}	71	5,803	1.23×10^{-8}	38	3,204	4.33×10^{-4}
330	31	1,845	1.70×10^{-1}	70	5,721	3.75×10^{-8}	37	3,119	9.20×10^{-4}
	32	1,904	1.39×10^{-1}	71	5,803	2.70×10^{-8}	38	3,204	6.70×10^{-4}
350	31	1,845	2.69×10^{-1}	70	5,721	1.56×10^{-7}	37	3,119	2.00×10^{-3}
	32	1,904	2.23×10^{-1}	71	5,803	1.15×10^{-7}	38	3,204	1.49×10^{-3}
400	31	1,845	6.93×10^{-1}	70	5,721	2.95×10^{-6}	37	3,119	9.94×10^{-3}
	32	1,904	5.95×10^{-1}	71	5,803	2.26×10^{-6}	38	3,204	7.72×10^{-3}
450	31	1,845	1.45×10^{0}	70	5,721	2.91×10^{-5}	37	3,119	3.46×10^{-2}
	32	1,904	1.27×10^{0}	71	5,803	2.30×10^{-5}	38	3,204	2.78×10^{-2}

Born–Oppenheimer Molecular Dynamical simulations of atomic trajectories over the ωB97XD/aug-cc-pVTZ potential energy surface associated with the electronic ground state of W(CO)$_6$ and a time average over the 1,500–1,600 thermally distorted structures dumped from these simulations enables us to account on classical grounds for the contribution of all 33 vibrational eigenmodes of this compound in an anharmonic depiction as well as of their coupling with internal and external rotations, due for instance to Coriolis forces. Increasing the temperature from 298 and 310 K does not make in practice any observable difference in the ultimately obtained spherically averaged and resolution folded momentum distributions. When accounting with molecular dynamics for all vibrational and rotational degrees of freedom, a significantly stronger turn-up at low momentum is observed in the momentum distribution characterizing the HOMO (Fig. 5). This turn-up is, however, far to be strong enough to quantitatively reproduce the experimental profile in this region. Upon scrutinizing in details the results of our BOMD simulations at or near room temperature, it appears that the thermally induced structural distortions which have the most pronounced effect at low momenta correspond to bending of the W–C–O bond angles.

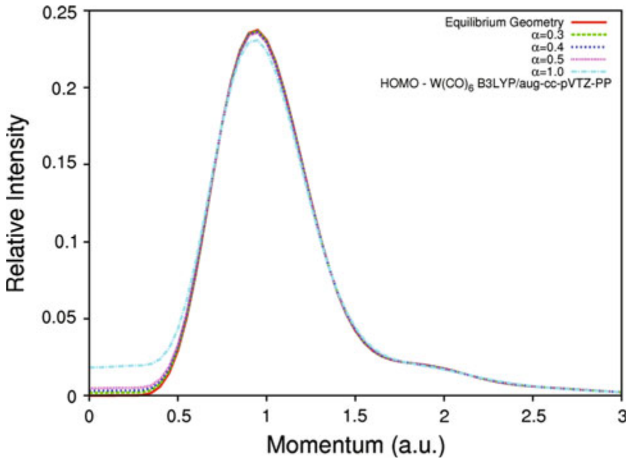

Fig. 4 Study of the consequences of structural distortions along the three first vibrational eigenmodes of W(CO)$_6$ upon the momentum profile characterizing the HOMO (without resolution folding). See text and Table 4 for a definition of the scaling factor α (results of single point calculation results at the B3LYP/aug-cc-pVTZ-PP level)

Similar remarks can be made regarding the influence of nuclear dynamics in the initial ground state upon the momentum profile characterizing the HOMO of Cr(CO)$_6$ and Mo(CO)$_6$. As our results indicate (Figs. 6, 7), compared with the available measurements, nuclear dynamics in the initial state is found in both cases to yield a significant albeit too weak turn-up of the frontier momentum densities at low momenta.

Starting from the vertical ionized state, the adiabatically relaxed molecular structures of the radical cation of the M(CO)$_6$ compounds (M=Cr, Mo, W) were found by systematically imposing tiny atomic displacements in the directions indicated by the vibrational eigenmodes associated with imaginary frequencies, and releasing thereafter all symmetry constraints during the geometry optimization process. Visual inspection along with careful verifications employing frequency analysis indicate that the molecular

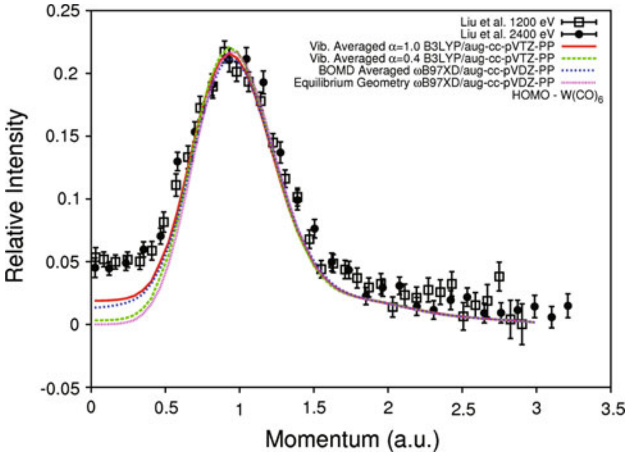

Fig. 5 Resolution folded ($E_0 = 2{,}400$ eV, $\Delta\theta = 0.53°$, $\Delta\phi = 0.84°$) and spherically averaged theoretical momentum distribution inferred for the HOMO of $W(CO)_6$ ($\varepsilon = 8.6$ eV), taking care of complications pertaining to nuclear dynamics in the initial state

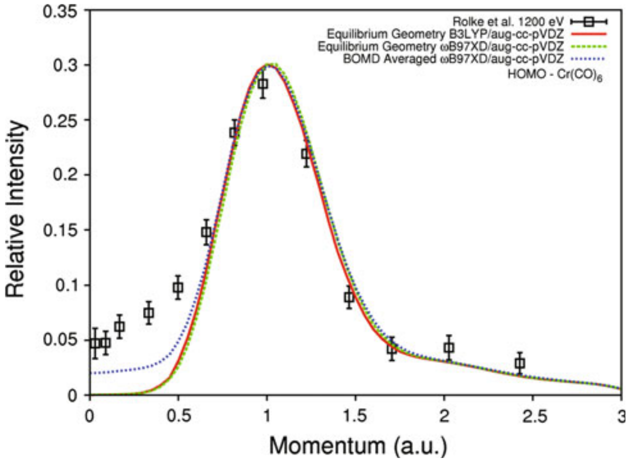

Fig. 6 Resolution folded ($E_0 = 1{,}200$ eV, $\Delta\theta = 0.60°$, $\Delta\phi = 1.20°$) and spherically averaged theoretical momentum distribution inferred for the HOMO of $Cr(CO)_6$ ($\varepsilon = 8.4$ eV), taking care of complications pertaining to nuclear dynamics in the initial state

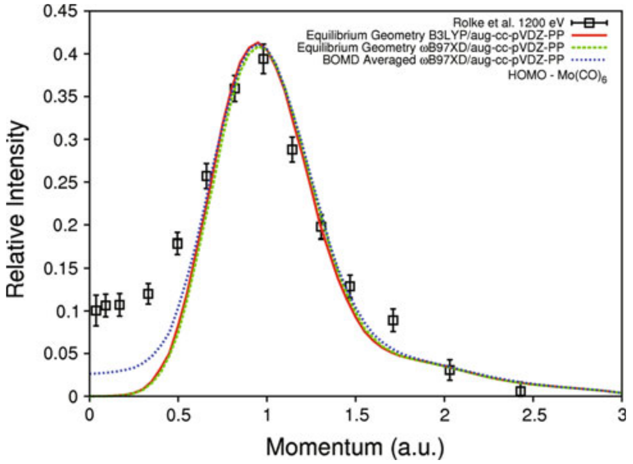

Fig. 7 Resolution folded ($E_0 = 1{,}200$ eV, $\Delta\theta = 0.60°$, $\Delta\phi = 1.20°$) and spherically averaged theoretical momentum distribution inferred for the HOMO of $Mo(CO)_6$ ($\varepsilon = 8.5$ eV), taking care of complications pertaining to nuclear dynamics in the initial state

structure of the radical cation of group 6 metal hexacarbonyl compounds can be discussed in terms of two structures of D_{3d} symmetry, which essentially differ by the extent of the angle (τ) in between the C–M bonds and the remaining C_3 rotation axis (Fig. 8). In these structures, the central metal, carbon and oxygen atoms remain perfectly co-linear. The interested reader is referred to Fig. 8 along with Tables 6, 7, 8 for a detailed comparison of these two structures with that of the neutral compound (of O_h symmetry), as well as for useful information regarding adiabatic relaxation energies from the vertical ionized state (ΔE_{rel}), and changes in frontier orbital energies due to the lowering of the symmetry point group. We note that releases of orbital energy degeneracies from the triply degenerate (T_{2g}) HOMO of the neutral into singly (A_{1g}) and doubly degenerate (E_g) orbitals upon imposing the D_{3d} structures of the cation do not exceed 0.15 eV. Since these levels cannot be individually resolved in EMS experiments, the corresponding momentum profiles have been summed to unravel the possible outcome of nuclear dynamics in the final state.

Upon examining Fig. 9, it is clear that final state dynamics associated with the Jahn–Teller distortions and release of symmetry constraints induced upon removal of an electron from the triply degenerate $2t_{2g}$ orbital of $W(CO)_6$ is also quite likely to induce a turn-up in the experimentally inferred momentum profiles for the $2t_{2g}^{-1}$ ionization channel, especially when considering the frontier momentum distribution for the adiabatically relaxed structure characterized by $\tau = 57.6°$. This turn-up arises because of the admixture of a fully symmetric (A_{1g}) orbital contribution (Table 8). Here again, this turn-up is on its own too weak to enable us to quantitatively reproduce experiment. Assuming a fully adiabatic ionization process, nuclear dynamics in the final state cannot account for more than one-third of the experimentally observed (e, 2e) ionization intensities at $p \rightarrow 0$. At this stage, it is worth reminding that such a depiction certainly overestimates the changes in the momentum densities induced by geometrical relaxation in the final state, during a real, that is, on a finite time scale, (e, 2e) ionization process. We note also that, within an adiabatic depiction, a Jahn–Teller distortion of the molecular structure of $W(CO)_6$ into a slightly flattened geometry characterized by $\tau = 53.5°$ only results in a barely visible turn-up (Fig. 9) in the low momentum region. Exactly the same remarks can be made (Figs. 10, 11) regarding the influence of nuclear dynamics in the final ionized state upon the momentum profile characterizing the HOMO of $Cr(CO)_6$ and $Mo(CO)_6$.

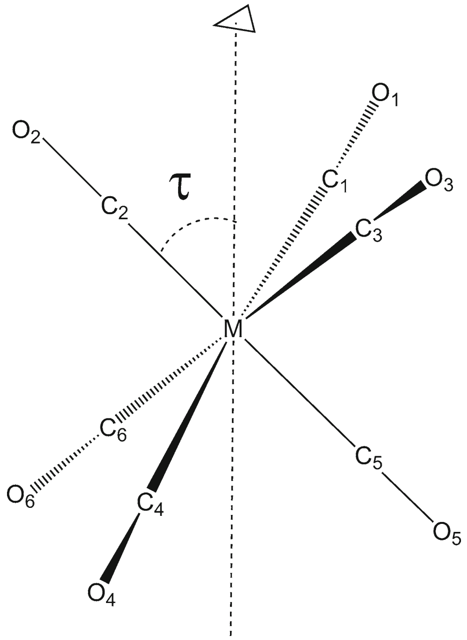

Fig. 8 Main geometrical parameters of the target group 6b metal hexacarbonyl compounds and of their radical cation

At last, it is worth noticing that on the experimental side [45], increasing the electron impact energy from 1.2 to 2.4 keV does have a small albeit discernable effect on the recorded momentum distributions for the HOMO of tungsten hexacarbonyl (Fig. 9). Note, in particular, that the agreement between theory and experiment slightly improves (beyond the reported statistical error [45]) at low momenta when resorting to an impinging electron beam with $E_0 = 2.4$ keV. In view of the *d*-like topology of the HOMO, which exhibits two perpendicular nodal planes intersecting at the location of the heavy metal atom, along with π-contributions from the CO groups (Fig. 12), it seems thus quite likely that, in spite of the negative conclusions by Liu et al. [45], distorted wave effects do play a role and converge more slowly upon increasing electron impact energies, than in the case of isolated atoms, due to the presence of many (13) scattering interference atomic centers in a target like W(CO)$_6$. The reader's attention is drawn on the fact that, whereas larger relative (e, 2e) intensities are obtained at low momenta when $E_0 = 1.2$ keV, significantly lower relative (e, 2e) intensities are on the contrary observed for the peak at ~0.9 a.u., compared with the results obtained at an impact energy of 2.4 keV. All in all, the experimental frontier momentum profile of W(CO)$_6$ seems thus far from being fully converging when E_0 increases from 1.2 to 2.4 keV. Note also that DWIA calculations indicate that, instead of vanishing as it should by virtue of symmetry constraints, the low momentum "turn-up" in the (e, 2e) ionization cross-sections for the 3d level of an atomic target like Ti still remains very prominent even at $E_0 = 2.4$ keV [44, 46]. Electron impact energies of the order of 10 keV or more might therefore be necessary for ensuring the convergence

Table 6 Comparison of the molecular geometries and frontier electronic structure of Cr(CO)$_6$ in its neutral ground state and lowest ionized (radical cation) state

Structure	τ (°)	R[Cr–C] in Å	R[C–O] in Å	$\theta(C_1\text{–Cr–}C_3)$ in °	$\theta(C_3\text{–Cr–}C_4)$ in °	$\Delta E_{\mathrm{rel}}^{a}$ (kcal/mol)	Frontier orbitals and their energies (eV)
O_h (neutral)	54.7	1.925	1.148	90.0	90.0	–	7.165 (T_{2g})
D_{3d} (1) (cation)	57.2	2.000	1.133	86.6	93.4	−8.333	6.583 (A_{1g})
							6.736 (E_g)
D_{3d} (2) (cation)	53.6	2.000	1.133	91.6	88.4	−7.096	6.663 (E_g)
							6.729 (A_{1g})

[a] Adiabatic relaxation energy from the vertical ionized state

Table 7 Comparison of the molecular geometries and frontier electronic structure of Mo(CO)$_6$ in its neutral ground state and lowest ionized (radical cation) state

Structure	τ (°)	R[Mo–C] in Å	R[C–O] in Å	$\theta(C_1\text{–Mo–}C_3)$ in °	$\theta(C_3\text{–Mo–}C_4)$ in °	$\Delta E_{\mathrm{rel}}^{a}$ (kcal/mol)	Frontier orbitals and their energies (eV)
O_h (neutral)	54.7	2.076	1.147	90.0	90.0	–	7.046 (T_{2g})
D_{3d} (1) (cation)	57.7	2.127	1.134	85.8	94.2	−6.056	6.591 (A_{1g})
							6.784 (E_g)
D_{3d} (2) (cation)	53.5	2.127	1.134	91.8	88.2	−4.693	6.699 (E_g)
							6.771 (A_{1g})

[a] Adiabatic relaxation energy from the vertical ionized state

Table 8 Comparison of the molecular geometries and frontier electronic structure of $W(CO)_6$ in its neutral ground state and lowest ionized (radical cation) states

Structure	τ (°)	R[W–C] in Å	R[C–O] in Å	$\theta(C_1–W–C_3)$ in °	$\theta(C_3–W–C_4)$ in °	ΔE^{a}_{rel} (kcal/mol)	Frontier orbitals and their energies (eV)
O_h (neutral)	54.7	2.072	1.149	90.0	90.0	–	7.063 (T_{2g})
D_{3d} (1) (cation)	57.6	2.114	1.136	86.1	93.9	−5.531	6.651 (A_{1g}) 6.839 (E_g)
D_{3d} (2) (cation)	53.5	2.114	1.136	91.8	88.2	−4.161	6.753 (E_g) 6.831 (A_{1g})

[a] Adiabatic relaxation energy from the vertical ionized state

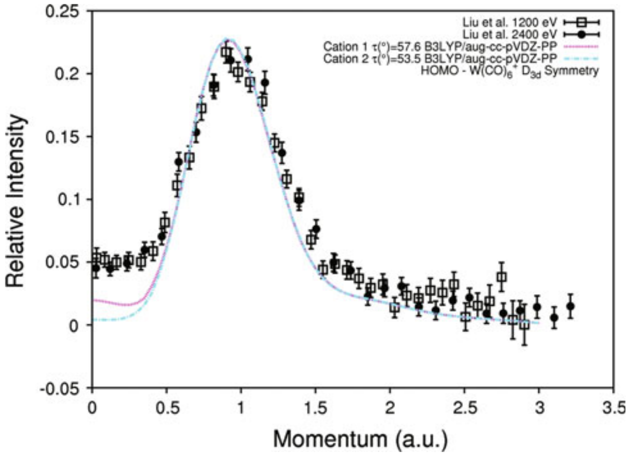

Fig. 9 Resolution folded ($E_0 = 2{,}400$ eV, $\Delta\theta = 0.53°$, $\Delta\phi = 0.84°$) and spherically averaged theoretical momentum distribution inferred for the HOMO of $W(CO)_6$ ($\varepsilon = 8.6$ eV), taking care of complications pertaining to nuclear dynamics in the initial states

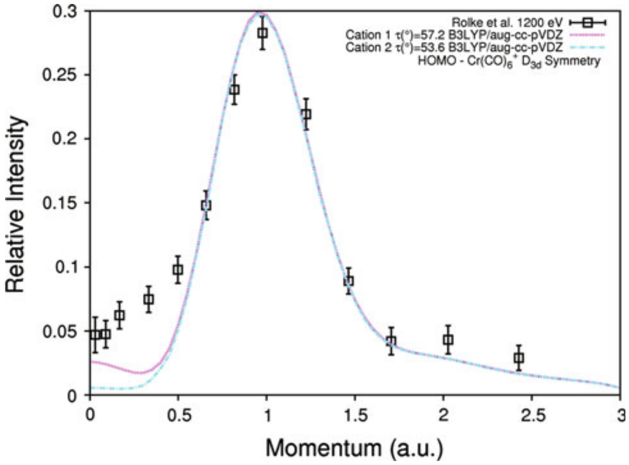

Fig. 10 Resolution folded ($E_0 = 1{,}200$ eV, $\Delta\theta = 0.60°$, $\Delta\phi = 1.20°$) and spherically averaged theoretical momentum distribution inferred for the HOMO of $Cr(CO)_6$ ($\varepsilon = 8.4$ eV), taking care of complications pertaining to nuclear dynamics in the initial states

of the momentum profiles of $W(CO)_6$, $Cr(CO)_6$, and $Mo(CO)_6$ to the high energy limit [102], at which the plane wave impulse approximation becomes valid.

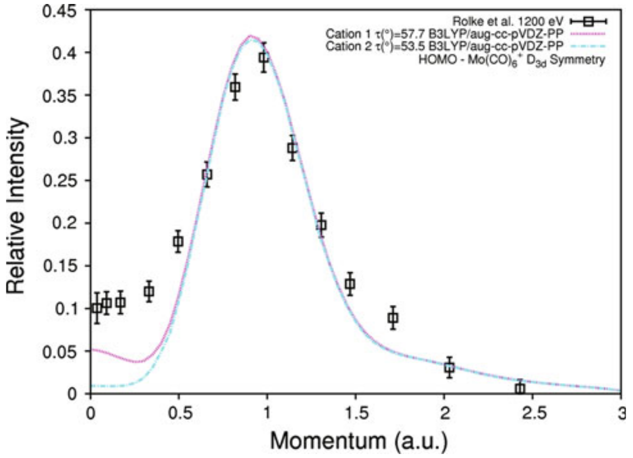

Fig. 11 Resolution folded ($E_0 = 1{,}200$ eV, $\Delta\theta = 0.60°$, $\Delta\phi = 1.20°$) and spherically averaged theoretical momentum distribution inferred for the HOMO of $Mo(CO)_6$ ($\varepsilon = 8.5$ eV), taking care of complications pertaining to nuclear dynamics in the initial states

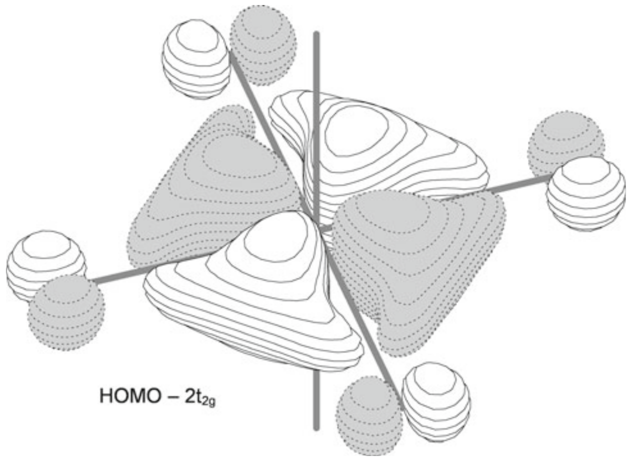

Fig. 12 Contour plot (contour value equal to 0.05) of the triply degenerate HOMO ($2t_{2g}$) of $W(CO)_6$ (this figure was made using MOLDEN [89])

5 Conclusions

The origin of the turn-up in the (e, 2e) ionization intensities which has been experimentally detected [43–45] in EMS studies at low electron momenta for the HOMO of group 6 (W, Cr, Mo) hexacarbonyl compounds has been reinvestigated, on the basis of large-scale calculations using the target Kohn–Sham approximations along with the standard hybrid B3LYP and dispersion-corrected ωB97XD exchange–correlation functionals. Our study invalidates the view [45] that the unexpectedly large (e, 2e) frontier orbital densities that were experimentally inferred in the low momentum region can be solely explained by nuclear displacements associated with the first three triply degenerate vibrational eigenmodes of these compounds. Indeed, at room temperature, an analysis of populations over these three vibrational eigenmodes ($1T_{2u}$, $1T_{1u}$, $1T_{2g}$) according to (Maxwell-)Botzmann thermostatistics indicate that these motions can only account for a very marginal fraction (a few % at most) of (e, 2e) ionization cross-sections at $p \rightarrow 0$.

Two different scenarios invoking nuclear dynamics in the initial ground state and nuclear dynamics in the final ionized state have been tested, on the ground of two very opposite models, assuming a vertical and an adiabatic depiction of the (e, 2e) reaction process, respectively. Both dynamics may partly contribute to the turn-up of (e, 2e) ionization intensities of the HOMO in the low momentum region, but none of them is on its own sufficient to explain this very large turn-up. Indeed, simulations employing Born–Oppenheimer molecular dynamics demonstrate that, at or near standard temperatures ($T = 298$ K or $T = 310$ K), thermally induced molecular motions on the potential energy surface associated with the electronic ground state can account for, at most, one-third of the experimentally observed (e, 2e) ionization cross-sections at $p \rightarrow 0$. Also, nuclear dynamics in the final state, in the form of Jahn–Teller distortions, can also only at best contribute for about the same ratio to these experimental cross-sections at or near zero electron momentum. In view of small but clearly observable differences in between EMS measurements at electron impact energies of 1.2 and 2.4 keV (Fig. 9), the only possible explanation we are left with is that both types of dynamical complications as well as distorted wave and post-collision (rescattering) effects in the continuum *cumulate* and yield *altogether* the experimentally observed turn-ups. Further EMS measurements, at much larger electron impact energies, with femtosecond time resolution as well as upon ultra-cooled supersonic molecular beams, are very much needed therefore for disentangling all these physical effects in a proper way on the experimental side. On theoretical side, the present study also most clearly emphasizes the need of thorough methodological and computational developments for quantitatively interpreting molecular EMS experiments upon large polyatomic systems beyond the plane wave impulse approximation. At the moment, a promising but still unexplored solution for investigating distorted wave effects in these systems consists in a molecular extension [6] of the BBK (Brauner, Briggs, and Klar) model [103] for the ionization of atoms.

Acknowledgments All calculations that were presented in this work have been performed on Compaq (HP) ES45 and ES47 workstations at Hasselt University, Belgium, and at the Flemish Supercomputer Center (Vlaams Supercomputer Centrum). This work has been supported by the FWO-Vlaanderen, the Flemish branch of the Belgian National Science Foundation, and by the Bijzonder OnderzoeksFonds of Hasselt University. The authors especially acknowledge financial support from a Research Program of the Research Foundation—Flanders (FWO_Vlaanderen; project number G.0350.09N, entitled “*From orbital imaging to quantum similarity in momentum space*”).

References

1. McCarthy IE, Weigold E (1991) Rep Prog Phys 54:789
2. Coplan MA, Moore JH, Doering JP (1994) Rev Mod Phys 66:985
3. Weigold E, McCarthy IE (1999) Electron Momentum Spectroscopy. Kluwer, New York
4. Neudatchin VG, Popov YV, Smirnov YF (1999) Physics-Uspehki 42:1017
5. Pang WN, Gao JF, Ruan CJ, Shang RC, Trofimov AB, Deleuze MS (2000) J Chem Phys 112:8043
6. Stia CR, Fojon OA, Weck PF, Hanssen J, Joulakian B, Rivarola RD (2002) Phys Rev A 66:052709
7. Champion C, Cappello CD, Houamer S, Mansouri A (2006) Phys Rev A 73:012717
8. Pickup BT (1977) Chem Phys 19:193
9. Öhrn Y (1981) Adv Quantum Chem 13:1
10. Deleuze M, Pickup BT, Delhalle J (1994) Mol Phys 83:655
11. Seabra GM, Kaplan IG, Zakrzewski VG, Ortiz JV (2004) J Chem Phys 121:4143
12. Duffy P, Chong DP, Casida ME, Salahub DR (1994) Phys Rev A 50:4704
13. Deleuze MS, Cederbaum LS (1997) Int J Quantum Chem 63:465
14. Golod A, Deleuze MS, Cederbaum LS (1999) J Chem Phys 110:6014
15. Ning CG, Ren XG, Deng JK, Su GL, Zhang SF, Knippenberg S, Deleuze MS (2006) Chem Phys Lett 421:52
16. Ning CG, Hajgató B, Huang YR, Zhang SF, Liu K, Luo ZH, Knippenberg S, Deng JK, Deleuze MS (2008) Chem Phys 343:19
17. Knippenberg S, François JP, Deleuze MS (2006) J Comp Chem 27:1703
18. Shojaei SHR, Hajgató B, Deleuze MS (2010) Chem Phys Lett 498:45
19. Deleuze MS, Pang WN, Salam A, Shang RC (2001) J Am Chem Soc 123:4049
20. Knippenberg S, Huang YR, Hajgató B, François JP, Deng JK, Deleuze MS (2007) J Chem Phys 127:174306
21. Morini F, Knippenberg S, Deleuze MS, Hajgató B (2010) J Phys Chem A 114:4400
22. Hajgató B, Deleuze MS, Morini F (2009) J Phys Chem A 113:7138
23. Takahashi M, Ogino R, Udagawa Y (1998) Chem Phys Lett 288:821
24. Ehara M, Ohtsuka Y, Nakatsuji H, Takahashi M, Udagawa Y (2005) J Chem Phys 122:234319

25. Deleuze MS, Knippenberg S (2006) J Chem Phys 125:104309
26. Huang CW, Shan X, Zhang Z, Wang EL, Li ZJ, Chen XJ (2010) J Chem Phys 133:124303
27. Brion CE, Zheng Y, Rolke J, Neville JJ, McCarthy IE, Wang J (1998) J Phys B 31:L223
28. Takahashi M, Saito T, Hiraka J, Udagawa Y (2003) J Phys B 36:2539
29. Nixon KL, Lawrance WD, Brunger MJ (2009) Chem Phys Lett 474:23
30. Takahashi M, Khajuria Y, Udagawa Y (2003) Phys Rev A 68:042710
31. Watanabe N, Takahashi M, Udagawa Y, Kouzakov KA, Popov YV (2007) Phys Rev A 75:052701
32. Takahashi M, Miyake Y, Watanabe N, Udagawa Y, Sakai Y, Mukoyama T (2007) Phys Rev Lett 98:013201
33. Ren XG, Ning CG, Deng JK, Zhang SF, Su GL, Huang F, Li GQ (2005) Phys Rev Lett 94:163201
34. Knippenberg S, Deleuze MS, Cleij TJ, François JP, Cederbaum LS, Eland JHD (2005) J Phys Chem A 109:4267
35. Knippenberg S, Hajgató B, François JP, Deleuze MS (2007) J Phys Chem A 111:10834
36. Knippenberg S, Hajgató B (2012) Spectrochim Acta A 102:2012
37. Li ZJ, Chen XJ, Shan X, Liu T, Xu KZ (2009) J Chem Phys 130:054302
38. Mingos DMP (1982) In: Wilkinson G (ed) Comprehensive organometallic chemistry, vol 3 of Comprehensive organometallic chemistry. Pergamon Press, New York
39. Huheey JE (1983) Inorganic chemistry: principles of structure and reactivity, 3rd edn. Harper International SI Edition, Cambridge
40. Cotton FA, Wilkinson G (1988) Advanced inorganic chemistry, 5th edn. Wiley-Interscience, New York
41. Schriver DF, Atkins PW (2006) Inorganic chemistry, 4th edn. Oxford University Press, Oxford
42. Higginson BR, Lloyd DR, Burroughs P, Gibson DM, Orchard AF (1973) J Chem Soc Faraday Trans 2:69
43. Chornay DJ, Coplan MA, Tossell JA, Moore JR, Baerends EJ, Rozendaal A (1985) Inorg Chem 24:877
44. Rolke J, Zheng Y, Brion CE, Chakravorty SJ, Davidson ER, McCarthy IE (1997) Chem Phys 215:191
45. Liu K, Ning CG, Luo ZH, Shi LL, Deng JK (2010) Chem Phys Lett 497:229
46. Brunger MJ, Braidwood SW, McCarthy IE, Weigold E (1994) J Phys B 27:L597
47. Takahashi M, Udagawa Y (2004) J Electron Spectrosc Rel Phenom 137:187
48. Landau LD, Lifshitz EM (1977) Quantum mechanics: non-relativistic theory. Pergamon, Oxford
49. Nicholson RJF, McCarthy IE, Weyrich W (1999) J Phys B 32:3873
50. Miyake Y, Takahashi M, Watanabe N, Khajuria Y, Udagawa Y, Sakai Y, Mukoyama T (2006) Phys Chem Chem Phys 8:3022
51. Champion C, Hanssen J, Hervieux PA (2002) Phys Rev A 65:022710
52. Builth-Williams JD, Bellm SM, Jones DB, Chaluvadi H, Madison DH, Ning CG, Lohmann B, Brunger MJ (2012) J Chem Phys 136:024304
53. McQuarrie DA (2000) Statistical mechanics. University Science Books, Sausalito
54. Carter AH (2001) Classical and statistical thermodynamics. Prentice Hall, Upper Saddle River
55. Helgaker T, Uggerud E, Jensen HJA (1990) Chem Phys Lett 173:145
56. Uggerud E, Helgaker T (1992) J Am Chem Soc 114:4265
57. Bolton K, Hase WL, Peslherbe GH (1998) In: Thompson DL (ed) Modern methods for multidimensional dynamics computation in chemistry. World Scientific, Singapore, p 143
58. Haile JMP (1997) Molecular dynamics simulation. Wiley, New York
59. Williams RW, Heilweil EJ (2010) Chem Phys 373:251
60. Joalland B, Rapacioli M, Simon A, Joblin C, Mardsen CJ, Spiegelman F (2010) J Phys Chem A 114:5846
61. Simon A, Rapacioli M, Lanza M, Joalland B, Spiegelman F (2011) Phys Chem Chem Phys 13:3359
62. Ramírez-Solís A, Jolibois F, Maron L (2011) Chem Phys Lett 510:21
63. Ning CG, Luo ZH, Huang YR, Hajgató B, Morini F, Liu K, Zhang SF, Deng JK, Deleuze MS (2008) J Phys B 41:175103
64. Levin VG, Neudatchin VG, Pavlitchenkov AV, Smirnov YF (1975) J Chem Phys 63:1541
65. Venkatesan TS, Mahapatra S, Cederbaum LS, Köppel H (2004) J Phys Chem A 108:2256
66. Köppel H, Domcke W, Cederbaum LS (1984) Adv Chem Phys 57:59
67. Deleuze MS, Hajgató B, Morini F, Knippenberg S (2010) J Phys Conf Ser 212:012020
68. Parr RG, Yang W (1989) Density functional theory of atoms and molecules. Oxford University Press, New York
69. Becke AD (1993) J Chem Phys 98:5648
70. Lee C, Yang W, Parr RG (1988) Phys Rev B 37:785
71. Chai JD, Head-Gordon M (2008) Phys Chem Chem Phys 10:6615
72. Dunning TH Jr (1989) J Chem Phys 90:1007
73. Kendall RA, Dunning TH Jr, Harrison R (1992) J Chem Phys 96:6796
74. Peterson K, Figgen D, Dolg M, Stoll H (2007) J Chem Phys 126:124101
75. Figgen D, Peterson KA, Dolg M, Stoll H (2009) J Chem Phys 130:164108
76. Peterson KA (2003) J Chem Phys 119:11099
77. Odoh OS, Schreckenbach G (2010) J Phys Chem A 114:1957
78. Frisch MJ, Trucks GW, Schlegel HB, Scuseria GE, Robb MA, Cheeseman JR, Scalmani G, Barone V, Mennucci B, Petersson GA, Nakatsuji H, Caricato M, Li X, Hratchian HP, Izmaylov AF, Bloino J, Zheng G, Sonnenberg JL, Hada M, Ehara M, Toyota K, Fukuda R, Hasegawa J, Ishida M, Nakajima T, Honda Y, Kitao O, Nakai H, Vreven T, Montgomery JA Jr., Peralta JE, Ogliaro F, Bearpark M, Heyd JJ, Brothers E, Kudin KN, Staroverov VN, Kobayashi R, Normand J, Raghavachari K, Rendell A, Burant JC, Iyengar SS, Tomasi J, Cossi M, Rega N, Millam JM, Klene M, Knox JE, Cross JB, Bakken CV, Jaramillo J, Gomperts R, Stratmann RE, Yazyev O, Austin AJ, Cammi R, Pomelli C, Ochterski JW, Martin RL, Morokuma K, Zakrzewski VG, Voth GA, Salvador P, Dannenberg JJ, Dapprich S, Daniels AD, Farkas Ö, Foresman JB, Ortiz JV, Cioslowski J, Fox DJ (2009) Gaussian 09, Revision B.1. Gaussian, Inc., Wallingford
79. Ren XG, Ning CG, Deng JK, Zhang SF, Su GL, Huang F, Li GQ (2005) Rev Sci Instrum 76:063103
80. Casida ME (1995) Phys Rev A 51:2005
81. Gritsenko OV, Braïda B, Baerends EJ (2003) J Chem Phys 119:1937
82. Janak JF (1978) Phys Rev B 18:7165
83. Vanfleteren D, Van Neck D, Ayers PW, Morrison RC, Bultinck P (2009) J Chem Phys 130:194104
84. Bawagan AO (1987) Ph.D. Thesis, University of British Columbia (UBC). See various contributions to the original HEMS program as recorded by Bawagan. The HEMS (now known as MOMAP) program has been extensively revised and extended at UBC by Cann NM and Cooper G
85. Duffy P, Casida ME, Brion CE, Chong DP (1992) Chem Phys 159(b):347
86. Bawagan AO, Brion CE (1990) Chem Phys 144:167
87. Bulirsch R, Stoer J (1991) Introduction to numerical analysis. Springer, New York

88. Press WH, Flannery BP, Teukolsky SA, Vetterling WT (1992) Richardson extrapolation and the Bulirsch-Stoer method. In: Numerical recipes in FORTRAN: the art of scientific computing. Cambridge University Press, Cambridge, 2nd edn., pp 718–725
89. Schaftenaar G, Noordik JH (2000) J Comput-Aided Mol Des 14:123
90. Vanlenthe E, Baerends E, Snijders J (1994) J Chem Phys 101:9783
91. Ehlers AW, Frenking G (1993) J Chem Soc Chem Commun 1709
92. Jonas V, Frenking G, Reetz MT (1992) J Comput Chem 13:919
93. Hay PJ, Wadt WR (1985) J Chem Phys 82:299
94. Hehre WJ, Ditchfield R, Pople PA (1972) J Chem Phys 56:2257
95. Shimanouchi T, Molecular vibrational frequencies. In: Lingstrom PJ, Mallard WG (eds) NIST Chemistry WebBook, NIST Standard Reference Database Number 69, National Institute of Standards and Technology, Gaithersburg MD, 20899, http://webbook.nist.gov
96. Shimanouchi T (1972) J Phys Chem Ref Data 6:993
97. Bérces A (1996) J Phys Chem A 100:16538
98. Mortimer RG (2003) Physical Chemistry, 3rd edn. Elsevier, London
99. Mc Quarrie DA, Simons JD (1997) Physical chemistry—a molecular approach. University Science Books, Sausalito
100. Atkins P, de Paula J (2010) Physical Chemistry, 9th edn. W. H. Freeman, New York
101. Herzberg G (1956) Molecular spectra and molecular structure; Part II. Infrared and Raman Spectra of Polyatomic Molecules, 07th Printing. D. Van Nostrand Company, Princeton
102. Takahashi M (2010) Oral remark at the international conference on many-particle spectroscopy of atoms, molecules, clusters, and surfaces; (MPS2012), held in Sendai. Japan, Sendai, 4–7 September 2010
103. Brauner M, Briggs JS, Klar J (1989) J Phys B 22:2265

Theor Chem Acc (2012) 131:1245
DOI 10.1007/s00214-012-1245-4

REGULAR ARTICLE

Radical electrophilicities in solvent

**Freija De Vleeschouwer · Paul Geerlings ·
Frank De Proft**

Received: 16 April 2012 / Accepted: 5 June 2012 / Published online: 16 June 2012

Abstract An electrophilicity scale for radicals in solution is reported using the electrophilicity index, an important quantity in conceptual density functional theory. Five different solvents were chosen, for which the static dielectric constant covers the entire range of nonpolar to polar solvents: *n*-hexane ($\varepsilon_r = 1.8819$), dichloromethane ($\varepsilon_r = 8.9300$), 2-propanol ($\varepsilon_r = 19.2640$), acetonitrile ($\varepsilon_r = 35.6880$) and water ($\varepsilon_r = 78.3553$). The calculations in solution were carried out within the polarizable continuum model through the Integral Equation Formalism (IEF-PCM) approach. For water, also conductor-like screening model (COSMO) calculations are reported. The electronic chemical potential remains almost constant when going from gas phase to solution. However, large decreases in chemical hardness can be observed, resulting in more electrophilic radicals compared to the gas phase, and even influencing the overall order of the previously established gas-phase scale. Both solvation models (COSMO and IEF-PCM) lead to essentially the same results.

Keywords Electrophilicity index · Conceptual DFT · Solvent effects · Chemical hardness

1 Introduction

Recently, we presented a radical electrophilic scale, global as well as local, for a set of 35 organic radicals in the gas phase (where the gas phase refers to calculations carried out on isolated molecules without the presence of solvent) [1]. This scale, based on the electrophilicity index as introduced by Parr et al. [2] (for a recent review see Chattaraj et al. [3]) and defined as the electronic chemical potential squared over two times the chemical hardness, has proven its value since assisting in classifying radical systems [4–10], explaining reaction behavior and introducing other chemical concepts like radical stability [11–14]. The question arises, though, as to whether the order of this gas-phase electrophilicity scale still holds for radicals in solution. Solvent effects can be very significant when considering electrophile/nucleophile interactions [15–17]. However, there is still a lot of debate about whether or in which cases gas-phase properties could be employed to describe concepts and reactions in solvent. Parr et al. [2], for instance, stated that gas-phase properties like the electrophilicity index can determine the reactivity in the case of for instance “a close encounter between the reacting species in a biological system,” because “solvent molecules have already been pushed out.” Another example is homolysis in solution where a caged radical pair is formed, that is, solvent molecules surround the initially formed radical pair, but none of the solvent molecules interferes between the two radical fragments. In order to escape the cage, one of the radicals needs to diffuse through the solvent [18]. If the diffusion rate is higher than the cage recombination rate, the radical fragments become “free radicals.” When such radicals approach each other from a larger distance, they will feel the effect of each other’s global electrophilicity, although affected by the

Published as part of the special collection of articles celebrating theoretical and computational chemistry in Belgium.

Electronic supplementary material The online version of this article (doi:10.1007/s00214-012-1245-4) contains supplementary material, which is available to authorized users.

F. De Vleeschouwer (✉) · P. Geerlings · F. De Proft
Eenheid Algemene Chemie (ALGC), Vrije Universiteit Brussel (VUB), Faculteit Wetenschappen, Pleinlaan 2,
1050 Brussels, Belgium
e-mail: fdevlees@vub.ac.be

presence of solvent molecules. Of course, not only can the presence of solvent alter the reactivity properties of the radical system; also, stronger radical–solvent interactions can come into play like radical addition to the solvent molecule, orbital interactions or the formation of a charge transfer complex [19].

Several studies have been performed to obtain more information about the effect of solvent on the properties and reactivity of different species. In 1986 Pearson estimated solution ionization potentials and electron affinities to obtain the effective electronic chemical potential and chemical hardness in solution for a set of neutral and charged species [20]. He concluded that the absolute electronegativity for small neutral molecules hardly changes going from gas phase to solvent, while the changes are much more pronounced for charged molecules. The chemical hardness values showed that neutral molecules become much softer in solution, although Pearson questioned their practical utility. De Luca et al. [21] applied three different approaches to compute the chemical hardness, already widely tested in gas phase, to species in solution, in order to evaluate the solvent effects on the chemical hardness. They found that for methods based on orbital energies (HOMO–LUMO gap and the internally resolved hardness tensor approach based on fractional occupation numbers), only a small dependency of the hardness on the solvent exists, in contradiction to the method based on total energy differences (from vertical electron affinity and vertical ionization potential) for which 50 % decreases in hardness values were detected.

Concerning the global electrophilicity index ω, Pérez et al. [22] looked into the effect of solvent on this particular property for a set of 18 electrophiles, using Parr's formula [2], applied to the solution phase:

$$\omega_{\mathrm{solv}} = \frac{\mu_{\mathrm{solv}}^2}{2\eta_{\mathrm{solv}}} \cong \frac{(IP_{\mathrm{solv}} + EA_{\mathrm{solv}})^2}{8(IP_{\mathrm{solv}} - EA_{\mathrm{solv}})} \tag{1}$$

where μ_{solv} is the electronic chemical potential [23] and η_{solv} the chemical hardness [24] in solvent. These two quantities were calculated by using the vertical ionization potential *IP* and electron affinity *EA* [20, 25], evaluated in solution. The electrophilicity index measures the energy stabilization when an optimal electronic charge transfer from the environment to the system occurs. Pérez et al. concluded that the electronic chemical potential for (most of) the series of neutral and more covalent electrophiles is almost unaffected by the solvent and that solvation makes the electrophile ligands softer than in the gas phase, again in agreement with Pearson's predictions. This means that for neutral systems, an enhancement of the electrophilicity is seen, controlled by changes in chemical hardness and the solvation energy, with a very small contribution from the electronic chemical potential of solvation. It also appears that μ_{solv} is dependent on the polarization charges induced in the environment within the reaction field approach, and according to that same approach, η_{solv} is independent of those charges [22, 26]. Meneses et al. [26] performed calculations using the continuum approach as well as the super-molecular approach to incorporate solvent effects. They discovered that "independent of the sign and magnitude of the charge, the chemical hardness always decreases upon solvation because the electrostatic potential decreases as the effective radius (solute radius plus a solvation layer) of the solute increases." However, there

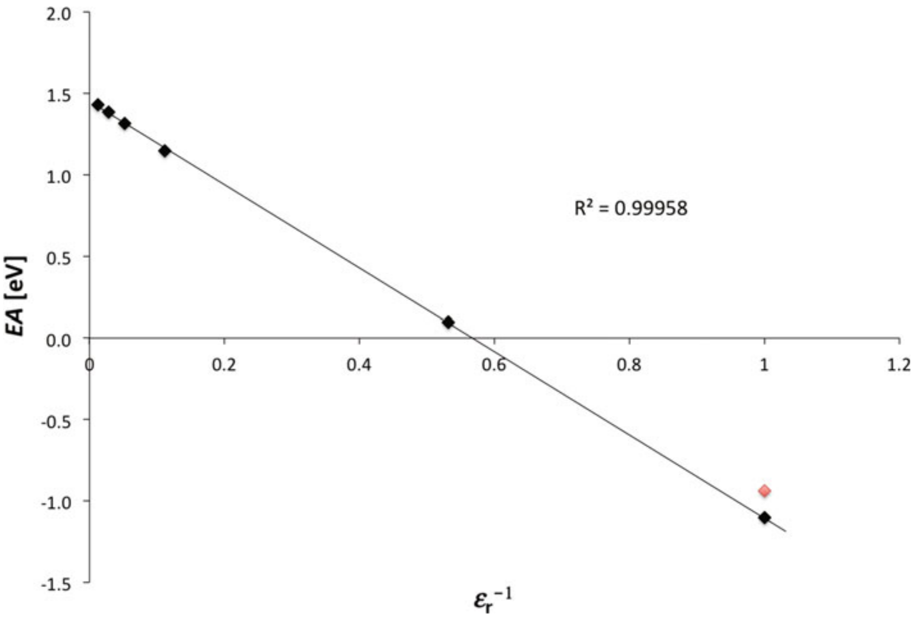

Fig. 1 Correlation between the vertical electron affinity *EA* (in eV) and the reciprocal of the static dielectric constant ε_r^{-1} for the 2-hydroxyprop-2-yl radical. At $\varepsilon_r^{-1} = 1$, the *red point* is the computed gas-phase *EA* and the *black point* is the extrapolated one

Table 1 The electronic chemical potential μ for the gas phase and 5 different solvents (using IEFPCM and COSMO) in eV

Radical	Gas phase	*n*-Hexane[a]	Dichloromethane[a]	2-Propanol[a]	Acetonitrile[a]	Water[a]	Water[b]
$C(OH)(CH_3)_2$	−3.0	−3.0	−3.0	−3.0	−3.0	−3.0	−3.0
$C(CH_3)_3$	−3.2	−3.2	−3.2	−3.2	−3.2	−3.2	−3.1
CH_2OH	−3.6	−3.6	−3.6	−3.6	−3.6	−3.6	−3.5
$CH(CH_3)_2$	−3.5	−3.5	−3.5	−3.5	−3.5	−3.5	−3.4
NO	−4.5	−4.4	−4.4	−4.4	−4.4	−4.4	−4.3
CH_2CH_3	−4.0	−4.0	−4.0	−4.0	−4.0	−4.0	−3.9
$CH_2CH_2CH_3$	−4.1	−4.0	−4.1	−4.1	−4.1	−4.1	−4.0
$CH_2C_6H_4(OCH_3)$	−3.6	−3.6	−3.7	−3.7	−3.7	−3.7	−3.7
$CH_3C(O)$	−4.3	−4.3	−4.2	−4.2	−4.2	−4.2	−4.2
CF_2CH_3	−4.6	−4.6	−4.6	−4.6	−4.6	−4.6	−4.6
$CH_2C_6H_4(CH_3)$	−3.8	−3.8	−3.9	−3.9	−3.9	−3.9	−3.9
CH_2CHCH_2	−4.2	−4.2	−4.2	−4.2	−4.2	−4.2	−4.2
HC(O)	−4.8	−4.7	−4.7	−4.7	−4.7	−4.6	−4.6
CH_3	−4.9	−4.8	−4.8	−4.8	−4.8	−4.8	−4.7
$CH_2C_6H_5$	−4.0	−4.0	−4.0	−4.1	−4.1	−4.1	−4.0
$CHCH_2$	−4.9	−4.9	−4.9	−4.9	−4.9	−4.9	−4.8
$CH_2C_6H_4(F)$	−4.0	−4.0	−4.0	−4.0	−4.1	−4.1	−4.0
$C_6H_4(CH_3)$	−4.8	−4.9	−5.0	−5.0	−5.0	−5.0	−5.0
$C_6H_4(OCH_3)$	−4.9	−4.9	−5.0	−5.1	−5.1	−5.1	−5.1
C_6H_5	−4.9	−4.9	−5.0	−5.0	−5.0	−5.1	−5.0
CCl_3	−4.9	−4.8	−4.8	−4.8	−4.8	−4.8	−4.8
$C(CN)(CH_3)_2$	−4.8	−4.7	−4.7	−4.7	−4.7	−4.7	−4.7
$C_6H_4(F)$	−5.2	−5.2	−5.3	−5.3	−5.3	−5.3	−5.2
CF_3	−6.0	−5.9	−5.9	−5.9	−5.9	−5.9	−5.8
NF_2	−6.6	−6.6	−6.6	−6.5	−6.5	−6.5	−6.5
$C_6H_4(CN)$	−5.6	−5.5	−5.4	−5.4	−5.4	−5.4	−5.3
NH_2	−6.7	−6.7	−6.7	−6.7	−6.7	−6.7	−6.5
$CH_2C_6H_4(CN)$	−4.8	−4.7	−4.6	−4.6	−4.6	−4.6	−4.5
OCH_3	−6.0	−6.1	−6.1	−6.1	−6.1	−6.1	−6.1
Tert-butoxycarbonylmethyl	−5.7	−5.7	−5.7	−5.7	−5.7	−5.7	−5.7
OCH_2CH_3	−5.9	−5.9	−6.0	−6.0	−6.0	−6.0	−6.0
$OCH_2C(CH_3)_3$	−5.7	−5.7	−5.9	−5.9	−5.9	−5.9	−5.9
CH_2CN	−5.9	−5.9	−5.8	−5.8	−5.8	−5.8	−5.7
SCH_3	−5.6	−5.6	−5.6	−5.6	−5.6	−5.6	−5.6
H	−7.3	−7.0	−6.8	−6.7	−6.7	−6.7	–
SCH_2CH_3	−5.5	−5.5	−5.6	−5.6	−5.6	−5.6	−5.5
NO_2	−6.6	−6.5	−6.5	−6.5	−6.5	−6.5	−6.3
OC_6H_5	−5.5	−5.5	−5.5	−5.5	−5.5	−5.5	−5.5
Tosyl	−5.6	−5.6	−5.7	−5.8	−5.8	−5.8	−5.8
Phenylsulfonyl	−5.7	−5.8	−5.9	−5.9	−5.9	−5.9	−5.9
OH	−7.5	−7.5	−7.5	−7.5	−7.5	−7.5	−7.4
SH	−6.4	−6.3	−6.3	−6.3	−6.3	−6.3	−6.2
2,2-Dimethyl-4,6-dioxo-1,3-dioxan-5-yl	−6.7	−6.7	−6.7	−6.7	−6.7	−6.7	−6.7
Br	−7.8	−7.7	−7.6	−7.6	−7.6	−7.6	−7.5
Cl	−8.4	−8.3	−8.3	−8.3	−8.3	−8.3	−8.2
F	−10.6	−10.6	−10.6	−10.6	−10.6	−10.6	−10.5
CN	−9.2	−9.1	−9.0	−9.0	−9.0	−9.0	−9.0

[a] Using IEF-PCM in Gaussian09

[b] Using COSMO in MOLPRO 2010.1

remains the problem of rigorously predicting the variations in chemical hardness for a system coupled to an external electric field.

In the context of our ongoing efforts in the field of conceptual DFT [27, 28], we will compute the electronic chemical potential, the chemical hardness and both the global and the local electrophilicity index for a set of uncharged radical systems in solvent. The resulting radical electrophilicity scales in solvent will be compared to the previously reported gas-phase scale. For water as a solvent, two different solvation methods (IEF-PCM and COSMO) will be applied to exclude artificial effects inherent to one of the two approaches.

2 Computational details

All calculations were performed within the Kohn–Sham framework. Geometries of all radical species were optimized in solvent at the B3LYP/6-311+G(d,p) level of theory [29–31] using both the polarizable continuum model through the integral equation formalism (IEF-PCM), as implemented in Gaussian09 [32], and the conductor-like screening model (COSMO), as implemented in MOLPRO 2010.1 [33]. The IEF-PCM method creates the solute cavity via a set of overlapping spheres [34–36]. The COSMO [37] model differs from the PCM model in that a scaled conductor boundary condition is used instead of the much more complicated dielectric boundary condition for the calculation of the polarization charges of a molecule in a continuum like with IEF-PCM. In the case of IEF-PCM, frequency calculations at the same level of theory were performed to ensure that all structures are minima on the potential energy surface.

3 Results and discussion

For this study, we use our extended database [11] of 47 radical systems, so 12 more than our previously published gas-phase radical electrophilicity scale [1], including C-, N-, O- and S-centered radicals, as well as some halogens, thus comprising a representative set of radicals for applications in organic chemistry. The structures can be retrieved from the Supporting Information. In order to compute the electrophilicity index, Parr's definition was applied to the solution phase as shown in Eq. 1, using IEF-PCM and—in the case of water—COSMO as the implicit solvation models. Five solvents were chosen, for which the static dielectric constant covers the entire range of nonpolar to polar solvents: *n*-hexane ($\varepsilon_r = 1.8819$), dichloromethane ($\varepsilon_r = 8.9300$), 2-propanol ($\varepsilon_r = 19.2640$), acetonitrile ($\varepsilon_r = 35.6880$) and water ($\varepsilon_r = 78.3553$).

3.1 Electronic chemical potential

The electronic chemical potential in solvent μ_{solv} is calculated using the finite difference approach as follows:

$$\mu_{\mathrm{solv}} \cong -\frac{IP_{\mathrm{solv}} + EA_{\mathrm{solv}}}{2}. \qquad (2)$$

For 10 out of the 47 radical systems, negative electron affinities were found. Cardenas et al. [38] found that, despite the ongoing debate about using negative instead of zero *EA*s, in the case of the chemical hardness it makes no difference which approach is used for metastable anions, and we expect the same results for the electronic chemical potential. In this paper, we choose to use negative *EA*s instead of zero ones. However, electron affinity calculations of metastable anions, mainly found in the gas phase, are mostly unreliable using standard quantum chemical techniques due to the temporary nature of those ions. One reliable possibility is to extrapolate the gas-phase *EA* from a series of solvent-based *EA*s, since the *EA*s correlate linearly with the reciprocal of the dielectric constant ε_r [39]. In order to check the accuracy of our computed gas-phase negative *EA*s, we compared those values with the values extrapolated from the solvent-phase *EA* calculations using IEF-PCM. The average deviation was around 0.1 eV with a maximal deviation of around 0.15 eV for the 2-hydroxyprop-2-yl radical as shown in Fig. 1. These deviations on the (negative) *EA*s have a minor influence on the electronic chemical potential, the chemical hardness and the electrophilicity indices since these electronic properties are dominated by the much larger (in absolute value) *IP*s.

Table 1 contains both the gas-phase and solvent μ-values, using IEF-PCM as the solvation model. For water, also the COSMO values are listed since this model works best for solvents with a large dielectric constant value. The COSMO values are very close to the IEF-PCM values, on the average within 0.1 eV. We find that the electronic chemical potential remains almost constant (average change of 2 %) going from gas phase to water with the largest change, an increase of 7 %, observed for the hydrogen atom. When comparing the low-to-high value ranking of the gas phase and water data, no important shifts are observed, which is in line with the literature, which says that for uncharged species the electronic chemical potential is in most cases almost unaffected by the solvent [20, 22].

3.2 Chemical hardness

Much larger changes are seen for the chemical hardness values. The chemical hardness in solvent η_{solv} is computed as follows, again using the finite difference approach:

$$\eta_{\mathrm{solv}} \cong IP_{\mathrm{solv}} - EA_{\mathrm{solv}}. \qquad (3)$$

Table 2 The chemical hardness η for the gas phase and 5 different solvents (using IEFPCM and COSMO) in eV

Radical	Gas phase	*n*-Hexane[a]	Dichloromethane[a]	2-Propanol[a]	Acetonitrile[a]	Water[a]	Water[b]
$C(OH)(CH_3)_2$	8.0	5.8	3.8	3.4	3.3	3.2	3.0
$C(CH_3)_3$	7.9	5.8	3.8	3.5	3.3	3.3	3.0
CH_2OH	9.2	6.6	4.1	3.8	3.6	3.5	3.3
$CH(CH_3)_2$	8.4	6.1	4.0	3.6	3.5	3.4	3.2
NO	11.6	8.7	6.0	5.6	5.4	5.3	4.9
CH_2CH_3	9.1	6.5	4.2	3.8	3.7	3.6	3.3
$CH_2CH_2CH_3$	8.6	6.2	4.0	3.7	3.6	3.5	3.2
$CH_2C_6H_4(OCH_3)$	6.1	4.2	2.5	2.2	2.1	2.1	1.9
$CH_3C(O)$	8.7	6.3	4.0	3.7	3.6	3.5	3.3
CF_2CH_3	9.6	7.2	4.9	4.6	4.5	4.4	4.1
$CH_2C_6H_4(CH_3)$	6.2	4.3	2.6	2.3	2.2	2.1	2.0
CH_2CHCH_2	7.8	5.4	3.3	3.0	2.9	2.8	2.6
HC(O)	9.9	7.1	4.6	4.2	4.1	4.0	3.7
CH_3	10.0	7.2	4.6	4.2	4.0	3.9	3.6
$CH_2C_6H_5$	6.4	4.5	2.6	2.4	2.3	2.2	2.0
$CHCH_2$	9.5	6.9	4.5	4.1	4.0	3.9	3.6
$CH_2C_6H_4(F)$	6.5	4.5	2.7	2.4	2.3	2.2	2.1
$C_6H_4(CH_3)$	8.3	6.2	4.2	3.9	3.8	3.7	3.5
$C_6H_4(OCH_3)$	8.4	6.3	4.3	4.0	3.9	3.8	3.6
C_6H_5	8.5	6.3	4.3	4.0	3.8	3.7	3.5
CCl_3	8.0	5.8	3.8	3.5	3.4	3.3	3.2
$C(CN)(CH_3)_2$	7.6	5.5	3.5	3.2	3.1	3.0	2.8
$C_6H_4(F)$	8.7	6.5	4.4	4.1	4.0	3.9	3.7
CF_3	10.8	8.2	5.7	5.4	5.2	5.2	4.9
NF_2	11.9	9.1	6.5	6.2	6.0	5.9	5.6
$C_6H_4(CN)$	8.4	6.3	4.4	4.1	4.0	3.9	3.7
NH_2	12.1	9.1	6.3	5.9	5.7	5.6	5.1
$CH_2C_6H_4(CN)$	6.0	4.2	2.5	2.2	2.1	2.0	1.9
OCH_3	9.5	6.8	4.3	3.9	3.7	3.6	3.2
Tert-butoxycarbonylmethyl	8.3	6.2	4.1	3.8	3.7	3.6	3.4
OCH_2CH_3	8.9	6.4	4.0	3.7	3.5	3.4	3.1
$OCH_2C(CH_3)_3$	8.2	6.0	3.9	3.5	3.4	3.3	3.0
CH_2CN	8.8	6.3	4.1	3.8	3.6	3.5	3.3
SCH_3	7.5	5.0	2.6	2.3	2.2	2.1	1.9
H	12.8	9.1	5.7	5.2	5.0	4.9	–
SCH_2CH_3	7.2	4.9	2.6	2.3	2.1	2.1	2.0
NO_2	10.3	7.6	5.1	4.8	4.6	4.5	4.1
OC_6H_5	6.7	4.6	2.7	2.4	2.3	2.2	2.1
Tosyl	6.8	4.8	3.0	2.7	2.6	2.5	2.4
Phenylsulfonyl	7.0	5.0	3.1	2.8	2.7	2.6	2.5
OH	11.6	8.3	5.3	4.9	4.7	4.6	3.9
SH	8.1	5.3	2.8	2.4	2.3	2.2	2.1
2,2-Dimethyl-4,6-dioxo-1,3-dioxan-5-yl	7.5	5.5	3.7	3.4	3.3	3.2	3.0
Br	8.4	5.6	3.1	2.7	2.6	2.5	2.2
Cl	9.4	6.4	3.7	3.3	3.2	3.1	2.8
F	14.3	10.7	7.5	7.1	6.9	6.8	6.3
CN	10.2	7.4	4.9	4.5	4.4	4.3	4.0

[a] Using IEF-PCM in Gaussian09

[b] Using COSMO in MOLPRO 2010.1

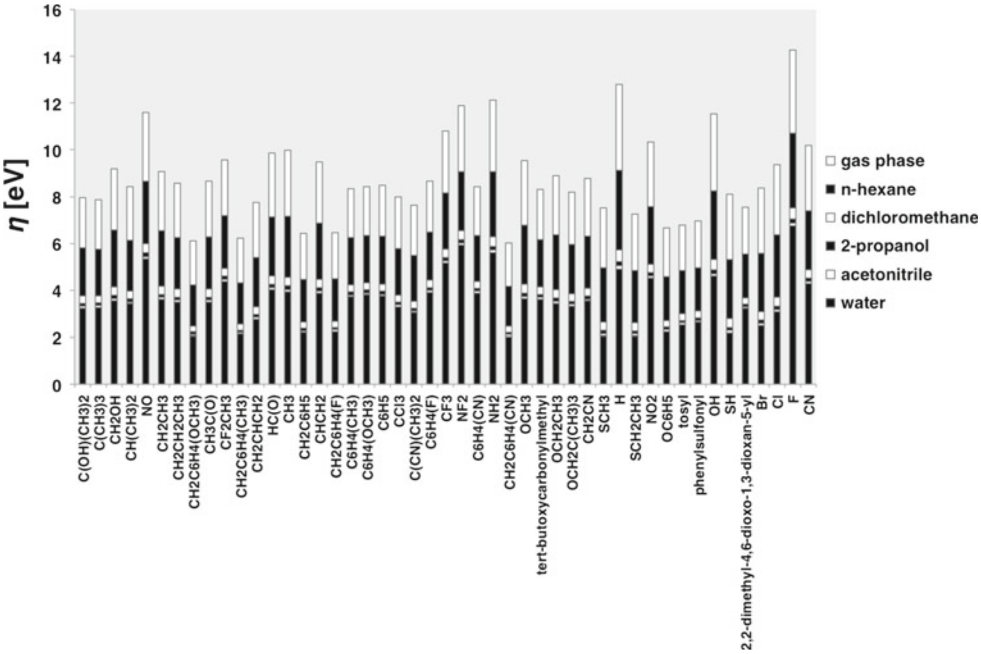

Fig. 2 The chemical hardness for a total of 47 radicals in gas phase and different solvents

All gas phase, IEF-PCM and COSMO values can be retrieved from Table 2. Again, for water, the COSMO values do not differ much from the IEF-PCM values, with the COSMO values on the average being 0.2–0.3 eV lower than the PCM values but with a correlation of more than 99 %. Figure 2 lists η for all radical systems ordered according to the gas-phase electrophilicities, starting with the values for water and adding up until the gas-phase values. All radicals become much softer in solvent, with changes from 50 to 73 % when gas-phase and water values are compared. The biggest changes are observed for the aliphatic thiyl radicals (R–S$^\cdot$), the para-substituted benzyl radicals, the phenoxy radical, chlorine and bromine, so radicals including highly polarizable (soft) atoms or groups. The smallest changes are observed for the para-substituted phenyl radicals, the N- and F-centered radicals as well as those radicals containing fluorine atoms (with the exception of *p*-fluorobenzyl). The first strong decrease (46.5 % of the overall difference is due to the gas phase/*n*-hexane change) can be linked to the actual solvation. This agrees with the findings of Meneses et al. [26]. The second strong decrease of 43.0 % (going from *n*-hexane to the more polar dichloromethane) is due to the increasing polarity of the solvent. Further changes are 6.0 % going from dichloromethane to 2-propanol, 2.4 % to acetonitrile and finally 1.5 % to water. These changes, in terms of percentage (100 % being the percentage when going from gas phase to water), are constant for every radical in the database and can be traced back to the estimation for changes in η upon solvation, derived from the approximate (generalized) reaction field Born's model: [22, 26, 40]

$$\Delta E_{\text{solv}} = -\frac{1}{2}\left(1-\frac{1}{\varepsilon_r}\right)\sum_A\sum_B Q_A Q_B \Gamma_{AB} \tag{4}$$

where Q_A and Q_B are the net charges of atoms A and B in the molecule and Γ_{AB} is a solute–solvent interaction integral. To get the estimation for the changes in chemical hardness in solution, we differentiate Eq. 4 twice with respect to the net charge:

$$\Delta\eta_{\varepsilon_r\leftarrow 1} = -\left(1-\frac{1}{\varepsilon_r}\right)\sum_A \Gamma_{AA}. \tag{5}$$

Note that within the continuum model of solvent effects, the changes in η are predicted to be negative. For the changes in percentage in η going from one solvent to another, Eq. 5 can be rewritten as follows:

$$\frac{\Delta\eta_{\varepsilon_{r,2}\leftarrow\varepsilon_{r,1}}}{\Delta\eta_{\varepsilon_{r,\max}\leftarrow 1}} = \frac{\left(\frac{1}{\varepsilon_{r,2}}-\frac{1}{\varepsilon_{r,1}}\right)}{\left(1-\frac{1}{\varepsilon_{r,\max}}\right)} \tag{6}$$

where $\varepsilon_{r,\max}$ stands for the maximal dielectric constant in our list, namely for water. The chemical hardness change in percentage is not a function of the type of radical within the solvent models applied in this study. This implies that for any solvent with a certain dielectric constant, the chemical hardness of any radical system listed in this work can be interpolated from the values in Table 2 with a good accuracy.

Table 3 The global electrophilicity index ω for the gas phase [1] and 5 different solvents (using IEFPCM and COSMO) in eV

Radical	Gas phase	*n*-Hexane[a]	Dichloromethane[a]	2-Propanol[a]	Acetonitrile[a]	Water[a]	Water[b]
$C(OH)(CH_3)_2$	0.581	0.774	1.217	1.339	1.395	1.434	1.492
$C(CH_3)_3$	0.651	0.870	1.336	1.459	1.516	1.556	1.632
CH_2OH	0.717	0.969	1.535	1.686	1.756	1.804	1.834
$CH(CH_3)_2$	0.720	0.978	1.530	1.675	1.742	1.787	1.842
NO	0.876	1.139	1.607	1.712	1.759	1.789	1.876
CH_2CH_3	0.891	1.220	1.925	2.108	2.191	2.248	2.313
$CH_2CH_2CH_3$	0.980	1.311	2.035	2.225	2.313	2.373	2.475
$CH_2C_6H_4(OCH_3)$	1.033	1.533	2.750	3.102	3.269	3.385	3.521
$CH_3C(O)$	1.083	1.443	2.224	2.428	2.521	2.585	2.681
CF_2CH_3	1.113	1.458	2.136	2.301	2.375	2.425	2.516
$CH_2C_6H_4(CH_3)$	1.157	1.685	2.946	3.307	3.477	3.595	3.722
CH_2CHCH_2	1.161	1.646	2.730	3.023	3.158	3.251	3.386
HC(O)	1.172	1.565	2.353	2.547	2.634	2.694	2.816
CH_3	1.209	1.632	2.524	2.751	2.854	2.924	3.046
$CH_2C_6H_5$	1.239	1.798	3.111	3.482	3.656	3.777	3.914
$CHCH_2$	1.252	1.711	2.661	2.902	3.011	3.086	3.210
$CH_2C_6H_4(F)$	1.265	1.807	3.046	3.391	3.552	3.663	3.781
$C_6H_4(CH_3)$	1.384	1.886	2.919	3.182	3.302	3.383	3.533
$C_6H_4(OCH_3)$	1.398	1.909	2.953	3.216	3.335	3.416	3.556
C_6H_5	1.405	1.913	2.946	3.207	3.325	3.406	3.553
CCl_3	1.480	1.999	3.028	3.280	3.393	3.470	3.573
$C(CN)(CH_3)_2$	1.495	2.051	3.179	3.463	3.592	3.680	3.857
$C_6H_4(F)$	1.579	2.101	3.120	3.370	3.482	3.559	3.694
CF_3	1.672	2.159	3.016	3.207	3.292	3.348	3.445
NF_2	1.849	2.391	3.287	3.478	3.560	3.615	3.795
$C_6H_4(CN)$	1.857	2.384	3.366	3.602	3.707	3.778	3.897
NH_2	1.871	2.468	3.543	3.786	3.893	3.964	4.216
$CH_2C_6H_4(CN)$	1.878	2.630	4.319	4.787	5.005	5.157	5.346
OCH_3	1.918	2.720	4.413	4.848	5.047	5.182	5.872
Tert-butoxycarbonylmethyl	1.930	2.607	3.949	4.283	4.434	4.537	4.750
OCH_2CH_3	1.940	2.747	4.483	4.939	5.148	5.290	5.921
$OCH_2C(CH_3)_3$	1.959	2.754	4.449	4.895	5.099	5.239	5.761
CH_2CN	2.003	2.715	4.100	4.435	4.585	4.686	4.921
SCH_3	2.054	3.103	5.939	6.849	7.295	7.611	7.915
H	2.063	2.662	4.001	4.346	4.503	4.610	–
SCH_2CH_3	2.078	3.121	5.935	6.838	7.279	7.593	7.791
NO_2	2.118	2.821	4.096	4.388	4.517	4.603	4.898
OC_6H_5	2.236	3.245	5.577	6.234	6.542	6.756	7.267
Tosyl	2.283	3.273	5.501	6.096	6.377	6.571	7.021
Phenylsulfonyl	2.358	3.345	5.514	6.094	6.361	6.545	6.959
OH	2.462	3.420	5.319	5.785	5.994	6.135	6.943
SH	2.520	3.755	7.054	8.101	8.612	8.973	9.345
2,2-Dimethyl-4,6-dioxo-1,3-dioxan-5-yl	3.017	4.078	6.095	6.582	6.799	6.947	7.279
Br	3.614	5.295	9.405	10.610	11.182	11.581	12.672
Cl	3.772	5.439	9.224	10.265	10.749	11.083	11.884
F	3.954	5.238	7.424	7.899	8.106	8.244	8.762
CN	4.119	5.607	8.397	9.050	9.339	9.534	10.156

[a] Using IEF-PCM in Gaussian09

[b] Using COSMO in MOLPRO 2010.1

Fig. 3 Correlation of the global electrophilicity index in water, calculated with IEF-PCM in Gaussian09 and with COSMO in MOLPRO 2010.1

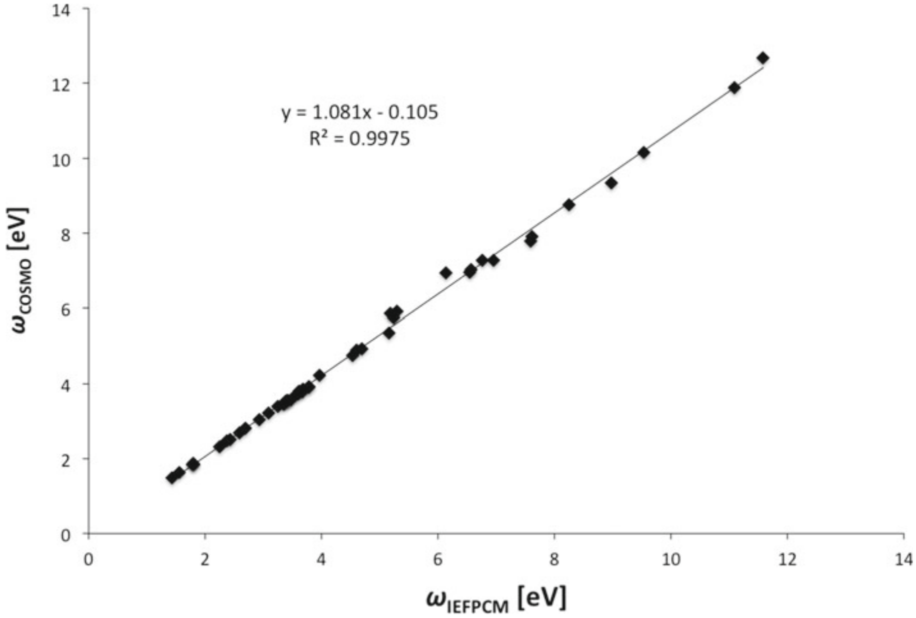

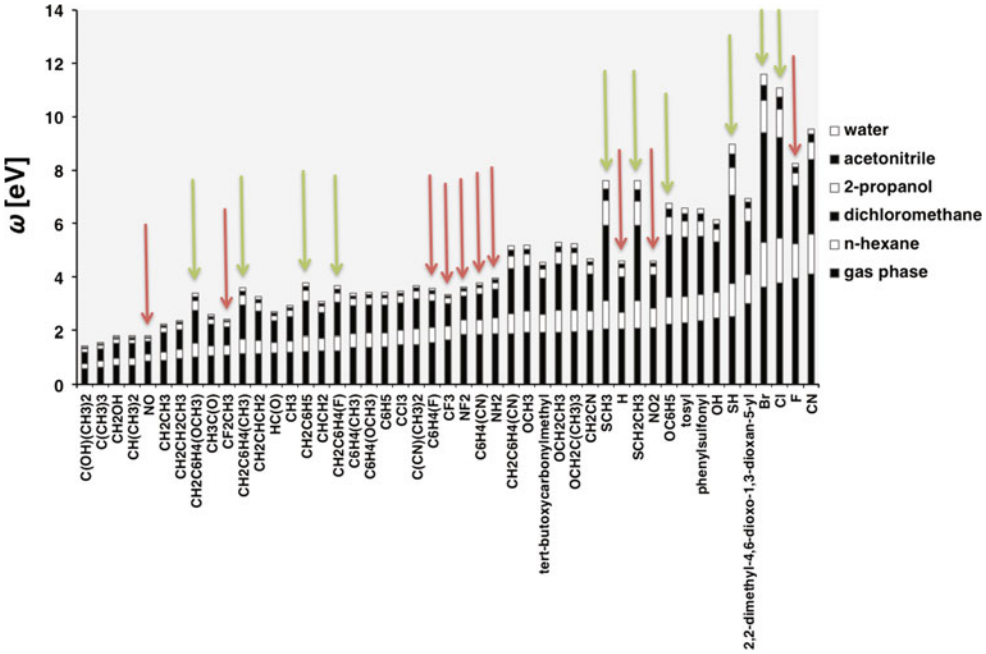

Fig. 4 Global electrophilicity index ω for a total of 47 radicals in gas phase and different solvents. *Green arrows*: radicals with the biggest increase in η. *Red arrows*: radicals with the lowest increase in η, going from gas phase to water

3.3 Global electrophilicity index

Combining the solvent effects on μ and η, we can determine the effect on the radical electrophilicity index ω. The values for ω in gas phase and solvent (IEF-PCM and COSMO) can be found in Table 3. In Fig. 3 the correlation between the IEF-PCM and COSMO electrophilicity values is depicted. The agreement between the two implicit solvation models is excellent with a correlation coefficient of 0.9975 and an almost perfectly linear 1-to-1 correspondence (slope of 1.081 and intercept of −0.105 eV). On the basis of this correlation, artifacts induced by the use of one of the two solvation models can be excluded. Figure 4 shows the global electrophilicity index for all radicals,

Table 4 The local electrophilicity index, condensed to the radical center, ω_{rc}^{+}, for the gas phase and 5 different solvents (using IEFPCM) in eV

Radical	Gas phase	*n*-Hexane[a]	Dichloromethane[a]	2-Propanol[a]	Acetonitrile[a]	Water[a]
$C(OH)(CH_3)_2$	0.254	0.387	0.697	0.786	0.829	0.858
$C(CH_3)_3$	0.376	0.544	0.849	0.923	0.964	0.993
CH_2OH	0.447	0.705	1.348	1.519	1.609	1.672
$CH(CH_3)_2$	0.460	0.717	1.285	1.440	1.509	1.556
NO	0.499	0.655	1.074	1.187	1.240	1.276
CH_2CH_3	0.502	0.763	1.423	1.618	1.710	1.775
$CH_2CH_2CH_3$	0.537	0.766	1.292	1.435	1.501	1.547
$CH_2C_6H_4(OCH_3)$	0.546	0.818	1.495	1.693	1.786	1.851
$CH_3C(O)$	0.555	0.735	1.059	1.133	1.165	1.187
CF_2CH_3	0.559	0.756	1.220	1.321	1.378	1.417
$CH_2C_6H_4(CH_3)$	0.571	0.843	1.503	1.693	1.782	1.844
CH_2CHCH_2	0.594	0.928	1.716	1.938	2.042	2.114
HC(O)	0.611	0.893	1.439	1.568	1.627	1.668
CH_3	0.621	0.955	1.707	1.920	2.019	2.087
$CH_2C_6H_5$	0.653	0.949	1.636	1.828	1.917	1.980
$CHCH_2$	0.654	0.887	1.391	1.520	1.578	1.618
$CH_2C_6H_4(F)$	0.693	1.015	1.709	1.891	1.975	2.033
$C_6H_4(CH_3)$	0.693	0.961	1.516	1.655	1.718	1.761
$C_6H_4(OCH_3)$	0.698	0.998	1.702	1.900	1.993	2.058
C_6H_5	0.699	0.960	1.484	1.615	1.675	1.715
CCl_3	0.712	1.000	1.631	1.797	1.872	1.924
$C(CN)(CH_3)_2$	0.767	1.037	1.540	1.657	1.709	1.744
$C_6H_4(F)$	0.781	1.164	1.995	2.218	2.321	2.391
CF_3	0.808	1.192	2.036	2.259	2.362	2.432
NF_2	0.811	1.189	2.015	2.235	2.336	2.405
$C_6H_4(CN)$	0.824	1.176	1.952	2.157	2.250	2.314
NH_2	0.929	1.323	2.149	2.363	2.460	2.527
$CH_2C_6H_4(CN)$	1.062	1.455	2.268	2.472	2.564	2.627
OCH_3	1.183	1.544	2.200	2.349	2.415	2.460
Tert-butoxycarbonylmethyl	1.188	1.612	2.523	2.757	2.864	2.936
OCH_2CH_3	1.208	1.653	2.553	2.779	2.881	2.951
$OCH_2C(CH_3)_3$	1.257	1.651	2.316	2.459	2.522	2.563
CH_2CN	1.286	1.755	2.682	2.908	3.011	3.080
SCH_3	1.311	1.942	3.295	3.656	3.819	3.931
H	1.330	1.945	3.259	3.607	3.766	3.876
SCH_2CH_3	1.416	2.034	3.377	3.724	3.882	3.990
NO_2	1.423	1.959	3.016	3.276	3.393	3.472
OC_6H_5	1.715	2.665	5.277	6.117	6.529	6.821
Tosyl	1.754	2.713	5.341	6.189	6.605	6.900
Phenylsulfonyl	1.822	2.410	3.488	3.734	3.843	3.915
OH	2.063	2.662	4.001	4.346	4.503	4.610
SH	2.378	3.314	5.185	5.645	5.851	5.991
2,2-Dimethyl-4,6-dioxo-1,3-dioxan-5-yl	2.475	3.702	6.999	8.049	8.560	8.923
Br	2.687	3.737	5.777	6.265	6.482	6.629
Cl	3.614	5.295	9.405	10.610	11.182	11.581
F	3.772	5.439	9.224	10.265	10.749	11.083
CN	3.954	5.238	7.424	7.899	8.106	8.244

[a] Using IEF-PCM in Gaussian09

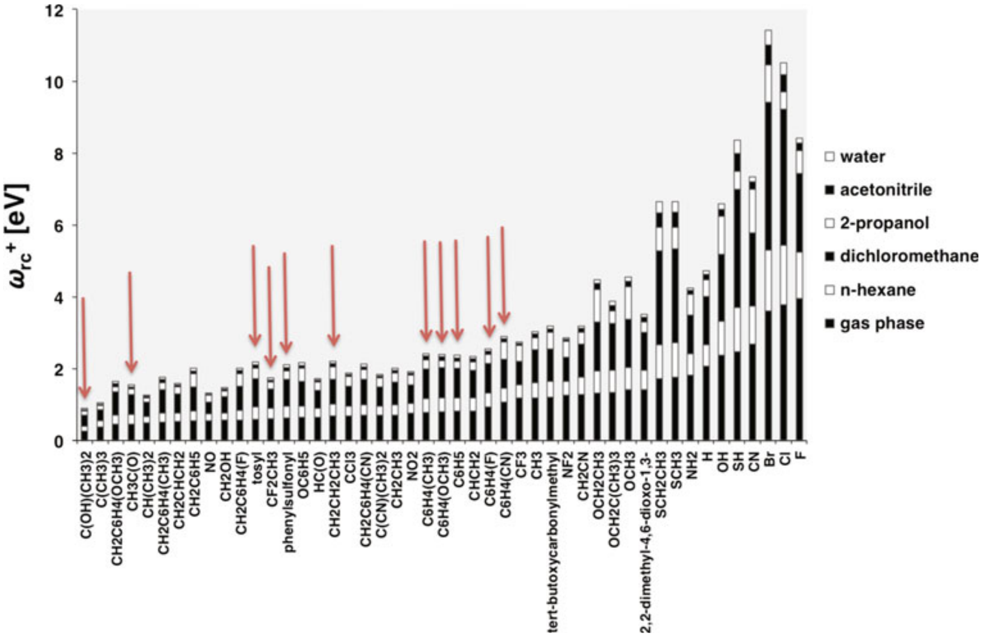

Fig. 5 Local electrophilicity index, condensed on the radical center, ω_{rc}^{+}, for a total of 47 radicals in gas phase and different solvents. The *arrows point* to those radicals for which the Fukui function for a nucleophilic attack f_{rc}^{+} shows the biggest increase, going from gas phase to water

starting with the gas-phase values and increasing up to the water values. Again, the radical systems are ordered according to the gas-phase electrophilicity. All radicals become more electrophilic as the solvent gets more polar. This enhancement in electrophilic power for neutral systems was already highlighted by Pérez et al. [22]. The differences in electrophilicity between the gas phase and the different solvents are following the hardness trend to a great extent. Increasing polarity of the solvent, however, plays a bigger role in the electrophilicity variations, because of the influence of μ_{solv} (squared property in Eq. 1), making the electrophilicity changes not as constant as is the case for the chemical hardness (all in terms of percentage). The overall change ($\omega_{\mathrm{water}} - \omega_{\mathrm{gas}}$) consists of the following average increases: 24.6 % from gas phase to *n*-hexane, 51.6 % to dichloromethane, 13.4 % to 2-propanol, 6.1 % to acetonitrile and finally 4.2 % to water, showing that increasing polarity has a bigger influence on the electrophilicity index than on the chemical hardness. We see that strong electrophilic and strong nucleophilic radicals are also in solution listed at the ends of the electrophilicity scale. The aliphatic thiyl radicals (R–S˙), the benzyl radicals, chlorine and bromine shift toward more electrophilicity because of their softer character in solvent. Fluorine and the radicals with fluorine substituents shift to a less electrophilic place in the table (except for *p*-fluorobenzyl). This confirms that all shifts of importance in the electrophilicity scales can be attributed to the changes in η (as visualized with the green and red arrows in Fig. 4). This also means that for any solvent with a certain dielectric constant, the global electrophilicity of any radical system listed in this work can be calculated from the values in Tables 1 and 2, using for instance an average value for the electronic chemical potential and an interpolated value (using Eq. 6 as mentioned in the previous section) for the chemical hardness.

3.4 Local electrophilicity index, condensed to the radical center

To describe the electrophilic character of a reactive site within a molecule, a local electrophilicity index $\omega^{+}(\mathbf{r})$ has been proposed [41, 42]. The condensed-to-atom k variant is defined as: [3]

$$\omega_k^{+} = \omega f_k^{+} \tag{7}$$

with f^{+} the Fukui function for nucleophilic attack [43]. For the computation of f^{+}, the Finite Differences Approximation (FDA) has been used. In this paper, atomic populations were obtained with the NPA method [44]. For the analysis of electrophile–nucleophile interactions, $\omega^{+}(\mathbf{r})$ is a better reactivity descriptor than the corresponding Fukui function, because the local electrophilicity index is a product of a global (ω) and a local index ($f^{+}(\mathbf{r})$). In this paper we solely report values for the local electrophilicity index condensed to the radical center, ω_{rc}^{+} (with rc = radical center). The values for ω_{rc}^{+} in gas phase and solvents (using IEF-PCM) can be retrieved from Table 4. A mixed influence on ω_{rc}^{+} is observed: on the one hand, the variations in chemical hardness (or in global electrophilicity) and on the other hand, the variations in the Fukui function f^{+}. The largest changes in f^{+} are encountered for the phenyl radicals, 2-hydroxyprop-2-yl, *n*-propyl, acetyl, 1,1-difluoroethyl, tosyl and sulfonyl (Fig. 5). They vary

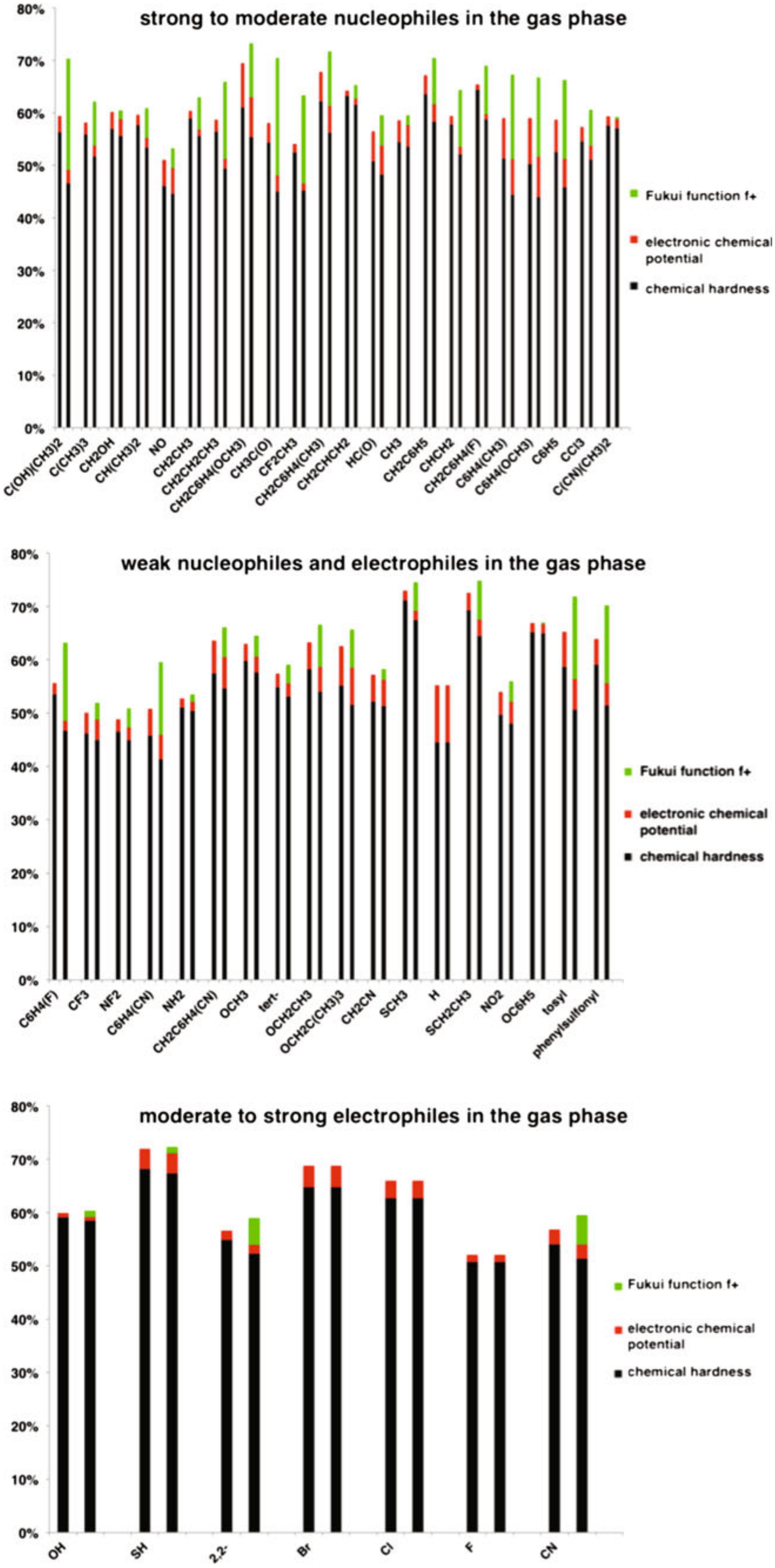

Fig. 6 The influence of the electronic chemical potential and the chemical hardness on the global electrophilicity differences between water and gas phase (*first bar* of each radical) as well as the influence of the global electrophilicity and the Fukui function f^{+} on the local electrophilicity differences (*second bar*)

from 0 % for the atomic radicals and the phenoxy radical to as much as 30 % for acetyl. The average increase is 9 %, much smaller than the change in chemical hardness (average decrease of 60 %), but much more pronounced than the change in electronic chemical potential (average change of 2 %). So the local descriptors are affected less by the solvent used, in agreement with Padmanabhan et al. [45]. The local electrophilicity index, however, is a combination of a local and a global descriptor so both local and global changes are combined. As both the local and the global descriptors change upon solvation, it is advisable to use ω_{rc}^{+} instead of f_{rc}^{+} when investigating and analyzing (intermolecular) electrophile–nucleophile interactions locally. Even though the changes in chemical hardness for any solvent can be predicted from the values in both gas phase and water and from the dielectric constants of those media using Eq. 6, the changes in Fukui function f_{rc}^{+} cannot be predicted straightforwardly and therefore require additional calculations in solution.

4 Conclusions

In summary, the global and local electrophilicity scales for radical systems in the gas phase, as introduced by De Vleeschouwer et al. [1], have been extended to electrophilicity scales for a larger set of radical systems in five different solvents, with a dielectric constant ranging from nonpolar to polar solvent situations. Both the global and local electrophilicity indices follow the trend in chemical hardness changes to a great extent, when going from the gas phase to solution, whereas the electronic chemical potential is found to be almost constant over all solvents and in the gas phase. In addition, it is shown that the chemical hardness changes in percentage are not a function of the type of radical, within the solvent models applied in this study, as can be derived from the approximate (generalized) reaction field Born's model. Figure 6 shows the division into portions due to η, μ and f^{+}, for the changes in ω and ω_{rc}^{+} between the gas phase and water. From these plots it can be seen which radicals are affected more by which property, concerning their change in electrophilicity index value. These new radical electrophilicity scales for solvents can be of great importance to organic chemists in the study of radical reactivity and selectivity in the solvents considered here or for other solvents through interpolation, in case of the global electrophilicity index.

Acknowledgments F.D.V. wishes to acknowledge the Research Foundation-Flanders (FWO) for a postdoctoral fellowship. F.D.P. and P.G. wish to acknowledge the Fund for Scientific Research-Flanders (FWO) and the Free University of Brussels for continuous support to their research group.

References

1. De Vleeschouwer F, Van Speybroeck V, Waroquier M, Geerlings P, De Proft F (2007) Org Lett 9:2721
2. Parr RG, Von Szentpaly L, Liu SB (1999) J Am Chem Soc 121:1922
3. Chattaraj PK, Sarkar U, Roy DR (2006) Chem Rev 106:2065
4. Godineau E, Schenk K, Landais Y (2008) J Org Chem 73:6983
5. Durand G, Choteau F, Pucci B, Villamena FA (2008) J Phys Chem A 112:12498
6. De Dobbeleer C, Pospisil J, De Vleeschouwer F, De Proft F, Marko IE (2009) Chem Comm 16:2142
7. Godineau E, Landais Y (2009) Chem Eur J 15:3044
8. Shih H-W, Vander Wal MN, Grange RL, MacMillan DWC (2010) J Am Chem Soc 132:13600
9. Pratsch G, Anger CA, Ritter K, Heinrich MR (2011) Chem Eur J 17:4104
10. Liautard V, Robert F, Landais Y (2011) Org Lett 13:2658
11. De Vleeschouwer F, Van Speybroeck V, Waroquier M, Geerlings P, De Proft F (2008) J Org Chem 73:9109
12. De Vleeschouwer F, De Proft F, Geerlings P (2010) J Mol Struct-Theochem 943, 1–3(Special Issue):94
13. De Vleeschouwer F, Jaque P, Geerlings P, Toro-Labbé A, De Proft F (2010) J Org Chem 75:4964
14. Hemelsoet K, De Vleeschouwer F, Van Speybroeck V, De Proft F, Geerlings P, Waroquier M (2011) Chem Phys Chem 12:1100
15. Mayr H, Patz M (1994) Ang Chem Int Ed Engl 33:938
16. Mayr H, Kuhn M, Gotta F, Patz MJ (1998) J Phys Org Chem 11:642
17. Mayr H, Ofial AR (2005) Pure Appl Chem 77:1807
18. Bauld NL (1997) Radicals, ion radicals, and triplets: the spin-bearing intermediates of organic chemistry. Wiley-VCH, New York
19. Graeme M, Solomon DH (2006) The chemistry of radical polymerization. Elsevier, Oxford
20. Pearson RG (1986) J Am Chem Soc 108:6109
21. De Luca G, Sicilia E, Russo N, Minerva T (2002) J Am Chem Soc 124:1494
22. Pérez P, Toro-Labbé A, Contreras R (2001) J Am Chem Soc 123:5527
23. Parr RG, Donnelly RA, Levy M, Palke WE (1978) J Chem Phys 68:3801
24. Parr RG, Pearson RG (1983) J Am Chem Soc 105:7512
25. Parr RG, Yang W (1989) Density functional theory of atoms and molecules. Oxford Science Publications, Oxford, New York
26. Meneses L, Fuentealba P, Contreras R (2006) Chem Phys Lett 433:54
27. Geerlings P, De Proft F, Langenaeker W (2003) Chem Rev 103:1793
28. Geerlings P, De Proft F (2008) Phys Chem Chem Phys 10:3028
29. Becke AD (1993) J Chem Phys 98:5648
30. Lee CT, Yang WT, Parr RG (1988) Phys Rev B 37:785
31. Hehre WJ (1976) Acc Chem Res 9:399
32. Frisch MJ et al (2009) Gaussian 09, B.1. Gaussian, Inc.
33. Werner H-J, Knowles PJ, Knizia G, Manby FR, Schütz M et al MOLPRO, version 2010.1, a package of ab initio programs
34. Cances E, Mennucci B, Tomasi J (1997) J Chem Phys 107:3032
35. Tomasi J, Mennucci B, Cances E (1999) J Mol Struct 464:211
36. Tomasi J, Mennucci B, Cammi R (2005) Chem Rev 105:2999
37. Klamt A, Schüürmann G (1993) J Chem Soc Perkin Trans 2:799
38. Cardenas C, Ayers PW, De Proft F, Tozer D, Geerlings P (2011) Phys Chem Chem Phys 13:2285
39. Puiatti M, Vera DMA, Pierini AB (2008) Phys Chem Chem Phys 10:1394
40. Constanciel R, Contreras R (1984) Theor Chim Acta (Berl) 65:1

41. Pérez P, Toro-Labbé A, Aizman A, Contreras RJ (2002) J Org Chem 67:4747
42. Chamorro E, Chattaraj PK, Fuentealba P (2003) J Phys Chem A 107:7068
43. Parr RG, Yang WT (1984) J Am Chem Soc 106:4049
44. Reed AE, Curtiss LA, Weinhold F (1988) Chem Rev 88:899
45. Padmanabhan J, Parthasarathi R, Sarkar U, Subramanian V, Chattaraj PK (2004) Chem Phys Lett 383:122

Theor Chem Acc (2012) 131:1246
DOI 10.1007/s00214-012-1246-3

REGULAR ARTICLE

S_5 graphs as model systems for icosahedral Jahn–Teller problems

**A. Ceulemans · E. Lijnen · P. W. Fowler ·
R. B. Mallion · T. Pisanski**

Received: 2 April 2012 / Accepted: 7 June 2012 / Published online: 26 June 2012

Abstract The degeneracy of the eigenvalues of the adjacency matrix of graphs may be broken by non-uniform changes of the edge weights. This symmetry breaking is the graph-theoretical equivalent of the molecular Jahn–Teller effect (Ceulemans et al. in Proc Roy Soc 468:971–989, 2012). It is investigated for three representative graphs, which all have the symmetric group on 5 elements, $\mathbf{S_5}$, as automorphism group: the complete graph K_5, with 5 nodes, the Petersen graph, with 10 nodes, and an extended K_5 graph with 20 nodes. The spectra of these graphs contain fourfold, fivefold, and sixfold degenerate manifolds, respectively, and provide model systems for the study of the Jahn–Teller effect in icosahedral molecules. The $\mathbf{S_5}$ symmetries of the distortion modes of the quintuplet in the Petersen graph yield a resolution of the product multiplicity in the corresponding $H \otimes (g + 2h)$ icosahedral Jahn–Teller problem. In the extended Petersen graph with 20 nodes, a selection rule prevents the Jahn–Teller splitting of the sextuplet into two conjugate icosahedral triplets.

Keywords Jahn–Teller effect · Icosahedral symmetry · $\mathbf{S_5}$ symmetry · Spectral graph-theory · Electronic/spectral degeneracy

1 Introduction

Symmetry may give rise to electronic degeneracy. A molecule in a degenerate state cannot be described by a single wave function. Instead, it will be characterized by a set of eigenfunctions, forming a so-called function space. Any linear combination of eigenfunctions corresponding to a direction in this space is a valid description of the state of the molecule. According to the Jahn–Teller (JT) theorem, this is not a stable situation. While the function space as a whole is an invariant of the molecular symmetry, this is not the case for the individual eigenfunctions. As a result, there will be an imbalance between the symmetric charge distribution of the nuclei and the non-symmetric charge distribution of the electronic state, giving rise to an electric force, which distorts the molecule to a structure of lower symmetry where the degeneracy is lifted [1, 2]. Molecular graphs are concise representations of molecules, which reduce a molecule to a set of atoms or 'nodes' connected by a network of bonds or 'lines' [3]. The graph-theoretical equivalent of the molecular symmetry group is the automorphism group of the graph. The elements of this group are the permutations of nodes that keep the bonding network of the graph intact. The 'states' of the graph correspond to the eigenfunctions and eigenvalues of its adjacency matrix, the latter being the *spectrum* of the graph. These analogies between molecules and graphs have

---

Published as part of the special collection of articles celebrating theoretical and computational chemistry in Belgium.

A. Ceulemans (✉) · E. Lijnen
Division of Quantum Chemistry and Physical Chemistry,
Department of Chemistry, K. U. Leuven, Celestijnenlaan 200F,
3001 Heverlee, Belgium
e-mail: arnout.ceulemans@chem.kuleuven.be

P. W. Fowler
Department of Chemistry, University of Sheffield,
Sheffield S3 7HF, UK

R. B. Mallion
School of Physical Sciences, University of Kent,
Canterbury CT2 7NH, UK

T. Pisanski
Faculty of Mathematics and Physics, University of Ljubljana,
Jadranska 19, 1000 Ljubljana, Slovenia

made us wonder whether there might also exist a graph-theoretical equivalent of the JT theorem. In a previous publication we have formulated the conjecture that *whenever the spectrum of a graph contains a set of non-zero degenerate eigenvalues, the roots of the Hamiltonian matrix over this set will show a linear dependence on edge distortions, which has the effect of lifting the degeneracy* [4]. The derivatives with respect to the distortion modes are the essential coupling parameters. These parameters are graph invariants. The graph-theoretical analogue of the JT theorem will hold whenever these parameters are different from zero. For non-bonding degenerate-eigenlevels, that is, with eigenvalue zero, there will be edge distortions in the active space that cannot couple to the degeneracy and then distortions of the vertex weights must also be included, in order to complete the JT Hamiltonian.

This conjecture has implications in both directions. It extends the notion of distortivity of a graph [5] by relating it to the coupling parameters associated with degeneracies in graph spectra. From the molecular point of view, graphs provide new models for the treatment of JT interactions. In the present article, we shall use the conjecture to study the JT effect for icosahedral orbital degeneracies. Three graphs of increasing complexity will be used in order to model fourfold, fivefold, and pairs of threefold degenerate-states in icosahedra. They are, respectively, the complete graph with five nodes, the Petersen graph, with 10 nodes, and an extended K_5 graph with 20 nodes. The automorphism group of each of these graphs is the symmetric group on five elements, $\mathbf{S_5}$, of order 120. The subgroup of even permutations is the alternating group, $\mathbf{A_5}$, of order 60. The symmetry point group of the icosahedron, $\mathbf{I_h}$, also has 120 elements, but it is not isomorphic to $\mathbf{S_5}$. Its rotational subgroup, $\mathbf{I}$, is, however, isomorphic to $\mathbf{A_5}$. The present treatment relies on this correspondence.

2 $\mathbf{S_5}$ graphs

In Fig. 1 we illustrate the three graphs of increasing sophistication on which the present treatment is based. The smallest graph in Fig. 1a is the fully connected 5-vertex graph, which is the skeleton of the simplex in 4D space. This is the complete graph with 5 vertices, known as K_5. Its automorphism group corresponds to the symmetric group on 5 elements. The corresponding permutations are denoted by their cycle structure. A mapping of type $\{a \rightarrow b\}\{b \rightarrow a\}\{c \rightarrow d\}\{d \rightarrow e\}\{e \rightarrow c\}$ has two cycles, of length 2 and 3, respectively, and is abbreviated as $(ab)(cde)$. All operations with the same cycle structure belong to the same conjugacy class, which is thus characterized uniquely by the cycle lengths. For the present example this is: {2,3}. For convenience, the character table of this group is reproduced here (Table 1). Irreducible representations (irreps) are denoted by the partitions of 5 cells in a Young tableau [6]. We have also introduced corresponding character labels, based on the icosahedral point group. The letters A, G, H, and I refer to one-, four-, five-, and sixfold degenerate representations, and the subscripts 1 or 2 distinguish representations that are symmetric or antisymmetric with respect to the $\mathbf{A_5}$ subgroup of even permutations. The A_2 irrep is the so-called pseudo-scalar representation. It is symmetric for even permutations and anti-symmetric for odd permutations. Multiplication by A_2 will interchange symmetric and anti-symmetric irreps. Note that all representations occur in pairs, apart from I, which has zero character for the odd permutations, and are thus not affected by multiplication with A_2.

The Petersen graph, shown in Fig. 1b, is a 10-vertex graph, which also has the $\mathbf{S_5}$ automorphism group. In Table 2 we list the corresponding cycle structure for the different $\mathbf{S_5}$ operations, as well as explicit forms of the generators. The Petersen graph is 3-regular and contains 15 edges. All these edges can be permuted into each other by the $\mathbf{S_5}$ operations, and they are therefore said to form a

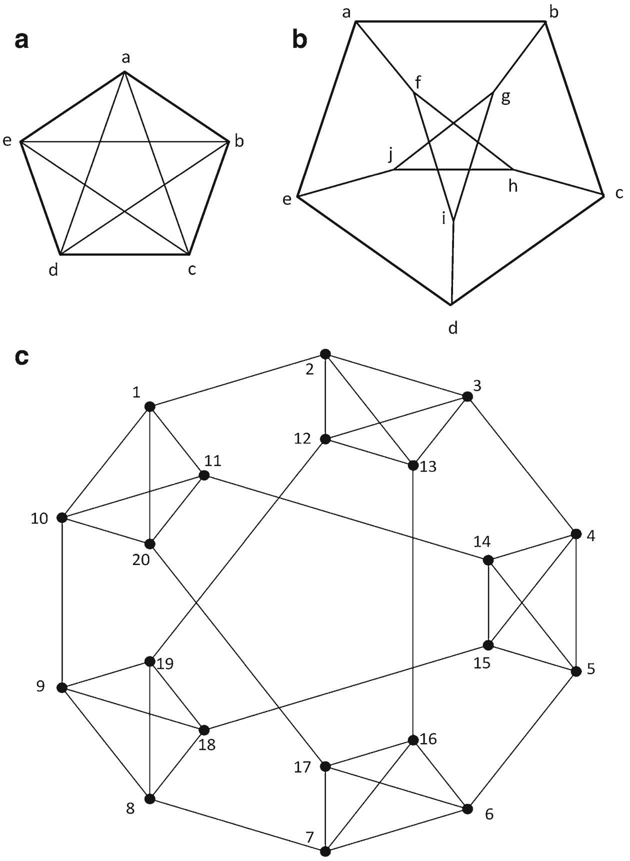

Fig. 1 Three graphs with automorphism group $\mathbf{S_5}$: **a** the complete 5-graph, K_5; **b** the (10-vertex) Petersen graph; **c** an extended K_5 graph with 20 vertices

Table 1 Character table for the symmetric group $\mathbf{S_5}$ and its alternating subgroup $\mathbf{A_5} \sim \mathbf{I}$ with: $\phi = \frac{1}{2}\left(1+\sqrt{5}\right) \quad -\phi^{-1} = \frac{1}{2}\left(1-\sqrt{5}\right)$

$\mathbf{S_5}$	$\{1^5\}$	$\{1^3,2\}$	$\{1^2,3\}$	$\{1,2^2\}$	$\{1,4\}$	$\{2,3\}$	$\{5\}$
	1	10	20	15	30	20	24
A_1 (5)	1	1	1	1	1	1	1
G_1 (4,1)	4	2	1	0	0	−1	−1
H_1 (3,2)	5	1	−1	1	−1	1	0
I $(3,1^2)$	6	0	0	−2	0	0	1
H_2 $(2^2,1)$	5	−1	−1	1	1	−1	0
G_2 $(2,1^3)$	4	−2	1	0	0	1	−1
A_2 (1^5)	1	−1	1	1	−1	−1	1

$\mathbf{A_5}$ $\mathbf{I}$	$\{1^5\}$ E 1	$\{1^2,3\}$ C_3 20	$\{1,2^2\}$ C_2 15	$\{5\}$ C_5 12	$\{5\}$ C_5^2 12
A	1	1	1	1	1
G	4	1	0	−1	−1
H	5	−1	1	0	0
T_1	3	0	−1	φ	$-\varphi^{-1}$
T_2	3	0	−1	$-\varphi^{-1}$	φ

Table 2 Cycle structure and generators for the Petersen graph

Class dimension	$\mathbf{S_5}$	Petersen	
1	$\{1^5\}$	$\{1^{10}\}$	(a)(b)(c)(d)(e)(f)(g)(h)(i)(j)
10	$\{1^3,2\}$	$\{1^4,2^3\}$	(a)(b)(c)(g)(ef)(dh)(ij)
20	$\{1^2,3\}$	$\{1,3^3\}$	(a)(efb)(dhg)(cji)
15	$\{1,2^2\}$	$\{1^2,2^4\}$	(a)(f)(be)(cd)(gj)(hi)
30	$\{1,4\}$	$\{2,4^2\}$	(ch)(agei)(bjdf)
20	$\{2,3\}$	$\{1,3,6\}$	(a)(efb)(gjhcdi)
24	$\{5\}$	$\{5^2\}$	(abcde)(fghij)

Table 3 Cycle structure and generators for the 20-graph

Class dimension	$\mathbf{S_5}$	20-graph	
1	$\{1^5\}$	$\{1^{20}\}$	(1)(2)…(20)
10	$\{1^3,2\}$	$\{1^6,2^7\}$	(1)(2)(13)(16)(17)(20)(3,12)(4,19)(5,8)(6,7)(9,14)(10,11)(15,18)
20	$\{1^2,3\}$	$\{1^2,3^6\}$	(15)(18)(1,17,13)(2,20,16)(3,11,6)(4,14,5)(10,7,12)
15	$\{1,2^2\}$	$\{2^{10}\}$	(1,10)(2,9)(3,8)(4,7)(5,6)(11,20)(12,19)(13,18)(14,17)(15,16)
30	$\{1,4\}$	$\{4^5\}$	(1,16,4,19)(2,13,3,12)(11,7,14,8)(10,17,5,18)(20,6,15,9)
20	$\{2,3\}$	$\{2,3^2,6^2\}$	(15,18) (1,13,17)(2,16,20)(3,7,11,12,6,10) (4,8,14,19,5,9)
24	$\{5\}$	$\{5^4\}$	(1,3,5,7,9)(10,2,4,6,8)(11,13,15,17,19)(20,12,14,16,18)

transitive set or an orbit. The Petersen graph is non-planar, which means that it cannot be drawn in the plane or on the surface of a sphere without intersections. It can, however, be mapped onto a projective plane.

A further graph with $\mathbf{S_5}$ symmetry is the 20-vertex graph shown in Fig. 1c. This graph is obtained as an extension of K_5 [7]. A comparison between K_5 and the 20-vertex graph shows that the original nodes of the complete graph K_5 are replaced, or 'truncated', by copies of K_4. In Table 3 we describe the corresponding cycle structure and generators. This graph is 4-regular and contains 40 edges. In contrast to the previous graphs, these edges form two separate orbits, an orbit of order 10 and an orbit of order 30. The edges of the five K_4 subgraphs form the 30-edge orbit, while the 10 remaining edges correspond to the original connectivity of the K_5 parent graph.

3 The complete 5-vertex graph K_5 and the fourfold degeneracy

The group of icosahedral rotations contains a maximal subgroup of tetrahedral rotations, **T**, describing rotations that leave an inscribed cube invariant. Euclid's construction of the dodecahedron is based on this relationship [8]. The ratio of the orders of the groups **I** and **T** is 60/12 = 5. Five different cubes can thus be inscribed. This set of cubes is doubly transitive, that is, there always exists a symmetry operation in the group that can map any ordered pair of elements of the set onto any other ordered pair. Clearly, the five elements of a doubly transitive set will thus correspond to the vertices of K_5. The spectrum of an n-vertex complete graph has one totally symmetric non-degenerate root, with eigenvalue $n-1$, while the remaining roots form a $(n-1)$-fold degenerate irrep, with eigenvalue -1. The graph spectrum is denoted $\left\{(n-1),(-1)^{n-1}\right\}$. The spectrum of K_5 thus contains a fourfold degenerate G representation, which may stand as a model for the icosahedral fourfold degenerate representation. The $G \otimes (g+h)$ Hamiltonian for this manifold has been described previously, and its relationship to the $\mathbf{S_5}$ graph has also been demonstrated [9, 10]. We briefly recapitulate the results. To apply the graph-theoretical JT theorem, we start from the eigenvectors associated with the -1 roots. They appear as linear combinations of the five nodes. Each node will be presented by a ket symbol. The *k*th eigenvector is given by:

$$|k> \;= \sum_{i=1}^{n} c_i^k |i> \tag{1}$$

In case of the orbital quadruplet, the components of the function space are labeled as (*a,x,y,z*) following the Boyle and Parker conventions [11]. The vertices are labeled as in Fig. 1a. The orthonormal form of the function space is given by:

$$\begin{aligned} |Ga> &= \frac{1}{2\sqrt{5}}(4|a> - |b> - |c> - |d> - |e>) \\ |Gx> &= \frac{1}{2}(-|b> + |c> - |d> + |e>) \\ |Gy> &= \frac{1}{2}(|b> - |c> - |d> + |e>) \\ |Gz> &= \frac{1}{2}(-|b> - |c> + |d> + |e>) \end{aligned} \tag{2}$$

The operator corresponding to the linear JT Hamiltonian is expressed as:

$$H = \sum_{i<j} \gamma\, \Delta r_{ij} (|i> <j| + |j> <i|) \tag{3}$$

Here, γ is a constant factor, corresponding to the first-order distance-derivative of the interaction-matrix element. The JT interaction matrix is obtained by acting with this operator in the function space. In general:

$$H_{kl} = \sum_i \sum_j \gamma\, \Delta r_{ij} \left(c_i^k c_j^l + c_j^k c_i^l \right) \tag{4}$$

As we have shown elsewhere, the coefficients in this expression correspond to the elements of the bond-order matrix [4]. Because the JT Hamiltonian is Hermitian and invariant under time reversal, it is represented by a symmetric matrix in a real function space. The symmetries of this interaction matrix will therefore correspond to the symmetrized direct square of the degenerate irrep of the function space. This part of the direct square is represented by square brackets. The corresponding character is given by [8]:

$$\chi^{[\Gamma]^2}(R) = \frac{1}{2}\left(\left(\chi^{\Gamma}(R)\right)^2 + \chi^{\Gamma}(R^2) \right) \tag{5}$$

In Table 4, we show how this applies to the direct square of the G representation. It reduces as follows:

$$[G \otimes G] = A_1 + G_1 + H_1 \tag{6}$$

The A_1 component is totally symmetric and cannot change the symmetry, but the G + H part of the interaction matrix contains the JT-active modes. On the other hand, the distortion space of the graph corresponds to the elongations and contractions of its edges (i.e., a decrease or increase in the weights of its edges). The automorphism group of the graph maps edges onto edges, which implies that the symmetry of the distortion space is given by the edge representation, denoted as Γ_e. Character reduction shows that the 10 edges transform in exactly the same way as the $[G \otimes G]$ symmetrized square. Hence, in the $\mathbf{S_5}$ graph the edge distortions, minus the totally symmetric component, coincide exactly with the JT modes that will lift the quadruplet degeneracy. This result can be shown to be true for every complete graph [10]. Indeed, in general, the edge representation can be obtained by forming the symmetrized square of the vertex representation, Γ_v. As mentioned earlier, for K_5 this vertex representation contains the totally symmetric component and an $(n - 1)$-fold degenerate irrep:

$$\Gamma_v = \Gamma_0 + \Gamma_{n-1} \tag{7}$$

The edges are formed by all pairwise combinations of vertices, omitting self-interactions. The latter interactions transform as Γ_v. The edge symmetries thus precisely correspond to the symmetrized square of Γ_v minus the on-site representation:

$$\begin{aligned} \Gamma_e &= [\Gamma_v \otimes \Gamma_v] - \Gamma_v \\ &= [(\Gamma_0 + \Gamma_{n-1}) \otimes (\Gamma_0 + \Gamma_{n-1})] - \Gamma_v \\ &= [\Gamma_{n-1} \otimes \Gamma_{n-1}] \end{aligned} \tag{8}$$

The full Hamiltonian for the G-state in the graph has been given elsewhere [9]. The molecular JT problem has two minimal-energy solutions: one tetrahedral along the G-distortion, and one trigonal, along a combination of G and H. The corresponding coupling constants depend on the

Table 4 Derivation of the characters for the symmetrized direct square $[G \otimes G]$ in $\mathbf{S_5}$

G	$\{1^5\}$	$\{1^3,2\}$	$\{1^2,3\}$	$\{1,2^2\}$	$\{1,4\}$	$\{2,3\}$	$\{5\}$
	1	10	20	15	30	20	24
χ(R)	4	2	1	0	0	−1	−1
χ^2(R)	16	4	1	0	0	1	1
$\chi(R^2)$	4	4	1	4	0	1	−1
[G × G]	10	4	1	2	0	1	0

The final row is the average of the two preceding rows (see Eq. 5)

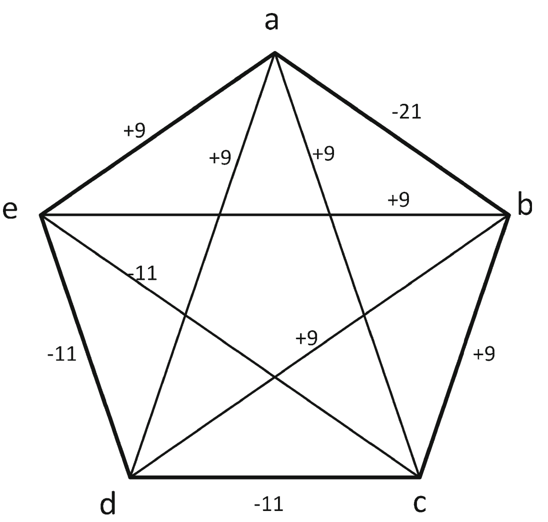

Fig. 2 Edge distortions of the complete graph K_5 that lead to an absolute trigonal minimum (unnormalized)

detailed nature of the molecular interactions. However, in a graph there is only one fundamental constant, γ, which implies that the ratio of the coupling constants for the different distortion modes will be fixed. For K_5, the respective slopes are $-\sqrt{3/5}\,\gamma \approx -0.775\,\gamma$ for the tetrahedral distortion, versus $-\sqrt{3/2}\,\gamma \approx -1.225\,\gamma$ for the trigonal distortion. Hence, the most efficient way to lift the degeneracy of this graph is by means of a trigonal distortion. The threefold symmetry is directed along one of the ten edges. Ten equivalent trigonal distortion paths thus exist. One of these is represented in Fig. 2. The map that connects adjacent minima is precisely the Petersen graph [9].

4 The Petersen graph and the fivefold degeneracy

The group of icosahedral rotations also contains a maximal pentagonal subgroup, $\mathbf{D_5}$, which leaves a pentagonal antiprism invariant. The ratio of group orders is 60/10 = 6, corresponding to the presence of six pentagonal directions. This set of six is also doubly transitive and therefore gives rise to a fivefold degenerate representation, which is the highest orbital degeneracy of the point groups. This quintuplet will appear in the spectrum of the fully connected graph on six elements, with the symmetric group $\mathbf{S_6}$ as automorphism group. In the same way as the quadruplet was related to K_5, the K_6-graph offers a model for analyzing the JT activity of the quintuplet. The connection is based on a special embedding of $\mathbf{I}$ in $\mathbf{S_6}$ and has been elaborated in previous contributions [2, 10]. At present, we propose a different model for the quintuplet symmetry breaking, using $\mathbf{S_5}$ instead of $\mathbf{S_6}$. For this purpose we investigate the 10-vertex Petersen graph. Its automorphism group is isomorphic with the symmetric group $\mathbf{S_5}$ on 5 objects, but in addition, it has a fivefold degenerate root. The graph spectrum is $\left\{3, 1^5, (-2)^4\right\}$. The Petersen graph is thus an example of an integral graph, one that has only integer eigenvalues. The 10 vertices of the Petersen graph can be shown to transform as:

$$\Gamma_v = A_1 + G_1 + H_1 \tag{9}$$

As was already mentioned in the previous section, the Petersen graph provides a map of the space of trigonal distortions of an icosahedron. Such distortions arise not only in the quadruplet but also in the quintuplet problem. Since the spectrum has both G and H states, tunneling ground states of the dynamic JT problem can have A, G, or H symmetries, and this may give rise to different JT dynamics [12]. The present section studies the H_1 state of the Petersen graph, which corresponds to the orbital quintuplet. If each node provides one electron, the fivefold degenerate level at $E = 1$ will host 8 electrons. The JT problem is thus concerned with distributing four electron pairs over five orbitals. The JT active modes can be identified by taking the symmetrized product of this representation minus the totally symmetric irrep.

$$[H_1 \otimes H_1] - A_1 = G_1 + H_1 + H_2 \tag{10}$$

The fifteen edges transform as:

$$\Gamma_e = A_1 + G_1 + H_1 + H_2, \tag{11}$$

which indicates that the edge distortions again correspond exactly with the JT-active modes plus the totally symmetric component. The subsequent analysis is based on the general treatment of the $H \otimes (g + 2h)$ JT Hamiltonian [13]. It starts with a symmetry adaptation of the five eigenvectors of our orbital quintuplet.

$$\begin{aligned}
|\theta\rangle &= \frac{1}{2\sqrt{3}}(-|b\rangle + 2|c\rangle - 2|d\rangle + |e\rangle + |h\rangle - |i\rangle)\\
|\varepsilon\rangle &= \frac{1}{2}(|b\rangle + |e\rangle - |h\rangle - |i\rangle)\\
|\xi\rangle &= \frac{1}{\sqrt{6}}(|a\rangle - |b\rangle + |f\rangle - |g\rangle - |h\rangle + |j\rangle)\\
|\eta\rangle &= \frac{1}{\sqrt{6}}(|a\rangle - |e\rangle + |f\rangle + |g\rangle - |i\rangle - |j\rangle)\\
|\zeta\rangle &= \frac{1}{\sqrt{6}}(-|a\rangle - |c\rangle - |d\rangle + |f\rangle + |g\rangle + |j\rangle)
\end{aligned} \tag{12}$$

A general eigenstate of the Hamiltonian can now be represented as:

$$|\Psi\rangle = \theta|\theta\rangle + \varepsilon|\varepsilon\rangle + \xi|\xi\rangle + \eta|\eta\rangle + \zeta|\zeta\rangle \tag{13}$$

with five normalized c-coefficients:

$$\theta^2 + \varepsilon^2 + \xi^2 + \eta^2 + \zeta^2 = 1 \tag{14}$$

Since the orbital quintuplet has eigenvalue different from zero, the full JT Hamiltonian can be expressed solely as a

Table 5 Normalized JT-active modes for the $H_1 \otimes (G_1 + H_1 + H_2)$ problem

	ab	*ae*	*af*	*cd*	*hj*	*ig*	*bg*	*de*	*fh*	*if*	*ej*	*bc*	*di*	*ch*	*gj*
Q_{G_1}															
$3\sqrt{10} \times Q_1$	2	2	2	2	2	2	−3	−3	−3	−3	−3	−3	2	2	2
$\sqrt{6} \times Q_2$	0	0	0	0	0	0	1	1	1	−1	−1	−1	0	0	0
$3\sqrt{2} \times Q_3$	1	−2	1	1	1	−2	0	0	0	0	0	0	1	−2	1
$\sqrt{6} \times Q_4$	1	0	−1	−1	1	0	0	0	0	0	0	0	1	0	−1
Q_{H_1}															
$3\sqrt{2} \times Q_5$	2	2	2	−1	−1	−1	0	0	0	0	0	0	−1	−1	−1
$4 \times Q_6$	0	0	0	1	1	−2	−1	0	1	−1	0	1	−1	2	−1
$4\sqrt{3} \times Q_7$	0	0	0	3	−3	0	−1	2	−1	1	−2	1	3	0	−3
$12 \times Q_8$	2	−4	2	−1	−1	2	3	−6	3	3	−6	3	−1	2	−1
$4\sqrt{3} \times Q_9$	2	0	−2	1	−1	0	3	0	−3	−3	0	3	−1	0	1
Q_{H_2}															
$\sqrt{6} \times Q_{10}$	0	0	0	1	1	1	0	0	0	0	0	0	−1	−1	−1
$4\sqrt{3} \times Q_{11}$	0	0	0	1	1	−2	3	0	−3	3	0	−3	−1	2	−1
$4 \times Q_{12}$	0	0	0	1	−1	0	1	−2	1	−1	2	−1	1	0	−1
$4\sqrt{3} \times Q_{13}$	2	−4	2	−1	−1	2	−1	2	−1	−1	2	−1	−1	2	−1
$4 \times Q_{14}$	2	0	−2	1	−1	0	−1	0	1	1	0	−1	−1	0	1

function of distortions of the 15 edges. As a 5 × 5 problem, the traceless JT matrix will contain 14 linearly independent active modes labeled Q_1 up to Q_{14}. Normalized expressions for these modes were derived in such a manner that $\{Q_1, Q_2, Q_3, Q_4\}$, $\{Q_5, Q_6, Q_7, Q_8, Q_9\}$, and $\{Q_{10}, Q_{11}, Q_{12}, Q_{13}, Q_{14}\}$ transform, respectively, as the G_1, H_1, and H_2 irreps of $\mathbf{S_5}$. The results are presented in Table 5. The JT Hamiltonian can be constructed straightforwardly using Eq. 4 and Table 5. In order to find the directions of maximal distortion, we shall follow the method of the iso-stationary function [14]. This method avoids the cumbersome diagonalization of the matrix and immediately leads to the directions of maximal distortion. One first adds to the Hamiltonian an isotropic term, which is proportional to the square of the radius of the active space and, in a molecular context, is called the harmonic restoring potential, V.

$$V = \frac{1}{2}\sum_{i=1}^{14} Q_i^2 \tag{15}$$

The eigenvalue corresponding to the state $|\Psi\rangle$ is given by:

$$E(Q) = V(Q) + \sum_{i,j} c_i c_j H_{ij}(Q) \tag{16}$$

The first term in this equation has a quadratic dependence on Q, whereas the second term has a linear dependence. By minimizing E with respect to the Q's, we thus obtain expressions for the stationary coordinates, $\|Q\|$, as a function of the c-coefficients (in units of γ):

$$\begin{aligned}
\|Q_1\| &= \frac{\sqrt{2}}{9\sqrt{5}}\left[7\theta^2 - 3\varepsilon^2 - 3\xi^2 - 3\eta^2 + 2\zeta^2 + 10\xi\zeta + 10\eta\zeta)\right] \\
\|Q_2\| &= \frac{\sqrt{2}}{3\sqrt{3}}\left[-\xi^2 + \eta^2 + 2\sqrt{3}\theta\varepsilon - 2\xi\zeta + 2\eta\zeta\right] \\
\|Q_3\| &= \frac{\sqrt{2}}{9}\left[-\theta^2 + 3\varepsilon^2 - 2\zeta^2 + 6\xi\eta + 2\xi\zeta + 2\eta\zeta\right] \\
\|Q_4\| &= \frac{2}{3\sqrt{3}}\left[\theta\xi + \theta\eta - 2\theta\zeta - \sqrt{3}\varepsilon\xi + \sqrt{3}\varepsilon\eta\right] \\
\|Q_5\| &= \frac{1}{9\sqrt{2}}\left[-\theta^2 + 3\varepsilon^2 - 2\zeta^2 - 6\xi\eta + 2\xi\zeta + 2\eta\zeta\right] \\
\|Q_6\| &= \frac{1}{3\sqrt{2}}\left[\theta\xi - \theta\eta - \sqrt{3}\varepsilon\xi - \sqrt{3}\varepsilon\eta\right] \\
\|Q_7\| &= \frac{1}{6\sqrt{3}}\left[\xi^2 - \eta^2 - 2\sqrt{3}\theta\varepsilon - 4\xi\zeta + 4\eta\zeta\right] \\
\|Q_8\| &= \frac{1}{18}\left[-5\theta^2 - 3\varepsilon^2 + 3\xi^2 + 3\eta^2 + 2\zeta^2 + 4\xi\zeta + 4\eta\zeta\right] \\
\|Q_9\| &= \frac{1}{3\sqrt{6}}\left[-\theta\xi - \theta\eta - 4\theta\zeta + \sqrt{3}\varepsilon\xi - \sqrt{3}\varepsilon\eta\right] \\
\|Q_{10}\| &= \frac{1}{3}\left[\sqrt{3}\theta\xi - \sqrt{3}\theta\eta + \varepsilon\xi + \varepsilon\eta + 2\varepsilon\zeta\right] \\
\|Q_{11}\| &= \frac{1}{3\sqrt{2}}\left[-\sqrt{3}\theta\xi + \sqrt{3}\theta\eta - \varepsilon\xi - \varepsilon\eta + 4\varepsilon\zeta\right] \\
\|Q_{12}\| &= \frac{1}{2\sqrt{3}}\left[\sqrt{3}\xi^2 - \sqrt{3}\eta^2 + 2\theta\varepsilon\right] \\
\|Q_{13}\| &= \frac{1}{2\sqrt{3}}\left[\theta^2 - \varepsilon^2 + \xi^2 + \eta^2 - 2\zeta^2\right] \\
\|Q_{14}\| &= \frac{1}{\sqrt{6}}\left[\sqrt{3}\theta\xi + \sqrt{3}\theta\eta + \varepsilon\xi - \varepsilon\eta\right]
\end{aligned} \tag{17}$$

The iso-stationary function is obtained by inserting these extremal coordinates into Eq. 16. Since the edge distortions were transformed according to the irreps of $\mathbf{S_5}$, the iso-stationary function naturally decomposes into three independent terms, one for each irrep.

$$\begin{aligned}\|E\| &= \|E\|_{G_1} + \|E\|_{H_1} + \|E\|_{H_2}\\ &= -\frac{16}{45}f_1 - \frac{1}{9}f_1 - \frac{1}{3}f_3 = E^{JT}_{G_1}f_1 + \frac{5}{4}E^{JT}_{H_1}f_1 + \frac{5}{4}E^{JT}_{H_2}f_3\\ &= -\frac{8}{35} + \frac{1}{21}(f_1 - f_3) = E^0 + E^1(f_1 - f_3) \end{aligned} \tag{18}$$

where f_1 and f_3 are fourth-order polynomials in the c-coordinates:

$$\begin{aligned} f_1 =& \frac{3}{8}\left(\theta^2+\varepsilon^2\right)^2 + \frac{1}{6}\left(\xi^2+\eta^2+\zeta^2\right)^2\\ &+\frac{1}{3}\left(\theta^2+\varepsilon^2\right)\left(\xi^2+\eta^2+\zeta^2\right) + \frac{5}{6}\left(\xi^2\eta^2+\eta^2\zeta^2+\zeta^2\xi^2\right)\\ &+\frac{5}{12}\left(\theta^2-\varepsilon^2\right)\left(2\zeta^2-\eta^2-\xi^2\right) - \frac{5}{2\sqrt{3}}\theta\varepsilon\left(\xi^2-\eta^2\right)\\ f_3 =& \frac{1}{8}\left(\theta^2+\varepsilon^2\right)^2 + \frac{1}{2}\left(\xi^2+\eta^2+\zeta^2\right)^2\\ &+\left(\theta^2+\varepsilon^2\right)\left(\xi^2+\eta^2+\zeta^2\right) - \frac{3}{2}\left(\xi^2\eta^2+\eta^2\zeta^2+\zeta^2\xi^2\right)\\ &-\frac{3}{4}\left(\theta^2-\varepsilon^2\right)\left(2\zeta^2-\eta^2-\xi^2\right) + \frac{3\sqrt{3}}{2}\theta\varepsilon\left(\xi^2-\eta^2\right) \end{aligned} \tag{19}$$

Although the current JT graph exhibits the instability of a fivefold degenerate level within $\mathbf{S_5}$ symmetry, its iso-stationary function exactly mimics that of the icosahedral quintuplet in the $H \otimes (g + 2h)$ JT problem [13], with the sole difference that in the present case the JT stabilization energies are no longer free parameters but are defined by the connectivity of the graph. The correspondence with the icosahedral symmetry group is explained by the permutational nature of the icosahedral fivefold representation. The exact values of these JT stabilization energies (in units of γ^2) are easily retrieved from the expressions in Eq. 18.

$$\begin{aligned} E^{JT}_{G_1} &= E^{JT}_{G} = -16/45\\ E^{JT}_{H_1} &= E^{JT}_{Ha} = -4/45\\ E^{JT}_{H_2} &= E^{JT}_{Hb} = -12/45 \end{aligned} \tag{20}$$

The extremal structure of the iso-stationary function has been extensively studied, and it was shown that the nature of the extrema depends on the exact values of the $E^{JT}_{G}, E^{JT}_{Ha}, E^{JT}_{Hb}$ parameters [13]. At present we shall not list all stationary points but shall instead limit ourselves to the ones corresponding with the absolute minima, providing in Table 6, energy, symmetry, and Hessian eigenvalues of the global minima (α orbit) and the transition states connecting these minima (γ orbit). Under the current regime ($E^1 > 0$), six equivalent pentagonal minima can be identified, forming the α orbit of Table 6. All these minima are equidistant in Q-space, and tunneling between all of them is equally probable and is mediated by the fifteen saddle points of the γ orbit. In this way, the topology of the dynamic JT system can be represented by the complete graph on six vertices with the vertices denoting the six $\mathbf{D_5}$ minima and the edges the fifteen tunneling pathways. The edge distortions leading to the α_2 minimum are shown in Fig. 3.

The rich topology of this tunneling graph results in closed cycles of lengths from three to six [15, 16]. Phase tracking in Q-space shows that all closed paths of length three give rise to a Berry phase of π [17]. Since these triangles form a basis for the cycle space of the graph, all other cycles can always be written as a sum of these three-cycles and their Berry phases will be equal to the sum of the Berry phases of the three-cycles involved, modulo 2π. As an example, the four-cycle (α_1–α_2–α_3–α_4) can be decomposed into the two three-cycles (α_1–α_2–α_4) and (α_2–α_3–α_4). Consequently, this four-cycle will have a Berry phase of $(\pi + \pi) \bmod 2\pi = 0$. In the current case, where all three-cycles carry a Berry phase of π, one can simply state that all odd cycles will have a Berry phase of π, while all even cycles will carry a Berry phase of zero. A special feature of the icosahedral point group is that the direct square of the quintuplet representation contains the H representation twice, giving rise to a product multiplicity of two H-modes in the corresponding JT problem: $H \otimes (g + 2h)$. This was solved previously by orthogonalization of the coupling coefficients [18]. The resulting couplings were labeled as H_a and H_b. It was later shown that this somewhat arbitrary multiplicity separation coincided with a different parentage in the $\mathbf{S_6}$ covering group [4, 19]. This also provided extra selection rules for several matrix elements. At present we see that the parent $\mathbf{S_5}$ group also provides a natural product separation as H_1 and H_2, which, moreover, also coincides with H_a and H_b. This is explained by the fact that the embedding of the icosahedral group in the complete 6-graph, K_6, contains $\mathbf{S_5}$ as an intermediate subgroup:

$$\mathbf{S}_6 \to \mathbf{S}_5 \to \mathbf{I}. \tag{21}$$

5 The 20-vertex graph and the sixfold degeneracy

The group $\mathbf{S_5}$ contains one sextuplet representation which in $\mathbf{A_5}$ splits into two triplets, labeled as the icosahedral T_1 and T_2 irreps. Clearly, since the icosahedral group cannot act transitively on a set of seven elements, we should not expect that it can host a sixfold degeneracy. In the context of the graph-theoretical JT theorem, this makes these triplets exceptional, since they cannot be related to the

Table 6 Energy, symmetry, and Hessian eigenvalues of the global minima (α orbit) and the transition states connecting these minima (γ orbit)

Orbit	Dim	Sym	Eigenvectors $(\theta, \varepsilon, \xi, \eta, \zeta)$	Energy	Hessian eigenvalues
α	6	$\mathbf{D_5}$	$\alpha_{1,2} = \frac{1}{\sqrt{10}}\left(\sqrt{3}, 1, \pm\sqrt{6}, 0, 0\right)$ $\alpha_{3,4} = \frac{1}{\sqrt{10}}\left(\sqrt{3}, -1, 0, \pm\sqrt{6}, 0\right)$ $\alpha_{5,6} = \frac{1}{\sqrt{5}}\left(0, \sqrt{2}, 0, 0, \pm\sqrt{3}\right)$	$E^{JT}_{(2^2,1)} = -4/15 = -36/135$	$\frac{4}{15}, \frac{4}{15}, \frac{4}{15}, \frac{4}{15}$
γ	15	$\mathbf{D_2}$	$(0, 0, 1, 0, 0)$ $(0, 0, 0, 1, 0)$ $(0, 0, 0, 0, 1)$ $\frac{1}{\sqrt{8}}\left(1, \sqrt{3}, \sqrt{2}, 0, \pm\sqrt{2}\right)$ $\frac{1}{\sqrt{8}}\left(1, \sqrt{3}, -\sqrt{2}, 0, \pm\sqrt{2}\right)$ $\frac{1}{\sqrt{8}}\left(1, -\sqrt{3}, 0, \sqrt{2}, \pm\sqrt{2}\right)$ $\frac{1}{\sqrt{8}}\left(1, -\sqrt{3}, 0, -\sqrt{2}, \pm\sqrt{2}\right)$ $\frac{1}{2}\left(\sqrt{2}, 0, 1, \pm 1, 0\right)$ $\frac{1}{2}\left(\sqrt{2}, 0, -1, \pm 1, 0\right)$	$\left(4E^{JT}_{(4,1)} + 5E^{JT}_{(3,2)} + 15E^{JT}_{(2^2,1)}\right)/24$ $= -33/135$	$-\frac{2}{9}, \frac{2}{9}, \frac{2}{9}, \frac{2}{9}$

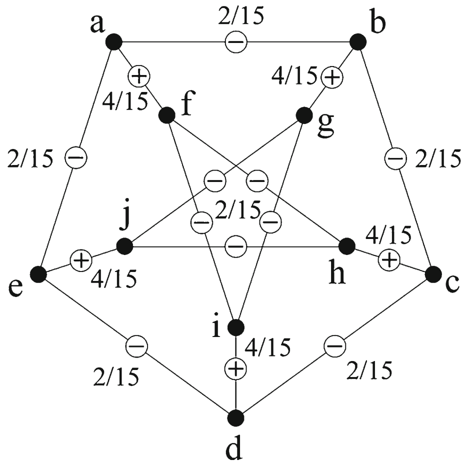

Fig. 3 Edge distortions of the Petersen graph leading to the α_2 minimum in the $H_1 \otimes (G_1 + H_1 + H_2)$ problem

embedding of a maximal subgroup of the icosahedral group. However, there exists an interesting relationship between both triplets, which points to a common sextuplet ancestor. The characters of the two T irreps are the same, except for the sign of the $\sqrt{5}$ (see Table 1). Such a pair of representations—which have opposite signs only for the irrational number appearing in their transformations—are known as irrational conjugates. As a result, the Clebsch-Gordan coupling coefficients for direct products involving these T states are likewise related [18]. These relationships may be used to explain some intriguing degeneracies in the multiplet terms, based on the icosahedral H and G shells. For some configurations, the T_1 and T_2 terms occur in pairs, with degenerate Coulomb energies [20, 21]. To explain these regularities, Judd and Lo have introduced a so-called kaleidoscopic operator that permutes the two triplets [22, 23]. In view of this conjugation between the two triplets, it is worthwhile to examine a model of JT activity in a sextuplet level of a graph with $\mathbf{S_5}$ symmetry. The 20-graph in Fig. 1c provides such a model. In this model an unexpected symmetry selection rule appears, which prevents the JT splitting of the sextuplet into two triplets.

The spectrum of the 20-graph is $\left\{4, 3^4, 0^5, (-2)^6, (-1)^4\right\}$. If each node were occupied by one electron, a closed shell would be obtained. Adding an extra electron would then give rise to a sixfold degenerate JT instability. It is possibly noteworthy that the eigenvectors of the sextuplet roots can be obtained in a special monomial form, with the same weight on each vertex. To this end, we use the embedding of a maximal subgroup of order 20, known as the Frobenius group, which is a meta-cyclic group containing one C_5-axis and five C_4-axes [24]. The intersection of this group with $\mathbf{I}$ is the pentagonal subgroup $\mathbf{D_5}$. Its character table is displayed in Table 7, and the subduction relations from $\mathbf{S_5}$ are as follows:

Table 7 Character table for the meta-cyclic MC5-4 Frobenius group, and the $\mathbf{S_5}$ cycle structure

	E $\{1^5\}$	$4C_5$ $\{5\}$	$5C_2$ $\{1,2^2\}$	$5C_4$ $\{1,4\}$	$5C_4^3$ $\{1,4\}$
A	1	1	1	1	1
B	1	1	1	-1	-1
Γ_1	1	1	-1	i	$-$i
Γ_2	1	1	-1	$-$i	i
G	4	-1	0	0	0

$$\begin{aligned} A_1 &\rightarrow A \\ A_2 &\rightarrow B \\ G_1 &\rightarrow G \\ G_2 &\rightarrow G \\ H_1 &\rightarrow B + G \\ H_2 &\rightarrow A + G \\ I &\rightarrow \Gamma_1 + \Gamma_2 + G \end{aligned} \tag{22}$$

We note that the complex conjugate non-degenerate irreps, Γ_1 and Γ_2, directly generate the sextuplet representation. According to induction theory, this process will yield at once the six eigenvectors in monomial form [25], where we use the sixfold axis as cyclic coset generator.

One of the eigenvectors is shown in Fig. 4. The five others may be obtained by acting on this with the sixfold generator specified in Table 3. The symmetrized square of the I representation can be obtained with the expression in Eq. 5, and reads:

$$[I \otimes I] = A_1 + A_2 + G_1 + 2H_1 + H_2 \tag{23}$$

On the other hand, the representations of the edge distortions can be obtained separately for each edge orbit, and they read:

$$\begin{aligned} \Gamma_{10}(e) &= A_1 + G_1 + H_1 \\ \Gamma_{30}(e) &= A_1 + 2G_1 + 2H_1 + H_2 + I \end{aligned} \tag{24}$$

When comparing the required JT modes in Eq. 23 with the available edge distortions in Eq. 24, it is observed that one of the JT modes, viz., the A_2, is missing from the space of the edge distortions. The vertex representation likewise does not contain this symmetry, so changes of vertex weights cannot provide such a symmetry breaking, either. On the other hand, the distortion space contains an I symmetry mode, which is not JT active. The latter case is not uncommon in the molecular JT effect, but the fact that one of the JT modes is missing is exceptional. In molecules this does not occur, except for the special case of linear molecules, which are JT inactive. In fact, these are the only exceptions to the JT effect in 3D space. On the other hand, when considering structures in higher-dimensional spaces, such as the hyper-octahedron, it happens that not all JT modes have counterparts in the hyperspace of the nuclear distortions [2]. From our present perspective, the absence of the A_2 mode is particularly intriguing since this mode breaks the $\mathbf{S_5}$ symmetry to $\mathbf{A_5}$, and its only effect on the representations is to split the sextuplet into two triplets:

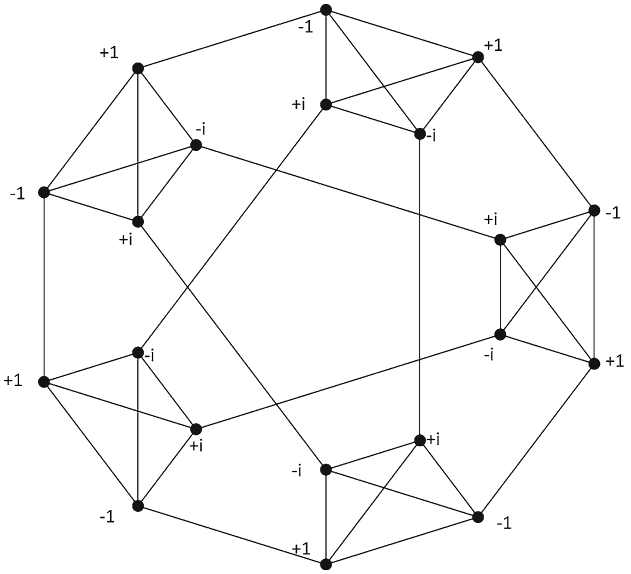

Fig. 4 Eigenvector of the sextuplet manifold in the 20-graph. The other components may be obtained by cyclic permutations under the $\{2,3^2,6^2\}$ operator of Table 3

$$I \rightarrow T_1 + T_2 \tag{25}$$

In fact, this branching provides the operator form for the A_2 mode. If we again work out the symmetrized square of the I irrep in the $\mathbf{A_5}$ subgroup, Eq. 23 becomes:

$$\begin{aligned} [I \otimes I] &= [(T_1 + T_2) \otimes (T_1 + T_2)] \\ &= [T_1 \otimes T_1] + [T_2 \otimes T_2] + T_1 \otimes T_2 \end{aligned} \tag{26}$$

The two T squares in the right-hand side of Eq. 26 both yield an A, which corresponds to the presence of two A-quantities in Eq. 23, but the symmetrized square of I can yield only one totally symmetric A_1, which will correspond to the trace of the sextuplet. The other A-quantity thus must be an A_2. This operator will be equal to the difference of the trace-operators for T_1 and T_2, which is precisely the operator that splits I into T_1 and T_2. The absence of such a mode in the distortion space leads us to the conclusion that, in this 20-graph, there is no distortion that can produce a neat separation of the two conjugate triplets. The only distortion that will partially distinguish both triplets is a distortion to $\mathbf{D_5}$ symmetry, using a component of the H representation, with the following subduction relation:

$$I \to \begin{cases} T_1 \to A_2 + E_1 \\ T_2 \to A_2 + E_2 \end{cases} \tag{27}$$

In this case, the E-components are resolved as E_1 and E_2 under the C_5-axis, but the non-degenerate level is the same for both triplets.

6 Conclusions

In this paper we have investigated three graphs with $\mathbf{S_5}$ symmetry as models for JT activity in icosahedral molecular problems. Such graph models can be used as pseudo-particle models of actual Jahn–Teller problems, the connection being based on the link between the automorphism group of the graph and the molecular symmetry group. In the case of the fivefold degenerate representation, the JT problem is characterized by a product multiplicity problem. Previous solutions of this were based on spherical symmetry and induction theory, as well as on subduction relations from the symmetric $\mathbf{S_6}$ groups. The present analysis shows that the intermediate $\mathbf{S_5}$ group is sufficient to obtain the same multiplicity resolution. From the graph-theoretical perspective, a further interesting feature was found in that the symmetry breaking of the sextuplet level into two triplets requires a pseudo-scalar operator, leading from $\mathbf{S_5}$ to $\mathbf{A_5}$, which was, however, absent from the edge-weight distortion space. This selection rule might provide a justification for the validity of Judd's 'kaleidoscopic' operator [22, 23]. It will also be interesting to examine the combined $(T_1 \oplus T_2)$ pseudo-JT problem. So far, only the $(T_{1g} \oplus T_{1u})$ adiabatic potential has been investigated [26].

Clearly, the graph-theoretical JT-conjecture must further be refined, since the last case shows that selection rules may prevent some modes of symmetry breaking by edge distortions. In which graphs this occurs, and why, are open questions.

Acknowledgments Financial support from the Flemish Science Foundation (FWO) is gratefully acknowledged. The work of TP has been partially financed by ARRS project P1—0294 and project N1—0011 within the EUROCORES Programme EUROGIGA (project GReGAS) of the European Science Foundation.

References

1. Bersuker IB, Polinger VZ (1989) Vibronic interactions in molecules and crystals. Springer, Berlin
2. Ceulemans A, Lijnen E (2010) Electronic degeneracy and vibrational degrees of freedom: the permutational proof of the Jahn–Teller theorem. In: Köppel H, Yarkony DR, Barentzen H (eds) The Jahn–Teller effect. Springer, Heidelberg, pp 25–50
3. Trinajstić N (1992) Chemical graph theory, 2nd edn. CRC Press, Boca Raton
4. Ceulemans A, Lijnen E, Fowler PW, Mallion RB, Pisanski T (2012) Graph theory and the Jahn–Teller theorem. Proc Roy Soc A 468:971–989
5. Fowler PW (2003) Symmetry aspects of distortivity in π systems. In: Ceulemans A, Chibotaru LF, Kryachko E (eds) Advances in quantum chemistry, vol 44. Elsevier, Amsterdam, pp 219–237
6. Pauncz R (1995) The symmetric group in quantum chemistry. CRC Press, Boca Raton
7. Pisanski T. If a graph G has n vertices, then the extension, defined as THE(G), has $n*n\text{-}n$ vertices. Namely, the vertices of THE(G) are ordered pairs of distinct vertices of G. If u and v are adjacent vertices of G then uv is adjacent to vu and for any other vertex w from G, different from u and v, the vertex uw is adjacent to uv (to be published)
8. Griffith JS (1961) The theory of transition-metal ions. Cambridge University Press, Cambridge
9. Ceulemans A, Fowler PW (1989) SO(4) symmetry and the static Jahn–Teller effect in icosahedral molecules. Phys Rev A 39:481–493
10. Ceulemans A, Lijnen E (2007) The Jahn–Teller effect in chemistry. Bull Chem Soc Jpn 80:1229–1240
11. Boyle LL, Parker YM (1980) Symmetry coordinates and vibration frequencies for an icosahedral cage. Mol Phys 39:95–109
12. Moate CP, O'Brien MCM, Dunn JL, Bates CA, Liu YM, Polinger VZ (1996) $H \otimes h$: a Jahn–Teller coupling that really does reduce the degeneracy of the ground state. Phys Rev Lett 77:4362–4365
13. Ceulemans A, Fowler PW (1990) The Jahn–Teller instability of fivefold degenerate states in icosahedral molecules. J Chem Phys 93:1221–1234
14. Ceulemans A (1987) The structure of Jahn–Teller surfaces. J Chem Phys 87:5374–5385
15. Ceulemans A, Lijnen E (2005) Berry phase and entanglement in the icosahedral $H \otimes (g \oplus 2\,h)$ Jahn–Teller system with trigonal minima. Phys Rev B 71:014305
16. Manini N, De Los Rios P (2000) Berry phase and ground-state symmetry in $H \otimes h$ dynamical Jahn–Teller systems. Phys Rev B 62:29–32
17. Berry MV (1984) Quantal phase factors accompanying adiabatic changes. Proc Roy Soc A 392:45–57
18. Fowler PW, Ceulemans A (1985) Symmetry relations in the property surfaces of icosahedral molecules. Mol Phys 54:767–785
19. Lijnen E, Ceulemans A (2007) The permutational symmetry of the icosahedral orbital quintuplet and its implication for vibronic interactions. Europhys Lett 80:67006
20. Plakhutin BN, Carbó-Dorca R (2000) Icosahedral symmetry structures with open-shell electronic configuration h^N ($N = 1$–9). Phys Lett A 267:370–378
21. Plakhutin BN, Arbuznikov AV (1997) Spectrum of states in icosahedral structures with g^N electronic configuration ($N = 1$–7). 2. Ab initio calculation of the C20 (Ih) molecule and its anions. J Struct Chem 38:501–510
22. Judd BR, Lo E (1999) Coulomb energies of icosahedral h orbitals. J Chem Phys 111:5706–5729
23. Lo E, Judd BR (1999) Implications of non-feasible transformations among icosahedral h orbitals. Phys Rev Lett 82:3224–3227
24. Voskresenskaya GV (2000) Metacyclic groups and modular forms. Math Notes 67:129–137
25. Ceulemans A, Beyens D (1983) Monomial representation of point-group symmetries. Phys Rev A 27:621–631
26. Ceulemans A, Chibotaru LF (1996) Icosahedral $T_{1u} + T_{1g}$ Jahn–Teller problem. Phys Rev B 53:2460–2462

Theor Chem Acc (2012) 131:1253
DOI 10.1007/s00214-012-1253-4

REGULAR ARTICLE

Mechanism of ketone hydrosilylation using NHC–Cu(I) catalysts: a computational study

Thomas Vergote · Thomas Gathy · Fady Nahra ·
Olivier Riant · Daniel Peeters · Tom Leyssens

Received: 29 March 2012 / Accepted: 23 June 2012 / Published online: 13 July 2012

Abstract The plausibility of the catalytic cycle suggested for the hydrosilylation of ketones by (NHC) copper(I) hydrides has been investigated by a theoretical DFT study. Model systems yield the necessary insight into the intrinsic reactivity of the system. Computations show the activation of the copper fluoride pre-catalyst, as well as both steps of the catalytic cycle to involve a 4-center metathesis transition state as suggested in the literature. These results show the reaction to be favored by the formation of van der Waals complexes resembling the transition states. Stabilizing electrostatic interactions between those atoms involved in the bond-breaking and bond-forming processes induces the formation of these latter. Both steps of the actual catalytic cycle show a free energy barrier of about 14.5 kcal/mol for the largest NHC ligands, with respect to the isolated reactants, hereby confirming the plausibility of the suggested cycle. The large overall exothermicity of the catalytic cycle of about 35 kcal/mol is in agreement with experimental observations.

Keywords N-heterocyclic diaminocarbene · Copper(I) · DFT · Hydrosilylation · Reactivity · Catalysis

1 Introduction

Carbonyl bond reduction, specifically of aldehydes and ketones, to the corresponding alcohol functionality via hydride transfer is a fundamental transformation in organic synthesis [1–5]. Transition metal catalysis has been successfully applied in the reduction of many carbonyl compounds via hydrogenation or hydrosilylation [1–5]. Hydrogenation reactions often proceed in good yields but require high pressure or elevated temperature. Moreover, if the reaction is part of a multistep synthesis, the resulting free alcohol often requires protection prior to the next synthetic step. In contrast, the softer reactions conditions of hydrosilylation turned out to be a major advantage, in addition to the fact that both the reduction and the protection steps are performed in a single, atom-efficient step.

The first catalytic hydrosilylation systems, based on rhodium, were developed in the early 1970s [6–8]. Traditionally, catalytic hydrosilylation of the carbonyl functionality was performed with precious, heavy metals ranging from Re, Rh, and Ru to Ir [9–18]. As the main drawback of these systems is the cost affiliated with these metals, during the two last decades efforts were taken in finding an efficient alternative system using less-expensive metals such as titanium [19–26], iron [27–29], manganese [30, 31], or zinc [32–35]. In 1984, Brunner and Miehling reported the first asymmetric hydrosilylation using a copper-diphosphine catalyst [36]. Since many copper-diphosphine catalytic systems were developed [37–43], the active species formed in situ was postulated to be a copper (I) hydride. Lipshutz and co-worker describe the formation of the CuH species in a system combining a catalytic quantity of CuCl/NaOt–Bu/diphosphine and a stoichiometric quantity ofhydrosilylating agent [44–48]. At the same time, Carreira et al. [49], as well as Riant et al. [41, 50–52],

---

Published as part of the special collection of articles celebrating theoretical and computational chemistry in Belgium.

Electronic supplementary material The online version of this article (doi:10.1007/s00214-012-1253-4) contains supplementary material, which is available to authorized users.

T. Vergote · T. Gathy · F. Nahra · O. Riant · D. Peeters ·
T. Leyssens (✉)
Institute of Condensed Matter and Nanosciences,
Université Catholique de Louvain, Place Louis Pasteur 1,
1348 Louvain-la-Neuve, Belgium
e-mail: tom.leyssens@uclouvain.be

reported CuF_2 systems as interesting precursors to copper hydride. Based on these results, Wu et al. [53] recently developed a highly asymmetric copper(II)-catalyzed hydrosilylation system.

N-Heterocyclic carbene (NHC) ligands [54–57], particularly of the type developed by Arduengo et al. [58], have emerged as efficient ligands in metal-mediated reactions [59–62]. Compared to tertiary phosphines, the NHC ligands are characterized by strong metal–ligand bonding, hereby minimizing ligand dissociation [54–57]. This latter is particularly interesting when performing mechanistic studies, as this will simplify the system under study. NHC ligands were shown to be interesting alternatives to phosphines for the copper-catalyzed hydrosilylation of carbonyl compounds. While (IPr)–CuCl (IPr = 1,3-bis(2,6-diisopropylphenyl)imidazol-2-ylidene) was an efficient catalyst for the hydrosilylation of unhindered ketones [63], (ICy)–CuCl (ICy = 1,3-bis(cyclohexyl)imidazol-2-ylidene) or (SIMes)-CuCl (SIMes = 1,3-bis(2,4,6-trimethylphenyl) imidazolin-2-ylidene) turned out to be effective for more challenging ketones [64]. The active species, formed in situ in the presence of a catalytic amount of NaOtBu and a stoichiometric quantity of hydrosilylating agent, is a copper(I) hydride. Yun et al. [65] reported that the use of copper(II) salts as catalytic precursor in combination with a NHC also leads to an effective hydrosilylation of ketones. Recently, a series of cationic bis-carbenic complexes, $[(NHC)_2–Cu]X$ (X = BF_4^- [66, 67], PF_6^- [66, 67], FHF^- [68]), has shown remarkable activity toward the hydrosilylation of ketones. Although, once more, the reaction pathway was not investigated, mono-carbenic intermediates are believed to be the active species. Interestingly, the first asymmetric (NHC)copper(I)-catalyzed ketone hydrosilylation was only developed recently by Gawley et al. [69].

In all of the above-mentioned studies, the suggested mechanism is based on the catalytic cycle shown in Scheme 1 [43, 64, 68, 70, 71], illustrated using a (NHC)copper(I) chloride complex. As the Cu–Cl bond cannot be cleaved in an efficient manner by a hydride source (such as silane), the complex needs to be activated through ligand exchange, replacing chlorine with an alkoxide or a fluoride. As stated in our previous work [68], depending on the reaction conditions, addition of a mild source of fluoride ($NEt_3 \cdot 3HF$) can lead to either a (NHC)Cu–F complex or a (NHC)Cu–FHF bifluoride complex. The copper(I) (bi)fluoride complexes are then expected to be activated through a σ-bond metathesis reaction with a silane to yield the desired copper(I) hydride catalyst, thought to be the active species [72]. This active species is then postulated to react with a ketone passing through a four-center transition state to form a copper alkoxide (*step 1*). Finally, the copper alkoxide undergoes a σ-bond metathesis with the hydrosilylating agent to regenerate the Cu–H complex and form the silylether product (*Step 2*). Although it has been suggested that (NHC)Cu–H species agglomerate in solution [73], no experimental evidence of this agglomeration in solution is available. However, this would imply that the equilibrium between monomeric and polymeric species is of prime importance for a complete understanding of the system under study. In this work, we do not investigate this aspect of the reaction, as it will only determine the final amount of free catalytic species available for catalysis but not the nature of the catalytic cycle itself.

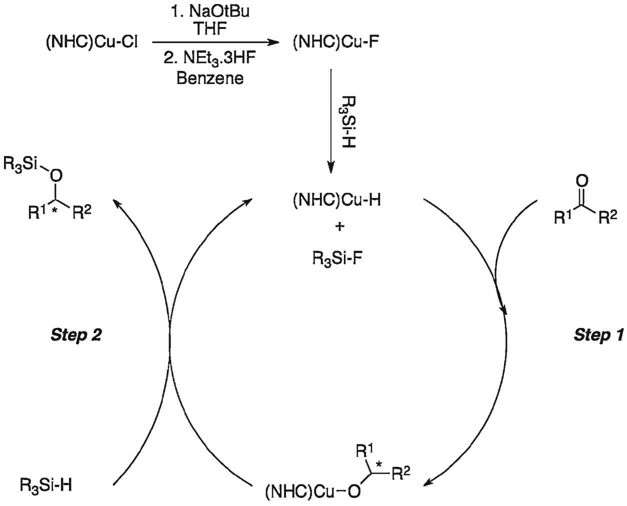

Scheme 1 Suggested cycle for the asymmetric hydrosilylation of ketones using (NHC) copper(I) catalysts

This mechanism is relatively similar to the one proposed for the hydrosilylation of ketones catalyzed by phosphine copper(I) complexes [39, 42, 43]. Although some computational studies concerning the hydrosilylation reaction of ketones using copper(I) diphosphine complexes have been reported in the literature [74–78], surprisingly, no such studies have been reported for (NHC)–Cu(I) complexes. As these complexes are more stable compared to diphosphine Cu(I) complexes, and hence are interesting from a mechanistic point of view, it is important to compare their overall reactivity with the diphosphine complexes, to verify if the plausibility of the suggested catalytic cycle still stands, and to highlight possible differences. In this paper, we use computational chemistry to verify the plausibility of the suggested cycle, investigating energetic, electronic, and structural properties. Differences in the diphosphine complexes will also be highlighted.

Our calculations were made on models of increasing complexity, ranging from the simplest acyclic NHC ligand (“ADC_H”) to the experimentally used unsaturated NHC ligands (shown in Scheme 2). Using a variety of NHC ligands, their effect on the catalytic cycle is studied. As our

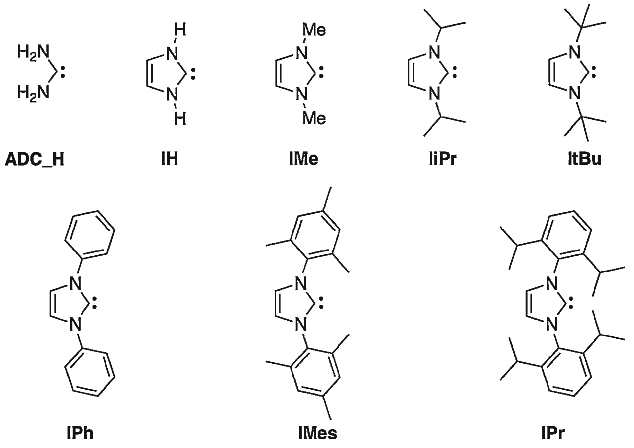

Scheme 2 Structure and acronyms of NHC ligands used throughout this work

first goal is to verify the plausibility of the catalytic cycles, as well as the effect of the NHC ligand, other reactants are modeled using formaldehyde and SiH_4 as model for, respectively, the ketone and silane species. The effect of a variation in ketone nature and silane nature could be studied at later stages, but goes beyond the scope of this contribution.

2 Computational details

Unless stated otherwise, all structures were fully optimized using Becke's three-parameter exchange functional [79] and the correlation functional of Lee, Yang, and Parr (B3LYP) [80], as implemented in the Gaussian 03 [81] series of programs. All possible conformations have been investigated and the most stable conformer is retained. Optimized geometries are provided as Supplementary material. Force constants were determined to characterize the stationary points, as well as to determine their entropies and free energies, based on a statistical thermodynamics treatment. For the transition state (TS), the correctness of the curvature and its corresponding eigenvector were checked in order to guarantee the quality of the obtained results. Accordingly, in some cases, intrinsic reaction coordinate (IRC) calculations were made to confirm the transition state corresponded to the actual reaction mechanism [82–85]. Reactants were allowed to interact on the potential energy surface (PES) and formed a van der Waals (VDW) intermolecular pre-reaction complex. van der Waals interaction energies should be taken as indicative, as DFT methods do not correctly account for dispersion interactions [86]. The Cu atom was described using an effective core potential to represent all but the valence n*d* and $(n + 1)s$ and outer core n*s* and *np* electrons [87–89]. The latter were described with a triple zeta contraction of the original double zeta basis set, and this combination is referred to as the LANL2DZ basis set. All non-metal atoms were described using the diffused and polarized 6-31++G(d,p) basis set [90, 91]. Natural bond orbitals (NBO) analysis was used to investigate electronic properties and charge distributions [92–95]. Density difference drawings were made using GAUSSVIEW [96]. Orange and blue zones indicate, respectively, an increase and decrease in electron density. Isodensity surfaces are shown at 0.01 $e^-/Bohr^3$ for Figs. 2 and 8 and at 0.005 $e^-/Bohr^3$ for Fig. 5.

To examine the basis set dependence, calculations using a larger basis set, 6-311G(2d,p) for all non-metal atoms and a def2-TZVP [97] basis set for Cu, were made using the (IMes)Cu-X model system. Results (Table S3 in the Supporting material) show a consistent shift up to 4 kcal/mol for all species involved in the transformation of the precatalyst, and of about 3 kcal/mol for the second step of the catalytic cycle, while almost no effect is observed for the first step. While these shifts do not change the energy ordering of the reactions paths, keeping the overall discussion unaltered, they are due to a basis set superposition error involving the fluorine and silicon atoms. The BSSE for the (IMes)Cu–F/SiH_4 and (IMes)Cu–OCH_3/SiH_4 complexes is a mere 1.0 kcal/mol using the LANL2DZ/6-31++G(d,p) basis set, but increases to 3.5 kcal/mol for these complexes using the def2-TZVP/6-311G(2d,p) (See Supporting Info, Table S1). This effect is no longer observed for the first step of the catalytic cycle, the BSSE for the (IMes)Cu–H/H_2CO system being a mere 0.3 kcal/mol with the def2-TZVP/6-311G(2d,p) basis set (instead of 0.9 kcal/mol for the LANL2DZ/6-31 ++G(d,p) basis set). This important BSSE for the CuF species can be reduced when introducing diffuse basis functions on the F and Si atoms.[1] Indeed, single-point calculations on the (IMes)Cu-X system with the all electrons def2-TZVP/6-311 ++G(2d,p) basis set show the basis set dependence on the whole catalytic cycle being negligible. As the main objective of this paper is to study the plausibility of the actual catalytic cycle, with the possibility of transposing the basis set used to larger systems in order to study the enantioselectivity, the smaller basis set was chosen throughout this work. To further check the reliability of our results, we have also decided to make additional calculations on the (IMes)Cu-X system using the pure GGA functional BP86 [98], and the B3PW91 [79, 99, 100] and MPW1PW91 [101] hybrid functionals, as these three were also proven effective for transition metal chemistry [102–104]. Results of single-point

---

[1] The BSSE contributes to an overestimation of the stabilization of these complexes with respect to isolated reactants. Excluding this contribution, the van der Waals complexes remain stabilized with respect to isolated reactants, and the overall discussion therefore remains unaltered.

calculations obtained with these functionals did not affect either the relative ordering of the reaction paths or the conclusions drawn from the energy ordering of the structures (i.e., consistent results with B3LYP). These numbers are therefore discussed in the Supporting Information only (Table S2). Finally, as concerns could arise because no polarization function is included in LANL2DZ, while polarization is taken into account for all non-metal atoms, single-point calculations were also made with the LANL2TZ(f) [89, 105, 106] basis set for Cu, which uses *f* polarization functions developed by Frenking's group [106]. In addition, we compared our results to the Stuttgart RSC 1997 (SDD) RECP [107–109] that contains an *f* function for the first-row transition elements. Once more, basis set dependence was found negligible (Table S3).

3 Results and discussion

The different parts of the catalytic cycle will be discussed separately, starting with a discussion on the activation of the pre-catalyst, followed by an investigation of the two steps of the actual catalytic cycle.

3.1 Activation of the pre-catalyst

Once the pre-catalyst formed, this species reacts with a hydrosilane via a σ bond metathesis reaction to yield the active copper hydride species. As shown in Scheme 3, the formation of a σ bond between the copper and hydrogen atoms occurs through transmetalation [46, 72, 110] passing by a 4-center transition state.

Table 1 shows the relative energy, enthalpy, and free energy of the van der Waals complexes and transition states. The reaction is guided by the initial formation of an energetically favored van der Waals complex between the pre-catalyst and the SiH_4 hydrogenating agent.

The electrostatic interaction between the negatively charged fluorine atom and the positively charged copper atom, as well as the interaction between the negatively charged hydrogen atom and the positively charged silicon atom (Table S4), most likely explains the driving force for the formation of this complex.

As expected for a σ bond metathesis, the transition states are characterized by increased Cu–F and Si–H bond lengths, while Cu–H and Si–F bonds become shorter. Investigation of how the electronic density changes upon the formation of the transition state can help to clarify the actual reaction mechanism. Figure 2 shows the differential density between, respectively, the transition state and the sum of both reactants at transition-state geometry. As shown in this figure, the transition state is characterized by a strong decrease in electron density around the copper atom, and a strong increase between the Si and F atoms, corresponding to the breaking of the Cu–F bond, in favor of the formation of the Si–F bond. The formation of the copper hydride bond and breaking of the Si–H bond can also be observed, but seem less advanced. The 4-center σ bond metathesis should therefore be characterized as an asynchronous concerted reaction, with the breaking of the Cu–F bond (or formation of the Si–F bond) being slightly more advanced than the transfer of the silicon-linked hydrogen atom to the copper atom.

To get a more quantitative measurement of synchronicity/asynchronicity, Wiberg indexes [111] and NBO bond orders (B_i) were calculated. B_i were computed using the NBO program as implemented in Gaussian 03, and the synchronicity (S_y) was estimated using the concept proposed by Moyano et al. [112–114] (for more details, see section V in the Supporting information).

Bond indexes were calculated for the four bonds involved in the σ-bond metathesis reaction, meaning Cu–F, Cu–H, Si–H, and Si–F bonds (Fig. 2); all other bonds remain practically unaltered during the process (Fig. 1).

Calculating Wiberg indexes B_i for reactant complexes, TS, and products complexes allows locating the position of the TS between reactant and product (Table 2). For simplicity, only results for NHC = ADC_H, IH, and IMes are shown in Table 2 as these are representative of the entire set of species studied (See Supporting material, Table S5–S7).

Table 2 shows that the Cu–F bond has disappeared up to approximately 90 % at the TS, while this is a mere 44 % for the Si–H bond. In parallel, the Si–F bond has formed to an extent of 67 %, whereas the Cu–H bond has barely been formed (38 %). A similar observation is made for all studied NHC ligands, leading to synchronicity values of $S_y = 0.78–0.80$, which is in agreement with the structural

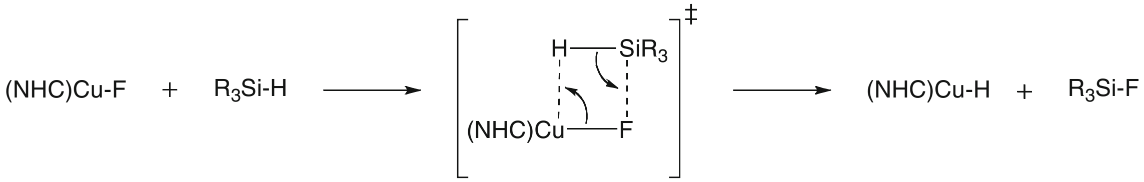

Scheme 3 Activation of the pre-catalyst

Table 1 Relative energy ΔE, enthalpy, and free energy (ΔH; ΔG) with respect to reactants for the pre-catalyst activation reaction

Pre-catalyst	van der Waals complex	TS	van der Waals complex	Products
(ADC_H)Cu–F	−1.2 (0.0; 6.2)	5.7 (6.0; 17.2)	−3.8 (−3.2; 4.8)	0.3 (−0.3; −0.6)
(IH)Cu–F	−1.2 (0.1; 6.0)	5.8 (6.1; 17.0)	−4.3 (−3.6; 4.4)	0.5 (−0.1; −0.4)
(IMe)Cu–F	−1.4 (−0.1; 6.4)	6.0 (6.4; 17.5)	−1.2 (−0.6; 7.4)	0.9 (0.3; 0.1)
(IiPr)Cu–F	−1.4 (−0.2; 5.8)	6.3 (6.7; 17.2)	−1.0 (−0.3; 6.8)	1.0 (0.4; 0.1)
(ItBu)Cu–F	−1.5 (−0.3; 5.9)	7.3 (7.6; 17.8)	−0.7 (0.0; 7.1)	0.3 (−0.3; −0.4)
(IPh)Cu–F	−1.8 (−0.5; 6.7)	6.5 (6.9; 17.6)	−1.0 (−0.4; 7.0)	0.8 (0.2; −0.1)
(IMes)Cu–F	−1.7 (−0.4; 6.1)	6.4 (6.8; 17.6)	−0.5 (0.1; 9.0)	1.4 (0.7: −0.9)
(IPr)Cu–F	−1.6 (−0.3; 8.2)	6.6 (7.0; 18.8)	¯0.1 (0.6; 9.9)	1.1 (0.5; 0.2)

Values are given in kcal/mol

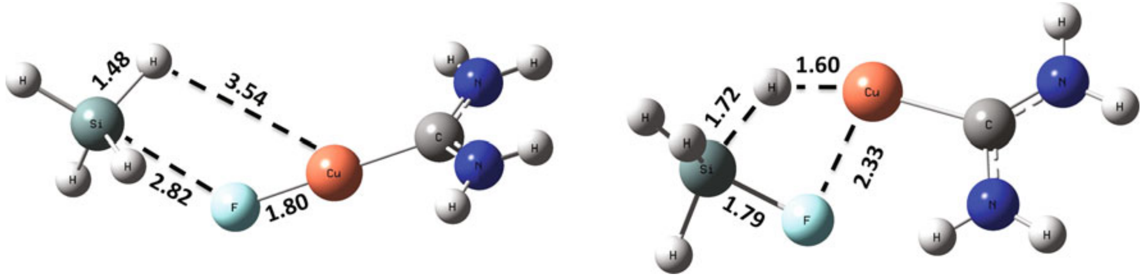

Fig. 1 Initial van der Waals complex and transition-state structure for the reaction between (ADC_H)Cu–F and SiH_4. Bond lengths are given in Å

Table 2 NBO analysis for the activation of the pre-catalyst

Pre-catalyst	Cu–F	Cu–H	Si–F	Si–H	δB_{AV}	S_y
(ADC_H)Cu–F						
B_i^R	0.2351	0.0011	0.0280	0.9473	0.597	0.79
B_i^{TS}	0.0250	0.2298	0.3548	0.5342		
B_i^P	0.0030	0.6084	0.5169	0.0017		
%Ev	90.52	37.66	66.84	43.69		
(IH)Cu–F						
B_i^R	0.2326	0.0011	0.0295	0.9471	0.599	0.78
B_i^{TS}	0.0225	0.2296	0.3552	0.5337		
B_i^P	0.0021	0.6159	0.5129	0.0061		
%Ev	91.15	37.17	67.38	43.93		
(IMes)Cu–F						
B_i^R	0.2170	0.0006	0.0327	0.9484	0.582	0.79
B_i^{TS}	0.0297	0.2107	0.3664	0.5523		
B_i^P	0.0028	0.5802	0.5371	0.0256		
%Ev	87.44	36.25	66.16	42.82		

Wiberg bond indexes (B_i), % evolution through the reaction coordinate ($\%E_v$), average bond index variation (δB_{AV}), and synchronicity parameters (S_y)

and electronic parameters (See Supporting material, Table S11), and confirms the qualitative interpretation shown in Fig. 2. As the Cu–F bond breaking ($\%E_v \approx 90$ %) is more advanced than all of the other bond changes at the transition state, the $Cu^{\delta+}$–$F^{\delta-}$ polarization of this bond is expected to be a determining factor in this reaction.

The activation reactions show a free energy barrier[2] of about 18 kcal/mol (Table 1). The more important barrier for the IPr NHC ligand can be explained by an increased steric effect around the copper atom. Table 1 confirms the

---

[2] Free energy barriers are reported with respect to isolated reactants.

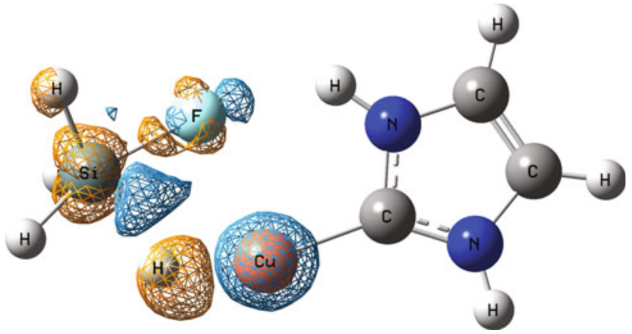

Fig. 2 Density difference between transition state and sum of reactants at transition-state geometry

importance of such a steric effect, showing a slight increase in free energy barrier when going from NHC = ADC_H to NHC = IMes.

These free energy barriers are relatively important, especially for a catalytic reaction, and in particular when compared to the ones obtained for diphosphines ligands [74]. The high barriers could be indicative of a different activation mechanism in solution. Calculations in solution on alternative mechanisms are currently ongoing.

The activation mechanism is nearly thermoneutral ($\Delta H = -0.3$–0.7 kcal/mol). As mentioned above, the fluorine atom is essential to the activation of the pre-catalyst, as other copper halogen complexes show little to no reactivity. Our results show that this observation is most likely due to the strong polarization of the Cu–F bond.

3.2 Catalytic cycle

Once activated, the copper hydride species enters the catalytic cycle. The proposed mechanism for the hydrogenation of ketones occurs through a two-step cycle as presented in Scheme 4. A first step concerns the formation of a copper alkoxide, through a σ metathesis similar to that observed for the activation of the pre-catalyst. In a second step, another 4-center transition state between this alkoxide and a hydrosilane leads to a silylated ether, and the reactivated catalyst. The alcohol can be recovered through hydrolysis of the silylated ether. Due to the fact the alkoxide complex is not observed experimentally, the reduction of the ketone is suggested to be the rate-limiting step.

As for the activation of the pre-catalyst, a stabilized van der Waals complex is observed between the catalyst and the reacting ketone during the first step of the cycle. The orientation of the molecules in this complex is favorable to the formation of the 4-center transition state (Fig. 3). Table 3 shows the relative energies, enthalpies, as well as free energies of the species involved in the first step of the catalytic cycle.

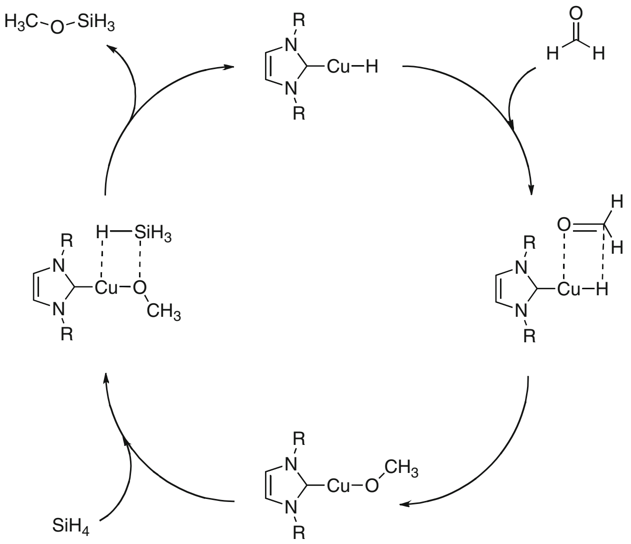

Scheme 4 The proposed mechanism for the hydrogenation of ketones by copper(I) hydride catalysts

The results show the formation of the van der Waals complex to be energetically favored by about 5 kcal/mol. The more important stabilization for NHC = ADC_H and IH complexes is not due to reduced steric effects but due to the formation of a strong hydrogen bond between the ketone oxygen atom and hydrogen atom fixed on the heterocyclic nitrogen (See Fig. 3). In true experimental systems, such interaction is not expected to occur. On the other hand, the slightly less important stabilization for the ItBu and IPr ligands can be explained by an increased steric hindrance around the copper atom.

As shown in Fig. 3, the van der Waals complexes are structurally close to the transition state, hence explaining the small energetic differences between both. At the transition state, elongated C–O and Cu–H bonds and reduced Cu–O and C–H distances characterize the complexes.

As for the activation of the pre-catalyst, the density differences at the transition state (Fig. 4) point toward an asynchronous concerted reaction mechanism, with the Cu–H–C rearrangement being more advanced than the formation of the Cu–O bond. Figure 4 shows a decrease in electron density along the Cu–H axis, as well as an increase along the H–C axis. The electron density of the C=O double bond is apparently displaced yielding a supplementary lone pair on the oxygen atom. In a second instance, the increased electronic density on the oxygen atom will be transferred to the Cu atom to complete the σ bond metathesis.

Bond indexes were, once more, calculated to give a more quantitative analysis of the transition-state asynchronicity. For this analysis, Cu–H, Cu–O, π(C–O), and C–H bonds were considered. Calculated Wiberg indexes for NHC = ADC_H, IH, and IMes are reported in Table 4.

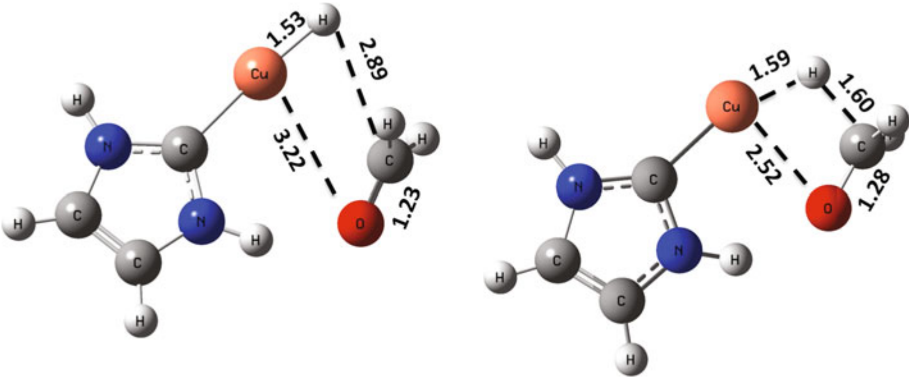

Fig. 3 Reactant van der Waals complex (*left*) and transition-state (*right*) structure for the reaction between (IH)Cu–H and H_2CO. Bond lengths are given in Å

Table 3 Relative energy ΔE, enthalpy, and free energy (ΔH; ΔG) with respect to (NHC)Cu–H and H_2CO reactants during the first step of the catalytic cycle

NHC=	van der Waals complex	TS	Products
ADC_H	−7.9 (−6.4; 3.1)	−1.8 (−0.8; 9.9)	−33.3 (−28.5; −18.8)
IH	−9.1 (−7.6; 2.3)	−2.5 (−1.6; 8.8)	−33.3 (−28.5; −18.9)
IMe	−4.9 (−3.6; 4.2)	−0.9 (−0.0; 11.2)	−33.5 (−28.7; −18.7)
IiPr	−4.9 (−3.5; 4.4)	−0.3 (0.6; 10.9)	−33.3 (−28.5; −18.9)
ItBu	−3.6 (−2.2; 5.0)	2.3 (3.2; 13.9)	−32.8 (−28.7; −18.5)
IPh	−4.9 (−3.5; 5.0)	0.4 (1.3; 12.6)	−33.5 (−28.7; −18.5)
IMes	−5.1 (−3.6; 7.4)	−0.6 (0.4; 14.5)	−33.8 (−28.9; −18.5)
IPr	−3.9 (−2.4; 7.0)	0.1 (1.0; 14.2)	−33.6 (−28.8; −19.6)

Values in kcal/mol

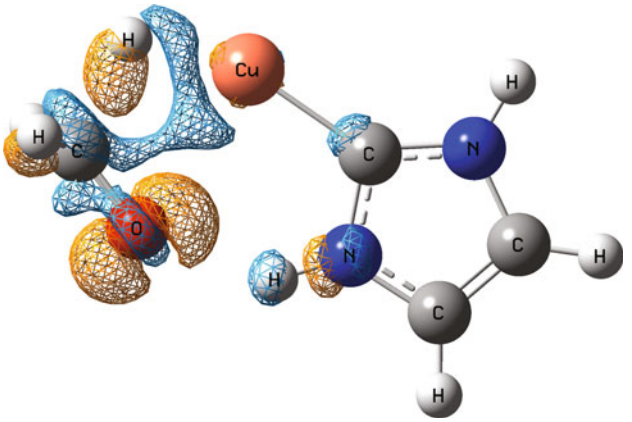

Fig. 4 Density difference between transition state and sum of reactants at transition-state geometry

According to these results, the Cu–H and π(C–O) bonds have been broken to approximately 50 % and 45 % at the TS, whereas the C–H bond has formed up to about 40–48 %. In agreement with the electronic density differences, the Cu–O bond has only been formed to a mere 4–13 %. Considering the Cu–H–C rearrangement to be more advanced than the formation of the Cu–O bond, the TS can be characterized as asynchronous, with the calculated S_y values ranged from 0.70 to 0.75. δB_{AV} average values of about 0.35 can be seen as indicative of early transition states.

For the reaction to take place, free energy barriers ranging from 9 to 15 kcal/mol with respect to the isolated reactants have to be overcome (Table 3).

As this first step of the catalytic cycle involves an electron transfer from the Cu–H bond to the ketone carbon atom, a more pronounced hydride character of the active Cu–H complex possibly explains the difference in reactivity for the different NHC ligands [76]. However, no relationship is found between the electronic population of the hydride and the free energy activation barrier $\Delta G^{\neq}$. Table S8 (in Supporting information) also confirms there to be almost no difference in charge of the hydrogen atom in the initial van der Waals complexes as NHC ligands considered in this study are similar from an electronic point of view (i.e., weak influence of the N substituents on electronic properties), and hence, this factor does not explain the difference in reactivity. However, the series of ligands considered here strongly differ from a steric point of view. To study steric effects, the "percent buried volume" ($\%V_{\mathrm{Bur}}$) defined as the percent of the total volume of a sphere occupied by a ligand, introduced by Nolan and Cavallo [115–123], is used. To measure the $\%V_{\mathrm{Bur}}$, we examined the DFT-optimized geometries of the free ligands by using a software developed by Cavallo et al., which is available free from charge [124, 125].[3] Table 5

---

[3] Optimized structures of (NHC)Cu–H complexes were transformed to *xyz* format using the Open Babel 2.3.0 program [126] keeping only the atomic coordinates of elements belonging to the NHC ligand. These were used as raw data for $\%V_{\mathrm{Bur}}$ calculations with a distance of 2.10 Å for the metal–ligand bond. A compilation of $\%V_{\mathrm{Bur}}$ values is presented in Table 5.

Table 4 NBO analysis for the first step of the catalytic cycle

Catalyst	Cu–H	Cu–O	C–O	C–H	δB_{AV}	S_y
(ADC_H)Cu–H						
B_i^R	0.5657	0.0221	1.7823	0.0473	0.384	0.73
B_i^{TS}	0.2629	0.0436	1.4264	0.4630		
B_i^P	0.0021	0.3267	1.0107	0.9373		
%Ev	53.73	7.06	46.12	46.71		
(IH)Cu–H						
B_i^R	0.5612	0.0302	1.7554	0.0551	0.378	0.71
B_i^{TS}	0.2655	0.0444	1.4681	0.4794		
B_i^P	0.0020	0.3245	1.0138	0.9373		
%Ev	52.88	4.83	45.42	48.1		
(IMes)Cu–H						
B_i^R	0.5523	0.0144	1.8068	0.0530	0.347	0.75
B_i^{TS}	0.2900	0.0387	1.4622	0.4002		
B_i^P	0.0018	0.3093	1.0152	0.9365		
%Ev	47.65	8.24	43.53	39.30		

Wiberg bond indexes (B_i), % evolution through the reaction coordinate (%E_v), average bond index variation (δB_{AV}) ,and synchronicity parameters (S_y)

Table 5 %V_{Bur} for selected systems

Entry	NHC=	%V_{Bur}
1	ADC_H	20.4
2	IH	19.4
3	IMe	25.9
4	IiPr	27.0
5	ItBu	40.8
6	IPh	33.2
7	IMes	34.4
8	IPr	42.7

shows this parameter to increase as could be expected by looking at the size of the ligand, although the overall variation is small. Larger ligands such as the IMes ligand can be characterized by lower values, highlighting the importance of the structural occupation. Strong steric hindrance is shown for ItBu and IPr ligands, as they bring crowded methyl groups in the area surrounding the Cu atom (entries 5 and 8).

Analyzing the variation in free activation energy with respect to this parameter (Fig. 5), the importance of steric hindrance on the activation barrier of the first step of the

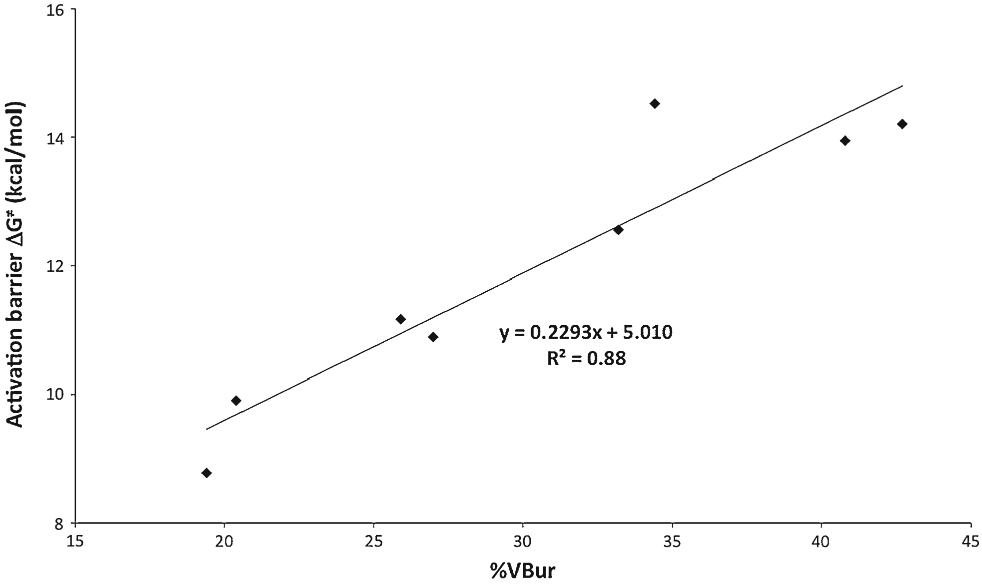

Fig. 5 Evolution of computed free activation barriers as a function of the %V_{Bur} for the first step of the catalytic cycle

Table 6 Relative energy ΔE, enthalpy, and free energy (ΔH; ΔG) with respect to (NHC)Cu–OCH_3 and SiH_4 reactants during the second step of the catalytic cycle

NHC=	van der Waals complex	TS	van der Waals complex	Products
ADC_H	−2.6 (−1.1; 8.5)	−1.0 (−0.5; 11.2)	−10.1 (−8.7; 1.6)	−5.0 (−5.0; −3.9)
IH	−2.8 (−1.3; 8.6)	−1.0 (−0.5; 9.7)	−11.2 (−9.8; 0.6)	−5.0 (−5.0; −3.8)
IMe	−2.8 (−1.3; 8.4)	−0.6 (0.1; 11.7)	−5.8 (−4.6; 3.6)	−4.8 (−4.8; −4.0)
IiPr	−2.9 (−1.4; 8.5)	−0.5 (−0.5; 13.6)	−5.7 (−4.5; 4.0)	−4.9 (−5.0; −4.6)
ItBu	−2.1 (−0.5; 9.1)	−0.9 (−0.3; 11.1)	−4.1 (−2.9; 3.4)	−5.4 (−5.5; −4.6)
IPh	−2.3 (−0.8; 8.6)	−1.0 (−1.0; 12.3)	−5.0 (−3.8; 2.3)	−4.7 (−4.8; −4.3)
IMes	−2.9 (−1.4; 8.4)	−0.1 (0.4; 13.1)	−4.8 (−3.5; 5.0)	−4.5 (−4.6; −4.2)
IPr	−2.5 (−0.8; 11.1)	0.6 (1.3; 15.6)	−4.5 (−4.5; 8.1)	−4.6 (−4.7; −3.1)

Values in kcal/mol

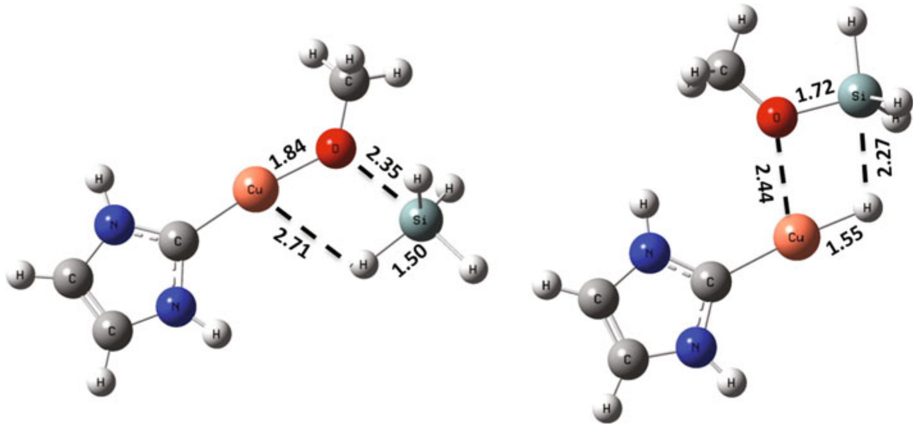

Fig. 6 Reactant van der Waals complex (*left*) and transition-state (*right*) structure for the reaction between (IH)Cu–OCH_3 and SiH_4. Bond lengths are given in Å

catalytic cycle is clearly highlighted, showing this step to be mainly under steric control.

The second step of the catalytic cycle concerns the regeneration of the catalyst, through the reaction of the Cu-alkoxide species with a silane molecule, yielding a silylated ether product. As for the previous steps, a σ metathesis reaction is suggested passing through a 4-center transition state. As for the previous steps, an energetically stabilized van der Waals complex is obtained between both compounds. The stabilizing interaction of about 3 kcal/mol (Table 6) is comparable to the energetic stabilization observed for the first step of the catalytic cycle. This interaction places the compounds in an orientation favorable to the 4-center transition state. As expected, the transition state is characterized by shortened Cu–H and Si–O bonds, and elongated SiH and Cu–O bonds, as shown in Fig. 6.

Density differences (Fig. 7) once more qualitatively show an asynchronous transition state with the Cu–O bond breaking/O–Si bond formation being more advanced compared to the hydrogen transfer toward the Cu atom. Wiberg indexes (Table 7) confirm this asynchronicity, although it being less pronounced compared to the previous steps ($S_y = 0.90$–0.95). At the TS, the Si–H and Cu–O bonds are broken at approximately 75 and 85 %, while almost 85 % of the Si–O bond has been formed. The Cu–H bond has only been formed up to about 60–65 %. δB_{AV} average values of about 0.75 indicate late transition states, which could be anticipated from their structure as shown in Fig. 6.

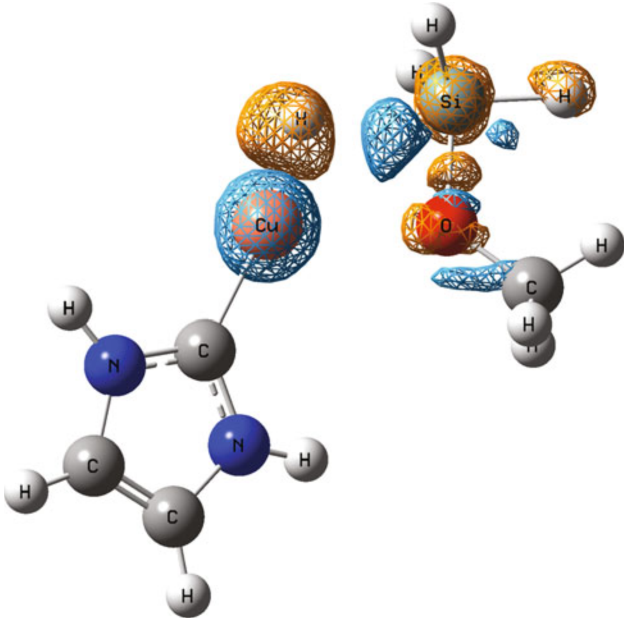

Fig. 7 Density difference between transition state and sum of reactants at transition-state geometry

For the reaction to take place, free energy barriers ranging from 9.5 to 15.5 kcal/mol have to be overcome

Table 7 NBO analysis for the second step of the catalytic cycle

Catalyst	Cu–O	Cu–H	Si–H	Si–O	δB_{AV}	S_y
(ADC_H)Cu–H						
B_i^R	0.2739	0.0056	0.9079	0.1233	0.804	0.95
B_i^{TS}	0.0407	0.4242	0.1791	0.5377		
B_i^P	0.0030	0.6140	0.0005	0.6040		
%Ev	86.08	68.80	80.32	86.21		
(IH)Cu–H						
B_i^R	0.2707	0.0056	0.9079	0.1310	0.760	0.91
B_i^{TS}	0.0334	0.3686	0.2645	0.5321		
B_i^P	0.0019	0.6158	0.0002	0.6012		
%Ev	88.28	59.49	70.88	85.30		
(IMes)Cu–H						
B_i^R	0.2614	0.0037	0.9191	0.1280	0.745	0.92
B_i^{TS}	0.0298	0.3630	0.2566	0.5355		
B_i^P	0.0012	0.6092	0.0004	0.6535		
%Ev	89.01	59.34	72.11	77.55		

Wiberg bond indexes (B_i), % evolution through the reaction coordinate ($\%E_v$), average bond index variation (δB_{AV}), and synchronicity parameters (S_y)

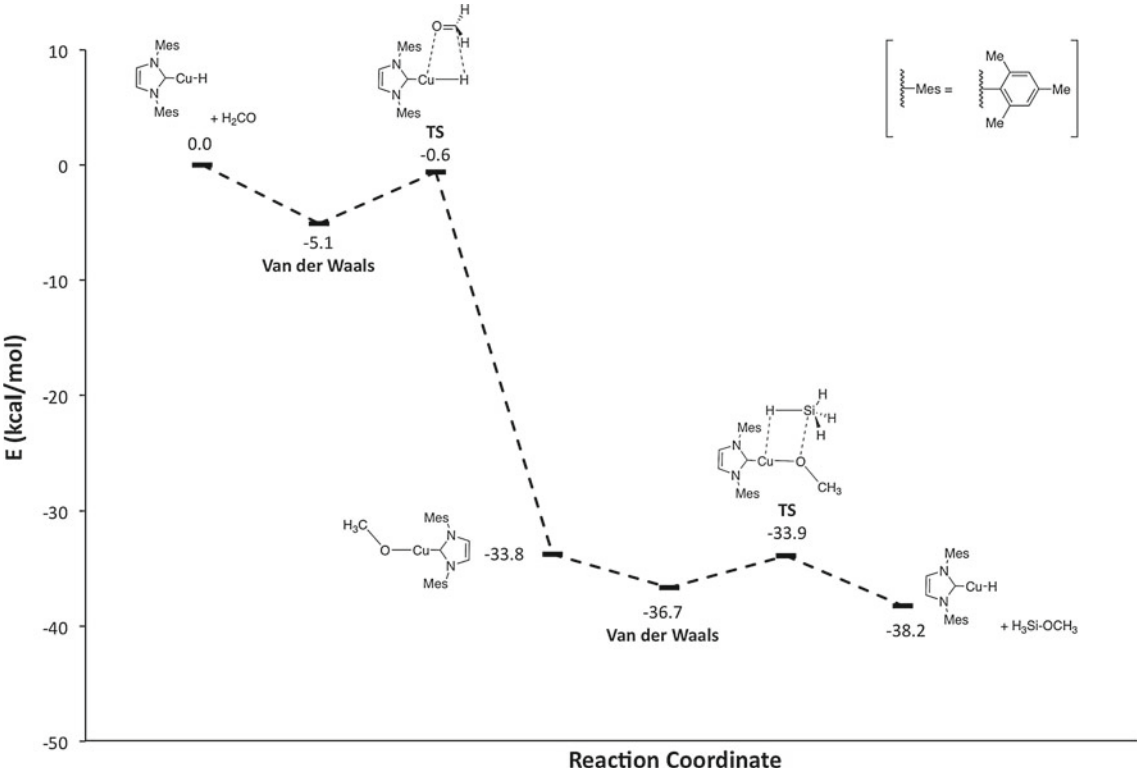

Fig. 8 Calculated B3LYP/6-31 ++G(d,p) potential energy surface (kcal/mol) for the catalytic cycle of hydrosilylation of formaldehyde by the (IMes)Cu–H catalyst

(Table 6), which are comparable to the barriers observed for the first step of the cycle (Fig. 8), and hence, the rate-determining step cannot be decided upon. Although the steric effect ($\%V_{\mathrm{Bur}}$) once more is important, it does not explain the variation in activation barrier as well as for the first step. Other effects such as bond strength and electronic effects are likely also important to explain the differences in activation barrier.

Steric effects likely have an increasing importance for the more crowed NHC ligands, as well as for larger ketones and silanes.

Energetic barriers are, nevertheless, substantially lower than free energy barriers of 51.13 and 56.70 kcal/mol calculated for the non-catalyzed hydrosilylation of formaldehyde and acetone, respectively. The low energetic barriers calculated in this work show the plausibility of the suggested catalytic cycle and furthermore explain the high turnover number observed for these types of catalyst.

The overall catalytic cycle shows an exothermicity of about 35 kcal/mol ($\Delta H = 33.5$ kcal/mol for the (IH)Cu–H molecule), which is driven by the transformation of a $\pi C = O$ bond and a σ Si–H bond into more stable σ C–H and σ O–Si bonds, and is in agreement with experimental observations.

4 Conclusions

In this paper, we have shown the theoretical validity of the suggested catalytic cycle for the hydrosilylation of ketones using N-heterocyclic diaminocarbenes Cu(I) hydride catalysts. The activation of the catalyst from a copper fluoride complex, as well as both steps of the catalytic cycle, involves a 4-center σ metathesis transition state. The reactants are guided toward these transition states, through the formation of energetically favored van der Waals complexes, formed through favorable electrostatic interactions. Analysis of transition states shows that the σ metathesis reactions studied here can be described as asynchronous concerted mechanisms, with the transfer from Cu-linked atoms occurring prior to the transfer toward the metal center.

For the reductive hydrosilylation of a ketone by SiH_4 to take place, a free energy barrier of about 14 kcal/mol (for the more realistic ItBu, IMes, and IPr models) with respect to the isolated reactants has to be overcome. Comparable energy barriers are obtained for the two successive steps of the catalytic cycle, not allowing to identify a rate-limiting step, if there should be one.

Finally, we noted an overall exothermicity of the catalytic cycle of about 35 kcal/mol, driven by the transformation of a $\pi C = O$ bond and a σ Si–H bond into more stable σ C–H and σ O–Si bonds.

Acknowledgments The authors would like to thank the Université Catholique de Louvain (Thomas Vergote is a UCL research assistant). They would also like to thank the Fond de la Recherche Scientifique de Belgique (FRS-FNRS) for funding computational resources provided by the supercomputing facilities of the Université Catholique de Louvain (CISM/UCL) and the Consortium des Equipements de Calcul Intensif en Fédération Wallonie-Bruxelles (CECI).

References

1. Smith MB, March J (2001) March's advanced organic chemistry. Wiley, New York
2. Ohkuma T, Noyori R (1999) Hydrogenation of carbonyl groups. In: Jacobsen EN, Pfaltz A, Yamamoto H (eds) Comprehensive asymmetric catalysis. Springer, Berlin, pp 199–246
3. Nishiyama H, Itoh K (2000) Asymmetric hydrosilylation and related reactions. In: Ojima I (ed) Catalytic asymmetric synthesis. Wiley, New York, pp 111–144
4. Corey EJ, Helal CJ (1998) Angew Chem Int Ed 37:1986–2012
5. Marciniec B, Maciejewski H, Pietraszuk C, Pawluć P (2009) Advances in silicon science, vol 1: hydrosilylation a comprehensive review on recent advances. Springer, Berlin
6. Ojima I, Nihonyanagi M, Nagai Y (1972) J Chem Soc Chem Commun 1972:938–938
7. Langlois N, Dang TP, Kagan HB (1973) Tetrahedron Lett 49: 4865–4868
8. Dumont W, Poulin J-C, Kagan HB (1973) J Am Chem Soc 95:8295–8299
9. Du G, Abu-Omar MM (2006) Organometallics 25:4920–4923
10. Ison EA, Trivedi ER, Corbin RA, Abu-Omar MM (2005) J Am Chem Soc 127:15374–15375
11. Nolin KA, Krumper JR, Pluth MD, Bergman RG, Toste FD (2007) J Am Chem Soc 129:14684–14696
12. Gade LH, Cesar V, Bellemin-Laponnaz S (2004) Angew Chem Int Ed 43:1014–1017
13. Nishiyama H, Sakaguchi H, Nakamura T, Horihata M, Kondo M, Itoh K (1989) Organometallics 8:846–848
14. Tao B, Fu GC (2002) Angew Chem Int Ed 41:3892–3894
15. Sawamura M, Ryoichi K, Ito Y (1994) Angew Chem Int Ed 33: 111–113
16. Zhu G, Terry M, Zhang X (1997) J Organomet Chem 547: 97–101
17. Nishibayashi Y, Takei I, Uemura S (1998) Organometallics 17:3420–3422
18. Chianese AR, Crabtree RH (2005) Organometallics 25:3066–3073
19. Nakano T, Nagai Y (1988) Chem Lett 17:481–484
20. Carter MB, SchiØtt B, Gutiérrez A, Buchwald SL (1994) J Am Chem Soc 116:11667–11670
21. Halterman R, Ramsey TM, Chen Z (1994) J Org Chem 59: 2642–2644
22. Xin S, Harrod JF (1995) Can J Chem 73:999–1002
23. Bandini M, Bernardi F, Bottoni A, Cozzi PG, Miscione GP, Umani-Ronchi A (2003) Eur J Org Chem 2003:2972–2984
24. Imma H, Mori M, Nakai T (1996) Syn Lett 1996:1229–1230
25. Mandini M, Cozzi PG, Nego L, Umani-Ronchi A (1999) Chem Comm 1999:39–40
26. Yun J, Buchwald SL (1999) J Am Chem Soc 121:5640–5644
27. Brunner H, Fisch K (1990) Angew Chem Int Ed 29:1131–1132
28. Shaikh NS, Enthaler S, Junge K, Beller M (2008) Angew Chem Int Ed 47:2497–2501
29. Langlotz BK, Wadepohl H, Gade LH (2008) Angew Chem Int Ed 41:4670–4674
30. Son SU, Paik S-J, Lee IS, Lee Y-A, Chung YK (1999) Organometallics 18:4114–4118
31. DiBiase Cavanaugh M, Gregg BT, Cutler AR (1996) Organometallics 15:2764–2769
32. Mimoun H, de Saint Laumer JY, Giannini L, Scopelliti R, Floriani C, Am J (1999) Chem Soc 121:6158–6166
33. Mimoun H (1999) J Org Chem 64:2582–2589
34. Ohkuma T, Hashiguchi S, Noyori R (1994) J Org Chem 59: 217–221

35. Bette V, Mortreux A, Savoia D, Carpentier J-F (2004) Tetrahedron 60:2837–2842
36. Brunner H, Miehling W (1984) J Organomet Chem 275:C17–C21
37. Lipshutz BH, Chrisman W, Noson K (2001) J Organomet Chem 624:367–371
38. Wu J, Ji J-X, Chan ASC (2005) Proc Nat Acad Sci 102: 3570–3575
39. Lee D-W, Yun J (2004) Tetrahedron Lett 45:5415–5417
40. Issenhuth JT, Dagorne S, Bellemin-Laponnaz S (2006) Adv Synth Catal 348:1991–1994
41. Riant O, Mostefaï N, Courmarcel J (2004) Synthesis 18:2943–2958
42. Lipshutz BH (2002) Copper(I)-mediated 1,2- and 1,4-Reductions. In: Krause N (ed) Modern organocopper chemistry. Wiley-VCH, Weinheim, pp 167–187
43. Riant O (2009) Copper(I) hydride reagents and catalysts. In: Rappoport Z, Marek I (ed) The chemistry of organocopper compounds. Wiley, pp 731–773
44. Lipshutz BH, Noson K, Chrisman W (2001) J Am Chem Soc 123:12917–12918
45. Lipshutz BH, Lower A, Noson K (2002) Org Lett 4:4045–4048
46. Lipshutz BH, Caires CC, Kuipers P, Chrisman W (2003) Org Lett 5:3085–3088
47. Lipshutz BH, Frieman BA (2005) Angew Chem 117:6503–6506
48. Lipshutz BH, Frieman BA (2005) Angew Chem Int Ed 44:6345–6348
49. Czekelius C, Carreira EM (2004) Org Lett 6:4575–4578
50. Sirol S, Courmarcel J, Mostefaï N, Riant O (2001) Org Lett 3: 4111–4113
51. Courmarcel J, Mostefaï N, Sirol S, Choppin S, Riant O (2001) Isr J Chem 41:231–240
52. Mostefaï N, Sirol S, Courmarcel J, Riant O (2007) Synthesis 8:1265–1271
53. Yu F, Zhou JN, Zhang XC, Sui YZ, Wu FF, Xie LJ, Chan ASC, Wu J (2011) Chem Eur J 17:14234–14240
54. Díez-González S, Nolan SP (2005) Annu Rep Prog Chem Sect B 101:171–191
55. Herrmann WA (2002) Angew Chem Int Ed 41:2162–2187
56. Bourissou D, Guerret O, Gabbai FP, Bertrand G (2000) Chem Rev 100:39–91
57. Arduengo AJ III (1999) Acc Chem Res 32:913–921
58. Arduengo AJ III, Harlow RL, Kline M (1991) J Am Chem Soc 113:361–363
59. Navarro O, Kelly RA III, Nolan SP (2003) J Am Chem Soc 125:16194–16195
60. Viciu MS, Germaneau RF, Nolan SP (2002) Org Lett 4: 4053–4056
61. Lee CW, Choi T-L, Grubbs RH (2002) J Am Chem Soc 124: 3224–3225
62. Herrmann WA, Bohm VPW, Gstottmayr CWK, Grosche M, Reisinger CP, Weskamp TJ (1999) Organomet Chem 586: 563–565
63. Kaur H, Zinn FK, Stevens ED, Nolan SP (2004) Organometallics 23:1157–1160
64. Díez-González S, Kaur H, Zinn FK, Stevens ED, Nolan SP (2005) J Org Chem 70:4784–4796
65. Yun J, Kim D, Yun H (2005) Chem Comm 2005:5181–5183
66. Díez-González S, Scott NM, Nolan SP (2006) Organometallics 25:2355–2358
67. Díez-González S, Stevens ED, Scott NM, Petersen JL, Nolan SP (2008) Chem Eur J 14:158–168
68. Vergote T, Nahra F, Welle A, Luhmer M, Wouters J, Mager N, Riant O, Leyssens T (2012) Chem Eur J 18:793–798
69. Albright A, Gawley RE (2011) J Am Chem Soc 133:19680–19683
70. Díez-González S, Nolan SP (2008) Acc Chem Res 41:349–358
71. Díez-González S, Nolan SP (2008) Aldrichimica Acta 41:43–51
72. Ito H, Ishizuka T, Okumura T, Yamanaka H, Tateiwa J-I, Sonoda M, Hosomi A (1999) J Organomet Chem 574:102–106
73. Mankad NP, Laitar DS, Sadighi JP (2004) Organometallics 23:3369–3371
74. Gathy T, Peeters D, Leyssens T (2009) J Organomet Chem 694: 3943–3950
75. Gathy T, Leyssens T, Peeters D (2011) Comp Theor Chem 970: 23–29
76. Gathy T, Riant O, Peeters D, Leyssens T (2011) J Organomet Chem 696:3425–3430
77. Issenhuth J-T, Notter F-P, Dagorne S, Dedieu A, Bellemin-Laponnaz S (2010) Eur J Inorg Chem 2010:529–541
78. Zhang W, Li W, Qin S (2012) Org Biomol Chem 10:597–604
79. Becke AD (1993) J Chem Phys 98:5648–5653
80. Lee C, Yang W, Parr RG (1988) Phys Rev B37:785–789
81. Frisch MJ, Trucks GW, Schlegel HB, Scuseria GE, Robb MA, Cheeseman JR, Montgomery JA Jr, Vreven T, Kudin KN, Burant JC, Millam JM, Iyengar SS, Tomasi J, Barone V, Mennucci B, Cossi M, Scalmani G, Rega N, Petersson GA, Nakatsuji H, Hada M, Ehara M, Toyota K, Fukuda R, Hasegawa J, Ishida M, Nakajima T, Honda Y, Kitao O, Nakai H, Klene M, Li X, Knox JE, Hratchian HP, Cross JB, Bakken V, Adamo C, Jaramillo J, Gomperts R, Stratmann RE, Yazyev O, Austin AJ, Cammi R, Pomelli C, Ochterski JW, Ayala PY, Morokuma K, Voth GA, Salvador P, Dannenberg JJ, Zakrzewski VG, Dapprich S, Daniels AD, Strain MC, Farkas O, Malick DK, Rabuck AD, Raghavachari K, Foresman JB, Ortiz JV, Cui Q, Baboul AG, Clifford S, Cioslowski J, Stefanov BB, Liu G, Liashenko A, Piskorz P, Komaromi I, Martin RL, Fox DJ, Keith T, Al-Laham MA, Peng CY, Nanayakkara A, Challacombe M, Gill PMW, Johnson B, Chen W, Wong MW, Gonzalez C, Pople JA (2004) Gaussian 03, revision C.02. Gaussian, Wallingford
82. Fukui K (1970) J Phys Chem 74:4163–6161
83. Fukui K (1981) Acc Chem Res 14:363–368
84. Gonzalez C, Schlegel HB (1989) J Chem Phys 90:2154–2161
85. Gonzalez C, Schlegel HB (1990) J Phys Chem 94:5523–5527
86. Grimme S, Antony J, Ehrlich S, Krieg H (2010) J Chem Phys 132:154104–154123
87. Hay PJ, Wadt WR (1985) J Chem Phys 82:270–283
88. Hay PJ, Wadt WR (1985) J Chem Phys 82:284–298
89. Hay PJ, Wadt WR (1985) J Chem Phys 82:299–310
90. Hehre WJ, Ditchfield R, Pople JA (1972) J Chem Phys 56:2257–2261
91. Hariharan PC, Pople JA (1973) Theor Chim Acta 28:213–222
92. Foster JP, Weinhold F (1980) J Am Chem Soc 102:7211–7218
93. Reed AE, Weinhold F (1983) J Chem Phys 78:4066–4073
94. Reed AE, Weinstock RB, Weinhold F (1985) J Chem Phys 83: 735–746
95. Reed AE, Weinhold F (1985) J Chem Phys 83:1736–1740
96. Keith T, Millam J (2006) Gaussview, version 4.1.2, R. Dennington, II, Semichem, Inc., Shawnee
97. Weigend F, Ahlrichs R (2005) Phys Chem Chem Phys 7:3297–3305
98. Perdew JP (1986) Phys Rev B 33:8822–8824
99. Becke AD (1988) Phys Rev A 38:3098–3100
100. Perdew JP (1991) Beyond the local density approximation. In: Ziesche P, Esching H (eds) Electronic structure of solids '91. Akademie Verlag, Berlin, pp 11–20
101. Adamo C, Barone V (1998) J Chem Phys 108:664–675
102. Quintal MM, Karton A, Iron MA, Boese AD, Martin JML (2006) J Phys Chem 110:709–716
103. Sousa SF, Fernandes PA, Ramos MJ (2007) J Phys Chem A 111: 10439–10452
104. Schultz NE, Zhao Y, Truhlar DG (2005) J Phys Chem A 109: 11127–11143

105. Roy LE, Hay PJ, Martin RL (2008) J Chem Theory Comput 4:1029–1031
106. Ehlers AW, Bihme M, Dapprich S, Gobbi A, Hollwaerth A, Jonas V, Kokler KF, Stegmann R, Veldkamp A, Frenking G (1993) Chem Phys Lett 208:111–114
107. Bergner A, Dolg M, Kuechle W, Stoll H, Preuss H (1993) Mol Phys 80:1431–1441
108. Kaupp M, Schleyer PVR, Stoll H, Preuss H (1991) J Chem Phys 94:1360–1366
109. Dolg M, Stoll H, Preuss H, Pitzer RM (1993) J Phys Chem 97:5852–5859
110. Mahonney WS, Bretensky DM, Stryker JM (1988) J Organomet Chem 110:291–294
111. Wiberg K (1968) Tetrahedron 24:1083–1096
112. Moyano A, Pericas M, Valenti E (1989) J Org Chem 54:573–582
113. Lecea B, Arrieta A, Roa G, Ugalde J, Cossio F (1994) J Am Chem Soc 116:9613–9619
114. Heredia MM, Lorono M, Cordova T, Chuchani G (2005) J Mol Struct: Theochem 770:131–137
115. Cavallo L, Correa A, Costabille C, Jacobsen H (2005) J Organomet Chem 690:5407–5413
116. Hillier AC, Sommer WJ, Yong BS, Petersen JL, Cavallo L, Nolan SP (2003) Organometallics 22:4322–4326
117. Bazinet P, Ong T-G, O'Brien JS, Lavoie N, Bell E, Yap GPA, Korobkov I, Richeson DS (2007) Organometallics 26:2885–2895
118. Fortman GC, Scott NM, Linden A, Stevens ED, Dorta R, Nolan SP (2010) Chem Comm 46:1050–1052
119. Clavier H, Correa A, cavallo L, Escuerdo-Adán EC, Benet-Buchholz J, Slawin AMZ, Nolan SP (2009) Eur J Inorg Chem 2009:1767–1773
120. Viciu MS, Navarro O, Germaneau RF, Kelly RA III, Sommer W, Marion N, Stevens ED, Cavallo L, Nolan SP (2004) Organometallics 23:1629–1635
121. Dorta R, Stevens ED, Scott NM, Costabile C, Cavallo L, Hoff CD, Nolan SP (2005) J Am Chem Soc 127:2485–2495
122. Kelly RA III, Clavier H, Giudice S, Scott NM, Stevens ED, Bordner J, Samardjiev I, Hoff CD, Cavallo L, Nolan SP (2008) Organometallics 27:202–221
123. Urbina-Blanco CA, Bantreil X, Clavier H, Slawin AMZ, Nolan SP (2010) Beilstein J Org Chem 6:1120–1126
124. Poater A, Cosenza B, Correa A, Giudice S, Ragone F, Scarano V, Cavallo L (2009) Eur J Inorg Chem 2009:1759–1766
125. http://www.molnac.unisa.it/OMtools/sambvca.php
126. Available free of charge at: http://openbabel.sourceforge.net

Theor Chem Acc (2012) 131:1254
DOI 10.1007/s00214-012-1254-3

REGULAR ARTICLE

From atoms to biomolecules: a fruitful perspective

E. Cauët · T. Carette · C. Lauzin · J. G. Li · J. Loreau · M. Delsaut · C. Nazé · S. Verdebout · S. Vranckx · M. Godefroid · J. Liévin · N. Vaeck

Received: 17 April 2012 / Accepted: 26 June 2012 / Published online: 3 August 2012

Abstract We present a summary of the research activities of the “Quantum Chemistry and Atomic Physics” theoretical group of the “Chimie Quantique et Photophysique” Laboratory at Université Libre de Bruxelles. We emphasize the links between the three orientations of the group: theoretical atomic spectroscopy, structure, and molecular dynamics and list the perspectives of our collaboration.

Keywords Electronic correlation · Relativistic effects · Isotopic effects · Multiply excited states · Hollow atoms · *B*-spline basis set · Charge transfer · Photodissociation · Radiative association

1 Introduction

The “Quantum Chemistry and Atomic Physics” theoretical group of the ULB “Chimie quantique et Photophysique” (CQP) Laboratory actively participated in the series of “Quantum Chemistry in Belgium” meetings since the very first one (Namur 1995). During almost forty years, the seniors of this group (JL, MG, and NV) pursued the tradition of their predecessor, Georges Verhaegen, in investigating methodology transfers from atomic physics to quantum chemistry and vice versa. Among these developments, one finds the “atoms-in-molecules” approach[1] [105] that was developed to estimate the electron correlation molecular energy from atomic correlation energies [49] or the “transition states” method with fractional occupation numbers [67] to calculate atomic transition probabilities. Another tradition of our laboratory that the authors maintained, together with their colleagues Michel Herman and Jean Vander Auwera from the high resolution spectroscopy experimental group of the same laboratory, is to benefit from the theory-experiment synergy, as initiated by the tandem Reginald Colin—Georges Verhaegen in their study of BeH [41].

The present research activities of the theoretical group fit three main fields: ab initio atomic and molecular structures and quantum molecular dynamics. Some of the research subjects merge expertise from two different fields. For instance, the investigation of molecular dynamics is achieved by developing both wave packet propagation techniques [110] and molecular structure methodologies [112]. Another example is the continuous quest for new approaches to take electron correlation into account [174] that remains, since the beginning of ab initio calculations, the key for an adequate description of atomic [21] and molecular structures and properties [107]. A number of our research projects have direct astrophysical applications, including the determination of accurate atomic oscillator strengths and the investigation of isotopic and nuclear

Published as part of the special collection of articles celebrating theoretical and computational chemistry in Belgium.

E. Cauët · T. Carette · C. Lauzin · J. G. Li · J. Loreau ·
M. Delsaut · C. Nazé · S. Verdebout · S. Vranckx ·
M. Godefroid · J. Liévin · N. Vaeck (✉)
Chimie quantique et Photophysique, Université libre de
Bruxelles, 50, av. F.D. Roosevelt, CP160/09, 1050 Brussels,
Belgium
e-mail: nvaeck@ulb.ac.be

M. Godefroid
e-mail: mrgodef@ulb.ac.be

J. Liévin
e-mail: jlievin@ulb.ac.be

---

[1] Not to be confused with the Atoms In Molecules (AIM) approach of the late Richard Bader [6].

effects [71], the characterization of molecules suspected in space [137], the determination of rotational intensities to predict molecular abundances [29], or the calculation of rate constants for charge transfer processes [168, 169]. Contributions within each field may thus be very diverse and include also the calculation of atomic electroaffinities [20], time-dependent photodissociation processes [114], or DNA stacking properties [32]. We have gathered here some examples of our works which have been presented at the QCB meetings for more than 15 years now.

2 Theoretical atomic spectroscopy

The ab initio calculations of atomic structures are often dictated by high resolution spectroscopy laboratory experiments or by astrophysical observations that require reliable atomic parameters for their interpretation. The spectacular increase of the spectral resolution during the last two decades, in all domains of the electromagnetic spectrum, forced the theoreticians to improve their models and computational tools to achieve the needed accuracy in their atomic structures and dynamical properties calculations. This applies not only to laboratory measurements but also to observational spectroscopy for astrophysics and astronomy thanks to high resolution spectrometers coupled to ground-based or space telescopes.

We illustrate in the present section the important role of high resolution atomic structure calculations through specific examples, keeping in mind for their selection, that they should be of interest for the quantum chemistry community.

2.1 The partitioned correlation functions approach

It has been known for many years that variational methods can be used for targeting specific correlation effects by tailoring the configuration space [70]. We proposed a new method that was successfully applied for describing the total energy of the ground state of beryllium [174]. Independent sets of correlation orbitals, embedded in “Pair Correlation Functions (PCFs), are produced from separate multiconfiguration Hartree–Fock (MCHF) calculations [60]. These non-orthogonal one-electron functions span configuration state function (CSF) spaces that are coupled to each other by solving the associated generalized eigenvalue problem. The Hamiltonian and overlap matrix elements are evaluated using the biorthonormal orbital transformations and efficient counter-transformations of the configuration interaction eigenvectors [122]. Using this approach, we demonstrated the fast energy convergence in comparison with the conventional SD-MCHF method optimizing a single set of orthonormal one-electron orbitals for the complete configuration space. Very recently, we moved to a more general approach renamed the “Partitioned Correlation Function Interaction” approach [175] that keeps the same PCFI acronym, but that is not necessarily restricted to a pair partitioning. This original method is currently tested on the ground and the first excited state of neutral lithium, not only for the total energy, but also through the expectation values of the specific mass shift and hyperfine structure operators and radiative transition probabilities, using different models for tailoring the configuration space. We clearly identified the “contraction effect” as the source of inaccuracy for properties more sensitive than the energy, due to the use of fixed PCF eigenvector compositions. A progressive decontraction, up to the uncontracted non-orthogonal configuration interaction limit case, efficiently solves the problem by restoring the needed flexibility in the wave function. Let us illustrate the approach on $1s^2\ 2p\,{}^2P^{\mathrm{o}}$ of Li I for which the following four PCFs:

- the inner-shell ($1s$) double-excitations PCF,
- the inter-shell ($1s$, $2p$) single- and double-excitations PCF,
- the ($1s$, $1s$, $2p$) triple-excitations PCF,
- the inner-shell ($1s$) single-excitations PCF,

are built and optimized independently by the MCHF approach, keeping frozen the $1s$ and $2p$ orbitals from the HF solution. Each PCF brings its own basis of numerical orbitals, up to ($n = 10$; $l \leq 9$), in the “Uncontracted Partitioned Correlation Function Interaction”(UPCFI) eigenpair problem. The union of the four above PCFs reproduces the Complete Active Space (CAS) CSF expansion as far as the excitation families are concerned, but the variational richness of the one-electron basis is much larger than the one of the traditional CAS-MCHF calculation. Figure 1 illustrates the tremendous gain of our UPCFI approach compared with the CAS-MCHF method in the convergence pattern of the electric quadrupole hyperfine parameter b_{q} with respect to the size of the orbital active set(s). This parameter is defined as the following expectation value:

$$b_{\mathrm{q}} \equiv \left\langle \Gamma \mathrm{LSM}_L M_S \left| \sum_{i=1}^{N} 2C_0^{(2)}(i)\, r_i^{-3} \right| \Gamma \mathrm{LSM}_L M_S \right\rangle , \qquad (1)$$

calculated with $M_L = L$ and $M_S = S$ [71]. The ket $|\Gamma \mathrm{LSM}_L M_S\rangle$ defines the atomic state function and b_{q} represents the electric field gradient at the nucleus, produced by the electrons, interacting with the quadrupole moment of the nucleus, if any.

Even if the lithium atom is a three-electron system that can be described accurately by a single orthonormal

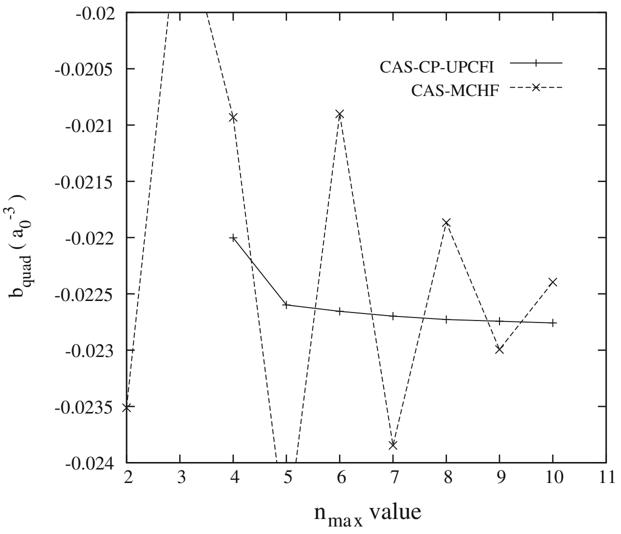

Fig. 1 Comparison of the CAS and uncontracted PCFI convergence patterns of the electric quadrupole hyperfine interaction parameter as a function of the size ($n_{\max}$) orbital active set

orbitals set, the PCFI method leads to an impressive improvement in the convergence pattern of all spectroscopic properties studied so far [175]. For larger systems, it becomes quickly hopeless to saturate the space occupied by all electrons with a single common set of orthonormal orbitals, and the PCFI method is a promising approach that might become competitive with the coupled-cluster approach [8] for getting high-quality correlated wave functions. The present study constitutes a major step in the current developments of both ATSP2K and GRASP2K packages [61, 90] that adopt the biorthonormal treatment for estimating energies, isotope shifts, hyperfine structures, and transition probabilities.

2.2 Nuclear effects on the electronic structure

During the last decade, our research group focused on various nuclear effects in atomic structures and dynamics. A major contribution [17] is the theoretical calculations of hyperfine-induced transitions that occur due to the fact that the total electronic quantum number **J** allowed by the coupling $\mathbf{J} = \mathbf{L} + \mathbf{S}$ cannot be "good" enough due to the hyperfine coupling $\mathbf{F} = \mathbf{J} + \mathbf{I}$, where **I** is the nuclear spin. The resulting **J**-mixing opens new decay processes that may affect the radiative lifetimes [1, 89] and may be observed in astrophysics [18]. The estimation of these subtle interaction mechanisms requires the evaluation of the complete hyperfine interaction matrix in the basis of the atomic states involved, all described by highly correlated and relativistic-corrected wave functions. The evaluation of the hyperfine constants and their comparison with observation brings sometimes surprises. For hyperfine structures of ^{15}N and ^{14}N spectral lines observed in the near-infrared [85], we estimated ab initio hyperfine constants [91] that disagree completely with the experimental parameters obtained by fitting the observed hyperfine spectra [85]. We proposed a new interpretation of the recorded weak spectral lines [21] as crossover signals, producing a new set of experimental hyperfine constants in very good agreement with the ab initio predictions. This exemplifies the crucial role of theoretical atomic structure calculations in the interpretation of high resolution spectroscopy experiments.

Another property, often relevant in chemistry, that can be isotope-dependent is the electron affinity. The theoretical estimation of this observable constitutes a real challenge [121], due to the delicate energy balance between the neutral atom and its negative ion. In the last years, we developed elaborated correlation models to estimate the isotope shift on the electron affinity in carbon, oxygen, sulfur, and chlorine [11, 20, 22], mainly motivated by the interpretation of the microscopy photodetachment experiments [10]. The estimation of the mass shift contributions becomes arduous for heavy systems since the recoil operator should be relativistically corrected [148]. We develop the algebra and the computational tools for allowing their calculation in the full relativistic scheme [63].

2.3 Relativistic effects in light elements

The ab initio calculation of atomic structures in light elements and ionic species definitely requires special care in the description of electron correlation beyond the single-configuration (not always single-Slater determinant) Hartree–Fock (HF) approximation. Although relativistic corrections are expected to become important for high-Z systems, they cannot be neglected at the level of high resolution at low Z. Moreover, in some situations, relativistic effects can be much larger than expected. These surprises occur in the case of near-degeneracies of non-relativistic levels that strongly mix through relativistic operators such as the spin–orbit interaction. In the present contribution, we illustrate how relativistic corrections can be large in fluorine, despite its low atomic number ($Z = 9$). Table 1 reports the theoretical values of the magnetic dipole hyperfine constant A_J for $2p^4 3p$ that are estimated using elaborate single- and double-multireference MCHF correlation models [23], together with the experimental value [158] for $^2D^o_{5/2}$. The calculations are performed using the multiconfiguration Hartree–Fock (MCHF) and Dirac–Fock (MCDF) methods. In both non-relativistic and relativistic models, the set of many-electron states selected to form the total wave function is constructed systematically using the "single- and double-multireference" approach. In the framework of MCHF, the relativistic effects are taken into account either in the Breit–Pauli (BP) approximation

Table 1 Theoretical and experimental hyperfine interaction constants A_J (in MHz) for neutral fluorine

Level	MCHF	MCHF-BP	RCI	MCDF	Exp [158]
$2p^4(^3P)3p\,^2D^o_{5/2}$	2,040	1,691	1,679	1,666	1,746 (1.5)
$2p^4(^3P)3p\,^4P^o_{5/2}$	788	1,007	1,004	1,002	

using the MCHF orbitals or through relativistic configuration interaction (RCI) calculations, in which the non-relativistic one-electron basis is converted to Dirac spinors using the Pauli approximation [22]. Relativistic effects can play a significant role on the hyperfine structures. The good agreement between the MCHF-BP, RCI, and MCDF results illustrates that these three methods are valid to capture relativistic effects in a system like fluorine. The remaining discrepancies between experiment and theory arise from higher-order electron correlation and relativistic corrections.

2.4 Electron densities from relativistic wave function

Ruthenium, rhodium, palladium, osmium, iridium, and platinum, having similar physical and chemical properties, constitute the so-called "platinum group". By looking at the position of the last three of these elements ($76 \leq Z \leq 78$) in the periodical table, the chemist immediately realizes the expected complexity of their electronic structures. Following the lanthanides, however, the 4*f* shell is filled by 14 electrons and the valence structures $5d^N\,6s^M$ of Os, Ir, Pt mainly differ in the (N, M) occupation numbers of the 5*d* and 6*s* atomic subshells. Osmium combined with rhenium, ruthenium or iron, produces compounds that are known as ultra-hard and incompressible materials [45], with a high recognized potential in the cutting tools and abrasives industry [93]. Osmium has a ground state $[\mathrm{Xe}]4f^{14}5d^66s^2\,{}^5D_4$ and the closeness of the valence shells with 4*f* makes an accurate description of its electronic wave function difficult to achieve. Moreover, relativistic effects are expected to be large with such a high number of protons [75]. We participate in the development of the computational atomic structure tools that are needed for getting a reliable description of such complex systems. Figure 2 displays the radial electron density $D(r)$ [12] of the osmium ground state, using three different models: HF, DF, and MCDF. The comparison between the HF and DF electron densities is striking and beautifully illustrates the importance of relativity for such a high-*Z* atom. But electron correlation is obviously crucial for many properties, although it is surprisingly difficult to visualize on the density itself [12]. The inset figure displays the magnified (×1,000) electron density difference between the single- and multiconfiguration pictures in the full relativistic scheme. The latter has been obtained by a single- and double-monoreference MCDF calculation, allowing one or two holes in the spectroscopic {4*f*, 5*d*, 6*s*} shells and adopting the {4*f*, 5*d*, 5*f*, 6*s*, 6*p*} orbital active set. As seen in this figure, the valence correlation induces some important reorganization of the electron cloud corresponding to an increase of the density in the outer region ($r > 1.5$ $\mathrm{a_0}$). A new program (RDENS) [104], designed as a module of GRASP2K [90] and its most recent version as far as the angular Racah–Wigner algebra is concerned [92], is under construction, on the basis of the relativistic extension of [12]. The possibility of getting reliable ab initio electron densities of complex atomic systems in ground and excited states, taking correlation and relativity into account, opens new perspectives in the context of ab initio DFT and its role in electronic structure theory [9, 73].

2.5 From doubly to multiply excited states in hollow atoms

In collision processes between slow highly charged ions (HCI) and neutral atoms or molecules, multiple electron capture into excited states of the ions is possible. Double capture is by far the most studied experimentally and theoretically [161] mainly because of the possibility to also reach those doubly-excited states radiatively from the ground state [16, 62]. Note that this research area is still very active, as illustrated by the recent reinvestigation of our pioneer work [161] on radiative transition probabilities

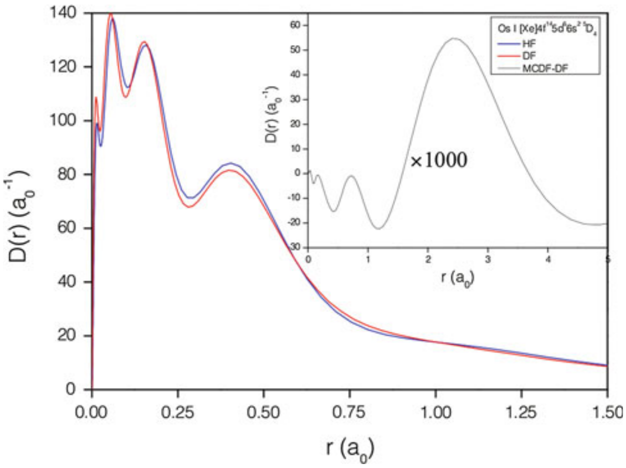

Fig. 2 Radial electron density $D(r)$ of the Os $[\mathrm{Xe}]4f^{14}5d^66s^2\,{}^5D_4$ ground state

and Auger rates of the $1s^2 3\ell 3\ell'$ states in Be-like ions [147]. The capture of three electrons from the neutral target into triply excited states is also possible but the analysis of the resulting electron spectra is much more complicated due to the complexity of the Auger decay cascade of the triply excited states. Vaeck and Hansen [163, 166] have carried out the first theoretical studies of the triply excited $3\ell 3\ell' 3\ell''$ and $3\ell 3\ell' n\ell''$ of N^{4+} and $1s^2 3\ell 3\ell' 3\ell''$ of N^{2+} and of their decay properties. The lifetimes of those triply excited states are dominated by Auger decay and assuming a statistical population of the manifolds, the average lifetime is about two orders of magnitude smaller than the average lifetime of corresponding the doubly-excited states (2.1×10^{-15} s compared with 1.0×10^{-13} s).

Multiple charge transfer processes can also take place in collision experiments between highly charged ions and metallic surfaces. At a certain distance from the metal, due to the large Coulomb potential, the ion pulls electrons out of the conduction band of the metal. These electrons populate excited levels of the ion until it is totally neutralized, leaving inner-shells empty. The resulting hollow atom, for which most of the electrons are in high-*n* levels, decays via cascades of autoionization and radiative processes while staying neutral due to the pick up of additional electrons. After, the hollow atom hits the surface and is stripped of its highly excited electrons. The ion then enters the surface and again captures electrons in excited levels (see [170] and the references therein).

The first challenge in the interpretation of the experimental results is the determination of the Auger rates of hollow atoms in front of the metallic surface. For N^{6+} at 600 eV in front of an Au surface, Vana et al. [172] observed about 20 electrons ejected in 10^{-14} s while for Th^{71+} in front of an Au surface, Aumayr et al. [4] measured the emission of between 160 and 260 electrons depending of the velocity of the ion. Using a single configuration average approach (SCA), Vaeck and Hansen [162, 164, 167] have determined the decay properties of hollow atoms of the type $1s^{0,1,2}np^N$ with $n = 2$–7 and $N = 2$–6 in nitrogen and obtained a lifetime for the neutral species of the order of 3–6×10^{-16} s in good agreement with the experimental data. These results have been confirmed for other atomic systems. For more complex systems, Palmeri et al [123] have developed a group-diagrammatic summation method which allows the calculation of Auger rates for configurations of the type $6f^N$ in $Th^{(44-N)+}$. Finally, the statistical properties of Hollow nitrogen have been investigated in the framework of the Random Matrix Theory by Vaeck and Kylstra [171].

When the ion enters the surface, lower energy levels start to be populated giving rise to interesting structures in the electron spectra. For N^{6+} colliding on a Ni(110) surface [3], the LMM and KLL structures have been partially interpreted using theoretical results [78]. The comparison between the electron spectrum resulting from the collision of N^{6+} and N^{7+} reveals three-electron Auger processes of the type K^2L^2L in which two electrons are stabilized while one is emitted [59]. The calculation of the decay rate of these processes is dominated by the non-orthogonality between the wavefunctions of the initial and final states [165].

Multiply excited states are characterized by very large configuration mixing which govern their decay properties. We hope that some of the methodology developed to study hollow atoms can open new perspectives for the calculation of complex molecular spectra involving autoionizing states or for the study of ion-pairs (heavy Rydberg) states [138] that will start soon in our laboratory.

3 Bridging atomic physics and quantum chemistry

3.1 Brillouin's theorem

We put a lot of effort in clarifying the connection between the Brillouin–Lévy–Berthier and Brillouin–Bauche–Labarthe–Froese Fischer theorems [69], leading to an interesting tool for analyzing the variational content of molecular wave functions [106]. Regarding Brillouin's theorem as a property of the Hartree–Fock wave function, one can use it to test the quality of the converged solution [68]. The Hartree–Fock problem for the general open-shell f^N case was solved by Gaigalas thanks to the Vilnius angular algebra [64]. In collaboration with Gaigalas, we proceeded to such systematic tests along the lanthanides and actinides for assessing the reliability of the code. This brings us to some mysterious discoveries: all Brillouin matrix elements that should be strictly zero for the converged HF solution are strictly zero. However, many other zeros appear as well, and these are still not understood despite our search in finding hidden symmetries within the quasi- and/or iso-spin formalisms.

3.2 The treatment of one-electron non-orthogonalities

For years, we faced the huge problem of dealing with radial non-orthogonalities arising from the independent optimization of the states involved in transition amplitudes, when using the Wigner–Fano–Racah algebra [56] for evaluating the matrix elements. The biorthogonal transformation algorithm developed by quantum chemists [115] was the key, after some necessary adaptation to the SO(3) spherical symmetry [122], to keep the advantages of the irreducible tensorial approach. These tools are now implemented for all one- and two-body operators in both the non-relativistic and relativistic packages [74] and are intensively used not only for the estimation of accurate transition probabilities, but also for energy differences and other properties as explained above in the PCFI section.

Bridging atomic physics and quantum chemistry is a rich inspiration source for new developments. Our recent work on the analysis of atomic physics calculations with methods from Quantum Chemistry [13] follows the same aim.

3.3 *B*-spline basis sets

B-splines are positive L^2 integrable piecewise polynomials of order K defined on a interval [0,R] from a recursive relation. *B*-splines have been used intensively in atomic physics to describe both the bond spectrum and the continuum of energy of atomic systems. One of the essential properties of the *B*-spline basis sets is their ”effective” completeness which allows the entire spectrum, including the continuum states, to be replaced by a pseudospectrum containing only a finite number of states. The pseudospectrum is constructed in such way that the low-lying states represent correctly the low-lying bound states of the real spectrum with the remaining pseudostates representing the remaining bound and continuum spectrum [76].

Using a truncated diagonalization method with these *B*-spline basis sets, we have calculated the decay properties of all doubly- excited $4\ell4\ell'$ and $4\ell5\ell'$ states of O^{6+} and Ne^{8+} populated during collisions between Ar and O^{8+} or Ne^{10+}, respectively [79, 80]. We have determined the degree of radiative stabilization of these doubly-excited states and compared it with the experimental results.

We took advantage of the effective completeness of the *B*-splines to predict the electronic rearrangement resulting from the β decay of ^{6}He and ^{6}He$^+$ in the framework of the sudden approximation [178] and by taking into account the recoil effects [179]. The shake off (ionization) probability of ^{6}Li^{2+} has been very recently measured in GANIL using a specially designed recoil ion spectrometer. This first measurement of an electron shake off following a β decay is in excellent agreement with our simple sudden approximation calculation [118].

The idea of using *B*-spline basis sets for the representation of vibrational molecular wave functions emerged rapidly. For a Morse potential and a two-dimensional Hénon–Heiles potential, we have assessed the efficiency of the *B*-splines over the conventional DVR (discrete variable representation) with a sine or a Laguerre basis sets [50]. In addition, the discretization of the vibrational continuum of energy when using the Galerkin method allows the calculation of photodissociation cross-sections in a time-independent approach.

The photodissociation of the molecular oxygen by UV solar radiation is the first step in the ozone-making reaction sequence

$$O_2 + h\nu \rightarrow O(^3P) + O(^3P)$$

$$O(^3P) + O_2 + M(M = O_2, N_2) \rightarrow O_3 + M$$

In the lower stratosphere, 90 % of the O_2 photodissociation results from transitions from the ground state $X^3\Sigma_g^-$ to the vibrational continua of the $A^3\Sigma_u^+, A'^3\Delta_u$ et $c^1\Sigma_u^-$ Herzberg states. Using a set a spectroscopic constants [87], we have constructed the RKR potential energy curves for the A, A′, c, and X states. The vibrational pseudospectra for all J values of these states have been obtained using 260 *B*-splines of order 13. The total cross section obtained in this work is compared to the available experimental and theoretical data in Fig. 3.

Finally, a *B*-spline method has also allowed the evaluation of the radiative decay probabilities of the six vibrational levels of the metastable $a^3\Sigma^+$ state of HeH$^+$. The transition $a^3\Sigma^+ \rightarrow X^1\Sigma^+$ is spin-forbidden, but acquires intensity through spin-orbit interaction with the singlet and triplet Π states [111].

4 Ab initio characterization of molecular structures

The evolution over the last decades of molecular ab initio calculations followed the spectacular methodological and

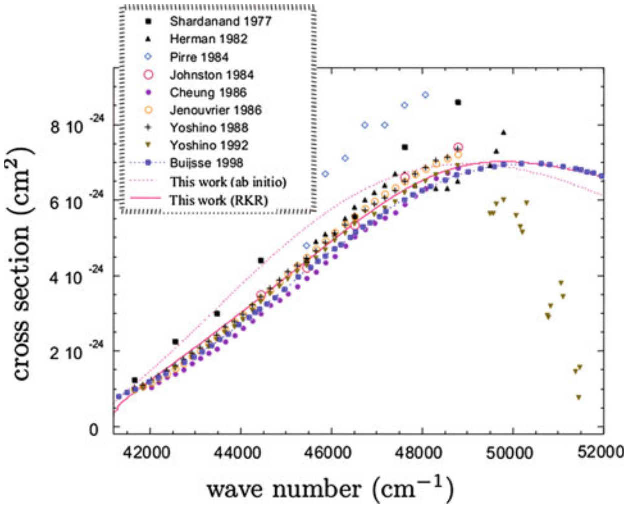

Fig. 3 Total photodissociation cross section for O_2 in the Herzberg states. “This work (ab initio)” corresponds to the use of ab initio potential energy curves and “This work (RKR)” to the use of RKR potentials constructed on the experimental data [87]. Comparison is made with the works of Shardanand and Prasad Rao [149], Herman and Mental [83], Pirre et al. [129], Johnston et al. [88], Cheung et al. [37], Jenouvrier et al. [86], Yoshino et al. [184], Yoshino et al. [185] and Buijsse et al. [19]

computational developments depicted in Sect. 2 for atomic calculations. It not only concerns the improvement of the methods of calculations for taking electron correlation and relativistic effects into account, and for treating excited states, but also the developments related to the nuclear degrees of freedom in molecules, like the handling of multi-dimensional potential energy surfaces [177] and the treatment of non-adiabatic couplings [53]. It also follows the increasing power of computer clusters allowing more accurate calculations on systems of increasing size. The size of a microscopic system is of course a subjective quantity, depending on both the number electrons and nuclei, the latter being equal to one for atoms and ranging from two to infinity for molecules, from diatomics to polymers. It is usually admitted that systems of two atoms or more belong to the world of "Chemistry", and specific theoretical developments are dedicated to different kinds of chemical objects. Application of Quantum Chemistry to biomolecules will be illustrated in Sect. 6 We will focus in this section on small molecules of atmospheric or astrophysical interest, for which a theoretical support to high resolution spectroscopy experiments is needed. As in the atomic case, we will highlight the theoretical efforts made for converging the calculated properties to experimental accuracy.

4.1 Determination of accurate molecular equilibrium properties

We first present some recent results on small hydrocarbons: methane, acetylene, and the methyl cation CH_3^+. Benchmark calculations have been performed on the determination of the equilibrium geometries of these species in their ground electronic state. These systems identified in numerous planetary atmospheres and interstellar medium present a renewed astrophysical interest [66, 102] and are extensively studied in high resolution laboratory experiments [14, 51].

The methyl cation CH_3^+ is involved in the interstellar reaction $C + H_3^+ \rightarrow CH^+ + H_2$, under study in our group [47].

Table 2 illustrates the convergence pattern up to the complete basis set limit (CBS) of the equilibrium CH bond distance in the ground ${}^1A_1'$ state (D_{3h} symmetry). Convergence is studied as a function of the extension (n = D, T, Q, 5 and 6) of the hierarchical aug-cc-pVnZ [54, 94] (AVnZ in short) and aug-cc-pCVnZ [182] (ACVnZ in short) basis sets. All calculations were performed using the internally-contracted multireference configuration interaction method (IC-MRCI) [95, 180] implemented in the MOLPRO program suite. The active spaces defining the multireference treatment coincide with the valence space for AVnZ calculations and with the full-(core + valence) active space for ACVnZ ones. All MRCI energies were corrected for Davidson's contribution for unlinked clusters [97]. CBS-extrapolation has been carried out on the energy, and not on the bond length value itself, as already done in other works [131]. Energies were extrapolated at each of the geometries scanned by the numerical derivative algorithm and numerical gradient optimizations have been applied to the extrapolated energies, as implemented in the MOLPRO code [181]. Extrapolations were separately applied [57, 173] at each geometry for the reference CASSCF energy and the dynamical correlation energy, using a simple exponential function [57] and a n^{-3} two-parameters form [81] respectively. The results show that, referring to the CBS value, one reaches the 0.1 pm accuracy at quintuple zeta level and that the introduction of the core and core-valence correlation (ACVnZ calculations) induces a contraction of the CH bond by 0.15 pm. Let us also note the agreement between IC-MRCI/AVnZ(CBS) and CCSD(T)-F12/VnZ-F12 frozen core results [46], with a faster convergence of the latter due to the use of explicit correlation.

In a similar study carried out on the ground electronic state of acetylene [107] at CCSD(T) level of theory, we found that the contribution of core electrons to the correlation energy decreases the CH equilibrium bond distance by a comparable amount (0.13 pm) as for CH_3^+. A similar contraction effect, but more pronounced (0.27 pm) as expected, is observed for the CC bond distance. The convergence of the ab initio equilibrium geometry to experimental accuracy was further addressed by also evaluating the effects of explicit triple and quadruple excitations (−0.014 and +0.042 pm for CC and CH, respectively), scalar relativistic corrections (−0.016 and −0.027 pm, respectively) and diagonal Born-Oppenheimer corrections (DBOC) (+0.013 and +0.003 pm respectively). Let us note that the DBOC calculations make use of the biorthogonal algorithm [115] cited in Sect. 3 The final ab initio values for both bonds, obtained by combining all mentioned contributions, are underestimated by about 0.02 pm with respect to the experimental values. Note that the latter were determined from a large number of ro-vibrational lines recorded for five isotopologues, providing thus a quite unique case for obtaining very accurate equilibrium parameters. These experimental values differ however from semi-empirical ones, also determined in Ref. [107] and based on results for ten isotopologues. Note also that non-adiabatic corrections are not taken into account in usual spectroscopic models. Above comparisons thus give an order of magnitude of the attainable accuracy on equilibrium geometries not only from ab initio calculations but also from experimental data.

Table 2 Convergence to CBS of the equilibrium CH bond length (in Å) of the ground electronic state of CH_3^+

n	D	T	Q	5	6	CBS
IC-MRCI/AV*n*Z	1.10380	1.09094	1.08951	1.08903	1.08898	1.08879
IC-MRCI/ACV*n*Z	1.10269	1.08967	1.08806	1.08758	1.08750	1.08729
CCSD(T)-F12/V*n*Z-F12 [46]	1.08913	1.08905	1.08875	–	–	–

Extensive calculations were also performed on methane [25–29], with the goal to predict the rotation–vibration spectrum which is of particular interest for evaluating methane abundance in planetary atmospheres. Our most recent results use an accurate potential energy surface calculated at the CCSD(T)/ACV5Z level of theory [119] and a dipole moment surface that we calculated at the IC-MRCI/ACV5Z level. The vibrational Schrödinger equation has been solved variationally, and perturbation theory was used to calculate the rotational spectrum of the ground vibrational state [29]. Note that the variational method developed for solving the vibrational problem, the vibrational mean field configuration interaction method (VMFCI) [26, 27], is directly inspired from electronic ab initio SCF/CI theory. The rotational spectrum calculated in that way is in very good agreement with the one recently recorded at the SOLEIL synchrotron [14] and with the atmospheric HITRAN database [142]. Note that part of this success comes from the accurate equilibrium geometry ensured by the use of the ACV5Z basis set in highly correlated calculations. As for the hydrocarbon systems mentioned above, the effect of core and core–valence correlation is to reduce the CH bond, by 0.02 pm in the case of methane.

4.2 Excited electronic structure of transition metal containing diatomics

Transition metal containing molecules have a potential astrophysical importance [109] and present an interest in catalysis and organometallic chemistry [24]. Numerous diatomic molecules MX made of a transition metal atom M and a second or third row atom X have been studied in laboratory using Fourier transform emission spectroscopy. Such experiments produce high resolution spectra covering a wide spectral range (typically from 0 to 25,000 cm^{-1}) and exhibit an intricate superposition of ro-vibrational bands. These spectra can usually not be assigned without a theoretical support. The complexity comes from the existence of many electronic states splitted by spin–orbit coupling and perturbed by non-adiabatic interactions. It also comes from the dense ro-vibrational structure conditioned by Franck–Condon factors and Hund's case angular momentum couplings. The electronic structure of the transition metal atom participating to the molecule formation is clearly at the origin of this complexity. As pointed out in Sect. 2, the transition metal is subject to relativistic effects and to important correlation effects arising from its valence shell $(n + 1)s^N nd^M$, coupled to the $ns^2\ np^6$ inner-shells and possibly to the 4*f* shell for sixth row elements. The high degeneracy of the low-lying transition metal atomic states and their splitting in the molecular $C_{\infty v}$ environment explain the high density of molecular electronic states in the spectral energy window. Providing a reliable energy scale of the molecular electronic states lying within this window is a challenge for ab initio calculations, but is a prerequisite to any spectroscopic assignment. Our group has provided a theoretical support for assigning the spectra of many transition metal containing diatomics recorded by Bernath's group (see for instance [132–135, 137]). The quantum chemistry approach we adopted for such systems is the CASSCF/IC-MRCI method, well adapted to excited state calculations with efficient account of electron correlation. Quasi-relativistic pseudo-potentials and corresponding basis sets are moreover used for the transition metal atom [2].

In many cases we found that the succession of electronic states drastically changes within an isovalent MX series. We showed for instance that the ground state of (IVb)-group chlorides changes from $^4\Phi$ to $^2\Delta$ from TiCl to HfCl, both states being quasi-degenerated for ZrCl [136]. We also showed that the low-lying quartet excited states are inverted in ZrF [152] with respect to ZrCl.

A similar situation is illustrated in Fig. 4 in the case of the diatomic nitrides of ruthenium, osmium, and iridium (transition metals of the "platinum group"), studied independently [132–134]. This choice of atoms for illustrating this topic rejoins the atomic physics interest in our group, pointed out in Sect. 2. The Figure shows that the low-lying electronic structure of the isovalent Ru and Os atoms can be described in terms of 4 main electronic configurations, labeled from (A) to (D), but that configurations (B), (C), and (D) are pushed to higher energies in OsN, with as a result a change of ground electronic state and an extension of the energy scale by more than 10,000 cm^{-1}. The reason for these changes can be interpreted in terms of the balance of correlation effects within the interacting shells (the natural orbitals of the IC-MRCI calculations of course move accordingly). Going from OsN to IrN corresponds to the addition of a single electron, which can tentatively be associated with different molecular orbitals from the analysis of the wave functions.

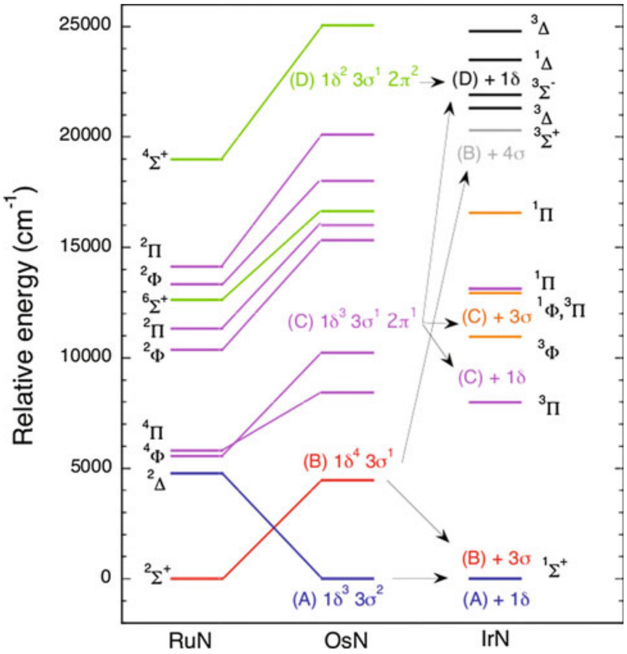

Fig. 4 Energy level diagram of the electronic states of RuN, OsN and IrN, from IC-MRCI calculations. *Colors* are used to mark states arising from the same configuration

4.3 Intermolecular potential energy surfaces of acetylene–rare gas complexes

High resolution infrared spectroscopy experiments carried out in our lab on acetylene-containing complexes motivated us to carry out large scale ab initio CCSD(T) calculations to support experimental results. Complexes are formed in a supersonic expansion allowing the detection of the complexes by means of cavity ring-down spectroscopy [52]. Accurate intermolecular potential energy surfaces (IPES) have been calculated for interpreting the $v_1 + v_3$ spectra of acetylene–rare gas complexes, the rare gas atom being argon, krypton, and xenon [101]. The spectra of the former two complexes have been studied experimentally [99, 100] but further theoretical help is needed for detailed analysis. IPES are defined by two coordinates R and θ, defining the Jacobi vector pointing from the center of mass of the acetylene moiety to the rare gas atom. Interaction energies were corrected for the basis set superposition error by means of the counterpoise approach [15]. Extensive test calculations have shown that the CCSD(T) method using all-electron AVQZ basis sets [54, 94] augmented by a set of ($3s3p2d1f$) midbond functions [157] provided interaction energy values close to the corresponding CBS limit. For krypton and xenon, multiconfigurational Dirac–Fock relativistic core potentials and corresponding AVQZ basis sets were used [126]. Table 3 illustrates the spectacular influence of both the correlation energy and the basis set on the stability of the global minimum of the acetylene–Kr complex. The positive values of the interaction energy at Hartree–Fock level shows how dispersion correlation effects determine the complex stability. Also note the importance of the basis set effect at CCSD(T) level, related to the description of the dispersion energy. The contributions of the scalar relativistic effects to the interaction energy have been evaluated to 1 and 2.3 % for acetylene–Kr and acetylene–Xe, respectively [101].

Table 3 Convergence to CBS of the interaction energy ΔE (in cm^{-1}) at the global minimum geometry of the acetylene–Kr complex

Method	Basis set	ΔE
HF	CBS(AV*n*Z + midbond)	+147.14
CCSD(T)	AVQZ	−141.39
CCSD(T)	CBS(AV*n*Z)	−153.11
CCSD(T)	AVQZ + midbond	−149.73

5 Non-adiabatic wavepacket molecular dynamics

Over the past decade, the Laboratoire de chimie quantique et photophysique of the ULB and the Laboratoire de chimie physique of the Université de Paris 11, Orsay have collaborated on the development of a strategy for the calculations of charge transfer cross-sections in ion-atom collision [110, 113, 168, 169],

$$A + B^{q+} \rightarrow A^{++}B^{(q-1)+}$$

This approach is based on a molecular description of the reaction in which the colliding particles engage in the reaction by the entrance channels corresponding to potential energy curves of the diatomic molecule AB^{q+}, form an unstable molecular bond, and dissociate into different exit channels. This method allows the use of conventional quantum chemistry program libraries for the calculation of the potential energy curves and of the coupling matrix elements which couple the entrance and exit channels in inelastic scattering. One of the expertise of the ULB team is the ab initio calculation of these time-independent parameters [112]. The dynamics of the nucleus is treated quantum mechanically, that is, the most appropriate approximation for low or very low collision energies encountered in the problems of interest in this proposal, by time-dependent wave packet propagation. For each collision energy, a Gaussian wave packet is prepared in the entrance channel and propagated on the coupled channels using the split-operator algorithm or the Chebyshev method. The cross-sections are extracted from the amplitude of the wave packets on the different exit channels at large internuclear distances using various numerical techniques such as the spectral projection or based on the properties of the flux operator [7].

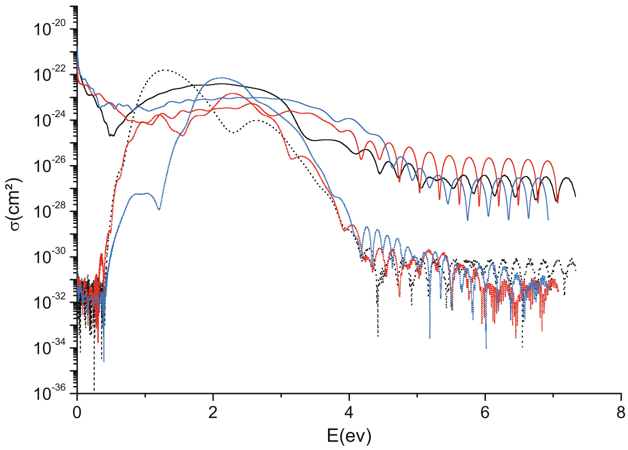

Fig. 5 Radiative association cross-sections of He($1s3s^3S$) + H^+ (*black curves*), He($1s3p\ ^3P^o$) + H^+ (*red curves*), and He($1s3d\ ^3D$) + H^+ (*blue curves*) toward the $b^3\Sigma^+$ state of HeH^+ with (*full lines*) and without (*dotted lines*) taking the vibrational dependence of the cross-sections into account

One of the advantages of time-dependent simulations is that they easily allow for the addition of the effect of an electromagnetic field on the dynamics, allowing the calculation of photodissociation and radiative association cross section for systems with one [151, 114] or two [5, 98] nuclear degrees of freedom. One example is the determination of the photodissociation and the radiative association cross-sections and rate constants of the molecular ion HeH^+, a species of particular interest in astrochemistry. We more specifically studied the difficulties met in extracting the cross-sections in systems which contain a very large number of coupled electronic states using a time-dependent method. Figure 5 shows the radiative association cross section of He($1s3s^3S$) + H^+, He($1s3p^3P^o$) + H^+, and He($1s3d^3D$) + H^+ toward the $b^3\Sigma^+$ state of HeH^+.

It is also possible to optimize the pulse of the laser to reach specific molecular states or reaction products, that is, quantum control. Orsay' LCP has a large expertise in that field and its application to chemical reactivity [120] and quantum computing [156]. In our approach, the control pulses are designed either by optimal control theory, by local control or by STIRAP (Stimulated Raman Adiabatic Passage). The most recent applications have been devoted to the implementation of quantum gates using states of cold diatomic molecules: using optimal control theory, we numerically implemented classical and quantum algorithms on hyperfine states of neighboring polar molecules in an optical trap. The prospect of operating intermolecular gates opens possibilities toward scalability and hyperfine states were shown to be good candidates for qubit encoding [124, 176].

6 Quantum chemical calculations of biomolecules and their environment

Research in theoretical and computational chemistry is also being carried out in our group with a special emphasis on applying quantum mechanics methods to molecular biophysics and chemical reactions in condensed matter. Dynamics and electronic structure theory calculations are being performed on large and complex systems to contribute to a better understanding of a variety of issues associated with biological and chemical structure and reactivity. In particular, a large effort of our research is being devoted to the elucidation of the mechanisms responsible for the radiation damage in DNA. Dynamics calculations are also being carried out with a special focus on the analysis of enzyme reactions and reactions occurring at the metal–solution interface. In addition, we are expanding our interests into molecular mechanics and combined quantum mechanical and molecular mechanical simulations of macro(bio)molecular systems. In this section, we summarize the contributions of modern quantum chemical calculations to the determination of the electronic properties of DNA bases, isolated or embedded in base clusters. In particular, the calculations discussed concern the characterization of the molecular energy levels and potential energy surfaces, which shed light on ionization and charge migration along DNA molecules. We mainly consider the estimation of key parameters, such as ionization energies (IEs) of DNA bases, which govern the charge injection into DNA. We also discuss the mechanisms of charge migration over stacked DNA bases and selected calculations performed on metal complexes used as DNA intercalators. Finally, the influence of the DNA environment and its effect on the IE quantities are described.

6.1 Isolated DNA bases and DNA base clusters

When trying to elucidate the effects of ionizing radiation on DNA, knowing the electronic structure of DNA is imperative. Indeed, detailed information about electronic properties of the DNA components will ultimately provide a fundamental understanding of the electronic factors that influence site-specific or sequence-specific radiation attack on DNA. Ab initio quantum mechanical calculations bring realistic descriptions of the Born–Oppenheimer potential energy surfaces of the neutral and cationic electronic states that govern the studied ionization properties of the DNA constituents. They also determine structures and relative energies of the relevant stationary points (minima and saddle points) on the corresponding potential energy surface and reveal the reaction pathways connecting them. A fundamental advantage is that quantum mechanical calculations reveal a direct relation between structure and energies, which is close to impossible to achieve via experimental approaches. On the monomer level, that is, isolated nucleobases, the application of quantum mechanical calculations has proven to be a powerful tool [58, 77, 96, 116, 150] because the interpretation of the experimental results is not yet complete owing to the frightening task of extracting contributions of numerous tautomers and conformers that can be produced under the experimental conditions (especially in the case of guanine and cytosine) [58, 96, 117, 160, 187]. Moreover, the advanced quantum mechanical calculations have been used as predictive tool for systems where no relevant experiment exists, such as hydrogen-bonding and π-stacking of nucleobases [35]. Thus, the improvement of quantum mechanical calculation techniques, together with the increase in computing power, allows today for precise analysis of ionization properties of clusters of DNA bases "in complete isolation", providing a detailed understanding of the intrinsic features of such systems. However, the application of the above-mentioned quantum mechanical calculations is far from being trivial given the ionization properties to be calculated and the size of the molecules and the interactions of interest. Stacking and H-bond interactions between nucleobases are still a challenge for quantum mechanical methods, the details of this have been reviewed in Refs. [31, 139, 154, 153]. The choice of the level of calculation well adapted to the studied problem is crucial.

While the ionization of isolated DNA bases and H-bonded base pairs has been studied extensively (see Ref. [35] and references therein), only a few ab initio IE calculations on π-stacked bases have been reported. Indeed, whereas the qualitative features of ionization of stacked systems, that is, the lowering of IE and the dependence of hole delocalization on the relative orientation of the fragments, can be easily explained by an electrostatic model [130] and simple molecular orbital analysis, as has been done by Sugiyama and Saito [143–146, 155, 186], the quantitative predictions are much more challenging. The influence of stacking interactions on guanine IE has been examined by employing single- and double-stranded model systems consisting of stacked guanine bases in orientations that occur in the standard B-form of DNA [30, 31, 36, 130, 143, 144, 155, 186]. Figure 6 summarizes the recent results concerning pure guanine single-strand stacked clusters. These include MP2 estimates using the polarized 6-31G(2d(0.8,0.2)) basis set. In this case, the geometries of the systems are not optimized and the values are vertical IEs. Stacking interactions in the GG dimer are found to reduce the vertical IE by 0.4 eV. A similar effect of stacking interactions on IEs has been reported in the case of the benzene dimer (0.53 eV) [127, 128] and the uracil dimer (0.34 eV) [72]. The IE lowering by stacking interaction is further confirmed for three, four, five, and six consecutive stacked guanines, in which the IE gradually drops with increasing number of nucleobase. The IE difference between dimer and trimer is 0.1 eV while the IE change between trimer and tetramer is larger (0.6 eV). In order to evaluate the IE sequence dependence, IEs were also estimated for different sequences of stacked DNA bases, in particular the human telomere sequence (TTAGGG) [36], which is essential for chromosomal stability and integrity, a function important for DNA damage. As depicted in Fig. 6, ionization energy calculations show that the G-rich human telomere sequence is particularly prone to oxidation and can act as a profound hole trap as deep as a sequence of five consecutive guanines. These calculations thus support the previously reported hypothesis of the protection of genes from oxidative damage by telomeric overhangs [82]. A molecular orbital analysis has been done explaining how unique the human telomeric sequence is and how modifications in the sequence are expected to induce changes in the electronic structure, with concomitant increase of the ionization energy.

Due to charge transfer between DNA bases, the chemical damage in irradiated DNA often occurs at sites other than where the original ionization takes place. For these reasons, the elucidation of the mechanisms responsible for the charge transfer phenomena in DNA is also a grand challenge in the current research on the oxidative damage of DNA. A key structural element, which determines the charge transfer properties of DNA, is the array of the π-stacked base pairs [159, 183]. DNA-mediated charge transfer has proven to be gated by base motions and, as such, to be sensitive to DNA conformation and stacking, with only certain base conformations being charge transfer active. A key theoretical result of our research has been the characterization, in gas phase, of very specific conformations of an ionized DNA stacking of two consecutive guanines, the most easily oxidized nucleic acid base, required for charge transfer to occur [32]. Our analysis relied on high-level multiconfigurational ab initio calculations: state-averaged CASSCF/MRCI and RASSCF/RASPT2. The ground and first two excited states of the radical cation have been characterized and the topology of the corresponding potential energy surfaces has been studied as a function of all intermolecular geometrical parameters. Relative translational motions of both guanines in their molecular planes have been demonstrated to govern the charge migration between the two bases. The reaction path describing the charge transfer from one guanine to another has been predicted. Five stationary point conformations of ionized guanine pairs (see Fig. 7) have been characterized corresponding to three minima (M1, M2 and M3) and two saddle points (S1 and S2). The corresponding relative energies with the percentages of the positive

Fig. 6 Vertical IEs (in eV) of B-form stacked contiguous guanines and the 5′-TTAGGG-3′ human telomere sequence

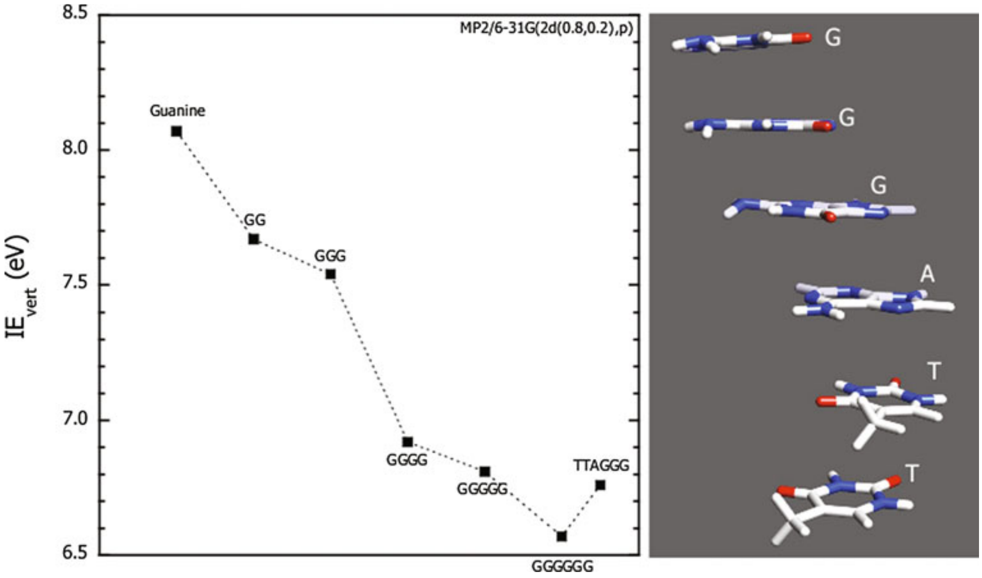

charge, calculated for each stationary point, on G5′ and G3′ are presented in Fig. 8. In addition, we have extended our study to a stacked sequence of three guanines isolated (GGG) and in interaction with the amino-acid arginine (GGGArg). The results of the calculations performed on these trimer geometries are promising and very exciting as they show that the charge transfer, first, proceeds in a multi-steps fashion, from one base to another, across the trimer and, second, may be modulated by a H-bond/cation-π stair motif, as the one found in GGGArg. These motifs are recurrently found at protein/DNA interfaces [140]. They can thus be viewed as stabilizing the stationary point conformations and modulating the charge transfer by the introduction of a positive charge in the vicinity of the guanine stack [141].

6.2 DNA intercalating complexes

In typical experiments designed to study the charge transfer in DNA, a donor and an acceptor of these charge carriers are intercalated in the stack of the DNA bases or chemically attached to the phosphate–sugar backbone. For a properly chosen donor and acceptor species, such chemical modifications enable the generation of holes under irradiation of the sample by light due to the removal of an electron from the nucleobase to the photoexcited donor. In the burgeoning area of DNA intercalation studies, transition metal intercalators have been a rich source of experimental data for decades and, in this context, the Ruthenium derived compounds have been extensively used. The rich chemical and structural diversity of the Ru(II) compounds has provided the biological chemists with a range of chemical, luminescent and photochemical probes to study DNA but also to potentially open new routes to diagnostic and therapeutic agents for various diseases. Indeed, when the photo-induced electron transfer is efficient, it has been shown experimentally that this may correlate with the single-strand cleavage of plasmid DNA. Extensive research has been performed on Ru(II) complexes in the presence of nucleic acids in Prof. A. Kirsch-De Mesmaeker′s research group [48, 55, 84, 103]. Recently, Prof. A. Kirsch-De Mesmaeker and Prof. M. Luhmer showed, for the first time, that the photoreaction of $[Ru(tap)_3]^{2+}$ and $[Ru(tap)_2(phen)]^{2+}$ with guanosine-5-monophosphate or *N*-acetyl-tyrosine gives rise to ^{1}H photo-CIDNP signals [125], that is, non-Boltzmann nuclear spin state distributions that has been detected by NMR spectroscopy as enhanced absorption or emission signals. However, the interpretation framework must be confirmed. In order to validate the experimental predictions, Density Functional Theory (DFT) calculations can be performed. These calculations are based on the determination of the electronic structure of the mono-reduced form of Ru(II) complexes in gas phase and aqueous solution. Recently, some of us showed that the electron spin density and the isotropic Fermi contact contribution to the hyperfine interactions with the ^{1}H nuclei agree remarkably well with the observed ^{1}H photo-CIDNP enhancements [34]. Thus, combined photo-CIDNP experiments and DFT calculations open up new important perspectives for the study of polyazaaromatic Ru(II) complexes photoreactions.

6.3 Influence of the DNA environment

As described in the earlier sections, ab initio studies have contributed to a fundamental understanding of the intricate effects of the different elements of the DNA environment, including bonding in nucleotides, H-bond and stacking

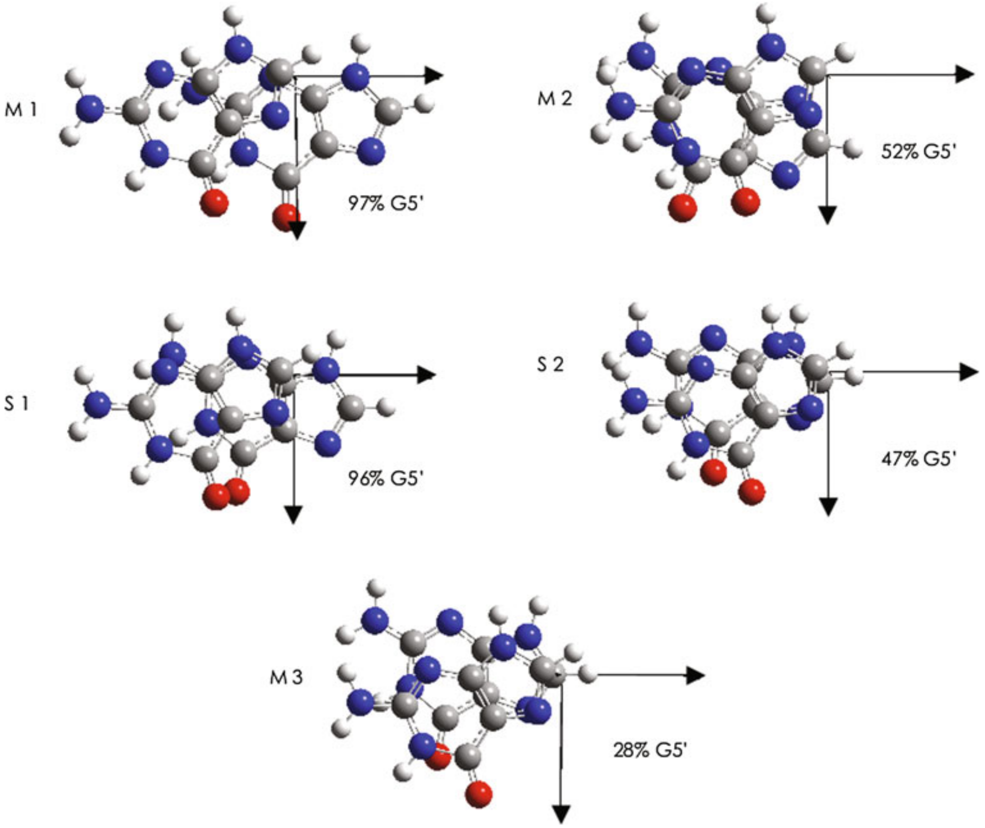

Fig. 7 Conformations of the ionized stacked cluster GG corresponding to the five stationary points (M for minimum and S for saddle point). The percentages of the positive charge on the guanine G5′ are also indicated

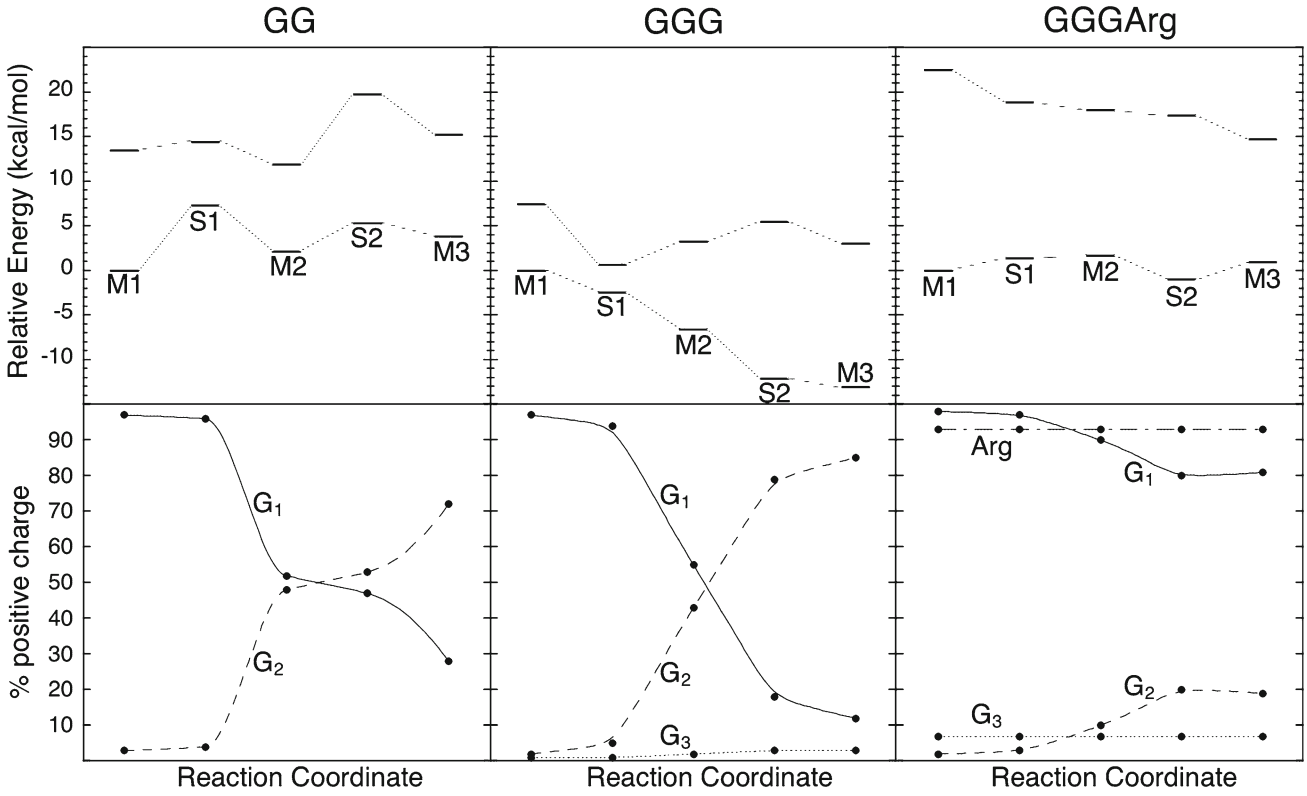

Fig. 8 *Top* relative energies (in kcal/mol) of the ground and first excited states, computed at the RASSCF/RASPT2/6-31G(d(0.2)) level of theory, for the ionized stacked clusters GG, GGG and GGGArg. The energies for the five optimized conformations represented in Fig. 7 have been calculated. *Bottom* percentages of the positive charge on each component of the clusters calculated for the ground state

Table 4 Results of CCSD(T)/aug-cc-pVDZ gas phase and QM/MM calculations of vertical IEs of DNA bases (in eV)

Nucleobase	Gas phase	QM/MM	Δ
Guanine	7.90	11.09	3.16
Adenine	8.23	11.55	3.32
Cytosine	8.65	11.98	3.33
Thymine	8.98	12.33	3.35

interactions between DNA bases but also solvation [38–40, 42–44, 125], on the IEs of each of the bases. However, it is important to have a global vision of the various aspects of the environmental effects to extrapolate these observations to predict the electronic properties of DNA bases in a biologically relevant aqueous environment. The DNA bases embedded in the DNA helix experience very special electrostatic interactions with the solution structure outside the helix. Indeed, a long-range solvent structure is created by the presence of the negatively charged phosphates of the backbone and the positive counterions. All these effects can cause important changes in the electronic structure of the DNA bases and the next step is thus to ask what the electronic properties of DNA bases are if we take these into account. The modeling of the DNA solution is an important challenge with many thousands of participating atoms. While significant progress is being made in the development of quantum chemical approaches applicable to large systems, it is clear that to treat complex biological systems such as DNA we still need to integrate different computational methodologies with diverse accuracies and cost. The goal of our research is to gain better insight into the effect of the native DNA environment on the IEs of the nucleobases, with the aid of the hybrid quantum mechanics/molecular mechanics (QM/MM) approach. The QM/MM approach consists of embedding a quantum mechanics calculation in a classical molecular mechanics model of the environment [65, 108]. The coupling between the QM region treated by quantum mechanics and the MM region treated with classical molecular mechanics must be able to describe both bonded and non-bonded interactions, such as electrostatic and van der Waals interactions, between the two regions. The use of the QM/MM approach allows thus to provide an explicit molecular description of the environmental effects taking into account the local structure of the solvent and the coordination of counterions in solution. This QM/MM approach has been used to computationally estimate the ionization energies of nucleobases within the biological environment showing the large effect on these properties [33]. The predicted energies are collected in Table 4 in which they are compared to the corresponding gas phase values. For the first time, the application of the QM/MM approach to the study of the ionization process of DNA shows how the negative phosphate groups of the DNA double helix and positive counterions induce a long-range molecular structure of the solvent creating, in the center of the DNA helix, a noticeably amplified electric potential. This potential shifts the ionization energy threshold of DNA bases by 3.2–3.3 eV relative to the gas phase. The QM/MM model has also been applied to IE calculations of clusters of DNA bases. The important IE shift due to solvation surrounding DNA remains at the same level as for single DNA bases. The results of this study have lead to detailed and reliable information about IEs of the DNA components providing a fundamental understanding of the electronic factors that influence site-specific or sequence-specific electron detachment on the genetic material.

7 A fruitful perspective

One of the main advantages of our group is a shared expertise dedicated to a wide range of problems. We plan to apply this advantage toward new perspectives. For example, one goal common to the three orientations of our respective research fields is to expand the size of the systems under study toward biological molecules, heavy atoms and ions, molecules containing transition metal atoms, molecular complexes or dynamics at ice surfaces. We will also approach the determination of new properties that will necessitate further theoretical developments, such as atomic and molecular photoionization cross-sections. Finally, we plan to carry on with the methodological transfers from electronic ab initio methods to nuclear dynamics (molecular vibration–rotation). All those projects are closely connected with experiments and will keep tightened all the members of the laboratory.

Acknowledgments SVe, CN, MD, and SVr are grateful to the "Fonds pour la formation la Recherche dans l'Industrie et dans l'Agriculture" of Belgium for a PhD grant (Boursier F.R.S.-FNRS). MG, JL, JGL, and NV thank the Communauté française of Belgium (Action de Recherche Concertée) and the Belgian National Fund for Scientific Research (FRFC/IISN Convention) for financial support.

References

1. Aboussaïd A, Godefroid M, Jönsson P, Froese Fischer C (1995) Phys Rev A 51:2031–9
2. Andrae D, Häussermann U, Dolg M, Stoll H, Preuss H (1990) Theor Chim Acta 77:123
3. Arnau A, Aumayr F, Echenique PM, Grether M, Heiland W, Limburg J, Morgenstern R, Roncin P, Schippers S, Schuch R, Stolterfoht N, Varga P, Zouros TJM, Winter HP (1997) Surf Sci Rep 27:113
4. Aumayr F, Kurz H, Schneider D, Briere MA, McDonald JW, Cunningham CE, Winter HP (1993) Phys Rev Lett 71:1943

5. Bacchus-Montabonel M-C, Vaeck N, Lasorne B, Desouter-Lecomte M (2003) Chem Phys Lett 374:307–313
6. Bader R (1994) Atoms in molecules: a quantum theory. Oxford University Press, USA
7. Baloïtcha E, Desouter-Lecomte M, Bacchus-Montabonel M-C, Vaeck N (2001) J Chem Phys 114:8741–51
8. Bartlett RJ (2010) Mol Phys 108(21–23):2905–2920
9. Bartlett RJ (2010) Mol Phys 108(21–23):3299–3311
10. Blondel C, Delsart C, Dulieu F (1996) Phys Rev Lett 77(18):3755–3758
11. Blondel C, Delsart C, Valli C, Yiou S, Godefroid M, Eck SV (2001) Phys Rev A 64:052504
12. Borgoo A, Scharf O, Gaigalas G, Godefroid M (2010) Comput Phys Commun 181:426–439
13. Borgoo A, Godefroid M, Geerlings P (2011) In: Hoggan P, Brändas E, Maruani J, Delgado-Barrio PPG (eds) Advances in the theory of quantum systems in chemistry and physics, progress in theoretical chemistry and physics, B22, chap 9, Springer, Dordrecht, pp 139–171
14. Boudon V, Pirali O, Roy P, Brubach J-B, Manceron L, Vander Auwera J (2010) J Quant Spectrosc Radiat Transfer 111: 1117–1129
15. Boys S, Bernardi F (1970) Mol Phys 19:553
16. Brage T, Froese Fischer C, Vaeck N, Godefroid M, Hibbert A (1993) Phys Scr 48:533–545
17. Brage T, Judge P, Aboussaïd A, Godefroid M, Froese Fischer C, Jönsson P, Ynnerman A, Leckrone D (1998) Astrophys J 500:507–521
18. Brage T, Judge PG, Proffitt CR (2002) Phys Rev Lett 89(28): 281101
19. Buijsse B, van der Zande JW, Eppink ATJB, Parker DH, Lewis RS, Gibson ST (1998) J Chem Phys 108:7229
20. Carette T, Drag C, Scharf O, Blondel C, Delsart C, Froese Fischer C, Godefroid M (2010) Phys Rev A 81:042522
21. Carette T, Nemouchi M, Jönsson P, Godefroid M (2010) Eur Phys J D 60:231–242
22. Carette T, Godefroid M (2011) Phys Rev A 83:062505
23. Carette T, Li J, Nemouchi M, Godefroid M (2012) Phys Rev A (work in progress)
24. Casado MA, Perez-Torrente JJ, Ciriano MA, Oro LA, Orejon A, Claver C (1999) Organometallics 18:3035–3044
25. Cassam-Chenaï P (2003) J Quant Spectrosc Radiat Transfer 82:251–277
26. Cassam-Chenaï P, Liévin J (2003) Int J Quantum Chem 93: 245–264
27. Cassam-Chenaï P, Liévin J (2006) J Comput Chem 27:627–640
28. Cassam-Chenaï P, Bouret Y, Rey M, Tashkun SA, Nikitin AV, Tyuterev VG (2012) Int J Quantum Chem 112:2201–2220
29. Cassam-Chenaï P, Liévin J (2012) J Chem Phys 136:174–309
30. Cauët E, Dehareng D, Liévin J (2006) J Phys Chem A 110(29):9200–9211
31. Cauët E, Liévin J (2007) Adv Quantum Chem 52:121–147
32. Cauët E, Liëvin J (2009) J Phys Chem A 113(36):9881–9890
33. Cauët E, Valiev M, Weare JH (2010) J Phys Chem B 114(17):5886–5894
34. Cauët E, Bogatko S, Mugeniwabagara E, Fusaro L, Kirsch-De Mesmaeker A, Luhmer M, Vaeck N (2010) Inorg Chem 49(17):7826–7831
35. Cauët E (2011) In: Marissa J, Campbell (eds) Quantum mechanical methods related to ionization of nucleic acid bases. Nova Publishers, New York
36. Cauët E (2011) J Biomol Struct Dyn 29(3):557–561
37. Cheung AS-C, Yoshino K, Parkinson WH, Guberman SL, Freeman DE (1986) Planet Space Sci 34:1007
38. Close DM (2004) J Phys Chem A 108(46):10376–10379
39. Close DM, Crespo-Hernández CE, Gorb L, Leszczynski J (2005) J Phys Chem A 109(41):9279–9283
40. Close DM, Crespo-Hernandez CE, Gorb L, Leszczynski J (2006) J Phys Chem A 110(23):7485–7490
41. Colin R, de Greef D, Goethals P, Verhaegen G (1974) Chem Phys Lett 25(1):70–73
42. Colson AO, Besler B, Sevilla MD (1993) J Phys Chem 97(51):13852–13859
43. Crespo-Hernández CE, Arce R, Ishikawa Y, Gorb L, Leszczynski J, Close DM (2004) J Phys Chem A 108(30): 6373–6377
44. Crespo-Hernandez CE, Close DM, Gorb L, Leszczynski J (2007) J Phys Chem B 111(19):5386–5395
45. Cumberland RW, Weinberger MB, Gilman JJ, Clark SM, Tolbert SH, Kaner RB (2005) J Am Chem Soc 127(20):7264–7265
46. Cunhade Miranda BK, Alcaraz C, Elhanine M, Noller B, Hemberger P, Fischer I, Garcia GA, Soldi-Lose H, Gans B, Vieira Mendes LA, Boyé-Péronne S, Douin S, Zabka J, Botschwina P (2010) J Phys Chem A 114:4818–4830
47. Delsaut M (2012) Ph.D. thesis, Université libre de Bruxelles (work in progress)
48. Deroo S, Le Gac S, Ghosh S, Villien M, Gerbaux P, Defrancq E, Moucheron C, Dumy P, Kirsch-De Mesmaeker A (2009) Eur J Inorg Chem 2009(4):524–532
49. Desclaux JP, Moser CM, Verhaegen G (1971) J Phys B At Mol Phys 4(3):296
50. Dian A (2002) PhD thesis, Université Libre de Bruxelles
51. Didriche K, Herman M (2010) Chem Phys Lett 496:1–7
52. Didriche K, Lauzin C, Foldes T, de Ghellinck D'Elseghem Vaernewijck X, Herman M (2010) Mol Phys 108:2155
53. Domcke WD (2011) In Domcke WD, Yarkoni DR, Köppel H (eds) Conical intersections. Theory, computation and experiment. Advanced series in physical chemistry, vol 17. World scientific Publishing Co, Singapore
54. Dunning T (1989) J Chem Phys 90:1007
55. Elias B, Kirsch-De Mesmaeker A (2006) Coordin Chem Rev 250(13–14):1627–1641
56. Fano U (1965) Phys Rev A 140:67–75
57. Feller D (1992) J Chem Phys 96:6104
58. Feyer V, Plekan O, Richter R, Coreno M, Vall-llosera G, Prince KC, Trofimov AB, Zaytseva IL, Moskovskaya TE, Gromov EV, Schirmer J (2009) J Phys Chem A 113(19):5736–5742
59. Folkerts L, Das J, Bergsma SW, Morgenstern R (1992) Phys Lett A 163:73
60. Froese Fischer C (1977) The Hartree–Fock method for atoms. A numerical approach. Wiley, New York
61. Froese Fischer C, Tachiev G, Gaigalas G, Godefroid M (2007) Comput Phys Commun 176:559–579
62. Gaardsted JO, Andersen T, Haugen HK, Hansen JE, Vaeck N (1991) J Phys B At Mol Phys 24:4363–4377
63. Gaidamauskas E, Nazé C, Rynkun P, Gaigalas G, Jönsson P, Godefroid M (2011) J Phys B At Mol Phys 44(17):175003
64. Gaigalas G, Froese Fischer C (1996) Comput Phys Commun 98:255–264
65. Gao J, Truhlar DG (2002) Annu Rev Phys Chem 53:467–505
66. Gibb EL, Van Brunt KA, Brittain SD, Rettig TW (2007) Astrophys J 660:1572
67. Godefroid M, Berger JJ, Verhaegen G (1976) J Phys B At Mol Phys 9(13):2181
68. Godefroid M, Liévin J, Metz JY (1987) J Phys B At Mol Phys 20:3283–96
69. Godefroid M, Liévin J, Metz JY (1991) Int J Quant Chem XL:243–264
70. Godefroid M, Jönsson P, Froese Fischer C (1998) Phys Scr T78:33–46

71. Godefroid M, Froese Fischer C, Jönsson P (2001) J Phys B At Mol Phys 34:1079–1104
72. Golubeva AA, Krylov AI (2009) Phys Chem Chem Phys 11(9):1303–11
73. Grabowski I, Lotrich V, Hirata S (2010) Mol Phys 108(21–23): 3313–22
74. Grant I (2006) Relativistic atomic structure. In: Drake GWF (ed) Atomic, molecular and optical physics handbook. American Institute of Physics, Woodbury, New York, pp 325–357
75. Grant I (2007) Relativistic quantum theory of atoms and molecules. Theory and computation. Atomic, optical and plasma physics. Springer, New York
76. Hansen J, Bentley M, van der Hart H, Lister G, Shen YT, Vaeck N (1993) Phys Scr T47:7–17
77. Hanus M, Ryjácek F, Kabelác M, Kubar T, Bogdan TV, Trygubenko SA, Hobza P (2003) J Am Chem Soc 125(25): 7678–7688
78. Hansen JE, Schraa O, Vaeck N (1992) Phys Scr T41:41–44
79. van der Hart HW, Vaeck N, Hansen JE (1994) J Phys B At Mol Phys 27:3489–3514
80. van der Hart HW, Vaeck N, Hansen JE (1995) J Phys B At Mol Phys 28:5207–5228
81. Helgaker T, Klopper W, Koch H, Noga J (1997) J Chem Phys 106:9639
82. Heller A (2000) Spiers memorial lecture. On the hypothesis of cathodic protection of genes. Faraday Discussions 116:1–13. http://dx.doi.org/10.1039/B006196O
83. Herman J, Mental J (1982) J Geophys Res 87:8967
84. Herman L, Ghosh S, Defrancq E, Mesmaekera AKD (2008) J Org Chem 21(7–8):670–681
85. Jennerich R, Keiser A, Tate D (2006) Eur Phys J D 40:81–89
86. Jenouvrier A, Coquart B, Mérienne MF (1986) J Quant Spectrosc Radiat Transfer 36:249
87. Jenouvrier A, Mérienne MF, Coquart B, Carleer M, Fally S, Vandaele AC, Hermans C, Colin R (1999) J Mol Struct 198:136
88. Johnston HS, Paige M, Yao F (1984) J. Geophys. Res. 89:11661
89. Johnson W (2010) Can J Phys 99:1–9
90. Jönsson P, He X, Froese Fischer C, Grant I (2007) Comput Phys Commun 177:597–622
91. Jönsson P, Carette T, Nemouchi M, Godefroid M (2010) J Phys B At Mol Phys 43:115,006
92. Jönsson P, Gaigalas G, Bieroń J, Froese Fischer C, Grant I (2012) Comput Phys Commun (submitted)
93. Kaner R, Gilman J (2010) Osmium diboride compounds and their uses. Patent US 7,645,308 B2
94. Kendall RA, Dunning TH Jr (1992) J Chem Phys 96:6796
95. Knowles PJ, Werner HJ (1992) Theor Chim Acta 84:95–103
96. Kostko O, Bravaya K, Krylov A, Ahmed M (2010) Phys Chem Chem Phys 12(12):2860–2872
97. Langhoff R, Davidson ER (1974) J Chem Phys 8:62
98. Lasorne B, Bacchus-Montabonel MC, Vaeck N, Desouter-Lecomte M (2004) J Chem Phys 120:1271–1278
99. Lauzin C, Didriche K, Macko P, Demaison J, Liévin J, Herman M (2009) J Phys Chem A 113:2359
100. Lauzin C, Didriche K (2011) Phys Chem Chem Phys 751:2359
101. Lauzin C, Cauët E, Demaison J, Herman M, Stoll H, Liévin J (2012) Mol Phys (submitted)
102. Lefèvre F, Forget F (2009) Nature 460:720–723
103. Le Gac S, Rickling S, Gerbaux P, Defrancq E, Moucheron C, Kirsch-De Mesmaeker A (2009) Angew Chem Int Ed 48(6): 1122–1125
104. Li J, Gaigalas G, Godefroid M (2012) Comput Phys Commun (work in progress)
105. Liévin J, Breulet J, Clercq P, Metz J (1982) Theor Chim Acta 61:513–537
106. Liévin J, Vaeck N (1990) Int J Quant Chem 62:521–541
107. Liévin J, Demaison J, Herman M, Fayt A, Puzzarini C (2011) J Chem Phys 134:064119
108. Lin H, Truhlar D (2007) Theor Chim Acta 117:185–199
109. Lindgren B, Olofsson G Astron (1980) Astrophysics 84:300–303
110. Loreau J, Sodoga K, Lauvergnat D, Desouter-Lecomte M, Vaeck N (2010) Phys Rev A 82:012708
111. Loreau J, Liévin J, Vaeck N (2010) J Chem Phys 133:114302
112. Loreau J, Liévin J, Palmeri P, Quinet P, Vaeck N (2010) J Phys B At Mol Phys 43:065101
113. Loreau J, Ryabchenko S, Dalgarno A, Vaeck N (2011) Phys Rev A 84:052720
114. Loreau J, Urbain X, Lecointre J, Vaeck N (2011) Phys Rev A 84:053412
115. Malmqvist PA (1986) Int J Quant Chem XXX:479–494
116. Marian CM (2007) J Phys Chem A 111(8):1545–1553
117. Mons M, Piuzzi F, Dimicoli I, Gorb L, Leszczynski J (2006) J Phys Chem A 110(38):10921–10924
118. Naviliat-Cuncic O (2012) Laboratoire de Physique Corpusculaire, U.d.C.B.N.: private communication
119. Nikitin AV, Rey M, Tyuterev VG (2011) Chem Phys 501:179
120. Ndong M, Bomble L, Sugny D, Justum Y, Desouter-Lecomte M (2007) Phys Rev A 76(4):043424
121. de Oliveira G, Martin JML, de Proft F, Geerlings P (1999) Phys Rev A 60(2):1034–1045
122. Olsen J, Godefroid M, Jönsson P, Malmqvist PA, Froese Fischer C (1995) Phys Rev E 52:4499–4508
123. Palmeri P, Quinet P, Zitane N, Vaeck N (2001) J Phys B At Mol Phys 34:4125–4139
124. Pellegrini P, Vranckx S, Desouter-Lecomte M (2011) Phys Chem Chem Phys 13:18864
125. Perrier S, Mugeniwabagara E, Kirsch-De Mesmaeker A, Hore PJ, Luhmer M (2009) J Am Chem Soc 131(34):12458–12465
126. Peterson KA, Figgen D, Goll E, Stoll H, Dolg M (2003) J Chem Phys 119:11113
127. Pieniazek PA, Krylov AI, Bradforth SE (2007) J Chem Phys 127(4):044317
128. Pieniazek PA, Bradforth SE, Krylov AI (2008) J Chem Phys 129(7):074104
129. Pirre M, Rigaud P, Huguenin D (1984) Geophys Res Lett 11:1199
130. Prat F, Houk KN, Foote CS (1998) J Am Chem Soc 120(4):845–846
131. Puzzarini C, Heckert M, Gauss J (2008) J Chem Phys 128: 194108
132. Ram RS, Liévin J, Bernath PF (1998) J Chem Phys 109: 6329–6337
133. Ram RS, Liévin J, Bernath PF (1999) J Chem Phys 111: 3449–3456
134. Ram RS, Liévin J, Bernath PF (1999) J Mol Spectrosc 197:133–146
135. Ram RS, Adam AG, Tsouli A, Liévin J, Bernath P (2000) J Mol Spectrosc 202:116
136. Ram RS, Adam A, Sha W, Tsouli A, Liévin J, Bernath PF (2001) J Chem Phys 114:3977–3987
137. Ram RS, Liévin J, Bernath PF (2009) J Mol Spectrosc 256
138. Reinhold E, Ubachs W (2005) Mol Phys 103:1329
139. Riley KE, Pitoňák M, Černý J, Hobza P (2010) J Chem Theory Comput 6(1):66–80
140. Rooman M, Liévin J, Buisine E, Wintjens R (2002) J Mol Biol 319(1):67–76
141. Rooman M, Cauët E, Liévin J, Wintjens R (2011) J Biomol Struct Dyn 28(6):949–953
142. Rothman LS, Gordon IE, Barbe A, Benner D Chris, Bernath PF, Birk M, Boudon V, Brown LR, Campargue A, Champion J-P, Chance K, Coudert LH, Dana V, Devi VM, Fally S, Flaud J-M, Gamache RR, Goldman A, Jacquemart D, Kleiner I, Lacome N,

Lafferty WJ, Mandin J-Y, Massie ST, Mikhailenko SN, Miller CE, Moazzen-Ahmadi N, Naumenko OV, Nikitin AV, Orphal J, Perevalov VI, Perrin A, Predoi-Cross A, Rinsland CP, Rotger M, Šimečková M, Smith MAH, Sung K, Tashkun SA, Tennyson J, Toth RA, Vandaele AC, Vander Auwera J (2009) J Quant Spectrosc Radiat Transfer 110:533–572

143. Saito I, Takayama M, Sugiyama H, Nakatani K, Tsuchida A, Yamamoto M (1995) J Am Chem Soc 117(23):6406–6407
144. Saito I, Takayama M, Sugiyama H, Nakamura T (1997) J Photochem Photobiol A 106(1–3):141–144
145. Saito I, Nakamura T, Nakatani K, Yoshioka Y, Yamaguchi K, Sugiyama H (1998) J Am Chem Soc 120(48):12686–12687
146. Saito I, Nakamura T, Nakatani K (2000) J Am Chem Soc 122(13):3001–3006
147. Sang C, Jiao Y, Sun Y, Gou B (2011) Eur Phys J D 64:203–207
148. Shabaev V, Artemyev A (1994) J Phys B At Mol Phys 27:1307–1314
149. Shardanand, Prasad Rao AD (1977) J Quant Spectrosc Radiat Transfer 17:433
150. Shukla M, Leszczynski (2006) J Chem Phys Lett 429(1–3): 261–265
151. Sodoga K, Loreau J, Lauvergnat D, Justum Y, Vaeck N (2009) Desouter-Lecomte M. Phys Rev A 80:033417
152. Soorkia S, Shafizadeh N, Liévin J, Gaveau MA, Pothier C, Mestdagh J-M, Soep B, Field RW (2011) J Phys Chem A 115:9620–9632
153. Šponer J, Jurečka P, Hobza P (2006) Computational studies of RNA and DNA. Springer, Berlin, pp 343–388
154. Šponer J, Riley KE, Hobza P (2008) Phys Chem Chem Phys 10(19):2595–2610
155. Sugiyama H, Saito I (1996) J Am Chem Soc 118(30):7063–7068
156. Sugny D, Bomble L, Ribeyre T, Dulieu O, Desouter-Lecomte M (2009) Phys Rev A 80(4):042325
157. Tao FM, Pan YK (1992) J Chem Phys 97:4989
158. Tate DA, Aturaliye DN (1997/09/1/) Phys Rev A 56:1844
159. Treadway CR, Hill MG, Barton JK (2002) Chem Phys 281(2–3):409–428
160. Trofimov AB, Schirmer J, Kobychev VB, Potts AW, Holland DMP, Karlsson L (2006) J Phys B At Mol Phys 39(2):305
161. Vaeck N, Hansen JE (1989) J Phys B At Mol Phys 22(20):3137
162. Vaeck N, Hansen JE (1991) J Phys B At Mol Phys 24:L469–L475
163. Vaeck N, Hansen JE (1992) J Phys B At Mol Phys 25:3613–3619
164. Vaeck N, Hansen JE (1992) Surf Sci 269(270):596–600
165. Vaeck N, Hansen JE (1992) J Phys B At Mol Phys 25:3613–3619
166. Vaeck N, Hansen JE (1992) J Phys B At Mol Phys 25:3267–3282
167. Vaeck N, Hansen JE (1995) J Phys B At Mol Phys 28:3523–3543
168. Vaeck N, Desouter-Lecomte M, Liévin J (1999) J Phys B At Mol Phys 32:409–428
169. Vaeck N, Bacchus-Montabonel M-C, Baloïtcha E, Desouter-Lecomte M (2001) Phys Rev A 63:042704
170. Vaeck N, Hansen JE, Palmeri P, Quinet P, Zitane N, Godefroid M, Fritzsche S, Kylstra N (2001) Phys Scr 2001(T95):68
171. Vaeck N, Kylstra N (2002) Phys Rev A 65:062502
172. Vana M, Aumayr F, Lemell C, Winter HP (1995) Int J Mass Spectrom Ion Proc 149(150):45
173. Varandas A (2007) J Chem Phys 127:114316
174. Verdebout S, Jönsson P, Gaigalas G, Godefroid M, Froese Fischer C (2010) J Phys B At Mol Phys 43:074017
175. Verdebout S, Rynkun P, Jönsson P, Gaigalas G, Godefroid M, Froese Fischer C (2012) J Phys B At Mol Phys (in preparation)
176. Vranckx S, Jaouadi A, Pellegrini P, Bomble L, Vaeck N, Desouter-Lecomte M (2012) Advances in atom and single molecule machines (submitted)
177. Wales D (2003) Energy Landscapes. With applications to clusters, biomolecules and glasses. Cambridge University Press, Cambridge
178. Wauters L, Vaeck N (1996) Phys Rev C 53:497–500
179. Wauters L, Vaeck N, Godefroid M, van der Hart H, Demeur M (1997) J Phys B At Mol Phys 30:4569–4589
180. Werner HJ, Knowles PJ (1988) J Chem Phys 89:5803–5814
181. Werner HJ, Knowles PJ, Knizia G, Manby FR, Schütz M, Celani P, Korona T, Lindh R, Mitrushenkov A, Rauhut G, Shamasundar KR, Adler TB, Amos RD, Bernhardsson A, Berning A, Cooper DL, Deegan MJO, Dobbyn AJ, Eckert F, Goll E, Hampel C, Hesselmann A, Hetzer G, Hrenar T, Jansen G, Köppl C, Liu Y, Lloyd AW, Mata RA, May AJ, McNicholas SJ, Meyer W, Mura ME, Nicklass A, O'Neill DP, Palmieri P, Pflüger K, Pitzer R, Reiher M, Shiozaki T, Stoll H, Stone AJ, Tarroni R, Thorsteinsson T, Wang M, Wolf A (2010) Molpro, version 2010.1, a package of ab initio programs. See http://www.molpro.net
182. Woon DE, Dunning TH Jr (1995) J Chem Phys 103:4572
183. Ye YJ, Jiang Y (2000) Int J Quant Chem 78(2):112–130
184. Yoshino K, Cheung AS-C, Esmond JR, Parkinson WH, Freeman DE, Guberman SL, Jenouvrier, Coquart B, Mérienne M-F (1988) Planet Space Sci 12
185. Yoshino K, Esmond JR, Cheung AS-C, Freeman DE, Parkinson WH (1992) Planet Space Sci 40:185
186. Yoshioka Y, Kitagawa Y, Takano Y, Yamaguchi K, Nakamura T, Saito I (1999) J Am Chem Soc 121(38):8712–8719
187. Zhou J, Kostko O, Nicolas C, Tang X, Belau L, de Vries MS, Ahmed M (2009) J Phys Chem A 113(17):4829–4832

Theor Chem Acc (2012) 131:1255
DOI 10.1007/s00214-012-1255-2

REGULAR ARTICLE

Stabilization of merocyanine by protonation, charge, and external electric fields and effects on the isomerization of spiropyran: a computational study

Renuka Ganesan · F. Remacle

Received: 28 February 2012 / Accepted: 3 July 2012 / Published online: 27 July 2012

Abstract Protonation, charging, and field effects on the thermal isomerization of a nitrospiropyran (SP) modified by a thiolated etheroxide chain into merocyanine (MC) are computationally studied at the DFT level. The ring opening leads to *cis*-MC conformers that then isomerize to the more stable trans forms. While the closed neutral spiropyran is more stable than the conjugated open forms, the merocyanine conformers are significantly stabilized by protonation, electron attachment, and ionization. For protonation on the pyran oxygen atom and electron attachment, the MC conformers are more stable than SP, and unlike for the neutral species, the ring opening is spontaneous at room temperature. Moreover, for the pyran oxygen-protonated form, the ring opening to the *cis*-merocyanine becomes barrierless. On the other hand, barriers comparable to the neutral remain along the thermal pathway to the *cis*-merocyanine conformer for ionization or electron attachment, and the barrier for isomerization is significantly higher for the N-protonated SP form. External field effects on the neutral reaction path show that ring opening to the *cis*-merocyanine is favored when the field reduces the electron density on the pyran part, as also induced by the local field due to O protonation.

Keywords Thermal isomerization of spiropyran · Field effects · Protonation effect · Charging effects · Quantum chemistry

1 Introduction

Spiropyran (SP) are well-known photochromes that can reversibly photoisomerize to a conjugated open form, the merocyanine (MC). The SP molecule is made of two orthogonal moieties, an indole part and a benzopyran part (see Fig. 1). The absorption of UV light causes the cleavage of the weak C4–O9 bond of the colorless closed SP form that isomerizes first to *cis*-open-MC conformers and then to more stable trans-MC ones [1–5]. All the MC conformers absorb in the visible. The conversion from a close SP form to an open planar conjugate MC form is accompanied by changes in optical, polarization, and transport properties. This reversible switching of properties upon isomerization makes spiropyran derivatives attractive candidates for designing optical switching [6–10] and storage [7, 11–13] devices, sensors [14–17] and cell imaging [18, 19].

The photochemical isomerization of various spiropyran molecules in different media (gas phase, solution, monolayers, polymers) has been extensively experimentally [1–3, 20–30] and theoretically [31, 32] studied in order to understand the reaction mechanism. Less studied, however, are the effect of protonation, charge, and external fields on the isomerization pathway of this electrocyclic reaction. It was recently reported that the rate of isomerization of the SP form is considerably increased by protonation of the

---

Published as part of the special collection of articles celebrating theoretical and computational chemistry in Belgium.

Electronic supplementary material The online version of this article (doi:10.1007/s00214-012-1255-2) contains supplementary material, which is available to authorized users.

R. Ganesan · F. Remacle (✉)
Department of Chemistry, B6c, University of Liège,
4000 Liège, Belgium
e-mail: fremacle@ulg.ac.be

F. Remacle
University of Liege and FNRS (Fonds National de la Recherche Scientifique), Liège, Belgium

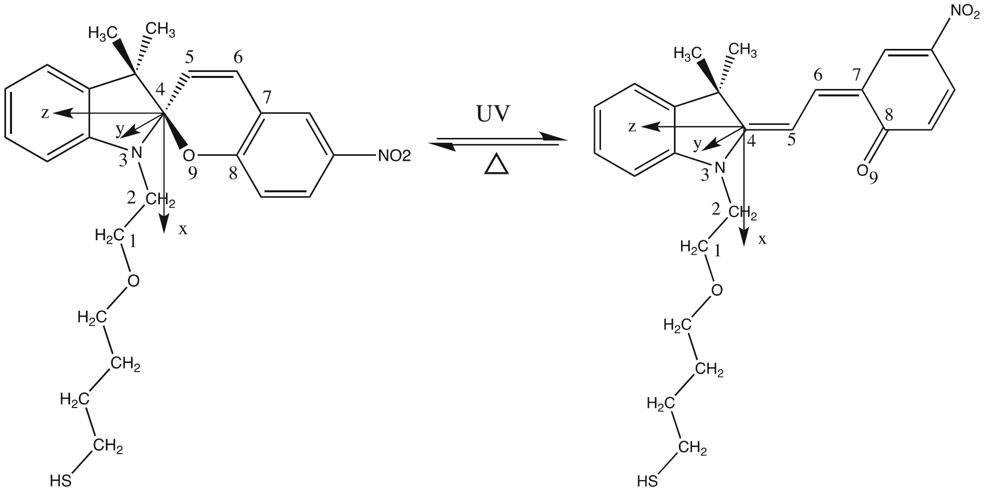

Fig. 1 Isomerization of the thiol, $(CH_2)_2O(CH_2)_4SH$, derivative of 1′,3′-dihydro-1′-R,3′,3′-dimethyl-6-nitrospiro[2H-1-benzopyran-2,2′-[2H]indole]. The carbon C4 is chiral. The spiro (SP) form is the R closed conformer (*left*) and the merocyanine (MC) the open one (*right*). The open conformers are defined by three dihedral angles α = N3–C4–C5–C6, β = C4–C5–C6–C7, γ = C5–C6–C7–C8

pyran O at room temperature [33]. This experimental finding is supported by semi-empirical computations which report that the ring opening of the O-protonated form to *cis*-MC becomes barrierless [34]. Stimulated by these results and in view of potential use of the charged and protonated forms as well as applying static fields in the design of molecular logic devices, we investigated protonation, charging, and field effects on the thermal isomerization pathway using density functional theory (DFT). For each of these effects, the Gibbs energies are calculated along the reaction coordinate. While the photoinduced SP to MC isomerization is usually faster than the thermal route, it is important to understand which processes can occur in the dark route for designing efficient and reliable devices.

Experimental photochemical studies of the neutral isomerization pathway in the gas phase [23] and in organic media [5, 35, 36] show that the ring opening of SP proceeds through several steps involving MC conformers as intermediates. They are labeled by three letters indicating a cis(C) or a trans(T) value for the α, β, γ angles defined in Fig. 1 [37]. In the first step, SP absorbs in the UV region, and the C4–O9 bond cleavage (see Fig. 1) leads to the metastable cis (CCC)-MC. The other steps are isomerizations between the different MC conformers. The most stable TTC conformer can be reached via the CCC, CTC, or TCC conformers that are metastable. The photo-activated pathways are not yet fully characterized. Uncertainties remain about the relative stability of some intermediates, like that of the CCC conformer with respect to the CTC one [38]. The reverse reaction can be induced thermally or via VIS excitation.

We focus on the 1′,3′-dihydro-1′-R,3′,3′-dimethyl-6-nitrospiro[2H-1-benzopyran-2,2′-[2H]indole] [21, 22] shown in Fig. 1 which is modified by a thiolated etheroxide chain (R = $(CH_2)_2O(CH_2)_4SH$) [13, 39–41]. Because the linker can take different conformations, there exist several stable SP conformers. In addition, the SP form has two enantiomers because the carbon atom C4 is chiral [42]. The R enantiomer is shown in Fig. 1. For each of the stable conformers of the SP form, several open MC conformers which differ by the values of three torsional dihedral angles α, β, and γ are stable. The TTC conformer is shown in Fig. 1.

We report detailed computations of the thermal reaction path and energetics of the isomerization reaction for the two enantiomers of two conformers of the SP form which differ by the value of the dihedral angle involving the linker, the C1–C2–N3–C4 dihedral angle (see Fig. 1). Our motivation for doing so is that while they are very close in energy and almost isoenergetic, the two conformers exhibit different reaction paths because of the difference of the steric hindrance due to the ligand on the ring opening. We then report on external field effects on the thermal isomerization mechanism of the neutral species. The SP form has two protonation sites: on the O atom of the pyran moiety and on the N atom of the indole part. We investigated the thermal reaction paths for both protonation sites, as well as those for the SP cation and anion.

2 Computational methodology

We use density functional theory as implemented in the suite of quantum chemistry programs Gaussian09 [43]. The choice of the functional and basis set needs to satisfy two requirements. The first one is to account correctly for the dispersion interactions that stabilize the SP form. These interactions occur between the CH_3 group on the indole part and the pyran part and induce two weak H-bonds between the H atom of the CH_3 group and the O atom of the pyran. (These bonds are indicated in Fig. 2 below). In addition to these, in the SP form, there is also a weak H-bond between a CH_2 group (H-C1 or H-C2) of the linker close to the N3 atom of the indole and the O9 atom of the

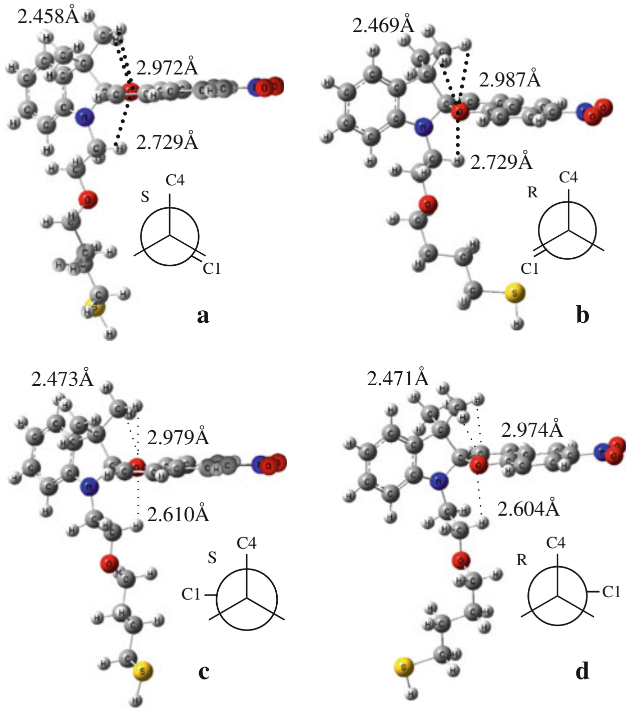

Fig. 2 Equilibrium geometries of the conformers of SP molecule shown in Fig. 1 **a** S-SP1; $\theta = d(C1–C2–N3–C4) = 127.2°$, **b** R-SP1; $\theta = -127.6°$, **c** S-SP2; $\theta = -79.4°$, **d** R-SP2; $\theta = 79.7°$. Important H-bond between the O of the pyran and the CH_3 group of the indole and the CH_2 group of the linker, respectively, are indicated in dotted lines. For a given conformer, the two enantiomers S and R have opposite sign of the dihedral angle θ. Both enantiomers exhibit the same H-bond pattern. For S-SP2 and R-SP2, conformers with initial dihedral angle of +127° and −127° relax to stable SP2 conformers with $\theta = |79|°$

pyran (see Fig. 2 below). When the ring is opened, a stronger H-bond takes place between the O9 and the H–C5 or H–C6 group but overall the dispersions interactions are much weaker in the MC forms. The dispersions interactions occurring in the SP form make it more stable than the MC form in the neutral state which is what is observed experimentally [42]. To account for them correctly, it is necessary to use long range interaction corrected functionals [44–47]. The second effect that needs to be taken into account is the distortion of the electron density induced by applying an external static electric field. For doing so, large basis sets with diffuse functions are necessary. We use the 6-311+G(d,p) and the 6-311++G(d,p) basis sets. Two functionals were systematically investigated: B3LYP [48] and the long range interaction corrected CAM-B3LYP [45, 49]. The B3LYP/6-311++G(d,p) level accounts for the H-bond in the MC form but fails to correctly describe the long range interactions in SP and leads to numerically degenerate SP and MC conformers. On the other hand, the long range interaction corrected CAM-B3LYP/6-311+G(d,p) level leads to the experimental stability order for the neutral species, SP being more stable than MC. In addition, for this level, tests show that the energy differences between conformers, field free and in the presence of a static field do not vary when going to the larger 6-311++G(d,p) basis set (see Tables S1 and S2). We therefore report results for the CAM-B3LYP/6-311+G(d,p) level throughout the paper and when of interest, we mention results for the B3LYP functional. We also report below results obtained with the long range interaction corrected M06-2X [46] functional for the SP form which is prone to dispersion interactions.

All stable minima and TS were checked by frequency computations at the same level and the geometries of the TS confirmed by IRC computations.

3 Thermal isomerization of the neutral

Since we focus in this paper on the protonated and charged species isomerization pathways and on field effects, establishing the energetics of the thermal reaction path of the neutral thio-nitrospiropyran shown in Fig. 1 is important for comparisons at the same computational level. In addition, our study of the neutral thermal isomerization pathway provides understanding on the role of the steric hindrance and weak interactions between the linker and the SP or MC units. These effects are of interest for the isomerization of an anchored spiropyran, which is often the case for sensing, logic or storage device applications. The reason is that while the isomerization of the neutral SP to MC is usually induced by photoactivation, the MC conformers being less stable than the SP form, the back isomerization can occur thermally. The characterization of the isomerization barriers between the different merocyanine conformers is also of interest as the final steps of the forward photochemical pathways.

We first investigated the relative stabilities of the different conformers. Those are mainly of the MC form. However, the SP form has two enantiomers because it has a chiral center, C4 in Fig. 1. In addition, several almost isoenergetic conformers of the SP and the MC are possible because of the different conformations of the linker chain. Among those, we investigated in details two conformers of the SP form that differ by the value of the dihedral angle d(C1–C2–N3–C4) (see Fig. 1). These two conformers have a different pathway for the opening of the cycle due to differences in the steric hindrance of the linker. Since each of them has two isoenergetic enantiomers, we report on the isomerization pathways of four SP conformers. Their computed equilibrium geometries are shown in Fig. 2, and the energetics and some relevant geometry parameters of each conformers are reported in Table 1. The pair of enantiomers that we call SP1 is the lowest in energy when

Table 1 Relative ZPE corrected and free energies (kJ mol^{-1}) of the SP and MC conformers as well as of the transition states along the isomerization pathways reported in Fig. 3, computed at CAM-B3LYP/6-311+G(d,p) level (with respect to S-SP1)

Conformer	ΔE $ZPE_{corrected}$	ΔG	C4–O9	θ	α	β	γ
S-SP1	0.0	0.0	1.467	127.2	124.9	−1.5	−2.2
S-SP2	1.3	4.2	1.474	−79.4	131.8	−2.5	−4.9
R-SP1	0.5	2.8	1.466	−127.6	−128.3	1.9	3.8
R-SP2	1.3	4.9	1.474	79.7	−131.3	2.4	4.7
TTCa	40.3	35.8	4.133	85.7	178.2	178.4	−1.4
TTTa	45.3	42.5	4.977	95.4	178.0	179.0	179.9
CTCa	47.4	50.9	4.148	86.9	−8.9	178.8	−0.9
CTTa	51.0	48.3	5.019	94.3	−11.7	−178.3	174.2
S-CCCa	68.1	68.4	2.637	95.4	42.5	16.7	14.1
CCTa	85.2	78.1	5.275	84.0	22.7	26.0	−176.7
TCTa	115.9	113.0	5.339	87.6	179.7	−3.0	178.7
TTCb	41.7	38.5	4.128	−84.7	−178.3	−177.8	1.8
TTTb	47.9	44.6	4.970	−98.2	−178.6	−178.3	−179.7
CTCb	53.2	51.2	4.115	−94.5	10.8	178.6	2.7
CTTb	51.0	51.5	5.026	−93.9	11.4	178.6	−174.4
R-CCCb	70.1	68.7	2.636	−98.2	−42.8	−16.6	−13.4
CCTb	94.9	98.0	5.292	−123.3	17.6	35.6	−175.7
TCTb	116.8	112.2	5.339	−87.8	179.8	3.9	−178.4
TS1	68.8	73.0	2.361	101.9	62.1	11.6	14.9
TS2	125.4	118.3	3.354	89.6	−3.6	94.4	−4.9
TS3	115.2	113.3	4.042	88.9	90.9	−178.8	1.7
TS4	125.2	121.4	3.342	90.0	179.2	−88.5	−0.1
TS5	70.8	74.5	2.374	−104.6	−61.5	−11.8	−14.5
TS6	117.9	123.3	3.389	−91.8	5.9	−96.0	4.7
TS7	118.0	116.9	4.038	−88.0	−91.1	179.4	−1.9
TS8	125.3	121.3	3.339	−90.2	−179.2	88.7	−0.1
TS9	123.6	128.0	3.413	−95.6	−4.0	98.8	−6.0
TS10	122.3	119.2	3.327	−79.2	179.2	−87.0	−1.4
TS11	123.3	119.2	3.359	96.6	−0.2	−94.4	2.9
TS12	122.2	118.3	3.330	79.5	−179.3	87.1	1.4

The corresponding values of the C4–O9 bond (in Å) and dihedral angles θ = d(C1–C2–C3–N4), α = N3–C4–C5–C6, β = C4–C5–C6–C7, γ = C5–C6–C7–C8 (in degree) (see Fig. 1) are also reported. The difference between the ΔE $ZPE_{corrected}$ and ΔG for S-SP1 is −173.8 kJ mol^{-1}

computed at the CAM-B3LYP/6-311+G(d,p). They correspond to a value of the dihedral angle d(C1–C2–N3–C4) of |127|°. The second pair of stable enantiomers exhibits a value of the dihedral angle d(C1–C2–N3–C4) of |79|° and is called SP2. The SP2 enantiomers are also isoenergetic within numerical accuracy, see Table 1. On the other hand, the SP1 and SP2 conformers differ by the trans (SP1)- or the cis (SP2)-orientation of the C1–C2 bond of the linker with respect to the C4–O9 bond of the pyran. This difference leads to more steric hindrance for the opening of the C4–O9 bond for the SP2 conformers and to higher energy barriers as discussed below. It also plays a role in N-protonated isomerization pathway (see Sect. 5).

The order of stability of the SP1 and SP2 conformers depends on the relative strength of the two kinds of H-bonds that can take place : those between the CH_3 group of the indole and O of the pyran and the H-bond between one of the CH_2 group of the linker and the O of pyran, see Fig. 2. In the S-SP2 conformer, the H-bond takes place between the C1 carbon of the linker and the O of the pyran part, while for the S-SP1, it is the C2 carbon of the linker that is involved. The SP1 and SP2 conformers are computed to be numerically quasi degenerate. The energy difference between them being small, their order of stability depends on the functional used. At the CAM-B3LYP/6-311+G(d,p) level, the linker-pyran H-bond is stronger in SP2 and leads to a more rigid geometry for SP2 with systematically slightly larger vibrational frequencies for the lowest normal modes (see Fig. 2). The computed free energy difference at 298 K between the S-SP1 and S-SP2 conformers is 4.2 kJ/mol. This energy difference is mainly due to the entropy effect, the zero point energy (ZPE) corrected energy difference between two conformers being 1.3 kJ/mol, see Table 1. The same is true at the B3LYP/6-311+G(d,p) level, see Table S3. On the other hand, at the M06-2X/6-311+G(d,p) level, both kinds of H-bond are stronger in SP2 than in SP1, which leads to a reverse of the order of stability with respect to the CAM-B3LYP level, SP2 being more stable than SP1 by 1.7 kJ/mol for electronic energies, see Table S3.

The two enantiomers of a given conformer follow the same reaction pathway. However, the opening of the C4–O9 bond in the R and S enantiomers of SP1 and SP2 does not lead to the same family of MC conformers, again because of a different orientation of the linker. S-SP1 and R-SP2 lead to positive values of the dihedral angle θ ranging between +84.0° and +95.4° in the planar MC conformers (labeled MCa), while for R-SP1 and S-SP2, the values of the dihedral angle θ are negative and range between −84.7° and −123.3° (labeled MCb) (see Table 1). The energies and geometries are reported in Table 1 and in Fig. S1 of the ESM. Each conformer of MCa is quasi isoenergetic with the corresponding MCb one with free energy differences in the range 0.5–3.0 kJ/mol except the CCT conformer for which the computed energy difference between CCTa and CCTb is 19.9 kJ/mol. Note that this conformer is not involved in the reactions we discussed below. Barriers for isomerization among the MCa or the MCb conformers are in the range of 50–70 kJ mol^{-1}, see Table 1 and Fig. 3. The stability order of MCa open conformers at the CAM-B3LYP/6-311+G(d,p) level is computed to be:

$$\mathrm{TTCa} > \mathrm{TTTa} > \mathrm{CTTa} > \mathrm{CTCa} > \mathrm{CCCa} > \mathrm{CCTa} > \mathrm{TCTa} \quad (1)$$

while for the MCb conformers, we get:

$$\mathrm{TTCb} > \mathrm{TTTb} > \mathrm{CTCb} > \mathrm{CTTb} > \mathrm{CCCb} > \mathrm{CCTb} > \mathrm{TCTb} \quad (2)$$

The TCC conformer is not stable because of the steric hindrance due to the methyl group and relaxes to the SP conformer upon geometry optimization. A trans configuration for the dihedral angle β has less steric hindrance. In agreement with ref [50], conformers that are trans (T) for the β dihedral angle (TTC, TTT, CTC, CTT) are therefore computed to be more stable than conformers that are cis for that angle (CCC, CCT, TCT). TTC and TTT are found to be more stable than other MC conformers in agreement with refs [21, 51, 52]. In the gas phase, SP is more stable than TTC. The zero point energy (ZPE) corrected energy difference between the S-SP1 and TTCa is 40.3 kJ/mol at the CAM-B3LYP/6-311+G(d,p) level and the free energy difference is 35.8 kJ/mol at 298 K, see Table 1. (Using the B3LYP functional without long range corrections, SP and TTC are closer in energy, ΔG is 14.5 kJ/mol at B3LYP/6-31G(d,p) and 1.2 kJ/mol at B3LYP/6-311 ++G(d,p), see Table S1. The larger stability of the SP form implies that the thermal back isomerization to SP is spontaneous at room temperature, in agreement with experimental results [42]. On the other hand, as we report below, charging or protonation of the SP stabilizes the MC forms compared to the SP one. In the case of the anion and the O-protonated species, the order of stability is reverted and MC is more stable than SP, making the forward reaction (ring opening) spontaneous at room temperature.

The neutral isomerization pathways for the SP1 and the SP2 conformers were first screened using a grid in the α and β dihedral angles while keeping all other coordinates frozen. Since varying these angles de facto implies a variation of the CO bond length, the identified stable points (maxima and minima) were then relaxed and the transition state geometries confirmed by IRC. All the maxima and minima are checked by frequency calculation. The two pathways important for the thermal isomerization and for comparison with the charged species are reported in Fig. 3 for each enantiomer of the SP1 and SP2 conformers. For a given conformer, the reaction pathways of the two enantiomers are identical within numerical accuracy.

The reaction pathway for the SP1 conformer (Fig. 3a, b) involves as a first intermediate the metastable CCC MC conformer, which can easily revert to the SP form. The computed barrier at room temperature from S-SP1 to CCCa is 73.0 kJ/mol (Fig. 3a), while the reverse barrier is only 4.6 kJ/mol. The computed transition state theory (TST) forward rate constant is 9.7×10^{-1} s^{-1}, while the backward rate is 9.7×10^{11} s^{-1}. For this reason, the CCC conformer has not been unambiguously identified experimentally [38]. Its geometry is distorted and not fully planar, unlike that of the more stable MC conformers. To reach the more stable CTCa and TTCa MC open conformers, one needs to cross two other high barriers (49.9 kJ/mol and 62.4, respectively). For these two final steps, the forward reaction is faster than the backward one. The TST forward and backward rates between each intermediate are reported in Table S4. Since the neutral TTC and CTC forms are higher in energy than the SP1 closed conformer, at room temperature, it is the colorless SP1 form that is by far preponderant. We also report in Fig. 3a and b a second reaction pathway, which goes directly via a single TS from the S-SP1 to the TTCa form with a barrier 121.4 kJ/mol. This pathway will be shown to be of interest for comparison with the pathways of the charged species.

As alluded to above, for the SP2 conformer (see Fig. 2c, d), the reaction path is different because of the steric hindrance of the (thiol derivative) linker: at the equilibrium geometry,

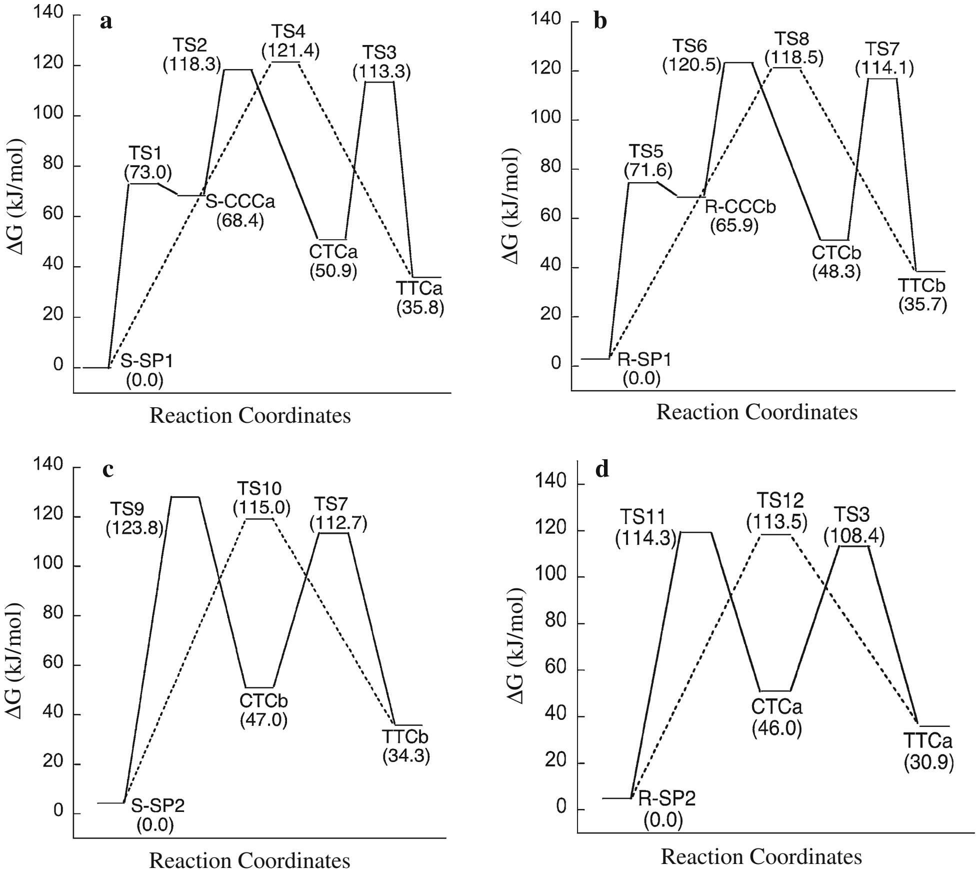

Fig. 3 The two investigated thermal reaction pathways of the isomerization reaction of S-SP1 (**a**), R-SP1 (**b**), S-SP2 (**c**), R-SP2 (**d**) to MC. The free energies are calculated at the CAM-B3LYP/6-311+G(d,p) level in the gas phase at room temperature and reported with respect to the S-SP1 conformer in all four panels. Energy differences in parenthesis are computed with respect to corresponding stable SP conformer for each panel. The multistep reaction path is shown in solid line and the direct one in dotted ones. See also Table 1

the linker is positioned in the ring opening direction. For this reason, the CCC conformer is not stable for the SP2 form. SP2 is isomerizing directly to CTC via a very high barrier of 123.8 kJ/mol (Fig. 3c). CTC is not chiral anymore and can isomerize to TTC as in Fig. 3a and b. On the other hand, the direct one step isomerization from SP2 to TTC has a barrier of 115.0 kJ/mol at CAM-B3LYP/6-311+G(d,p) level (see Table 1). This energy barrier is slightly lower than that of the isomerization of the SP1 conformer discussed above.

4 Field effects on the neutral reaction pathway

We first report on the effect of a static external field on the electrocyclic reaction leading to ring opening. The effect of the static field is to distort the electronic density and to change the distribution of partial charges. Our motivation is to investigate whether reasonable field strength of about 1 V/nm, as typically applied in break junctions, could distort the electron density strongly enough to induce the ring opening of the SP form. Significant field effects have been recently reported by Shaik et al. [53] on another electrocyclic reaction, the one step Diels-Adler reactions between butadiene and ethylene and between maleic anhydride and cyclopentadiene. The situation is more complex in the case of the isomerization of the SP because the most favorable reaction path is multistep and involves several intermediates. Our conclusion is that while the electronic density is significantly distorted, as shown in Fig. 4 below, reasonable field strength cannot lead to a ring opening.

We started by systematically analyzing the changes in the distribution of the electron density between the two moieties for increasing field strengths of different orientations with respect to the molecular frame shown in Fig. 1 for the neutral S-SP1 conformer (see Fig. 2a) at its field-free equilibrium geometry. As pointed out in Ref. [53], in Gaussian09, the direction of the applied external field corresponds to the displacement of negative charges. Since the reaction coordinate for the opening of the C4–O9 bond has components in the y and z directions, we concentrated on these two directions. The field effects along the x direction mainly affect the linker part. The effects on the relative energies of the TS and the metastable intermediates for field strengths of 1.3 V/nm applied the x, y, and z directions (see Fig. 1) are reported in Table S5. We show in Fig. 4 the difference, $\rho_{F=0} - \rho_{F_z}$, between the field-free and field-distorted isocontours of the one-electron density of SP for a field strength of 1.3 V/nm applied in the

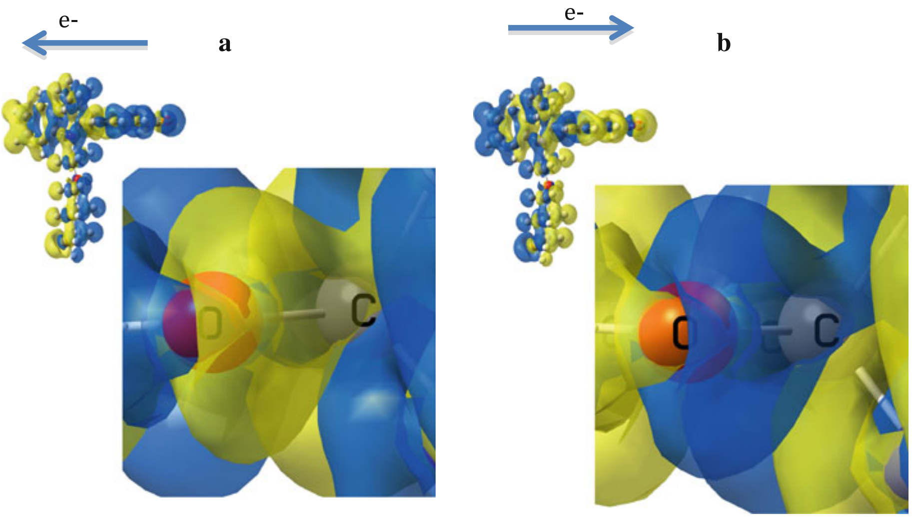

Fig. 4 Zoom on the C4–O9 bond of an isocontour of the density difference, $\rho_{F=0} - \rho_{F_z}$, where $\rho_{F=0}$ is field free and ρ_{F_z} is computed for an external field strength of 1.3 V/nm applied in *z* direction (*panel a*) and $-z$ direction (*panel b*) at the CAM-B3LYP/6-311+G(d,p) level for the equilibrium geometry of the field free S-SP1 molecule. Isocontour value is 0.0001 |e|/Å^3. The insets show the overall molecule oriented as in Fig. 1. A positive difference is shown in *blue* and a negative one in *yellow*. A negative difference (*yellow*, *panel a*) indicates that the finite field electron density is larger than that of the neutral. A positive difference (*blue*, *panel b*) indicates that the electron density of the neutral is larger than that of the field distorted one so that the field has decreased the density on the C4–O9 bond. Accordingly, the z component of the dipole moment computed for a field applied in the $+z$ direction is 0.3 D which is smaller than that of the neutral (2.8 D), while the dipole moment computed for a field applied in the $-z$ direction is +5.3 D, which is larger than that of the neutral. See Fig. S2 for the difference between the field free and the field distorted isocontours of the one-electron density of the TTCa open form

$+z$ (Fig. 4a) and $-z$ (Fig. 4b) directions (see Fig. 1). The figures show specifically the C4–O9 bond and the insets the entire molecule. As a general rule, an orientation of the external field that favors a decrease of electron density on the pyran moiety, in particular on the C4–O9 bond, favors ring opening. This corresponds to the $-z$ direction and $-y$ directions for which the electron density increases on the nitrobenzene part moiety and decreases on the indoline part and on the C4–O9 bond of the pyran (see Fig. 4b).

We then optimized the geometries of the intermediates reported in Fig. 3 and in Table 1 for a field strength of 0.0025 a.u. (corresponding to 1.3 V/nm) applied in the $+z$, $-z$, $+y$, and $-y$ directions. The results are reported in Table 2. Partial charges were computed for the field-free and the finite-field equilibrium geometries. The changes in partial charges while small at this field strength reflect the changes induced in the localization of the electron density of the applied external field shown in Fig. 4 and are reported in Table S6 of the ESM. The changes in partial charges are larger when computed using the MK [54] approach than using the NBO [55] one. The MK partial charges increase significantly on the C4 (positive, 20–40 %) and O9 (negative, a few %) atoms for field applied in the $+y$ and $+z$ direction. They decrease but to a smaller extent when the field is applied in the $-y$ and $-z$ directions. The NBO analysis [55] gives smaller partial charge changes. This analysis also gives a small increase of electron density on the C4–O9 bond when the field is applied in the $+y$ and $+z$ directions and a decrease for field applied in the opposite directions. The changes in the equilibrium geometry C4–O9 bond length induced by the external field are consistent with the changes in the localization of the electron density and in the computed partial charges reported above. The C4–O9 bond length increases by 0.01 Å for a field strength of 0.0025 a.u. applied in the $-y$ and $-z$ direction which favors the bond opening. For a stronger field of 0.005 au (2.6 V/nm), the C4–O9 bond length increased is of about 0.03 Å at the B3LYP/6-311 ++G(d,p) level.

A field applied in the $-y$ and $-z$ directions lowers the barrier for the ring opening step, between S-SP1 and S-CCCa, from 73.0 kJ/mol (field free) to 61.9 kJ/mol for a field applied in the $-y$ and 60.2 kJ/mol for a field applied in the $-z$ direction (Table 2). A similar trend in the lowering of the barrier is induced by the effect of a nitro group in para to C4–O9 bond in spiropyran. The nitro group, being an electron attractor, also depletes the electron density on the C4–O9 bond [31]. When the static field is applied in the $+y$ direction, the trans-MC CTCa and TTCa conformers are less stable than SP by 42.5 and 20.8 kJ/mol, respectively, while when the field applied in the $-z$ direction, the CTCa and TTCa conformers are less stable than S-SP1 by 27.2 and 16.4 kJ/mol but more stable than in the field-free case (see Table 2). On the other hand, a field

Table 2 Relative free energies (kJ mol^{-1}) for the two reaction pathways of the neutral molecule (see Fig. 3) computed at CAM-B3LYP/6-311+G(d,p) level for an external electric field of 1.3 V/nm applied in the y and z directions (see Fig. 1)

Conformer	Field free	y	$-y$	z	$-z$
S-SP1	0.0	13.0	−16.1	5.9	−10.7
CCCa	68.4	83.7	39.7	79.1	45.6
CTCa	48.3	55.5	44.7	68.7	16.5
TTCa	35.8	33.8	30.5	52.8	5.7
TS1	73.0	88.7	45.8	84.8	49.5
TS2	118.3	124.6	109.6	120.6	105.7
TS3	113.3	118.1	97.5	150.4	64.4
TS4	121.4	126.6	110.5	121.7	111.1

The relative energies of the conformers and TS at finite field are reported with respect to field free S-SP1 conformer. All computed frequencies of the stable conformers are real, and the TS have a single imaginary frequency only

applied in the $-z$ direction does not favor the isomerization from CCC to CTC. Overall, it is therefore not possible to find a single field orientation that leads to a significantly faster isomerization rate from SP to TTC. If, however, one is interested in controlling one isomerization step along the reaction pathway, like for example as recently reported for the TTC and the TTT MC conformers, [52] field effects can be significant. Since SP and MC have rather large dipole moments, the computed values at the CAM-B3LYP/6-311+G(d,p) are 9.8 D for TTC compared to 6.4 D for SP, the molecules could be oriented and the switching between two forms controlled by applying a static electric field.

5 O and N protonation effects

Compared to applying a static external field, fully charging the molecule, either by removing or adding an electron or by adding a proton, significantly modifies the relative stability of the close and open conformers and the reaction pathways.

A recent experimental study on protonation effect [56] as well as previous studies [33, 34] shows that protonation on the pyran oxygen considerably stabilizes the open form, see Fig. 5. These studies report that the colorless SP opens to *cis*-MC by protonation of the pyran oxygen at room temperature. Isomerization to the most stable MC TTC conformers can be induced by UV light. The reverse reaction can be triggered by moving to a basic solution or by VIS light. Protonation on the N atom of the indole cycle was also observed as a side product [33].

Our computations fully confirm this effect. Protonation on the O of the pyran significantly decreases the electron density on the C4–O9 bond, which leads to the opening of the bond. Upon O protonation, both enantiomers of the SP1 and SP2 forms are found unstable. They relax to the open *cis*-$TCCOH^+$ conformer (as shown in Fig. 6, see also Table S7) that was not identified in the neutral reaction pathway. On the other hand, protonating the SP form on the N atom accumulates electron density on the C4–O9 and the indoline part, which stabilizes significantly the SP forms, see Fig. 6 and Table S8. The effects of O and N protonation are similar to those reported above for externally applied electric fields. The difference is that the local field created by protonation is stronger than those induced by a reasonable field strength. Protonation on the O of the pyran is strong enough to lead to the opening of the C4–O9 bond, while reasonable field strengths (< than 2.6 V/nm) remove electron density from that bond (Fig. 4b) and accumulate electron density on the nitrobenzene part but do not trigger bond opening. N protonation accumulates electron density of the C4–O9 bond and leads to a larger stabilization of the SP form than external fields applied in the $+z$ and $+y$ directions. The analog of Fig. 4 computed for protonation effects on the one electron density difference is reported in the ESM, Fig. S3.

The computed reaction pathways for the O-protonated SP are reported in Fig. 7 (see also Table S7) for the two enantiomers of the SP1 and SP2 conformers. Upon geometry optimization, $SPOH^+$ is not stable and relaxes to the stable $TCCOH^+$. The $CCCOH^+$ conformer is found slightly more stable than the $TCCOH^+$ conformers (by 3–7 kJ mol^{-1}) except for R-SP2 where it is $TCCOH^+$ which is more stable by 18.7 kJ mol^{-1}. The *cis*-$MCOH^+$ conformers then isomerize to trans-$MCOH^+$.

As in the case of the neutral (see Fig. 3), the protonated S-SP1 and R-SP2 go to protonated MCa conformers, while R-SP1 and S-SP2 lead to MCb conformers. The $CCCOH^+$ and $TCCOH^+$ conformers do not isomerize easily to the stable trans-O-protonated MC form. The computed barriers for the isomerization of $CCCOH^+$ to $CTCOH^+$ are of the order of 120 kJ mol^{-1}. The second isomerization between $CTCOH^+$ and $TTCOH^+$ is easier, with computed barriers of the order 20 kJ mol^{-1}.

For the N-protonated SP, there are two possible ways for the proton to bind to the N atom (see Fig. S4). This in total

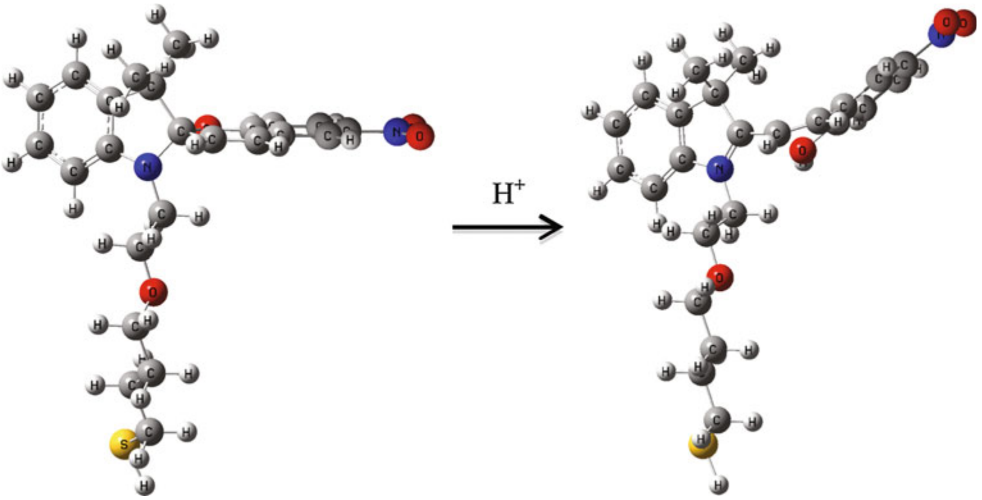

Fig. 5 S-SP1(left) and protonated open stable TCCOHa$^+$ (*right*) calculated at CAM-B3LYP/6-311+G(d,p). Note that the SP-O-protonated form is not stable

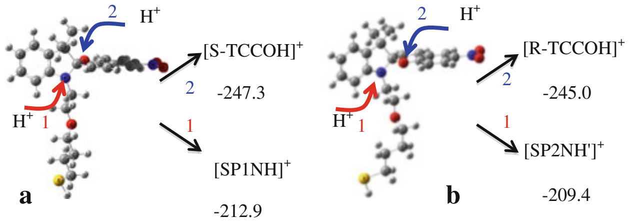

Fig. 6 **a** Protonation on O and on N of S-SP1 conformer, **b** protonation on O and on N of R-SP2 conformer, as for the neutral case, both enantiomers of a given conformer react in the same way (see Fig. 7). The protonation free energies (kJ mol^{-1}) for the reaction SP + H_3O^+ – > SPH^+ + H_2O are computed at the CAM-B3LYP/6-311 + G(d,p) level at room temperature. Note that while protonation on the O leads to the open *cis*-TCCOH$^+$ conformer (see Table S7), protonation on the N atom leads to a stable close SP conformer (see Table S8)

leads to eight possible conformers of the N-protonated form. When the N–H bond is in a trans configuration with respect to the C4–O9 bond of the benzopyran, the conformer is named as SPNH$^+$, while it is called SPNH'$^+$ when the N–H bond is cis with respect to the C4–O9 bond. The enantiomers of SP1NH$^+$ are more stable than the SP1NH'$^+$ ones by about 13.3 kJ/mol. On the other hand, the R and S enantiomers of SP2NH$^+$ and SP2NH'$^+$ are found to be isoenergetic. In the case of N protonation, the close conformers are considerably more stable than the open ones (by about 100 kJ/mol). No stable CCCNH$^+$ conformer could be identified in the reaction pathways. Upon ring opening, the SP1 enantiomers go to CTCNH$^+$ conformer with very high barriers of 190 kJ/mol (see Table S8).

To summarize, for all conformers of SP, the protonation of the O of the pyran leads to a localization of positive charge on the benzopyran part, which favors the opening of the C–O bond and the conversion to a distorted TCCOH$^+$ conformer without any barrier. On the contrary, the N-protonated form is very stable for all SP conformers and compared to the neutral case significantly more stable than the open MC conformers.

6 Electron attachment and ionization effects

Experimental studies of the electrochemical oxidation and reduction of nitro SP compounds in different environments show that oxidation takes place on the indole part of the SP and reduction at the NO_2 group of the benzopyran part of the SP [57–60]. Without a NO_2 group, SP does not exhibit electroactivity [61]. We report in this section on the isomerization reaction pathways for the anion and the cation of S-SP1 conformer. The isomerization pathways are summarized in Fig. 8 and compared with field and protonation effects.

The vertical attachment of an electron to the neutral S-SP1 form leads to a localization of the extra electron density on the benzopyran part mainly on the NO_2 group. This density corresponds to that of the LUMO of the neutral, see Fig. 9a. Since the ring opening and the breaking of the C4–O9 bond is favored by a decrease of electron density on the benzopyran part, the computed barrier for ring opening remains high, similar to neutral one, and is equal to 85.9 kJ/mol (see Fig. 8a, f). The difference is that the CCCa$^-$ anion is more stable than the S-SP1$^-$ anion by 8.6 kJ/mol, so that the back reaction is not spontaneous, unlike what is found for the neutral. Being stable, it is also likely that the CCCa$^-$ conformer could be easily identified spectroscopically. The CTCa$^-$ and TTCa$^-$ anions are also more stable than S-SP1$^-$ by 43.9 and 59.0 kJ/mol, respectively, (see Fig. 8f and Table S9) and the forward isomerization barrier of the CCCa$^-$ conformer to the more stable open CTCa$^-$conformer is computed to be 16.6 kJ/mol, which leads to a very fast isomerization rate of 7.9 × 10^9 s^{-1}. The computed TST

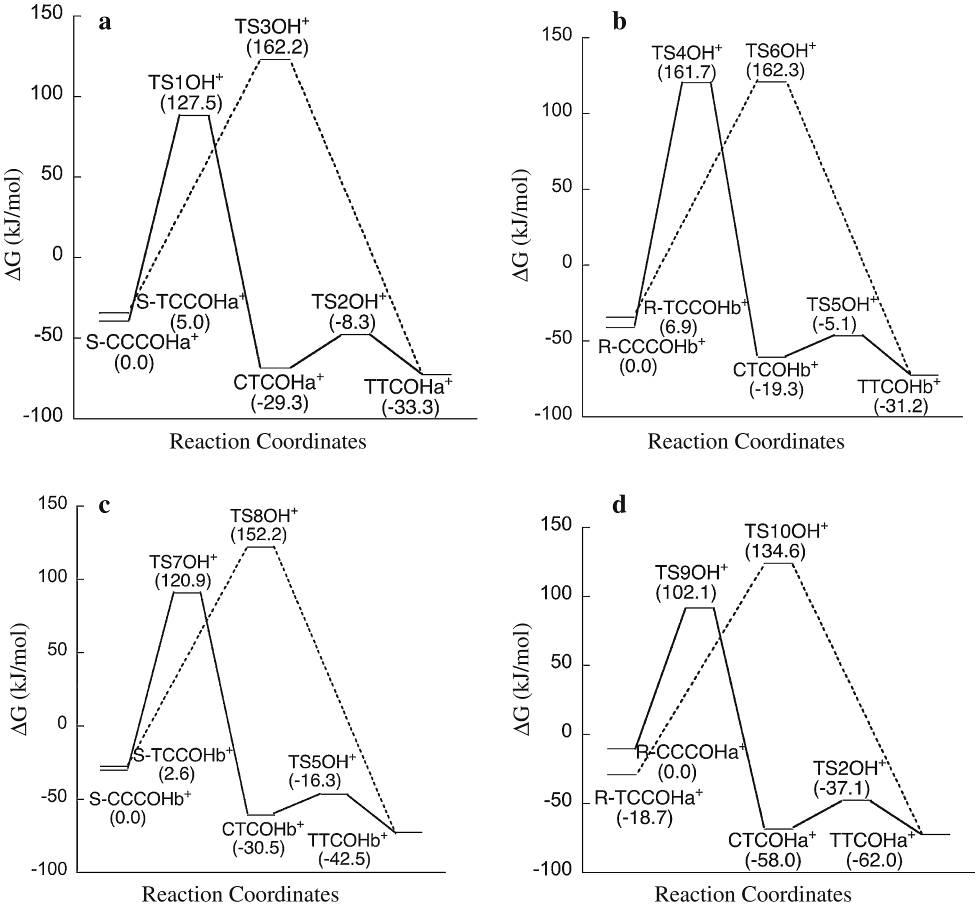

Fig. 7 **a** Free energy profile for the protonated SP: **a** S-SP1, **b** R-SP1, **c** S-SP2, **d** R-SP2 computed with respect to the stable N-protonated S-SP1 conformer. Energies in parenthesis are computed with respect to the stable corresponding $CCCOH^+$. The free energies are calculated at CAM-B3LYP/6-311+G(d,p) level in the gas phase at room temperature. See also Table S7

rates are reported in Table S10. In the case of the anion, we also identified a different reaction path involving the $TCCa^-$ conformer. This reaction pathway involves fewer intermediates and does not exist for the neutral. The $CCCa^-$ conformer can isomerize to the $TCCa^-$ intermediate by crossing a barrier of 42.1 kJ/mol. One can then reach $TTCa^-$ in an essentially barrierless manner (the computed barrier is 4.7 kJ/mol). Since the anion forms of MCs are stabilized compared to the SP anion, the backward reaction is not spontaneous but can be induced by VIS light. However, unlike in the case of protonation on the O of the pyran (see Fig. 8b), the ring opening to $CCCa^-$ is not spontaneous, the computed rate constant is 5.4×10^{-3} s^{-1} (see Table S10), the thermal reaction is slow but occurs spontaneously. The next reaction steps involving isomerization between the MC forms are much faster.

Upon vertical ionization, a hole is made in the indoline part, which leads to a decrease of the electron density and partial charge on the N atom. The hole density corresponds to the density of the HOMO of the neutral, see Fig. 9b. Upon geometry relaxation, the geometry of the S-SP1 cation is distorted with respect to that of the neutral (in particular the α dihedral angle) but remains more stable than that of the open $CCCa^+$ MC conformer by 28.8 kJ/mol (see Fig. 8e and Table S11). The energy difference is smaller than in the case of the neutral (see Fig. 8a) and the barrier height for the isomerization to $CCCa^+$ is computed equal to 73.6 kJ/mol. $S\text{-}SP1^+$ remains more stable than $TTCa^+$ by 8.3 kJ/mol while for the neutral S-SP1 is more stable than TTCa by 35.8 kJ/mol. The energy barrier for the isomerization of CCCa to TTCa is 60.4 kJ/mol, the TS of this isomerization step being similar to the TS4 of the neutral. Unlike for the reaction paths of the neutral (Figs. 3, 8a) and of the anion (Fig. 8f), the reaction path of the cation involves only two intermediates. The computed rates of isomerization can be found in the Table S12. Contrary to electron attachment, the isomerization of the SP cation is not spontaneous at room temperature. The isomerization pathway is similar to that of the neutral.

7 Concluding remarks

Protonation, charge, and field effects affect the thermal reaction path of the isomerization of spiropyran. Since these effects are likely to occur when the isomerization takes place in solution or in a break junction, it is of interest to characterize them in order to design reliable sensing,

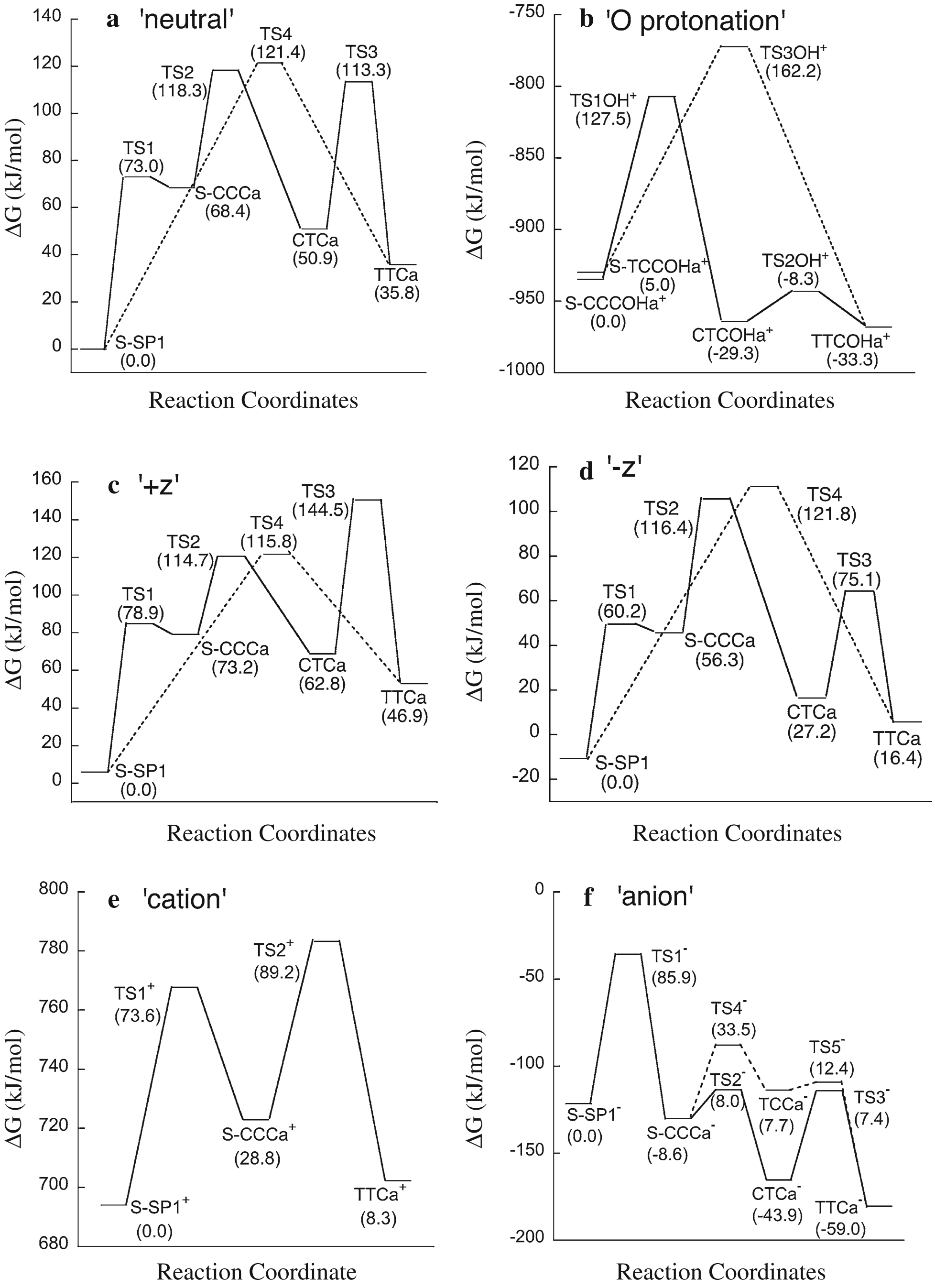

Fig. 8 The thermal reaction pathways of the isomerization reaction of S-SP1 to MCa under different conditions: **a** neutral, **b** proton attachment **c** field (1.3 V/nm) applied in the *z* direction, **d** field (1.3 V/nm) applied in the $-z$ direction **e** removing an electron **f** adding an electron. The free energies are calculated at the CAM-B3LYP/6-311+G(d,p) level in the gas phase at room temperature and reported with respect to neutral S-SP1. Energy differences in parenthesis are computed with respect to corresponding SP conformer for **a**, **c**–**f**, in **b** computed with respect to S-CCCOHa$^+$ conformer

logic, or storage devices. Our computational results are summarized in Fig. 8 above. They show that charge effects stabilize the open MC conformers with respect to the close SP form and reverse the order of stability in the case of electron attachment (Fig. 8f) and protonation on the O of the pyran (Fig. 8b), so that the ring opening becomes spontaneous at room temperature. While a marked increase of the rate for ring opening was experimentally reported for the oxygen-protonated form, [33] the cation and the anion reaction pathways have not yet been experimentally investigated. The largest effect on the reaction pathway occurs in the case of protonation on the O of the pyran moiety for which we could not identify a stable SP form. Upon relaxation, the stable conformer is an open *cis*-MCOH$^+$ conformer. The latter then isomerizes to the trans-MC form. For the anion (Fig. 8f), the CCC form is more stable than the SP one, as well as all the trans-MC conformers. In the case of the cation (Fig. 8e), the CCC and TTC conformers remain less stable than SP. While the ring opening is barrierless for protonation on the O of the pyran

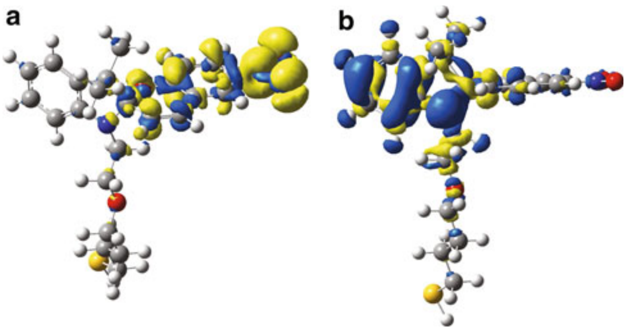

Fig. 9 Isocontour (0.002 |e|/Å^3) of the density difference between the neutral S-SP1 and the S-SP1 anion, $\rho_{SP} - \rho_{SP-}$, (**a**) and the S-SP1 cation, $\rho_{SP} - \rho_{SP+}$ (**b**) computed at the CAM-B3LYP/6-311 + G(d,p) level. In (**a**), the geometry is rotated by 30° with respect to S-SP1 (see Fig. 2). One can see that the extra electron density is localized on the benzopyran part and particularly on the nitro group. On the other hand, the hole is localized on the indoline part (**b**)

moiety, for the anion and the cation, the computed rates are of the same order of magnitude as those computed for the neutral. The N-protonated SP form is found very stable.

As a general rule, the electrocyclic reaction leading to ring opening is favored when the electron density of the pyran part is reduced. The decrease of the electron density on the C4–O9 bond leads to the stable TCC form in the case of protonation on O9 (Fig. 8b) and to a decrease of the barrier height to reach CCC upon application of an external electric field that withdraw electron density from that bond (Fig. 8d).

Acknowledgments We thank Prof. I. Willner (Hebrew University of Jerusalem), Prof. R. Weinkauf (University of Dusseldorf), and Dr. S. Karthäuser (FZ Jülich) for stimulating discussions. The work of FR and RG was supported by the EC FET project MOLOC and the ARC grant of the French Community of Belgium NANOFORCE.

References

1. Lenoble C, Becker RS (1986) Photophysics, photochemistry, kinetics, and mechanism of the photochromism of 6’-nitroindolinospiropyran. J Phys Chem 90:62–65
2. Chibisov AK, Gorner H (1997) Photoprocesses in spiropyran-derived merocyanines. J Phys Chem A 101:4305–4312
3. Minkin VI (2004) Photo-, thermo-, solvato-, and electrochromic spiroheterocyclic compounds. Chem Rev 104:2751–2776
4. Minkin VI, Metelitsa AV, Dorogan IV, Lukyanov BS, Besugliy SO, Micheau J-C (2005) Spectroscopic and theoretical evidence for the elusive intermediate of the photoinitiated and thermal rearrangements of photochromic spiropyrans. J Phys Chem A 109:9605–9616
5. Buntinx G, Poizat O, Foley S, Sliwa M, Aloise S, Lokshin V, Samat A (2010) Sub-picosecond transient absorption spectroscopy of substituted photochromic spironaphthoxazine compounds. Dyes Pigm 89:305–312
6. Willner I (1997) Photoswitchable biomaterials: en route to optobioelectronic systems. Acc Chem Res 30:347–356
7. Berkovic G, Krongauz V, Weiss V (2000) Spiropyrans and spirooxazines for memories and switches. Chem Rev 100:1741–1754
8. Wen G, Yan J, Zhou Y, Zhang D, Mao L, Zhu D (2006) Photomodulation of the electrode potential of a photochromic spiropyran-modified Au electrode in the presence of Zn2+: a new molecular switch on the electronic transduction of the optical signals. Chem Commun 2006(28):3016–3018
9. Fukushima K, Vandenbos AJ, Fujiwara T (2007) Spiropyran dimer toward photo-switchable molecular machine. Chem Mater 19:644–646
10. Bardavid Y, Goykhman I, Nozaki D, Cuniberti G, Yitzchaik S (2011) Dipole assisted photogated switch in spiropyran grafted polyaniline nanowires. J Phys Chem C 115:3123–3128
11. Raymo FM, Alvarado RJ, Giordani S, Cejas MA (2003) Memory effects based on intermolecular photoinduced proton transfer. J Am Chem Soc 125:2361–2364
12. Tomizaki K-y, Mihara H (2007) Phosphate-mediated molecular memory driven by two different protein kinases as information input elements. J Am Chem Soc 129:8345–8352
13. Riskin M, Gutkin V, Felner I, Willner I (2008) Photochemical and electrochemical encoding of erasable magnetic patterns. Angew Chem Int Ed 47:4416–4420
14. Winkler JD, Bowen CM, Michelet V (1998) Photodynamic fluorescent metal ion sensors with parts per billion sensitivity. J Am Chem Soc 120:3237–3242
15. Ren J, Tian H (2007) Thermally stable merocyanine form of photochromic spiropyran with aluminium ion as a reversible photo-driven sensors in aqueous solution. Sensors 7:3166–3178
16. Scarmagnani S, Walsh Z, Slater C, Alhashimy N, Paull B, Macka M, Diamond D (2008) Polystyrene bead-based system for optical sensing using spiropyran photoswitches. J Mater Chem 18:5063–5071
17. Shiraishi Y, Adachi K, Itoh M, Hirai T (2009) Spiropyran as a selective, sensitive, and reproducible cyanide anion receptor. Org Lett 11:3482–3485
18. Zhu M-Q, Zhu L, Han JJ, Wu W, Hurst JK, Li ADQ (2006) Spiropyran-based photochromic polymer nanoparticles with optically switchable luminescence. J Am Chem Soc 128:4303–4309
19. Zhu L, Wu W, Zhu M-Q, Han JJ, Hurst JK, Li ADQ (2007) Reversibly photoswitchable dual-color fluorescent nanoparticles as new tools for live-cell imaging. J Am Chem Soc 129:3524–3526
20. de Leon L, Biewer MC (2000) Preparation of self-assembled monolayers with specific intermolecular interactions. Tetrahedron Lett 41:3527–3530
21. Wohl CJ, Kuciauskas D (2005) Excited-state dynamics of spiropyran-derived merocyanine isomers. J Phys Chem B 109:22186–22191
22. Holm A-K, Mohammed OF, Rini M, Mukhtar E, Nibbering ETJ, Fidder H (2005) Sequential merocyanine product isomerization following femtosecond UV excitation of a spiropyran. J Phys Chem A 109:8962–8968
23. Poisson L, Raffael KD, Soep B, Mestdagh J-M, Buntinx G (2006) Gas-phase dynamics of spiropyran and spirooxazine molecules. J Am Chem Soc 128:3169–3178
24. Stitzel S, Byrne R, Diamond D (2006) LED switching of spiropyran-doped polymer films. J Mater Sci 41:5841–5844
25. Kalisky Y, Orlowski TE, Williams DJ (1983) Dynamics of the spiropyran-merocyanine conversion in solution. J Phys Chem 87:5333–5338
26. Tamaki T, Sakuragi M, Ichimura K, Aoki K (1989) Laser photolysis studies of nitrospiropyrans intramolecularly linked with a triplet quenching or sensitizing side group. Chem Phys Lett 161:23–26

27. Helmut G (1998) Photochemical ring opening in nitrospiropyrans: triplet pathway and the role of singlet molecular oxygen. Chem Phys Lett 282:381–390
28. Emsting NP (1989) Transient optical absorption spectroscopy of the photochemical spiropyran-merocyanine conversion. Chem Phys Lett 159:526–531
29. Zhang JZ, Schwartz BJ, King JC, Harris CB (1992) Ultrafast studies of photochromic spiropyrans in solution. J Am Chem Soc 114:10921–10927
30. Chibisov AK, Gorner H (2001) Photochromism of spirobenzopyranindolines and spironaphthopyranindolines. Phys Chem Chem Phys 3:424–431
31. Sheng Y, Leszczynski J, Garcia AA, Rosario R, Gust D, Springer J (2004) Comprehensive theoretical study of the conversion reactions of spiropyrans: substituent and solvent effects. J Phys Chem B 108:16233–16243
32. Maurel F, Aubard J, Millie P, Dognon JP, Rajzmann M, Guglielmetti R, Samat A (2006) Quantum chemical study of the photocoloration reaction in the napthoxazine series. J Phys Chem A 110:4759–4771
33. Wojtyk JTC, Wasey A, Xiao N-N, Kazmaier PM, Hoz S, Yu C, Lemieux RP, Buncel E (2007) Elucidating the mechanisms of acidochromic spiropyran-merocyanine interconversion. J Phys Chem A 111:2511–2516
34. Hisayoshi S (1997) Molecular orbital calculations for acid induced ring opening reaction of spiropyran. Dyes Pigm 33:229–237
35. Buback J, Kullmann M, Langhojer F, Nuernberger P, Schmidt R, Wurthner F, Brixner T (2010) Ultrafast bidirectional photoswitching of a spiropyran. J Am Chem Soc 132:16510–16519
36. Krysanov SA, Alfimov MV (1984) Picosecond flash photolysis of photochromic spiropyrans. Laser Chem 4:129–138
37. Cottone G, Noto R, La Manna G (2004) Theoretical study of spiropyran-merocyanine thermal isomerization. Chem Phys Lett 388:218–222
38. Ernsting NP, Dick B, Arthen-Engeland Th (1990) The Primary photochemical reaction step of unsubstituted indolino-spiropyrans. Pure Appl Chem 62:1483–1488
39. Ipe BI, Mahima S, Thomas KG (2003) Light-induced modulation of self-assembly on spiropyran-capped gold nanoparticles: a potential system for the controlled release of amino acid derivatives. J Am Chem Soc 125:7174–7175
40. Riskin M, Willner I (2009) Coupled electrochemical/photochemical patterning and erasure of ag 0 nanoclusters on au surfaces. Langmuir 25:13900–13905
41. Piantek M, Schulze G, Koch M, Franke KJ, Leyssner F, Kruger A, Navio C, Miguel J, Bernien M, Wolf M, Kuch W, Tegeder P, Pascual JI (2009) Reversing the thermal stability of a molecular switch on a gold surface: ring-opening reaction of nitrospiropyran. J Am Chem Soc 131:12729–12735
42. Kiebwetter R, Pustet N, Brandl F, Mannschreck A (1999) 1′, 3′, 3′-Trimethyl-6-nitrospiro[2H-1-benzopyran-2,2′-indoline]: its thermal enantiomerization and the equilibration with its merocyanine. Tetrahedron Asymmetry 10:4677–4687
43. Frisch MJ, Trucks GW, Schlegel HB, Scuseria GE, Robb MA, Cheeseman JR, Scalmani G, Barone V, Mennucci B, Petersson GA, Nakatsuji H, Caricato M, Li HPHX, Izmaylov AF, Bloino J, Zheng G, Sonnenberg JL, Hada M, Ehara M, Toyota K, Fukuda R, Hasegawa J, Ishida M, Nakajima YT, Honda Y, Kitao O, Nakai H, Vreven T, Montgomery JA, JEP Jr, Ogliaro F, Bearpark M, Heyd JJ, Brothers E, Kudin KN, Staroverov VN, Kobayashi R, Normand J, Raghavachari K, A Rendell K, Burant JC, Iyengar SS, Tomasi J, Cossi M, Rega N, Millam JM, Klene M, Knox JE, Cross JB, Bakken V, Adamo C, J Jaramillo C, Gomperts R, Stratmann RE, Yazyev O, Austin AJ, Cammi R, Pomelli C, Ochterski JW, Martin RL, Morokuma K, Zakrzewski VG, Voth GA, Salvador P, Dannenberg JJ, Dapprich S, Daniels AD, Farkas JÖ, Foresman B, Ortiz JV, Cioslowski J, Fox DJ (2009) Gaussian 09 Revision A.1
44. Wang Y-G (2009) Examination of DFT and TDDFT methods II. J Phys Chem A 113:10873–10879
45. Yanai T, Tew DP, Handy NC (2004) A new hybrid exchange–correlation functional using the Coulomb-attenuating method (CAM-B3LYP). Chem Phys Lett 393:51–57
46. Zhao Y, Truhlar D (2008) The M06 suite of density functionals for main group thermochemistry, thermochemical kinetics, noncovalent interactions, excited states, and transition elements: two new functionals and systematic testing of four M06-class functionals and 12 other functionals. Theor Chem Account 120:215–241
47. Sumimoto M, Kawashima Y, Yokogawa D, Hori K, Fujimoto H (2012) Influences of dispersion and long-range corrections on molecular structures of three types of lithium phthalocyanine dimer. Int J Quantum Chem. doi:10.1002/qua.24072
48. Becke A (1993) Density-functional thermochemistry. III. The role of exact exchange. J Chem Phys 98:5648–5652
49. Mohan N, Vijayalakshmi KP, Koga N, Suresh CH (2010) Comparison of aromatic NH$\cdots\pi$, OH$\cdots\pi$, and CH$\cdots\pi$ interactions of alanine using MP2, CCSD, and DFT methods. J Comput Chem 31:2874–2882
50. Futami Y, Chin MLS, Kudoh S, Takayanagi M, Nakata M (2003) Conformations of nitro-substituted spiropyran and merocyanine studied by low-temperature matrix-isolation infrared spectroscopy and density-functional-theory calculation. Chem Phys Lett 370:460–468
51. Hobley J, Malatesta V, Millini R, Montanari L, Neil Parker WO (1999) Proton exchange and isomerisation reactions of photochromic and reverse photochromic spiro-pyrans and their merocyanine forms. Phys Chem Chem Phys 1:3259–3267
52. Buback J, Nuernberger P, Kullmann M, Langhojer F, Schmidt R, Wurthner F, Brixner T (2011) Ring-closure and isomerization capabilities of spiropyran-derived merocyanine isomers. J Phys Chem A 115:3924–3935
53. Meir R, Chen H, Lai W, Shaik S (2010) Oriented electric fields accelerate diels–alder reactions and control the endo/exo selectivity. ChemPhysChem 11:301–310
54. Singh UC, Kollman PA (1984) An approach to computing electrostatic charges for molecules. J Comput Chem 5:129–145
55. Reed AE, Weinstock RB, Weinhold F (1985) Natural population analysis. J Chem Phys 83:735–746
56. Shiraishi Y, Itoh M, Hirai T (2010) Thermal isomerization of spiropyran to merocyanine in aqueous media and its application to colorimetric temperature indication. Phys Chem Chem Phys 12:13737–13745
57. Campredon M, Giusti G, Guglielmetti R, Samat A, Gronchi G, Alberti A, Benaglia M (1993) Radical ions and germyloxyaminoxyls from nitrospiro[indoline-naphthopyrans]. A combined electrochemical and EPR study. J Chem Soc Perkin Trans 2:2089–2094
58. Preigh MJ, Stauffer MT, Lin F-T, Weber SG (1996) Anodic oxidation mechanism of a spiropyran. J Chem Soc Faraday Trans 92:3991–3996
59. Jukes RTF, Bozic B, Hartl F, Belser P, De Cola L (2006) Synthesis, photophysical, photochemical, and redox properties of nitrospiropyrans substituted with Ru or Os Tris(bipyridine) complexes. Inorg Chem 45:8326–8341
60. Wagner K, Byrne R, Zanoni M, Gambhir S, Dennany L, Breukers R, Higgins M, Wagner P, Diamond D, Wallace GG, Officer DL (2011) A multiswitchable poly(terthiophene) bearing a spiropyran functionality: understanding photo- and electrochemical control. J Am Chem Soc 133:5453–5462
61. Zhi JF, Baba R, Hashimoto K, Fujishima A (1995) A Multifunctional electro-optical molecular device. The photoelectrochemical behavior of spirobenzopyrans in dimethylformamide. Ber Bunsenges Phys Chem 99:32–39

Theor Chem Acc (2012) 131:1257
DOI 10.1007/s00214-012-1257-0

REGULAR ARTICLE

Ewald-type formulas for Gaussian-basis studies of one-dimensionally periodic systems

Joseph G. Fripiat · Frank E. Harris

Received: 11 May 2012 / Accepted: 10 July 2012 / Published online: 27 July 2012

Abstract The history of computations at Namur and elsewhere on the electronic structures of stereoregular polymers is briefly reviewed to place the work reported here in the context of related efforts. Our earlier publications described methods for the formal inclusion of Ewald-type convergence acceleration in band-structure computations based on Gaussian-type orbitals, and that work is here extended to include a discussion of the calculation of total energies. It is noted that the continuous nature of the electronic density leads to different functional forms than are encountered for point-charge lattice sums. Examples are provided to document the correctness and convergence properties of the formulation.

Keywords Total energy · Stereoregular polymers · Ewald method

Published as part of the special collection of articles celebrating theoretical and computational chemistry in Belgium.

J. G. Fripiat (✉)
Laboratoire de Chimie Théorique, Unité de chimie physique théorique et structurale, FUNDP–University of Namur,
Rue de Bruxelles, 61, 5000 Namur, Belgium
e-mail: joseph.fripiat@fundp.ac.be

F. E. Harris
Department of Physics, University of Utah,
Salt Lake City, UT 84112, USA
e-mail: harris@qtp.ufl.edu

F. E. Harris
Quantum Theory Project, University of Florida,
Gainesville, FL 32611, USA

1 Introduction

In the laboratories of the University of Namur, the authors and their colleagues have a long history in the development of methods for the study of one-dimensionally periodic systems described quantum-mechanically at the Hartree-Fock and correlation levels using expansions in Gaussian-type atomic orbitals. This work, which was started under the direction of Professor J. M. André, led to the creation of the program known as PLH [1]. That program, designed for the study of the structural and electronic properties of linear polymers, evaluated the lattice sums as direct-space expansions. Further work, directed by Professor J. Delhalle, led to the development of an approach that combined direct- and reciprocal-space concepts to yield an Ewald-type method [2]. That work appeared in the Ph.D. dissertation of Flamant [3], in a paper that included the present authors [4], and in later publications that are referred to where appropriate in the present communication.

The past 20 years have seen a renewal of interest in lattice summation methods, catalyzed by the advances in high-performance computing and the ability thereby provided to approach molecular dynamics and condensed-phase structural problems that had previously seemed inaccessible. In this respect, an important development was the so-called fast multipole method (FMM) [5]. With its help, the electrostatic energies of arrays of charged particles can be evaluated in computing times that are nearly linear in the number of particles. One of the strengths of FMM is that the charge distribution need not be periodic, and methods of Ewald character can be combined with FMM concepts for studies of periodic systems [6].

While FMM has opened the door to greatly improved efficiency in lattice sum evaluation, it may be useful to observe that (unlike the Ewald procedure) it is not a fundamentally new algorithm. FMM is in our opinion better viewed as an intelligently designed direct-space approach wherein (1) the charges in various regions are described in terms of a (truncated) set of their multipole moments; (2) multipole moments from regions that are sufficiently separated are used to compute energy contributions; (3) the regions, their size, and their moment truncation levels are chosen to optimize efficiency at a specified level of accuracy, and (4) any short-range energetic contributions that cannot be described accurately as multipole interactions are computed exactly and explicitly.

The situation becomes more complicated when, instead of point-charge arrays, one encounters continuous charge distributions of known functional forms, as occurs when orbitals are introduced to describe localized electron distributions in systems with periodicity in one or more dimensions. It is possible to use FMM methods for such systems, as was shown, for example, by Strain et al. [7]. However, in addition to the possibility of simply representing an orbital by its moments (and thereby foregoing any processing based on its specific form), one may alternatively be able to use properties of the orbitals to make further mathematical analyses that lead to gains in computational efficiency. Such an approach is represented in two efforts of which we are aware:

1. the periodic-system code CRYSTAL [8] manipulates direct-space lattice sums involving Gaussian-type orbitals (GTOs) in a way such that (at least for systems with linear periodicity) they are represented using the Euler-Maclaurin summation formula [9]. Although the Euler-Maclaurin formula is asymptotic (i.e., formally not convergent), this approach leads to highly satisfactory results in typical computations.
2. The work of our group (cited above), which makes explicit use of the transformational properties of the GTOs to obtain rapidly convergent analytical formulas for all the lattice sums entering Hartree-Fock (HF) and post-HF computations.

At this juncture, it is not clear which of the three currently identified approaches (FMM or those discussed in the preceding paragraph) will be the most efficient for various classes of problems. However, the present authors' experience indicates that there are problems of practical importance in which a full exploitation of the analytical properties of the basis functions has been found advisable. It therefore seems appropriate to encourage researchers to proceed in accord with their individual interests.

The present communication, which deals with computations of the total energy in one-dimensionally periodic systems, completes an exposition started in a recent paper from our group [10], in which we developed Ewald-type formulas for GTO-based band-structure computations in stereoregular polymers. The work of our group showed how the integrations in the nonperiodic directions can be carried out analytically to yield exact closed formulas for the terms in the remaining one-dimensional lattice summations. Although the Ewald transformation for GTOs leads, for the direct-space part, to complementary error functions (as also found for expansions involving point charges), the reciprocal-space contribution was found to be significantly different, being expressible in terms of a family of incomplete Bessel functions [11] whose numerical features had not previously been fully investigated. Consequently, our research effort included not only the formal aspects of the manipulation of the lattice summations to reach rapid convergence, but also the development of methods for the numerical evaluation of the relevant special functions. A satisfying aspect of the analysis is that the use of a comprehensive formal development enables the subsequent pursuit of whatever numerical methods seem most appropriate, in contrast to a situation in which the formal problem is solved via the introduction of a specific numerical method that is then not easily modified.

Formulas for the total energy of course include the nuclear–nuclear repulsion, which during the computation must be offset by half the electron–nuclear attraction energy to reach a finite, convergent result. This, in turn, means that the formalism for the nuclear–nuclear term must be developed in a way consistent with that for the other energy contributions so that a proper divergence cancelation is achieved. This problem was addressed for spherically symmetric orbitals by Flamant [3], and the present communication extends the analysis to orbitals of general symmetry. Because our results are expressed in terms of the first-order density matrix, they can be further extended without essential modification to more general GTO-based calculations that include electron correlation.

2 Total energy—basic formulas

We assume that the Hartree-Fock orbitals of our problem have already been determined, based on a Fock matrix $F_{ab}(k)$ whose subscripts a and b label Bloch states built from basis GTO's and whose argument k is a Bloch-wave vector in units such that the Brillouin zone is of unit length. Our methods for the calculation of $F_{ab}(k)$ and related quantities were reported in detail in our previous work [10].

Included in $F_{ab}(k)$ are Coulomb and exchange electron–electron terms, as well as k-dependent electron–nuclear and kinetic-energy matrices $V_{ab}(k)$ and $T_{ab}(k)$. We also note that $F_{ab}(k)$, $V_{ab}(k)$, and $T_{ab}(k)$ are scaled such that the corresponding overlap matrix element has the value $S_{ab}(k)$. All these k-dependent quantities are assumed known.

From the occupied Hartree-Fock orbitals, we can obtain the first-order density matrix $P_{ab}(k)$, and the total energy (per unit cell) then takes the form

$$E_T = \frac{1}{2}\int_{-1/2}^{1/2} \mathrm{d}k \sum_{ab} P_{ba}(k) \times \left[F_{ab}(k) + T_{ab}(k) + V_{ab}(k) + n_e^{-1} S_{ab}(k) U\right], \quad (1)$$

where U is twice the nuclear–nuclear repulsion energy:

$$U = \frac{1}{a_0}\sum_{AB} Q_A Q_B u(\mathbf{B} - \mathbf{A}), \quad (2)$$

$$u(\mathbf{R}) = \sum_{v=-\infty}^{\infty}{}' \frac{1}{|\mathbf{R} + v\hat{\mathbf{z}}|}. \quad (3)$$

Here, n_e is the number of electrons per unit cell, and Q_A and Q_B are nuclear charges at respective points $\mathbf{A}$ and $\mathbf{B}$ in the unit cell, with positions expressed as fractions of the cell dimension, which is a_0. The unit vector $\hat{\mathbf{z}}$ is in the direction of periodicity, and the prime on the v summation indicates that the term $v = 0$ is to be omitted if $A = B$. The factor $n_e^{-1} S_{ab}(k)$ in Eq. (1) simply causes the summation and integration of the U term of Eq. (1) to reduce to U. The present placement of U facilitates the combined treatment of $V_{ab}(k) + n_e^{-1} S_{ab}(k)\, U$.

The quantities $V_{ab}(k)$ and U are formally divergent, but when $V_{ab}(k)$ is used in $F_{ab}(k)$, the divergence cancels against a similar singularity in the electron–electron interaction. When both these kinds of contributions are treated by an Ewald procedure, the divergent contributions combine to give a finite (but nonzero) result. In Eq. (1) here, we can use for $V_{ab}(k)$ the same Ewald formulation as was used in our previous work, but will need to use a compatible Ewald formula for U and consider the limiting behavior of $V_{ab}(k) + n_e^{-1} S_{ab}(k)\, U$. Since the only divergence in the Ewald formulas is at the origin point of the Fourier-space sums, we may evaluate all the terms of $V_{ab}(k)$ and the decomposition of U individually except for the single divergent term of each and then for the divergent terms take the limit of their sum.

3 Nuclear–nuclear term

A rather direct way of obtaining the Ewald decomposition of the nuclear–nuclear lattice sum uses the error function, defined as

$$\mathrm{erf}(x) = \frac{2}{\pi^{1/2}}\int_0^x e^{-t^2}\mathrm{d}t, \quad (4)$$

and its complement $\mathrm{erfc}(x)$, defined as $1 - \mathrm{erf}(x)$. At $x = 0$, $\mathrm{erf}(x) = 0$ and $\mathrm{erfc}(x) = 1$, while at $x = \infty$, $\mathrm{erf}(x) = 1$ and $\mathrm{erfc}(x) = 0$. Thus, these functions partition unity in a way dependent on the value of x. We use these properties by writing

$$u(\mathbf{R}) = \sum_{v=-\infty}^{\infty}{}' \frac{\mathrm{erf}\left(\frac{|\mathbf{R}+v\hat{\mathbf{z}}|}{\tau^{1/2}}\right) + \mathrm{erfc}\left(\frac{|\mathbf{R}+v\hat{\mathbf{z}}|}{\tau^{1/2}}\right)}{|\mathbf{R} + v\hat{\mathbf{z}}|}. \quad (5)$$

Here, τ is a separation constant (not necessarily equal to those used for V_{ab} or the electron–electron terms). Larger values of τ make the erfc term of the partitioning (the direct-space contribution) more important. Smaller values of τ cause emphasis on the erf term, which will be transformed into Fourier space.

The erf term of Eq. (5) is now subjected to a Poisson transformation, adding a contribution from $v = 0$ if it was missing and then subtracting it again external to the transformation. Before the Poisson transformation, this term, which we call $u_{\mathrm{FS}}(\mathbf{R})$, can be written as an integral:

$$u_{\mathrm{FS}}(\mathbf{R}) = \frac{2}{(\pi\tau)^{1/2}}\left[\sum_{v=-\infty}^{\infty}\int_0^1 e^{-|\mathbf{R}+v\hat{\mathbf{z}}|^2 t^2/\tau}\mathrm{d}t - \delta_{\mathbf{R},0}\right]. \quad (6)$$

After the transformation, u_{FS} becomes (temporarily disregarding problems associated with the singularity at $\mu = 0$)

$$u_{\mathrm{FS}}(\mathbf{R}) = \sum_{\mu=-\infty}^{\infty} e^{2\pi i\mu R_z} K_0(\pi^2\tau\mu^2, |\mathbf{R}_0|^2/\tau) - \frac{2\delta_{\mathbf{R},0}}{(\pi\tau)^{1/2}}. \quad (7)$$

In the right-hand side of Eq. (7) appear the component of $\mathbf{R}$ in the direction of periodicity, denoted R_z, and the two-dimensional remainder of $\mathbf{R}$ perpendicular to that direction, denoted $\mathbf{R}_0$. Reaching Eq. (7) requires a number of steps, but they are similar to those used for V_{ab} and other lattice sums in Ref. [10]. The function K_0 is an incomplete Bessel function that always occurs when a lattice of GTO's is subjected to a Poisson transformation, with integral representation

$$K_0(x, y) = \int_1^{\infty} e^{-xt-y/t}\mathrm{d}t. \quad (8)$$

A detailed account of this function was recently published by one of the present authors [12], and methods for its numerical evaluation were reviewed by both of us [13].

Turning now to the term of u_{FS} with $\mu = 0$, which we denote χ_{nn}, we identify its limiting behavior as $\mu \to 0$, first for the case $\mathbf{R}_0 \neq 0$. Using Eq. (C12) of Ref. [10], we find

$$\chi_{nn} = -2\ln\mu - \ln(\pi^2|\mathbf{R}_0|^2) - 2\gamma_{\mathrm{E}} - E_1(|\mathbf{R}_0|^2/\tau). \quad (9)$$

Here, γ_{E} is the Euler-Mascheroni constant, and E_1 is an exponential integral [14]. The quantity χ_{nn} contains the only singular contribution to U; it diverges logarithmically as $\mu \to 0$.

Summarizing and simplifying,

$$U = \frac{1}{a_0}\sum_{AB} Q_A Q_B \times \left[\sum_{\mu\neq 0} e^{2\pi i\mu(B_z-A_z)} K_0(\pi^2\tau\mu^2, |\mathbf{B}_0-\mathbf{A}_0|^2/\tau) + \chi_{\text{nn}} + {\sum_{v=-\infty}^{\infty}}' \frac{\operatorname{erfc}(\tau^{-1/2}|\mathbf{B}-\mathbf{A}+v\hat{\mathbf{z}}|)}{|\mathbf{B}-\mathbf{A}+v\hat{\mathbf{z}}|} - \frac{2\delta_{AB}}{(\pi\tau)^{1/2}}\right] \tag{10}$$

4 Singularity cancellation

To see how the singularities cancel, we first note that the only singular term of $V_{ab}(k)$ (from Ref. [10]) arises from the $\mu = 0$ limit of its term with all the quantum numbers $n = l = m = 0$. Thus, we write

$$V_{ab}(k) = V_{ab}(k)|_{\text{nonsing}} - \frac{S_{ab}(k)}{a_0}\sum_{A} Q_A \chi_{\text{ne}}(A), \tag{11}$$

where

$$\chi_{\text{ne}}(A) = \lim_{\mu=0} K_0\left(\pi^2(\eta_{ab}+\tau_{\text{ne}})\mu^2, \frac{|\mathbf{P}_0-\mathbf{A}_0|^2}{\eta_{ab}+\tau_{\text{ne}}}\right). \tag{12}$$

Here, τ_{ne} is the separation constant for $V_{ab}(k)$, $\eta_{ab} = 1/(\alpha_a + \alpha_b)$, where α_a and α_b are GTO screening parameters, and $\mathbf{P}_0$ is the component perpendicular to $\hat{\mathbf{z}}$ of the centroid of the GTO product *ab*, as given in Eq. (7) of Ref. [10]. Note that χ_{ne} also depends upon the orbitals *a* and *b*; the notation for χ becomes too cumbersome if that dependence is shown explicitly.

Evaluating the limit in Eq. (12), we find

$$\chi_{\text{ne}}(A) = -2\ln\mu - \ln(\pi^2|\mathbf{P}_0-\mathbf{A}_0|^2) - 2\gamma_{\text{E}} - E_1\left(\frac{|\mathbf{P}_0-\mathbf{A}_0|^2}{\eta_{ab}+\tau_{\text{ne}}}\right). \tag{13}$$

The χ_{ne} exhibit a logarithmic divergence as $\mu \to 0$ that must cancel against the similar divergence in χ_{nn}.

Combining all the χ terms, and inserting for those coming from $V_{ab}(k)$ the quantity $n_e^{-1}\sum_B Q_B$ (which is unity), the singularities and several finite contributions cancel, and we have

$$\begin{aligned}\left[V_{ab}(k) + n_e^{-1}S_{ab}(k)U\right]_{\text{sing}} &= \frac{S_{ab}(k)}{a_0 n_e}\sum_{AB} Q_A Q_B[\chi_{\text{nn}} - \chi_{\text{ne}}(A)] \\ &= \frac{S_{ab}(k)}{a_0 n_e}\sum_{AB} Q_A Q_B\left[\ln\left(\frac{|\mathbf{P}_0-\mathbf{A}_0|^2}{|\mathbf{B}_0-\mathbf{A}_0|^2}\right) + E_1\left(\frac{|\mathbf{P}_0-\mathbf{A}_0|^2}{\eta_{ab}+\tau_{\text{ne}}}\right) - E_1\left(\frac{|\mathbf{B}_0-\mathbf{A}_0|^2}{\tau}\right)\right].\end{aligned} \tag{14}$$

Equation (14) requires further manipulation if any of the quantities $\mathbf{B}_0{-}\mathbf{A}_0$ or $\mathbf{P}_0{-}\mathbf{A}_0$ vanish. In any such case, we must replace the exponential integral by its small-argument limit, which then causes cancellation of the corresponding logarithm. The substitution involved corresponds to

$$E_1\left(\frac{|\mathbf{R}|^2}{\tau}\right) \longrightarrow -\gamma_{\text{E}} + \ln\tau - \ln|\mathbf{R}|^2, \tag{15}$$

and has the result that if the entire system is linear, Eq. (14) reduces to

$$\left[V_{ab}(k) + n_e^{-1}S_{ab}(k)U\right]_{\text{sing}} = \frac{n_e S_{ab}(k)}{a_0}\ln\left(\frac{\eta_{ab}+\tau_{\text{ne}}}{\tau}\right). \tag{16}$$

5 Convergence rates

The ultimate rate of convergence of the μ and v summations in Eq. (10) is determined by the asymptotic behavior of the functions erfc(x) and $K_0(x, y)$, and in particular, the dominant contributions thereto at large x, which are exponentially decaying:

$$\operatorname{erfc}(x) \sim e^{-x^2}f(x), \qquad K_0(x,y) \sim e^{-x-y}f(x,y); \tag{17}$$

$f(x)$ and $f(x, y)$ are not important for the ultimate convergence rate. From Eq. (17), we see that when $\tau \neq 0$, both the summations converge at a quadratically exponential rate, with their relative rates dominated (for μ) by the decay of $\exp(-\pi^2\tau\mu^2)$ and (for v) by the decay of $\exp(-\tau^{-1}v^2)$. Both these forms are in contrast to the slow and conditional convergence obtained when terms of $1/\mu$ dependence (but opposing signs) are summed.

The above analysis is consistent with our original objective in partitioning the energy contributions: larger τ enhances the convergence rate of the Fourier-space sum (that containing K_0) while diminishing its importance to the overall result. Smaller τ enhances the convergence rate of the direct-space sum (that containing erfc) while moving energetic contributions to the Fourier representation.

The optimum overall summation extent (in the limit of high accuracy) may now be obtained by requiring that both summations converge at the same ultimate rate; this objective is achieved by setting their exponential rates equal when $\mu = v$, yielding

$$\pi^2\tau = \tau^{-1}, \tag{18}$$

with solution $\tau = 1/\pi \approx 0.32$.

A similar analysis can be applied to the partitioning of the energetic contributions of V_{ab}. As indicated in Ref. [10], the condition for equal direct- and Fourier-space ultimate convergence rates reduces to

$$\pi^2(\eta_{ab}+\tau_{\text{ne}}) = \frac{1}{\eta_{ab}+\tau_{\text{ne}}}, \tag{19}$$

with solution $\tau_{\text{ne}} = \pi^{-1} - \eta_{ab}$. This result is meaningful only if $0 < \eta_{ab} < \pi^{-1}$. If this condition is not met, the optimum value of τ_{ne} is zero, corresponding to computation entirely in Fourier space.

We close this section with two observations. First, the number of summation terms is only a partial criterion for maximizing computational efficiency. The relative effort of evaluating individual terms of the two summations is also relevant; current evaluation methods are faster for a direct-space term than for a Fourier-space term, indicating that Eqs. (18) and (19) are only starting points for highly tuned evaluations.

Second, the ultimate convergence rate may not be relevant if the accuracy we seek causes summation terms to be deemed negligible before the limiting behavior is reached. We observe this phenomenon in the examples to follow.

6 Numerical tests

In order to demonstrate the correctness and the convergence of this formulation, we now present illustrative computations of that portion of the total energy that includes the nuclear–nuclear repulsion and the offsetting electron–nuclear attraction. This contribution to the total energy arises from the last two terms within the square brackets of Eq. (1) and contains the singular terms that must cancel; we denote it E_{ne} and observe that it has the form

$$E_{\mathrm{ne}} = \frac{1}{2}\int_{-1/2}^{1/2} dk \sum_{ab} P_{ba}(k)\left[V_{ab}(k) + n_e^{-1} S_{ab}(k) U\right]. \qquad (20)$$

Our test system consists of a linear chain of H_2 molecules, with a single $1s$ Gaussian orbital, of functional form $\exp(-\alpha r^2)$, on each atom. We used two geometries, with the first, designated $H_{2\|}$, consisting of molecules that are aligned on the z-axis (the direction of translational periodicity). The second geometry, designated $H_{2\perp}$, consists of molecules whose orientation is perpendicular to the z-axis. All computations were made for a unit cell of length $a_0 = 3.0$ bohr and containing one H_2 molecule with its internuclear distance fixed at 1.42 bohr. For computational simplicity, we used a density matrix with diagonal elements $P_{pp} = S_{pp}^{-1}$ ($p = a$ and b) and with off-diagonal elements set to zero.

In the case $H_{2\|}$, the vectors $\mathbf{R}_0$, $\mathbf{A}_0$, and $\mathbf{P}_0$ (which describe "projections" perpendicular to the direction of periodicity) vanish for all choices of orbitals and nuclei. This causes all the incomplete Bessel functions appearing in the computations to reduce to exponential integrals, with all the singular terms collapsing to the form given in Eq. (16) of the present communication. A more comprehensive test is provided by the case $H_{2\perp}$, because the projection vectors do not vanish for $a \neq b$ and $A \neq B$, thereby providing a test for the general case of Eq. (14).

The first test we applied was to verify that our formulas for E_{ne} can give the same results as conventional "direct-space" (DS) computations. Fixing the separation constant τ at the near-optimum value 0.3 and setting τ_{ne} also to 0.3 (a value that will sometimes be far from optimal), we computed E_{ne} for several values of the GTO exponent α, both by the method of the present communication and by a conventional DS formula. The results are shown in Table 1. Because of the wide range of the α values and the non-optimal choice of τ_{ne} some of the summations needed for Table 1 converged extremely slowly. We arranged to keep up to 1001 terms in the lattice summations, achieving adequate convergence for all the table entries except for the DS sums at $\alpha = 0.1$. It is clear that the present and conventional methods are in agreement.

We next considered issues related to the rate of convergence of E_{ne}, restricting attention to the single GTO exponent $\alpha = 0.5$ bohr^{-2}. We carried out two sets of computations; in the first set, summarized in Table 2, we kept the electron–nuclear partitioning constant τ_{ne} at 0.3 and varied the nuclear–nuclear constant τ over a wide range of values. The table reports the overall value of E_{ne}, which should be (and is) independent of the value of τ, and also indicates the numbers of terms N larger in absolute value than 10^{-8} in the direct-space (DS) and Fourier-space (FS) series for U appearing in Eq. (10). The N values are expressed as ranges when they differ significantly for different atom pairs. As expected, an increase in τ increases the importance of the direct-space summation of U and reduces its convergence rate; the opposite trends are noted for for the Fourier-space summation of U.

The table also includes the total number of significant terms, $N_{\mathrm{DS}} + N_{\mathrm{FS}}$; we see that it is a minimum in a broad

Table 1 Energies E_{ne}, hartrees: this work ($\tau = \tau_{\mathrm{ne}} = 0.3$) and by conventional direct-space computation (DS), for various GTO exponents α

	α bohr^{-2}	E_{ne} (this work)	E_{ne} (DS)
$H_{2\|}$	0.1	−0.003 139	−0.003 141
	0.5	−1.080 911	−1.080 911
	1.0	−1.591 596	−1.591 596
	10.0	−5.046 265	−5.046 265
	100.0	−15.957 691	−15.957 691
$H_{2\perp}$	0.1	−0.194 889	−0.194 890
	0.5	−1.104 350	−1.104 350
	1.0	−1.592 786	−1.592 786
	10.0	−5.046 265	−5.046 265
	100.0	−15.957 691	−15.957 691

Table 2 Electrostatic energy E_{ne} (hartrees) and the numbers of significant terms in the direct-space and Fourier-space series of Eq. (10) as a function of the separation constant τ

	τ	E_{ne}	N_{DS}	N_{FS}	$N_{DS} + N_{FS}$
$H_{2\parallel}$	0.001	−1.080 911	1	79	80
	0.01	−1.080 911	1	25	26
	0.1	−1.080 911	3	7	10
	0.3	−1.080 911	5	5	10
	1.0	−1.080 911	7–9	3	10–12
	10.0	−1.080 911	25	1	26
	100.0	−1.080 911	73	1	74
$H_{2\perp}$	0.001	−1.104 350	1	13–79	14–80
	0.01	−1.104 350	1	13–25	14–26
	0.1	−1.104 350	3	7	10
	0.3	−1.104 350	5	5	10
	1.0	−1.104 350	7	3	10
	10.0	−1.104 350	25	1	26
	100.0	−1.104 350	73	1	74

region centered about the theoretical value, 0.32. Finally, we note that N_{FS} has a wide range of values for $H_{2\perp}$ at small τ. This behavior is caused by a combination of extremely slow convergence and the fact that when $A \neq B$, the large nonzero value of the second argument of the Bessel function K_0, namely $|\mathbf{B}_0 - \mathbf{A}_0|^2/\tau$, makes all the summation terms smaller, see Eq. (17), and fewer of them remain larger in magnitude than 10^{-8}.

Our second set of test computations was with the nuclear–nuclear separation constant τ set to 0.3, with the nuclear–electron constant τ_{ne} varied. These studies are summarized in Table 3, where we are studying the rates of convergence of the series for V_{ab}, given as Eqs. (53)–(55) of Ref. [10]. Again, we verify that the overall value of E_{ne} is independent of the separation constants. We also see, as expected, that the number of significant terms (greater in absolute value than 10^{-8}) in the direct-space series for V_{ab} increases with τ_{ne}.

If we now look at the total number of significant terms in the V_{ab} expansions, we see that they do not indicate a minimum at any intermediate value of τ_{ne}. Because of the presence of the quantity η_{ab}, which in this case is $1/2\alpha = 1$, Eq. (19) does not predict an optimum positive value of τ_{ne}, and the best choice for this parameter is predicted to be zero. The data in Table 3 are consistent with this prediction: The table shows the total number of terms, $N_{DS} + N_{FS}$, to be a minimum at $\tau = 0$, indicating that the optimum partitioning of V_{ab} is entirely to Fourier space.

The data in Table 3 do not show the wild variation in N_{FS} that was exhibited by the expansion of U for $H_{2\perp}$. The difference in behavior is due to the fact that for V_{ab} the second argument of K_0 depends upon $(\eta_{ab} + \tau_{ne})^{-1}$, and not on τ^{-1} as in the nuclear–nuclear contribution.

Table 3 Electrostatic energy E_{ne} (hartrees) and the numbers of significant terms in the direct-space and Fourier-space series appearing in Eqs. (53)–(55) of Ref. [10] as a function of the separation constant τ_{ne}

	τ_{ne}	E_{ne}	N_{DS}	N_{FS}	$N_{DS} + N_{FS}$
$H_{2\parallel}$	0.0	−1.080 911	0	7	7
	0.1	−1.080 911	5–7	5	10–12
	0.3	−1.080 911	7–9	3	10–12
	1.0	−1.080 911	11–13	3	14–16
	2.0	−1.080 911	13–15	1	14–16
	10.0	−1.080 911	25–27	1	26–28
	100.0	−1.080 911	73–75	1	74–76
$H_{2\perp}$	0.0	−1.104 350	0	7	7
	0.1	−1.104 350	7	5	12
	0.3	−1.104 350	7–9	3	10–12
	1.0	−1.104 350	11	3	14
	2.0	−1.104 350	15	1	16
	10.0	−1.104 350	27	1	28
	100.0	−1.104 350	75	1	76

7 Conclusions

This paper completes the work presented in Ref. [10] by showing how the Ewald technique can be applied to compute the Hartree-Fock total energy for infinite systems of one-dimensional periodicity in a basis of Gaussian-type orbitals. A key aspect of the present contribution is the method for combining correctly the singularities appearing in the nuclear–nuclear and nuclear–electron interaction terms. These singularities are a manifestation of the fact that these two terms diverge if treated separately. The correctness and adequacy of the approach are validated by the presentation of sample computations.

Acknowledgments FEH was supported by US National Science Foundation Grant PHY-0601758. JGF is grateful to Professors J. M. André and B. Champagne for their support. JGF thanks the FNRS for financial support making possible his visits to QTP at the University of Florida during these last years. We thank Professor Joseph Delhalle for his continuing interest in this work and for many fruitful discussions. Part of this research has been funded by BELSPO (IAP P6/27 network "Functional Supramolecular Systems").

References

1. André JM, Moseley DH, Champagne B, Delhalle J, Fripiat JG, Brédas JL, Vanderveken DJ, Vercauteren DP (1993) Methods and techniques in computational chemistry: METECC-94. In: Clementi E (eds) STEF, Cagliari, pp 423–480
2. Ewald PP (1921) Ann Phys Leipzig 64:253
3. Flamant I (1998) Fourier space restricted Hartree-Fock method for the electronic structure calculation of stereoregular polymers. Ph.D. dissertation, Facultés Universitaires Notre-Dame de la Paix
4. Flamant I, Fripiat JG, Delhalle J, Harris FE (2000) Theor Chem Acc 104:350

5. Ambrosiano J, Greengard L, Rokhlin V (1988) Comput Phys Commun 48:117
6. Lambert CG, Darden TA, Board JA Jr. (1996) J Comput Phys 126:274
7. Strain MC, Scuseria GE, Frisch MJ (1996) Science 271:51
8. Pisani C, Dovesi R, Roetti C, Causà M, Orlando R, Casassa S, Saunders VR (2000) Int J Quantum Chem 77:1032
9. Saunders VR, Freyria-Fava C, Dovesi R, Roetti C (1994) Comput Phys Commun 84:156
10. Fripiat JG, Delhalle J, Flamant I, Harris FE (2010) J Chem Phys 132:044108
11. Terras R (1991) J Comput Phys 39:233
12. Harris FE (2008) J Comput Appl Math 215:260
13. Harris FE, Fripiat JG (2009) Int J Quantum Chem 109:1728
14. Abramowitz, M, Stegun, I (eds) (1964) Handbook of mathematical functions. Dover, New York

Theor Chem Acc (2012) 131:1259
DOI 10.1007/s00214-012-1259-y

REGULAR ARTICLE

Smoothed Gaussian molecular fields: an evaluation of molecular alignment problems

Laurence Leherte · Daniel P. Vercauteren

Received: 29 February 2012 / Accepted: 11 July 2012 / Published online: 28 July 2012

Abstract Several smoothed Gaussian-based descriptors used in a molecular superposition algorithm are presented. One descriptor, as detailed in a previous work (Leherte in J Comput Chem 27:1800–1816, 2006), is the full electron density approximated through the promolecular atomic shell approximation (PASA) (Amat and Carbó-Dorca in J Chem Inf Comput Sci 40:1188–1198, 2000). Herein, we additionally present a new descriptor, that is, the charge density of a molecule calculated via the Poisson equation. The Coulomb potential as approximated by Good et al. (J Chem Inf Comput Sci 32:188–191, 1992) and atom-based functions such as hydrogen bond donor or acceptor properties, lipophilicity as detailed in the work of Totrov (Chem Biol Drug Des 71:15–27, 2008) were also considered. A Monte Carlo/Simulated Annealing superposition method is applied to a set of six families of drug molecules, that is, elastase inhibitors, ligands of endothiapepsins, trypsins, thermolysins, p38 MAP kinases, and rhinovirus, all of them already reported in the literature, for discussing superposition problems. The results show that the descriptor selection can be guided by the nature of the interactions expected to occur between the drug molecules and their receptor. They also emphasize the particular efficiency of the PASA descriptor for molecules characterized by significant shape properties.

Keywords Promolecular electron density distribution · Poisson equation · Coulomb potential · Smoothing · Molecular alignment · Similarity index

1 Introduction

Since at least two decades, the use of Gaussian functions for the evaluation of the molecular similarity has been an attractive strategy as both it allows short calculation times and it is very easy to implement [1]. Indeed, using such functions, similarity measures are directly related to distances between the atoms that constitute the molecular structures to be compared [2, 3]. In molecular modelling, it is indeed common to access the shape of a molecule by fitting spheres at the atom locations, such as the well-known van der Waals (vdW) spheres [4], or by considering Gaussian functions as presented, for example, by Good and Richards [5] and Grant and Pickup [6–8]. In order to consider some hardness of the atoms when bound in a molecule, Good and Richards [5] used atomic electron density (ED) distributions, which are set to zero beyond the vdW radius of the atoms. Grant et al. [6–8] compared the conventional hard sphere representation and a Gaussian-based model and proposed applications in the field of shape comparison using the so-called shape multipoles or moments. Their work led, notably, to the implementation of the program ROCS [9]. Later, applications were reported by Haigh et al. [10] who suggested a transferable and fast shape fingerprint approach based on Grant et al.'s works. Maggiora and coworkers [11] used spherically symmetric Gaussian functions located on selected atoms

---

Published as part of the special collection of articles celebrating theoretical and computational chemistry in Belgium.

Electronic supplementary material The online version of this article (doi:10.1007/s00214-012-1259-y) contains supplementary material, which is available to authorized users.

L. Leherte (✉) · D. P. Vercauteren
Laboratoire de Physico-Chimie Informatique, Unité de Chimie Physique Théorique et Structurale, Facultés Universitaires Notre-Dame de la Paix (FUNDP), Rue de Bruxelles 61, 5000 Namur, Belgium
e-mail: laurence.leherte@fundp.ac.be

and characterized by adjustable magnitudes and widths to modulate the degree of details needed to achieve protein alignments. Within such a representation, each amino acid of a protein is described by a linear combination of a limited number of Gaussians. Their approach was implemented in the program MIMIC [12]. Duncan and Olson [13] also defined molecular surfaces as a sum over atomic Gaussian functions. In their work, emphasis was given on the resolution of these surfaces, which can be modified by convolving the ED distribution function with a Gaussian function of selected variance. On such bases, various applications were proposed in the fields of molecular comparison and molecular complementarity, as well as in visual interpretation of molecular surfaces. Klebe et al. [14] established a mathematical formalism for the evaluation of molecular similarity in three-dimensional (3D) QSAR studies. Similarity was evaluated between a given molecule and a spherical probe and was calculated at each point of a 3D grid as a summation over atomic contributions [14]. More recently, Totrov [15] described a molecule through seven 3D atomic property fields (APFs) calculated from Gaussians functions centred on the constituting atoms. These atomic properties are hydrogen bond donor, hydrogen bond acceptor, sp^2 hybridization, lipophilicity, size, charge, and electronegativity. The author identified 21 atom types and associated them a value for each of those seven properties. Totrov's approach is close to the procedure described by Lemmen et al. [16] in the program FLEXS wherein physicochemical properties such as hydrophobicity, charge, hydrogen bonding are approximated by a set of Gaussian functions centred on atoms or other regions defined by the user. Proschak et al. [17] applied a molecular shape description expressed as a summation over atomic Gaussian functions to define molecular surface elements useful in surface matching calculations and implemented their approach in the program "Shapelets". Chan et al. [18] used Gaussians to define a scoring function for their alignment procedure. The function is calculated as a summation over Gaussian terms depending upon the distances occurring between atoms characterized by a given property (size, hydrophobicity). The authors implemented their scoring function in the program MOE [19].

Superposition of molecules is a problem that involves many local solutions. A way to reduce the number of possible alignments is to lower the resolution of the molecular field under consideration, in order words, to lower the level of details by smoothing the 3D scalar field [11, 13, 20]. This can easily be achieved through a convolution product with a Gaussian function, as proposed by Kostrowicki et al. [21]. Another approach consists in limiting the number of points representing the molecules, such as in the studies of Glick et al. [22, 23], wherein the atoms are clustered based on their separating distances. We also used such an approach by representing molecular systems as graphs of smoothed ED critical points [24, 25].

Following a work we previously achieved on molecular similarity of promolecular ED distribution functions [20], we expand here the concepts presented before through the calculation of charge density (CD) distributions calculated from smoothed electrostatic potential functions via the Poisson equation. The advantage of Gaussian functions in evaluating various similarity measures is again considered to easily calculate integrals such as the overlap and the so-called Laplacian ones at low cost.

In this paper, we treat various molecular similarity problems through the study of six different families of molecules, as already detailed in the literature. The selected families are the TOMI and DFKi elastase ligands [26–29], inhibitors of endothiapepsins [16, 20, 30], trypsins [16, 18, 31, 32], thermolysins [16, 17, 30–32], human rhinovirus HRV14 [16, 18, 32], and of p38 mitogen-activated proteins (MAP) [18, 32].

We first used a promolecular description of the ED distribution function of the various molecules, as reported before [20]. We also apply the formalism obtained for the CD calculated from smoothed electrostatic potential functions through the Poisson equation. Such a CD distribution function was previously considered to design, through its topological properties, reduced point charge models for proteins [33]. This new aspect is considered in comparison with the method described by Good et al. [34] to superpose Coulomb potential functions and implemented by us in combination with a smoothing approach. Finally, we also considered a smoothed version of the APFs developed by Totrov [15].

Flexibility is not considered in the present work as we compare alignments to discuss the efficiency of the various smoothed molecular fields under consideration without the influence of the conformation. As shown by the results, the various molecular fields can provide different results and their efficiency can vary with the nature of the interactions involved between the molecules and their receptor.

In the next section, we briefly recall the mathematical expressions needed to superpose the molecules and to evaluate the corresponding similarity degree. We detail the new expressions related to CD distribution functions and smoothing in general. Thereafter, we present the molecular systems under study and discuss the alignment results. Conclusions and perspectives are provided at the end of the paper.

2 Theoretical background

In this section, it is described how smoothed Gaussian-based scalar fields can be calculated analytically and how similarity measures and indices are evaluated.

2.1 Promolecular electron density distributions

In their work related to the Promolecular Atom Shell Approximation (PASA), Amat and Carbó-Dorca used atomic Gaussian ED functions that were fitted on 6-311G atomic basis set results [35]. In the PASA approach that is considered in the present work, a promolecular ED distribution ρ_A is represented analytically as a weighted summation over the nat atomic ED distributions ρ_a, which are described in terms of series of three squared 1s Gaussian functions fitted from atomic basis set representations [36]:

$$\rho_A = \sum_{a \in A}^{\text{nat}} \rho_a \tag{1}$$

with:

$$\rho_a(\mathbf{r}) = Z_a \sum_{i=1}^{3} w_{a,i} \left[\left(\frac{2\varsigma_{a,i}}{\pi} \right)^{34} \mathrm{e}^{-\varsigma_{a,i}|\mathbf{r}-\mathbf{R}_a|^2} \right]^2 \tag{2}$$

where Z_a, $\mathbf{R}_a$, and $w_{a,i}$ and $\varsigma_{a,i}$, are the atomic number of atom a, its position vector, and the two fitted parameters, respectively.

To generate smoothed 3D ED functions, ρ_A is directly expressed as the solution of the diffusion equation according to the formalism presented by Kostrowicki et al. [21]:

$$\rho_{a,t}(\mathbf{r}) = \sum_{i=1}^{3} s_{a,i} \quad \text{where} \quad s_{a,i} = \alpha_{a,i}\mathrm{e}^{-\beta_{a,i}|\mathbf{r}-\mathbf{R}_a|^2} \tag{3}$$

with:

$$\begin{aligned} \alpha_{a,i} &= Z_a w_{a,i} \left(\frac{2\varsigma_{a,i}}{\pi} \right)^{3/2} \frac{1}{\left(1 + 8\varsigma_{a,i} t\right)^{3/2}} \quad \text{and} \\ \beta_{a,i} &= \frac{2\varsigma_{a,i}}{\left(1 + 8\varsigma_{a,i} t\right)} \end{aligned} \tag{4}$$

where t is the smoothing degree of the ED, unsmoothed EDs being obtained by imposing $t = 0$ bohr^2.

When using the PASA description, only the non-hydrogen atoms of the molecular structures are considered. It is done so to limit the calculation time of the alignment procedures. The advantage of such a descriptor thus relies in the fact that no a priori knowledge of the protonation state of the molecules is required.

2.2 Coulomb potential and charge density distribution functions

The electrostatic potential function generated by a molecule A is approximated by a summation over its atomic contributions using the Coulomb equation:

$$\Phi_A(\mathbf{r}) = \sum_{a \in A}^{\text{nat}} \frac{q_a}{|\mathbf{r} - \mathbf{R}_a|} \tag{5}$$

q_a being the net charge of atom a. A smoothed version of the potential generated by atom a, $\Phi_{a,t}(r)$, can be expressed as [37]:

$$\Phi_{a,t}(r) = \frac{q_a}{r} \operatorname{erf}\left(\frac{r}{2\sqrt{t}} \right) \tag{6}$$

where t is the smoothing parameter and erf stands for the error function. From the potential given in Eq. 6, the corresponding analytical CD function $\rho_{a,t}(r)$ can be obtained from the Poisson equation:

$$-\nabla^2 \Phi_{a,t} = \frac{\rho_{a,t}}{\varepsilon_0} \tag{7}$$

and expressed as:

$$\rho_{a,t}(r) = \frac{q_a}{(4\pi t)^{3/2}} \mathrm{e}^{-r^2/4t} \tag{8}$$

In such a formalism, $\rho_{a,t}(r)$ cannot be calculated at $t = 0$. Indeed, that situation corresponds to the original Coulomb potential for which the solution of the Poisson equation is zero.

2.3 Approximation of the Coulomb potential function

In their paper, Good et al. [34] approximated the r^{-1} term in the Coulomb potential by a sum over three Gaussian functions:

$$\frac{1}{r} = \sum_{i=1}^{3} \lambda_i \mathrm{e}^{-\sigma_i r^2} \tag{9}$$

where the three (λ_i, σ_i) pairs are (0.3001, 0.0499), (0.9716, 0.5026), and (0.1268, 0.0026 Å^{-2}). A visualization of that approximate function clearly shows that the fit of r^{-1} is acceptable only at distances r that are larger than about 1 Å; the asymptotic behaviour of r^{-1} at $r = 0$ is indeed not satisfied.

A smoothed version can be given by relationships similar to Eqs. 3 and 4:

$$\left(\frac{1}{r} \right)_t = \sum_{i=1}^{3} \frac{\lambda_i}{(1 + 8\sigma_i t)^{3/2}} \mathrm{e}^{-\frac{\sigma_i}{(1+8\sigma_i t)} r^2} \tag{10}$$

The discrepancies between the Good and Hodgkin's approximation and the original r^{-1} function are strongly reduced when the smoothing factor t differs from zero. This is particularly due to the fact that the infinite asymptotic behaviour at $r = 0$ of function r^{-1} is not present any longer in Eq. 6.

2.4 Atomic property fields

The different 3D atomic property fields $P_i(r)$ selected by Totrov [15], that is, hydrogen bond donor, hydrogen bond acceptor, sp^2 hybridization, lipophilicity, charge, and electronegativity, are represented through Gaussian functions:

$$P_i(\mathbf{r}) = \sum_{a \in A}^{\text{nat}} \varphi_{i,a} \mathrm{e}^{-\frac{|\mathbf{r}-\mathbf{R}_a|^2}{\lambda^2}} \tag{11}$$

where $\varphi_{i,a}$ stands for the atomic property i associated with atom a (Table 1 of Ref. [15]), and the so-called effective distance parameter λ is set equal to 1.2 Å [15, 16].

Similar to Eq. 10, a smoothed version of Eq. 11 was implemented as follows:

$$P_{i,t}(\mathbf{r}) = \sum_{a \in A}^{\text{nat}} \frac{\phi_{i,a}}{\left(1 + 8\frac{1}{\lambda}t\right)^{3/2}} \mathrm{e}^{-\frac{1/\lambda}{\left(1+8\frac{1}{\lambda}t\right)}|\mathbf{r}-\mathbf{R}_a|^2} \tag{12}$$

When using such a description, most of the hydrogen atoms of the molecular structure are eliminated from the superposition procedure, and only the polar ones, as described by Totrov [15], are kept. In the implementation we set up, a global field descriptor is calculated as a summation over all seven above-mentioned $P_i(r)$ fields.

2.5 Evaluation functions for the alignment of smoothed distribution functions

The selection of a 3D scalar field as a relevant property to determine the similarity degree between two molecules A and B has led to several definitions of similarity measure [2, 38].

The well-known overlap similarity measure is defined by:

$$I_{AB,\text{overlap}} = \int \mathrm{d}\mathbf{r} \rho_{A,t}(\mathbf{r}) \rho_{B,t}(\mathbf{r}) \tag{13}$$

where t is the smoothing degree of the ED.

Another quantity used in our previous work [20] is the so-called Laplacian similarity measure $I_{AB,\text{Laplacian}}$:

$$I_{AB,\text{Laplacian}} = \int \mathrm{d}\mathbf{r} \rho_{A,t}(\mathbf{r}) T \rho_{B,t}(\mathbf{r}) \tag{14}$$

where the operator T is related to the Laplacian operator ∇^2 :

$$\nabla^2 = \frac{\partial^2}{\partial x^2} + \frac{\partial^2}{\partial y^2} + \frac{\partial^2}{\partial z^2} \tag{15}$$

by $T = -\nabla^2/2$. It has been shown that the $I_{AB,\text{Laplacian}}$ similarity measure can be seen as the overlap integral of the gradient of the ED [2, 39]. In the latter reference, the use of the density gradient in quantum similarity measures is thoroughly described and is evaluated versus the overlap similarity measure.

Similarity measures are involved in several well-known similarity index formulae [2, 38, 40] such as the Carbó (also known as Cosine) index:

$$S_{AB,\text{Carbo}} = \frac{I_{AB}}{\sqrt{I_{AA}}\sqrt{I_{BB}}}, \tag{16}$$

the Hodgkin–Richard (also known as Dice) index:

$$S_{AB,\text{Hodgkin}} = \frac{I_{AB}}{\frac{1}{2}(I_{AA} + I_{BB})}, \tag{17}$$

and the 3D shape Tanimoto similarity index:

Table 1 PDB access codes and net charge (in |e$^-$|) of the molecules considered in the present work

	Structure number												
	1	2	3	4	5	6	7	8	9	10	11	12	13
Elastase	1PPF	4EST											
	0	0											
Endothiapepsin	2ER7	4ER1	4ER2	5ER1	5ER2								
	−1	0	−1	−1	0								
Trypsin	1PPH	1TNH	1TNI	1TNJ	1TNK	1TNL	3PTB						
	+1	+1	+1	+1	+1	+1	+1						
Thermolysin	1THL	1TLP	1TMN	2TMN	3TMN	4TLN	4TMN	5TLN	5TMN	6TMN			
	−2	−2	−2	−1	0	0	−2	−1	−2	−2			
P38	1A9U	1BL6	1BL7	1DI9	1M7Q	1OUK	1OUY	1OVE	1OZ1	1W7H	1W84	1WBO	1YQJ
	0	0	+1	0	+1	+1	+1	+1	0	0	0	0	+1
HRV14	2R04	2R06	2R07	2RM2	2RR1	2RS1	2RS3	2RS5					
	0	0	0	0	0	0	0	0					

$$S_{AB,\mathrm{Tanimoto}} = \frac{I_{AB}}{I_{AA} + I_{BB} - I_{AB}} \tag{18}$$

$S_{AB,\mathrm{Tanimoto}}$ was found to be efficient for the superposition of 3D fields, both in the position space [9] and in the momentum space wherein emphasis is given to the long-range variations of the electron density [41]; it is known to be more sensitive to size differences between two structures. It was also found to be efficient in superpositions of endothiapepsin ligands [20].

2.6 Superposition algorithm

Using a Monte Carlo/Simulated Annealing algorithm (MC/SA), rigid pair alignments were achieved at smoothing degrees t varying between 1.7 and 1.4 bohr^2. The two values were selected after the studies presented in [42, 43], which report topological analyses of PASA and Poisson-based CD distribution functions. Best performances of the approach were observed at values of t where the critical points (local maxima and/or minima) of the smoothed 3D fields correspond to known interaction sites of the ligands [25] or to locations of point charges on amino acids [33, 43].

Our superposition algorithm consists of a sequence of MC loops carried out at linearly decreasing acceptance rates. First of all, the structure to be aligned on the reference molecule is translated to locate the two centres of mass at the same position. At each step of a MC loop, the structure to be aligned is displaced by random translation and rotation steps. The maximal translation and rotation displacements were set equal to 0.5 Å and 0.5 rad, respectively. The new alignment is evaluated using S_{AB} and is accepted only if it is probable enough, that is:

$$p = e^{-\beta\left(S_{AB}^{\mathrm{old}} - S_{AB}^{\mathrm{new}}\right)} > \xi \tag{19}$$

where ξ is a random number selected between 0 and 1. The parameter β controls the acceptance rate of the MC loop. Twenty values are regularly selected between 0.001 and 0.1. The best alignment, that is, the alignment with the highest S_{AB} value, obtained at a given value of β, is used as the starting point of the MC loop at the next β value. The number of iterations per MC loop was set equal to 10,000.

Starting with the PASA molecular description, several calculations were achieved at $t = 1.7$ and 1.4 bohr^2. It was also considered to work at a given β value and let t vary from a high to a low smoothing value during the MC/SA procedure. This last option did not bring real improvements versus the first option. Indeed, the MC/SA algorithm is built to maximize the similarity degree S_{AB}. Starting with a highly smoothed ED and going to a less well-smoothed ED leads to values of S_{AB} that tend to decrease for a given alignment. Nevertheless, the simultaneous variation of t and β during the MC/SA procedure appeared to provide rather good results, with a high performance on the alignment convergence. The MC/SA parameters to be considered when using the PASA description were finally set to a simultaneous and linear decrease in t and β from 1.7 to 1.4 bohr^2 and from 0.1 to 0.001, respectively. Even if ED contours obtained at $t = 1.7$ and 1.4 bohr^2 are very similar as depicted for endothiapepsin ligand 4 (Fig. 1), letting t vary during the superposition procedure seems to favour the search for a global solution.

When considering the CD and APF descriptors, it appeared that the calculation of the similarity measures should better involve positive integrals (overlap, Laplacian) only, that is, the superposition of negative distributions onto positive distributions (or inversely) should not participate to the total value of S_{AB}. This is done to avoid unfavourable partial alignments of the molecules. Looking at the CD contours illustrated in Fig. 1 for endothiapepsin ligand 4, one clearly distinguishes a larger positive isocontour 0.0002 e$^-$/bohr^3 corresponding to the positive NH_3^+ end (left side of the structures in Fig. 1), that is spread away from the molecular skeleton versus its PASA counterpart. It is also seen, for example, that aromatic groups (right side of the structures in Fig. 1) tend to be surrounded by positive regions while the inner part of the ring itself leads to a negatively charged area.

When using the smoothed Coulomb potential description, one first wished to emphasize the overlap of the electrostatic potential acting in regions of space remote from the molecular skeleton itself, that is, beyond the so-called solvent accessible surface of the molecule. In that case, one first used the overlap similarity measure with the Hodgkin similarity index as Good et al. [44] reported that this last index is sensitive to the magnitude of the 3D descriptor field. It, however, appeared that the Laplacian–Tanimoto combination was more efficient.

To evaluate the success of the alignments, the coordinates of the non-hydrogen atoms of the aligned molecules were compared to the corresponding coordinates of their expected (crystallographic) position. An rmsd value was calculated to quantify this degree of success.

3 Applications and results

All 3D coordinates of the molecular systems studied in this paper were retrieved from the Protein Data Base (PDB) [45]. Table 1 reports the PDB access codes of the various systems. Based on the atomic hybridization states, H atoms were added to the structures with the program VEGA ZZ [46, 47]. Protonation states were considered as found in the literature. All end NH_2 and COOH groups in peptides were systematically ionized. Charges were added with the same

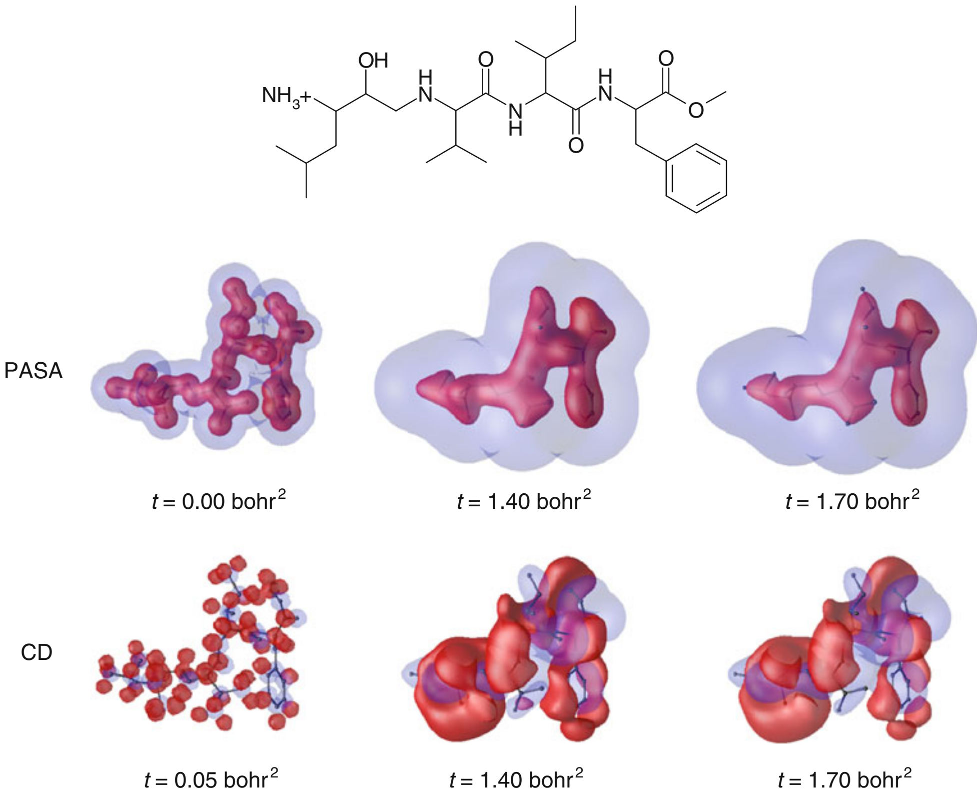

Fig. 1 2D representation and isocontours of the PASA ED (0.0002 in *light blue* and 0.075 e$^-$/bohr^3 in *dark red*) and of the CD (-0.0002 in *light blue* and 0.0002 e$^-$/bohr^3 in *dark red*) of endothiapepsin ligand 4, calculated at various smoothing degrees *t*. The molecular skeleton is displayed using *sticks* (H are not shown for clarity)

program using the Gasteiger–Marsili [48, 49] scheme. 2D representations of all molecular structures studied in this paper are presented in Online Resources 1–6.

Within each family of ligands, all possible pair alignments were carried out, that is, the largest structure on the smallest and inversely. The best solution observed among the two so-obtained was kept.

3.1 Alignment results for the elastase TOMI/DFKi system

The system is particular in that the turkey ovomucoid inhibitor, TOMI (PDB access code 1PPF), is an elastase inhibitor consisting of 56 residues (814 atoms), that is, characterized by a size drastically larger than the difluoroketone inhibitor, DFKi (PDB access code 4EST), with 70 atoms (Online Resource 1). Due to that particularity, it has been the subject of several studies [26–29] regarding their alignment using molecular similarity-based techniques.

The desired alignment of TOMI and DFKi, that is, the expected crystallographic solution, is obtained using the PASA descriptor with the conditions applied throughout this paper, that is, *t* varying from 1.70 to 1.40 bohr^2, and with the Laplacian Tanimoto similarity measure and index. The corresponding degree of similarity S_{AB} is equal to 0.0697, and the rmsd value of the TOMI structure is 2.26 Å (Fig. 2a). The low value of S_{AB} is due to the size difference in the two structures, leading to similarity measures that differ by an order of magnitude. In the present case, $I_{AA,\mathrm{Laplacian}} = 21.052$, $I_{BB,\mathrm{Laplacian}} = 1.966$, and $I_{AB,\mathrm{Laplacian}} = 1.450$, at $t = 1.4$ bohr^2. The use of the Laplacian similarity measure allows to emphasize the importance of the shape of the molecular skeletons. Another similarity measure choice, like “overlap”, will force the overlap between the drug DFKi and the helix of TOMI, that is, a high-density region (Fig. 2b).

All other descriptors did not provide the right alignment under the calculation conditions used in the present work. This suggests that the molecular shape is the main information required to align the molecules.

3.2 Alignment results for the endothiapepsin ligands

Endothiapepsin is a single-chain proteinase of 330 amino acids. The structure is largely of *β*-sheet type and consists of two related lobes of approximately 170 amino acids each. The active site resides in a pronounced cleft between the lobes. Inhibitors have been shown, by X-ray crystallography, to bind in the active site cleft in extended conformations. A detailed comparison of the X-ray structures of 21 inhibitor complexes is given by Bailey and Cooper [50]. The hydrogen bonds that position the inhibitor main chain in the active site cleft are largely conserved from one

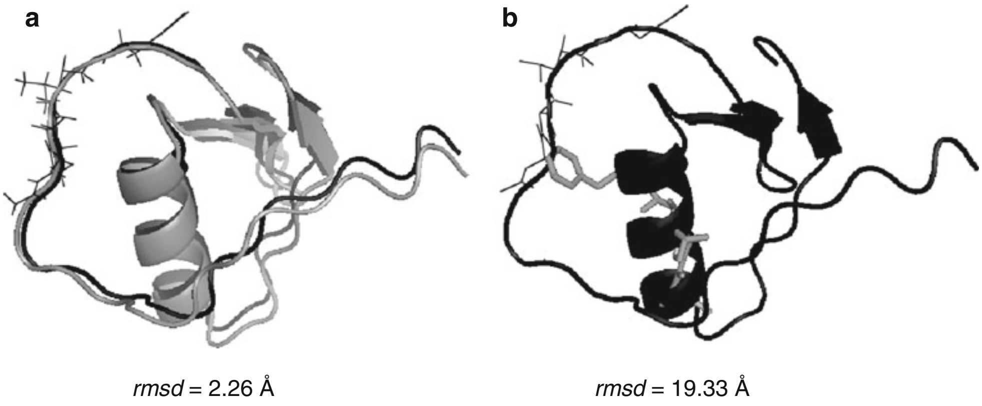

Fig. 2 **a** Superimposition of the crystallographic structure of TOMI (*black ribbon*), DFKi (*black wire*), and the MC/SA orientation of TOMI versus DFKi (*grey*) obtained with the PASA descriptor smoothed at *t* varying between 1.7 and 1.4 bohr^2 using **a** the Laplacian similarity measure and **b** the overlap similarity measure (H are not shown for clarity)

inhibitor to another, implying that the largest determinants of specificity are the vdW contacts between the enzyme and the ligand side chains. Side chains of the inhibitors can adopt different conformations to compensate for greater or lesser occupation of the neighbouring residues.

The five ligands considered in this work were selected following the work of Lemmen et al. [16] (Online Resource 2). For convenience, the five molecules will be numbered 1–5 further in the text (Table 1).

Alignments achieved using the PASA descriptor together with the Laplacian and Tanimoto similarity evaluators showed that the only problematic case occurred when one superposed ligands 2 and 4 (Table 2). Indeed, the obtained similarity degree S_{AB}, 34 %, is higher than the S_{AB} degree calculated for molecules in the experimental orientation, $S_{AB} = 22$ % at $t = 1.40$ bohr^2, where a partial overlap is observed. With the CD descriptor, this problem is cancelled since $S_{AB\ \mathrm{expected}}$, 25 %, is larger than $S_{AB\ \mathrm{full\ overlap}}$, 17 %, and a good alignment is obtained between the two ligands 2 and 4 (Table 2). With the CD descriptor, a misalignment remains between ligands 2 and 5. A deeper insight showed that this is due to non-convergence of the algorithm, with $S_{AB\ \mathrm{expected}} = 23$ % at $t = 1.40$ bohr^2, rather than 20 %, as shown in Table 2. Thus, with PASA, only 9 alignments over 10 are successful while one can expect a 100 % success when using the CD descriptor. Lemmen et al. [16] obtained a success rate of 70 %. Besides the use of the PASA and CD distributions functions, the Coulomb potential descriptor did not provide satisfactory alignment results (Table 2). Indeed, only one superposition is characterized by a rmsd value <2 Å, and rmsd values beyond 20 Å suggest that some superposition results completely diverge from the expected ones. The APF descriptor is efficient, except for all alignments that involve ligand 2 (Table 2). This is due to the absence of a negatively charged carboxylate group. Indeed, when present, the two negative oxygen of the carboxylate bear a highly negative charge descriptor value $\varphi_{i,a}$ of −1.5 as well as a highly positive hydrogen bond value, 1.5, in the framework of the APF representation. It is then possible to slightly improve the efficiency of the APF-based alignments, with a success rate of 8 over 10 alignments, by working with the size component of the APF representation only (Table 2).

Thus, one concludes that the orientation of the drug molecules in the binding pocket of the receptor is mainly governed by their shape, a property that is often related to vdW contacts discussed above.

3.3 Alignment results for the trypsin ligands

Trypsins belong to the family of serine proteases and are constituted by about 245 amino acid residues. Their active site contains a serine residue, located at the junction of two β-barrel domains. The seven ligands (Table 1) considered in this work were taken from the work of Chan et al. [18]. Except for the largest ligand, 1PPH, all of them present a rather similar structure (Online Resource 3) that consists in an aromatic group and a positively charged amine group separated by aliphatic linkers of different lengths. All molecules thus bear a net +1 charge. Ligand 1TNI (ligand 3), with a longer linker, assumes a binding mode that is slightly different from the other molecules. The positively substituted phenyl moiety of the larger molecule (ligand 1) is oriented in a similar manner as benzamidine (ligand 7) and faces the negatively charged carboxylate group of residue Asp189 of trypsin while also interacting through hydrogen bonds [51].

None of the alignments involving the largest structure (ligand 1), achieved using either the PASA or the CD descriptor, provided satisfactory results (Online Resources 7 and 8). Indeed, all rmsd values are larger than 5 Å. In such cases, the positively charged N atom of the small ligands is aligned with the SO_2 group of ligand 1 (Fig. 3). This leads to a higher similarity measure due to the larger density distribution of the sulphonate group of ligand 1. With the CD descriptor, two positive regions appear at the level of the $C(NH_2)_2^+$ and SO_2 groups of atoms and

Table 2 Best pair alignment results, in terms of S_{AB} values (%), obtained using the Laplacian Tanimoto MC/SA procedure with various descriptors smoothed at t varying between 1.7 and 1.4 bohr^2 for the five endothiapepsin ligands

	1	2	3	4
PASA				
1	–			
2	35 (0.81)	–		
3	34 (0.16)	40 (0.42)	–	
4	27 (0.72)	**34 (11.14)** $S_{AB\ \mathrm{expected}} = 22$	32 (1.42)	–
5	51 (0.47)	49 (0.52)	48 (0.45)	**36 (0.44)**
CD				
1	–			
2	22 (0.73)	–		
3	**31 (1.19)**	29 (0.28)	–	
4	24 (0.93)	**25 (1.65)** $S_{AB\ \mathrm{full\ overlap}} = 17$	25 (0.96)	–
5	41 (0.54)	**20 (8.67)** $S_{AB\ \mathrm{expected}} = 23$	45 (0.60)	28 (0.80)
Coulomb electrostatic potential				
1	–			
2	8 (10.58)	–		
3	**90 (1.62)**	8 (12.24)	–	
4	1 (41.31)	4 (8.79)	1 (40.00)	–
5	40 (21.00)	10 (8.40)	39 (2.32)	38 (17.64)
APF				
1	–			
2	17 (0.33)	–		
3	60 (0.87)	28 (11.61)	–	
4	**25 (1.24)**	35 (8.92)	31 (1.30)	–
5	60 (0.77)	21 (8.27)	67 (0.61)	27 (0.93)
Size component of the APF				
1	–			
2	36 (0.55)	–		
3	45 (0.37)	44 (0.67)	–	
4	32 (0.74)	30 (9.90)	38 (1.89)	–
5	36 (0.40)	**23 (0.76)**	31 (0.74)	51 (15.99)

The reference molecules are mentioned in the first row; otherwise, results are shown in bold. rmsd values (Å) of the aligned molecules are given in parentheses

misalignments are also observed (Fig. 3). Therefore, the only way to superpose the ligands is to consider a descriptor that involves information well beyond the molecular skeleton, that is, the Coulomb electrostatic potential, or to consider other properties as those in the APF formalism. Figure 3 illustrates that with the Coulomb potential descriptor, there is only one main positive region located around the amidino groups of ligands 1 and 7. The expected alignment can thus be obtained for these two compounds (Fig. 3). Indeed, with that last approach, ones notices that all small molecules tend to be superposed on the correct branch of ligand 1. The Coulomb potential alignments are not ideal, that is, rmsd can be larger than 2 Å, except for the alignment of ligands 1 and 7, with rmsd = 0.36 Å (Online Resource 9). Besides that, the alignment of the small structures versus another did not show significant improvements versus the PASA and CD descriptors. Finally, if one accepts the alignments characterized by rmsd values between 2 and 3 Å, the approach is 100 % successful. In their work, Lemmen et al. [16] also obtained a 100 % success, that is, for each pair of superposed molecules, at least one alignment is correct among the two possible ones. These authors did, however, not consider the largest structure 1PPH in their work. Values

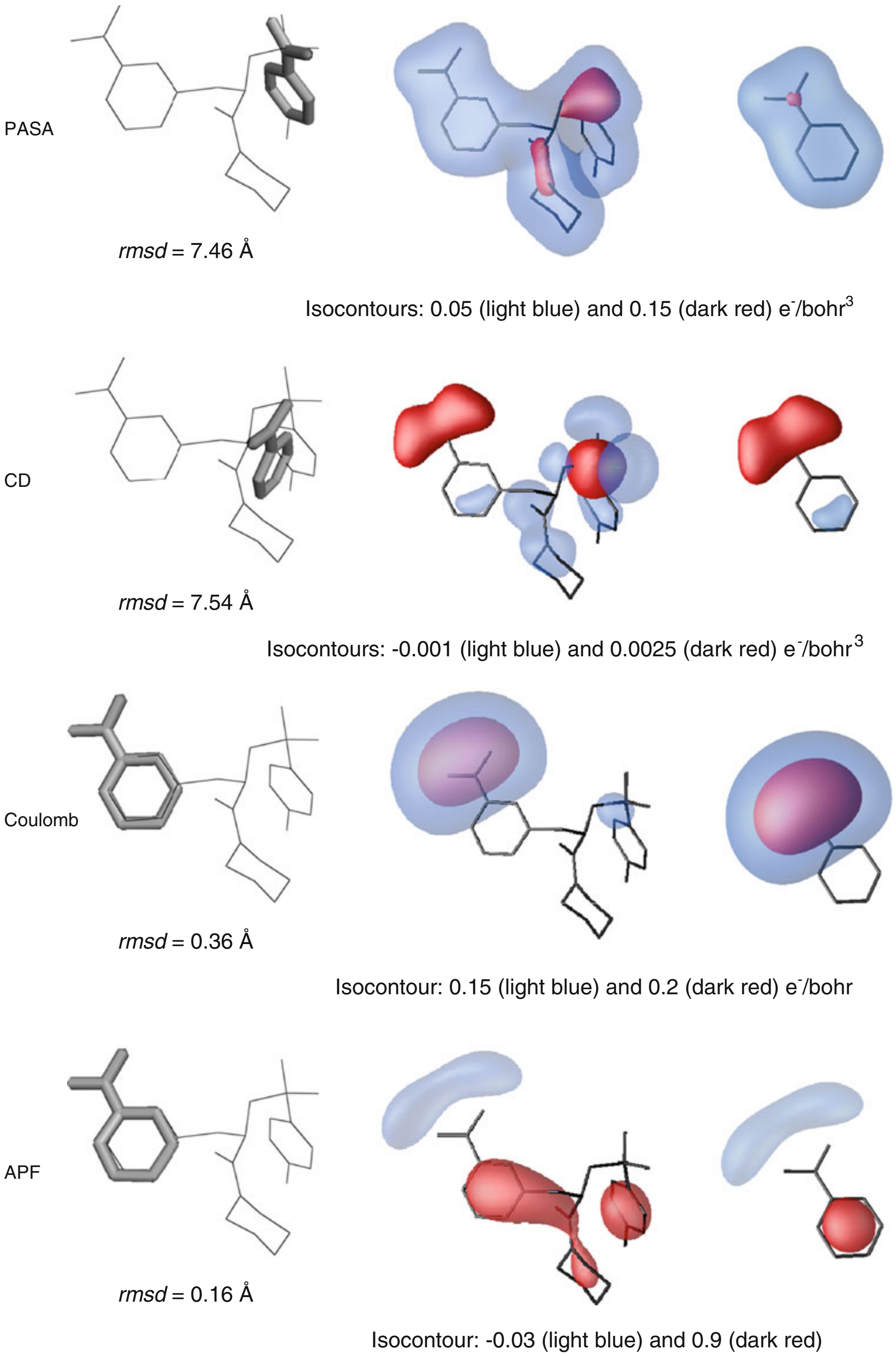

Fig. 3 *Left* Superimpositions of the structures of trypsin ligand 1 (*black wire*) and ligand 7 (*grey stick*) obtained using the MC/SA algorithm with various descriptors smoothed at t varying between 1.7 and 1.4 bohr^2. Isocontours of the PASA ED, CD Coulomb potential, and APF of trypsin ligands 1 (*middle*) and 7 (*right*) calculated at $t = 1.4$ bohr^2. The molecular skeleton is displayed using *sticks* (H are not shown for clarity)

of 80 [18], 73 [32], and 57 % [32] are also reported in the literature. Additional tests carried out using the Coulomb potential descriptor at $t = 1.0$ bohr^2 (Online Resource 9) to determine whether the resolution may lead to lower rmsd values did not show improvements versus the procedure involving a variation of t from 1.70 to 1.40 bohr^2.

The use of the APF descriptor led, as with the Coulomb potential descriptor, to a desired positioning of the aligned ligands (Online Resource 10). The rather high values of rmsd, beyond 2 Å, often characterize shifted molecules, that is, the positive group is well aligned while the aromatic cycle is misaligned as shown for ligands 3 and 7 (Fig. 4). This happens for six alignments, marked "shifted" in Online Resource 10. The alignment of ligands 1 and 6 is characterized by a wrong inversed orientation, with rmsd = 2.21 Å only, and $S_{AB} = 14\ \%$. A good alignment could be expected at the same similarity degree, that is, $S_{AB} = 14\ \%$. An additional run was achieved at $t = 0.50$ bohr^2, which tends to show that these shifted positions are not due to the smoothing of the APF field (Online Resource 10). Indeed, nine pairs are misaligned, one inversed orientation is obtained, as well as a completely wrong result for ligands 2 and 7 with rmsd = 5.40 Å.

Superposing the trypsin ligands thus requires a descriptor that is able to differentiate high-density regions of different chemical natures and electric charges by taking into consideration descriptor distributions spread around the molecular skeleton like the Coulomb potential.

3.4 Alignment results for the thermolysin ligands

Thermolysin, a calcium-binding zinc endopeptidase consisting of 316 amino acid residues, involves a pronounced active site cleft formed at the junction of the two lobes characterizing its structure. Ten thermolysin ligands were considered in the present study (Table 1). Two structures, 2TMN and 4TLN, examined by Lemmen et al. [16], were added to the set of eight ligands studied by Chan et al. [18]. Among these ten ligands, 5TMN and 6TMN differ by a small moiety, as shown in Online Resource 4, that is, an O atom replacing a NH group. When bound in the receptor, the molecules are linked to a Zn cation. More precisely, inhibitors 4TLN and 5TLN bind to the receptor with their hydroxamate group complexed to the Zn, while molecules like 1TLP, 2TMN, 4TMN, 5TMN, and 6TMN are coordinated to the Zn by phosphoryl oxygens. Binding to the receptor also occurs through hydrogen bonds with the NH groups of the molecular skeletons. The ionization state of 4TLN and 5TLN was selected following the work of Matthews and coll. [52, 53] who favoured the anionic form of the NHOH moiety. A positive NH_3^+ group is also assumed in structure 4TLN [53]. The structure of 2TMN involves a protonated N atom located next to P, as described by Matthews and coworkers [53, 54]. Finally, O atoms of the phosphoramidate groups in 1TLP, 4TMN, 5TMN, and 6TMN are charged as represented in the work of Gresh et al. [55].

The use of the PASA descriptor (Online Resource 11) provides an overall success rate, 27 over 45 alignments, that is slightly less good than the one obtained with the CD

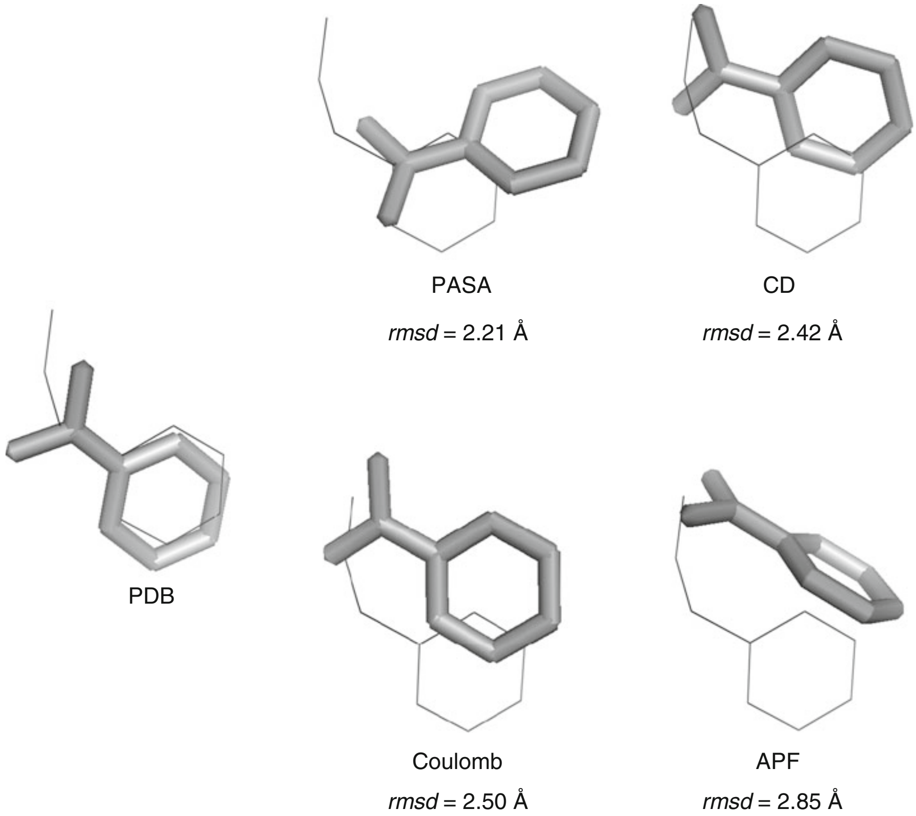
PASA *rmsd* = 2.21 Å

CD *rmsd* = 2.42 Å

PDB

Coulomb *rmsd* = 2.50 Å

APF *rmsd* = 2.85 Å

Fig. 4 Superimposition of the structures of trypsin ligand 3 (*black wire*) and ligand 7 (*grey stick*) in its crystallographic orientation (PDB), and in the MC/SA orientations obtained using the PASA ED, CD, Coulomb potential, and APF descriptors smoothed at *t* varying between 1.7 and 1.4 bohr^2 (H are not shown for clarity) descriptor, that is, 30 good solutions (Online Resource 12). All rmsd values of the successful alignments are lower than 2 Å, except for the superimposition of ligands 6 and 10 with the PASA descriptor, rmsd = 2.62 Å, and the superposition of ligands 7 and 10 with the CD descriptor, rmsd = 2.66 Å. Proper alignments are expected with unchanged S_{AB} values between ligands 2 and 6 using the PASA and CD descriptors. The main difference between the PASA and CD-based results lies in the type of alignments that were achieved with success. For example, all nine alignments involving ligand 8 led to expected results with the CD descriptor, while only three were obtained as desired with PASA. Combining both sets of results leads to a total success rate of 36 over 45 solutions, that is, 80 %. This may suggest that a combination of shape- and charge-dependent descriptors needs to be envisaged for further work with those ligands. The case of ligands 4 and 10 is depicted in Fig. 5, which illustrates that the wrong alignment observed with the CD descriptor occurs due to the large negative region of ligand 4 located at the level of PO_3^{2-}. An additional run carried out with a NH group, replacing the NH_2^+ moiety, did not modify at all the alignment results. The use of the smoothed Coulomb potential (Online Resource 13) did not bring any overall improvement over PASA, especially for all superpositions involving ligand 4, the smallest one, and ligand 5; 17 good solutions, characterized by rmsd < 2 Å, were obtained. Seven alignments correspond to shifted molecules versus their expected orientation. As for the PASA descriptor, the APF one (Online Resource 14) leads to mixed results, with a success rate of 20 over 45 alignments. These good solutions are all characterized by rmsd < 2.5 Å. For ligands 6 and 8, we have to mention that an additional APF type was considered for the negatively charged N atoms of the hydroxamate groups occurring in both ligands. The selected parameters were −0.5 for hydrogen bond donor, 1.5 for hydrogen bond acceptor, 0.0 for sp^2 hybridization, −1.0 for lipophilicity, 0.0 for size, −1.5 for charge, and −1.5 for electronegativity.

Only molecules 1–3, 5, and 7–10 were considered in the work by Chan et al. [18], while molecules 2–9 were studied by Lemmen et al. [16]. If one restricts our analyses to the eight structures involved in each of those previous studies, one gets a maximal success rates of 82 % (23 alignments over 28) and 64 % (18 alignments over 28) with the CD descriptor that are of the same order of magnitude as the literature values of 93 % [18] and 61 % [16], respectively. Only alignments with rmsd < 2 Å were considered, as in the literature [16, 18]. On the whole, most of the wrong superposition results obtained with the CD descriptor (Online Resource 12) involve molecules 4–6, that is, the smallest structures. As already discussed, structure 8 that is a bit larger in size is always well aligned with CD. The particular case of ligands 1 and 8 is illustrated in Fig. 6. The use of the CD descriptor allowed to correctly superpose the functional moieties that are expected to bind to the Zn ion, that is, the carboxylate and the hydroxamate groups, respectively, and the remaining C=O functions (Fig. 6b). On the contrary, PASA tends to superpose the –NH–CH_2–CH_2–OH tail of molecule 8 with the fused rings of ligand 1 (Fig. 6a) to maximize S_{AB}.

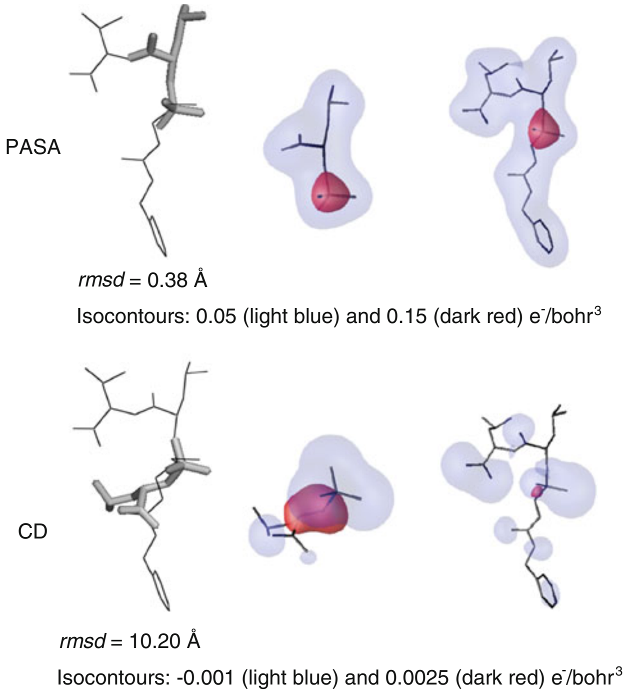

Fig. 5 *Left* Superimpositions of the structures of thermolysin ligand 4 (*grey stick*) and ligand 10 (*black wire*) obtained using the MC/SA algorithm with various descriptors smoothed at t varying between 1.7 and 1.4 $bohr^2$. Isocontours of the PASA ED and CD of thermolysin ligands 4 (*middle*) and 10 (*right*) calculated at $t = 1.4$ $bohr^2$. The molecular skeleton is displayed using *sticks* (H are not shown for clarity)

A careful analysis of the molecular structures is thus required to select a descriptor for this family of molecules in order to determine whether an emphasis is to be given on isosterism or on the electric charge of the functional groups.

3.5 Alignment results for the p38 ligands

Among the four members of the p38 MAP kinase family, the most studied isoform is p38α, a target for anti-inflammatory drugs. The primary sequence reported in the PDB consists of 360–379 amino acid residues forming secondary structures of types α and β. Thirteen ligands (Table 1), able to bind in the ATP-binding pocket located between the N- and C-terminal lobes of p38α, were studied following the work of Chan et al. [18]. The 2D structures are reported

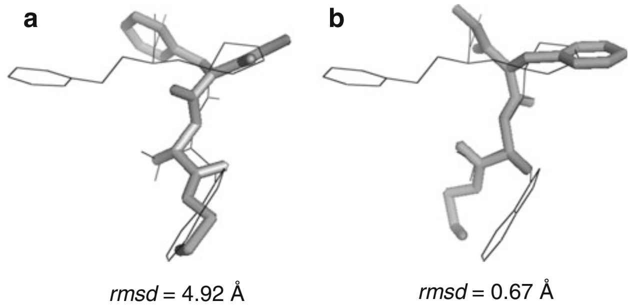

Fig. 6 Superimposition of the structures of thermolysin ligand 1 (*black wire*) and ligand 8 (*grey stick*) obtained using the MC/SA algorithm with the **a** PASA and **b** CD descriptors smoothed at *t* varying between 1.7 and 1.4 bohr^2 (H are not shown for clarity)

in Online Resource 5; the protonation states were selected according to the work of Chan et al. [18]. The p38 ligands interact with the receptor mainly through hydrogen bonding, π-stacking, and hydrophobic interactions. A study of the crystalline complexes shows that the ligands bind in different arrangements in the same binding pocket, as illustrated in Fig. 6 of [18]. Ligand 1WBO is particularly small as it results from fragment-based lead discovery studies, and all four ligands 5–8, that is, 1M7Q, 1OUK, 1OUY, and 1OVE bind in a similar way. Additionally, all those four ligands contain halogen atoms, their pyridyl/pyrimidyl protonated nitrogen form a hydrogen bond with the main chain NH of Met109, and their aryl substituent occupies a hydrophobic pocket [57]. Ligand 1DI9 binds in a mode different from the others, but still interacts with Met109 and Thr106 [58]. The seven remaining ligands, that is, ligands 1–3, 9–11, and 13, bind in a similar fashion; the inhibitors interact with the receptor through hydrogen bonds between their pyridyl/pyrimidyl moieties and Met109, and their respective aromatic groups occupy a lipophilic pocket involving Thr106 [59–62]. Only some of them, ligands 1–3 and 9, are halogenated. A hydrogen bond may be involved with Lys58 [63]. A superposition of the thirteen ligands in their crystallographic orientation is given in Fig. 7 to classify them according to their binding fashion. Such different binding patterns made the superposition between members of the different binding families rather unsuccessful. For example, success rate values of 43 [18] and 27 % [32] were reported in the literature.

Similarity indices and rmsd values are given in Online Resources 15–18 for all alignments obtained with the PASA, CD, Coulomb potential, and APF descriptors, respectively. Alignments between molecules that bind in a similar fashion are highlighted in light and dark grey in the Tables of the Online Resources and the corresponding total number of expected good alignments is 27. With the PASA descriptor, an overall success rate of 37 % (29 alignments over 78) was obtained. When considering molecules in similar binding families, seventeen alignments over 27 were satisfactory, that is, 63 %, all with rmsd below 2.1 Å. With the CD and Coulomb potential descriptors, only eight good alignments were obtained. Moreover, those eight alignments are characterized by a larger rmsd limit value, that is, 2.9 Å. One can additionally observe that with PASA, three alignments did not converge towards the expected solutions. Indeed, proper alignments can be obtained for ligands 2 and 7 ($S_{AB} = 41$ %), 6 and 8 ($S_{AB} = 51$ %), and 7 and 11 ($S_{AB} = 36$ %). This brings the success rate of the PASA-based superposition procedure to a value of 67 % for the alignments obtained using molecules of the same binding families. In comparison, the corresponding success rate reached by Chan et al. [18] is 78 %. In both Chan et al.'s work and in ours, a 100 % success is reached for the family of structures 5–8. With the APF descriptor, only eight expected alignments are obtained, all with rmsd < 2 Å. Beyond that value, the rmsd value cannot be associated with a good alignment. For instance, the incorrect superposition of ligands 6 and 13, illustrated in Fig. 8, is characterized by rmsd = 2.77 Å.

According to the superposition results, the molecular similarity in the ligands of the p38 MAP kinases is mainly shape-dependent. Most of these ligands involve halogen atoms, which guide the alignment procedure. For ligands

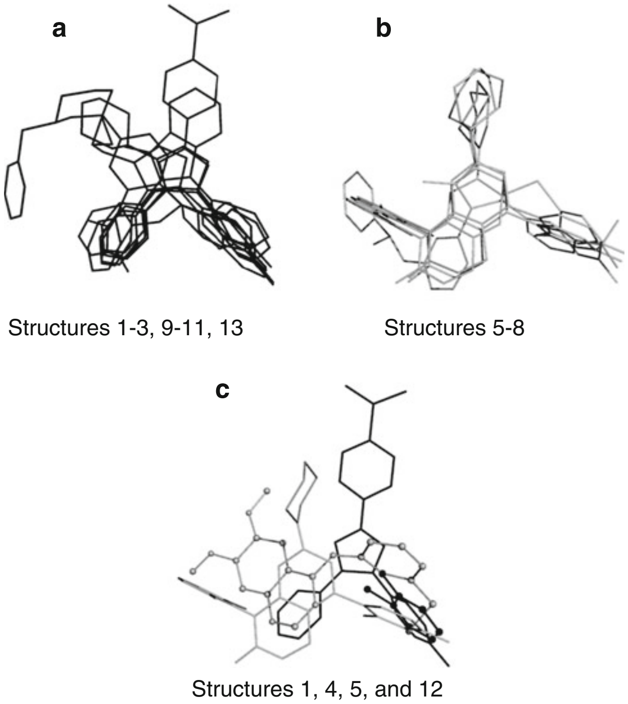

Fig. 7 Superimpositions of the p38 ligands according to their binding mode: **a** ligands *1–3*, *9–11*, and *13*; **b** ligands *5–8*; **c** ligands *5* (*grey*) and *12* (*black ball*-and-*stick*) are displayed together with ligands 1 (*black*) and *4* (*grey ball*-and-*stick*) for comparison with the two binding families (**a**) and (**b**) (H are not shown for clarity)

5–8, the CD descriptor also provides acceptable results, due to the presence of NH_2^+ moieties in all four molecules, and hence can be adequately superposed based on that charged group.

3.6 Alignment results for the HRV14 ligands

Eight antiviral compounds binding to the coating protein of human rhinovirus 14 (Table 1) were considered as in the work of Lemmen et al. [16]. The RHV14 coat protein has four subunits named VP1–VP4 with 289, 262, 236, and 68 amino acid residues, respectively. The HRV14 viral capsid consists of 60 copies of each subunit. VP1 to VP3 are located at the viral capsid surface, while VP4 is buried deeper in the virion, close to the capsid/RNA interface. All ligands are rather extended molecules composed of heterocycles at both ends, which are separated by an aliphatic chain and an aromatic group that act as linkers (Online Resource 6). The HRV14 inhibitors show two distinct binding modes [56] that differ in the orientation of the ligand. A reverse binding mode is observed for ligands 2RM2, 2RR1, 2RS1, and 2RS3 that are characterized by a seven carbon long linker and two methylated five-membered rings, versus 2R04, 2R06, 2R07, and 2RS5. Those last four molecules are all characterized by a shorter linker, constituted of five C atoms, with no or only one methylated five-membered ring. The binding pocket of the receptor is mainly hydrophobic as shown in Fig. 2 of [64] and is essentially composed of residues of VP1 that form a β-barrel.

As observed in the studies of Lemmen et al. [16] and Tervo et al. [56], the use of molecular fields does not always allow to detect reverse orientations. Nevertheless, among all descriptors used in the present work, PASA is able to adequately superimpose ligands of the two orientations. The particular cases of ligands 2–3 and 2–4 are presented in Fig. 9 for the various descriptors. When using the PASA descriptor (Online Resource 19), all alignments between molecules binding in a similar orientation, that is, molecules 1–3 and 8, and molecules 4–7, are successful and are all characterized by rmsd < 1 Å. It is noteworthy to mention that the alignment of molecules binding in a different orientation is also satisfying, as illustrated in Fig. 9 for ligands 2 and 4, except for four cases: ligands 1 and 4, 3 and 4, 3 and 7, and 4 and 8, the success rate being 12 over 16. With the charge-dependent descriptors, like CD (Online Resource 20), Coulomb potential (Online Resource 21), and APF (Online Resource 22), almost all alignments of molecules binding in the same orientation are correct, with rmsd < 1 Å, while no correct alignments between ligands of two inverse orientations are found, that is, rmsd > 10 Å, as also observed by Tervo et al. [56]. An illustration that emphasizes the similarity of the electrostatic potential isocontours explaining the incorrect alignments of ligands of different binding orientations can be found in Fig. 2 of Ref. [56]. The superposition problem occurring between ligands 2 and 4 is not strictly dependent on the shape of the molecules. Indeed, the use of the size component of the APF descriptor only did not provide any good results either. Thus, the nature of the atoms constituting the molecules should also be considered.

Regarding the performance of other approaches, Lemmen et al. [16] obtained a success rate of 100 % when aligning molecules of the same orientations only. Overall values of about 50 % were obtained by Chan et al. [18] and the programs ROCS and FLEXS [32].

One thus concludes that the PASA descriptor, which is able to involve the shape and size of the molecules, as well as the chemical nature of the atoms, is essential for aligning as desired the molecules of the rhinovirus ligand family, and charge effect should be avoided.

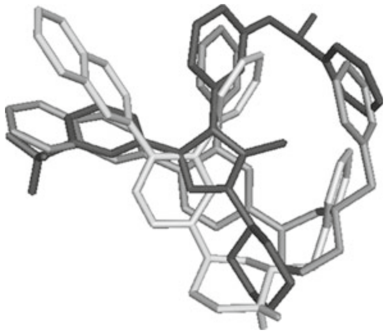

Fig. 8 Superimposition of the structures of p38 ligand 6 (*black stick*) and ligand 13 in its crystallographic orientation (*dark grey stick*), and in the MC/SA orientation obtained using the APF descriptor smoothed at *t* values between 1.7 and 1.4 bohr^2 (*light grey stick*) (H are not shown for clarity)

4 Conclusions

In the present work, a Monte Carlo/Simulated Annealing rigid superposition algorithm was applied to six families of drug molecules, that is, elastase inhibitors, and ligands of endothiapepsins, trypsins, thermolysins, p38 MAP kinases, and rhinovirus, for which various alignment problems were reported in the literature.

All molecules were described using each of the four following smoothed molecular fields, that is, the promolecular atomic shell approximation (PASA) of the full electron density (ED) [35], a charge density (CD) calculated using the Poisson equation [33], the Coulomb electrostatic potential [34], and the Atomic Property Fields (APF) described by Totrov [15].

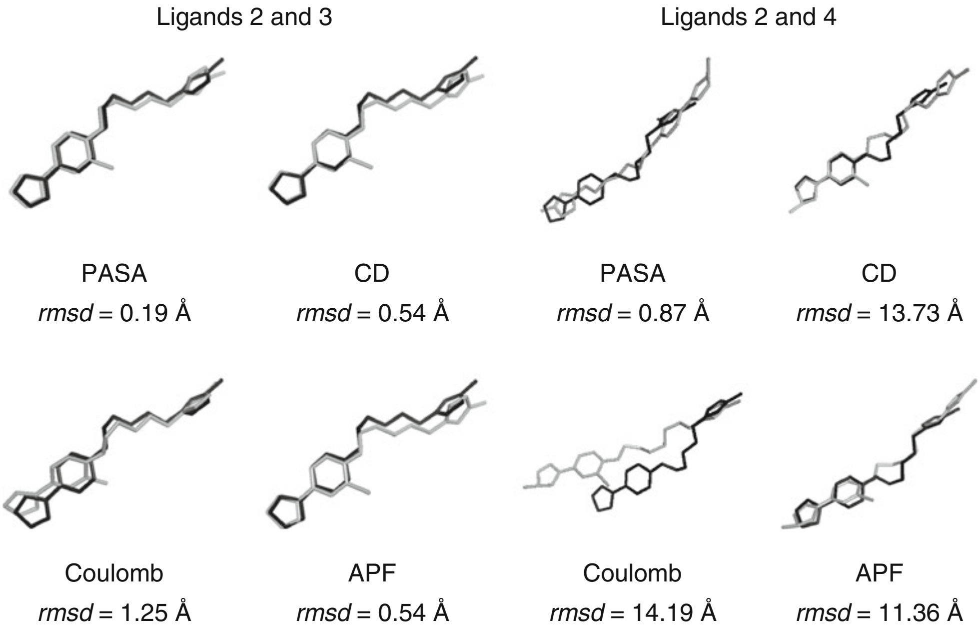

Fig. 9 Superimposition of the structures of HRV14 ligand 2 (*black stick*) and (*left*) ligand 3 (*grey stick*), and (*right*) ligand 4 (*grey stick*) in their MC/SA orientation obtained using the PASA ED, CD, Coulomb potential, and APF descriptors smoothed at t varying between 1.7 and 1.4 bohr^2 (H are not shown for clarity)

All descriptor fields were smoothed to lower the number of local solutions. An additional consequence of that smoothing resides in the levelling of the similarity degree values. This involves that in some cases, several different alignment solutions may occur with the same similarity degrees as for the desired alignments. The smoothing degree was selected following previous studies wherein it was shown that the topological properties of the promolecular ED and the CD distribution functions could be related to molecular features such as pharmacophore elements and/or amino acid residues in larger biomolecules [20, 33]. It was observed that a simultaneous change in the "temperature" during the simulated annealing process, carried out together with a decrease in the smoothing degree, favoured the convergence to global solutions.

With this work, it was first noticed that the use of a rmsd value to evaluate the pair-wise alignments is appropriate for selected ranges of values. All alignments characterized by rmsd smaller or equal to 2 Å correspond to expected solutions. Beyond 3 Å, all can be considered as inadequate. Between 2 and 3 Å, they mostly correspond to displaced alignments but, in some less frequent cases, to false positives. For large peptide structures, such as the elastase ligand TOMI, it can correspond to a good solution.

On the whole, the PASA descriptor field appeared to be the best choice to superpose amino acid sequences, like the two elastase inhibitors, and molecules interacting mainly through van der Waals contacts with their receptor. This was especially clear for molecules of the elastase, endothiapepsin, and rhinovirus ligand families. Alignments of the ligands of the p38 MAP kinase family provided slightly less successful results versus the other methods proposed in the literature. When the shape of the molecules is not the essential component to consider in the description of the molecules, the use of property fields such as the CD and the Coulomb potential can bring a real improvement versus PASA, especially in the families of trypsin and thermolysin inhibitors. A 100 % success was obtained for trypsin when using the smoothed Coulomb potential as a descriptor.

It is thus considered that the descriptor to select for the alignments is strongly dependent upon the nature of the interactions between the drug molecules and their receptor. Additional parameters that are difficult to control during superpositions, but that may affect the results if considered, are flexibility, hydration state, presence of metallic ions or clusters, etc. In addition, working with ligands of very different size, or which partly overlap in the receptor, is always a challenge, but it appeared that these difficulties may also be overcome by an adequate choice of the descriptor, as shown, for example, with the elastase and endothiapepsin ligands. Working with several descriptors may also allow to cumulate adequate alignment information.

To extend and/or improve the superposition results, different strategies could be considered. Besides the inclusion of flexibility, one approach consists in aligning at least three molecules at a time, as discussed by Mestres et al. [65]. Such considerations would, however, lead to additional local solutions to the superposition problems.

One also might to combine several similarity degrees, obtained using different descriptors such as PASA, CD, Coulomb potential, as done in the present work by using the seven APF descriptors of Totrov [15], and by Mestres et al. [65].

5 Online resources

The 2D structure and protonation states of all molecules considered in the present work are given in the Online Resources, as well as the alignment results, in terms of similarity degrees S_{AB} and rmsd values, for the trypsins, thermolysins, p38 MAP kinases, and rhinovirus ligands.

Acknowledgments The authors thank the reviewers for their comments. They also acknowledge L. Piela for fruitful discussions, the support of the F.R.S.–F.R.F.C. (convention no. 2.4.617.07.F), and the ''Facultés Universitaires Notre-Dame de la Paix'' (FUNDP) for the use of the Interuniversity Scientific Computing Facility (ISCF) Center.

References

1. Maggiora GM, Shanmugasundaram V (2004) Methods in molecular biology. In: Bajorath J (ed) Chemoinformatics: concepts, methods, and tools for drug discovery, vol 275. Humana Press, Totowa
2. Bultinck P, Gironés X, Carbó-Dorca R (2005) In: Lipkowitz KB, Larter R, Cundari TR (eds) Reviews in computational chemistry, vol 21. Wiley-VCH, Hoboken
3. Carbó-Dorca R, Besalú E, Mercado LD (2011) Communications on quantum similarity, Part 3: a geometric-quantum similarity molecular superposition algorithm. J Comput Chem 32:582–599
4. Connolly ML (1996) NetSci's science center: computational chemistry 1996. http://www.netsci.org/Science/Compchem/feature14.html. Accessed 11 Jan 2012
5. Good AC, Richards WG (1993) Rapid evaluation of shape similarity using Gaussian functions. J Chem Inf Comput Sci 33:112–116
6. Grant JA, Pickup BT (1995) A Gaussian description of molecular shape. J Phys Chem 99:3503–3510
7. Grant JA, Gallardo MA, Pickup BT (1996) A fast method of molecular shape comparison: a simple application of a Gaussian description of molecular shape. J Comput Chem 17:1653–1666
8. Grant JA, Pickup BT (1997) Gaussian shape methods. Comput Simul Biomol Syst 3:150–176
9. Nicholls A, MacCuish NE, MacCuish JD (2004) Variable selection and model validation of 2D and 3D molecular descriptors. J Comput Aided Mol Des 18:451–474
10. Haigh JA, Pickup BT, Grant JA, Nicholls A (2005) Small molecules shape-fingerprints. J Chem Inf Model 45:673–684
11. Maggiora GM, Rohrer DC, Mestres J (2001) Comparing protein structures: a Gaussian-based approach to the three-dimensional structural similarity of proteins. J Mol Graph Model 19:168–178
12. Mestres J, Rohrer DC, Maggiora GM (1997) MIMIC: a molecular-field matching program. Exploiting applicability of molecular similarity approaches. J Comput Chem 18:934–954
13. Duncan BS, Olson A (1993) Shape analysis of molecular surfaces. Biopolymers 33:231–238
14. Klebe G, Abraham U, Mietzner T (1994) Molecular similarity indices in a comparative analysis (CoMSIA) of drug molecules to correlate and predict their biological activity. J Med Chem 37:4130–4146
15. Totrov M (2008) Atomic property fields: generalized 3D pharmacophoric potential for automated ligand superposition, pharmacophore elucidation and 3D QSAR. Chem Biol Drug Des 71:15–27
16. Lemmen C, Lengauer T, Klebe G (1998) FLEXS: a method for fast flexible ligand superposition. J Med Chem 41:4502–4520
17. Proschak E, Rupp M, Derksen S, Scneider G (2008) Shapelets: possibilities and limitations of shape-based virtual screening. J Comput Chem 29:108–114
18. Chan SL, Labute P (2010) Training a scoring function for the alignment of small molecules. J Chem Inf Model 50:1724–1735
19. Molecular Operating Environment (MOE), 2011.10 (2011) Chemical Computing Group Inc., Montreal
20. Leherte L (2006) Similarity measures based on Gaussian-type promolecular electron density models: alignment of small rigid molecules. J Comput Chem 27:1800–1816
21. Kostrowicki J, Piela L, Cherayil BJ, Scheraga HA (1991) Performance of the diffusion equation method in searches for optimum structures of clusters of Lennard-Jones atoms. J Phys Chem 95:4113–4119
22. Glick M, Robinson DD, Grant GH, Richards WG (2002) Identification of ligand binding sites on proteins using a multi-scale approach. J Amer Chem Soc 124:2337–2344
23. Glick M, Grant GH, Richards WG (2002) Docking of flexible molecules using multiscale ligand representations. J Med Chem 45:4639–4646
24. Leherte L (2001) Application of multiresolution analyses to electron density maps of small molecules: critical point representations for molecular superposition. J Math Chem 29:47–83
25. Leherte L, Meurice N, Vercauteren DP (2005) Influence of conformation on the representation of small flexible molecules at low resolution: alignment of endothiapepsin ligands. J Comput Aided Mol Des 19:525–549
26. Masek BB, Merchant A, Matthew JB (1993) Molecular skins: a new concept for quantitative shape matching of a protein with its small molecule mimics. Proteins 17:193–202
27. Perkins TDJ, Mills JEJ, Dean PM (1995) Molecular surface-volume and property matching to superpose flexible dissimilar molecules. J Comput Aided Mol Des 9:479–490
28. Poirrette AR, Artymiuk PJ, Rice DW, Willett P (1997) Comparison of protein surfaces using a genetic algorithm. J Comput Aided Mol Des 11:557–569
29. Robinson DD, Lyne PD, Richards WG (2000) Partial molecular alignment via local structure analysis. J Chem Inf Comput Sci 40:503–512
30. Klebe G, Mietzner T, Weber F (1994) Different approaches toward an automatic structural alignment of drug molecules: applications to sterol mimics, thrombin and thermolysin inhibitors. J Comput Aided Mol Des 8:751–778
31. Vieth M, Hirst JD, Brooks CL III (1998) Do active site conformations of small ligands correspond to low free-energy solution structures? J Comput Aided Mol Des 12:563–572
32. Chen Q, Higgs RE, Vieth M (2006) Geometric accuracy of three-dimensional molecular overlays. J Chem Inf Model 46:1996–2002
33. Leherte L, Vercauteren DP (2011) Charge density distributions derived from smoothed electrostatic potential functions: design of protein reduced point charge models. J Comput Aided Mol Des 25:913–930
34. Good AC, Hodgkin EE, Richards WG (1992) Utilization of Gaussian functions for the rapid evaluation of molecular similarity. J Chem Inf Comput Sci 32:188–191

35. Amat L, Carbó-Dorca R (2000) Molecular electronic density fitting using elementary Jacobi rotations under atomic shell approximation. J Chem Inf Comput Sci 40:1188–1198
36. Amat L, Carbó-Dorca R (1997) Quantum similarity measures under atomic shell approximation: first order density fitting using elementary Jacobi rotations. J Comput Chem 18:2023–2039. http://iqc.udg.es/cat/similarity/ASA/funcset.html. Accessed 12 Jan 2012
37. Hart RK, Pappu RV, Ponder JW (2000) Exploring the similarities between potential smoothing and simulated annealing. J Comput Chem 21:531–552
38. Robert D, Carbó-Dorca R (1998) A formal comparison between molecular quantum similarity measures and indices. J Chem Inf Comput Sci 38:469–475
39. Carbó-Dorca R, Mercado LD (2010) Commentaries on quantum similarity (1): density gradient quantum similarity. J Comput Chem 31:2195–2212
40. Maggiora GM, Petke JD, Mestres J (2002) A general analysis of field-based molecular similarity indices. J Math Chem 31:251–270
41. Cooper DL, Allan NL (1995) In: Carbó R (ed) Molecular similarity and reactivity: from quantum chemical to phenomenological approaches. Kluwer, Dordrecht
42. Leherte L (2004) Hierarchical analysis of promolecular full electron-density distributions: description of protein structure fragments. Acta Crystallogr Sect D 60:1254–1265
43. Leherte L, Vercauteren DP (2009) Coarse point charge models for proteins from smoothed molecular electrostatic potentials. J Chem Theory Comput 5:3279–3298
44. Good AC, Peterson SJ, Richards WG (1993) QSAR's from similarity matrices. Technique validation and application in the comparison of different similarity evaluation methods. J Med Chem 36(1993):2929–2937
45. Berman HM, Westbrook J, Feng Z, Gilliland G, Bhat TN, Weissig H, Shindyalov IN, Bourne PE (2000) The protein data bank. Nucleic Acids Res 28:235–242. http://www.rcsb.org/pdb. Accessed 12 Jan 2012
46. Pedretti A, Villa L, Vistoli G (2002) VEGA: a versatile program to convert, handle, and visualize molecular structure on Windows-based PCs. J Mol Graph 21:47–49
47. Pedretti A, Villa L, Vistoli G (2004) VEGA—an open platform to develop chemo-bio-informatics applications, using plug-in architecture and script programming. J Comput Aided Mol Des 18:16–173. http://www.vegazz.net/. Accessed 12 Jan 2012
48. Gasteiger J, Marsili M (1980) Iterative partial equalization of orbital electronegativity: a rapid access to atomic charges. Tetrahedron 36:3219–3222
49. Marsili M, Gasteiger J (1981) π Charge distribution from molecular topology and π orbital electronegativity. Croat Chem Acta 53:601–614
50. Bailey D, Cooper JB (1994) A structural comparison of 21 inhibitor complexes of the aspartic proteinase from *Endothia parasitica*. Protein Sci 3:2129–2143
51. Turk D, Stürzebecher J, Bode W (1991) Geometry of binding of the Nα-tosylated piperidines of *m*-amidino-, *p*-amidino- and *p*-guanidino phenylalanine to thrombin and trypsin—X-ray crystal structures of their trypsin complexes and modeling of their thrombin complexes. FEBS 287:133–138
52. Holmes MA, Matthews BW (1981) Binding of hydroxamic acid inhibitors to crystalline thermolysin suggests a pentacoordinate zinc intermediate in catalysis. Biochemistry 20:6912–6920
53. Matthews BW (1988) Structural basis of the action of thermolysin and related zinc peptidases. Acc Chem Res 21:333–340
54. Tronrud DE, Monzingo AF, Matthews BW (1986) Crystallographic structural analysis of phosphoramidates as inhibitors and transition-state analogs of thermolysin. Eur J Biochem 157:261–268
55. Gresh N, Roques BP (1997) Thermolysin-inhibitor binding: effect of the His^{231} → Ala mutation on the relative affinities of thiolate versus phosphoramidate inhibitors—A model theoretical investigation incorporating a continuum reaction field hydration model. Biopolymers 41:145–164
56. Tervo AJ, Rönkkö T, Nyrönen TH, Poso A (2005) BRUTUS: optimization of a grid-based similarity function for rigid-body molecular superposition. 1. Alignment and virtual screening applications. J Med Chem 48:4076–4086
57. Stelmach JE, Liu L, Patel SB, Pivnichny JV, Scapin G, Singh S, Hop CECA, Wang Z, Strauss JR, Cameron PM, Nichols EA, O'Keefe SJ, O'Neill EA, Schmatz DM, Schwartz CD, Thompson CM, Zaller DM, Doherty JB (2003) Design and synthesis of potent, orally bioavailable dihydroquinazolinone inhibitors of p38 MAP kinase. Bioorg Med Chem Lett 13:277–280
58. Shewchuk L, Hassell A, Wisely B, Rocque W, Holmes W, Veal J, Kuyper LF (2000) Binding mode of the 4-anilinoquinazoline class of protein kinase inhibitor: X-ray crystallographic studies of 4-anilinoquinazolines bound to cyclin-dependent kinase 2 and p38 kinase. J Med Chem 43:133–138
59. Wang Z, Canagarajah BJ, Boehm JC, Kassicà S, Cobb MH, Young PR, Abdel-Meguid S, Adams JL, Goldsmith EJ (1998) Structural basis of inhibitor selectivity in MAP kinases. Structure 6:1117–1128
60. Gill AL, Frederickson M, Cleasby A, Woodhead SJ, Carr MG, Woodhead AJ, Walker MT, Congreve MS, Devine LA, Tisi D, O'Reilly M, Seavers LCA, Davis DJ, Curry J, Anthony R, Padova A, Murray CW, Carr RAE, Jhoti H (2005) Identification of novel p38α MAP kinase inhibitors using fragment-based lead generation. J Med Chem 48:414–426
61. Tamayo N, Liao L, Goldberg M, Powers D, Tudor YY, Yu V, Wong LM, Henkle B, Middleton S, Syed R, Harvey T, Jang G, Hungate R, Dominguez C (2005) Design and synthesis of potent pyridazine inhibitors of p38 MAP kinase. Bioorg Med Chem Lett 15:2409–2413
62. Perry JJP, Harris RM, Moiani D, Olson AJ, Tainer JA (2009) p38α MAP kinase C-terminal domain binding pocket characterized by crystallographic and computational analyses. J Mol Biol 391:1–11
63. Trejo A, Arzeno H, Browner M, Chanda S, Cheng S, Comer DD, Dalrymple SA, Dunten P, Lafargue J, Lovejoy B, Freire-Moar J, Lim J, Mcintosh J, Miller J, Papp E, Reuter D, Roberts R, Sanpablo F, Saunders J, Song K, Villasenor A, Warren SD, Welch M, Weller P, Whiteley PE, Zeng L, Goldstein DM (2003) Design and synthesis of 4-azaindoles as inhibitors of p38 MAP kinase. J Med Chem 46:4702–4713
64. Hadfield AT, Oliveira MA, Kim KH, Minor I, Kremer MJ, Heinz BA, Shepard D, Pevear DC, Rueckert RR, Rossmann MG (1995) Structural studies on human rhinovirus 14 drug-resistant compensation mutants. J Mol Biol 253:61–73
65. Mestres J, Rohrer DC, Maggiora GM (1999) A molecular-field-based similarity study of non-nucleoside HIV-1 reverse transcriptase inhibitors. J Comput Aided Mol Des 13:79–93

Theor Chem Acc (2012) 131:1261
DOI 10.1007/s00214-012-1261-4

REGULAR ARTICLE

Ab initio quantum chemical and ReaxFF-based study of the intramolecular iminium–enamine conversion in a proline-catalyzed reaction

Pierre O. Hubin · Denis Jacquemin ·
Laurence Leherte · Jean-Marie André ·
Adri C. T. van Duin · Daniel P. Vercauteren

Received: 29 February 2012 / Accepted: 3 July 2012 / Published online: 9 August 2012

Abstract Among all strategies used by organic chemists to control the stereoselectivity of reactions, organocatalysis, which consists in using the chirality of a small organic molecule, is an increasingly popular method. The proline-catalyzed aldol reaction was one of the first reported cases that demonstrated the power of organocatalysis in the field of asymmetric synthesis. Previous theoretical contributions focused on the reaction mechanism using quantum mechanics (QM) methods. We here present a theoretical study about one specific step of the proline-catalyzed aldol reaction, namely, the conversion of the iminium intermediate into the corresponding enamine. It consists of an intramolecular rearrangement that involves the transfer of a hydrogen atom. First, we investigate this transfer using modern QM models, that is, density functional theory calculations with the M06-2X functional. On the basis of these QM results, we then assess the performance of a reactive force field, ReaxFF, used in combination with molecular dynamics simulations in order to provide a complementary light on this reaction.

Keywords ReaxFF · Force field development · Molecular dynamics simulation · Organocatalysis · Reaction pathway · Proline catalysis · Enamine · Iminium · Solvent effects · DFT · M06-2X

1 Introduction

The ability to control the stereoselectivity of organic reactions is an important key for experimental chemists. As two enantiomers present the same energy, a source of chirality is required to achieve enantioselective synthesis. An efficient approach to induce the chirality in a product is to take advantage of a chiral catalyst, like enzymes or organometallic compounds [1]. During the last decade, a new class of chiral catalysts has been identified, leading to the emergence of so-called organocatalysis [1–3]. The common characteristic of this class of compounds is not only their composition (carbon, hydrogen, nitrogen, oxygen, or sulfur atoms), but also their relative compactness [1]. A well-known example is (s)-proline that catalyzes asymmetric aldol reactions (Scheme 1) with a large yield as well as with a significant enantiomeric excess [4]. This reaction is indeed one of the first reported cases that demonstrated that a small organic molecule could induce an asymmetric reaction [4]. Other organocatalysts were

---

Published as part of the special collection of articles celebrating theoretical and computational chemistry in Belgium.

Electronic supplementary material The online version of this article (doi:10.1007/s00214-012-1261-4) contains supplementary material, which is available to authorized users.

P. O. Hubin (✉) · L. Leherte · D. P. Vercauteren (✉)
Laboratoire de Physico-Chimie Informatique, University of Namur, 61, rue de Bruxelles, 5000 Namur, Belgium
e-mail: phubin@student.fundp.ac.be

D. P. Vercauteren
e-mail: daniel.vercauteren@fundp.ac.be

D. Jacquemin
CESIAM UMR CNRS 6230, Université de Nantes,
2, rue de la Houssinière, BP 92208, 44322 Nantes 3, France

J.-M. André
University of Namur, Académie Royale de Belgique,
61, rue de Bruxelles, 5000 Namur, Belgium

A. C. T. van Duin
Department of Mechanical and Nuclear Engineering,
Pennsylvania State University, 136 Research East Building,
University Park, PA 16802, USA

later found to be efficient in several reaction paths [1–3, 5–8]. Previous studies, mainly relying on quantum mechanics (QM) techniques, focused on the proline-catalyzed aldol reaction and managed to rationalize the observed selectivity [9–15]. It was proposed that the crucial step to explain the stereoselectivity of the reaction is the C–C bond formation and that the mechanism is controlled mainly by the possibility to form a hydrogen bond and by steric hindrance [9–15]. Even if these studies were quite complete, they lacked information about environment and conformational effects, especially for large molecules. It is due to the relatively large computational cost that QM techniques require. Additionally, the mechanistic questions concerning the proline-catalyzed aldol reaction are still not completely resolved. Though the enamine pathway [9–14] is generally accepted, other explanations partially based on the experimental facts [16–18] propose that oxazolidinone intermediates are likely to occur in the mechanism [17].

Our present contribution is devoted to one of the early step of the proline-catalyzed aldol reaction, namely the conversion of the iminium intermediate formed by proline and an aldehyde into the corresponding enamine (Scheme 1). It corresponds to an intramolecular rearrangement involving the transfer of one hydrogen atom. In this paper, first, a fresh theoretical look at the iminium–enamine conversion is proposed by considering different possible paths for the proton transfer with modern QM techniques and the reactive force field (FF), ReaxFF [19]. This last one is combined with molecular dynamics (MD) simulations to shed a complementary light on several aspects of the reaction. The ReaxFF potential establishes a relation between the bond order and the distance between atoms. Consequently, it is able to handle the breaking and formation of chemical bonds during simulations, allowing thus to investigate chemical reactions. It was originally designed and applied to problems related to hydrocarbons [19], but was subsequently extended to many other families of chemicals [20–23]. For instance, ReaxFF parameters were recently developed to model proton transfer in glycine conformers surrounded by water molecules [23]. Combining a reactive FF with MD simulations to investigate chemical reactions is specifically helpful to take into account effects of the environment. It, instead, still remains a challenge for QM techniques to model explicit solvation due to the large computational cost associated with hundreds of solvent molecules, whereas it is a tractable process in the framework of classical MD simulation.

Our paper is organized as follows. First, we compare the performances of several QM models for mimicking the proton transfer reactions, considering both thermodynamic (relative stabilities of intermediates) and kinetic (values of energetic barriers) parameters. To this end, CCSD(T) [24] energies were computed to obtain reliable benchmarks and to adequately assess the quality of lighter ab initio schemes, notably of several density functional theory (DFT) hybrids. This first step allowed selecting an efficient and accurate QM method to investigate the hydrogen atom transfer in the present framework. In a second stage, we consider different possible conformations for the reagent and the product (Fig. 1), the possibility to have a water-assisted proton transfer, as well as the impact of polar (water and acetonitrile) and apolar (benzene) solvents via QM calculations. Information obtained from ReaxFF MD simulations carried out with explicit water molecules surrounding the reactive species gives insight into the effect of water on the reaction. The selected QM method is also used to estimate the reliability of ReaxFF to model the reaction step framed in Scheme 1.

2 Computational methods

All QM calculations were performed using Gaussian09 [25] aiming at generating an accurate description of the investigated reaction from both thermodynamic and kinetic point of views in order to guide the ReaxFF simulations. Consequently, we concentrated on the definition of a theoretical method which can provide reliable results for the intermediates and the transition states (TS). Four functionals were tested: B3LYP [26], BMK [27], ωB97X-D [28], and M06-2X [29], the former being the *classical* functional used in many simulations of organic reactions, while the three latter are well recognized as more adequate for the investigation of the TS. MP2 [30] geometry optimizations and CCSD(T) single point energy computations on the MP2 structures were also carried out to allow a balanced assessment of the *pros* and *cons* of each functional. Calculations performed to provide comparisons

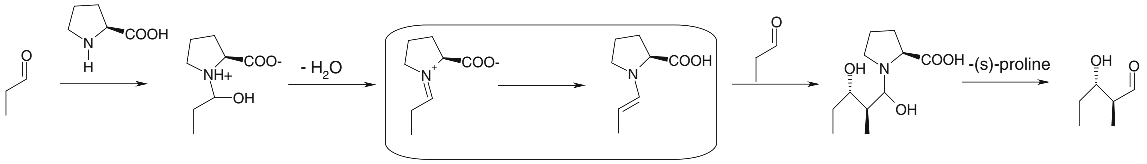

Scheme 1 Representation of the major steps of the proline-catalyzed aldol reaction of propionaldehyde following the enamine pathway [12]. The present contribution focuses on the framed step

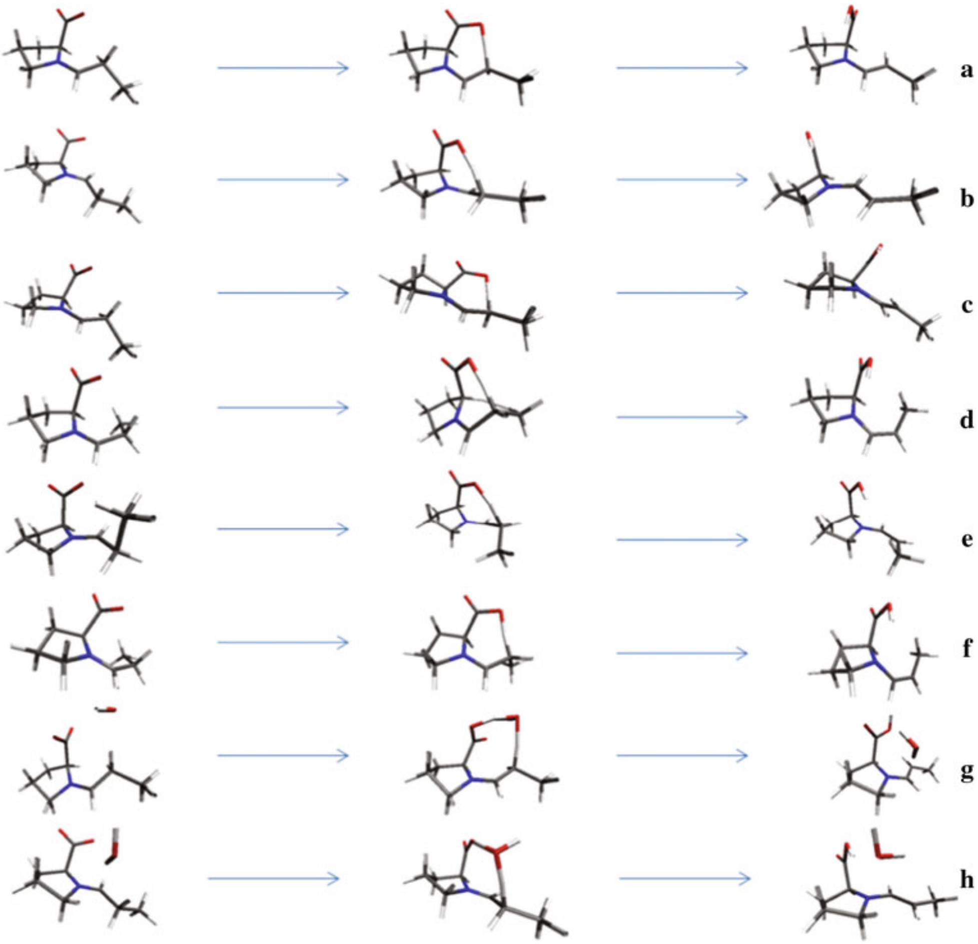

Fig. 1 Sketch of eight conformations of the iminium (*left*) and enamine (*right*) intermediates as well as the transition states (*center*). **a** E *s-cis endo*, **b** E *s-trans endo*, **c** E *s-cis exo*, **d** Z *s-cis endo*, **e** Z *s-trans endo*, **f** Z *s-cis exo*, **g** E *s-cis endo* complexed with one water molecule, and **h** E *s-trans endo* complexed with one water molecule. Carbon, hydrogen, oxygen, and nitrogen atoms are sketched in *gray*, *white*, *red*, and *blue*, respectively. One should notice that the notations regarding the iminium intermediates are defined following the enamine that is formed, for example, iminium E *s-cis endo* being the conformation of iminium leading to the enamine with the E geometry of the double bond, the *s-cis* conformation, and the *endo* conformation of the proline cycle

between the four functionals were done with the 6-311 ++G(d,p) atomic basis set. In the latter steps, the M06-2X/6-31 + G(d,p) scheme was used to investigate several aspects of the reaction as this more compact basis set provided results very similar to its more extended counterpart (see Supplemental Materials Table S2 for a brief comparison of the two basis sets). Vibrational frequencies of all optimized structures were systematically computed to ensure that local minima (no imaginary frequency) or TS (one imaginary frequency) are described. Regarding the TS, the imaginary frequency was checked to correspond to the hydrogen atom transfer between iminium and enamine. The bulk solvent interactions at the QM level were taken into account via the IEF (integral equation formalism)-PCM (polarizable continuum model) method [31].

In the second stage of our work, the program LAMMPS [32] was used to carry out MD simulations of the hydrogen atom transfer in combination with ReaxFF. Before performing simulations of the reaction, we had to assess the performances of the FF for our system. To this end, molecular mechanics (MM) minimizations were done with LAMMPS to compare both geometrical and energetic criteria obtained at the QM and MM levels. Specific FF parameters relevant to the studied reaction were obtained through an optimization process of ReaxFF. The procedure consisted in a single-parameter optimization as described in another contribution [33]. We initially started our investigations with ReaxFF parameters developed for a study regarding the proton transfers in glycine isomers [23]. These parameters were subsequently modified to reproduce QM relative energies related to compounds that include functional groups relevant to our study. MMFF94 [34], another FF for which specific parameters for the iminium and enamine functional groups were already available, was also used with the program Tinker [35] to compare the performances of both FF's.

MD simulations in vacuum were performed in a cubic periodic box of 8,000 Å^3 in the canonical NVT ensemble. Tests were also carried out using the microcanonical NVE ensemble but led to large variation of the temperature between the reactant and the product. The temperature was maintained to 100 K with a Nosé-Hoover thermostat [36] so as to limit thermal fluctuation of the energy. As emphasized in a previous study, it indeed appeared that a relatively low temperature was needed to characterize both intermediates with significant energy values [23]. The iminium intermediate was also put in a box containing solvent molecules to characterize the influence of explicit solvation on the reaction. The number of solvent molecules was fixed to reach the density observed at atmospheric pressure. The temperature for the solvated simulations was also maintained to 100 K. Another important point regarding the simulation of the reaction concerns the triggering of the hydrogen atom transfer. Indeed, while one could in principle expects the reaction to occur spontaneously, this, in practice, can require extremely long simulations to be observed. Consequently, a specific strategy was adopted to trigger the reaction. It consisted in imposing a constraint to force the atoms which are going to form a new bond to come closer. The constraint was set up using the steered-MD function of LAMMPS [37] with a spring constant of 1.0 kcal/mol Å^2, sufficient to trigger the reaction within 10 ps for most considered cases. It was not imposed during the whole simulation; a period of equilibration was applied before and after imposing the constraint. The time step was fixed to 0.1 fs when the constraint was acting and to 0.25 fs (in vacuum) or 0.5 fs (with explicit water molecules) otherwise. The choice of a relatively short time step is consistent with the study of chemical reactions involving fast movements of atoms. Especially, we figured out that a 0.1 fs time step was necessary to trigger the reaction without the occurrence of any other undesired event.

3 Results and discussion

3.1 Comparison of QM methods

In this section, we assess the performances of four functionals, B3LYP, BMK, ωB97X-D, and M06-2X, for estimating the relative stabilities of the intermediates and the reaction energy barrier. Benchmarks were obtained with several wavefunction methods using single point energies computed on the MP2 geometries (Table 1). The CCSD(T)/6-311++G(d,p) energy values were in agreement with complete size basis-set extrapolation calculations, that is, CBS/QB3 and G3MP2 approaches, regarding the stability of iminium versus enamine with deviations smaller than 0.6 kcal/mol.

First, it is noticed that MP2 gives values in the line of the CCSD(T) ones. Regarding the four functionals, one sees that BMK and ωB97X-D are particularly efficient for estimating energy barriers but less reliable for predicting the relative stability of the intermediates (errors exceeding 3 kcal/mol). With B3LYP, the energy barrier is also underestimated, an expected outcome for a hybrid functional incorporating a relatively small fraction of *exact* exchange [27, 29, 38, 39]. M06-2X provides very accurate values for intermediates and, though less satisfying for the TS, this *meta*-GGA hybrid functional emerges as adequate for the investigation of the considered reaction. It is indeed the only functional to yield errors smaller than 20 % for both criteria.

Table 1 6-311 ++G(d,p) relative stabilities of the iminium and enamine intermediates and energy barriers associated with the conversion of iminium into enamine for the E *s-cis endo* case, both non-hydrated and water-assisted

QM method	Non-hydrated		Water-assisted	
	Relative stability (kcal/mol)	Energy barrier (kcal/mol)	Relative stability (kcal/mol)	Energy barrier (kcal/mol)
CCSD(T)[a]	14.35	13.20	7.02	22.08
CCSD[a]	15.81 (10.2)	14.23 (7.8)	8.30 (18.2)	24.43 (10.6)
MP4(SDQ)[a]	15.28 (6.5)	13.99 (6.0)	7.79 (11.0)	24.09 (9.1)
MP2	15.00 (4.5)	11.88 (10.0)	7.34 (4.6)	19.15 (13.3)
B3LYP	12.18 (15.1)	10.24 (22.4)	8.27 (17.8)	17.76 (19.6)
BMK	11.19 (22.0)	12.53 (5.1)	5.89 (16.1)	21.93 (0.7)
ωB97XD	10.22 (28.8)	13.78 (4.4)	6.63 (5.6)	19.02 (13.9)
M06-2X	15.13 (5.4)	10.96 (17.0)	8.36 (19.1)	18.05 (18.3)

Zero point vibrational energy (ZPVE) was not taken into account. Relative errors (percentages) with respect to CCSD(T) are given in parentheses

[a] Single point calculation using the MP2 geometry

Among the parameters that influence the reaction, we tested the possibility for a water molecule to mediate the proton transfer. The results reported in Table 1 show the performances of each functional when one single water molecule is complexed with the reactive species.

Though the error of M06-2X for the relative stability is larger, 19.1 %, than for the non-hydrated case, 5.4 %, it remains quite consistent with relative discrepancies below 20 %, an acceptable threshold for our purposes. It is worth highlighting that ωB97X-D performs very well, 5.6 and 13.9 % of errors with respect to CCSD(T), for the water-assisted case, although it was significantly less efficient for the non-hydrated case, 28.8 %, confirming its performances when hydrogen bonds with water molecules play a key role [39]. BMK underestimates the relative energy between the intermediates but it gives a result very close to CCSD(T) for the energy barrier, with an error inferior to 1 %. However, for the non-hydrated case, this functional implies an error superior to 20 % regarding the relative stability.

Combining both non-hydrated and water-assisted cases, one can draw several conclusions. BMK and ωB97X-D behave similarly; they predict energy barriers (especially BMK) rather well but underestimate the relative stability of the intermediates. This error remains limited when the

Table 2 M06-2X/6-31 + G(d,p) relative stabilities and energy barriers for the eight considered cases

	Relative stability (kcal/mol)	Energy barrier (kcal/mol)
E *s-cis endo* (a)	15.14	10.25
E *s-trans endo* (b)	14.77	21.31
E *s-cis exo* (c)	15.88	10.03
Z *s-cis endo* (d)	14.77	11.06
Z *s-trans endo* (e)	11.62	25.80
Z *s-cis exo* (f)	14.94	10.46
E *s-cis endo* + 1 H_2O (g)	13.34	11.91
E *s-trans endo* + 1 H_2O (h)	7.41	16.34

ZPVE corrections were not taken into account. Labels (a)–(h) correspond to those of Fig. 1

absolute value is small but becomes problematic for larger values. B3LYP provides results of average accuracy regarding the relative stability and underrates the energy barriers. M06-2X slightly overestimates the relative stability of the intermediates with an error becoming significant when the absolute value is particularly small. Like B3LYP, it underestimates energy barriers.

In short, we selected the M06-2X functional for all further calculations because it emerges as a suitable compromise for estimating both energy barriers and relative stabilities between intermediates and it is the most consistent method for the two considered cases, non-hydrated and water-assisted. Let us add that the conclusions regarding the selected functional are limited to the case investigated here, and it should not be inferred that it is adequate for any type of reactions.

3.2 Conformational issues

The M06-2X/6-31 + G(d,p) approach was used to investigate conformational aspects of the reaction. Six possible forms of the starting iminium intermediate were considered focusing on three parameters: the conformation of the proline cycle (*endo* or *exo*) [14], the relative position of the methyl group *versus* the carboxylate (*s-cis* or *s-trans*) [15], and the two conformations that may lead to the E or Z configuration of the enamine. Cases (a) to (f) are illustrated in Fig. 1; the results are summarized in Table 2. One should notice that a total of eight cases could have been considered. However, the Z and E *s-trans exo* forms of the iminium were too unstable to be located. The possibility for the hydrogen atom transfer to occur through a water molecule, cases (g) and (h), was also considered (Table 2).

The enamine conformer (b) is of similar stability than its counterpart (a), 0.05 kcal/mol, but the corresponding energy barrier for (b), 21.31 kcal/mol, is far larger than (a), 10.25 kcal/mol. It can be explained by the distance separating the two atoms forming the new bond; the O···H distance is indeed 2.49 Å in iminium (a) but 3.29 Å in iminium (b). We therefore evaluated the possibility to convert enamine (a) into (b). Such a conversion seems energetically allowed: the TS to pass from one form to the other was localized, and the energy barrier associated with this transformation is 6.72 kcal/mol, which is lower than the energy barrier of the reaction, 10.25 kcal/mol. The conformation of the proline cycle, *endo* or *exo*, has a rather negligible impact from both thermodynamic and kinetic points of views. The reaction probably occurs regardless of the starting conformation of the five-membered ring. Comparing cases (a) and (d), the E species are generally favored over the Z ones: the iminium and enamine isomers (a) are more stable than their counterpart (d). The barrier for the formation of the enamines E is also a bit smaller by 0.81 kcal/mol. The difference between (d) and (e) is similar to the one noticed between (a) and (b): the energy barrier associated with the *s-trans* isomer, 25.80 kcal/mol, being much larger than the one of the *s-cis* one, 11.06 kcal/mol.

The sizeable energy barriers in the *s-trans* cases are related to the distances between the oxygen and the hydrogen atoms, and they can be potentially decreased if a water molecule assists the transfer of the hydrogen. This scenario was investigated by comparing the energy barriers of the water-assisted transfer for the E *endo s-cis* (g) and E *endo s-trans* (h) structures. The corresponding TS may be viewed in Fig. 1. The results shown in Table 2 indicate that the hypothesis is verified: the energy barrier is decreased by 4.97 kcal/mol for the *s-trans* case and slightly increased for the *s-cis* one, 1.66 kcal/mol. This is consistent with previously published data [15].

Our conclusion is thus that the transfer is more likely to happen from the E *s-cis endo* form of the iminium to yield the enamine E *s-cis endo*, which is probably in equilibrium with the E *s-trans endo* one.

As mentioned in the introduction, there is an alternative mechanistic pathway supporting that the iminium–enamine conversion occurs through an oxazolidinone intermediate. We tested the possibility to form oxazolidinone from the E *endo s-trans* isomer of the iminium. It turns out that the energy barrier for this conversion is very low, 0.20 kcal/mol. Moreover, this oxazolidinone species is more stable than the other considered intermediates, the difference being 7.44 kcal/mol regarding the enamine E *endo s-trans*. These results are not particularly surprising since, on the one hand, it is known from experimental observations that oxazolidinones are easily isolated in the reaction mixture, although it is nearly never the case for enamines, and, as on the other hand, similar theoretical results were already reported in literature. Nevertheless, the oxazolidinone formed must be subsequently opened to yield a negatively charged enamine and no element proves that this particular step is kinetically favored over the direct iminium–enamine conversion, especially if no base is added in the reaction mixture to allow the elimination process. Sharma et al. [15] investigated the possibility for the oxazolidinone opening to occur in presence of trimethylamine and found a Gibbs free energy of activation of 18.0 kcal/mol with the B3LYP functional. As far as we are concerned, those values of energy barriers are too close to completely rule out one or another pathway which may also vary following the reaction conditions.

To this point, we did not take into account entropic effects. A summary of the influence of these contributions is given in "Supplemental Materials." Globally, the enthalpic contribution is clearly predominant from both thermodynamic and kinetic point of views, an expected outcome for an intramolecular reaction. Consequently, for the rest of the work, only enthalpic contributions are considered, these ones being directly comparable with the FF potential energies.

3.3 Solvation effects

Experimentally, the low solubility of proline in common organic solvents is a problem for the proline-catalyzed aldol reaction [40]. The problem can be circumvented by using polar aprotic solvents like DMSO [4]. Water can also be used as co-solvent; it speeds up the reaction and allows using only stoichiometric quantities of ketones [40]. The reaction still works when performed in water with no other co-solvent, but to the price of a loss of selectivity [40].

To model bulk effects of solvents such as acetonitrile and water, we used the IEF-PCM algorithm. First, single points were computed on the vacuum geometries. The second step consisted in optimizing the geometries of the structures under implicit solvation. A summary of the different approaches and results for the E *s-cis endo* case is presented in Table 3.

The global trend can be summarized as follows: the more the description of the solvent is complete, the more the iminium intermediate is stabilized with respect to the enamine and the TS. In terms of implicit solvation, the last observation is easily understood since the stabilizing effect of polar solvents is larger for polar solutes. The dipole moment of iminium in vacuum computed at the M06-2X/6-31 + G(d,p) level is indeed 9.94 D, which is 1.52 (4.49) D larger than the TS (enamine) dipole moment. This implies that the energy barrier in polar solvents is increased with respect to vacuum [12, 41]. Similarly, the relative stability of iminium *versus* enamine is shifted in favor of the former, the effect being larger when the geometry optimization is carried out with implicit solvation.

Table 3 M06-2X/6-31 + G(d,p) relative stabilities between the two intermediates and energy barriers for the case E *s-cis endo* considering several solvent models

	Relative stability (kcal/mol)	Energy barrier (kcal/mol)
1: Vacuum	15.14	10.25
2: Implicit solvation, single point energy (IEF-PCM, CH_3CN)	2.37	15.37
3: Implicit solvation, geometry optimization (IEF-PCM, CH_3CN)[a]	0.31	18.13
4: Implicit solvation, geometry optimization (IEF-PCM, water)	−5.56	18.82
5: Five explicit water molecules + implicit solvation (IEF-PCM, water)[b]	−7.57	24.48

ZPVE corrections were not taken into account

[a] The enamine conformation considered in 1, 2, and 3 is not the same than in 4 and 5

[b] The geometries of the solutes are the ones optimized in 4

To model explicit solvation, single point energies were computed on systems composed of solute molecules (whose geometries were optimized at the M06-2X/6-31 + G(d,p) level with implicit solvation) surrounded by five molecules of water, the rest of the solvent being treated implicitly. To set up the position of the solvent molecules, we relied on MD simulations carried out with ReaxFF with explicit solvent molecules. However, five water molecules are not sufficient to completely describe the first solvation shell. For this reason, the positions of the water molecules were adjusted to ensure the comparison of similar situations for iminium, enamine, and the TS. Let us precise that in this case the solvent molecules do not play an active role in the reaction (they do not mediate the hydrogen atom transfer) but may stabilize one intermediate over the other and tune the height of the barrier. The explicit water molecules stabilize even more the iminium intermediate, which becomes more stable than the enamine by 7.57 kcal/mol. In addition, the energy barrier is raised by 5.56 kcal/mol. This outcome suggests that using only implicit solvation yields an underestimation of the stability of iminium. This additional stabilization of iminium originates in the strong hydrogen bonds between the carboxylate group and water molecules. This observation is consistent with what can be deduced from the ReaxFF MD simulations of the reaction. Following the evolution of the system composed by the iminium intermediate surrounded by 104 molecules of water, it is seen that both oxygen atoms of the carboxylate are close to hydrogen atoms of water.

The mean distances computed during the simulation are 1.67 ± 0.07 and 1.64 ± 0.04 Å. These short distances suggest an interaction stronger than a simple H-bond, and it is consistent with the raise of the barrier of the reaction. The hydrogen atom transfer is indeed less likely to occur when the oxygen of the carboxylate is involved in a strong interaction with water molecules.

3.4 Validation of the FF

To evaluate the performances of ReaxFF for the reaction, we compare the reference QM results, obtained with the M06-2X functional and the 6-31 + G(d,p) basis set, with MM geometry optimizations and single point energy calculations. When it is possible, we also compare these results with MMFF94 data [34], another FF that contains specific parameters for the iminium and enamine functional groups.

Our first criterion to evaluate ReaxFF is the energy. We compare relative energies between several intermediates of the reaction obtained from the optimized QM and FF geometries. Selected results are presented in Table 4, the five top lines correspond to relative energies of selected isomers, for example, E *s-cis endo versus* E *s-trans endo*, whereas the bottom three lines imply different molecules. For the first category, ReaxFF performances are quite similar to MMFF94 ones: MMFF94 is slightly better for the comparison of the enamine E *s-cis endo* (a) and Z *s-cis endo* (d), but it was impossible to locate two different conformations for the iminium conformers (a) and (d) with MMFF94. Actually, the geometry optimization systematically yields the conformer (a), regardless of the starting point.

MMFF94 cannot be used to compare the structural isomers as it does not grant meaningful comparison between molecules with different connectivities. The computed energy indeed depends on the atom types that change between iminium and enamine. ReaxFF is able to qualitatively reproduce QM results: the enamine intermediates remain more stable than iminium ones, though the difference is slightly overestimated by ReaxFF.

Table 4 Relative energies (in kcal/mol) of optimized structures of several intermediates with different QM (M06-2X/6-31 + G(d,p) and FF (ReaxFF and MMFF94) methods

Structures[a]	M06-2X	ReaxFF	MMFF94
Enamine (b)/(a)[b]	−0.05	0.03	0.59
Iminium (b)/(a)	−0.42	−0.13	0.37
Enamine (d)/(a)	2.09	6.02	3.63
Iminium (d)/(a)	1.71	3.44	0.00
Enamine (h)/(g)	0.63	−3.82	−6.09
Iminium (a)/enamine (a)	15.14	19.52	–
Iminium (d)/enamine (d)	14.77	16.94	–
Iminium (g)/enamine (g)	13.34	16.10	–

[a] Relative energies are computed by subtracting the energy of the second structure to the first

[b] Labels (a)–(h) refer to cases presented in Fig. 1

For the water-assisted cases, one notes that the structure of the enamine E *s-trans endo* (h) optimized with ReaxFF is close to the QM structure, but it is not the case with MMFF94, the water molecule in the optimized geometry departing from its initial position (*cfr* Supplemental Materials). This explains the large error, 6.72 kcal/mol, observed for MMFF94 in that case.

In short, from these data one can conclude that ReaxFF provides results that are comparable to those obtained with MMFF94 for conformers. In general, ReaxFF is able to satisfactorily reproduce QM predictions.

Turning toward the performances of ReaxFF to describe structures perturbed by variations of bond lengths, valence angles, and torsion angles, we compared four potential energy curves as presented in Fig. 2 for key structural parameters (*cfr* Fig. 3 for atom labels). We selected the following strategy: starting from the equilibrium geometry of the QM level of reference, we progressively modified a geometrical parameter and computed QM and ReaxFF single point energies on the obtained structures.

Both bonds are particularly interesting since one is broken, C1-H24, and the other is formed, O15-H24, during the reaction. One notes that ReaxFF reproduces well the bond stretching energies. There is a deviation when the bond lengths are constrained to very small values, for example, 0.7 Å. However, this is not problematic since such situation does not take place in actual chemical reactions. One can also notice that the equilibrium values of the bond lengths are well reproduced by the FF.

As for bond lengths, the position of the minimum for the C20-C1-H24 valence angle is well reproduced by the FF. The curvature is also similar for large angles. For small angles, however, ReaxFF energies are significantly overestimated. To explain this discrepancy, one must refer to the form of ReaxFF. As bond orders are calculated on the basis of distances between atoms, it must prevent the atoms from being involved in more bonds than expected. Thus, an overcoordination penalty term is present in the FF. If one focuses on the geometry of the iminium when the C20-C1-H24 valence angle is constrained to 60° (Fig. 4), one sees that the hydrogen atom H24 is simultaneously close, with distances lower than 1.4 Å, to two carbon atoms, C1 and C20. It follows that H24 and C20 are largely overcoordinated, and thus the overcoordination penalty becomes very large, around 90 kcal/mol. To show that the deviation from QM results is not due to the valence angle description of ReaxFF, we plotted the valence angle energy term in function of the C20-C1-H24 angle (Fig. 4) and the MM *versus* QM discrepancy diminishes.

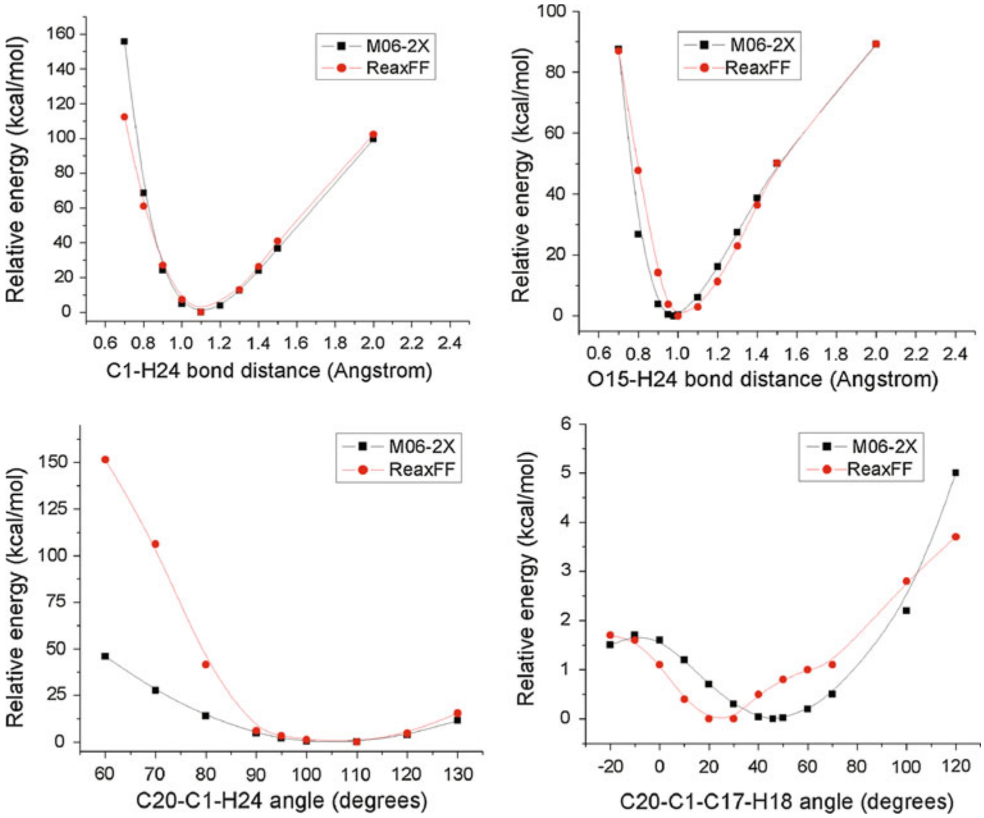

Fig. 2 Relative energy versus the C1-H24 bond length in iminium E s-*cis endo* (*top left*), the O15-H24 bond length in enamine E *s-cis endo* (*top right*), the C20-C1-H24 valence angle (*bottom left*), and the C20-C1-C17-H18 torsion angle (*bottom right*) in iminium E s-*cis endo* as obtained at the M06-2X/6-31 + G(d,p) level and with ReaxFF. Labels of the atoms are given in Fig. 3

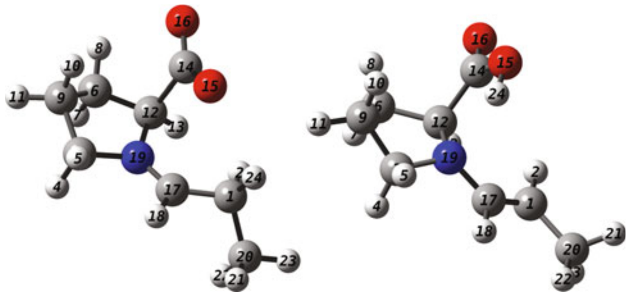

Fig. 3 Sketch of the iminium (*left*) and enamine (*right*) E *s-cis endo* 3D structures with labeled atoms. Colors of the atoms are given in Fig. 1

For the C20-C1-C17-H18 torsion angle in iminium, one notes that the position of the minimum is shifted to smaller angles, 20°, with respect to the QM equilibrium value, 45°. However, the energy difference between these conformations is quite small, that is, less than 2 kcal/mol in the range −20–70°. This small value indicates that the torsion angle is likely to vary significantly during simulations (*cfr* Sect. 3.5).

One can conclude that QM results are reasonably reproduced by ReaxFF. Consequently, one can be confident to find reliable results regarding the investigated reaction with the MD simulations of the hydrogen atom transfer, as described below.

3.5 ReaxFF MD simulations

Let us now focus on the results of the ReaxFF MD simulations. As mentioned in Sect. 2, a constraint was applied on the system to trigger the reaction. The evolution with time of the C···H and H···O distances throughout the simulation is presented in Fig. 5. The C···H distance first fluctuates around a value of 1.1 Å, which corresponds to a C–H σ-bond. After the reaction (34 ps), the distance varies on a larger range since the atoms are not bonded anymore in the enamine structure. The H···O distance decreases gradually before the hydrogen atom is transferred, a direct consequence of the constraint. Once the transfer is triggered, the reaction happens on a very short time scale (about 0.25 ps). This makes the characterization of the TS less straightforward. The solution adopted to tackle the problem was to select an atomic configuration characteristic of the TS and perform a new MD simulation with this configuration as starting point after having fixed the

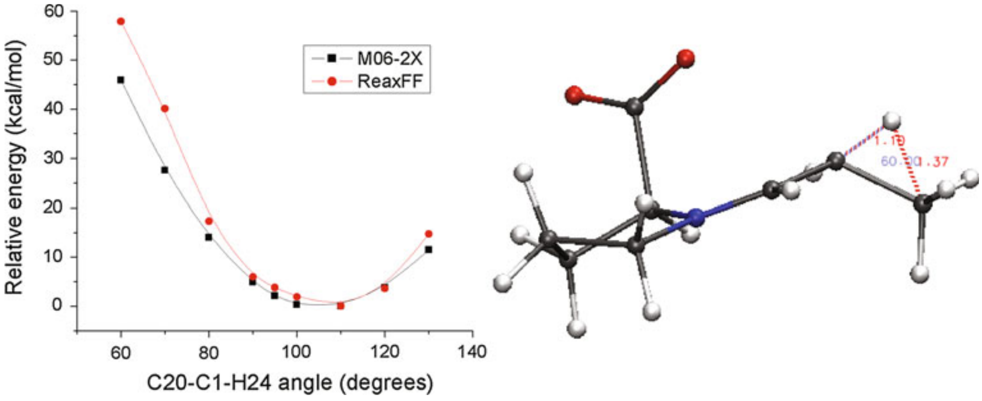

Fig. 4 Comparison between the total QM energy and the valence angle ReaxFF energy contribution for different values of the C20-C1-H24 valence angle in iminium E *s-cis endo*. The structure when the angle is constrained to 60.0° is illustrated on the *right*. Colors and labels of the atoms are given in Figs. 1 and 3, respectively

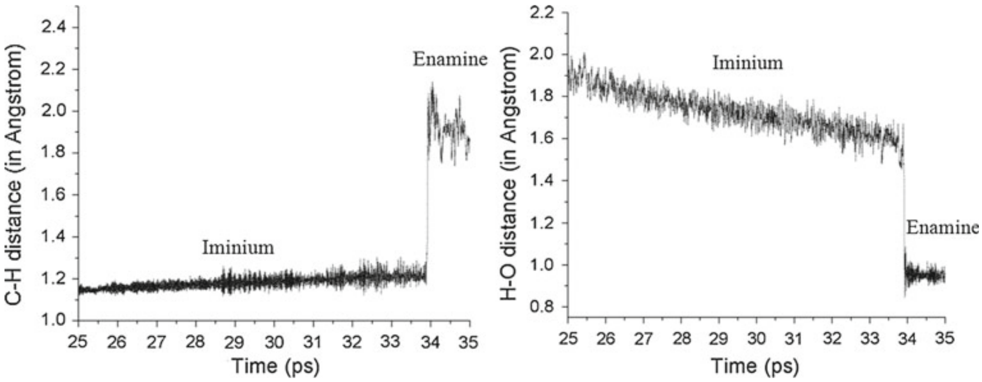

Fig. 5 Evolution of C···H (*left-broken bond*) and H···O (*right-formed bond*) distances during the ReaxFF MD simulation of the conversion of iminium E *s-cis endo* into the corresponding enamine at a temperature of 100 K (NVT ensemble) in vacuum

positions of the three atoms directly involved in the hydrogen atom transfer, that is, C1, H24, and O15.

A summary of the relative stabilities and energy barriers obtained with the M06-2X/6-31 + G(d,p) scheme (*cfr* Table 2) as well as deduced from the MD simulations in vacuum carried out using ReaxFF is presented in Table 5. The energy values of the intermediates from the MD simulations were determined by averaging the potential energies over a time range of 5 ps. For the TS, energies were evaluated on the basis of simulations in which the positions of the atoms involved in the hydrogen atom transfer were held fixed. Errors on the potential energies estimated via the standard deviations stay between 1.0 and 1.5 kcal/mol. Let us mention that we here considered potential energy values obtained from the simulations carried out in vacuum because they can be directly compared to QM energies (without any ZPVE, neither thermal, nor entropic corrections). Explicit solvation effects deduced from simulations cannot be easily related to implicit QM ones, due to the huge difference between the considered systems. Moreover, the parameterization of ReaxFF for this study was performed on the basis of QM results obtained in vacuum, without implicit solvation data. All those reasons explain why the simulations in vacuum are taken into account at this point to compare QM and MD simulations results. Let us also emphasize that it is much easier to extract relative stabilities between intermediates and energy barriers from simulations in vacuum; standard deviations associated with the mean values of potential energies being indeed much larger when considering simulations carried out in a box of water molecules.

From Table 5, it is seen that ReaxFF overshoots the stability of enamine with errors in the range 2.5–4.0 kcal/mol. ReaxFF also slightly overestimates energy barriers,

Table 5 Relative stabilities between the iminium and enamine intermediates and energy barriers associated with the conversion of iminium into enamine in six cases as obtained with the M06-2X/6-31 + G(d,p) scheme and as deduced from the ReaxFF MD simulations at a temperature of 100 K (NVT ensemble) in vacuum

	M06-2X		ReaxFF	
	Relative stability (kcal/mol)	Energy barrier (kcal/mol)	Relative stability (kcal/mol)	Energy barrier (kcal/mol)
E *s-cis endo*	15.14	10.25	18.4	11.2
E *s-trans endo*	14.77	21.31	17.7	27.2
E *s-cis exo*	15.88	10.03	20.0	12.9
Z *s-cis endo*	14.77	11.06	17.5	13.0
Z *s-trans endo*	11.62	25.80	15.7	31.0
Z *s-cis exo*	14.94	10.46	17.2	11.5

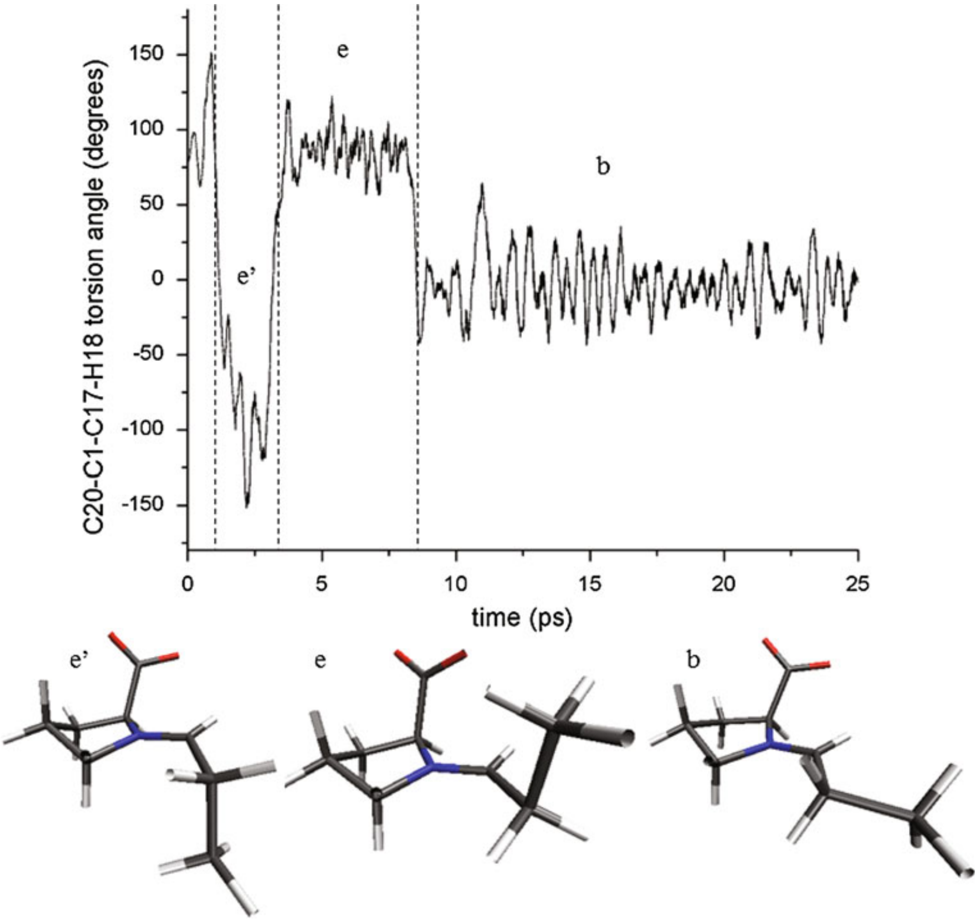

Fig. 6 Evolution of the C20-C1-C17-H18 torsion angle value of the iminium Z *s-trans endo* during the ReaxFF MD simulation performed at 100 K (NVT ensemble) in vacuum. The three conformations, (*e'*), (*e*), and (*b*), encountered during the simulation are illustrated below, labels correspond to the ones given in Fig. 1. Colors and labels of the atoms are given in Figs. 1 and 3, respectively

that is, between 1 and 3 kcal/mol for the *s-cis* cases, for which M06-2X energy barriers are predicted around 10 kcal/mol. The overestimation is slightly larger, around 5 kcal/mol, for the *s-trans* cases, which are predicted around 20–25 kcal/mol with the QM method. ReaxFF results can also be compared to CCSD(T) benchmarks: in the E *s-cis* case, the overestimation using ReaxFF is 4.0 kcal/mol for the relative stability between intermediates and 2.0 kcal/mol regarding the energy barrier. For *s-cis* isomers, it is clear, on the basis of the computed standard deviations, 1.0–1.5 kcal/mol, that ReaxFF cannot precisely indicate whether the hydrogen atom transfer takes place from one specific conformer of the iminium intermediate. Nevertheless, ReaxFF reproduces correctly the much higher energy barriers needed to initiate the hydrogen atom transfer from the *s-trans* forms.

As mentioned in Sect. 3.4, the C20-C1-C17-H18 torsion angle in iminium is relatively flexible. This statement concerned the iminium E *s-cis endo*. From Fig. 6, one sees that this torsion angle in the iminium Z *s-trans endo* is indeed very flexible; three main conformations are observed during the ReaxFF MD simulation. The last one, the most significant if the times passed in each conformation are compared, does not correspond to the Z *s-trans endo* iminium but rather to the E *s-trans endo* (Fig. 6). A much longer simulation of 400 ps was also carried out confirming that the major conformation of iminium was E. The same behavior was observed for the Z *s-cis exo* iminium that had the tendency to switch to the E conformation during the simulation. It is particularly interesting since energy barriers for the *s-cis* isomers are too close to conclude that one is kinetically favored over the other. This switch between E and Z conformations constitutes a thermodynamic argument, showing that iminium is more likely to adopt an E conformation and can thus be converted into E configurations of the enamine.

4 Conclusions

Our theoretical investigation regarding the understanding of the conversion of iminium into enamine in the framework of a proline-catalyzed aldol reaction emphasizes that the reactive force field (FF), ReaxFF, used in combination with molecular dynamics (MD) simulations is a relevant method to investigate the mechanism of proton transfers in iminium–enamine conversions. This approach should be extended to model other steps of proline-catalyzed reactions. ReaxFF simulations allow investigating the evolution of the system in time, which is useful to assess the likelihood of a given conformational change. Combining MD simulations with explicit inclusion of the solvent is a powerful tool to rationalize the interactions it may form with the solute.

First, we showed that similar conclusions regarding the relative stability of intermediates and energy barriers could be drawn either from ReaxFF MD simulations or from DFT calculations at the M06-2X/6-31 + G(d,p) level. Regarding the particular studied step of the reaction, one showed that the iminium–enamine conversion is more likely to yield an E enamine and that the energy barrier for the reaction is also smaller starting from the *s-cis* isomer of iminium relatively to the *s-trans* one.

We now plan to investigate other steps of the reaction. Particularly, we will focus on the possibility to form the enamine through the opening of the oxazolidinone intermediate. The C–C bond formation step, which is significant to explain the stereoselectivity of the proline-catalyzed aldol reaction, will also be considered. The modeling of other solvents is another perspective for future work.

Acknowledgments The authors acknowledge the support of the F.R.S.-FRFC (convention no. 2.4.617.07.F), and the “Facultés Universitaires Notre-Dame de la Paix” (FUNDP) for the use of the Interuniversity Scientific Computing Facility (ISCF) Center. They are also thankful to Prof. S. Lanners (FUNDP) for fruitful discussions. DJ indebted to the *Régions des Pays de Loire (recrutement sur poste stratégique)* and to the ERC StG program (Grant: Marches–278845) for financial support.

References

1. MacMillan DWC (2008) Nature 455:304–308
2. Dalko PI, Moisan L (2004) Angew Chem Int Ed 43:5138–5175
3. Geary LM, Hultin PG (2009) Tetrahedron Asymmetry 20:131–173
4. List B, Lerner RA, Barbas CF III (2000) J Am Chem Soc 122:2395–2396
5. Doyle AG, Jacobsen EN (2007) Chem Rev 107:5713–5743
6. Ouellet SG, Tuttle JB, MacMillan DWC (2005) J Am Chem Soc 127:32–33
7. Reisman SE, Doyle AG, Jacobsen EN (2008) J Am Chem Soc 130:7198–7199
8. Yang HY, Hong JB, MacMillan DWC (2007) J Am Chem Soc 129:7004–7005
9. Bahmanyar S, Houk KN (2001) J Am Chem Soc 123:11273–11283
10. Bahmanyar S, Houk KN (2001) J Am Chem Soc 123:12911–12912
11. Bahmanyar S, Houk KN, Martin HJ, List B (2003) J Am Chem Soc 125:2475–2479
12. Allemann C, Gordillo R, Clemente FR, Cheong PH-Y, Houk KN (2004) Acc Chem Res 37:558–569
13. Clemente FR, Houk KN (2005) J Am Chem Soc 127:11294–11302
14. Allemann C, Um JM, Houk KN (2010) J Mol Catal A 324:31–38
15. Sharma AK, Sunoj RB (2010) Angew Chem Int Ed 49:6373–6377
16. Klussmann M, Iwamura H, Mathew SP, Wells DH Jr, Pandya U, Armstrong A, Blackmond DG (2006) Nature 441:621–623
17. Seebach D, Beck AK, Badine DM, Limbach M, Eschenmoser A, Treasurywala AM, Hobi R (2007) Helv Chim Acta 90:425–471
18. Kanzian T, Lakhdar S, Mayr H (2010) Angew Chem Int Ed 49:9526–9529
19. van Duin ACT, Dasgupta S, Lorant F, Goddard WA III (2001) J Phys Chem A 105:9396–9409
20. Chenoweth K, Cheung S, van Duin ACT, Goddard WA III, Kober EM (2005) J Am Chem Soc 127:7192–7202
21. Chenoweth K, van Duin ACT, Goddard WA III (2008) J Phys Chem A 112:1040–1053
22. Zhang L, Zybin SV, van Duin ACT, Dasgupta S, Goddard WA III, Kober EM (2009) J Phys Chem B 113:10619–10640
23. Rahaman O, van Duin ACT, Goddard WA III, Doren DJ (2011) J Phys Chem B 115:249–261
24. Raghavachari K, Trucks GW, Pople JA, Head-Gordon M (1989) Chem Phys Lett 157:479–483
25. Gaussian 09, Revision B01, Frisch MJ, Trucks GW, Schlegel HB, Scuseria GE, Robb MA, Cheeseman JR, Scalmani G, Barone V, Mennucci B, Petersson GA, Nakatsuji H, Caricato M, Li X, Hratchian HP, Izmaylov AF, Bloino J, Zheng G, Sonnenberg JL, Hada M, Ehara M, Toyota K, Fukuda R, Hasegawa J, Ishida M, Nakajima T, Honda Y, Kitao O, Nakai H, Vreven T, Montgomery, Jr JA, Peralta JE, Ogliaro F, Bearpark M, Heyd JJ, Brothers E, Kudin KN, Staroverov VN, Kobayashi R, Normand J, Raghavachari K, Rendell A, Burant JC, Iyengar SS, Tomasi J, Cossi M, Rega N, Millam JM, Klene M, Knox JE, Cross JB, Bakken V, Adamo C, Jaramillo J, Gomperts R, Stratmann RE, Yazyev O, Austin AJ, Cammi R, Pomelli C, Ochterski JW, Martin RL, Morokuma K, Zakrzewski VG, Voth GA, Salvador P, Dannenberg JJ, Dapprich S, Daniels AD, Farkas Ö, Foresman JB, Ortiz JV, Cioslowski J, Fox DJ, Gaussian, Inc, Wallingford CT, 2010
26. Becke AD (1993) J Chem Phys 98:1372–1377
27. Boese AD, Martin JML (2004) J Chem Phys 121:3405–3416
28. Chai JD, Head-Gordon M (2008) Phys Chem Chem Phys 10:6615–6620
29. Zhao Y, Truhlar DG (2008) Theor Chem Acc 120:215–241
30. Møller C, Plesset MS (1934) Phys Rev 46:618–622
31. Tomasi J, Mennucci B, Cammi R (2005) Chem Rev 105:2099–3093
32. Plimpton SJ (1995) J Comp Phys 117:1–19
33. van Duin ACT, Baas JMA, van de Graaf B (1994) J Chem Soc, Faraday Trans 90:2881–2895
34. Halgren TA (1996) J Comp Chem 17:490–519
35. Ponder J (2011) Tinker 5.1.09, program available on: http://dasher.wustl.edu/tinker/. Last consulted on 2 December 2011
36. Shinoda W, DeVane R, Klein ML (2007) Mol Sim 33:27–36
37. Izrailev S, Stepaniants S, Isralewitz B, Kosztin D, Lu H, Molnar F, Wriggers W, Schulten K (1998) Computational molecular dynamics: challenges, methods, ideas. In: Deuflhard P, Hermans J, Leimkuhler B, Mark AE, Reich S, Skeel RD (eds) Lecture notes in computational science and engineering, vol 4. Springer, Berlin, pp 39–65
38. Wodrich MD, Corminboeuf C, Schleyer PVR (2006) Org Lett 8:3631–3634
39. Burns LA, Vazquez-Mayagoitia A, Sumpter BG, Sherrill CD (2011) J Chem Phys 134:84107–84114
40. Pihko PM, Laurikainen KM, Usano A, Nyberg AI, Kaavi JA (2006) Tetrahedron 62:317–328
41. Rankin KN, Gauld JW, Boyd RJ (2002) J Phys Chem A 106:5155–5159

Theor Chem Acc (2012) 131:1273
DOI 10.1007/s00214-012-1273-0

REGULAR ARTICLE

Density functional theory for the description of charge-transfer processes at TTF/TCNQ interfaces

Tanguy Van Regemorter · Maxime Guillaume · Gjergji Sini · John S. Sears · Victor Geskin · Jean-Luc Brédas · David Beljonne · Jérôme Cornil

Received: 27 April 2012 / Accepted: 28 August 2012 / Published online: 15 September 2012

Abstract In the field of organic electronics, a central issue is to assess how the frontier electronic levels of two adjacent organic layers align with respect to one another at the interface. This alignment can be driven by the presence of a partial charge transfer and the formation of an interface dipole; it plays a key role for instance in determining the rates of exciton dissociation or exciton formation in organic solar cells or light-emitting diodes, respectively. Reliably modeling the processes taking place at these interfaces remains a challenge for the computational chemistry community. Here, we review our recent theoretical work on the influence of the choice of density functional theory (DFT) methodology on the description of the charge-transfer character in the ground state of TTF/TCNQ model complexes and interfaces. Starting with the electronic properties of the isolated TTF and TCNQ molecules and then considering the charge transfer and resulting interface dipole in TTF/TCNQ donor–acceptor stacks and bilayers, we examine the impact of the choice of DFT functional in describing the interfacial electronic structure. Finally, we employ computations based on periodic boundary conditions to highlight the impact of depolarization effects on the interfacial dipole moment.

Keywords DFT · Partial charge transfer · TTF/TCNQ · Organic electronics · Interface dipole · Interfaces

1 Introduction

A key characteristic of organic electronic devices is their multilayered structure resulting in the presence of multiple interfaces that have a large impact on the overall device performance. Thus, a detailed understanding of the processes taking place between the layers is of crucial importance. The Schottky–Mott model is the simplest picture that can be applied to interfaces between organic conjugated materials. In this model, two adjacent layers share a common vacuum level at the interface. If this were to hold true, the energetic characteristics of the interface could be designed by tailoring separately the electronic properties of the two materials. However, numerous experimental studies based in particular on photoemission electron spectroscopy have demonstrated that this picture is usually not valid [1, 2]. In fact, an additional electrostatic potential is generally present at the donor/acceptor interface and shifts the vacuum level of one layer with respect to the other; this, in turn, modulates the relative alignment of the electronic levels of the interfacial components [3]. This additional potential is associated with the formation of an interface dipole layer (IDL); the IDL originates in charge-transfer processes between the donor and acceptor molecules and/or in polarization effects induced by the asymmetry of the electrostatic environment at the interface

---

Published as part of the special collection of articles celebrating theoretical and computational chemistry in Belgium.

T. Van Regemorter (✉) · M. Guillaume · V. Geskin · D. Beljonne · J. Cornil
Laboratory for Chemistry of Novel Materials, University of Mons, Place du Parc 20, 7000 Mons, Belgium
e-mail: tanguy.vanregemorter@umons.ac.be

G. Sini · J. S. Sears · J.-L. Brédas
School of Chemistry and Biochemistry and Center for Organic Photonics and Electronics, Georgia Institute of Technology, 30332-0400 Atlanta, Georgia

G. Sini
Laboratoire de Physicochimie des Polymères et des Interfaces (LPPI), Université de Cergy-Pontoise, 5 Gay-Lussac, 95031 Cergy-Pontoise Cedex, France

as compared to the bulk of the individual materials [4, 5]. In the case of donor and acceptor moieties that are weakly coupled, either a vanishing or a complete charge transfer is expected. In the latter instance, a multiconfigurational quantum chemical approach is needed to properly account for the biradical character of the charge-transfer state [6]. In contrast, in cases where there is significant overlap between the molecular orbitals of the two components, a partial charge transfer is expected. In a one-electron picture, this implies that a fraction of an electron is transferred from the highest occupied levels of the donor to the lowest unoccupied levels of the acceptor. In the context of perturbation theory, the contribution of each possible charge-transfer pathway is proportional to the electronic coupling between the two relevant molecular orbitals and inversely proportional to their energy separation [7]. In small molecules that exhibit large energy differences between consecutive frontier electronic levels, the transfer is generally dominated by the coupling between the HOMO of the donor and LUMO of the acceptor (since this corresponds to the lowest energy pathway), except when symmetry effects make this coupling negligible.

In order to assess the most appropriate quantum mechanical methodology to describe a partial interfacial charge transfer and its contribution to the interface dipole, we have chosen to investigate a model interface consisting of a strong donor, the tetrathiafulvalene molecule (TTF), and a strong acceptor, the tetracyanoquinodimethane molecule (TCNQ). These molecules are known to present a significant charge transfer when in a parallel configuration [8].

In this contribution, we survey our recent theoretical work addressing the choice of the functional in density functional theory (DFT) to describe the charge-transfer character in the ground state of TTF/TCNQ model complexes [9, 10]. First, we examine how the nature of the functional impacts the electronic properties of isolated TTF or TCNQ molecules or stacks of each species. Through comparison to benchmark calculations, we then examine the impact of the functional choice on the computed charge transfer and associated interface dipole in TTF/TCNQ stacks. This study encompasses hybrid DFT functionals with a low percentage of HF exchange (B3LYP [11, 12], TPSSh [13], B97-1 [14–16], and PBE0 [16]), hybrid functionals with a high percentage of HF exchange (BMK [17], BHandH [18], BHLYP [18], M05-2X [19], M06-2X [20], and M06-HF [20]), and long-range corrected (LRC) functionals, also referred to as ω-functionals hereafter (ωB97X [21], ωB97X-D [22], as well as LRC-ωPBEh [23]). The influence of the basis set will not be discussed here since it was previously shown to play only a minor role in comparison with the choice of functional for the properties of interest [10]. Finally, we consider the influence of the environment on the interface dipole and partial charge transfer via depolarization effects.

2 Theoretical results

2.1 Isolated molecules

In this section, we investigate the impact of the percentage of exact exchange (% HF) on the computed electronic properties of isolated TTF and TCNQ molecules. In Fig. 1a, we present the evolution of the energy of the HOMO (highest occupied molecular orbital) and HOMO-1 level of an isolated TTF molecule and of the LUMO (lowest unoccupied molecular orbital) level of an isolated TCNQ molecule from several DFT functionals with varying amounts of HF exchange. Figure 1b shows the evolution of the corresponding donor/acceptor gap (E[LUMO$_{\mathrm{TCNQ}}$]-E[HOMO$_{\mathrm{TTF}}$]). It is worth noting that these values evolve linearly as a function of the percentage of HF exchange in the functional.

In the limit of large separation, the fundamental gap of a TTF/TCNQ complex should approach the difference between the ionization potential (IP) of TTF and the electron affinity (EA) of TCNQ. However, in the case of semilocal DFT functionals, the HOMO values differ largely from the IP and provide a HOMO–LUMO gap far below (by over 1 eV) the fundamental gap. This is due to the lack of derivative discontinuity (the finite jump in the exchange-correlation potential when passing through an integer

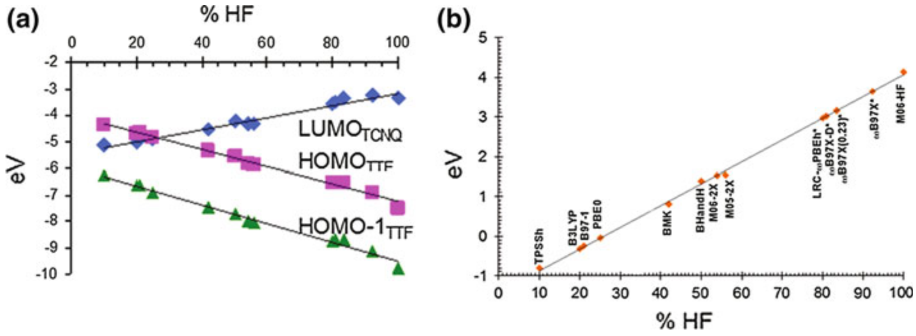

Fig. 1 **a** Computed HOMO$_{\mathrm{TTF}}$, HOMO-1$_{\mathrm{TTF}}$, and LUMO$_{\mathrm{TCNQ}}$ energies as a function of the percentage of HF exchange. The %HF for ω-functionals are effective values (see text for details). **b** Computed E[HOMO$_{\mathrm{TTF}}$]-E[LUMO$_{\mathrm{TCNQ}}$] for various DFT functionals varying by the degree of HF exchange (*orange diamonds*). This figure is adapted from [9]

number of electrons). On the other hand, the HF HOMO–LUMO gap is too large compared to the fundamental gap. Thus, the inclusion of some amount of exact exchange by constructing hybrid functionals can improve the comparison between the HOMO–LUMO gap and the fundamental gap. Note that hybrid functionals can be considered as a special case of the generalized Kohn–Sham (GKS) scheme [24–26] designed with the intention to remedy the DFT gap problem. For the TTF/TCNQ example, the M06-HF functional, which contains 100 % HF exchange, provides for the largest E[$\mathrm{LUMO}_{\mathrm{TCNQ}}$]-E[$\mathrm{HOMO}_{\mathrm{TTF}}$] energy gap among all DFT functionals considered here, slightly over 4 eV. It is topped only by the HF value itself, 4.87 eV. At the other extreme, the TPSSh functional (that contains just 10 % HF exchange) and the other functionals with a low fraction of HF exchange (B3LYP, B97-1, and PBE0) yield the $\mathrm{LUMO}_{\mathrm{TCNQ}}$ lower in energy than the $\mathrm{HOMO}_{\mathrm{TTF}}$. Since the experimental gas-phase values for the ionization potential of TTF and the (exothermic) electron affinity of TCNQ are 6.7 eV [27] and 2.8 eV [28], respectively, this behavior is qualitatively wrong and represents an artifact of these methodologies. Given that a positive value for E[$\mathrm{HOMO}_{\mathrm{TTF}}$]-E[$\mathrm{LUMO}_{\mathrm{TCNQ}}$] should be expected, the functionals containing more than 40–50 % HF exchange (i.e., BMK, BHandH, M05-2X, M06-2X, and M06-HF) and the ω-functionals provide at least a reasonably physical description. Comparing the theoretical energy differences with the difference between the experimental IP value for TTF and EA value for TCNQ (3.9 eV), it is found that the ωB97X with a standard value for $\omega = 0.3$ provides reliable results. With regard to the LRC, or ω-functionals, it is not possible to assign explicit values for the percentage of HF exchange. A simple linear regression was used [9] to approximate the relationship between the computed gaps and the percentage of exact exchange, see Fig. 1. This relation has been employed to assign *effective* percentages of exact exchange to the ω-functionals. As we will show, a proper description of the GKS HOMO–LUMO gap will become increasingly important as we build from the example of a single TTF and a single TCNQ to the model interfaces considered below.

2.2 Isolated stacks

A proper description of interfacial electronic properties requires going beyond a simple two-molecule representation containing one donor and one acceptor unit [10]. In order to assess the validity of LRC functionals for systems of large size, we have computed the evolution of the $\mathrm{HOMO}_{\mathrm{TTF}}$ and $\mathrm{LUMO}_{\mathrm{TCNQ}}$ in isolated one-dimensional stacks containing from one to five layers. We compared the ωB97X functional, which gave the most reliable results in the previous section, to the BHLYP functional that also ensures a positive HOMO–LUMO gap for isolated molecules. Figure 2 exhibits a rapid inversion of the two energy levels with BHLYP: $\mathrm{LUMO}_{\mathrm{TCNQ}}$ lies below $\mathrm{HOMO}_{\mathrm{TTF}}$ already for a stack of two layers. On the other hand, no inversion is observed with ωB97X and $\mathrm{HOMO}_{\mathrm{TTF}}$ always stays below $\mathrm{LUMO}_{\mathrm{TCNQ}}$. Though the shape of the curves is similar for both functionals, it is the initial wider gap of the LRC functional that prevents the levels to cross at least for the stack sizes under consideration. It is worth noticing that such an inversion does occur in the three-dimensional band structure of the TTF/TCNQ co-crystal that presents adjacent columns of TTF and TCNQ molecules (in contrast to the interfacial geometry considered below) due to the increased widths of the bands [29].

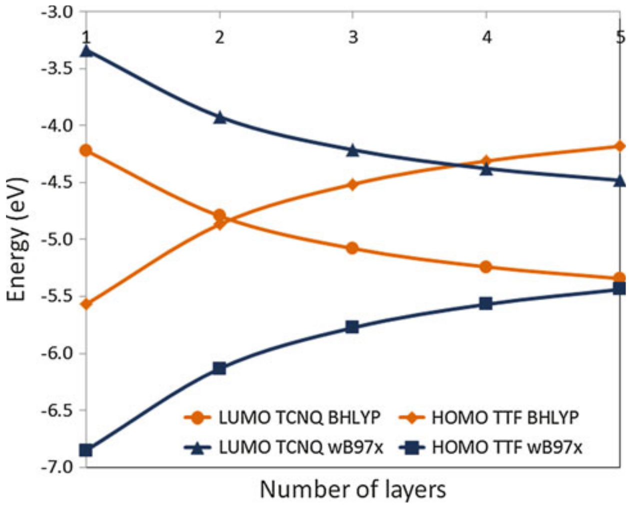

Fig. 2 Evolution of the energy of the HOMO of TTF and LUMO of TCNQ in isolated stacks of growing size, as calculated with the BHLYP and ωB97X functionals. This figure is adapted from [10]

2.3 TTF/TCNQ complex

As a first step, we have studied the influence of the nature of the functional on the charge-transfer character in the ground state of a cofacial TTF/TCNQ complex with the two molecules separated by $\sim$3.5 Å. It is worth stressing that CASSCF and CAS-MRCI calculations, used as benchmark in the previous studies, rule out a complete electron transfer in the ground state [9, 10]. Only a partial charge transfer (lower than 0.15 $|e|$) takes place, which validates the use of a mono-determinantal closed-shell approach such as DFT. However, the shift of the frontier orbitals correlated with the amount of HF exchange should affect the amount of charge transferred.

The electronic coupling between the HOMO of TTF and LUMO of TCNQ generally governs the amount of charge transfer and is very sensitive to the relative orientations/positions of the molecules forming the complex [30]. This is

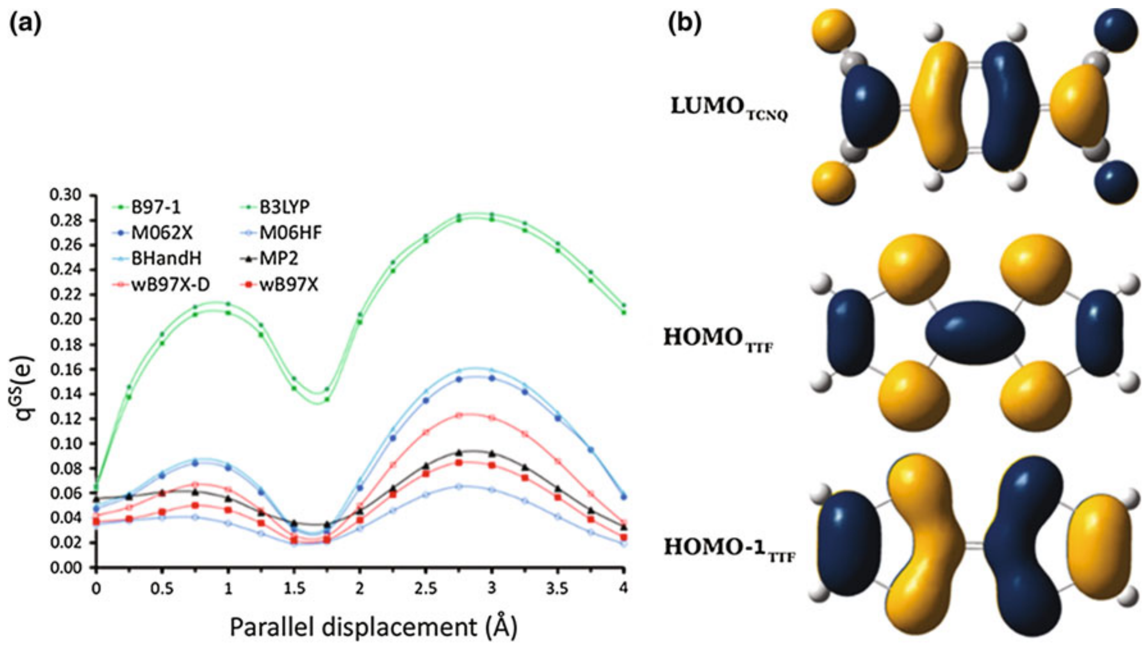

Fig. 3 **a** NPA charges transferred in the ground state (q^{GS}), as calculated with the different functionals, plotted as a function of the horizontal displacement at a fixed interplanar distance of 3.45 Å for the TTF/TCNQ model system. **b** Sketch of the HOMO-1_{TTF}, $HOMO_{TTF}$, and $LUMO_{TCNQ}$ orbitals. This figure is adapted from [9]

shown in Fig. 3a that depicts the evolution of the natural population analysis (NPA) charge q^{GS} transferred as a function of the longitudinal displacement of one molecule of the complex. For a given parallel-displaced geometry, the $HOMO_{TTF}$/$LUMO_{TCNQ}$ overlap (and the corresponding electronic coupling) varies as a function of the relative positions of the $HOMO_{TTF}$ and $LUMO_{TCNQ}$ nodal surfaces displayed in Fig. 3b. The minimum observed in the q^{GS} values for parallel displacements around 1.75 Å and the maximum observed for displacements of ca. 3.0 Å are consistent with the $HOMO_{TTF}$/$LUMO_{TCNQ}$ couplings of 0.075 and 0.708 eV calculated at these geometries, respectively, using the procedure described in Ref. [9] (absolute values with the ωB97X functional). The importance of employing functionals with a high admixture of HF exchange can be seen when considering the q^{GS} values for the parallel-displaced structures obtained with B3LYP and B97-1, which greatly overestimate the contribution from the $HOMO_{TTF}$/$LUMO_{TCNQ}$ coupling and underestimate the energy gap, and as a result, the amount of charge transferred. For a given geometry, the electronic coupling can still vary largely as a function of the choice of DFT functional. This is demonstrated in Fig. 4, where the electronic coupling between HOMO-1_{TTF} and $LUMO_{TCNQ}$ follows a nearly linear dependence upon the amount of exchange, increasing by a factor of ∼2.3 in going from the TPSSh functional (10 % HF) to the M06-HF functional (100 % HF).

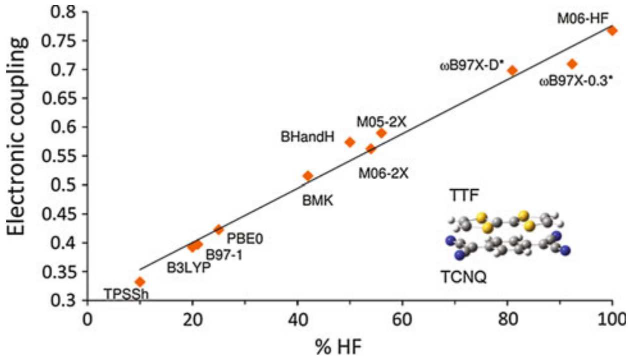

Fig. 4 Electronic coupling (eV) between HOMO-1_{TTF} and $LUMO_{TCNQ}$ for the cofacial TTF/TCNQ model system (with an intermolecular distance of 3.45 Å), as calculated with various functionals and plotted as a function of % HF exchange. This figure is adapted from [9]

The natural population analysis (NPA) charges in the ground state (q^{GS}) for the cofacial and the parallel-displaced configuration at 3.0 Å are plotted in Fig. 5 as a function of the fraction of exact exchange. For the perfectly cofacial geometry, the ground-state charge transfer varies by only 0.05 e^- among the functionals, with a maximum value of 0.08 |e| for TPSSh. The small values calculated in the case of the cofacial geometry are a consequence of the symmetry of the $HOMO_{TTF}$ and $LUMO_{TCNQ}$ orbitals (Fig. 3b), which leads to a vanishing electronic coupling. The small charge transfer in fact arises from interactions between HOMO-1_{TTF} and $LUMO_{TCNQ}$ (which have a larger energy difference). This situation is very different in the

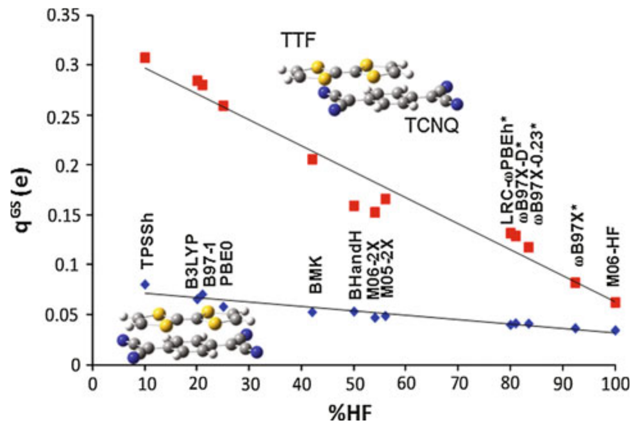

Fig. 5 NPA charge transferred in the ground state (qGS) calculated with the different functionals plotted as a function of the HF exchange for the cofacial (*blue*) and parallel-displaced (*red*) configurations of the TTF/TCNQ model complex. This figure is adapted from [9]

parallel-displaced configuration where the amount of charge transferred increases by up to 0.3 |e|, see Fig. 5.

The poor description of the frontier orbital energies provided by functionals containing only a small percentage of HF exchange (i.e., TPSSh, B97-1, B3LYP, and PBE0) results in an overestimation of the q^{GS} values. On the other hand, the functionals containing more than 50 %HF exchange (i.e., BHandH, M052X, M062X, M06HF, and the ω-functionals) give q^{GS} values lower than 0.2 e^-. When considering the MP2 value of 0.095 e^- as a reference, it can be seen that the ωB97X functional, with the standard value for ω (0.23 bohr^{-1}), provides reliable results. This is also consistent with the comparison made above between the computed HOMO–LUMO gaps and the ~3.9 eV experimental difference between IP(TTF) and EA(TCNQ), for which the ωB97X functional also provides a reasonable estimate (namely 3.65 eV).

2.4 Large TTF/TCNQ stacks

We now turn to a description of the evolution of the charge transfer between cofacial TTF and TCNQ stacks of increasing size using different DFT functionals. We start here with the displaced geometry of the complex characterized by a 3-Å translation (that yields the largest charge transfer) and include additional TTF and TCNQ molecules in perfect cofacial orientation. This results in a slip-stacked structure between a cofacial stack of TTF and a cofacial stack of TCNQ. The term "layer" used in the following corresponds to one molecule of TTF and one molecule of TCNQ on each side. For example, the stack represented in Fig. 6a has three layers (i.e., 3 TTF and 3 TCNQ).

The evolution with stack size of the dipole moment along the stacking axis, as calculated with BHLYP and a SVP basis set, is presented in Fig. 6a which clearly shows that the dipole moment along the stacking axis reaches unrealistic values of about 90 Debyes in the largest stacks; in addition, no convergence is reached with system size. This behavior appears to be in contradiction with UPS measurements that point to a vacuum level shift around 0.6 eV, associated with a much smaller interface dipole [31, 32]. In order to understand the origin of these large dipole moments, we have performed a Mulliken charge analysis on a stack comprising six layers, see Fig. 7a.

Figure 7a highlights the large delocalization of the charges within the entire stack. The molecules at the interface bear a significant charge that decreases along the stack though without vanishing at the end of the stack. The evolution with stack size of the charge distribution

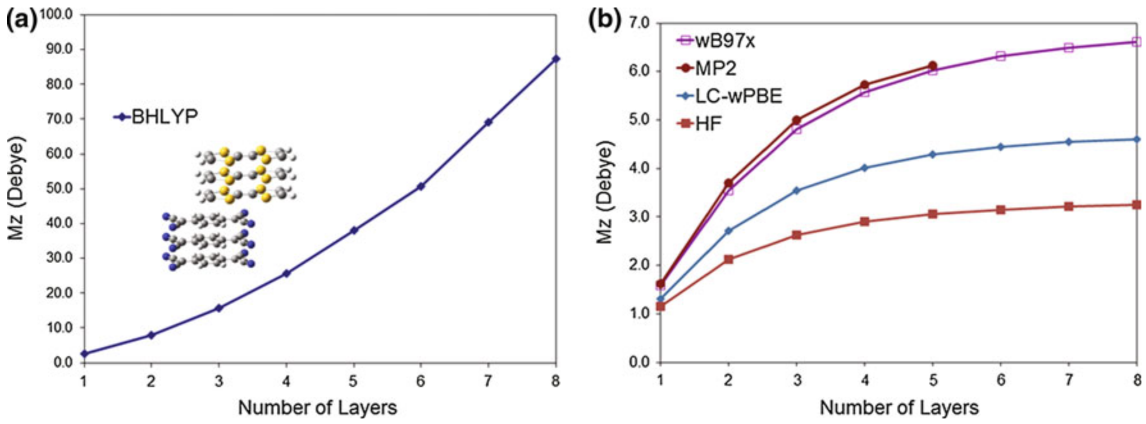

Fig. 6 **a** Evolution of the dipole moment along the stacking axis with an increasing number of layers, as calculated with the BHLYP functional; N layers correspond to a stack including N TTF and N TCNQ molecules. **b** Evolution of the dipole moment along the stacking axis with the number of layers for two long-range-corrected DFT functionals (LC-ωPBE and ωB97X), MP2 and HF methodologies (SVP basis set). This figure is adapted from [10]

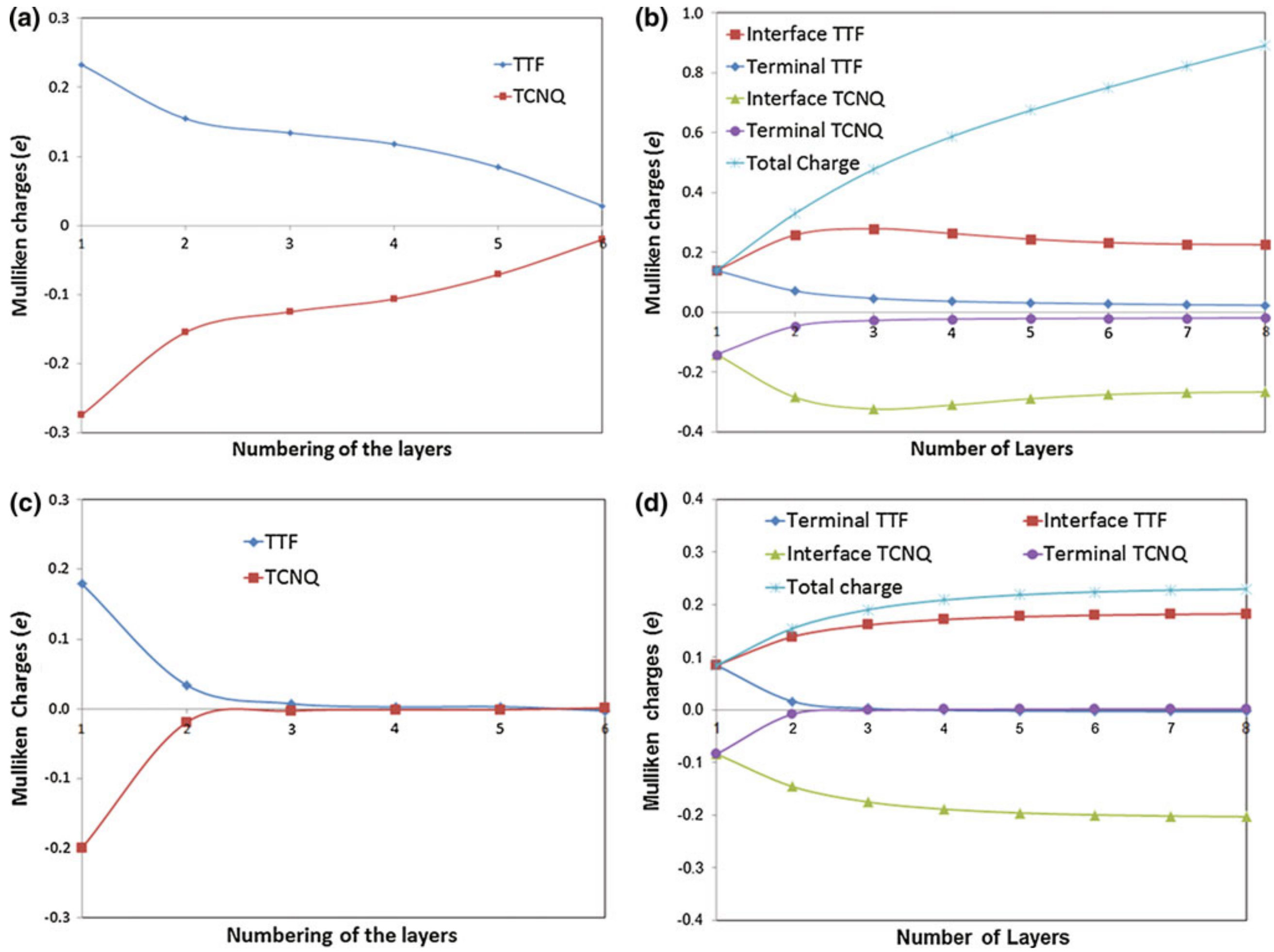

Fig. 7 **a** Evolution of the charge per molecule within a stack of six layers, as calculated with BHLYP (*blue diamond*: charges on TTF—*red square*: charges on TCNQ); layer 1 stands next to the interface. **b** Evolution of the charge (BHLYP) on the interfacial and terminal TTF or TCNQ molecule as a function of stack size, from one to eight layers. **c** Evolution of the charge per molecule within a stack of six layers, as calculated with ωB97X (*blue diamond*: charges on TTF—*red square*: charges on TCNQ); layer 1 stands next to the interface. **d** Evolution of the charge (ωB97X) on the interfacial and the terminal TTF or TCNQ molecule as a function of stack size, from one to eight layers. This figure is adapted from [10]

(BHLYP) in the interfacial and terminal molecules is depicted in Fig. 7b. The charge on the interfacial TTF and TCNQ molecule progressively increases in going from one to three layers and starts slowly decreasing beyond four layers. On the other hand, the charge on the terminal TTF or TCNQ molecule is reduced with the increase in stack size, though a residual charge is always present on the outermost molecule, which explains the continuous increase in dipole moment (Fig. 6a). In addition, the total charge transferred between the two sides of the stack also increases gradually with the size of the system (Fig. 7b). This unphysical evolution of the dipole moment linked with the rapid crossing of $\text{LUMO}_{\text{TCNQ}}$ and HOMO_{TTF} discussed above rules out the use of BHLYP to study extended donor–acceptor complexes. The pronounced charge delocalization is most likely related to the poor description of the long-range interactions in the BHLYP functional. Accordingly, we next turn to LRC functionals and present in Fig. 6b the evolution of the dipole for stacks containing from one to eight layers, using the LC-ωPBE and ωB97X functionals as well as Hartree–Fock and MP2 methods with the SVP basis set.

The dipole moment calculated with LC-ωPBE and ωB97X for an eight-layer stack amounts to 4.61 and 6.61 D, respectively, and appears to have nearly converged. Furthermore, ωB97X fits best the values obtained with MP2 considered as benchmark. Note that the dipole moment calculated with the HF method converges with the number of layers, but tends to an upper limit around 3.25 D for a stack of eight layers due to the HOMO–LUMO gap overestimation which reduces the amount of charge transfer. In order to understand the difference in behavior between BHLYP and ωB97X, the Mulliken charge distribution within a stack of six TTF/TCNQ layers obtained at the ωB97X level (Fig. 7c, d) has been compared with the corresponding distribution at the BHLYP level (Fig. 7a, b).

Figure 7 illustrates that the charges are delocalized along the entire stack with the BHLYP functional. On the other hand, the charge distribution obtained with ωB97X is strongly localized on the interfacial molecules. It gets vanishingly small already on the third layer of the stack and decreases even further away from the interfacial region. This evolution explains the saturation of the dipole moment.

Speculating about the performance of the ωB97X functional and, from a broader point of view, about the reasons of success or failure of a given density functional approximation (DFA), the following should be taken into account. There are a number of inherent shortcomings that may affect DFAs, namely the self-interaction error (SIE), the absence of derivative discontinuities (DD), and the wrong description of the asymptotic behavior of Coulomb terms which are all intricately related. In turn, there are well-documented systematic failures of DFAs that are a priori a direct consequence of these limitations. Understanding the relationship between the shortcomings and failures of DFAs is important in order to look for remedies but not always simple, so that a partial remedy often precedes complete understanding. It is therefore difficult to clearly identify which improvement in the ωB97X functional determines its success in our study. Indeed, the main motivation for using LRC hybrid functionals is initially to cure the wrong asymptotic behavior. To do so, the Hartree–Fock exchange is fully (e.g., LC-ωPBE, ωB97X) or partially (e.g., CAM-B3LYP) restored in the long-range (LR) component of the 1/r potential separated for this purpose in two parts with the help of a partition function. The short-range (SR) component remains treated as before range separation is introduced, with a local (e.g., ωB97) or semilocal (e.g., ωB97X) DFA. The reason for which it is preferable to introduce HF exchange in the LR only rather than everywhere in space can be related to a subtle balance of errors between exchange and correlation components of optimized XC DFAs in the electron-rich SR. Interestingly, it was quickly noticed that some LRC functionals are particularly successful in improving on the DD and SIE shortcomings. Altogether, this contributes to a better description of charge transfer between non-covalently bound fragments [33, 34].

2.5 Two-dimensional interfaces

The use of a simple vertical stack is clearly a very crude model to describe the electronic processes taking place at most organic/organic interfaces. It has been previously shown that the depolarization effects in aggregates of higher dimensionality can strongly reduce the interfacial dipole [35–37]. In order to gauge this effect, we have performed 2D periodic boundary conditions (PBC) calculations along the *x*- and *y*-axes (perpendicular to the stacking axis) to replicate the perfect vertical stack considered in the previous section. The PBC method implemented within Gaussian 09 was used with the functionals and basis set that perform best for the individual stack, that is, ωB97X and SVP. The lattice parameters are equal to a = 7.5 Å and b = 11.5 Å, resulting in a distance of 3.1 Å between the closest atoms of a given molecule and its image. The size of the stack considered for the PBC calculations was limited to four layers of TTF/TCNQ molecules since it has been previously observed (Fig. 7c) that the charges per molecule vanish almost completely beyond three layers.

The calculated dipole moments are collected in Table 1 and drop when moving from 1D to 2D structures. This decrease can be as large as 80 % of the initial value in some cases. The saturation of the dipole moment along the z-axis for a stack of three layers correlates well with the Mulliken charge distributions presented in Table 2. These charges are mostly confined within the interfacial layer when applying PBC in the plane while they are more delocalized for an isolated out-of-plane stack.

Table 1 Evolution of the dipole moment (in Debye) along the z-axis as a function of the number of layers using PBC along the (*x*, *y*) plane versus the dipole moment obtained for the isolated stacks

Number of layers	μ_z (D)—PBC	μ_z (D)—isolated stack
1	0.725	1.593
2	0.764	3.547
3	0.982	4.811
4	0.984	5.570

The values are presented for stacks size from one to four layers

Table 2 Mulliken charges on TTF and TCNQ within the first and second layers for the isolated stack and for the stack repeated along the *x*- and *y*- axes using PBC for stacks from one to four layers

Charges |e|	1	2	3	4
Isolated stack				
TTF layer 2	–	0.016	0.027	0.029
TTF interface	0.084	0.139	0.161	0.129
TCNQ interface	−0.084	−0.146	−0.175	−0.148
TCNQ layer 2	–	−0.008	−0.013	−0.015
PBC				
TTF layer 2	–	0.003	0.005	0.004
TTF interface	0.060	0.071	0.070	0.070
TCNQ interface	−0.060	−0.072	−0.074	−0.074
TCNQ layer 2	–	−0.001	0.000	−0.001

3 Conclusions

This work stresses the importance of choosing the appropriate DFT functional to describe the electronic properties at an organic/organic interface. For this purpose, we have investigated, for model donor/acceptor systems, the evolution of the frontier orbital energies with an increased fraction of exact exchange. There, a linear increase in the HOMO–LUMO gap is observed as a function of the percentage of HF exchange, and the ωB97X functional was identified as the most promising functional in comparison with experimental data. The underestimation of the $\mathrm{HOMO_{TTF}}$/$\mathrm{LUMO_{TCNQ}}$ gap for functionals with a small amount of HF exchange was found to be the dominating factor explaining the drastic overestimation of the partial charge transferred for a TTF/TCNQ complex placed in a cofacial position. In addition, for large stacks of TTF/TCNQ, the BHLYP functional with 50 % HF exchange shows a disproportionate charge delocalization that results in an unrealistic interface dipole. Again, the ωB97X functional gives a much more realistic behavior in comparison with the values obtained with MP2, which underlines the importance of a well-balanced description of the short- and long-range interactions.

Finally, we have highlighted the major impact of the depolarization effects on the amount of charge transferred at a model interface, using periodic boundary conditions. A drop in interface dipole by as much as 80 % of the value obtained for an isolated stack can be observed.

Acknowledgments The authors acknowledge the European project MINOTOR (FP7-NMP-228424) for financial support. The work in Mons is also partly supported by the Interuniversity Attraction Pole IAP 6/27 of the Belgian Federal Government and by the Belgian National Fund for Scientific Research (FNRS/FRFC). J.C. and D.B. are FNRS Research Fellows. The work at Georgia Tech has been partly supported by the Center for Advanced Molecular Photovoltaics, Award No. KUS-C1-015-21, made by King Abdullah University of Science and Technology (KAUST); the Georgia Research Alliance; and the STC Program of the National Science Foundation under Award DMR-0120967.

References

1. Shen C, Kahn A, Hill I (2001) In: Salaneck WR, Seki K, Kahn A, Pireaux J-J (eds) Conjugated polymer and molecular interfaces: science and technology for photonic and optoelectronic applications. Marcel Dekker, New York, pp 351–400
2. Veenstra SC, Jonkman HT (2003) J Polym Sci Pol Phys 41:2549
3. Ishii H, Sugiyama K, Ito E, Seki K (1999) Adv Mater 11:605
4. Braun S, Salaneck WR, Fahlman M (2009) Adv Mater 21:1450–1472
5. Verlaak S, Beljonne D, Cheyns D, Rolin C, Linares M, Castet F, Cornil J, Heremans Adv P (2009) Funct Mater 19:3809–3815
6. Geskin V, Stadler R, Cornil J (2009) Phys Rev B 80:085411
7. Mulliken RS, Person WB (1969) J Am Chem Soc 91:3409
8. Avilov I, Geskin V, Cornil J (2009) Adv Funct Mater 19:624–633
9. Sini G, Sears JS, Brédas J-L (2011) J Chem Theory Comput 7:602–609
10. Van Regemorter T, Guillaume M, Fuchs A, Lennartz C, Geskin V, Beljonne D, Cornil J, J Chem Phys (submitted to)
11. Becke AD (1993) J Chem Phys 98:5648–5652
12. Lee CT, Yang WT, Parr RG (1988) Phys Rev B 37:785–789
13. Tao JM, Perdew JP, Staroverov VN, Scuseria GE (2003) Phys Rev Lett 91:146401
14. Hamprecht FA, Cohen AJ, Tozer DJ, Handy NC (1998) J Chem Phys 109:6264–6271
15. Ernzerhof M, Scuseria GE (1999) J Chem Phys 110:5029–5036
16. Adamo C, Barone V (1999) J Chem Phys 110:6158–6170
17. Boese AD, Martin JML (2004) J Chem Phys 121:3405–3416
18. as implemeted in Gaussian09
19. Zhao Y, Schultz NE, Truhlar DG (2006) J Chem Theory Comput 2:364–382
20. Zhao Y, Truhlar DG (2008) Acc Chem Res 41:157–167
21. Chai JD, Head-Gordon M (2008) J Chem Phys 128:084106
22. Chai JD, Head-Gordon M (2008) Phys Chem Chem Phys 10:6615–6620
23. Rohrdanz MA, Martins KM, Herbert JM (2009) J Chem Phys 130:054112
24. Seidl A, Görling A, Vogl P, Majewski JA, Levy M (1996) Phys Rev B 53:3764
25. Kronik L, Stein T, Refaely-Abramson S, Baer R (2012) J Chem Theory Comput 8:1515
26. Lichtenberger DL, Johnston RL, Hinkelmann K, Suzuki T, Wudl F (1990) J Am Chem Soc 112:3302–3307
27. Compton RN, Cooper CD (1977) J Chem Phys 66:4325–4329
28. Ishibashi S, Kohyama M (2000) Phys Rev B 62:7839
29. Fraxedas J et al (2003) Phys Rev B 68:195115
30. Brédas JL, Calbert JP, da Silva DA, Cornil J (2002) Proc Natl Acad Sci USA 99:5804–5809
31. Braun S, Liu X, Salaneck WR, Fahlman M (2010) Org Electron 11:212–217
32. Yuge R, Miyazaki A, Enoki T, Tamada K, Nakamura F, Hara M (2002) J Phys Chem B 106:6894–6901
33. Vydrov OA, Scuseria GE, Perdew JP (2007) J Chem Phys 126:154109
34. Haunschild R, Henderson TM, Jiménez-Hoyos CA, Scuseria GE (2010) J Chem Phys 133:134116
35. Cornil D, Olivier Y, Geskin V, Cornil J (2007) Adv Funct Mater 17:1143–1148
36. Natan A, Kronik L, Haick H, Tung RT (2007) Adv Mater 19:4103–4117
37. Heimel G, Rissner F, Zojer E (2010) Adv Mater 22:2494–2513

Theor Chem Acc (2012) 131:1284
DOI 10.1007/s00214-012-1284-x

REGULAR ARTICLE

Implementation in the Pyvib2 program of the localized mode method and application to a helicene

Vincent Liégeois · Benoît Champagne

Received: 3 July 2012 / Accepted: 21 September 2012 / Published online: 27 October 2012

Abstract In this paper, after reviewing key elements for simulating and interpreting IR, Raman, VCD, and ROA spectra, as well as after describing the localized mode procedure, we present a graphical user interface to carry out the normal mode localizations and we illustrate its application on the ROA spectra of the [19]helicene molecule. The overall procedure consists of four steps, and therefore, a specific interface has been designed for each of them. The first and most important part of the procedure is the selection of the mode ensemble under which the localization procedure is performed. Then, during our step-by-step guided tour of the localized mode procedure in Pyvib2, we highlight the importance of the ordering of the localized modes and the importance to set correctly the phase factor between the localized modes. Finally, the vibrational coupling matrix ($\tilde{\boldsymbol{\Omega}}$), the intensity coupling matrix ($\tilde{\boldsymbol{I}}$), and the unitary transformation matrix ($\boldsymbol{U}$) can be analyzed from their representation in the different panels. The ROA spectrum of the [19]helicene molecule is dominated by the positive peaks associated with two normal modes. From the localized mode procedure, we have identified the atomic displacements of these modes as a few-node combination of localized modes characterized by atomic displacements that look like the motion of a "claw".

Keywords Vibrational spectroscopy · Raman optical activity · Ab initio calculation · Helicene · Localized mode method

1 Introduction

Vibrational signatures are witnesses of the structure, the reactivity, and the properties of molecules, supramolecules, and polymers. Their large number enables to probe the different moieties and functions of the system whereas it complexifies the spectra, making often difficult a straightforward interpretation. This is why simulation and interpretation tools are receiving more and more interest. About a decade ago, our lab initiated a project on simulating vibrational spectra, looking first at Raman and hyper-Raman spectroscopies [1, 2] and then focusing on sum frequency generation (SFG) [3, 4] and vibrational Raman optical activity (ROA) [5–7]. These approaches were initially based on the time-dependent Hartree-Fock (TDHF) method before electron correlation was treated within density functional theory (DFT) or wavefunction methods. In order to be efficient to unravel experimental spectra, these simulation approaches should, however, be combined with efficient visualization and interpretation tools like the Pyvib2 program [8].

The Pyvib2 program [8], first developed by Fedorovsky in Fribourg university (Switzerland), is a tool to plot and analyze vibrational spectra, and in particular infrared absorption (IR), vibrational circular dichroism (VCD), Raman and ROA spectra. This program was initially designed to display the experimental data from the Raman/ROA spectrometer developed by Hug in Fribourg as well as to represent the calculated spectra from the Gaussian [9] or Dalton [10] packages, providing therefore original tools

Published as part of the special collection of articles celebrating theoretical and computational chemistry in Belgium.

V. Liégeois (✉) · B. Champagne
Laboratoire de Chimie Théorique, Facultés Universitaires
Notre-Dame de la Paix, rue de Bruxelles, 61,
5000 Namur, Belgium
e-mail: vincent.liegeois@fundp.ac.be

to unravel the structure/spectra relationships. Some of its key features are (1) the decomposition scheme [11] introduced by Hug that divides the intensity into group coupling matrices (GCMs) or atomic contribution patterns (ACPs) and (2) the interface to analyze the coupling between normal modes of two similar molecules [12, 13]. This program was released as an open-source program and is used by the scientific community worldwide.

For many years, models have been developed to interpret vibrational spectra, leading to rules of thumb that can be used straightforwardly for a preliminary assignment. Among new methods, the localized mode method developed by Jacob and Reiher [14] is mostly devoted to the analysis of the normal modes of polymer chains, where the localized modes are translated (or rototranslated) along the polymer chain. However, one can also use this procedure to obtain the localized modes associated with systems with point group symmetry. This method consists in localizing the vibrational normal modes through a unitary transformation of the normal modes of one specific band. From this, the total band intensity as well as the coupling between the localized modes that gives rise to the band shape can be analyzed. Unfortunately, this method was, up to now, only implemented in a local python program written by Jacob. Our purpose and the topic of this paper was therefore to extend the functionalities of Pyvib2 by implementing a graphical user interface (GUI) in order to carry out the mode localization and the subsequent analysis. The targets encompass its applicability to (1) any kind of molecules and to (2) a broad range of vibrational spectroscopies. The structure of this new tool implemented into Pyvib2 is presented in this paper together with the theoretical aspects underlying the analysis (Sects. 2, 3). Then, in order to illustrate the procedure and the kind of analysis that can be performed, the ROA signatures of the [19]helicene molecule are analyzed. Owing to their remarkable structural, electronic, and optical properties [15–23], helicenes have attracted a renewed interest. For instance, in a previous study [24], we have found that the ROA spectrum of the [6]helicene molecule was dominated by one positive band at around 1,350 cm^{-1}. Therefore, using this implementation of the localized mode approach, we investigate here the origin of this specific signature for a longer chain. Section 4 provides computational details for the calculation of the vibrational normal modes and the ROA intensities of the [19]helicene molecule. At last, Sect. 5 describes the 4 step procedure: (1) selection of a band of normal modes, (2) mode localization, (3) setting of the phase factor, and (4) analysis of the vibrational and intensity coupling matrices together with the analysis of the specific ROA signature of the [19]helicene molecule, exemplifying the procedure and the kind of results that can be obtained from the GUI interface. Section 6 ends this article by drawing conclusions.

2 Vibrational normal modes and IR, Raman, VCD, and ROA intensities

We introduce here basic aspects of vibrational spectroscopies that will be needed further on to describe the localized mode procedure and their analysis. The vibrational normal modes constitute a basis in which the mass-weighted Hessian, $H^m_{i\alpha,j\beta} = \frac{1}{\sqrt{m_i m_j}}\left(\frac{\partial^2 E}{\partial R_{i\alpha}\partial R_{j\beta}}\right)_0$, is diagonal [25]:

$$\boldsymbol{Q}^T \boldsymbol{H}^m \boldsymbol{Q} = \boldsymbol{H}^q \tag{1}$$

The individual elements of $\boldsymbol{H}^q$ are equal to the squares of the angular frequencies, $H^q_{pp} = \omega_p^2 = 4\ \pi^2\ \nu_p^2$, with ν_p being the pth vibrational frequency. The pth column of the unitary matrix $\boldsymbol{Q}$, denoted $\boldsymbol{Q}_p$, is the pth normal mode in terms of mass-weighted Cartesian coordinates. The components of this mode in terms of Cartesian coordinates $\boldsymbol{Q}^c_p$ is then expressed as $Q^c_{i\alpha,p} = (1/\sqrt{m_i})Q_{i\alpha,p}$. In the matrix terms, the indices i and j denote atomic nuclei while α and β are used for Cartesian components (x, y, z).

Within the harmonic approximation, the Raman, ROA [for a naturally polarized incident light (n) in the scattered circularly polarized (SCP) scheme] [26–28], IR, and VCD [29–32] intensities associated with the pth vibrational normal mode respectively read:

$$\begin{aligned} {}^n\mathrm{d}\sigma(\theta)_{\mathrm{SCP},p} \\ = \frac{1}{90}\frac{1}{c^4}\omega_p^3\omega_0\frac{\hbar}{2\Delta\omega_p}\underbrace{\frac{1}{16\pi^2\epsilon_0^2}[\mathrm{A}\cdot a_p^2 + \mathrm{B}\cdot\beta_p^2]}_{I_p^{\mathrm{Raman}}\ [\mathrm{m}^4\mathrm{Kg}^{-1}]}\mathrm{d}\Omega\ [\mathrm{m}^2/\mathrm{sr}] \end{aligned} \tag{2}$$

$$\begin{aligned} -\Delta^n\mathrm{d}\sigma(\theta)_{\mathrm{SCP},p} = \frac{1}{90}\frac{1}{c^4}\omega_p^3\omega_0 \\ \times\frac{\hbar}{2\Delta\omega_p}\underbrace{\frac{1}{c16\pi^2\epsilon_0^2}[\mathrm{C}\cdot aG'_p + \mathrm{D}\cdot\beta_{\mathrm{G}p}^2 + \mathrm{E}\cdot\beta_{\mathrm{A}p}^2]}_{I_p^{\mathrm{ROA}}\ [\mathrm{m}^4\mathrm{Kg}^{-1}]}\mathrm{d}\Omega\ [\mathrm{m}^2/\mathrm{sr}] \end{aligned} \tag{3}$$

$$\int\limits_{\mathrm{band}_p} \epsilon(\bar{\nu})\mathrm{d}\bar{\nu} = I_p^{\mathrm{IR}} = \frac{N_A\pi}{3c\epsilon_0\hbar}\Delta\bar{\nu}_p D_{0\rightarrow 1_p}\ [\mathrm{m\ mol}^{-1}] \tag{4}$$

$$\int\limits_{\mathrm{band}_p} \Delta\epsilon(\bar{\nu})\mathrm{d}\bar{\nu} = I_p^{\mathrm{VCD}} = \frac{4N_A\pi}{3c^2\epsilon_0\hbar}\Delta\bar{\nu}_p R_{0\rightarrow 1_p}\ [\mathrm{m\ mol}^{-1}] \tag{5}$$

where c is the speed of light in vacuum, $\omega_0 = 2\pi\nu_0$ is the angular frequency of the laser beam, ω_p the angular frequency of the scattered light, $\Delta\omega_p$ ($\Delta\bar{\nu}_p$) corresponds to the vibrational transition associated with the normal coordinate Q_p, ϵ_0 is the electric constant (formerly vacuum permittivity), $\hbar$ is the Planck constant divided by 2π, and N_A is the Avogadro number. $D_{0\rightarrow 1p}$ and $R_{0\rightarrow 1p}$ are the dipole and rotational strength, respectively, while a_p^2, β_p^2, aG'_p, $\beta_{\mathrm{G}p}^2$, $\beta_{\mathrm{A}p}^2$ are the two Raman and the three ROA invariants. A, B, C, D, and E are multiplicative factors that are function of the scattering angle θ. For instance, for the backward-scattering intensity, they amount to 90, 14, 0, 48, and 16, respectively. The Raman I_p^{Raman} and ROA I_p^{ROA} intensities [underbraced quantities in Eqs. (2) and (3)] are expressed in Å^4/amu (SI units: m^4 Kg^{-1}). These units are obtained while using polarizability volumes [33], that is, the polarizability divided by $4\pi\epsilon_0$. In the following, the Raman and ROA intensities will refer to these quantities instead of the scattering cross sections ${}^n\mathrm{d}\sigma(\theta)_{\mathrm{SCP},\ p}$ and $-\Delta^n\mathrm{d}\sigma(\theta)_{\mathrm{SCP},p}$. The main difference is that I_p^{Raman} and I_p^{ROA} intensities do not depend anymore on the vibrational frequency $\Delta\omega_p$.

The Raman (Eq. 2) and ROA (Eq. 3) invariants require the evaluation of the first-order derivatives of three polarizability tensors: $(\partial\alpha/\partial R_{i\alpha})$, $(\partial A/\partial R_{i\alpha})$, and $(\partial G'/\partial R_{i\alpha})$. A review by Buckingham [34] defines all these polarizabilities. The dipole strength and rotational strength entering into the IR (Eq. 4) and VCD (Eq. 5) intensities require the calculation of the atomic polar tensors (APTs, $\boldsymbol{P}_{i\alpha} = \partial\boldsymbol{\mu}/\partial R_{i\alpha}$) and of the atomic axial tensors (AATs, $\boldsymbol{M}_{i\alpha}$), respectively. The Raman and ROA invariants [11] as well as the dipole and rotational strengths [31] have the form:

$$\begin{aligned} a_p^2 &= \frac{1}{9}\sum_{\mu,\nu}\left(\frac{\partial\alpha_{\mu\mu}}{\partial Q_p}\right)_0\left(\frac{\partial\alpha_{\nu\nu}}{\partial Q_p}\right)_0 \\ &= \sum_{i\alpha}\sum_{j\beta} Q^c_{i\alpha,p}Q^c_{j\beta,p}\underbrace{\frac{1}{9}\sum_{\mu,\nu}\left(\frac{\partial\alpha_{\mu\mu}}{\partial R_{i\alpha}}\right)_0\left(\frac{\partial\alpha_{\nu\nu}}{\partial R_{j\beta}}\right)_0}_{V(a^2)_{i\alpha,j\beta}} \end{aligned} \tag{6}$$

$$\begin{aligned} \beta_p^2 &= \frac{1}{2}\sum_{\mu,\nu}\left[3\left(\frac{\partial\alpha_{\mu\nu}}{\partial Q_p}\right)_0\left(\frac{\partial\alpha_{\mu\nu}}{\partial Q_p}\right)_0 - \left(\frac{\partial\alpha_{\mu\mu}}{\partial Q_p}\right)_0\left(\frac{\partial\alpha_{\nu\nu}}{\partial Q_p}\right)_0\right] \\ &= \sum_{i\alpha}\sum_{j\beta} Q^c_{i\alpha,p}Q^c_{j\beta,p} \\ &\quad \underbrace{\frac{1}{2}\sum_{\mu,\nu}\left[3\left(\frac{\partial\alpha_{\mu\nu}}{\partial R_{i\alpha}}\right)_0\left(\frac{\partial\alpha_{\mu\nu}}{\partial R_{j\beta}}\right)_0 - \left(\frac{\partial\alpha_{\mu\mu}}{\partial R_{i\alpha}}\right)_0\left(\frac{\partial\alpha_{\nu\nu}}{\partial R_{j\beta}}\right)_0\right]}_{V(\beta^2)_{i\alpha,j\beta}} \end{aligned} \tag{7}$$

$$\begin{aligned} aG'_p &= \frac{1}{9}\sum_{\mu,\nu}\left(\frac{\partial\alpha_{\mu\mu}}{\partial Q_p}\right)_0\left(\frac{\partial G'_{\nu\nu}}{\partial Q_p}\right)_0 \\ &= \sum_{i\alpha}\sum_{j\beta} Q^c_{i\alpha,p}Q^c_{j\beta,p}\underbrace{\frac{1}{9}\sum_{\mu,\nu}\left(\frac{\partial\alpha_{\mu\mu}}{\partial R_{i\alpha}}\right)_0\left(\frac{\partial G'_{\nu\nu}}{\partial R_{i\beta}}\right)_0}_{V(aG')_{i\alpha,j\beta}} \end{aligned} \tag{8}$$

$$\begin{aligned} \beta_{\mathrm{G}p}^2 &= \frac{1}{2}\sum_{\mu,\nu}\left[3\left(\frac{\partial\alpha_{\mu\nu}}{\partial Q_p}\right)_0\left(\frac{\partial G'_{\mu\nu}}{\partial Q_p}\right)_0 - \left(\frac{\partial\alpha_{\mu\mu}}{\partial Q_p}\right)_0\left(\frac{\partial G'_{\nu\nu}}{\partial Q_p}\right)_0\right] \\ &= \sum_{i\alpha}\sum_{j\beta} Q^c_{i\alpha,p}Q^c_{j\beta,p} \\ &\quad \underbrace{\frac{1}{2}\sum_{\mu,\nu}\left[3\left(\frac{\partial\alpha_{\mu\nu}}{\partial Q_p}\right)_0\left(\frac{\partial G'_{\mu\nu}}{\partial Q_p}\right)_0 - \left(\frac{\partial\alpha_{\mu\mu}}{\partial Q_p}\right)_0\left(\frac{\partial G'_{\nu\nu}}{\partial Q_p}\right)_0\right]}_{V(\beta_{\mathrm{G}}^2)_{i\alpha,j\beta}} \end{aligned} \tag{9}$$

$$\begin{aligned} \beta_{\mathrm{A}p}^2 &= \frac{\omega_0}{2}\sum_{\mu,\nu}\sum_{\lambda,\kappa}\left[\left(\frac{\partial\alpha_{\mu\nu}}{\partial Q_p}\right)_0\left(\frac{\epsilon_{\mu\lambda\kappa}\partial A_{\lambda\kappa\nu}}{\partial Q_p}\right)_0\right] \\ &= \sum_{i\alpha}\sum_{j\beta} Q^c_{i\alpha,p}Q^c_{j\beta,p}\underbrace{\frac{\omega_0}{2}\sum_{\mu,\nu}\sum_{\lambda,\kappa}\left[\left(\frac{\partial\alpha_{\mu\nu}}{\partial Q_p}\right)_0\left(\frac{\epsilon_{\mu\lambda\kappa}\partial A_{\lambda\kappa\nu}}{\partial Q_p}\right)_0\right]}_{V(\beta_{\mathrm{A}}^2)_{i\alpha,j\beta}} \end{aligned} \tag{10}$$

$$D_{0\rightarrow 1_p} = \frac{\hbar}{2\Delta\omega_p}\sum_{i\alpha}\sum_{j\beta} Q^c_{i\alpha,p}Q^c_{j\beta,p}\sum_{\mu} P_{i\alpha,\mu}P_{j\beta,\mu} \tag{11}$$

$$R_{0\rightarrow 1_p} = \hbar^2\sum_{i\alpha}\sum_{j\beta} Q^c_{i\alpha,p}Q^c_{j\beta,p}\Im\left[\sum_{\mu} P_{i\alpha,\mu}M_{j\beta,\mu}\right] \tag{12}$$

In the above summations, the indices μ, ν, λ, and κ are components of the electric or magnetic fields (x, y, z). $\epsilon_{\mu\lambda\kappa}$ is the antisymmetric unit tensor of Levi-Civita. The subscript 0 indicates that the properties are evaluated at the equilibrium geometry.

3 Localization of vibrational normal modes

The localized mode procedure [14] consists in performing a unitary transformation on a subset of k normal modes ($\boldsymbol{Q}^{\mathrm{sub}}$) belonging to a specific band in order to obtain localized modes,

$$\tilde{\boldsymbol{Q}}^{\text{sub}} = \boldsymbol{Q}^{\text{sub}}\boldsymbol{U} \tag{13}$$

where the unitary transformation $\boldsymbol{U}$ is chosen in such a way that it yields the "most localized" modes $\tilde{\boldsymbol{Q}}^{\text{sub}}$, that is, it maximizes a criterion that measures how localized a set of modes $\tilde{\boldsymbol{Q}}^{\text{sub}}$ is. Note that throughout this paper, a tilde is used on all quantities that refer to localized modes instead of vibrational normal modes. Two different localization criteria have been proposed and are available in the program: the "atomic-contribution" and the "distance" criteria [14]. The first one refers to the sum of the squares of the atomic contributions to the modes, while the second is based on the distance between the "centers" of the modes, which can be defined by weighting the atomic coordinates. Nevertheless, both criteria lead to similar patterns of the localized modes.

In the basis of the localized modes, the mass-weighed Hessian is not longer diagonal:

$$\tilde{\boldsymbol{Q}}^{T,\text{sub}}\boldsymbol{H}^{m,\text{sub}}\tilde{\boldsymbol{Q}}^{\text{sub}} = \tilde{\boldsymbol{H}}^{\text{sub}} = \boldsymbol{U}^{T}\boldsymbol{H}^{q,\text{sub}}\boldsymbol{U} \tag{14}$$

The diagonal elements of the matrix $\tilde{\boldsymbol{H}}^{\text{sub}}$ are squares of fictitious angular frequencies $\tilde{H}_{ll}^{\text{sub}} = \tilde{\omega}_l^2 = 4\pi^2\tilde{v}_l^2$ of the localized modes l while the off-diagonal elements $\tilde{H}_{lm}^{\text{sub}}$ can be interpreted as the couplings between the localized modes l and m. However, the numerical values of the couplings are not easy to analyze as they refer to squares of angular frequencies instead of vibrational frequencies. Therefore, it is useful to introduce a new quantity, the vibrational coupling matrix $\tilde{\boldsymbol{\Omega}}$, defined as [14]:

$$\tilde{\boldsymbol{\Omega}} = \boldsymbol{U}^{T}\boldsymbol{\Omega}\boldsymbol{U} \tag{15}$$

where $\boldsymbol{\Omega}$ is the diagonal matrix with $\Omega_{pp} = \bar{v}_p = \omega_p/(2\pi c)$, the wavenumbers of the vibrational normal modes. As seen in [14], the diagonal elements of the coupling matrix $\tilde{\Omega}_{ll}$ can be interpreted as the wavenumbers of the localized modes, while the off-diagonal elements $\tilde{\Omega}_{lm}$ can be understood as coupling constants. It should be noted that the frequencies of the localized modes obtained as the diagonal elements of $\tilde{\boldsymbol{\Omega}}$ are, in general, different from those calculated as the square root of the diagonal elements of $\tilde{\boldsymbol{H}}^{\text{sub}}$, even if the differences between the two are generally quite small. The maximum difference amounts to 1.2 cm^{-1} in our test case (see below).

We can now write the expression of the Raman, ROA, IR, and VCD intensities associated with these localized modes simply by replacing in Eqs. (6) to (12) the normal mode coordinates by the localized mode coordinates. Similarly, the intensity coupling matrix ($\tilde{\boldsymbol{I}}$) is defined as the intensity between any l and k pair of localized modes:

$$\tilde{I}_{lm}^{\text{Raman}} = \frac{1}{16\pi^2\epsilon_0^2}\sum_{i\alpha}\sum_{j\beta}\tilde{Q}_{i\alpha,l}^{c}\tilde{Q}_{j\beta,m}^{c}[\text{A}\cdot V(a^2)_{i\alpha,j\beta} + \text{B} \cdot V(\beta^2)_{i\alpha,j\beta}][\text{m}^4\text{Kg}^{-1}] \tag{16}$$

$$\tilde{I}_{lm}^{\text{ROA}} = \frac{1}{c16\pi^2\epsilon_0^2}\sum_{i\alpha}\sum_{j\beta}\tilde{Q}_{i\alpha,l}^{c}\tilde{Q}_{j\beta,m}^{c}[\text{C}\cdot V(aG')_{i\alpha,j\beta} + \text{D}\cdot V(\beta_{\text{G}}^2)_{i\alpha,j\beta} + \text{E}\cdot V(\beta_{\text{A}}^2)_{i\alpha,j\beta}]\ [\text{m}^4\text{Kg}^{-1}] \tag{17}$$

$$\tilde{I}_{lm}^{\text{IR}} = \frac{N_A}{12c^2\epsilon_0}\sum_{i\alpha}\sum_{j\beta}\tilde{Q}_{i\alpha,l}^{c}\tilde{Q}_{j\beta,m}^{c}\sum_{\mu}P_{i\alpha,\mu}P_{j\beta,\mu}\ [\text{m mol}^{-1}] \tag{18}$$

$$\tilde{I}_{lm}^{\text{VCD}} = \frac{4N_A\pi\hbar}{3c^2\epsilon_0}\sqrt{\Delta\bar{v}_l\Delta\bar{v}_m} \times \sum_{i\alpha}\sum_{j\beta}\tilde{Q}_{i\alpha,l}^{c}\tilde{Q}_{j\beta,m}^{c}\Im\left[\sum_{\mu}P_{i\alpha,\mu}M_{j\beta,\mu}\right]\ [\text{m mol}^{-1}] \tag{19}$$

The diagonal elements of this matrix, $\tilde{I}_{ll}$, are referred to as the intensities of the lth localized modes, while the off-diagonal values, $\tilde{I}_{lm}$, are the intensity coupling terms. The intensity coupling matrix $\tilde{\boldsymbol{I}}$ can be used to understand the shapes of the band (i.e., how the intensity of a band is spread over all the normal modes, see also below). Indeed, the intensity associated with each vibrational normal mode (I_p) of one band is related to the intensity coupling matrix $\tilde{\boldsymbol{I}}$ and to the unitary transformation $\boldsymbol{U}$:

$$I_p = \sum_{lm}U_{pl}U_{pm}\tilde{I}_{lm} \tag{20}$$

Since the trace of a matrix is conserved along a unitary transformation (Eq. 20), the total intensity of the band $\sum_p I_p$ is equal to the sum of the intensities of the localized modes, $\sum_l \tilde{I}_{ll}$. Moreover, since the atomic displacements of the localized modes are usually similar, so are their intensities. The total intensity of the band can therefore be investigated simply by analyzing the intensity of one localized mode. For the band shape, the intensity coupling matrix $\tilde{\boldsymbol{I}}$ together with the transformation matrix $\boldsymbol{U}$ (eigenvectors of $\tilde{\boldsymbol{\Omega}}$) describes how the intensities of the localized modes are distributed in the vibrational normal modes. One should note, however, that the intensity coupling matrix $\tilde{I}_{lm}^{\text{VCD}}$ for the VCD intensity depends on the geometric mean of the wavenumbers of the two localized modes l and m. Therefore, Eq. (20) is not strictly fulfilled (neither is the equality between the sum of the intensities over the normal modes and the localized modes) even if the deviation is quite small.

4 Computational aspects

In the following, we illustrate the implementation of the localized mode procedure for the analysis of the Raman and ROA spectra of the [19]helicene molecule. The structure as well as the vibrational frequencies and normal modes was determined using the analytical coupled-perturbed Kohn-Sham [35] procedure together with the 6-31G* basis set [36]. The hybrid B3LYP exchange-correlation functional was selected owing to its recognized performance for calculating vibrational frequencies [37]. However, to account for the systematic error due to approximate exchange-correlation functional and anharmonicity effects, a multiplicative factor of 0.96 [37–39] was employed to scale the B3LYP vibrational frequencies.

The geometry derivatives of the three polarizability tensors entering into the Raman and ROA invariants were calculated using the rDPS:3-21G (reduced diffuse polarization function and shell augmented) basis set introduced by Zuber and Hug [40]. It consists of the 3–21++G [41] basis set augmented by a set of p diffuse functions (of exponent 0.2) on the hydrogen atoms. The derivatives are evaluated at the TDHF level for the Cartesian displacements [5] and are transformed afterward into the geometrical derivatives with respect to the vibrational normal coordinates, with the normal coordinates calculated using the CPKS procedure. The calculations were performed using the GAUSSIAN 09 [9] quantum chemistry packages.

While the electron correlation effects in the simulation of vibrational spectroscopies are, till now, most of the time treated by DFT [42–46], other approaches such as coupled-cluster are becoming available [47–49]. Nevertheless, such methods are still in their early stages and are restricted to small molecules. The Pyvib2 program is, however, not limited to any kind of method and can thus analyze the vibrational signatures coming for any quantum chemistry package providing the implementation of a parser.

A typical incident light wavelength of 532 nm was adopted in all optical tensor calculations. The Maxwell–Boltzmann ($1/[1 - e^{(-\hbar\Delta\omega_p/(k_b T))}]$) factor with $T = 298.15$ K is used to account for the T-dependence of the populations of the vibrational levels.

5 Localized mode method using pyvib2

The procedure to obtain and analyze the localized modes consists of four different steps:

1. The selection of the normal modes that constitute an ensemble (a band) on which we perform the unitary transformation.
2. The mode localization for a given choice of localized criterion (the atomic-contribution or the distance criterion).
3. The setting of the phase factor for each localized mode.
4. The analysis of the vibrational and intensity coupling matrices.

Each of these steps requires a specific input from the user and therefore a specific graphical interface has been developed for each step.

5.1 Determination of the normal mode ensemble

As explained earlier, the localization procedure consists in performing a unitary transformation on a subset of normal

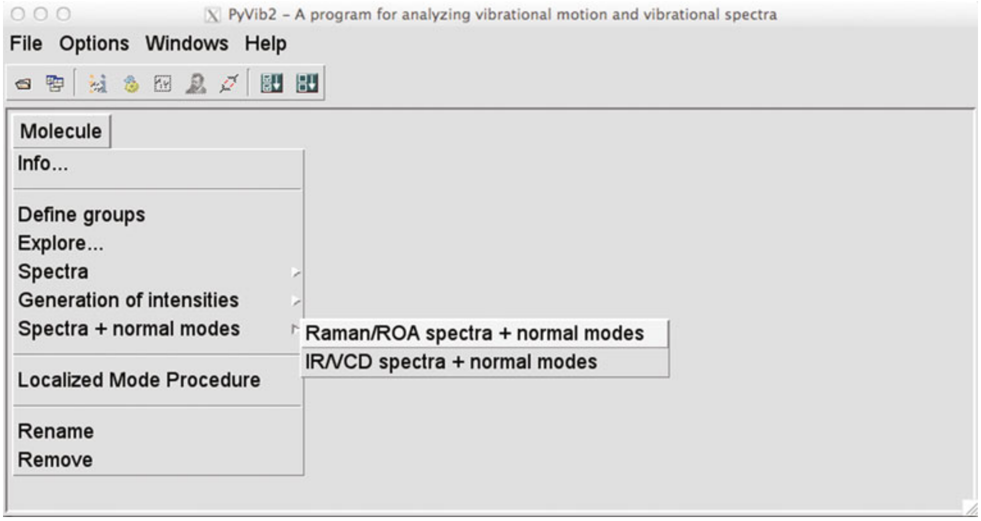

Fig. 1 Screenshot of the options available for analyzing a molecule

modes that belong to a band. This means that we need to select an ensemble of normal modes having similar atomic displacements along the chain, though different phases between the different units of the chain. Most of the time, these modes have similar wavenumbers, but for molecules constituted of only carbon and hydrogen atoms, the frontier between two successive bands can be difficult to assess. Nevertheless, the interface enables to visualize simultaneously the vibrational normal modes and the simulated Raman and ROA spectra. One should note that a similar interface has also been developed for the IR and VCD spectra.

After loading the file into the program, different options are available, see Fig. 1. The `Explore` option loads a window to represent the atomic displacements of the vibrational normal modes, while the `Spectra` option displays the various vibrational spectra. The `Generation of Intensities` option uses the decomposition scheme [11] and renders the group coupling matrices (GCMs) and the atomic contribution patterns (ACPs). The

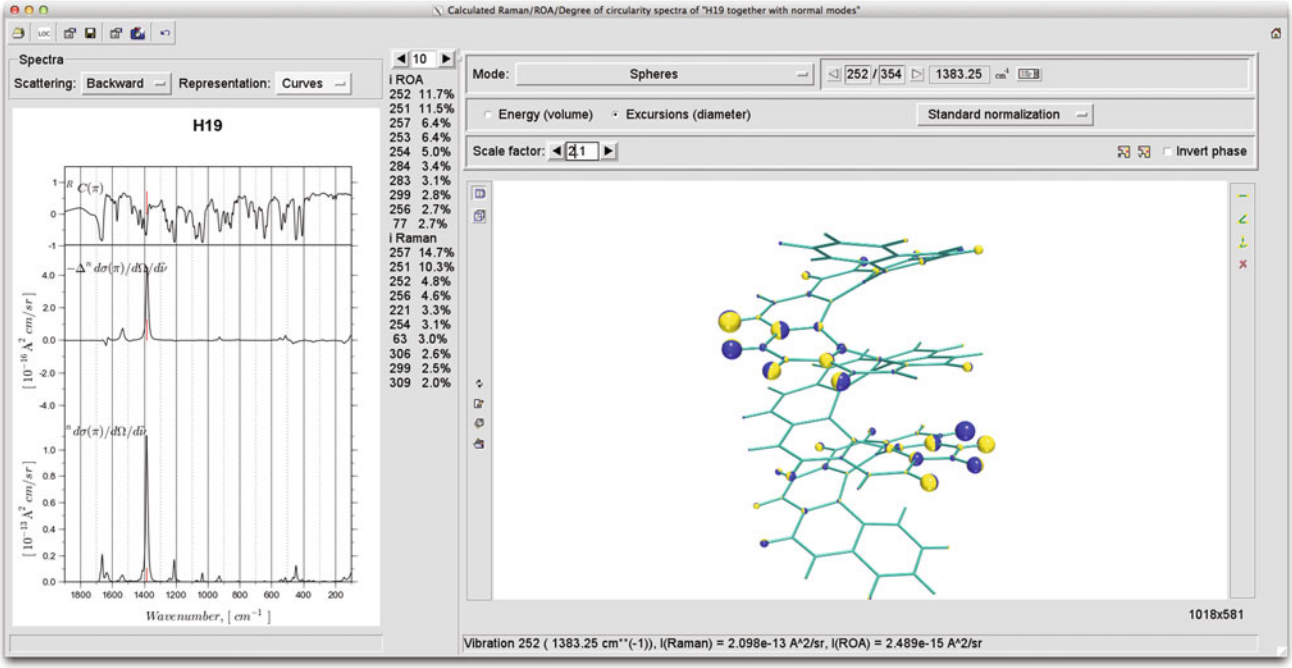

Calculated Raman/ROA/Degree of circularity spectra of "H19 together with normal modes"

Spectra
Scattering: Backward
Representation: Curves

10
i ROA
252 11.7%
251 11.5%
257 6.4%
253 6.4%
254 5.0%
284 3.4%
283 3.1%
299 2.8%
256 2.7%
77 2.7%
i Raman
257 14.7%
251 10.3%
252 4.8%
256 4.6%
221 3.3%
254 3.1%
63 3.0%
306 2.6%
299 2.5%
309 2.0%

Mode: Spheres
252 / 354 1383.25 cm-1
○ Energy (volume) ● Excursions (diameter)
Standard normalization
Scale factor: 2.1
☐ Invert phase

1018x581

Vibration 252 (1383.25 cm**(-1)), I(Raman) = 2.098e-13 A^2/sr, I(ROA) = 2.489e-15 A^2/sr

Fig. 2 Screenshot of the window that plots the spectra together with the representation of the atomic displacements of a selected vibrational normal mode

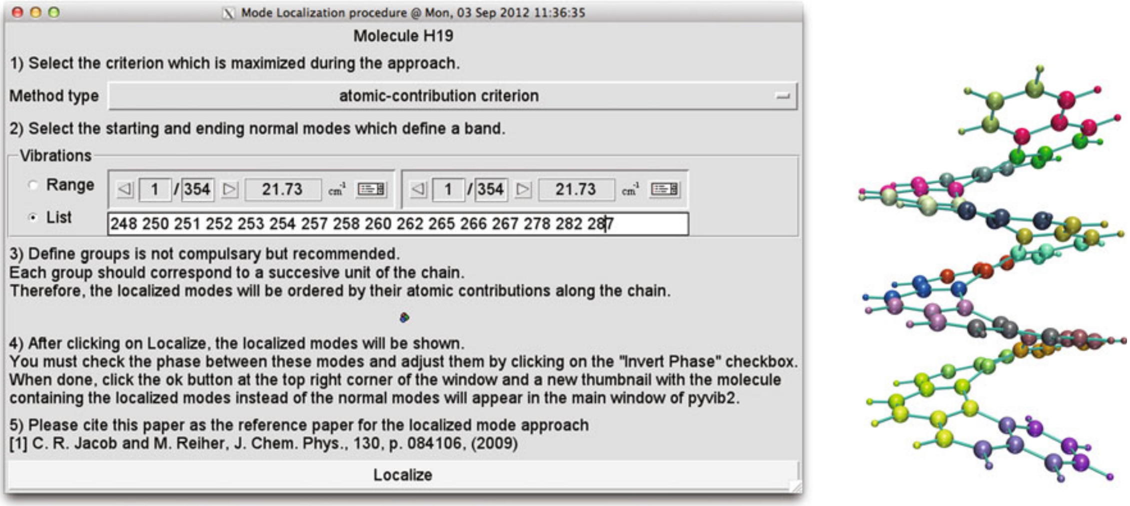

Mode Localization procedure @ Mon, 03 Sep 2012 11:36:35

Molecule H19

1) Select the criterion which is maximized during the approach.

Method type: atomic-contribution criterion

2) Select the starting and ending normal modes which define a band.

Vibrations
○ Range 1 / 354 21.73 cm-1 1 / 354 21.73 cm-1
● List 248 250 251 252 253 254 257 258 260 262 265 266 267 278 282 287

3) Define groups is not compulsary but recommended.
Each group should correspond to a succesive unit of the chain.
Therefore, the localized modes will be ordered by their atomic contributions along the chain.

4) After clicking on Localize, the localized modes will be shown.
You must check the phase between these modes and adjust them by clicking on the "Invert Phase" checkbox.
When done, click the ok button at the top right corner of the window and a new thumbnail with the molecule containing the localized modes instead of the normal modes will appear in the main window of pyvib2.

5) Please cite this paper as the reference paper for the localized mode approach
[1] C. R. Jacob and M. Reiher, J. Chem. Phys., 130, p. 084106, (2009)

Fig. 3 *Left* Screenshot of the window to launch the "localized mode procedure"; *Right* groups definition

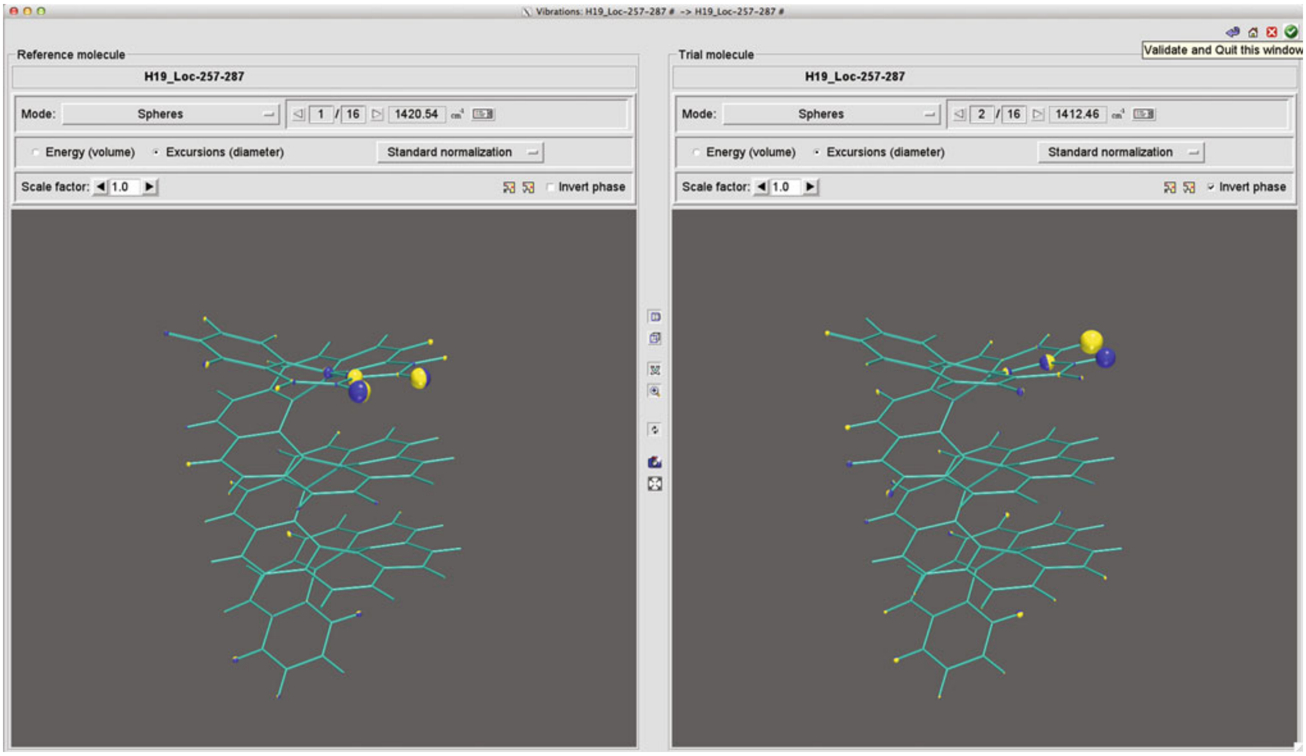

Vibrations: H19_Loc-257-287 # -> H19_Loc-257-287 #

Reference molecule: H19_Loc-257-287

Mode: Spheres 1 / 16 1420.54 cm⁻¹

○ Energy (volume) ● Excursions (diameter) Standard normalization

Scale factor: 1.0 ☐ Invert phase

Trial molecule: H19_Loc-257-287

Mode: Spheres 2 / 16 1412.46 cm⁻¹

○ Energy (volume) ● Excursions (diameter) Standard normalization

Scale factor: 1.0 ☑ Invert phase

Fig. 4 Screenshot of the window to set the phase factors on the localized modes

`Spectra normal modes` option displays a window to analyze simultaneously the spectra with the normal modes. Figure 2 is an example of such window where mode 252 is selected. On the left, one can see the ROA (middle) and Raman (bottom) spectra together with the degree of circularity (top). In both spectra, the red bars indicate the intensity of the selected sketched mode. The list displayed in the center of the window gives the most intense modes for both the Raman and ROA together with the percentage of their intensity relative to the sum of the intensity of the modes that appears within the wavenumber range of the spectra. For the [19]helicene molecule, the Raman and ROA spectra are dominated by two positive peaks corresponding to modes 251 and 252, which belong to one intense positive band. This signature is similar to the one observed previously for a smaller [6]helicene [24]. On the right side of the window, the atomic displacements of the selected mode are displayed using spheres on each atom. The direction of the displacement of an atom is given by the line joining the two poles of different color while the magnitude of the displacement is given by the radius of the sphere. The atomic displacements associated with the most intense mode (mode 252) involve the stretching of the C–C bond between two neighboring rings and the wagging of two hydrogen atoms at the exterior of the helicene close to the C–C stretching bond. The displacements of these two H atoms and these C atoms look therefore like a claw. The same displacement is found in every junction of two neighboring rings, some of them with the same phase and some with the opposite phase. This same pattern is also found in other modes but with different phases between the different sites. As we have 19 rings, we should find something like 18 similar modes. After close inspection of the vibrational normal modes in the vicinity of modes 251 and 252, it was possible to select 16 similar modes. The two missing modes come from the fact that at the extremity of the chain, this “claw” displacements are mixed with the wagging of the H atoms. The 16 modes numbers (and wavenumbers) are 248 (1,378.8 cm^{-1}), 250 (1,379.6 cm^{-1}), 251 (1,381.6 cm^{-1}), 252 (1,383.3 cm^{-1}), 253 (1,384.7 cm^{-1}), 254 (1,387.2 cm^{-1}), 257 (1,389.4 cm^{-1}), 258 (1,392.8 cm^{-1}), 260 (1,397.1 cm^{-1}), 262 (1,403.0 cm^{-1}), 265 (1,415.1 cm^{-1}), 266 (1,426.4 cm^{-1}), 267 (1,438.7 cm^{-1}), 278 (1,502.6 cm^{-1}), 282 (1,526.9 cm^{-1}), 287 (1,556.8 cm^{-1}).

5.2 Localized mode procedure

Figure 3 illustrates the window that launches the localized mode procedure and is obtained after selecting `Localized Mode Procedure` in Fig. 1. The first step in the procedure consists in selecting the localization criterion.

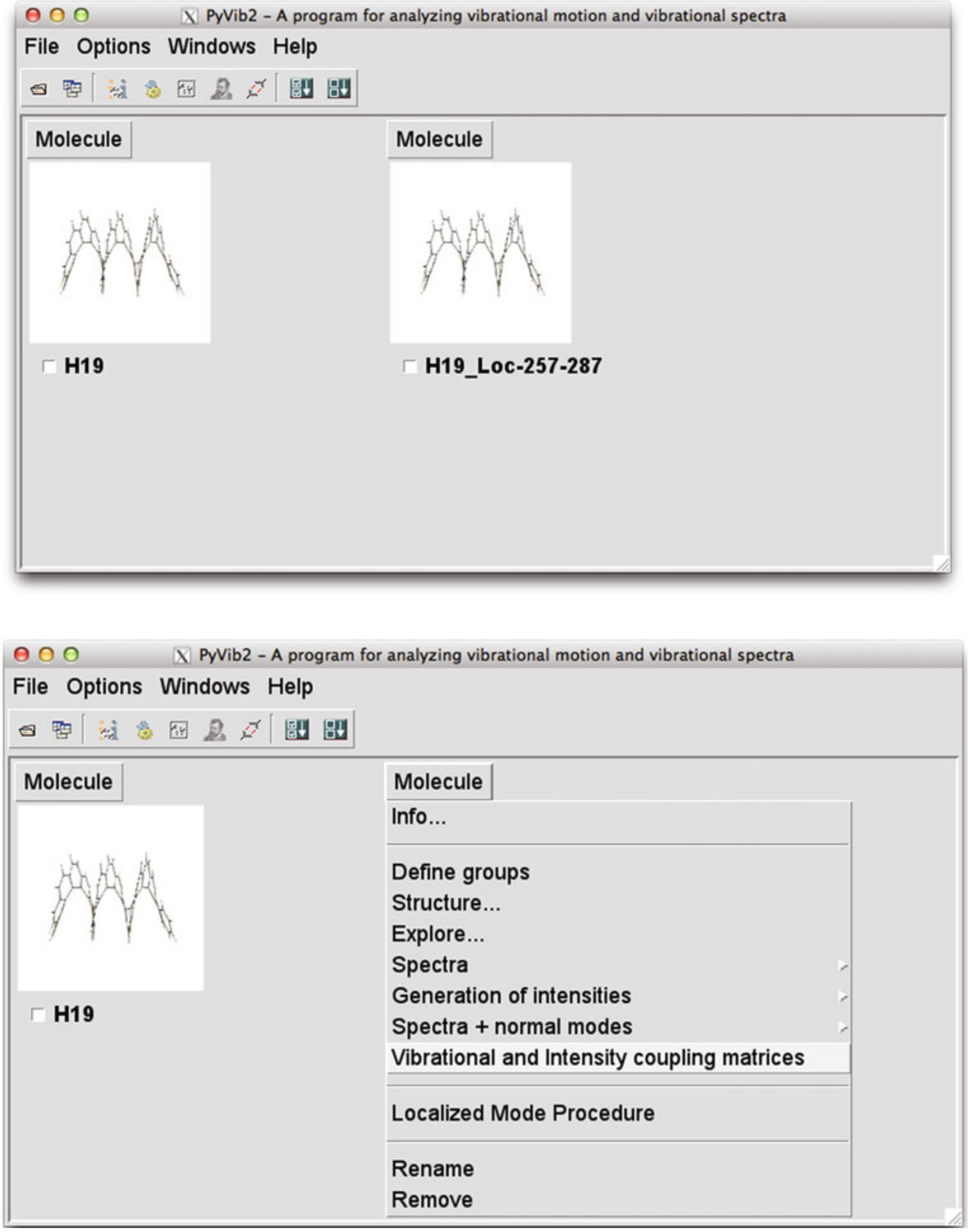

Fig. 5 Screenshot of the main window after the mode localization has been performed

Two choices are available: the "atomic-contribution" criterion and the "distance" criterion [14] but in practice, both of them give similar localized modes and the "atomic-contribution" criterion is used in our example. The next step is to input the ensemble of normal modes among which the localization is performed. Either a continuous range of modes or a list of "individual" modes can be given. In our example, we give the list of the 16 modes reported before. The last step before clicking on the `Localize` button is the definition of groups. This step is not compulsory but highly recommended to help analyzing the vibrational and intensity coupling matrices ($\tilde{\boldsymbol{\Omega}}$ and $\tilde{\boldsymbol{I}}$). Indeed, by default, the localized modes obtained have no particular order, that is, the first localized mode in the list can have atomic displacements in the middle of the chain, while the next localized mode in the list can have atomic contribution on one extremity of the chain. However, since it is more handy that the successive localized modes involve atomic displacements localized on successive neighboring sites, we therefore define successive groups composed of atoms ranging from one side of the chain to the other. Figure 3 exemplifies the groups defined for the [19]helicene with "group 1" being the 3 C atoms and their H atoms on one extremity of the chain, "group 2" containing 4 C atoms and 2 H atoms just below "group 1", and so one up to "group 20", which contains the last 3 C atoms and their H atoms at the other extremity of the molecule. The localized mode are ordered in such a way that localized mode 1 has most of its atomic contributions on the first groups while the last localized mode presents atomic contributions mostly centered on the last groups. The number of groups can be different from the number of modes to localize but best orderings are obtained if the atoms constituting a group are the same as those which contribute to the localized modes. This is the reason why the different groups (except the two terminal groups) are made of 4 C atoms and two H atoms, similar to the "claw" displacement corresponding to the normal mode pattern. It is important to notice that the group definition does not influence the generation of the localized mode (only the criterion does) but only provides a way to order them with respect to their position along the chain.

5.3 Set the phase factors on the localized modes

In addition to the ordering of the localized mode, it is important to set the correct phase factor on the localized modes. Indeed, in the analysis, the localized modes constitute a basis set in which each normal mode can be expressed. For instance, the sign of the vibrational coupling between two localized modes is changed if their relative phase is inverted. It is therefore crucial that two localized modes contain similar atomic displacements (without phase shift) but translated (or rototranslated) to the next unit of the chain. However, since the normal mode (as eigenvectors of the mass-weighted Hessian) are not affected by a change of sign of all their contributions, so are the localized modes. Therefore, at the end of the localized mode procedure, a first attempt to set the phase is made by defining the vibrational coupling between two successive neighbors to be positive. Nevertheless, one cannot predict the sign of these couplings, and we therefore need to confirm manually the phase factor for all the localized modes relative to one localized mode taken as reference. Figure 4 shows the interface that was developed for this purpose. The left panel represents the atomic displacements of mode 1 taken as reference (any other mode could have been chosen), while the right panel shows the atomic displacements of another mode. In this particular example, in order to obtain in-phase atomic displacements for modes 1 and 2, the `Invert phase` box was checked. For all the modes except the reference one, the atomic displacements have to be examined and the `Invert phase` box checked if required. When all the modes are inspected, we can click on the top right button that says `Validate and Quit this window`. A new "thumbnail" with the molecule will be created on the main window (Fig. 5). This molecule is different from the original one by the fact that the transformation matrix between the Cartesian coordinates and the mode coordinates is the $\tilde{\boldsymbol{Q}}_l$ matrix, which defines the set of localized modes. The same analyses as for the original molecule can be conducted here, but wherever normal modes are involved ($\boldsymbol{Q}_p$), the localized modes ($\tilde{\boldsymbol{Q}}_l$) are used instead. For instance, using the `Spectra` option will plot the peaks associated with the localized modes (Eqs. 16–19). Moreover, an additional option is available under the name `Vibrational and Intensity coupling matrices` which provides a new window (Figs. 6, 7, 8, 9) with four panels to analyze the localized modes.

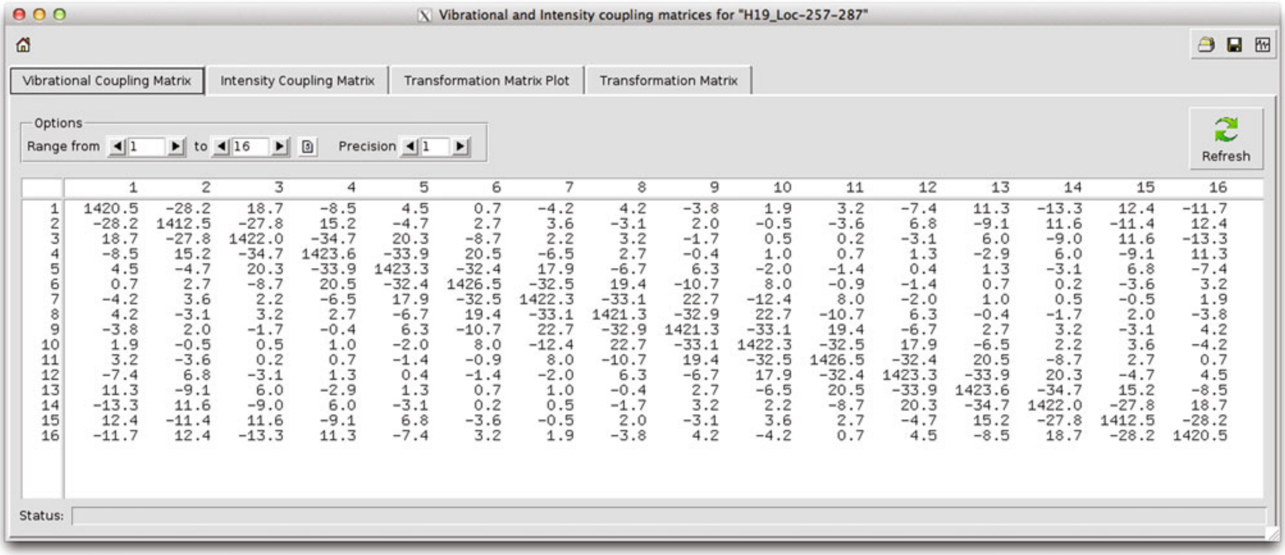

Range from 1 to 16

Precision 1

	1	2	3	4	5	6	7	8	9	10	11	12	13	14	15	16
1	1420.5	-28.2	18.7	-8.5	4.5	0.7	-4.2	4.2	-3.8	1.9	3.2	-7.4	11.3	-13.3	12.4	-11.7
2	-28.2	1412.5	-27.8	15.2	-4.7	2.7	3.6	-3.1	2.0	-0.5	-3.6	6.8	-9.1	11.6	-11.4	12.4
3	18.7	-27.8	1422.0	-34.7	20.3	-8.7	2.2	3.2	-1.7	0.5	0.2	-3.1	6.0	-9.0	11.6	-13.3
4	-8.5	15.2	-34.7	1423.6	-33.9	20.5	-6.5	2.7	-0.4	1.0	0.7	1.3	-2.9	6.0	-9.1	11.3
5	4.5	-4.7	20.3	-33.9	1423.3	-32.4	17.9	-6.7	6.3	-2.0	-1.4	0.4	1.3	-3.1	6.8	-7.4
6	0.7	2.7	-8.7	20.5	-32.4	1426.5	-32.5	19.4	-10.7	8.0	-0.9	-1.4	0.7	0.2	-3.6	3.2
7	-4.2	3.6	2.2	-6.5	17.9	-32.5	1422.3	-33.1	22.7	-12.4	8.0	-2.0	1.0	0.5	-0.5	1.9
8	4.2	-3.1	3.2	2.7	-6.7	19.4	-33.1	1421.3	-32.9	22.7	-10.7	6.3	-0.4	-1.7	2.0	-3.8
9	-3.8	2.0	-1.7	-0.4	6.3	-10.7	22.7	-32.9	1421.3	-33.1	19.4	-6.7	2.7	3.2	-3.1	4.2
10	1.9	-0.5	0.5	1.0	-2.0	8.0	-12.4	22.7	-33.1	1422.3	-32.5	17.9	-6.5	2.2	3.6	-4.2
11	3.2	-3.6	0.2	0.7	-1.4	-0.9	8.0	-10.7	19.4	-32.5	1426.5	-32.4	20.5	-8.7	2.7	0.7
12	-7.4	6.8	-3.1	1.3	0.4	-1.4	-2.0	6.3	-6.7	17.9	-32.4	1423.3	-33.9	20.3	-4.7	4.5
13	11.3	-9.1	6.0	-2.9	1.3	0.7	1.0	-0.4	2.7	-6.5	20.5	-33.9	1423.6	-34.7	15.2	-8.5
14	-13.3	11.6	-9.0	6.0	-3.1	0.2	0.5	-1.7	3.2	2.2	-8.7	20.3	-34.7	1422.0	-27.8	18.7
15	12.4	-11.4	11.6	-9.1	6.8	-3.6	-0.5	2.0	-3.1	3.6	2.7	-4.7	15.2	-27.8	1412.5	-28.2
16	-11.7	12.4	-13.3	11.3	-7.4	3.2	1.9	-3.8	4.2	-4.2	0.7	4.5	-8.5	18.7	-28.2	1420.5

Fig. 6 Screenshot of the panel that analyzes the vibrational coupling matrix $\tilde{\boldsymbol{\Omega}}$

Table 1 Vibrational coupling matrix $\tilde{\mathbf{\Omega}}$

	1	2	3	4	5	6	7	8	9	10	11	12	13	14	15	16
1	1,420.5	−28.2	18.7	−8.5	4.5	0.7	−4.2	4.2	−3.8	1.9	3.2	−7.4	11.3	−13.3	12.4	−11.7
2	−28.2	1,412.5	−27.8	15.2	−4.7	2.7	3.6	−3.1	2.0	−0.5	−3.6	6.8	−9.1	11.6	−11.4	12.4
3	18.7	−27.8	1,422.0	−34.7	20.3	−8.7	2.2	3.2	−1.7	0.5	0.2	−3.1	6.0	−9.0	11.6	−13.3
4	−8.5	15.2	−34.7	1,423.6	−33.9	20.5	−6.5	2.7	−0.4	1.0	0.7	1.3	−2.9	6.0	−9.1	11.3
5	4.5	−4.7	20.3	−33.9	1,423.3	−32.4	17.9	−6.7	6.3	−2.0	−1.4	0.4	1.3	−3.1	6.8	−7.4
6	0.7	2.7	−8.7	20.5	−32.4	1,426.5	−32.5	19.4	−10.7	8.0	−0.9	−1.4	0.7	0.2	−3.6	3.2
7	−4.2	3.6	2.2	−6.5	17.9	−32.5	1,422.3	−33.1	22.7	−12.4	8.0	−2.0	1.0	0.5	−0.5	1.9
8	4.2	−3.1	3.2	2.7	−6.7	19.4	−33.1	1,421.3	−32.9	22.7	−10.7	6.3	−0.4	−1.7	2.0	−3.8
9	−3.8	2.0	−1.7	−0.4	6.3	−10.7	22.7	−32.9	1,421.3	−33.1	19.4	−6.7	2.7	3.2	−3.1	4.2
10	1.9	−0.5	0.5	1.0	−2.0	8.0	−12.4	22.7	−33.1	1,422.3	−32.5	17.9	−6.5	2.2	3.6	−4.2
11	3.2	−3.6	0.2	0.7	−1.4	−0.9	8.0	−10.7	19.4	−32.5	1,426.5	−32.4	20.5	−8.7	2.7	0.7
12	−7.4	6.8	−3.1	1.3	0.4	−1.4	−2.0	6.3	−6.7	17.9	−32.4	1,423.3	−33.9	20.3	−4.7	4.5
13	11.3	−9.1	6.0	−2.9	1.3	0.7	1.0	−0.4	2.7	−6.5	20.5	−33.9	1,423.6	−34.7	15.2	−8.5
14	−13.3	11.6	−9.0	6.0	−3.1	0.2	0.5	−1.7	3.2	2.2	−8.7	20.3	−34.7	1,422.0	−27.8	18.7
15	12.4	−11.4	11.6	−9.1	6.8	−3.6	−0.5	2.0	−3.1	3.6	2.7	−4.7	15.2	−27.8	1,412.5	−28.2
16	−11.7	12.4	−13.3	11.3	−7.4	3.2	1.9	−3.8	4.2	−4.2	0.7	4.5	−8.5	18.7	−28.2	1,420.5

Table 2 Unitary transformation matrix U_{pl} values

	1,379.8	1,380.9	1,383.8	1,386.4	1,388.1	1,392.3	1,397.4	1,408.2	1,427.5	1,484.5	1,502.1	1,546.8
1,422.0	18.83	19.37	21.60	−33.79	9.67	32.11	−38.08	36.15	−37.99	40.21	22.75	−14.24
1,423.6	33.52	28.66	44.03	−34.37	23.45	18.55	1.75	−8.55	30.61	−37.12	−34.72	21.07
1,423.3	31.22	6.02	38.79	14.30	32.51	−38.89	35.04	−27.26	−0.63	22.48	39.17	−26.43
1,426.5	8.27	−29.34	24.39	38.27	31.91	−29.90	−12.46	39.78	−31.12	0.73	−36.41	32.68
1,422.3	−21.06	−47.46	20.22	13.19	33.20	24.42	−38.90	0.92	37.11	−21.09	19.79	−35.99
1,421.3	−45.12	−25.55	9.33	−28.89	34.35	24.90	25.51	−35.97	−16.56	32.47	−5.10	35.93
1,421.3	−45.10	25.57	−9.34	−28.88	34.33	−24.92	25.52	35.97	−16.56	−32.47	−5.10	−35.93
1,422.3	−21.03	47.47	−20.22	13.20	33.18	−24.45	−38.89	−0.92	37.11	21.09	19.79	35.99
1,426.5	8.29	29.33	−24.40	38.26	31.92	29.89	−12.47	−39.78	−31.12	−0.72	−36.40	−32.68
1,423.3	31.24	−6.04	−38.79	14.29	32.54	38.88	35.03	27.25	−0.63	−22.49	39.17	26.43
1,423.6	33.53	−28.67	−44.02	−34.37	23.43	−18.57	1.75	8.55	30.61	37.13	−34.71	−21.07
1,422.0	18.83	−19.37	−21.58	−33.79	9.65	−32.14	−38.08	−36.16	−37.99	−40.21	22.74	14.24
Int:	1.57e+00	1.01e+01	2.66e+00	1.02e+01	9.50e+00	6.45e−01	1.21e+00	2.24e−01	3.16e−01	2.38e−01	−1.55e−01	4.82e−01
Percent:	4.20	27.09	7.14	27.30	25.50	1.73	3.24	0.60	0.85	0.64	0.42	1.29

The localized modes *l* constitute the lines of the table, while the columns are the “optimum” normal modes *p*. The ROA backward-scattering intensities (in Å^4/amu) associated with the “optimum” normal modes are given at the bottom of the table together with their percentage

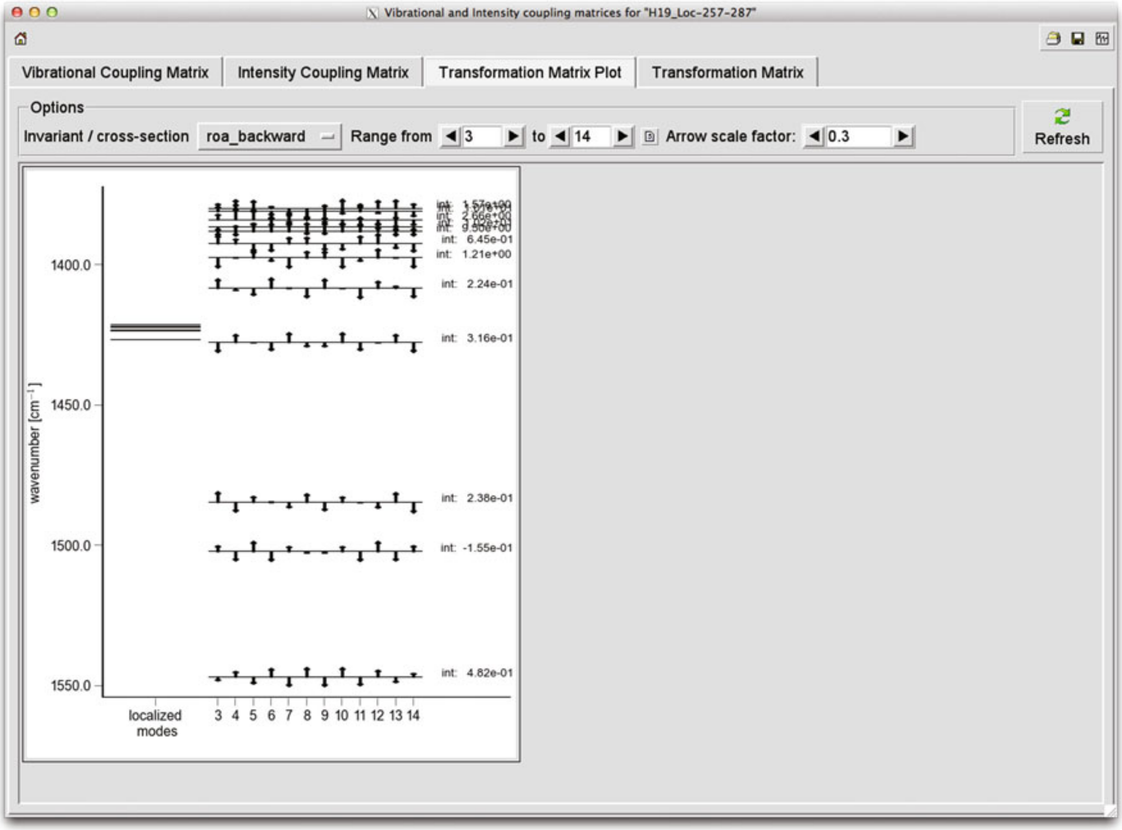

Invariant / cross-section roa_backward

Range from 3 to 14

Arrow scale factor: 0.3

Fig. 7 Screenshot of the panel that analyzes the unitary transformation matrix ***U*** using a graphical representation of the matrix. The ROA backward-scattering intensities (in Å^4/amu) associated with the "optimum" normal modes are also given

5.4 Analysis of the vibrational and intensity coupling matrices

Now that we have obtained the localized modes, we can interpret the normal modes as combinations of the localized modes, which form a basis set. The first quantity of interest is the vibrational coupling matrix (Eq. 15), which defines the coupling (in wavenumbers) between two localized modes. We can see here the benefit of ordering the localized modes. Indeed, the coupling between modes l and $l+1$ ($\tilde{\Omega}_{l,l+1}$) now corresponds to the coupling between two localized modes that have atomic contributions on neighboring sites. Their vibrational coupling matrix is similar to the coupling matrix between two or more states. Let's consider a two-state model with two states $|\psi_1\rangle$ and $|\psi_2\rangle$ of identical energy $E = \alpha$ coupled by an interaction term $V = \beta$. The wavefunction $|\Psi_i\rangle = C_{1i}|\psi_1\rangle + C_{2i}|\psi_2\rangle$ is obtained by solving the following set of equations:

$$\begin{pmatrix} \alpha & \beta \\ \beta & \alpha \end{pmatrix} \begin{pmatrix} C_{1i} \\ C_{2i} \end{pmatrix} = \lambda_i \begin{pmatrix} C_{1i} \\ C_{2i} \end{pmatrix} \tag{21}$$

It has two solutions: $\Psi_1 = \sqrt{2}/2(\psi_1 + \psi_2)$ with $\lambda_1 = \alpha + \beta$, and $\Psi_2 = \sqrt{2}/2(\psi_1 - \psi_2)$ with $\lambda_2 = \alpha - \beta$. If the coupling β is positive, the in-phase combination is higher in energy than the out-of-phase combination, while the order is reversed when β is negative. The problem we are solving in the localized mode procedure (Eq. 15) is the reverse one. Indeed, we already know the eigenvalues of the vibrational coupling matrix $\tilde{\mathbf{\Omega}}$ that are the frequencies of the normal modes. By defining a criterion, we find the transformation matrix ***U*** (corresponding to the eigenvectors of $\tilde{\mathbf{\Omega}}$) in order to define the vibrational coupling matrix $\tilde{\mathbf{\Omega}}$. By doing so, we can now better understand the normal modes. For instance, in our example of the [19]helicene molecule, the vibrational coupling matrix is dominated by negative contributions from first-nearest neighbors together with smaller absolute contributions for the second-nearest neighbors (Fig. 6 and Table 1). The coupling pattern is therefore slightly more sophisticated than in the simple two-state model, but the conclusion is similar: since the most intense coupling is negative, the in-phase normal mode will be at lower wavenumber while the out-of-phase normal mode will be at higher wavenumber. This is further illustrated in Fig. 7 which sketches the positions in wavenumbers of the normal modes together with up and down arrows illustrating the contribution of each localized

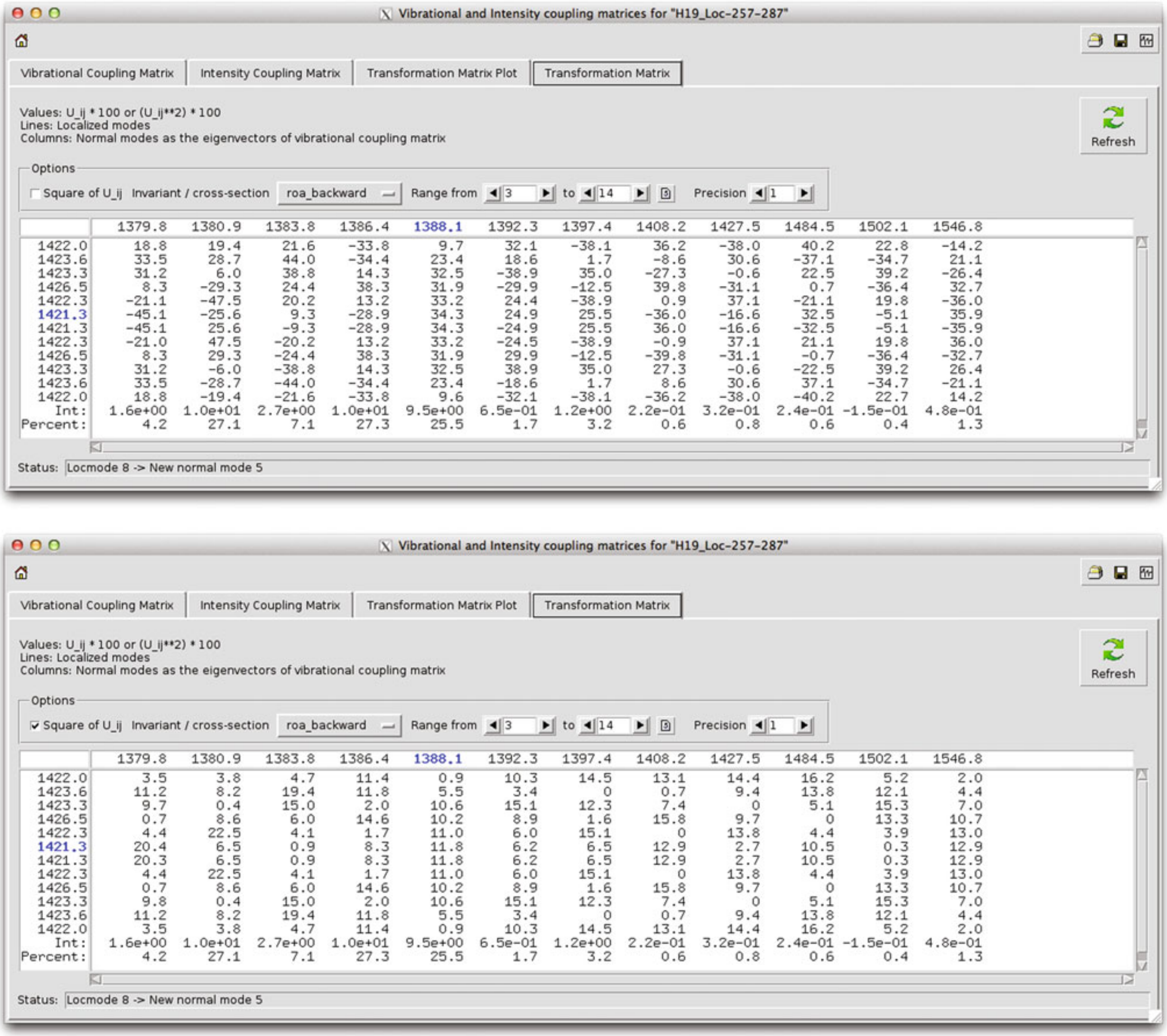

Values: U_ij * 100 or (U_ij**2) * 100
Lines: Localized modes
Columns: Normal modes as the eigenvectors of vibrational coupling matrix

Options

☐ Square of U_ij Invariant / cross-section roa_backward Range from 3 to 14 Precision 1

	1379.8	1380.9	1383.8	1386.4	1388.1	1392.3	1397.4	1408.2	1427.5	1484.5	1502.1	1546.8
1422.0	18.8	19.4	21.6	-33.8	9.7	32.1	-38.1	36.2	-38.0	40.2	22.8	-14.2
1423.6	33.5	28.7	44.0	-34.4	23.4	18.6	1.7	-8.6	30.6	-37.1	-34.7	21.1
1423.3	31.2	6.0	38.8	14.3	32.5	-38.9	35.0	-27.3	-0.6	22.5	39.2	-26.4
1426.5	8.3	-29.3	24.4	38.3	31.9	-29.9	-12.5	39.8	-31.1	0.7	-36.4	32.7
1422.3	-21.1	-47.5	20.2	13.2	33.2	24.4	-38.9	0.9	37.1	-21.1	19.8	-36.0
1421.3	-45.1	-25.6	9.3	-28.9	34.3	24.9	25.5	-36.0	-16.6	32.5	-5.1	35.9
1421.3	-45.1	25.6	-9.3	-28.9	34.3	-24.9	25.5	36.0	-16.6	-32.5	-5.1	-35.9
1422.3	-21.0	47.5	-20.2	13.2	33.2	-24.5	-38.9	-0.9	37.1	21.1	19.8	36.0
1426.5	8.3	29.3	-24.4	38.3	31.9	29.9	-12.5	-39.8	-31.1	-0.7	-36.4	-32.7
1423.3	31.2	-6.0	-38.8	14.3	32.5	38.9	35.0	27.3	-0.6	-22.5	39.2	26.4
1423.6	33.5	-28.7	-44.0	-34.4	23.4	-18.6	1.7	8.6	30.6	37.1	-34.7	-21.1
1422.0	18.8	-19.4	-21.6	-33.8	9.6	-32.1	-38.1	-36.2	-38.0	-40.2	22.7	14.2
Int:	1.6e+00	1.0e+01	2.7e+00	1.0e+01	9.5e+00	6.5e-01	1.2e+00	2.2e-01	3.2e-01	2.4e-01	-1.5e-01	4.8e-01
Percent:	4.2	27.1	7.1	27.3	25.5	1.7	3.2	0.6	0.8	0.6	0.4	1.3

Status: Locmode 8 -> New normal mode 5

Values: U_ij * 100 or (U_ij**2) * 100
Lines: Localized modes
Columns: Normal modes as the eigenvectors of vibrational coupling matrix

Options

☑ Square of U_ij Invariant / cross-section roa_backward Range from 3 to 14 Precision 1

	1379.8	1380.9	1383.8	1386.4	1388.1	1392.3	1397.4	1408.2	1427.5	1484.5	1502.1	1546.8
1422.0	3.5	3.8	4.7	11.4	0.9	10.3	14.5	13.1	14.4	16.2	5.2	2.0
1423.6	11.2	8.2	19.4	11.8	5.5	3.4	0	0.7	9.4	13.8	12.1	4.4
1423.3	9.7	0.4	15.0	2.0	10.6	15.1	12.3	7.4	0	5.1	15.3	7.0
1426.5	0.7	8.6	6.0	14.6	10.2	8.9	1.6	15.8	9.7	0	13.3	10.7
1422.3	4.4	22.5	4.1	1.7	11.0	6.0	15.1	0	13.8	4.4	3.9	13.0
1421.3	20.4	6.5	0.9	8.3	11.8	6.2	6.5	12.9	2.7	10.5	0.3	12.9
1421.3	20.3	6.5	0.9	8.3	11.8	6.2	6.5	12.9	2.7	10.5	0.3	12.9
1422.3	4.4	22.5	4.1	1.7	11.0	6.0	15.1	0	13.8	4.4	3.9	13.0
1426.5	0.7	8.6	6.0	14.6	10.2	8.9	1.6	15.8	9.7	0	13.3	10.7
1423.3	9.8	0.4	15.0	2.0	10.6	15.1	12.3	7.4	0	5.1	15.3	7.0
1423.6	11.2	8.2	19.4	11.8	5.5	3.4	0	0.7	9.4	13.8	12.1	4.4
1422.0	3.5	3.8	4.7	11.4	0.9	10.3	14.5	13.1	14.4	16.2	5.2	2.0
Int:	1.6e+00	1.0e+01	2.7e+00	1.0e+01	9.5e+00	6.5e-01	1.2e+00	2.2e-01	3.2e-01	2.4e-01	-1.5e-01	4.8e-01
Percent:	4.2	27.1	7.1	27.3	25.5	1.7	3.2	0.6	0.8	0.6	0.4	1.3

Status: Locmode 8 -> New normal mode 5

Fig. 8 Screenshot of the panel that analyzes the unitary transformation matrix ***U***. The ROA backward-scattering intensities (in Å^4/amu) associated with the "optimum" normal modes are given at the bottom of the table together with their percentage

mode to a given normal mode [obtained from the unitary matrix ***U***, Eq. 13]. One observes that the mode at 1547 cm^{-1} has alternating up and down arrows meaning an out-of-phase combination (maximum of nodes), while the modes at lower frequencies have less nodes. Figure 8 represents the unitary transformation matrix ***U***. The top figure contains the values of U_{pl}*100 while the bottom figure contains U_{pp}^2*100 values for each localized modes l (lines of the table) and each normal modes p (columns of the table). The U_{pl}^2*100 quantities correspond to the percentages of a localized modes l in a normal mode p (as well as the other way around), with the sum of all terms in each column (or each line) equal to one. From the U_{pl}*100 values, we directly see the contributions of the localized modes l to a given normal mode p. For instance, the normal mode at 1,388.1 cm^{-1} has only positive terms and therefore corresponds to the in-phase mode, while the mode at 1,546.8 cm^{-1} is the out-of-phase combination (See also Table 2).

In Figs. 7, 8, and 9, only a subset of the localized modes has been taken into account: mode 3 to mode 14 (without modes 1, 2, 15, 16). By doing so, the normal modes are not the "real" normal modes but are "optimum" normal modes constructed as the eigenvectors of a subset of the vibrational coupling matrix $\tilde{\mathbf{\Omega}}$. Indeed, we can choose to get rid of the localized modes that have atomic contributions localized at the two extrema of the chain in order to have a more ideal "polymer-like" coupling matrix.

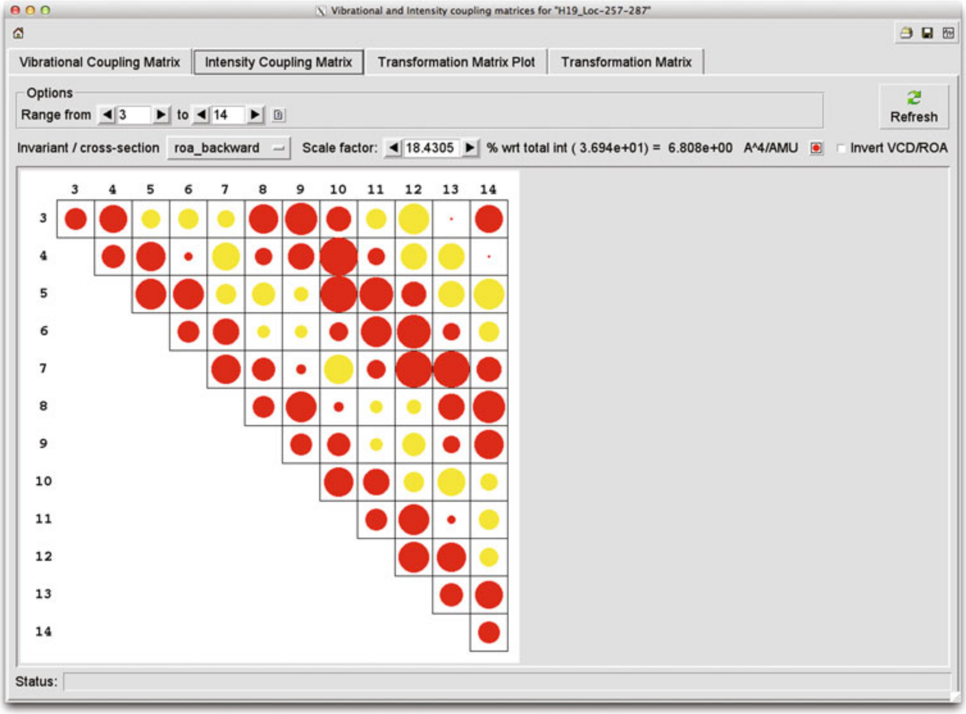

Vibrational and Intensity coupling matrices for "H19_Loc-257-287"

Range from 3 to 14

Invariant / cross-section roa_backward

Scale factor: 18.4305 % wrt total int (3.694e+01) = 6.808e+00 A^4/AMU

☐ Invert VCD/ROA

Status:

Fig. 9 Screenshot of the panel that analyzes the intensity coupling matrix $\tilde{\boldsymbol{I}}$

The eigenvectors of such subblocks of the vibrational coupling matrix $\tilde{\boldsymbol{\Omega}}$ give normal modes that are slightly different from the "real" normal modes. The intensity values given in Figs. 7 and 8 and Table 2 are therefore the intensities associated with the "optimum" normal modes and are equal to the intensity of the "real" normal modes only when all the localized modes are considered. As said before, in order to be able to have this kind of conclusion, it is crucial to have set the phase factor correctly for every localized modes.

At last, Fig. 9 is the window which represents the intensity coupling matrix ($\tilde{I}_{lm}$, Eq. 20). The diagonal elements of the matrix are the intensities associated with the localized modes, while the off-diagonal elements are the intensity coupling values. In our example, the intensity coupling terms are mostly positive with a few negative but smaller (in amplitude) contributions, which means that normal modes having a few nodes will have the highest intensities. Indeed, in Eq. (20), U_{pl} and U_{pm} will have the same sign for an in-phase normal mode p, and therefore, its intensity will be the (weighted) sum of all the terms in the intensity matrix. On the contrary, for an out-of-phase mode p, the U_{pl} and U_{pm} will have the same sign if $l = m + 2n$ and will have opposite sign if $l = m + (2n + 1)$. The intensity of such mode will therefore be the (weighted) sum of the diagonal terms of the vibrational coupling matrix minus the sum of the first off-diagonal terms plus the sum of the second off-diagonal terms minus the sum of the third off-diagonal terms, ... Since most of these terms are positive, the different contributions will cancel out to give a very small intensity for an out-of-phase normal mode. Indeed, in Fig. 8 and Table 2, one observes that the intensity for the out-of-phase mode at 1,546.8 cm^{-1} is 20 times smaller than the intensity of the in-phase mode at 1,388.1 cm^{-1} (0.482 vs. 9.50 Å^4/amu).

6 Conclusions and outlook

In this paper, we have reviewed key elements for simulating and interpreting IR, Raman, VCD, and ROA spectra as well as for analyzing them by using the localized mode procedure. Then, we have presented a graphical user interface (GUI) to carry out the localization of the vibrational normal modes and have illustrated its application on the ROA spectra of the [19]helicene molecule. The overall procedure consists of four steps, and therefore, a specific interface has been designed for each of them. The first and most important part of the procedure consists in selecting the mode ensemble under which the localization procedure is performed. Then, during our step-by-step guided tour of the localized mode procedure in Pyvib2, we have highlighted the importance of the ordering of the localized modes and the importance to set correctly the phase factor between the localized modes. Finally, the vibrational coupling matrix ($\tilde{\boldsymbol{\Omega}}$), the intensity coupling matrix ($\tilde{\boldsymbol{I}}$), and the unitary transformation matrix ($\boldsymbol{U}$) can be analyzed from their representation in the different panels.

The ROA spectrum of the [19]helicene molecule is dominated by two positive peaks associated with the normal modes 251 and 252. From the localized mode procedure, we have identified the atomic displacements of these modes as combinations of localized modes characterized by atomic displacements that look like the motion of a “claw”. Moreover, the intensity coupling matrix ($\tilde{\boldsymbol{I}}$) is shown to contain mainly positive terms, which explains why it is the in-phase combination and the combination with only a few nodes that give the most intense peaks in this band. At last, the vibrational coupling term ($\tilde{\boldsymbol{\Omega}}$) between two neighboring localized modes is negative and, as a result, the normal mode which is an in-phase combination of the localized modes is situated at lower wavenumber than the out-of-phase combination. One should note that such signature (one positive peak in the 200–2,000 cm^{-1} region) is quite unusual. Indeed, the ROA spectrum presents most of the time a succession of positive and negative peaks. The specific π-electron delocalization in the helicene molecule must be responsible for this remarkable spectrum.

Other tools such as the ACP and the GCM analyses can be applied on the localized modes by using the `Generation of Intensities` option from the thumbnail of the molecule obtained from the localized mode procedure. The main advantage of using such tools on the localized modes instead on the normal modes is that the atomic displacements of the localized modes are centered on a small part of the chain on the contrary to the normal modes that are delocalized over the whole structure. This kind of analysis has been successfully used in the past to understand the difference in signature between the α-helix and the 3_{10} helix conformations of an 20-unit oligomer of alanine [14, 50, 51] or between the $(\mathrm{TG})_\mathrm{N}$ and the $(\mathrm{GG})_\mathrm{N}$ conformation of a 20-unit polypropylene chain [52]. Thanks to this implementation in Pyvib2, we hope that such strategy will be used to analyze the vibrational signatures of various synthetic or bio-related oligomers.

Acknowledgments The authors thank Maxim Federovsky and Werner Hug for fruitful discussions about the Pyvib2 program and Christoph Jacob and Markus Reiher for discussions about the localized mode methodology. V.L. thanks the Fund for Scientific Research (F.R.S-FNRS) for his Postdoctoral Researcher position. The calculations were performed on the Interuniversity Scientific Computing Facility (ISCF) installed at the FUNDP, for which we gratefully acknowledge financial support from the F.R.S.-FNRS (Convention No. 2.4.617.07.F), and from the FUNDP.

References

1. Quinet O, Champagne B (2002) J Chem Phys 117:2481
2. Quinet O, Champagne B, Rodriguez V (2004) J Chem Phys 121:4705
3. Mani A, Schultz Z, Caudano Y, Champagne B, Humbert C, Dreesen L, Gewirth A, White JO, Thiry PA, Peremans A (2004) J Phys Chem B 108:16135
4. Guthmuller J, Cecchet F, Lis D, Caudano Y, Mani AA, Thiry PA, Peremans A, Champagne B (2009) ChemPhysChem 10:2132
5. Liégeois V, Ruud K, Champagne B (2007) J Chem Phys 127:204105
6. Drooghaag X, Marchand-Brynaert J, Champagne B, Liégeois V (2010) J Phys Chem B 114:11753
7. Liégeois V, Champagne B (2011) J Phys Chem A 115:13706
8. Fedorovsky M (2007) Pyvib2, a program for analyzing vibrational motion and vibrational spectra. http://pyvib2.sourceforge.net
9. Frisch MJ, Trucks GW, Schlegel HB, Scuseria GE, Robb MA, Cheeseman JR, Scalmani G, Barone V, Mennucci B, Petersson GA, Nakatsuji H, Caricato M, Li X, Hratchian HP, Izmaylov AF, Bloino J, Zheng G, Sonnenberg JL, Hada M, Ehara M, Toyota K, Fukuda R, Hasegawa J, Ishida M, Nakajima T, Honda Y, Kitao O, Nakai H, Vreven T, Montgomery JA Jr., Peralta JE, Ogliaro F, Bearpark M, Heyd JJ, Brothers E, Kudin KN, Staroverov VN, Kobayashi R, Normand J, Raghavachari K, Rendell A, Burant JC, Iyengar SS, Tomasi J, Cossi M, Rega N, Millam JM, Klene M, Knox JE, Cross JB, Bakken V, Adamo C, Jaramillo J, Gomperts R, Stratmann RE, Yazyev O, Austin AJ, Cammi R, Pomelli C, Ochterski JW, Martin RL, Morokuma K, Zakrzewski VG, Voth GA, Salvador P, Dannenberg JJ, Dapprich S, Daniels AD, Farkas ö, Foresman JB, Ortiz JV, Cioslowski J, Fox DJ (2009) Gaussian 09 Revision A.1. Gaussian Inc., Wallingford, CT
10. Dalton, a molecular electronic structure program, Release Dalton2011 (2011) see http://daltonprogram.org/.
11. Hug W (2001) Chem Phys 264:53
12. Hug W, Fedorovsky M (2008) Theor Chem Acc 119:113
13. Fedorovsky M (2006) Comput Lett 2:233
14. Jacob CR, Reiher M (2009) J Chem Phys 130:084106
15. Martin RH (1974) Angew Chem Int Ed 13:649
16. Autschbach J, Patchkovskii S, Ziegler T, van Gisbergen SJA, Baerends EJ (2002) J Chem Phys 117:581
17. Furche F, Ahlrichs R, Wacksmann C, Weber E, Sobanski A, Vögtle F, Grimme S (2000) J Am Chem Soc 122:1717
18. Autschbach J, Ziegler T, van Gisbergen SJA, Baerends EJ (2002) J Chem Phys 116:6930
19. Spassova M, Asselberghs I, Verbiest T, Clays K, Botek E, Champagne B (2007) Chem Phys Lett 439:213
20. Botek E, Champagne B (2007) J Chem Phys 127:204101
21. Verbiest T, Elshocht SV, Kauranen M, Hellemans L, Snauwaert J, Nuckolls C, Katz TJ, Persoons A (1998) Science 282:913
22. Verbiest T, Sioncke S, Persoons A, Vyklicky L, Katz TJ (2002) Angew Chem Int Ed 41:3882
23. Jansík B, Rizzo A, Ågren H, Champagne B (2008) J Chem Theory Comput 4:457
24. Liégeois V, Liégeois V (2009) J Comput Chem 30:1261
25. Wilson EB, Decius JC, Cross PC (1980) Molecular vibrations: the theory of infrared and Raman vibrational spectra (Dover Books on Chemistry). Dover Publications, New York
26. Barron LD, Buckingham AD (1971) Mol Phys 20:1111
27. Hug W (2002) In: Chalmers JM, Griffiths PR (eds) Handbook of vibrational spectroscopy. Wiley, New York, p 175
28. Barron LD (2004) Molecular light scattering and optical activity, 2 edn. Cambridge University Press, Cambridge
29. Stephens PJ (1985) J Phys Chem 89:748
30. Stephens PJ (1987) J Phys Chem 91:1712
31. Cheeseman JR, Frisch MJ, Devlin FJ, Stephens PJ (1996) Chem Phys Lett 252:211
32. He Y, Bo W, Dukor RK, Nafie LA (2011) Appl Spectrosc 65:699
33. Neugebauer J, Reiher M, Kind C, Hess B (2002) J Comput Chem 23:895
34. Buckingham AD (1967) Adv Chem Phys 12:107
35. Komornicki A, Fitzgerald G (1993) J Chem Phys 98:1398
36. Hehre WJ, Ditchfield R, Pople JA (1972) J Chem Phys 56:2257
37. Scott AP, Radom L (1996) J Phys Chem 100:16502
38. Irikura KK, Johnson RD III, Kacker RN (2005) J Phys Chem A 109:8430

39. Merrick J, Moran D, Radom L (2007) J Phys Chem A 111:11683
40. Zuber G, Hug W (2004) J Phys Chem A 108:2108
41. Binkley JS, Pople JA, Hehre WJ (1980) J Am Chem Soc 102:939
42. Pecul M, Rizzo A (2003) Mol Phys 101:2073
43. Reiher M, Liégeois V, Ruud K (2005) J Phys Chem A 109:7567
44. Pecul M, Ruud K (2005) Int J Quantum Chem 104:816
45. Cheeseman JR, Shaik MS, Popelier PLA, Blanch EW (2011) J Am Chem Soc 133:4991
46. Cheeseman JR, Frisch MJ (2011) J Chem Theory Comput 7:3323
47. Perera SA, Bartlett RJ (1999) Chem Phys Lett 314:381
48. Crawford TD, Ruud K (2011) ChemPhysChem 12:3442
49. Joshi SP, Dutta AK, Pal S, Vaval N (2012) Chem Phys 403:25
50. Jacob CR, Luber S, Reiher M (2009) J Phys Chem B 113:6558
51. Jacob CR, Luber S, Reiher M (2009) Chem Eur J 15:13491
52. Liégeois V, Jacob CR, Champagne B, Reiher M (2010) J Phys Chem A 114:7198

Theor Chem Acc (2012) 131:1289
DOI 10.1007/s00214-012-1289-5

REGULAR ARTICLE

Time-dependent density functional theory study of charge transfer in collisions

Guillermo Avendaño-Franco · Bernard Piraux · Myrta Grüning · Xavier Gonze

Received: 12 April 2012 / Accepted: 26 September 2012 / Published online: 17 October 2012

Abstract We study the charge transfer between colliding ions, atoms, or molecules, within time-dependent density functional theory. Two particular cases are presented, the collision between a proton and a Helium atom, and between a gold atom and a butane molecule. In the first case, proton kinetic energies between 16 keV and 1.2 MeV are considered, with impact parameters between 0.31 and 1.9 Å. The partial transfer of charge is monitored with time. The total cross-section is obtained as a function of the proton kinetic energy. In the second case, we analyze one trajectory and discuss spin-dependent charge transfer between the different fragments.

Keywords Time-dependent density functional theory · Charge transfer · Collisions

Published as part of the special collection of articles celebrating theoretical and computational chemistry in Belgium.

G. Avendaño-Franco · B. Piraux · X. Gonze (✉)
Université Catholique de Louvain (UCL), NAPS-Chemin des étoiles 8 bte L7.03.01, 1348 Louvain-la-Neuve, Belgium
e-mail: xavier.gonze@uclouvain.be

G. Avendaño-Franco
e-mail: guillermo.avendano@uclouvain.be

B. Piraux
e-mail: bernard.piraux@uclouvain.be

M. Grüning
Center for Computational Physics and Physics Department, Universidade de Coimbra, Rua Larga, 3004-516 Coimbra, Portugal
e-mail: myrta@teor.fis.uc.pt

1 Introduction

For more than two decades, density functional theory (DFT) has been used as a reliable tool to describe the electronic structure, total energy, and associated characteristics of molecules and solid-state materials, in the adiabatic approximation [1, 2]. The level of accuracy achieved by DFT is acceptable for a range of purposes in quantum chemistry with a better balance between accuracy and computational cost than more sophisticated approaches based on interacting electronic wave function theory (WFT) [3].

However, quantum chemistry is not restricted to the description of static (or adiabatic) phenomena. Collision dynamics, or the description of systems excited with femtosecond lasers, requires time-dependent approaches. Phenomena like photoionization, excitation, and ionization by electron impact, charge transfer processes [4, 5], atomic scattering, and interstellar chemistry, also call for theoretical support.

For many years, the atomic physics community has been using highly accurate WFT to investigate time-dependent phenomena, including the electronic correlation effects, with impressive success [6]. However, even with present computational resources, only a few electrons can be tackled when such approaches are followed.

Several routes to avoid the treatment of many-body wave functions in collisions, still accounting for adiabatic effects, have been explored. Without being exhaustive, let us mention the approach from Saalmann et al. [7], in which the authors study an exact case with one electron, time-dependent Hartree-Fock (TD-HF), that was used in [8] to explore the charge exchange in the collision $He^{2+} + He$, and many studies based on non-adiabatic hopping between hypersurfaces [9].

Time-dependent density functional theory (TD-DFT) [10] shares with DFT a favorable scaling with the number of electrons and allows one to compute the evolution of the electronic structure with a time-dependent Hamiltonian, a characteristic that traditionally was only possible from first principles using WFT. In the past few years, TD-DFT has been used by a few groups to study ion–atom collisions : Keim et al. [11] used a basis generator method (BGM) to examine the collisions of bare ions with helium, with excellent agreement with the experimental results from Rudd et al. [12, 13], while Wang et al. [14] examined proton–Argon and proton–Neon [15] collisions, also with reasonable agreement with experimental data. In the latter case, the authors went beyond the analysis of the single electron transfer channel and explored different methods to quantify the double electron transfer. The study of more complex phenomena has been also undertaken recently: collisions between atomic oxygen and graphite clusters [16], and studies of the stopping power of ions impacting on surfaces [17, 18].

Within a long-term effort aiming at the description of the transfer of charges occurring in secondary ion mass spectrometry [19–21], we explore the use of TD-DFT for collisions between ion, atom, and molecule. In the line of Keim, Wang, and coworkers, [11, 14, 15, 22], we examine first the transfer of charge during a simple proton–atom collision, namely the proton–Helium case. We base our analysis on tools that will scale easily to more complex physical situations : the combination of real-space integrated density representation and Hirshfeld partitioning [23] of charge between atoms. Then, we explore the collision between a gold atom and a butane molecule, and apply the same analysis tools. The charge transfer is quantified for each spin channel.

2 Theoretical background

Time-dependent density functional theory (TD-DFT) is an extension of ground-state DFT (GS-DFT) to solve the electronic structure problem under a time-dependent Hamiltonian. Its foundations are similar in purpose to those in GS-DFT, although the set of theorems and their mathematical demonstrations are considerably different. More detailed references about the TD-DFT formalism can be found in [24]. In what follows, we will consider the combination of TD-DFT, for the electronic system, with a classical representation of nuclei motion.

In the presence of a time-dependent Hamiltonian, WFT solves the Schrödinger equation

$$i\frac{\partial}{\partial t}\Psi(\{\mathbf{r}\},t) = \hat{H}(\{\mathbf{r}\},t)\Psi(\{\mathbf{r}\},t), \tag{1}$$

where the Hamiltonian $\hat{H}$ and the wave function Ψ are functions of the spatial coordinates of N electrons $\{\mathbf{r}\} = \{r_1, r_2, \ldots, r_N\}$ and the time. The Hamiltonian is decomposed as:

$$\begin{aligned}\hat{H}(\{\mathbf{r}\},t) &= \hat{T}(\{\mathbf{r}\}) + \hat{W}(\{\mathbf{r}\}) + \hat{V}_{ext}(\{\mathbf{r}\},t)\\ &= -\frac{1}{2}\sum_{i=1}^{N}\nabla_i^2 + \frac{1}{2}\sum_{i,j=1}^{N}\frac{1}{|\mathbf{r}_i - \mathbf{r}_j|}\\ &\quad + \sum_{i=1}^{N} v_{ext}(\mathbf{r}_i,t)\end{aligned} \tag{2}$$

In the case of scattering, without electromagnetic fields, the dependence with time of the Hamiltonian comes from the classical path followed by M point-like nuclei. In such case, the external potential $v_{ext}(\mathbf{r}_i, t)$ can be written:

$$v_{ext}(\mathbf{r},t) = -\sum_{k=1}^{M}\frac{Z_k}{|\mathbf{r} - \mathbf{R}_k(t)|} \tag{3}$$

where Z_k denotes the charge of the nucleus k and $\mathbf{R}_k$ denotes its position.

Once Eq. (1) has been solved, the many-body wave function Ψ defines the electronic density

$$n(\mathbf{r},t) = N\int d^3\mathbf{r}_2 d^3\cdots d^3\mathbf{r}_N|\Psi(\mathbf{r},\mathbf{r}_2,\ldots,\mathbf{r}_N,t)|^2 \tag{4}$$

TD-DFT uses the real scalar field $n(\mathbf{r}, t)$ as the basic variable, instead of the many-body wave function. The foundations of this switch from wave functions to the density as a fundamental quantity comes from the so-called Runge-Gross theorem [10] that establishes a one-to-one correspondence between the external potential $v_{ext}(\mathbf{r}, t)$ and the density $n(\mathbf{r}, t)$. In a similar way as GS-DFT is implemented, TD-DFT also uses an artificial set of non-interacting N wave functions, where the Hamiltonian for each of them is a functional of the time-dependent density. An evolution equation for non-interacting electrons replaces Eq. (1). An initial condition must provided. In our case of collisions between ions, atoms, and/or molecules, we assume that both target and projectile start from their electronic ground state, so that the Hohenberg-Kohn theorem establishes that the ground-state density is sufficient to determine the many-body ground state. Explicitly, let $\phi_i(\mathbf{r}, t)$ be the one-electron orbital, the evolution equation reads :

$$i\frac{\partial}{\partial t}\phi_i(\mathbf{r},t) = \hat{H}_{KS}(\mathbf{r},t)\phi_i(\mathbf{r},t) \tag{5}$$

with the Hamiltonian $\hat{H}_{KS}(\mathbf{r},t)$ separated in terms of

$$\begin{aligned}\hat{H}_{KS}[n](\mathbf{r},t) &= -\frac{\nabla^2}{2} + v_{ext}(\mathbf{r},t)\\ &\quad + v_{Hartree}[n](\mathbf{r},t) + v_{xc}[n](\mathbf{r},t)\end{aligned} \tag{6}$$

where $v_{Hartree}(\mathbf{r}, t)$ is the classical Hartree potential.

We will rely on the so-called adiabatic local density approximation (ALDA) to describe the exchange-correlation time-dependent functional $v_{xc}[n](\mathbf{r}, t)$, based on the exchange-correlation of a free electron-gas [25–28].

Simulations of collisions were performed using the software package Octopus [29, 30]. Octopus is an implementation of TD-DFT based on a real-space grid discretization. The simulation space is a parallelepiped whose longer axis is along the direction of collision. In general, the projectile and target are placed sufficiently far from each other inside the simulation box. However, for the specific case of proton projectile, the initial position could be also at the frontier or outside the simulation box. The ground state is computed first and used as initial condition for the time evolution. The time evolution is also discretized, the optimal time step is very dependent, not only on the velocity of the ions, but also on the kinetic energy of the electrons. To reduce the number of electrons involved in the dynamics, the description of core electrons is implemented using norm-conserving pseudopotentials (see, e.g., Chap. 11 in [2]). In that case, particular attention has to be paid to avoid overlappings of the cutoff radius of those pseudopotentials that could induce artefacts in the simulation.

During the time evolution, the electrons are treated quantum-mechanically (TD-DFT) and the nuclei are point particles treated classically using a modified Ehrenfest formalism, as described in [31, 32]. The algorithm used to approximate the evolution operator is the approximated enforced time-reversal symmetry (AETRS) as implemented on Octopus. The exponential of the Hamiltonian is expanded using a Krylov subspace approximation of the action of the exponential and the evolution follows the technique described in [33]. The Perdew-Zunger's exchange-correlation [34] is used, and the core electrons are represented using norm-conserving pseudopotentials from Troullier and Martins [36]

3 Proton impacting Helium

Our first case corresponds to the simulation of a collision between a proton and a Helium atom. This is a well-studied problem in atomic physics [11, 13, 37–40], for which a wealth of experimental data as well as results from higher levels of theory are available.

For the simulation, a rectangular parallelepiped of 16.94 Å along the direction of impact and 10.58 Å in the transversal directions is used. The simulation box is defined by its extremes (−8.47, −5.29, −5.29) and (8.47, 5.29, 5.29). The spacing between points in the mesh is 0.1 Bohr (that is, 0.0529 Å). The total number of points in the mesh is $321 \times 201 \times 201 = 12968721$ grid points plus some extra points outside of the boundary to properly compute spatial derivatives.

The Helium atom originally located along the major central axis of the parallelepiped is impacted by a proton that starts in one of the faces of the box with a certain kinetic energy and impact parameter. The starting coordinates for the He target is (−4.2, 0, 0), and for the proton projectile is (−8.47, b, 0), where b is the impact parameter (the perpendicular distance between the path of a projectile and the center of the target)

In scattering processes, usually only the final product of the collision is considered. First principles methods also allow to understand the dynamics during the collision. With the aim to gain understanding of computational as well as physical aspects, we monitor the dynamics of the electronic structure during the entire evolution. However, the amount of data accumulated per time step is quite large, and thus must be handled with care. To fix the idea, the storage of electronic density for 12968721 grid points will require a binary file of about 96 MB. Supposing a total of 25,000 time steps, storing the data each hundred steps will require 24 GB. Instead of storing such amount of data for post-processing purposes only, we decided to introduce small modifications to the Octopus source code to extract the relevant data in a more detailed way during the execution, focusing on selected integrated quantities, described later. Those modifications are only affecting the output of the density : the physics and algorithms implemented in Octopus were not changed.

As the kinetic energy of the proton spans several orders of magnitude, the time step needs to be properly adjusted for each value of kinetic energy. The optimal value was computed for the most energetic proton in such a way that the total energy of the system be constant under a tolerance of 0.03 eV. The larger deviations for the total energy occurs when the proton reaches the closest distance with the He nucleus. After the time step was scaled proportionally for the different energies in such a way that the same number of time steps are needed to move the proton the entire length of the simulation box. The number of time steps required to move the proton from one side of the box to the opposite one is around 30,000. The simulation is stopped at 25,000 time steps when the proton is sufficiently far from the He nucleus and around 3 Å far from the end of the simulation box. At this point, the electronic capture is complete.

As the proton follows its path, coming close to the Helium atom, the electronic structure of the latter is perturbed. Depending on the initial kinetic energy of the projectile and its impact parameter, some charge is ejected out of the Helium atom region and either becomes attached to the proton projectile, or is ejected in all direction of space, including backwards the direction of impact.

In the TD-DFT formalism for a two-electron spin-saturated system such as the Helium atom, only one Kohn-

Sham orbital is explicitly treated. Contrary to WFT, the knowledge of the final state of the system does not allow a unambiguous interpretation of the final result in terms of probabilities of one- and two-electron transfer. However, the one-electron transfer probability is much larger than the two-electron transfer probability, and in the present context, we will assume that the charge density outside the Helium region is a direct image of the one-electron transfer process. This is consistent with the results obtained in [14, 15]

Figure 1 presents several snapshots of the time evolution of the electronic density inside the simulation box, for a typical collision. For the purpose of visualization, the electronic density is integrated in planes perpendicular to the direction of propagation, inside discs of different radii in the $y - z$ plane. One notices that before the collision, the lines for radii larger or equal to $R = 1.59$ Å are undistinguishable from the line obtained in the whole plane, while the spread between different radii increases steadily after the collision, meaning that the electronic charge that is localized within 1.59 Å before the collision, is scattered and occupies the whole simulation box after the collision, as expected.

To measure the amount of charge being transferred to the proton, we integrate the charge around the two nuclei after the scattering and when they are sufficiently separated to measure a stable number of electrons to each of them. In this simulation, the proton carries at the end about 0.4 electrons in a sphere of 1 Å of radius.

In order to examine the stability of the quantitative estimation of the charge transfer, Fig. 2 presents the evolution of the integrated charge in slices of 2 Å, centered on each atom. For completeness, we also present in this graph, the integral of the charge density in the region of space with x lower than -1 (called "Back-scattering slice"), and with x larger than $+1$ (called "Forward-scattering slice").

At the beginning of the simulation, using a slice of 2 Å for the Helium atom, a charge 1.967 electrons is inside the "Helium slice," the charge that spills out of the slice represents the tail of the charge density, split in 0.018

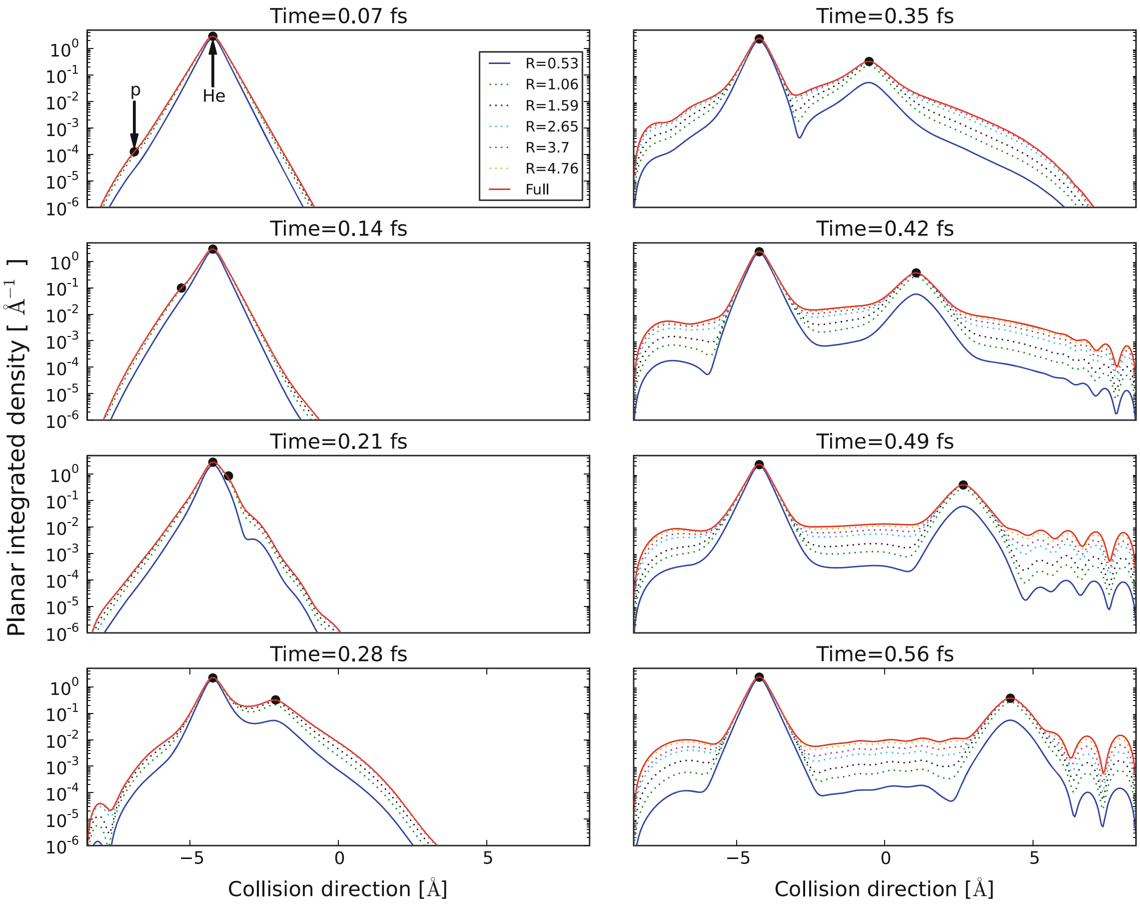

Fig. 1 Snapshots of the integrated planar charge density during a typical proton-Helium collision. The impact parameter is 0.74 Å, the initial kinetic energy of the proton is 26.8 keV. The direction of propagation is x. The *different lines* show the density integrated inside a disc of radius R (in Å) in the $y - z$ plane (or inside the full box) centered on a line that passes through the Helium atom at rest. *Small black dots* are used to show the locations of the nuclei in the direction x (see text)

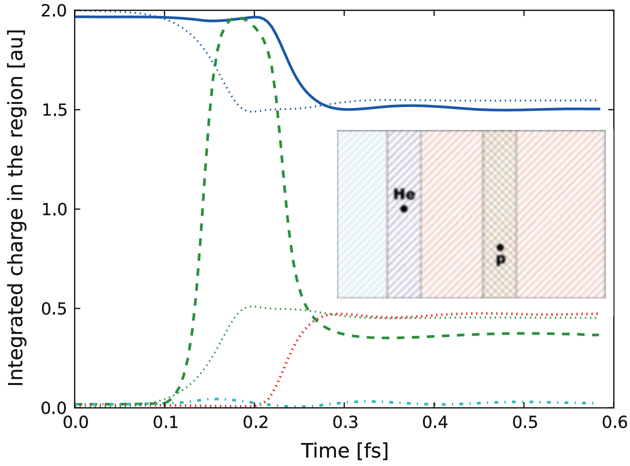

Fig. 2 Amount of charge present in different regions of space during the proton-He collision. The initial kinetic energy and impact parameter are the same than the ones used in Fig. 1. Full line (*blue*) : integrated charge in a slice with x between -5.2 and -3.2, that is, between -1 and $+1$ Å with respect to the Helium atom, defining the "Helium slice". *Dotted line* (*red*): integrated charge with x higher than -3.2, that is, in the "Forward-scattering slice". *Dash-dotted line* (*light blue*): integrated charge with x lower than -3.2, that is, in the "Back-scattering slice". *Dashed line* (*green*): integrated charge in a moving slice, with the difference in x with respect to the proton being between -1 and $+1$, that is, in the "Proton slice". Note that this slice overlaps first with the "Back-scattering slice", then with the "Helium slice", then with the "Forward-scattering slice". *Small dotted line* (*blue*), upper: Hirshfeld charge for the Helium nucleus. *Small dotted line* (*green*), lower: Hirshfeld charge for the proton

electrons for the "Back-scattering slice" and 0.015 electrons for the "Forward-scattering slice." It means that more than 98 % of the charge is initially contained inside the "Helium slice." As the proton gets closer to the Helium, part of the charge associated with the He is also associated with the proton, as the two slices overlap. Finally, when the proton leaves the region of interaction, some charge follows the proton, reducing the charge associated the Helium atom.

The charges associated with proton and He stabilizes around a well-defined value. While the back-scattered charge is quite small, the difference between forward-scattered charge and the charge centered on the proton, after the collision, is non-negligible and calls for further analysis, especially with respect to its angular dependence. Artefacts due to the reflecting nature of the simulation box must also be analyzed. At the end of the time simulation corresponding to Fig. 2, the charge present in the "Back-scattering slice" is 0.023, the charge present in the "Helium slice" is 1.504, the charge present in the "Forward-scattering slice" is 0.473, while the charge present in the "Proton slice" is 0.367.

Figure 2 also presented the Hirshfeld partitioning [23] of the total charge, as a function of time. The Hirshfeld partitioning attributes the charge at each point in space either to the Helium or to the proton, according to a weight that is proportional to the radial densities of the neutral (ground state) Helium or Hydrogen atoms. The implementation of this partitioning is rather easy. Although it completely neglects the possibility that a fraction of electronic charge density might not be attributed to one of both atoms, it constitutes a useful characterization tool that can be transposed easily to more complex situations, as described in the next section [41]. For the present proton–Helium case, after the collision, the Hydrogen Hirshfeld charge is 0.453 and the Helium Hirshfeld charge is 1.547. The Helium Hirshfeld charge is slightly higher than the charge in the "Helium slice." It seems to gather most of the charge excluded from the "Back-scattering slice." Analogously, the proton Hirshfeld charge is larger than the "proton slice charge," and smaller than the charge in the "Forward-scattering slice." In both cases, they stabilize after the collision and can be used to perform an analysis of the transfer of charge.

As seen on Fig. 2, the amount of charge being transferred becomes stable for a given value of initial kinetic energy and impact parameter. The understanding of the long-term evolution of the charge clearly identified to be in the He and H regions seems rather obvious, unlike the charge in other regions.

In Fig. 3, we examine one aspect of the behavior of the charge that remains between the two nuclei. In this respect, we define the planar average velocity as the integral of the local current divided by the local density in the plane perpendicular to the x direction. This figure shows the planar average velocity during the proton–He collision for a reference plane in the scattering region at $x = -0.5$ Å. As the proton approaches the He atom ($t < 0.20$ fs), the charge oscillates at the reference plane, inducing oscillations in the charge velocity. Immediately after the proton–He atom collision ($x = -4.2$ Å, $t = 0.21$ fs), some charge crosses the reference plane, causing a sudden jump in the charge velocity shown in Fig. 3. When the proton crosses the reference plane, ($t = 0.35$ fs), the charge crosses the plane with the same velocity as the proton, as is evident in the plateau found around 0.35 fs. After the crossing of the proton, the velocity of the charge in the plane decreases exponentially. Also, some charge goes back to the Helium atom, visible as a negative value in the current along y. The quantification of the amount of charge going in the different channels (including, e.g., electron scattering) has not been attempted.

Figure 4 gathers the electronic charge transfer values, after collision, as a function of the initial kinetic energy of the projectile, for several values of the impact parameter. Assuming an exponential behavior of the electronic capture as a function of the impact parameter, the capture cross-section based on the proton slice integrated charge density

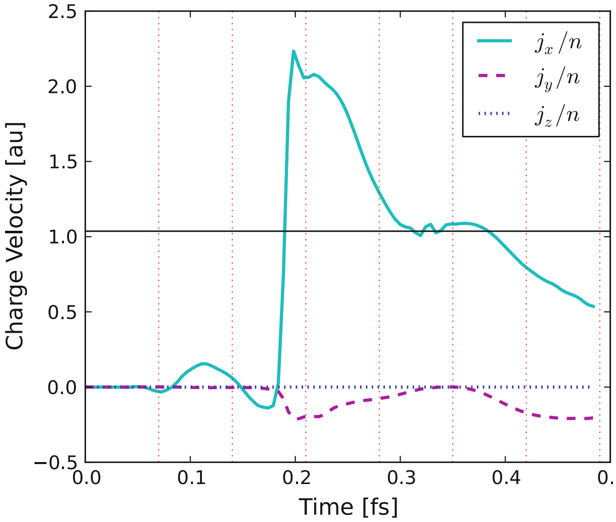

Fig. 3 Components of the planar average charge velocity (j/n) as a function of time, for the plane $x = -0.5$ Å. The physical conditions shown here are the same as Fig. 2; the *vertical dashed red lines* indicate the times of the snapshots of Fig. 1. The velocity of the proton is also shown with a *horizontal line*

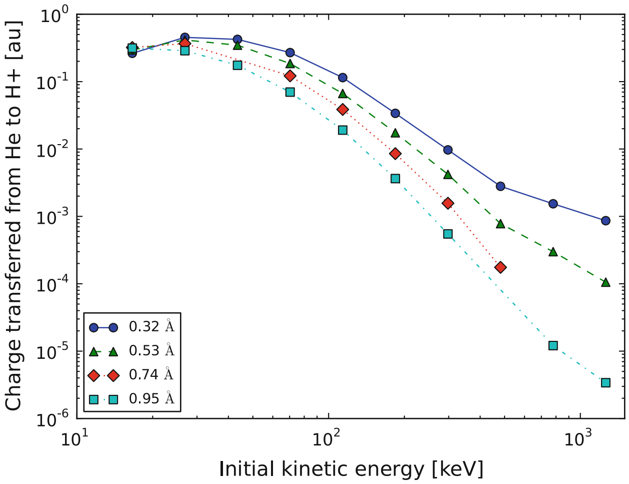

Fig. 4 Electronic charge capture for the proton–Helium collision, as function of the initial kinetic energies for several different impacts parameters. The charge depicted is the charge from the proton slice when the transfer is completed

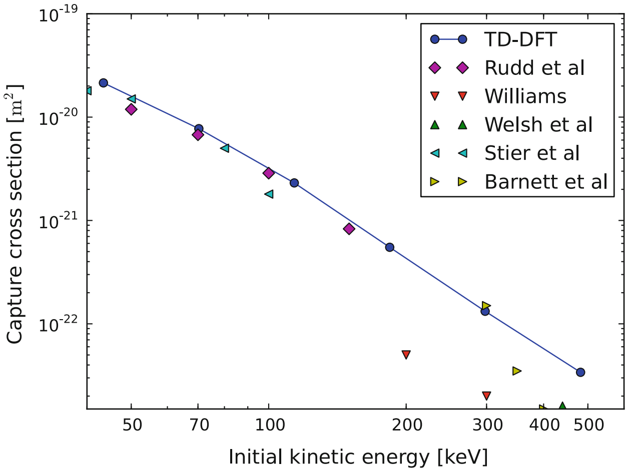

Fig. 5 Electronic capture cross-section by proton in Helium. Experimental results [12, 42–45] are shown for comparison

can be computed as a function of the initial kinetic energy of the projectile. The corresponding data are presented in Fig. 5. There is a good agreement with the experimental data [12, 42–45] in the energy range where they agree (below 150 keV).

One can wonder why the agreement is quite good, although it is well known that TD-DFT usually overestimates charge transfer [46, 47]. However, during collisions, the electronic transfer occurs close to the nuclei, where the electronic density is high. The contribution to the capture cross-section is dominated by collisions with small impact parameter. The known problem, actually related to the presence of region of spaces weakly populated (exponential decay of the wave function) seems not to be encountered here. Even the lack of a non-local exchange [48] does not affect the capture cross-section. We performed some additional calculations, with the self-interaction correction present in Octopus. We observed that differences in the final outcome of the simulation are negligible.

4 Gold–Butane collision

The collision of an atom of gold and a molecule of butane includes some extra challenges compared with the previous case. Instead of two electrons, now we have a total of 113 electrons. By using pseudopotentials, the number of electrons treated explicitly can be reduced to 37. The gold atom being spin-polarized, we have to treat independently each spin channel. The total number of Kohn-Sham spin orbitals to be handled is thus 37.

As the butane molecule and the gold atom are bigger than the entities of the previous case, the simulation box needs also to be bigger: the box is 22 Å along the direction of collision and 10.5 Å in the transversal directions. As the projectile (Au) now contains electrons, its initial position must be inside of the box.

In the proton–Helium case, the mass ratio between projectile and target was 1:2. With Au as projectile, the proportion is inverted to about 3:1. The simulation presented in Fig. 6 shows an atom of gold, with initial kinetic energy of 23.9 keV, impacting the bond region between two carbon atoms of the butane molecule. We observe that the gold atom breaks the molecule precisely on that bond and continues its path without major deflection. Two fragments are formed from the former butane : one CH_3 ion

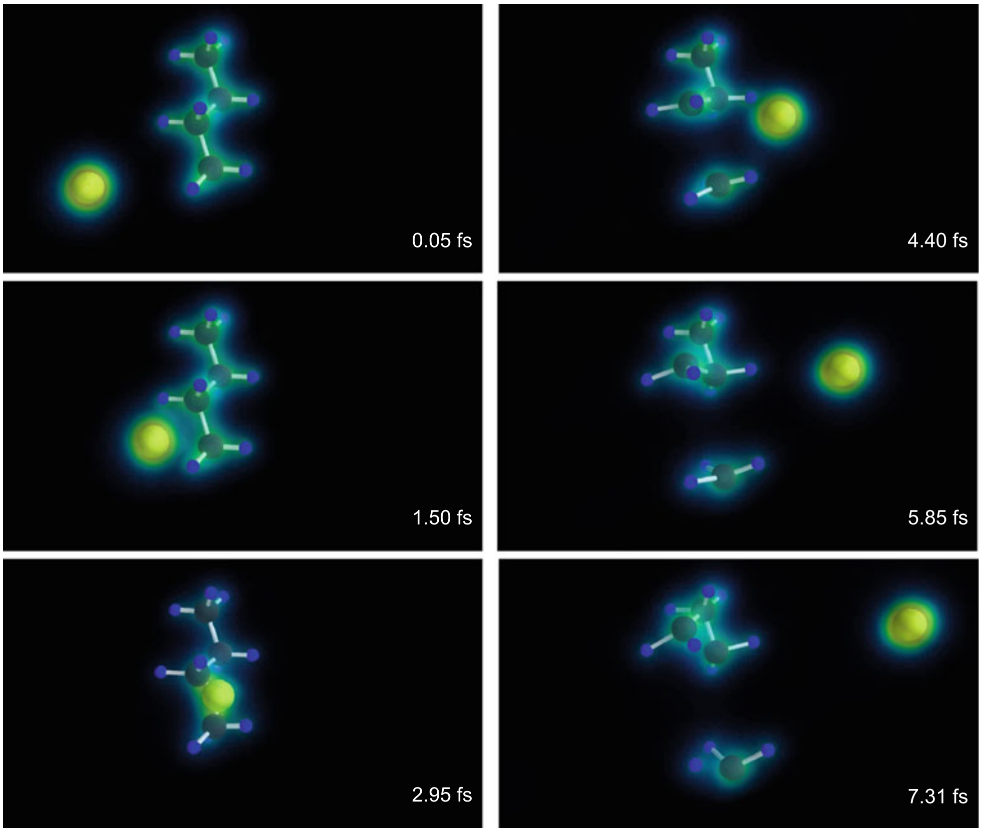

Fig. 6 Snapshots of the collision of a gold atom with a butane molecule. The initial kinetic energy of the projectile is 23.9 keV

(lower part of each sub-figure) and one C_3H_7 ion (upper part of each sub-figure). However, the latter can be seen to decompose in a CH_2 entity (moving upwards), and a C_2H_5 entity (nearly static).

This work is intended to simulate the kind of processes occurring in secondary ion mass spectrometry (SIMS). From a SIMS perspective, the fragmentations present in our simulations should be similar to those occurring in organic polymers due to secondary collision of the atoms from a gold deposit surface as is the case in metal-assisted SIMS (MetA-SIMS). They should have an important role in the ionization of those organic fragments, allowing them to be identified when sputtered.

Following the same methodology than the one used to understand the case of proton and He collision, the planar-integrated density was computed along the direction of impact. It is represented in Fig. 7. As for the proton–Helium collision, such charge density representation allows to visualize the dynamic evolution of the electronic clouds. The two clouds, initially well separated, merge, and then separate, while a small component is present outside of the two major regions.

For kinetic energies as high as in the case presented, and with similarly large impact parameter, the fragments of the butane molecule acquire a relatively small velocity, making easier to partition the charge. We also tested lower kinetic energy cases. However, for some of these, the fragments have a velocity close to the one of the projectile. Measures of charge based on a one-dimensional integrated partition of the space are not as effective. The partition of space must be three-dimensional (as was done with cylinder for the proton–Helium collision) to provide usable results.

In Fig. 8, the Hirshfeld analysis is carried out for each spin component. It shows a well-defined reallocation of the spins charges for the gold atom. As the total amount of charge for each component remains constant, it means that the spin rearrangement is done at expenses of the spin components of the carbon and hydrogen atom. While the charge and spin on the gold atom quickly stabilizes after the collision, on each fragment, the time-dependent Hirshfeld analysis shows some fluctuation between atoms, which is expected (even is confined in a fragment, the electrons continue to oscillate, due to the Ehrenfest dynamics). For a well-separated fragment, like the CH_3 going downwards on Fig. 6, the stabilization is expected to be faster than for each atom separately.

In Table 1, we provide the position, velocity, and Hirshfeld charges (for each spin channel), for each atom, as well as for the C_2H_5, CH_2 and CH_3 fragments, at the

Fig. 7 Planar-integrated charge density, during the simulation of an atom of gold in collision with a butane molecule, corresponding to the six snapshots of Fig. 6. Each spin contribution is considered independently

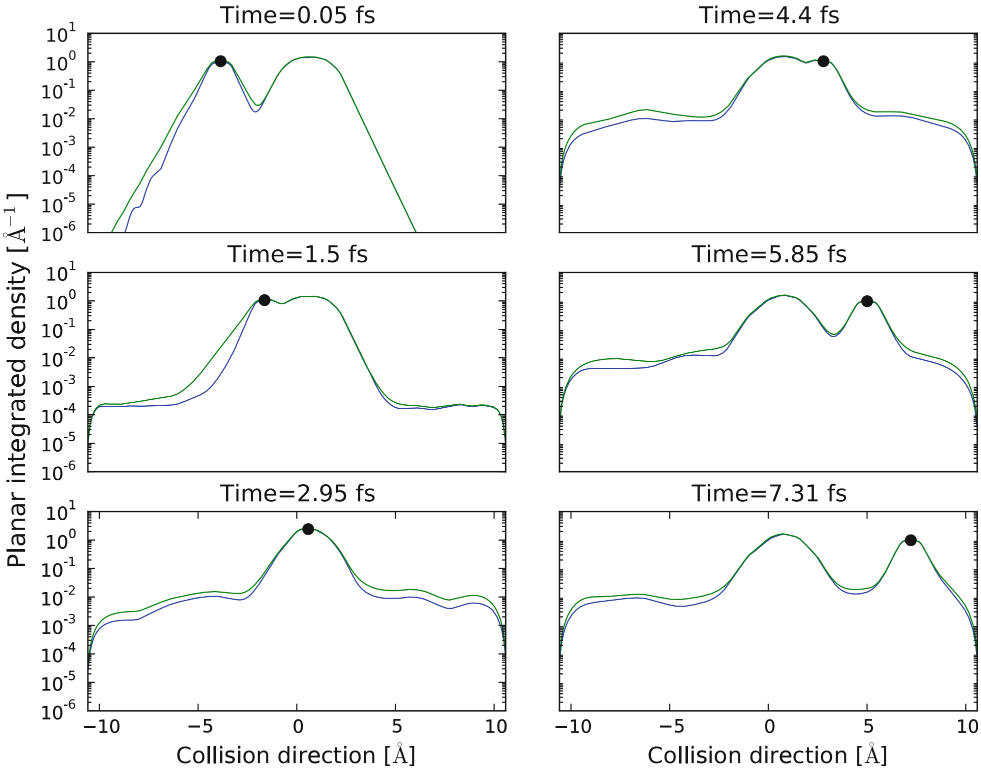

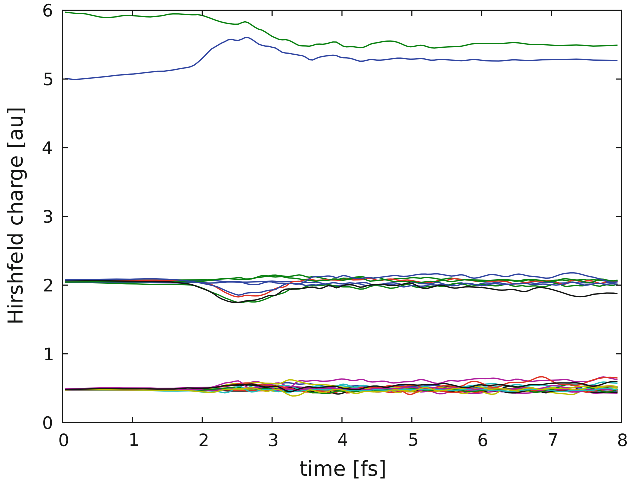

Fig. 8 Evolution of the Hirshfeld charges, during the simulation of the collision between an atom of gold and a butane molecule, with the same parameters as in Fig. 6. Each spin contribution is displayed independently for each atom. The *upper curves* are for the spin up and spin down Hirshfeld charges on the gold atom. The Carbon Hirshfeld charges start at a value of about two (for both spin up and spin down, making four valence electrons for each carbon atom as expected), and the Hydrogen Hirshfeld charges start at a value of about one half (for both spin up and spin down, making one valence electrons for each hydrogen atom as expected)

beginning, and at the end of our simulation. Note that in Fig. 6, the x axis runs diagonal in the perspective of the snapshots. Also, the butane molecule is not symmetric with respect to the impact axis.

The Hirshfeld analysis shows that the gold atom loses a charge of 0.477 electrons in the spin up channel and gains a charge of 0.280 electrons in the spin down channel, with a global loss of 0.197 electrons. The CH_3 fragment charge change (U,D) is (+0.297, −0.135), for a global gain of 0.162 electrons, the CH_2 fragment charge change (U,D) is (+0.134, −0.039), for a global gain of 0.095 electrons, the C_2H_5 fragment charge change (U,D) is (+0.047, −0.106), for a global loss of 0.059 electrons.

5 Conclusions

In the present study, we have analyzed the charge transfer due to collisions, using time-dependent density functional theory. We focused first on the collision of a proton with an atom of Helium, for which we tested analysis tools that would scale also for more complex systems. The agreement with experimental data for scattering cross-section is reasonably good. We apply the same methodology to describe the transfer of charge due to a collision between an atom of gold and a molecule of butane. We find that the slice representation allows for an easy visualization of the whole phenomena, allowing to gauge the charge partitioning in different region of space. The Hirshfeld partitioning yields complementary quantitative information, although the emission of electrons is missing from such representation. In the case of the gold–butane collision, there is a cross-

Table 1 Initial and final conditions for the simulation of a collision between an atom of gold and a molecule of butane

Atom	Initial		Final		
	Position [Å]	Charge (U, D) [a.u.]	Position [Å]	Velocity [Å·fs^{-1}]	Charge (U,D) [a.u]
C	(1.225, 1.773, 0.167)	(2.072, 2.072)	(1.230, 1.789, 0.173)	(2.4e-03, 1.0e-02, 5.7e-03)	(2.065, 2.044)
H	(0.248, 2.202, 0.450)	(0.476, 0.476)	(0.221, 2.229, 0.502)	(−2.7e-03, 2.7e-02, 3.2e-02)	(0.480, 0.464)
H	(1.508, 2.202, −0.811)	(0.476, 0.476)	(1.555, 2.229, −0.855)	(3.5e-02, 2.6e-02, −2.0e-02)	(0.468, 0.444)
H	(1.968, 2.108, 0.909)	(0.475, 0.475)	(2.026, 2.136, 0.972)	(2.3e-02, 1.6e-02, 2.3e-02)	(0.465, 0.460)
C	(1.151, 0.259, 0.093)	(2.045, 2.044)	(1.173, 0.326, 0.170)	(8.8e-03, 1.3e-02, 2.1e-02)	(2.079, 2.041)
H	(0.894, −0.157, 1.086)	(0.477, 0.477)	(0.874, −0.169, 1.174)	(−1.3e-02, −3.1e-03, 1.6e-02)	(0.511, 0.484)
H	(2.145, −0.157, −0.165)	(0.477, 0.476)	(2.466, 0.202, 0.194)	(6.0e-02, 9.7e-02, 9.6e-02)	(0.478, 0.453)
C	(0.136, −0.222, −0.922)	(2.050, 2.042)	(0.393, 1.372, −0.835)	(3.1e-02, 3.3e-01, 1.1e-02)	(2.076, 1.995)
H	(−0.862, 0.180, −0.667)	(0.489, 0.479)	(−0.989, 1.155, −0.394)	(2.4e-02, 1.9e-01, 3.2e-02)	(0.602, 0.558)
H	(0.391, 0.180, −1.921)	(0.477, 0.477)	(0.500, 0.725, −2.230)	(2.2e-02, 1.3e-01, −3.2e-02)	(0.473, 0.407)
C	(0.072, −1.750, −0.987)	(2.075, 2.070)	(0.332, −3.364, −0.967)	(3.9e-02, −3.3e-01, 3.2e-03)	(2.177, 1.844)
H	(−0.206, −2.154, 0.008)	(0.479, 0.477)	(−0.144, −2.656, 0.306)	(3.3e-02, −1.2e-01, 1.7e-02)	(0.545, 0.541)
H	(1.066, −2.154, −1.265)	(0.475, 0.475)	(1.546, −3.125, −1.527)	(7.2e-02, −2.3e-01, −3.6e-02)	(0.508, 0.466)
H	(−0.677, −2.084, −1.735)	(0.481, 0.475)	(−0.700, −2.701, −2.097)	(4.2e-02, −1.3e-01, −8.1e-03)	(0.578, 0.510)
Au	(−3.930, −0.987, −0.987)	(5.972, 5.009)	(7.218, −0.989, −0.998)	(1.5e+00, −8.5e-04, −2.8e-03)	(5.495, 5.289)
C_2H_5	(1.216, 1.055, 0.158)	(6.500, 6.497)	(1.241, 1.104, 0.211)	(8.2e-03, 1.5e-02, 1.6e-02)	(6.547, 6.391)
CH_2	(0.083,−0.165, −0.975)	(3.017, 2.998)	(0.302, 1.310, −0.903)	(3.0e-02, 3.1e-01, 9.2e-03)	(3.151, 2.959)
CH_3	(0.070, −1.826, −0.989)	(3.511, 3.497)	(0.312, −3.257, −0.995)	(4.1e-02,−3.0e-01, 7.4e-04)	(3.808, 3.362)

The gold atom has an initial velocity of 1.53 Å ·fs^{-1} in the positive x direction, and the butane molecule is initially at rest, asymmetrically. The Hirshfeld charge associated to each atom is decomposed into its up (U) and down (D) contribution

exchange of spin charge density between the gold atom and butane molecule (or fragments).

While in the case of the proton–Helium collision, we were able to lead a full sampling of the parameter space (impact parameter, kinetic energy of the projectile), the configuration space for the gold–butane case is much larger, as the orientation of the butane molecule is to be described in a three-parameter space, the whole characterization having to be done in a five-dimensional space. Monte-Carlo techniques should be used to investigate such a parameter space.

Acknowledgments We acknowledge many discussions with A. Delcorte and O. Restrepo related with secondary ion mass spectrometry, and with Y. Popov concerning the proton–Helium collision. This work was supported by the Communauté française de Belgique, through the Action de Recherche Concertée 07/12-003 “Nanosystèmes hybrides metal-organiques”, and by the FRS-FNRS Belgium (FRFC Grant 2.4.589.09.F).

References

1. Parr RG, Yang W (1994) Density-functional theory of atoms and molecules. Oxford University Press, New York
2. Martin RM (2004) Electronic structure: basic theory and practical methods. Cambridge University Press, London
3. Matta CF (2010) How dependent are molecular and atomic properties on the electronic structure method? Comparison of Hartree-Fock, DFT, and MP2 on a biologically relevant set of molecules. J Comp Chem 31:1297. doi:10.1002/jcc.21417
4. Yabana K, Tazawa T, Abe Y, Bo zek P (1998) Time-dependent mean-field description for multiple electron transfer in slow ion-cluster collisions. Phys Rev A 57:R3165. doi:10.1103/PhysRevA.57.R3165
5. Kirchner T, Horbatsch M, Lüdde HJ (2002) Time-dependent independent-particle model calculation of multiple capture and ionization processes in $p-\mathrm{Ar}, \bar{p}-\mathrm{Ar}$, and $\mathrm{He}^{2+}-\mathrm{Ar}$ collisions. Phys Rev A 66:052719. doi:10.1103/PhysRevA.66.052719
6. Vanroose W, Martin F, Rescigno TN, McCurdy CW (2005) Complete photo-induced breakup of H_2 molecule as a probe of molecular electron correlation. Science 310:1787. doi:10.1126/science.1120263
7. Saalmann U, Schmidt R (1996) Non-adiabatic quantum molecular dynamics: basic formalism and case study Z. fr. Phys D 38:153. doi:10.1007/s004600050077
8. Kulander KC, Devi KR, Sandhya , Koonin SE (1982) Time-dependent Hartree-Fock theory of charge exchange: Application to $\mathrm{He}^{2+} + \mathrm{He}$. Phys Rev A 25:2968. doi:10.1103/PhysRevA.25.2968
9. Tully JC (1990) Molecular dynamics with electronic transitions. J Chem Phys 93:1061. doi:10.1063/1.459170
10. Runge E, Gross EKU (1984) Density-functional theory for time-dependent systems. Phys Rev Lett 52:997. doi:10.1103/PhysRevLett.52.997
11. Keim M, Achenbach A, Lüdde HJ, Kirchner T (2005) Time-dependent density functional theory calculations for collisions of bare ions with helium. Nucl Instrum Meth B 233:240. doi:10.1016/j.nimb.2005.03.114
12. Rudd ME, DuBois RD, Toburen LH, Ratcliffe CA, Goffe TV (1983) Cross sections for ionization of gases by 5-4000-keV protons and for electron capture by 5-150-keV protons. Phys Rev A 28:3244. doi:10.1103/PhysRevA.28.3244

13. Rudd ME, Kim YK, Madison DH, Gallagher JW (1985) Electron production in proton collisions: total cross sections. Rev Mod Phys 57:965. doi:10.1103/RevModPhys.57.965
14. Wang F, Xu XC, Hong XH, Wang J, Gou BC (2011) A theoretical model for electron transfer in ion-atom collisions: calculations for the collision of a proton with an argon atom. Phys Lett A 375:3290. doi:10.1016/j.physleta.2011.07.032
15. Wang F, Hong XH, Wang J, Gou BC, Wang JG (2012) Comparison of three methods for calculation of electron transfer probability in $H^+ + Ne$. Phys Lett A 376:469. doi:10.1016/j.physleta.2011.11.031
16. Isborn CM, Li X, Tully JC (2007) Time-dependent density functional theory Ehrenfest dynamics: collisions between atomic oxygen and graphite clusters. J Chem Phys 126:134307. doi:10.1063/1.2713391
17. Pruneda JM, Sánchez-Portal D, Arnau A, Juaristi JI , Artacho E (2007) Electronic stopping power in LiF from first principles. Phys Rev Lett 99:235501. doi:10.1103/PhysRevLett.99.235501
18. Pruneda JM, Sánchez-Portal D, Arnau A, Juaristi JI, Artacho E (2009) Heating electrons with ion irradiation: a first-principles approach. Nucl Instrum Meth B 267:590. doi:10.1016/j.nimb.2008.11.012
19. Delcorte A, Bour J, Aubriet F, Muller JF, Bertrand P (2003) Sample metallization for performance improvement in desorption/ionization of kilodalton molecules:quantitative evaluation, imaging secondary ion MS, and laser ablation. Anal Chem 75:6875. doi:10.1021/ac0302105
20. Restrepo OA, Prabhakaran A, Hamraoui K, Wehbe N, Yunus S, Bertrand P, Delcorte A (2010) Mechanisms of metal-assisted secondary ion mass spectrometry: a mixed theoretical and experimental study. Surf Interface Anal 42:1030. doi:10.1002/sia.3203
21. Restrepo OA, Delcorte A (2011) Molecular dynamics study of metal-organic samples bombarded by kiloelectronvolt projectiles. Surf Interface Anal 43:70. doi:10.1002/sia.3411
22. Wang F, Hong X, Wang J, Kim KS (2011) Coordinate space translation technique for simulation of electronic process in the ion–atom collision. J Chem Phys 134:154308. doi:10.1063/1.3581820
23. Hirshfeld FL (1977) Bonded-atom fragments for describing molecular charge densities. Theo Chim Acta 44:129. doi:10.1007/BF00549096
24. Marques MAL, Gross EKU (2004) Time-dependent density functional theory. Annu Rev Phys Chem 55:427. doi:10.1146/annurev.physchem.55.091602.094449
25. Marques M, Gross E (2003) In: Fiolhais C, Nogueira F, Marques M (eds) A primer in density functional theory. Springer, Berlin. doi:10.1007/3-540-37072-2
26. Marques M, Ullrich C, Nogueira F, Rubio A, Burke K, Gross EKU (2006) Time-dependent density functional theory. Springer, Berlin. doi:10.1007/b11767107
27. Engel E, Dreizler RM (2011) Density functional theory. Springer, Berlin. doi:10.1007/978-3-642-14090-7
28. Gross EKU, Maitra N (2012) Fundamentals of time-dependent density functional theory. Springer, Berlin. doi:10.1007/978-3-642-23518-4
29. Marques MAL, Castro A, Bertsch GF, Rubio A (2003) Octopus: a first-principles tool for excited electron-ion dynamics. Comput Phys Commun 151:60. doi:10.1016/S0010-4655(02)00686-0
30. Castro A, Heiko A, Oliveira M, Rozzi CA, Andrade X, Lorenzen F, Marques MAL, Gross EKU, Rubio A (2006) Octopus: a tool for the application of time-dependent density functional theory. Phys Status Solidi (b) 243:2465. doi:10.1002/pssb.200642067
31. Alonso JL, Andrade X, Echenique P, Falceto F, Prada-Gracia D, Rubio A (2008) Efficient formalism for large-scale *Ab Initio* molecular dynamics based on time-dependent density functional theory. Phys Rev Lett 101:096403. doi:10.1103/PhysRevLett.101.096403
32. Andrade X, Castro A, Zueco D, Alonso JL, Echenique P, Falceto F, Rubio Ángel (2009) Modified Ehrenfest formalism for efficient large-scale ab initio molecular dynamics. J Chem Theo Comp 5:728. doi:10.1021/ct800518j
33. Castro A, Marques MAL, Rubio A (2004) Propagators for the time-dependent Kohn–Sham equations. J Chem Phys 121:3425. doi:10.1063/1.1774980
34. Perdew JP, Zunger A (1981) Self-interaction correction to density-functional approximations for many-electron systems. Phys Rev B 23:5048. doi:10.1103/PhysRevB.23.5048
35. Perdew JP, Wang Y (1992) Accurate and simple analytic representation of the electron-gas correlation energy. Phys Rev B 45:13244. doi:10.1103/PhysRevB.45.13244
36. Troullier N, Martins JL (1991) Efficient pseudopotentials for plane-wave calculations. Phys Rev B 43:1993. doi:10.1103/PhysRevB.43.1993
37. Belkic D (1978) A quantum theory of ionisation in fast collisions between ions and atomic systems. J Phys B At Mol Phys 11:3529. doi:10.1088/0022-3700/11/20/015
38. Belkic D, Gayet R, Salin A (1979) Electron capture in high-energy ion-atom collisions. Phys Rep 56:279. doi:10.1016/0370-1573(79)90035-8
39. Mergel V, Dörner R, Achler M, Khayyat Kh, Lencinas S, Euler J, Jagutzki O, Nüttgens S, Unverzagt M, Spielberger L, Wu W, Ali R, Ullrich J, Cederquist H, Salin A, Wood CJ, Olson RE, Belkić Dž, Cocke CL, Schmidt-Böcking H (1997) Intra-atomic electron-electron scattering in *p*-He collisions (Thomas Process) investigated by cold target recoil ion momentum spectroscopy. Phys Rev Lett 79:387. doi:10.1103/PhysRevLett.79.387
40. Hasan A, Tooke B, Zapukhlyak M, Kirchner T, Schulz M (2006) Kinematically complete experiment on transfer excitation in intermediate-energy $p + He$ collisions. Phys Rev A 74:032703. doi:10.1103/PhysRevA.74.032703
41. Meister J, Schwarz WHE (1994) Principal components of ionicity. J Phys Chem 98:8245. doi:10.1021/j100084a048
42. Stier PM, Barnett CF (1956) Charge exchange cross sections of hydrogen ions in gases. Phys Rev 103:896. doi:10.1103/PhysRev.103.896
43. Barnett CF, Reynolds HK (1958) Charge exchange cross sections of hydrogen particles in gases at high energies. Phys Rev 109:355. doi:10.1103/PhysRev.109.355
44. Williams JF (1967) Measurement of charge-transfer cross sections for 0.25- to 2.5-MeV protons and hydrogen atoms incident upon hydrogen and helium gases. Phys Rev 157:97. doi:10.1103/PhysRev.157.97
45. Welsh LM, Berkner KH, Kaplan SN, Pyle RV (1967) Cross sections for electron capture by fast protons in H_2, He, N_2, and Ar. Phys Rev 158:85. doi:10.1103/PhysRev.158.85
46. Jamorski C, Foresman JB, Thilgen C, Lüthi HP (2002) Assessment of time-dependent density-functional theory for the calculation of critical features in the absorption spectra of a series of aromatic donor–acceptor systems. J Chem Phys 116:8761. doi:10.1063/1.1465404
47. Dreuw A, Head-Gordon M (2004) Failure of time-dependent density functional theory for long-range charge-transfer excited states: the zincbacteriochlorin bacteriochlorin and bacteriochlorophyll spheroidene complexes. J Am Chem Soc 126:4007. doi:10.1021/ja039556n
48. Dreuw A, Weisman JL, Head-Gordon M (2003) Long-range charge-transfer excited states in time-dependent density functional theory require non-local exchange. J Chem Phys 119:2943. doi:10.1063/1.1590951

Theor Chem Acc (2013) 132:1291
DOI 10.1007/s00214-012-1291-y

REGULAR ARTICLE

A simple DFT-based diagnostic for nondynamical correlation

Uma R. Fogueri · Sebastian Kozuch ·
Amir Karton · Jan M. L. Martin

Received: 27 March 2012 / Accepted: 4 October 2012 / Published online: 5 December 2012

Abstract We propose a simple DFT-based diagnostic for nondynamical correlation effects, namely $A_\lambda = (1 - \mathrm{TAE}[X_\lambda C]/\mathrm{TAE}[XC])/\lambda$ where TAE stands for the molecular total atomization energy, XC is a pure-DFT exchange-correlation functional, and $X_\lambda C$ represents the corresponding hybrid with 100λ % Hartree–Fock-type exchange. The diagnostic is a good predictor for sensitivity of energetics to the level of theory, unlike most wavefunction-based diagnostics. For GGA functionals, A_λ values approaching unity indicate severe nondynamical correlation, while values between 0 and about 0.1 indicate systems where correlation is predominantly dynamical in character (or entirely absent). The diagnostic is only weakly sensitive to the basis set (beyond polarized valence double zeta) and can easily be applied to problems beyond the practical reach of wavefunction ab initio methods required for other diagnostics. We also propose a simple measure for the importance of dynamic correlation.

Keywords Nondynamical correlation · Density functional theory · Diagnostics · Ab initio · Thermochemistry

1 Introduction and background

When the Hartree–Fock reference determinant offers a very good zero-order description of the system, and no individual determinants or group of determinants make large contributions to the correlated many-body wavefunction, the molecule is said to be dominated by dynamical correlation. In such a scenario, the cluster expansion of the wavefunction converges rapidly, and a "gold standard" correlation method like CCSD(T) [1] truly comes very close to the exact (i.e., full CI) basis set correlation energy.

Deviations from this regime are, in the literature, interchangeably referred to as nondynamical correlation [2],[1] static correlation, near-degeneracy correlation, left-right correlation, and multireference effects [3].

In a very recent paper, Hollett and Gill (HG) [3] distinguish two types of nondynamical correlation, which they term Type A and B, while they designate dynamical correlation "Type D." A similar dichotomy was proposed earlier by Scuseria and Tsuchimoshi (ST) [4] who use the labels "left-right strong correlation" and "angular strong correlation," respectively, instead of "type A" and "type B".

"Type A static correlation," viz. "left-right strong correlation," is best illustrated by stretching H_2 to infinite

Published as part of the special collection of articles celebrating theoretical and computational chemistry in Belgium.

Electronic supplementary material The online version of this article (doi:10.1007/s00214-012-1291-y) contains supplementary material, which is available to authorized users.

U. R. Fogueri · J. M. L. Martin
Department of Chemistry, Center for Advanced Scientific Computing and Modeling (CASCaM), University of North Texas, Denton, TX 76201, USA

S. Kozuch · J. M. L. Martin (✉)
Department of Organic Chemistry, Weizmann Institute of Science, 76100 Rehovot, Israel
e-mail: gershom@weizmann.ac.il

A. Karton
School of Chemistry, University of Sydney, Sydney, NSW 2006, Australia

---

[1] The terms "dynamical" and "nondynamical" correlation appear to have been introduced first in Sinanoglu [2].

distance with RHF orbitals. Near r_e, the SCF wavefunction is an excellent zero-order description: as the bond is stretched, the σ_g and σ_u orbitals approach degeneracy, and eventually only a bideterminantal wavefunction will be an adequate zero-order approximation: a single-reference calculation using RHF orbitals will at large distance correspond to $H^+ + H^-$. However, as first noticed by Pople [5, 6], using UHF [7] orbitals not only are a lower energy obtained, but also correct dissociation is achieved: the single determinant is no longer an eigenfunction of the $\mathbf{S}^2$ operator but is able to capture some of the static correlation. Some systems exhibit such a "UHF instability" [8] even at their (experimental or high-level ab initio) equilibrium geometries: examples can be found in the first data column of Table 4.

Type A correlation energy is often, confusingly, referred to as "long-range" correlation: dispersion between noble gas atoms, which is purely dynamical in character, is of course likewise a long-range effect, albeit in a quite different way.

"Type B static correlation," viz. "angular strong correlation," is best illustrated [3] by comparing the correlation energy of helium-like ions with arbitrary Z with the valence correlation energy of beryllium-like ions, likewise with arbitrary Z [9]. In the He-like case, the 1s orbital never becomes quasidegenerate with any other, and Hartree–Fock is a good zero-order description throughout: in the limit for large Z, the "type D" (purely dynamical) correlation energy converges to a constant [10, 11]. In the Be-like case for $Z < 4.138$, the absolute energy gap between the 2s and 2p orbitals is small and a UHF instability exists. As Z is increased above the "isostability point" $Z = 4.138$, the gap actually widens in absolute terms but becomes ever smaller *relative* to the actual orbital energies: In fact, the correlation energy in the large-Z limit contains a term that goes up linearly with Z (!). As the type D correlation will asymptotically approach a constant like for the He series, type B static correlation will become the dominant contribution for large Z.

It may be clear in a qualitative sense how nondynamical correlation is defined, or at least experienced quantum chemists have an intuitive grasp of it [12].[2] However, for assessing the quality of quantum chemical predictions or the need for more computationally demanding ones, a quantitative or at least semiquantitative definition would be very helpful. Several such "multireference diagnostics" or "nondynamical correlation diagnostics" have been proposed over the years by wavefunction ab initio practitioners. These can basically be divided into two categories: wavefunction based and energy based. Values of various diagnostics for a representative selection of molecules can be found in Table 1, while those for the entire W4-11 set can be found in the Electronic Supporting Information.

Another perspective is offered by considering "Type A nondynamical correlation"/"left-right strong correlation" as a manifestation of quantum entanglement. A physically motivated measure of the latter is the von Neumann entropy [13], or the closely related correlation entropy [14, 15]

$$S_2 = -\sum_i \left(\frac{n_i}{2}\right) \ln \frac{n_i}{2} \tag{1}$$

where the n_i are the natural orbital occupation numbers. (Note that for a closed-shell, single-determinant Hartree–Fock wavefunction, $S_2 = 0$ since all n_i are either 2 or 0, and application of l'Hôpital's rule yields $\lim_{x\to 0^+} x \ln x = 0$.) Partitioning in spatial and spin correlation entropies has also been considered [16].

Entanglement is the central concept in the DMRG (density-matrix renormalization group) community [17]. In a recent study [18] on correlation effects in polycyclic aromatic hydrocarbons (PAHs), Mazziotti and coworkers employ Eq. (1) as a diagnostic for static correlation. They note that, as written, the expression is not intensive: As a workaround, applying it to CASSCF expansions for PAHs of different sizes, they truncated summations at the core and Rydberg ends of the CASSCF window such that they have the same number of NOs in each summation.

Out of the wavefunction-based diagnostics, perhaps the most widely used one is the T_1 diagnostic of Lee and Taylor [19], which is essentially nothing but the Frobenius norm of the single-excitation amplitude vector divided by the square root of the number of electrons correlated, $T_1 = ||\mathbf{t}_1||_2/\sqrt{n}$. (The denominator ensures that T_1 is approximately size-intensive.) Empirically, a T_1 of greater than 0.02 is said to indicate significant nondynamical correlation effects [16]. A closely related quantity is the D_1 diagnostic [20–22] of Janssen and Nielsen, which is the matrix norm of $\mathbf{t}_1$. T_1 is not foolproof by itself: for example [23], F_2 has a deceptively low $T_1 = 0.011$ despite being a notoriously "multireference" molecule (it is actually metastable at the SCF level), and $T_1 = 0.027$ for ozone only suggests mild problems for what is in fact a pathological system.

As for the largest T_2 amplitude in a CCSD calculation—another wavefunction-based diagnostic fairly widely employed in the coupled cluster community—it is actually larger for formaldehyde than for dioxygen (a much harder system to "get right"). Monitoring both T_1 and the largest T_2 amplitudes viz. C_2 coefficients will in practice detect

---

[2] Intuitive, empirical grasp of a concept was memorably expressed by Associate Justice Potter Stewart in the US Supreme Court decision in *Jacobellis versus Ohio* [12]: "Perhaps I could never succeed in intelligibly [defining it]. But I know it when I see it."

Table 1 Diagnostics for representative sample of W4-11 set, sorted by ascending %TAE[$T_4 + T_5$]

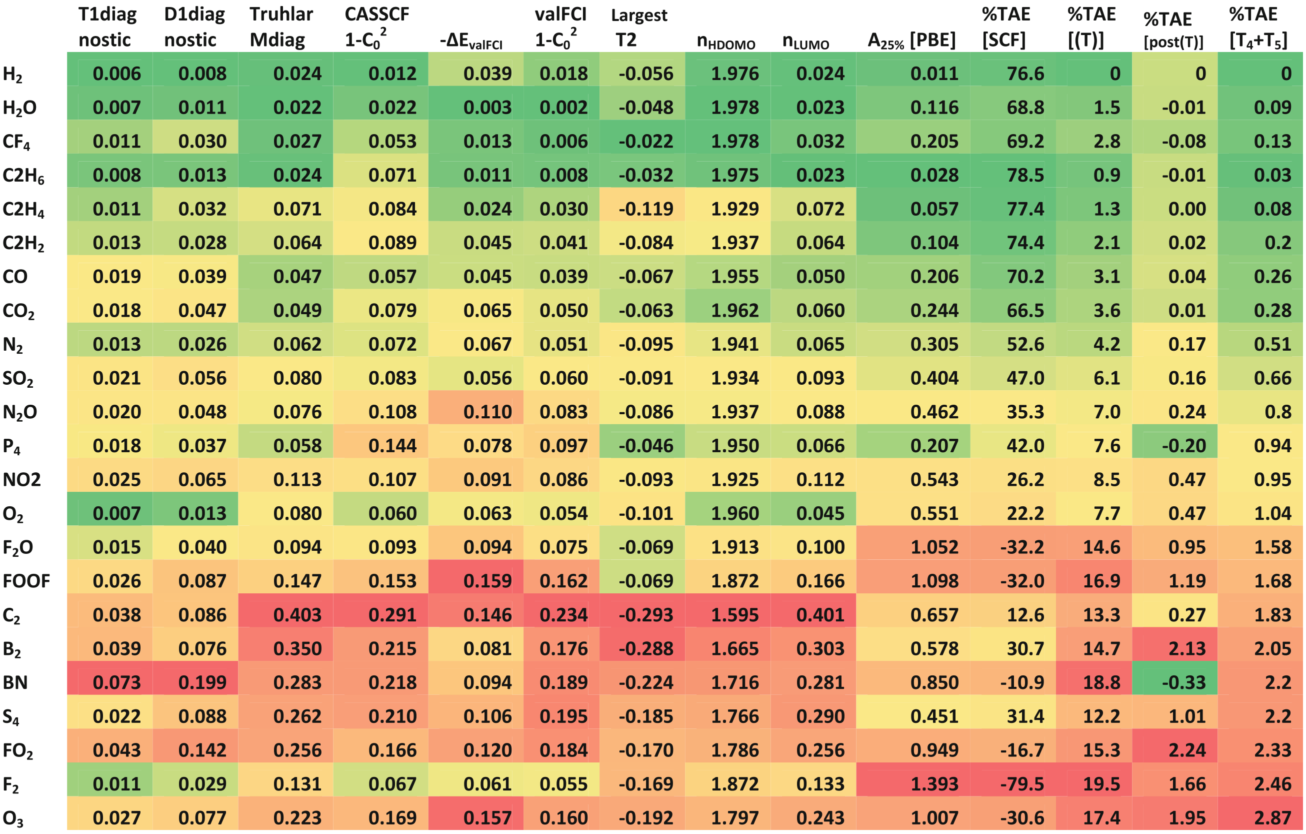

	T1diag nostic	D1diag nostic	Truhlar Mdiag	CASSCF $1\text{-}C_0^2$	$-\Delta E_{valFCI}$	valFCI $1\text{-}C_0^2$	Largest T2	n_{HDOMO}	n_{LUMO}	$A_{25\%}$ [PBE]	%TAE [SCF]	%TAE [(T)]	%TAE [post(T)]	%TAE [T_4+T_5]
H_2	0.006	0.008	0.024	0.012	0.039	0.018	-0.056	1.976	0.024	0.011	76.6	0	0	0
H_2O	0.007	0.011	0.022	0.022	0.003	0.002	-0.048	1.978	0.023	0.116	68.8	1.5	-0.01	0.09
CF_4	0.011	0.030	0.027	0.053	0.013	0.006	-0.022	1.978	0.032	0.205	69.2	2.8	-0.08	0.13
$C2H_6$	0.008	0.013	0.024	0.071	0.011	0.008	-0.032	1.975	0.023	0.028	78.5	0.9	-0.01	0.03
$C2H_4$	0.011	0.032	0.071	0.084	0.024	0.030	-0.119	1.929	0.072	0.057	77.4	1.3	0.00	0.08
$C2H_2$	0.013	0.028	0.064	0.089	0.045	0.041	-0.084	1.937	0.064	0.104	74.4	2.1	0.02	0.2
CO	0.019	0.039	0.047	0.057	0.045	0.039	-0.067	1.955	0.050	0.206	70.2	3.1	0.04	0.26
CO_2	0.018	0.047	0.049	0.079	0.065	0.050	-0.063	1.962	0.060	0.244	66.5	3.6	0.01	0.28
N_2	0.013	0.026	0.062	0.072	0.067	0.051	-0.095	1.941	0.065	0.305	52.6	4.2	0.17	0.51
SO_2	0.021	0.056	0.080	0.083	0.056	0.060	-0.091	1.934	0.093	0.404	47.0	6.1	0.16	0.66
N_2O	0.020	0.048	0.076	0.108	0.110	0.083	-0.086	1.937	0.088	0.462	35.3	7.0	0.24	0.8
P_4	0.018	0.037	0.058	0.144	0.078	0.097	-0.046	1.950	0.066	0.207	42.0	7.6	-0.20	0.94
NO2	0.025	0.065	0.113	0.107	0.091	0.086	-0.093	1.925	0.112	0.543	26.2	8.5	0.47	0.95
O_2	0.007	0.013	0.080	0.060	0.063	0.054	-0.101	1.960	0.045	0.551	22.2	7.7	0.47	1.04
F_2O	0.015	0.040	0.094	0.093	0.094	0.075	-0.069	1.913	0.100	1.052	-32.2	14.6	0.95	1.58
FOOF	0.026	0.087	0.147	0.153	0.159	0.162	-0.069	1.872	0.166	1.098	-32.0	16.9	1.19	1.68
C_2	0.038	0.086	0.403	0.291	0.146	0.234	-0.293	1.595	0.401	0.657	12.6	13.3	0.27	1.83
B_2	0.039	0.076	0.350	0.215	0.081	0.176	-0.288	1.665	0.303	0.578	30.7	14.7	2.13	2.05
BN	0.073	0.199	0.283	0.218	0.094	0.189	-0.224	1.716	0.281	0.850	-10.9	18.8	-0.33	2.2
S_4	0.022	0.088	0.262	0.210	0.106	0.195	-0.185	1.766	0.290	0.451	31.4	12.2	1.01	2.2
FO_2	0.043	0.142	0.256	0.166	0.120	0.184	-0.170	1.786	0.256	0.949	-16.7	15.3	2.24	2.33
F_2	0.011	0.029	0.131	0.067	0.061	0.055	-0.169	1.872	0.133	1.393	-79.5	19.5	1.66	2.46
O_3	0.027	0.077	0.223	0.169	0.157	0.160	-0.192	1.797	0.243	1.007	-30.6	17.4	1.95	2.87

$\Delta E_{\mathrm{valFCI}}$ is in Hartree, the remaining values are dimensionless

most problematic systems but for instance (see Table 1), the fairly mild scores of F_2O_2 (a.k.a. FOOF) on both criteria belie its highly problematic [24] character.

Another diagnostic that has been used over the years are the natural orbital occupations of the highest occupied and lowest virtual orbitals. The "*M* diagnostic" of Truhlar and coworkers [25] effectively condenses these into a single number:

$$M = \frac{1}{2}\left(2 - n_{\mathrm{HDOMO}} + n_{\mathrm{LUMO}} + \sum_{j\mathrm{SOMO}} |n_j - 1|\right) \qquad (2)$$

where n_i stands for the natural orbital (generalized) occupation number of orbital j, and, in a single-determinant picture, HDOMO would be the highest doubly occupied molecular orbital, LUMO the lowest unoccupied molecular orbital, and the SOMOs any singly occupied molecular orbitals. For the special case of 2-in-2 CASSCF on a closed-shell singlet, this reduces to $M = n_{\mathrm{LUMO}}$, which, with $x = n_{\mathrm{LUMO}}$, is also the low-x limit of the corresponding correlation entropy $S_2 = -(x/2)\ln(x/2) - (1-x/2)\ln(1-x/2)$.

Yet another criterion, known in various guises among people who carry out multireference calculations, is the coefficient C_0 (or its corresponding weight C_0^2) in a CISD or full-valence CASSCF wavefunction [26]. Since actually their deviation from unity is the true criterion, we report the CASSCF $1 - C_0^2$ in Table 1 instead. These two are not bulletproof, as the low $1 - C_0^2$ and moderate M for F_2 illustrate.

Various energetic criteria for nondynamical correlation were proposed by one of us [23] in an attempt to find reliable measures for inadequacy of the CCSD(T) method. Earlier, Handy and coworkers [27] proposed E[CASSCF, full valence] $-$ E[SCF], while Krylov et al. [28] proposed E[full CI, valence] $-$ E[SCF]. These latter two definitions differ through the orbital relaxation involved in CASSCF.

As an operational definition, we proposed [23] %TAE[$T_4 + T_5$], that is, the percentage of the molecular total atomization energy accounted for by connected quadruple and quintuple excitations. These are obtained a posteriori as a by-product of accurate W4 theory [23, 29] computational thermochemical calculations, but in view of their immense cost (the corresponding steps account for the lion's share of the CPU time in a typical W4 calculation), these are obviously not useful as a priori predictors. We did find two energy-based a priori diagnostics (requiring no more than a CCSD(T)/cc-pVTZ single point calculation) that are statistically very strongly correlated with %TAE[$T_4 + T_5$], namely %TAE[(T)] ($R^2 = 0.941$) and %TAE[SCF] ($R^2 = 0.810$). These latter statistics were obtained over a sample of 34 molecules spanning a wide range of multireference character: more recently, this analysis was repeated over the 140 molecules in the W4-11 benchmark dataset [30]: Upon elimination of the anomalous Be_2 diatomic (which is unbound at the CCSD level), we found essentially identical R^2 values of 0.94 and 0.80, respectively. This study also considered the basis set dependence of these diagnostics and found that they did not change significantly upon basis set expansion beyond cc-pVTZ [31]. It was also found [23, 30] that the T_1 and D_1 diagnostics correlate fairly poorly with %TAE[$T_4 + T_5$], with $R^2 = 0.36$ and 0.33, respectively, over the W4-11 set.

The reader might wonder why not use %TAE[post-CCSD(T)], that is, %TAE[$T_4 + T_5$] + %TAE[CCSDT − CCSD(T)], as a benchmark instead. However, the good performance of CCSD(T) itself results [32, 33] from a (mildly erratic) error compensation between T_4 (which universally increases TAE) and $T_3 - (T)$ (which almost universally decreases it), and hence highly problematic molecules like singlet C_2 look much more "well-behaved" on this criterion than they actually are.

The issue of nondynamical correlation not only vexes wavefunction ab initio practitioners, but also bedevils the presently much larger DFT developer and especially user community as well. While DFT is generally more resilient toward nondynamical correlation than, for example, many-body perturbation theory, it is common knowledge that, for example, "pure DFT" and hybrid DFT methods may yield very different answers in such multireference systems as early transition metal complexes.

As DFT (at least below the fifth rung of Jacob's Ladder [34][3]) is a single-determinant theory, diagnostics based on the structure of the multideterminantal wavefunction require additional wavefunction calculations, as do the %TAE[SCF] and %TAE[(T)] diagnostics. However, while preparing a lecture about the adiabatic connection [35] and hybrid DFT methods [36] for a graduate-level computational chemistry course, an alternative suggested itself, which is the subject of the present paper.

2 Methods

As our benchmark dataset, we used the 140 molecules in the W4-11 set, at fixed reference geometries taken from the supporting information to Ref. [30]. All calculations were performed on the Linux cluster of CASCaM (Center for Advanced Scientific Computing and Modeling) at the University of North Texas. CASSCF [37], valence-only full CI, and CCSD(T) calculations were carried out using the MOLPRO 2010.1 package [38] using full-valence active spaces in a cc-pVTZ basis set; for some of the largest molecules such as acetic acid, the lowest valence orbitals and the corresponding antibonding virtuals were taken out of the active space for technical reasons. For the open-shell systems, restricted open-shell wavefunctions were used. All DFT calculations were carried out using the Gaussian 09 program system [39] on the same computational platform; here, unrestricted Kohn–Sham orbitals were used for the open-shell systems. Orbital stability analyses were likewise carried out using Gaussian 09.

Total atomization energies (TAE_e values) were obtained as differences between the molecular energy and the sum of those of the neutral atoms in their respective ground states.

%TAE[post-CCSD(T)] and %TAE[$T_4 + T_5$] were taken from the Electronic Supporting Information of the W4-11 paper [30].

The following five DFT exchange-correlation functionals were considered: SVWN5 [40], BLYP [41–43], PBE [44], BB95 [45], and TPSS [46].

Full numerical data for the W4-11 dataset are given in the Electronic Supporting Information to the present paper.

3 Results and discussion

One can plot a molecule's total atomization energy and its various components (1-electron, Coulomb, exchange, correlation) as a function of the percentage of Hartree–Fock-like exchange. A representative such plot, for oxirane/ethylene epoxide (C_2H_4O), is given in Fig. 1. As can be seen there, while some components display just a hint of curvature, the dependence of both TAE and its various contributions exhibits surprisingly weak deviation from linearity. (It would be perfectly linear if the calculations were carried out in a post-LDA fashion.)

Zooming in a little, we do find that the ratio TAE(λ)/TAE(0) as a function of the fraction of HF exchange λ only shows some weak curvature (deviation from linearity) at the quadratic level (and essentially none at cubic and higher orders) for almost all the species. Even more conveniently, the dimensionless quantity $A_\lambda = (1 - \mathrm{TAE}(\lambda)/\mathrm{TAE}(0))/\lambda$ lends itself very well to linear regression to

---

[3] In this Biblical metaphor (Gen. 28:10–19) introduced by Perdew and Schmidt [34], Heaven is the exact solution and Earth the Hartree product. The first rung represents the local density approximation, the second rung generalized gradient approximations, the third rung meta-GGAs involving higher derivatives of the density, the fourth rung occupied-orbital-dependent functionals (of which hybrids are a special case), and the fifth rung virtual-orbital-dependent functionals (of which double-hybrids [56–58] are a special case).

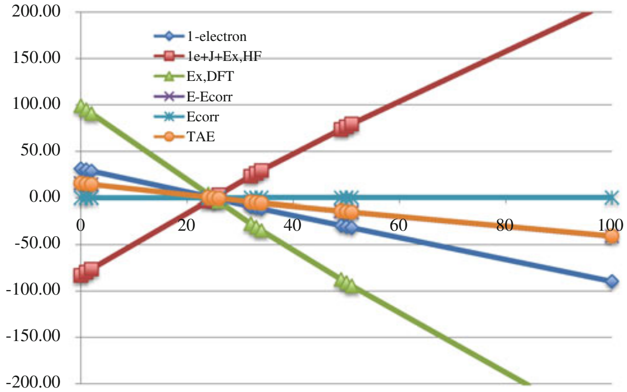

Fig. 1 Profile of different components to the PBE$_\lambda$/cc-pVTZ TAE$_e$ of oxirane as a function of the percentage of Hartree–Fock exchange. Values are in kcal/mol relative to λ = 25 % (PBE0)

$A_\lambda \approx S_\lambda + T_\lambda\lambda$, with $R^2 = 0.99$–0.9999 across the board (see Electronic Supporting Information). Typically, and consistent with the near-linearity of the TAE dependence, we find T_λ/S_λ on the order of 0.1, with the exception of a few species for which S_λ is very small to begin with and which are dominated by dynamical correlation (such as H_2 and B_2H_6). Large values of S_λ are found for molecules the quantum chemist intuitively thinks of as "basket cases" such as F_2O_2, O_3, etc.

Qualitatively, the same behavior is seen for all exchange-correlation functionals considered, but on average, we find S_λ[PBE]/S_λ[LDA] = 0.44 and S_λ[TPSS]/S_λ[PBE] = 0.76. It stands to reason that sensitivity to the percentage of HF exchange would decrease as one walks up the "Jacob's Ladder" [34]. S_λ[BLYP] is very similar to S_λ[PBE], and S_λ[BB95] is almost indistinguishable from S_λ[BLYP], suggesting not only that similar behavior is seen within rungs of Jacob's Ladder but also that the exchange functional affects values more than the correlation functional.

As can be seen in Table 2, squared correlation coefficients between S_λ for the four non-LDA functional combinations are universally very large, $R^2 = 0.993$–0.999. This suggests that they all essentially contain the same information.

How well do the S_λ parameters correlate with the more traditional nondynamical correlation indices? Correlation is largest with %TAE[SCF], with which R^2 vary from 0.96 to 0.97, and second largest with %TAE[(T)], all functionals yielding R^2 around 0.90.

Considering %TAE[$T_4 + T_5$] as the benchmark, the best statistical predictor is not surprisingly %TAE[(T)] with $R = 0.97$, with %TAE[SCF] and S_λ tied for second place. When it comes to %TAE[post-CCSD(T)] (error compensations and all), the DFT-based diagnostic in fact marginally outperforms %TAE[SCF] and %TAE[(T)].

Of the wavefunction-based diagnostics, the only one that has a reasonable correlation with %TAE[$T_4 + T_5$] is Truhlar's Mdiag, which for closed-shell species is effectively the average of HOMO and LUMO natural orbital occupations (as well as the low-n_i limit of the HOMO–LUMO correlation entropy). The T_1 diagnostic statistically correlates poorly with all energy-based diagnostics, except

Table 2 Squared correlation matrix of various diagnostics for nondynamical correlation for the W4-11 dataset less Be_2 (i.e., 139 molecules)

R^2 matrix	Sλ[BB95]	Sλ[PBE]	Sλ[TPSS]	Sλ[BLYP]	CASSCF 1-C$_0^2$	valFCI Ecorr	valFCI 1-C$_0^2$	CASSCF Mdiag	%TAE e[SCF]	%TAEe[(T)]	%TAEe[post(T)]	%TAEe[T4+T5]	T1
Aλ[BB95]	1.000	0.999	0.989	0.998	0.214	0.465	0.455	0.401	0.962	0.900	0.607	0.791	0.343
Aλ[PBE]		1.000	0.991	0.999	0.211	0.458	0.447	0.393	0.964	0.904	0.597	0.792	0.328
Aλ[TPSS]			1.000	0.993	0.209	0.438	0.436	0.396	0.971	0.900	0.606	0.797	0.306
Aλ[BLYP]				1.000	0.214	0.455	0.450	0.405	0.967	0.908	0.615	0.802	0.327
CASSCF 1-C$_0^2$					1.000	0.613	0.793	0.735	0.210	0.355	0.194	0.420	0.334
valFCI Ecorr						1.000	0.790	0.473	0.427	0.509	0.278	0.278	0.521
valFCI 1-C$_0^2$							1.000	0.821	0.429	0.616	0.409	0.409	0.698
Mdiag								1.000	0.394	0.555	0.442	0.654	0.425
%TAEe[SCF]									1.000	0.896	0.589	0.805	0.286
%TAEe[(T)]										1.000	0.593	0.938	0.383
%TAEe[post-CCSD(T)]											1.000	0.674	0.339
%TAEe[T4+T5]												1.000	0.378
T1													1.000

Between T_1 and D_1, $R^2 = 0.895$; correlations of D_1 with other diagnostics in this table are similar to or lower than those for T_1. For instance, with valFCI Ecorr and valFCI $1 - C_0^2R^2 = 0.278$ and 0.312, respectively

Unsurprisingly, the HOMO–LUMO correlation entropy tracks the CASSCF Mdiag very closely, with $R^2 = 0.953$

for the valence FCI correlation energy: its strongest correlation, aside from with the closely related D_1, is seen with $1 - C_0^2$ from a valence full CI calculation. (We note in passing that $1 - C_0^2$, the Truhlar M diagnostic, and the HOMO–LUMO correlation entropy all appear to contain very similar information.)

For diagnostic purposes, one wonders whether we really need to plot and fit such "HF exchange response curves," or can we, for a given fixed λ°, simply consider

$$A_{\lambda^\circ} = (1 - \mathrm{TAE}(\lambda^\circ)/\mathrm{TAE}(0))/\,\lambda^\circ \approx S_\lambda + \lambda^\circ \mathrm{T}_\lambda$$

As T_λ is not only small but also itself fairly well correlated with %TAE[$T_4 + T_5$], $R = 0.75$ in the PBE case, we can expect the correlation coefficient of A_{λ° with %TAE[$T_4 + T_5$] to be pretty constant. Not surprisingly, for values of λ° ranging from 0.05 to 1 (i.e., 5–100 %), A_{λ° has an essentially constant $R = 0.888$–0.893 with %TAE[$T_4 + T_5$]. We can, therefore, take a given arbitrary λ°, for example, 25%, in which case the equation reduces to $A_{25\,\%}[\mathrm{PBE}] = 4(1 - \mathrm{TAE(PBE0)/TAE(PBE)})$ or $A_{25\,\%}[\mathrm{BLYP}] = 4(1 - \mathrm{TAE(B1LYP)/TAE(BLYP)})$.

(While the present paper was being prepared for submission, a paper by Truhlar and coworkers [47, 48] was brought to our attention, in which $B1 = (\mathrm{BE_{BLYP}} - \mathrm{BE_{B1LYP}})/n_{\mathrm{bonds}}$ was considered for bond-breaking reactions.)

Returning to Table 1, and to the full table for the W4-11 set given in supporting information, we can state the following (for PBE or BLYP):

- A_λ values around or above 1 appear to indicate severe-to-pathological static correlation
- values around 0.5 appear to indicate moderate-to-severe nondynamical correlation
- values near 0.3 appear to indicate moderate nondynamical correlation
- near 0.15: mild
- below about 0.10: correlation is primarily dynamic in character

One advantage of A_λ is its relatively low cost. The cc-pVTZ basis set may still be out of reach for many practical problems, however, and therefore, the basis set dependence of the diagnostic is of interest. Table 3 lists correlation coefficients and deviation statistics (from near-basis-set-limit values with Jensen's pc-3 polarization consistent basis set [49–55]) for the LANL2DZ, 6-31G*, and 6-311G** basis sets. It is shown there that $R^2 \geq 0.98$ for basis sets of at least polarized double-zeta quality, while $R^2 \geq 0.995$ can be reached for triple-zeta double polarization or better basis sets. Only for small double-zeta basis sets like LANL2DZ or SDD could basis set dependence potentially become an issue.

Are we primarily dealing with Type A or Type B static correlation? One easy probe for that is to check for UHF instabilities (Table 4). Stability analysis using Gaussian 09 for RHF references reveals RHF/UHF energy lowerings for 29 out of 139 molecules, plus for Be_2 and Be atom: of these, the following exceed 10 kcal/mol: Be_2, BN($^1\Sigma^+$), $C_2(1\Sigma_g^+)$, $CH_2(^1A_1)$, FOOF, O_3, S_3, and S_4. Using B3LYP orbitals instead, only eight such instabilities are seen (three of which insignificant), which is reduced to just five (two of which insignificant) using BLYP orbitals. (The three species for which UBLYP is significantly lower in energy than RBLYP are the singlets BN, C_2, and CH_2.) This illustrates that, at equilibrium geometries, we are dealing chiefly with type B nondynamical correlation even with HF orbitals, and almost exclusively so using DFT orbitals. It also suggests that using DFT rather than HF orbitals as a reference (as is done, e.g., in double-hybrid functionals [56–58][4]) imparts greater resilience to at least type A static correlation. In fact, Cohen and Handy argue [59–62] that the exchange functional in DFT includes "left-right correlation." Huzak et al. [63] demonstrate that there is a clear analytical relationship between the extent of symmetry breaking and the inverse of the HOMO–LUMO gap. Note that in a Belgian collaboration on linear polyacenes [64], it was found that even naphthalene already exhibits a UHF instability, despite %TAE[SCF] = 75.5 and %TAE[(T)] = 1.56 values that are clearly in the "dynamical-dominated" range.[5] In the present work, we find quite low $A_{25\,\%}$[PBE] values of 0.067 and 0.075 for benzene and naphthalene, while the M_{diag} obtained from QCISD/cc-pVTZ natural orbitals are more "midrange" at 0.076 and 0.087, respectively. (The same holds true for the HOMO–LUMO correlation entropies.)

Finally, we note (Table 4) that both the absolute and the relative RHF/UHF energy lowerings exhibit fairly high

Table 3 Basis set sensitivity of $A_{50\,\%}$[PBE] as measured by the squared correlation coefficient with pc-3 results

	R^2 with pc-3
LANL2DZ	0.8375
SDD	0.8657
6-31G*	0.9911
6-311G**	0.9913
6-311G(2*d*,*p*)	0.9953
cc-pVTZ	0.9976
def2-SVP	0.9840
def2-TZVPP	0.9985
pc-1	0.9870
pc-2	0.9979
pc-3	1 by def.

---

[4] For the original concept of perturbation theory in a basis of Kohn–Sham orbitals, see: Görling and Levy [58].

[5] In fact, even benzene is marginally UHF-instable.

Table 4 UHF relaxation energy lowerings (kcal/mol) for the molecules in the W4-11 set

	HF	B3LYP	BLYP
AlH	0.33		
Be_2	12.93	0.20	
Be	0.20		
BH	4.08	0.03	0.02
BN	53.44	6.30	3.81
$C_2(1\Sigma^+_g)$	75.28	11.42	36.42
CCl_2	4.45		
CF_2	0.37		
CH_2C	0.42		
$CH_2(^1A_1)$	11.44	4.74	4.62
cis-HCOH	1.78		
cis-HONO	0.13		
cis-N_2H_2	1.34		
dioxirane	1.12		
F_2O	0.07		
F_2	6.27		
FOOF	24.96		
glyoxal	0.23		
HNO	3.50	0.18	0.12
NCCN	2.23		
O_3	53.66	1.70	
oxirene	1.50		
P_2	5.24		
S_2O	6.50		
S_3	16.45		
S_4(c2v)	34.16	1.17	
tr-HCOH	1.26		
tr-HONO	0.29		
tr-N_2H_2	1.21		

Absent entries mean the RHF solution is stable with respect to spin-symmetry breaking

For the values given, correlation coefficients with some diagnostics for nondynamical correlation are as follows: Truhlar *M*diag $R = 0.923$; HOMO–LUMO correlation entropy $S_{\text{corr}}R = 0.905$; CASSCF $1 - C_0^2 R = 0.840$. Correlation coefficients between (TAE[UHF] − TAE[RHF])/TAE total and various diagnostics are as follows: Truhlar *M*diag $R = 0.875$, $S_{\text{corr}}R = 0.869$, CASSCF $1 - C_0^2 R = 0.778$, %TAE[(*T*)] $R = 0.734$

correlation coefficients with the correlation entropy S_2 ($R = 0.905$ absolute, $R = 0.869$ relative) and with the (in fact, if perhaps not in intent) closely related *M* diagnostic. This again suggests that these diagnostics primarily measure type A static correlation, rather than the sum of both types A and B.

For the sake of completeness: what values of A_{λ° are obtained in situations where no correlation contribution at all is present? We considered two examples: $D_e[H_2^+]$ and IP(H). As neither has a correlation contribution of any kind, we expect A_{λ° values close to zero: in fact, we find $A_{25\,\%}$[PBE] = +0.056 and −0.011, respectively, acceptably close to zero. $A_{25\,\%}$[BB95] = 0.068 and −0.003, respectively, $A_{25\%}$[BLYP] = 0.068 and −0.004, respectively, while for $A_{25\%}$[TPSS], we find 0.074 and 0.000, respectively.

A reviewer inquired whether the M06L [65], M06 [66], M06-2X [66], and M06HF [67] family of functionals could be used for this diagnostic. Since the meta-GGA exchange and correlation parts of the M06 family [68] include dozens of adjustable parameters optimized over the training set at the given percentages of Hartree–Fock exchange (which are 0, 28, 56, and 100, respectively), the dependence of TAEs on the percentage of HF exchange is much weakened, as illustrated in Ref. [69, 70] for the BMK functional proposed there.

Defining $A_{\text{M06}} = (1 - \text{TAE[M06]/TAE[M06L]})/0.28$ and similarly for $A_{\text{M06}-2X}$ and $A_{\text{M06}-\text{HF}}$, and applying this to the W4-11 set, we find small negative values for systems dominated by dynamical correlation, rising to positive values in the 0.2–0.4 range for systems with severe static correlation. The correlation coefficients with %TAE[$T_4 + T_5$] are 0.79 for A_{M06}, 0.84 for $A_{\text{M06}-2X}$, and 0.85 for $A_{\text{M06}-\text{HF}}$. These are lower than for, for example, $A_{25\%}$[PBE] but still indicate somewhat useful predictive power, which may be useful for people carrying out application studies primarily using the M06 family (Table 3).

Finally, one might wonder whether a simple, convenient indicator for the importance of *dynamical* correlation could be generated from DFT data. If we eliminate the molecules with %[(*T*)] above 10% (i.e., cases with strong static correlation), we can consider, for a given correlation functional *C*,

$$D[C] = 1 - \text{TAE[HF]/TAE[HFC]}$$

where HF stands for straight Hartree–Fock, and HFC for the combination of pure Hartree–Fock exchange with DFT correlation functional *C*. *D*[*C*] has the following squared correlation coefficients R^2 with %TAE[SCF]: *D*[LYP] 0.907, *D*[PBE] 0.927, *D*[TPSS] 0.887, and *D*[B95] 0.948. If instead we consider the percentage of TAE accounted for by CCSD—which in the limit for a system with only dynamical correlation approaches the *entire* correlation contribution—then the R^2 values slightly increase to 0.923, 0.935, 0.902, and 0.952, respectively. Values for the W4-11 set can be found in the Electronic Supporting Information. We note that the idea of using DFT correlation functional using HF orbitals as a measure of dynamical correlation was, to the best of our knowledge, first suggested by Handy and coworkers [59, 60].

4 Conclusions

We propose a simple DFT-based diagnostic for nondynamical correlation effects, namely $A_\lambda = (\text{TAE}[XC] - \text{TAE}[X_\lambda C])/\lambda\text{TAE}[XC]$ where TAE stands for the molecular total atomization energy, *XC* is a pure-DFT exchange-correlation functional, and $X_\lambda C$ represents the corresponding hybrid with 100λ % Hartree–Fock-type exchange. The diagnostic is a good predictor for sensitivity of energetics to the level of theory, unlike most wavefunction-based diagnostics. $A_\lambda =$ values approaching unity indicate severe nondynamical correlation, while values between 0 and about 0.1 indicate that correlation is predominantly dynamic in character. The diagnostic converges rapidly with any basis set of polarized double-zeta or better quality and can easily be applied to problems beyond the practical reach of wavefunction ab initio methods required for other diagnostics.

We also can propose a simple gauge for the importance of dynamical correlation in a molecular binding (or reaction) energy: $D[C] = 1 - \mathrm{TAE[HF]/TAE[HFC]}$. Both indices can be computed with just three calculations: for example, using the BLYP exchange-correlation combination, one could make do with just BLYP, HFLYP, and HF calculations if $A_{100\ \%}$[BLYP] is acceptable, and an additional B1LYP calculation if $A_{25\ \%}$[BLYP] is preferred.

As a final remark, in the context of the present special issue, it might be observed that the present diagnostic touches on the area of conceptual density functional theory, which has been the focus of intense research activity in Belgium [71–73].

Acknowledgments J. M. L. M. is on leave of absence as the Thatcher Professor of Chemistry at the Weizmann Institute of Science. This research was supported in part by a startup grant from the University of North Texas from which the Martin group Linux cluster was purchased. U. R. F. acknowledges a research assistant fellowship from the Department of Chemistry at the University of North Texas, while S. K. and A. K. acknowledge Koshland and Australian Research Council postdoctoral fellowships, respectively. The authors would like to thank the reviewers for helpful comments, and Drs. Wanyi Jiang and Angela K. Wilson (U. of North Texas) for helpful discussions.

References

1. Raghavachari K, Trucks GW, Pople JA, Head-Gordon M (1989) Chem Phys Lett 157:479–483
2. Sinanoglu O (1964) Adv Chem Phys 6:315–412
3. Hollett JW, Gill PMW (2011) J Chem Phys 134:114111
4. Scuseria GE, Tsuchimoshi T (2009) J Chem Phys 131:164119
5. Seeger R, Pople JA (1977) J Chem Phys 66:3045
6. Pople JA, Binkley JS (1975) Mol Phys 29:599
7. Pople JA, Nesbet RK (1954) J Chem Phys 22:571
8. Ostlund NS (1972) J Chem Phys 57:2994
9. Linderberg J, Shull H (1961) J Mol Spectrosc 5:1
10. Englert BG, Schwinger J (1985) Phys Rev A 32:47 and references therein
11. Elliott P, Burke K (2009) Can J Chem 87(10):1485–1491
12. Supreme Court of the United States decision in *Jacobellis vs. Ohio* (1964) US Reports 378:184. URL:http://laws.findlaw.com/us/378/184.html
13. Zanardi P (2002) Phys Rev A 65:042101 and references therein
14. Ziesche P, Gunnarson O, John W, Beck H (1997) Phys Rev B 55:10270
15. Huang Z, Wang H, Kais S (2006) J Mod Opt 53:2543
16. Gersdorf P, John W, Perdew JP, Ziesche P (1997) Int J Quantum Chem 61:935
17. Murg W, Verstraete F, Legeza O, Noack RM (2010) Phys Rev B 82:205105 and references therein
18. Pelzer K, Greenman L, Gidofalvi G, Mazziotti DA (2011) J Phys Chem A 115:5632
19. Lee TJ, Taylor PR (1989) Int J Quantum Chem Symp S23:199–207
20. Janssen CL, Nielsen IMB (1998) Chem Phys Lett 290:423–430 (closed-shell)
21. Leininger ML, Nielsen IMB, Crawford TD, Janssen CL (2000) Chem Phys Lett 328:431–436 (open-shell)
22. Lee TJ (2003) Chem Phys Lett 372:362–367 (revised open-shell)
23. Karton A, Rabinovich E, Martin JML, Ruscic B (2006) J Chem Phys 125:144108
24. Karton A, Parthiban S, Martin JML (2009) J Phys Chem A 113:4802–4816 and references therein
25. Tishchenko O, Zheng J, Truhlar DG (2008) J Chem Theory Comput 4:1208–1219
26. Jiang W, DeYonker N, Wilson AK (2012) J Chem Theory Comput 8:460 and references therein
27. Mok DKW, Neumann R, Handy NC (1996) J Phys Chem 100:6225
28. Krylov AI, Sherrill CD, Byrd EFC, Head-Gordon M (1998) J Chem Phys 109:10669
29. Karton A, Taylor PR, Martin JML (2007) J Chem Phys 127:064104
30. Karton A, Daon S, Martin JML (2011) Chem Phys Lett 510:165–178
31. Dunning TH (1007) J Chem Phys 1989:90
32. Bak KL, Jørgensen P, Olsen J, Helgaker T, Gauss J (2000) Chem Phys Lett 317:116
33. Boese AD, Oren M, Atasoylu O, Martin JML, Kállay M, Gauss J (2004) J Chem Phys 120:4129–4141
34. Perdew JP, Schmidt K (2001) AIP Conf Proc 577:1
35. Harris J, Jones R (1974) J Phys F 4:117
36. Becke AD (1993) J Chem Phys 98:1372
37. Roos BO, Taylor PR, Siegbahn PEM (1980) Chem Phys 48:157–173
38. Werner H-J, Knowles PJ, Knizia G, Manby FR, Schütz M, Celani P, Korona T, Lindh R, Mitrushenkov A, Rauhut G, Shamasundar KR, Adler TB, Amos RD, Bernhardsson A, Berning A, Cooper DL, Deegan MJO, Dobbyn AJ, Eckert F, Goll E, Hampel C, Hesselmann A, Hetzer G, Hrenar T, Jansen G, Köppl C, Liu Y, Lloyd AW, Mata RA, May AJ, McNicholas SJ, Meyer W, Mura ME, Nicklaß A, O'Neill DP, Palmieri P, Pflüger K, Pitzer R, Reiher M, Shiozaki T, Stoll H, Stone AJ, Tarroni R, Thorsteinsson T, Wang M, Wolf A (2011) MOLPRO 2010.1, Departments of Chemistry, Universities of Cardiff, Wales and Stuttgart, Germany. http://www.molpro.net
39. Frisch MJ, Trucks GW, Schlegel HB, Scuseria GE, Robb MA, Cheeseman JR, Scalmani G, Barone V, Mennucci B, Petersson GA, Nakatsuji H, Caricato M, Li X, Hratchian HP, Izmaylov AF, Bloino J, Zheng G, Sonnenberg JL, Hada M, Ehara M, Toyota K, Fukuda R, Hasegawa J, Ishida M, Nakajima T, Honda Y, Kitao O, Nakai H, Vreven T, Montgomery JA Jr, Peralta JE, Ogliaro F, Bearpark M, Heyd JJ, Brothers E, Kudin KN, Staroverov VN, Kobayashi R, Normand J, Raghavachari K, Rendell A, Burant JC, Iyengar SS, Tomasi J, Cossi M, Rega N, Millam NJ, Klene M, Knox JE, Cross JB, Bakken V, Adamo C, Jaramillo J, Gomperts R, Stratmann RE, Yazyev O, Austin AJ, Cammi R, Pomelli C, Ochterski JW, Martin RL, Morokuma K, Zakrzewski VG, Voth GA, Salvador P, Dannenberg JJ, Dapprich S, Daniels AD, Farkas Ö, Foresman JB, Ortiz JV, Cioslowski J, Fox DJ (2009) Gaussian 09, Revision A.1. Gaussian, Inc., Wallingford, CT. http://www.gaussian.com
40. Vosko SH, Wilk L, Nusair M (1980) Can J Phys 58:1200
41. Becke AD (1988) Phys Rev A 38:3098
42. Lee C, Yang W, Parr RG (1988) Phys Rev B 37:785–789

43. Miehlich B, Savin A, Stoll H, Preuss H (1989) Chem Phys Lett 157:200–206
44. Perdew JP, BurkeK, Ernzerhof M (1996) Phys Rev Lett 77:3865–3868; erratum 78 (1997) 1396
45. Becke AD (1996) J Chem Phys 104:1040
46. Tao JM, Perdew JP, Staroverov VN, Scuseria GE (2003) Phys Rev Lett 91:146401
47. Schultz NE, Zhao Y, Truhlar DG (2005) J Phys Chem A 109:11127
48. Zhao Y, Tishchenko O, Gour JR, Li W, Lutz JJ, Piecuch P, Truhlar DG (2009) J Phys Chem A 113:5786
49. Jensen F (2001) J Chem Phys 115:9113
50. Jensen F (2002) J Chem Phys 116:3502
51. Jensen F (2002) J Chem Phys 116:7372
52. Jensen F (2002) J Chem Phys 117:9234
53. Jensen F (2012) J Chem Phys 136:094110
54. Jensen F (2008) J Phys Chem A 111:11198
55. Jensen F, Helgaker T (2004) J Chem Phys 121:3463
56. Grimme S (2006) J Chem Phys 124:034108
57. Kozuch S, Martin JML (2011) Phys Chem Chem Phys 13:20104 and references therein
58. Görling A, Levy M (1993) Phys Rev B 47:13105
59. Cohen AJ, Handy NC (2001) Mol Phys 99:403
60. Cohen AJ, Handy NC (2001) Mol Phys 99:607
61. Polo V, Grafenstein J, Kraka E, Cremer D (2002) Chem Phys Lett 352:469
62. Henderson TM, Scuseria GE (2010) Mol Phys 108:2511
63. Huzak M, Deleuze MS, Hajgato B (2011) J Chem Phys 135:104704 eq. (44)
64. Hajgato B, Szieberth D, Geerlings P, De Proft F, Deleuze MS (2009) J Chem Phys 131:224321
65. Zhao Y, Truhlar DG (2006) J Chem Phys 125:194101
66. Zhao Y, Truhlar DG (2008) Theor Chem Acc 120:215; erratum 119:525 (2008)
67. Zhao Y, Truhlar DG (2006) J Phys Chem A 110:13126
68. Zhao Y, Truhlar DG (2008) Acc Chem Res 41:157
69. Boese AD, Martin JML (2004) J Chem Phys 121:3405
70. Boese AD, Handy NC (2002) J Chem Phys 116:9559
71. Geerlings P, Ayers PW, Toro-Labbé A, Chattaraj PK, De Proft F (2012) Acc Chem Res 45(5):683–695
72. Geerlings P, De Proft F, Langenaeker W (2003) Chem Rev 103:1793
73. Geerlings P, De Proft F (2008) Phys Chem Chem Phys 10:3028

Theor Chem Acc (2013) 132:1300
DOI 10.1007/s00214-012-1300-1

REGULAR ARTICLE

Electronic structure analysis of small gold clusters Au_m ($m \leq 16$) by density functional theory

Giuseppe Zanti · Daniel Peeters

Received: 2 March 2012 / Accepted: 6 November 2012 / Published online: 1 December 2012

Abstract Small gold clusters Au_m ($m \leq 16$) were analyzed step by step using the density functional theory at B3LYP level with a Lanl2DZ pseudopotential to understand the rules governing the structures obtained for the most stable clusters. After a characterization by means of the NBO population analysis and spin densities, the particular electronic structure of such species was confronted to their structural parameters and stability. It appears that the most stable structures can be described in an original way through resonance structures resulting from an analysis of Au_m clusters into dimeric Au_2 subunits. These are arranged so as to promote: 1. A good overlap between bonding σ and anti-bonding σ* areas belonging to different Au_2 units. 2. A cyclic flow of electrons over the whole cluster. This model uses relatively simple chemical concepts in order to justify most of the structures already found in the literature as well as to establish a new approach explaining the structural transition from two- to three-dimensional configurations.

Keywords Clusters · Gold · Density functional calculations · Electronic structure

1 Introduction

Metal clusters are molecular-like entities, formed by assembling a small number of atoms ranging from a few to several hundreds [1]. Among them, gold nanoparticles are truly part of the emerging materials at the beginning of the twenty-first century. Over the past 20 years, gold clusters have attracted a particular interest for their potential applications in nanotechnologies as well as for their good catalytic performances [2, 3]. Their applications are so numerous that they are key materials in electronic, optic [4] even biomedical fields [5, 6]. Gold metal has for a long time been considered as a poor catalyst. Its high ionization potential explains its low affinity for small molecules such as H_2 and O_2. However, Professor Haruta found in his work that gold nanoparticles present a good catalytic activity [7–11]. Like most elements from the platinum group, these particles are able to activate the oxidation of H_2 or CO, even at low temperature [4, 9]. Such properties, which vary with the size of the system, are due to the presence of low coordination sites (surface/volume ratio larger than in the solid state) [12–14] but also to quantum size effects (filled electron shells) [15, 16]. For example, the reaction sites on Au_8 are not necessarily present on Au_7 since their electronic configuration and the geometric structure of these two clusters are completely different. This is illustrated by the study of CO oxidation efficiency by small gold clusters deposited on MgO, as a function of temperature and nuclearity [17, 18].

Due to the relative simplicity of the fundamental gold atomic configuration (only one 6*s* unpaired valence electron), the previous theoretical publications have mainly focused on geometrical structures rather than electronic aspects. However, several questions concerning the planar configuration of small size gold clusters remain open. Why

---

Published as part of the special collection of articles celebrating theoretical and computational chemistry in Belgium.

Electronic supplementary material The online version of this article (doi:10.1007/s00214-012-1300-1) contains supplementary material, which is available to authorized users.

G. Zanti · D. Peeters (✉)
Institute of Condensed Matter and Nanosciences,
Quantum Chemistry Group, Université catholique de Louvain,
Bâtiment Lavoisier, Place Louis Pasteur 1,
1348 Louvain-la-Neuve, Belgium
e-mail: daniel.peeters@uclouvain.be

is some symmetry more stable than others? What are the rules governing the geometry of the most stable structure? The nuclearity at which the transition to a three-dimensional structure takes place is another subject under debate. Many studies using in particular DFT [19–31] have attempted to provide some answers to these questions by simulating a large number of nuclear configurations. In this paper, we propose a model approach in which Au_m neutral gold clusters of small nuclearities are analyzed step by step in order to justify their structures and relative stability. The model connects structural parameters and relative stabilities to a detailed and original study of their electronic structure.

2 Methodology and results

Neutral gold clusters were computed using the density functional theory (DFT). This method was chosen because transition metal clusters present a great number of electrons and requires the introduction of electron correlation effects. DFT allows introducing some of this electronic correlation, while maintaining a good quality/computing time ratio. We opted for the B3LYP [32] exchange–correlation hybrid functional, which among others appears to give consistent results for the considered systems. Treating metal clusters requires an appropriate basis set, providing sufficient flexibility to describe as faithfully as possible electronic relocation while limiting the number of electrons and thus allowing computations to be completed in an affordable time. For these reasons, the Lanl2DZ [33–35][1] basis set was chosen, which deals explicitly with valence electrons through a split valence polarized basis set, retaining 19 electrons per Au atom ($5s^2$ $5p^6$ $5d^{10}$ $6s^1$). The remaining core electrons are modeled through an effective core potential taking into account some relativistic corrections (RECP). This choice, which is not the only possible one, has been done to preserve homogeneity with our previous publications on the subject [36] in which a more complete analysis of various functionals and ECP's was presented to justify our choice. Furthermore, it provides results that are consistent with most results published at the same level of methodology. All computations and geometry optimizations were carried out using the Gaussian 03 package [37].

As the number of possible structural isomers grows exponentially with the size of the cluster, it is essential to establish a strategy for exploring the different local potential energy surfaces (PES) that we will consider. Following a logical approach, the potential energy surfaces of Au_m clusters have been explored over a wide variety of geometries build on all symmetry point groups compatible with the chosen nuclearity. The analytical computation of the Hessian matrix under full symmetry relaxation conditions was performed for each point group and gives further information on the shape of the local hypersurface. Following downhill, the eigenvectors during the optimization processes allow for structural distortions and affect the system by introducing further stabilizing effects, such as a Jahn–Teller effect. This procedure leads to one or more true minima, which, after verifying the stability of the obtained stationary density, are retained and submitted to an analytical frequency computation. This optimization procedure was repeated for several spin multiplicities compatible with the odd or even number of electrons. For a selected nuclearity, we have retained those minima lying at most 6 kcal mol^{-1} (0.01 Hartree) above the global minimum. It appears that for neutral gold clusters, the lowest spin state is also the stable fundamental state. In agreement with other DFT studies [19–31], no high spin/low energy structures were ever found. This is not surprising as the gold atom has only one 6*s* valence electron available for forming metal–metal bonds. Singlets (closed shell, even number of gold atoms) and doublets (open shell, odd number of gold atoms) are thus the only spin multiplicities to be considered. All the optimized structures corresponding to these criteria are discussed below and used for comparing some selected properties.

Many bare gold clusters have already been obtained using DFT [19–31]. In this paper, we present and discuss our results and compare them to those that can be found in the literature. All Au_m lowest minima found during the optimization process are shown in Fig. 1 and those structures obtained for selected nuclearities are considered one by one. Relevant inter-atomic distances are presented in Fig. 2. It appears that the most favored structures for low nuclearities adopt preferentially planar configurations. These are observed for nuclearities up to 9. A three-dimensional transition occurs when pseudo-planar configurations become the favored structures. This transition takes place at $m = 10$ but the precise size for which gold clusters change from 2D planar structures to 3D structures remains an open question as this transition depends strongly on the method used [38]. Häkkinen and al. [39] suggest that planar structures are favored until Au_{13} while Xiao and Wang [20] suggest that the 2D–3D structural transition occurs at Au_{15}. The recent work of Assadollahzadeh and Schwerdtfeger with the B3PW91 functional [28] shows structures similar to ours. In this work, we will, from an electronic viewpoint, try to bring some arguments justifying this structural transition. The interested reader will find the Cartesian coordinates of all presented minima in the supporting information file.

---

[1] Figures have been drawn with Gaussview, Version 4.1.2, of Gaussian Inc.

Fig. 1 Most stable structures for Au_m clusters ($2 \leq n \leq 16$)

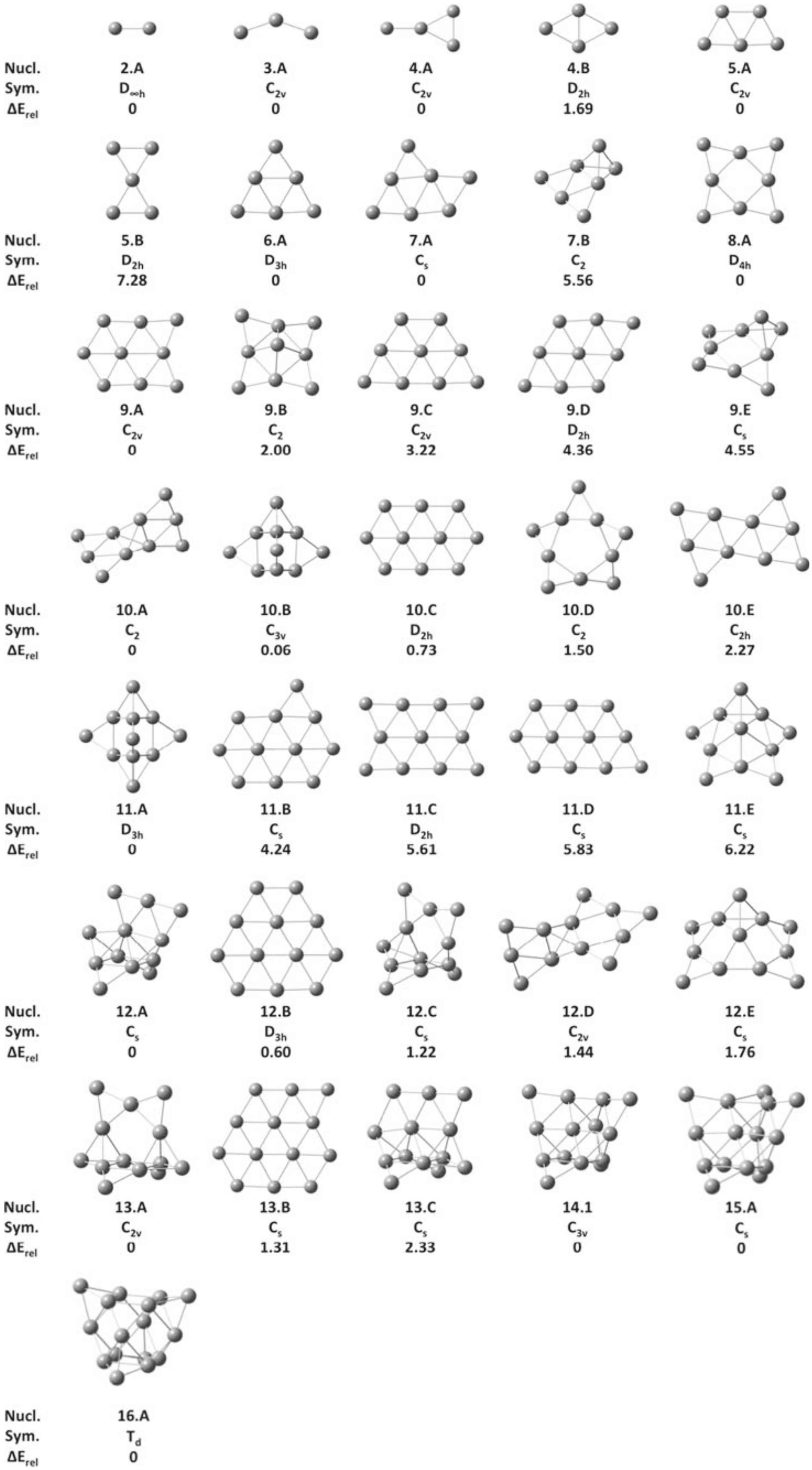

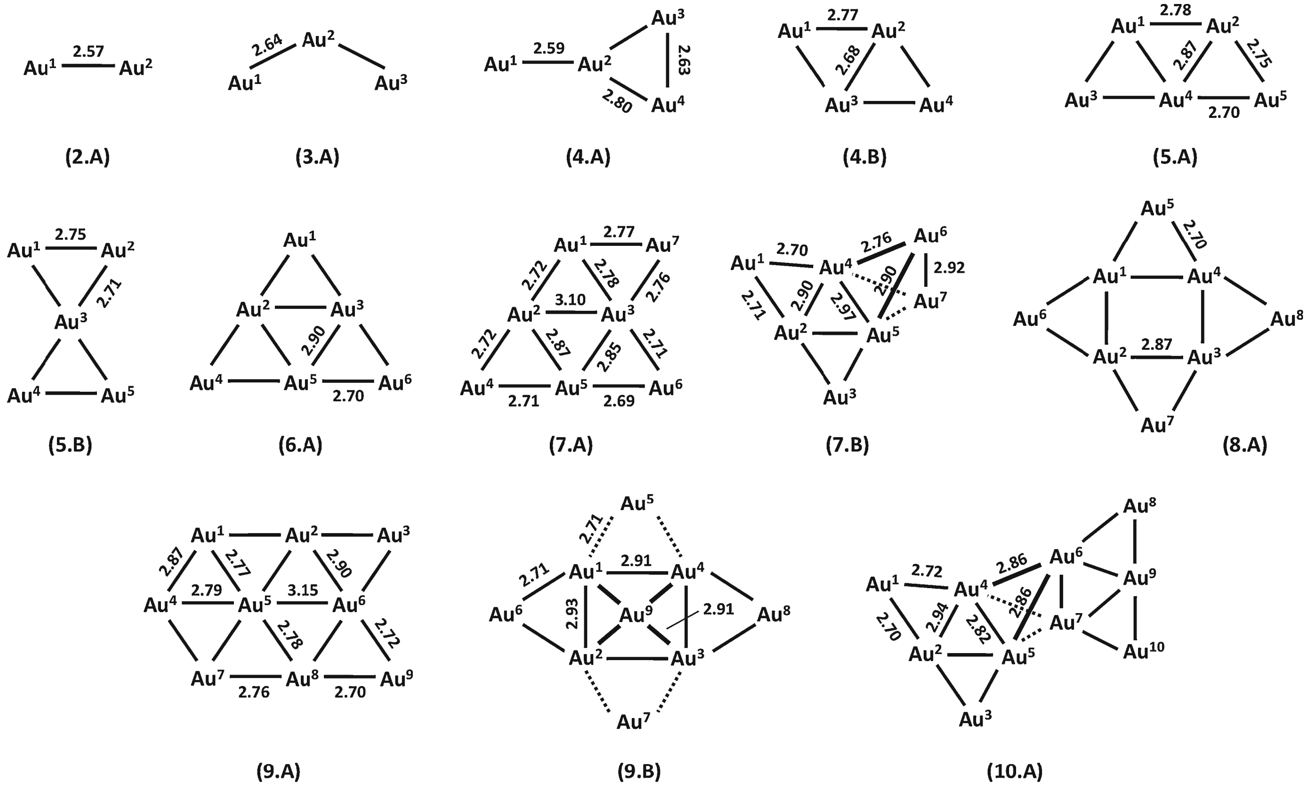

Fig. 2 Inter-atomic distances for Au_m clusters of small nuclearities

Fig. 3 Evolution of the cohesive energy of Au_m clusters as function of the nuclearity

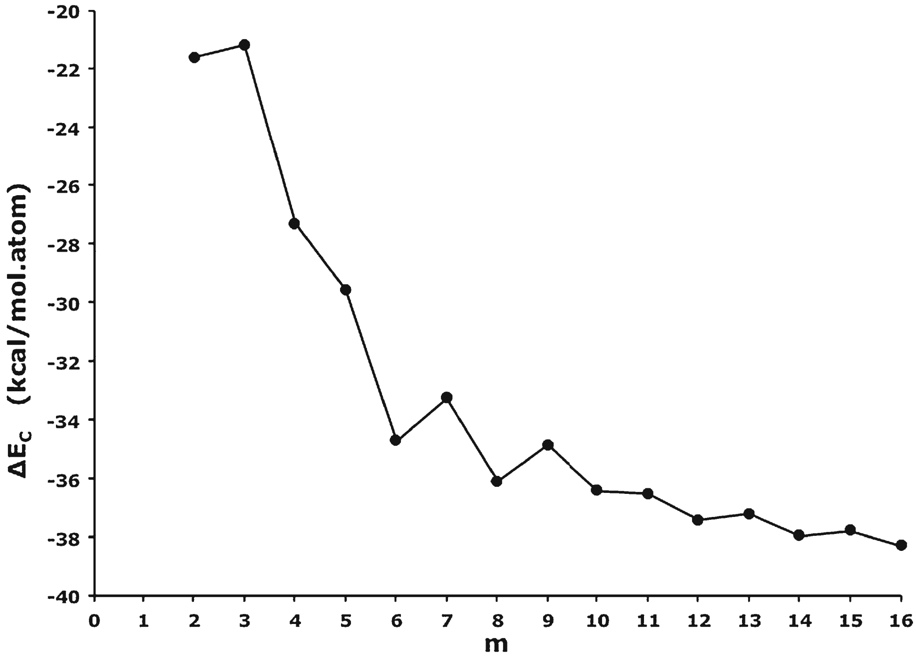

The relative stabilization energy of the clusters may be obtained by referring to the cohesive energy ΔE_C, which can be estimated from the energy released during the formation of metal clusters starting from isolated atoms:

$$\Delta E_C(\mathrm{Au}_m) = \frac{(E_{\mathrm{Au}(m)} - m\,E_{\mathrm{Au}})}{m}$$

where $E_{\mathrm{Au}(m)}$ is the computed energy of the gold cluster and E_{Au} stands for gold's atomic ground state energy.

The evolution of the cohesive energy ΔE_C for the most stable studied species is given in Fig. 3. As already discussed in a previous publication [36], the cohesive energy gets more exothermic with increasing nuclearity. Starting from these data, some other reaction energies can be obtained using thermodynamic cycles. Energetics of reactions such as $Au_{2n} \rightarrow n\ Au_2$ merit our attention and will be further commented on the discussion. The oscillations observed in Fig. 3 are due to the alternation between less stable open-shell and more stable closed-shell configurations. It appears also on the figure that the cohesive energy converges to a limit with increasing m that the stability gain for the first members of the series is impressive and that some configurations are particularly stable and merit further investigation to explain such properties. This is particularly true for Au_6 and Au_8.

To our knowledge, the electronic structure of gold clusters has never been studied through the natural population analysis [40–42], whereas this analysis provides relevant information about electron configurations, hybridization states, and charge transfers occurring between the various metal partners of the cluster. This method is useful to bring the complex vision of metal clusters into a more localized Lewis-like structure, which is easier to interpret for chemists. The electron cloud reorganization arising during the clustering process gives an idea of the orbital shapes involved in bonding and allows identifying potential reaction sites that may intervene in the growth process. This was achieved through the use of Δρ, a differential density function obtained by subtracting from the density of the cluster, the density of the isolated atoms maintained in the same nuclear configuration as the cluster.

$$\Delta\rho = \rho_{\text{cluster}} - \sum_{i=1}^{m} (\rho_{\text{atom}})_i$$

The electron density increase in bonding areas appears by positive Δρ values (blue color in the figures) while anti-bonding areas show negative Δρ values (red color). Finally, for open-shell systems, spin density, defined by subtracting β density to the α density, brings information on the unpaired electron distribution in the system.

$$\Delta\rho_{\text{spin}} = (\rho_{\text{cluster}})_\alpha - (\rho_{\text{cluster}})_\beta.$$

3 Discussion

As most of the discussion presented in this paper rests on the electronic structure of the Au_2 dimer, considered to be the subunit leading to a rationalization of the structure of these clusters, we will first focus on its electronic structure. Afterward, the analysis of even nuclearities, that is, closed-shell clusters, will be presented and we will show that their structures and relative stabilities may be rationalized by considering an assembly of such Au_2 subunits within the cluster. Finally, odd nuclearities will be discussed showing that their structure and stability may be described by the adsorption of a gold atom on the previous closed-shell cluster and respond to the same simple building principle even though the presence of an unpaired electron introduces some slight difference.

Table 1 Natural population analysis of the Au_2 dimer

Atom	Atomic population (e)			σ contribution (%)		
	6*s*	$5d_z^2$	$6p_z$	6*s*	$5d_z^2$	$6p_z$
Au	1.04	9.95	0.01	95.48	4.07	0.45

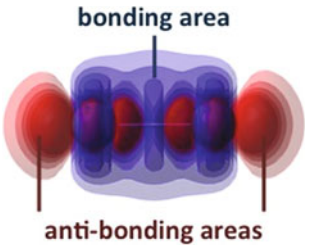

Fig. 4 Density differential functional of Au_2 dimer (5.10^{-3} e^-/bohr^3)

3.1 Dimer Au_2

In its atomic ground state, Au presents a $5d^{10}\ 6s^1$ open-shell valence configuration, which leads to a Au–Au stable chemical bond formed by the combination of the two 6*s* electrons. In this model, Au_2 is characterized by a σ doubly occupied bonding orbital (HOMO) and a σ* unoccupied anti-bonding orbital (LUMO). The natural population analysis shows that the 5*d* orbitals, lower in energy, remain largely separated on their respective atoms and that there contribution to the metal bond can be considered as negligible (Table 1). Furthermore, the occupancy numbers are very close to those of the isolated Au atom, removing the occurrence of any 6*s*–5*d* hybridization during the formation of the bond. The computed bond length (2.57 Å) is in accordance with other DFT studies and slightly longer than the experimental measurement (2.47 Å) [43]. The electronic reorganization following the combination of the two isolated atoms is illustrated through the differential density in Fig. 4. As seen, the valence electrons relocation takes place in a cylindrical region between the two nuclei, but outside the bond axis. Following the Berlin's diagram [44] approach of the Helmann Feynman electrostatic theorem, this area constitutes the bonding area or nucleophilic region of the dimer. A small electronic default appears along the bond axis completed by two large areas of lower density extending over both sides of the Au–Au bond. These are the anti-bonding areas or electrophilic regions. From this point of view, the Au_2 dimer seems able to play a double role: A donor, giving the electron density of its σ bonding orbital to an eventual acceptor site that should preferentially stand perpendicular to the bond axis; an electron acceptor receiving an excess of electron density into its empty anti-bonding σ* region. Of course, both interactions would lead to a weakening of the bond, anticipating a longer inter-atomic distance. This description is also consistent with the high polarizabilities of Au_2, which expresses in the cylindrical area outside the interatomic bond (lighter atoms, H_2 for example, would lead to a bonding density localized along the bond axis between the two nuclei). As these conclusions will be used later on to explain the structure of higher nuclearities, this behavior of the Au_2 dimer will be schematically represented by:

(2.A)

3.2 Closed-shell systems

Let us now consider higher closed-shell clusters and show in this section that closed-shell structures of Au_m clusters can be interpreted as an assembly of Au_2 dimeric subunits. A combined study of the electronic structure, inter-atomic distances, and stability properties realized on the obtained optimized geometries sustains this interpretation. It should be noted that despite the large number of existing papers on the subject, most present factual data on the clusters but none introduces the electronic facets of the problem to offer a model description.

3.2.1 Au_4: σ–σ* interaction

First of the series, the optimizations for the tetramer lead to two very stable planar structures and no stable low lying 3D structure can be found. The ground state corresponds to a C_{2v} *Y* shape structure (4.A) while the closest isomer, which is only 1.69 kcal mol^{-1} higher, is a D_{2h} rhombus (4.B). These two structures are those commonly found in the literature, although their relative stability depends on the functional or basis set used [25–28]. An analysis of structural parameters (Fig. 2) and charge distributions shows that four gold atoms, even in high symmetric structures, present important non-equivalent charges. This may however be explained if one admits that these two clusters result from the combination of two Au_2 units through a σ–σ* donor–acceptor interaction. In the 4A case, the two dimeric units are positioned in a perpendicular way while in the second case, they are positioned in a parallel, slightly shifted manner. The two configurations with their natural atomic charges are schematically illustrated below:

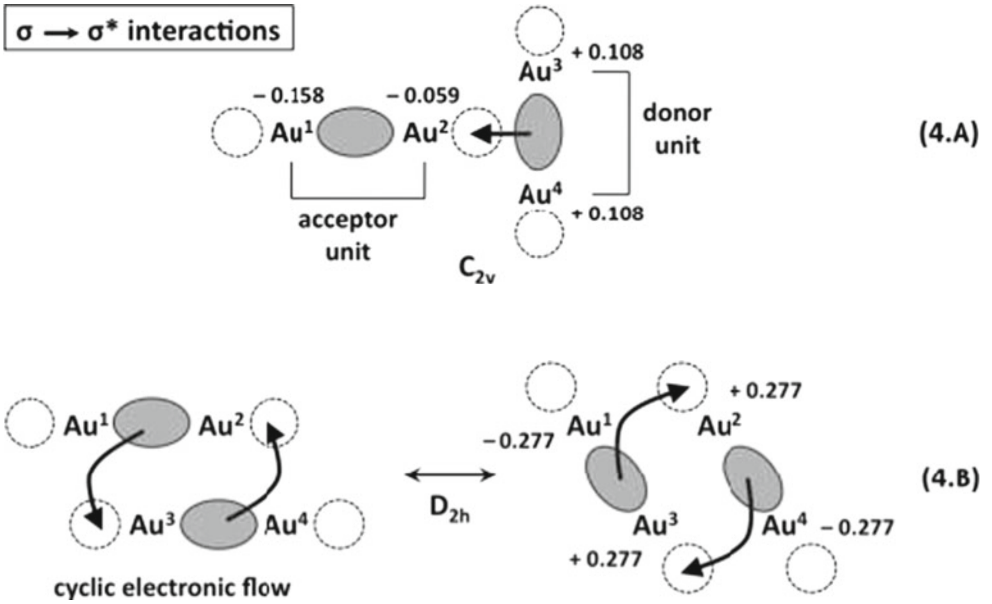

The most stable state (4.A) shows a relatively localized electronic structure where the two dimeric units, Au^{1-2} (2.59 Å) and Au^{3-4} (2.63 Å), are characterized by bond

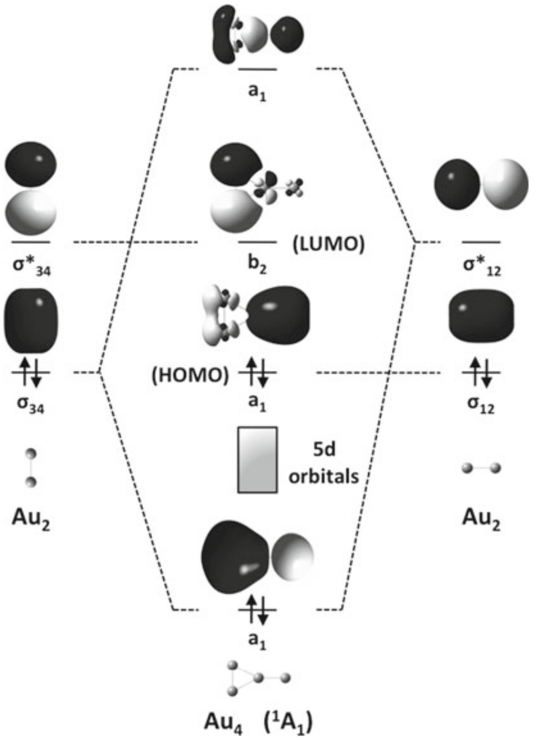

Fig. 5 Simplified orbital diagram of Au_4 in its (4.A) geometry obtained by the combination of two dimeric units

lengths close to those presented by the dimer. As anticipated in the Au_2 discussion, a small increase in bond length is observed and explained by the σ–σ* interaction that weakens the covalent bonds of both partners. These two distances are nevertheless shorter than the inter-unit Au^{2-3} and Au^{2-4} distances (2.80 Å), which do not respond to conventional covalent bonds. The NBO analysis calculates a $\sigma_{34} \rightarrow \sigma^*_{12}$ charge transfer of about 0.26 e$^-$, depicting an Au^{3-4} donor unit positively charged and an Au^{1-2} acceptor unit negatively charged (see diagram above). The σ_{12} and σ^*_{34} orbital populations remain substantially unchanged, justifying their negligible role in the charge transfer. These two latter orbitals correspond to the frontier orbitals as can be appreciated on the simplified orbital diagram of Fig. 5, which expresses the combination of two dimeric units.

The rhombohedral isomer (4.B) presents a more delocalized electronic structure. Nevertheless, its structure can also be described through an interaction between two Au_2 subunits, where each Au_2 subunit acts as a donor as well as an acceptor. This can be represented by two similar schemes, leading to two equivalent resonance structures. Unlike the more stable isomer (4.A), this spatial arrangement allows what we will call, as suggested by the arrows chaining, a "cyclic flow" of valence electrons on the entire structure. It is thus possible to write down two resonance structures depending on the arrows direction. This alternation representing the electron delocalization in a resonance phenomenon is responsible for longer bond lengths on the periphery (2.77 Å) while the central Au^{2-3} distance gets shorter (2.68 Å) to enhance σ–σ* overlap.

The energetic closeness of the two isomers suggests that this form of σ-aromaticity provides an additional gain in stability, which compensates the lower σ–σ* overlap. This interpretation is supported by the NBO analysis, which shows occupation numbers for σ and σ* orbitals of 1.6 and 0.4 e$^-$, respectively. The charge separation is larger than for the (4.A) isomer and may be related to the interaction between two dipoles. Following this description, one may admit that the relative stability of these two structures will largely depend on the amount of electron correlation introduced by the method, and depending on the nature of the chosen functional, the first or the latter will be favored.

These two minima belong to the same potential energy surface and are connected by a transition state following a

Fig. 6 Reaction pathway connecting both (4.A) and (4.B) minima accompanied by their density differential functional

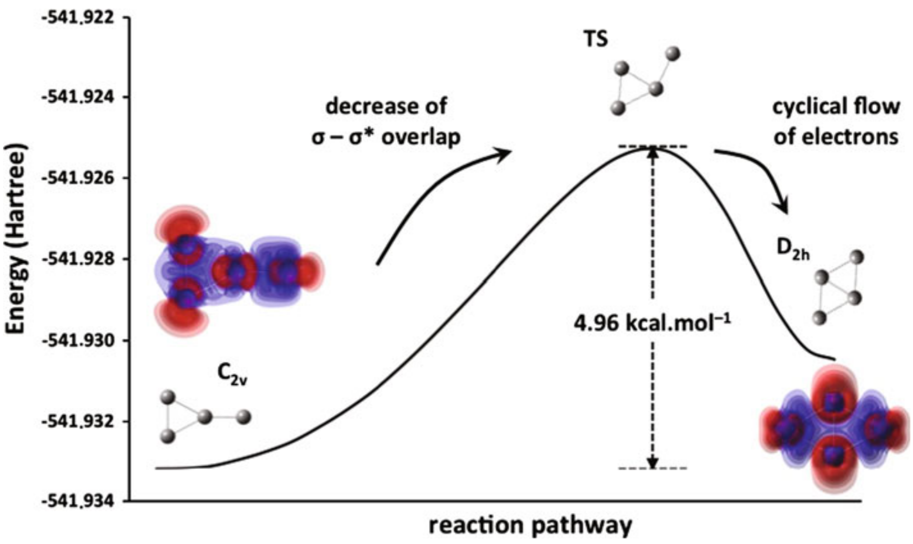

simple rotation in the plane of the two dimeric units. The calculated barrier is still very small (about 5 kcal mol^{-1}), since, going from (4.A) isomer to (4.B) isomer, the decrease in σ–σ* overlap is quickly counterbalanced by the cyclic flow of valence electrons on the entire structure. This behavior is illustrated in Fig. 6 along with the density delta function of the two minima. It should be mentioned that no stable three-dimensional structure of low energy has ever been identified. Such structures (D_{2d}) are high-order transition states lying at least 20 kcal mol^{-1} above the minima that reoptimize to (4.A) or (4.B). This is consistent with the σ–σ* interaction, which is maximized in a planar system, while the minimal interaction is obtained for a tetrahedral geometry.

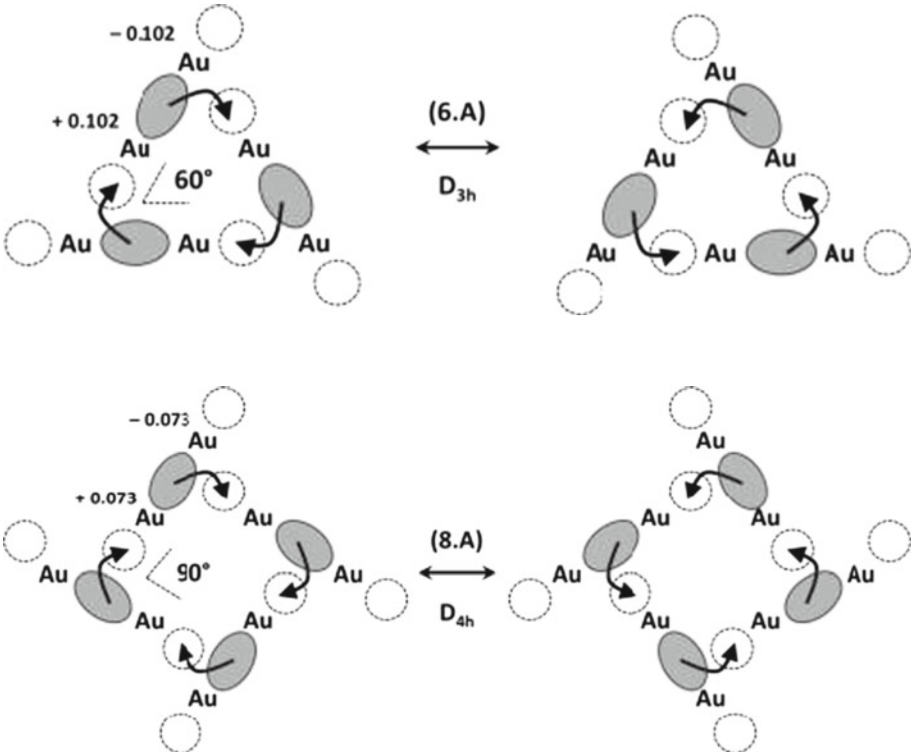

Finally, the stabilization energy induced by the association of two Au_2 subunits leading to the tetramer is estimated by the corresponding reaction energy to 22.8 and 21.1 kcal mol^{-1}, respectively, for (4.A) and (4.B). This large energy release is about one half of the binding energy of Au_2 (43.2 kcal mol^{-1}).

3.2.2 Au_6 and Au_8: σ aromaticity

As found for the tetramer, geometry optimizations show that the Au_6 hexamer and Au_8 octamer adopt very stable planar configurations, much lower in energy than any other structural isomers. Such configurations could already be anticipated from the electronic structure analysis carried out in the previous section. Thus, for these two clusters, the dimeric units are arranged, respectively, in D_{3h} (6.A) and D_{4h} (8.A) symmetry, preferred to the hexagonal or octagonal configuration. These symmetries maximize the σ–σ* interactions while allowing a good cyclic flow of valence electrons, which is associated with the σ-aromaticity concept [45].

No other nuclear configuration satisfies this double condition for such a small number of dimeric units. These two geometries are also found in the literature as the most stable, whatever the method of calculation performed [25–28]. As it is shown in Fig. 2, the dimeric part of the structure is easily recognized by bond lengths significantly shorter (2.70 Å) than the interatomic distances joining the central atoms (2.90 Å for Au_6 and 2.87 Å for Au_8). The natural populations are relatively similar to those found for the (4.B) tetramer isomer (σ: 1.6 e$^-$ and σ*: 0.4 e$^-$). The charge distribution shows that the negative charges are localized on the external atoms of the structure. Symmetry imposes of course the writing of two equivalent resonance structures, justifying the atomic charge alternation. The polarization of dimeric units, however, diminishes when their number increases. From the stability point of view, an increase is observed with the number of dimeric units. The comparison of three or four Au_2 subunits leads to stabilizations of, respectively, 76.5 and 115.8 kcal mol^{-1} which is more than three or four times the 21.1 kcal mol^{-1} value of (4.B). This is due to the amplifying effect of σ–σ* overlap which is better in Au_8 than in Au_6 and Au_4 (4.B). The σ–σ* overlaps are optimal in Au_8 as 90° angles link the dimeric units. For this reason, any other structural isomer lies much higher in energy. Finally, the differential densities of the two clusters, as illustrated in Fig. 7, highlight the domain of lower density located at the center of the structures.

3.2.3 Higher nuclearities: structural transition

When the size of the system becomes larger, in other words starting from five dimeric units, a structural transition to non-compact three-dimensional configurations (pseudo-planar geometries or cages) becomes possible while maintaining both good σ–σ* overlaps and some σ aromaticity. It is not uncommon to identify minima that adopt unconventional geometries, which may nevertheless be justified by an Au_2 units association. In order to illustrate this structural transition, we will consider the Au_{10} example, which presents a series of nearly degenerate minima reported in Fig. 1. The planar structure (10.C) has almost the same energy than the more stable (10.A) and (10.B). It is a matter of fact that this sequence will be modified by the methodology one uses and that inversions may appear. Our goal here is not to pretend that 3D is more stable than 2D at *m* equal to 10, but rather to show that both coexist and that the structure obtained for all these clusters obey to the same logic. The first two, (10.A) and (10.B), are three-dimensional, but they are based on slightly distorted Au_6 and Au_8 templates that maintain an aromatic character; for instance, the (10.A) isomer with D_2 symmetry shows two perpendicularly connected Au_5 units, each integrating two equivalent resonance structures favoring the cyclic flow as shown in the diagram below:

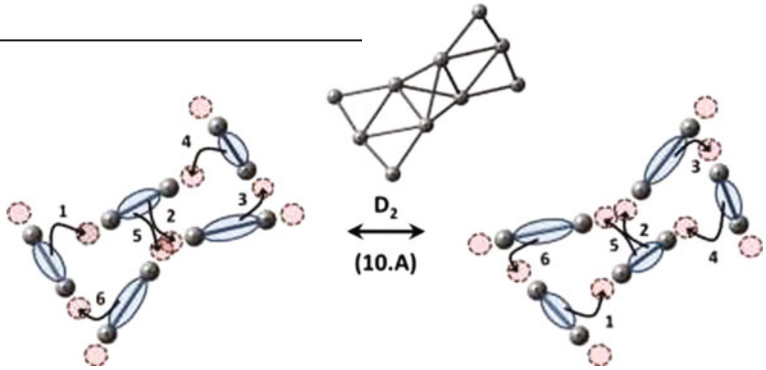

The (10.B) isomer with a C_{3v} symmetry is, in turn, stabilized by expressing its structure as a combination of three resonance structures.

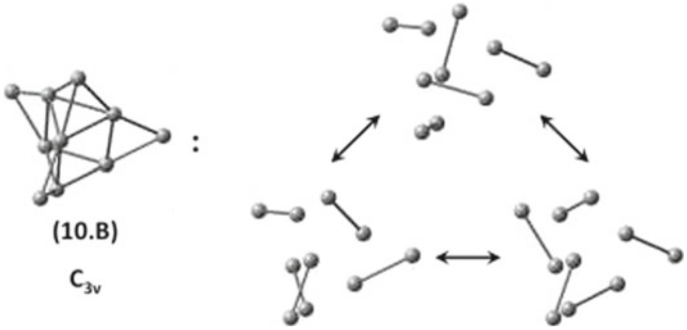

Isomer (10.D) is the next member of the Au_4 (D_{2h}), Au_6 (D_{3h}), and Au_8 (D_{4h}) planar sequence but this one must necessarily leave the plane in order to preserve angles close to 90° between the dimeric units. The number of σ–σ*

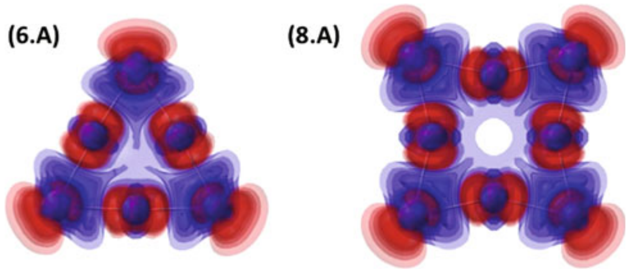

Fig. 7 Difference density of Au_6 (6.A) and Au_8 (8.A)

overlaps being less numerous than for (10.A) and (10.B) isomers, the (10.D) structure is a bit less stable.

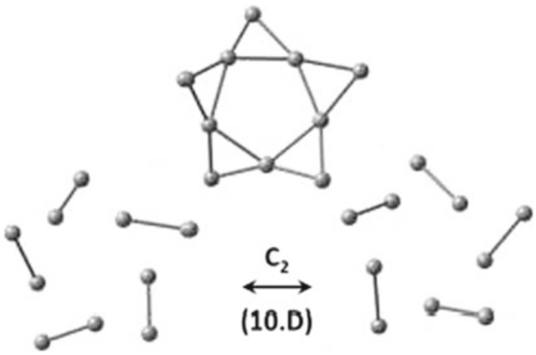

Finally, the (10.C) and (10.E) minima, located, respectively, at 0.73 and 2.27 kcal mol^{-1} of the most stable structure, correspond to the most stable planar configurations. In both cases, their predominant resonance structures are based on the Au_6 template. The largest stability of the (10.C) isomer compared to the (10.E) isomer may be explained by a larger delocalization of valence electrons.

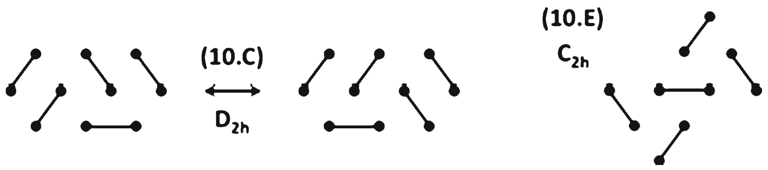

Even though the writing of resonance structures becomes more tedious, this discussion may be extended to higher nuclearities, leading finally to Au_{16}, the first cage structure. This remarkable structure is formed by the assembly of 8 dimeric units presenting T_d symmetry. Although it is difficult to translate in a 2D picture, the disposition of dimeric units and the high symmetry of this system provide many equivalent resonance structures and high σ–σ* overlaps, which bring a great stability to such configuration.

3.3 Open-shell systems

Building rules, established for closed-shell systems, may now be extended to the study of preferential structures and stabilities obtained for Au_m open-shell clusters.

3.3.1 Au_3: the "push pull" effect

The trimer can be described by a Au_2 dimeric unit to which an additional atom with an unpaired electron is added. Two donor–acceptor-type interactions are then possible between the two partners. On the one hand, the unpaired 6*s* electron of the additional atom acts as a donor toward the anti-bonding σ* orbital of the dimeric unit (acceptor). On the other hand, the bonding σ orbital of the dimeric unit acts as a donor toward the partially filled 6*s* orbital of the additional atom (acceptor). Following the model description presented above, the Au_3 trimer is expected to adopt a linear or triangular configuration according to the predominance of one of the two mentioned interactions. These two extreme situations are illustrated below:

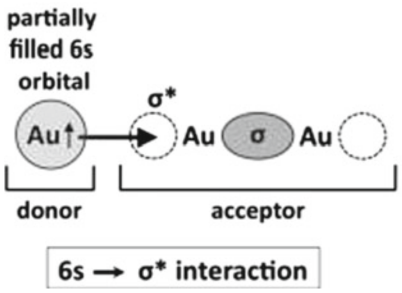

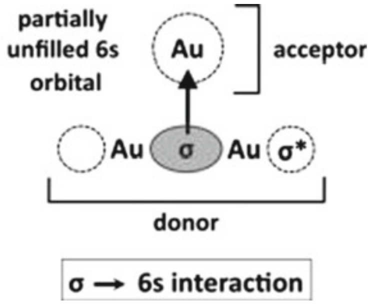

The geometry optimizations show that none of those two structures corresponds to a stable configuration. The ground state found is a bent C_{2v} structure with a 140° angle

Table 2 Electronic transfers involved in the localized description of Au_3 through the "push–pull" effect

	$Au_2 + Au$	Au_3	Charge transfer (e)
$\sigma_{Au(2)}$	2.00	1.82	–0.18
$6s_{Au}$ (β)	0.00	0.25	+0.18 (+0.07)
$6s_{Au}$ (α)	1.00	0.74	–0.26
$\sigma^*_{Au(2)}$	0.00	0.29	+0.26 (+0.03)
Total	3.00	3.10	0.00 (+0.10)

Numbers in parentheses are the contributions due to 5*d* orbitals

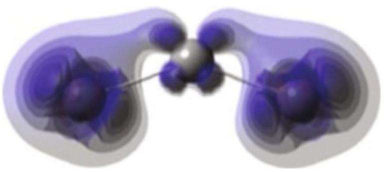

Fig. 8 Spin density of the trimer in its ground state (5.10^{-3} $e^-/bohr^3$)

(3.A). This structure is found in many DFT studies regardless of the functional or the basis set used [25–28] and has been observed experimentally [46]. Such intermediate geometry between two extreme situations (linear and triangular) suggests that both interactions have to be taken into consideration in order to predict the structure of the trimer. Indeed, by bending, the structure allows a synergistic combination of both interactions through an electronic effect and we may call "push–pull," which allows a cyclic flow of valence electrons. Two resonance structures for Au_3 may now be written, the unpaired electron being either at the right end, or at the left end of the resonance structure.

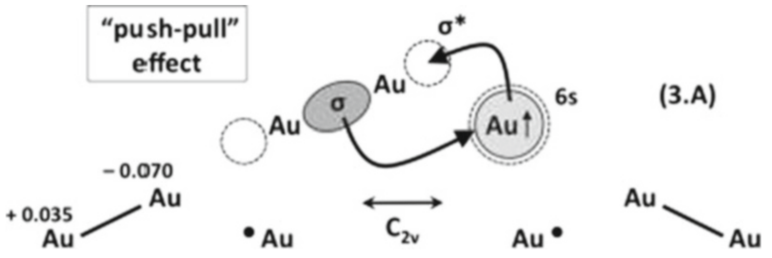

The structural parameters of the trimer can be linked to this electronic description. On the one hand, the computed bond lengths (2.64 Å) are in good agreement with the superposition of these two resonance structures. They are, therefore, slightly larger than in the case of the dimer. On the other hand, the angle of the structure (140°) complies with the dual interaction by adopting a median value to those adopted by the extreme structures (180° for linear and 90° for triangular). The charge transfers can be quantified by means of a NBO analysis and are listed in Table 2. Thus, although atomic populations of atoms located at the ends of the trimer show occupancy numbers ($5d^{9.95}$ $6s^{1.00}$) identical to those of the isolated atom, there is a $\sigma_{Au(2)} \rightarrow 6s_{Au}$ (β) transfer of 0.18 electron completed by a $6s_{Au}$ (α) $\rightarrow \sigma^*_{Au(2)}$ back transfer of 0.26 electron. Consequently, the trimer has a slight dipole moment and the central atom is negatively charged. Contributions due to the 5*d* orbitals ($5d_{Au(2)} \rightarrow 6s_{Au}$ (β) and $5d_{Au} \rightarrow \sigma^*_{Au(2)}$) are low and will not be discussed. The use of two resonance structures describing the trimer can still be justified using the spin density shown in Fig. 8. It shows that the majority of the unpaired electron distribution is located at the ends of the cluster. The figure also reveals the low contribution of the 5*d* orbitals of the central atom.

3.3.2 Au_5: competition between resonance structures

The most stable structure adopted by Au_5 is a trapezoidal planar geometry with C_{2v} symmetry (5.A). A D_{2h} planar isomer about 8 kcal mol^{-1} higher in energy could be identified (5.B). It corresponds to a flat minimum that can be connected to the previous structure by a very low barrier. These structures are also identified in other papers as being the lowest in energy [25–28]. They are listed on the reaction path (Fig. 9) along with their frontier orbitals. Considering the ground state (5.A), the localized subunit approach leads to three non-equivalent resonance structures depending on the position chosen for the *isolated* atom. These are shown below:

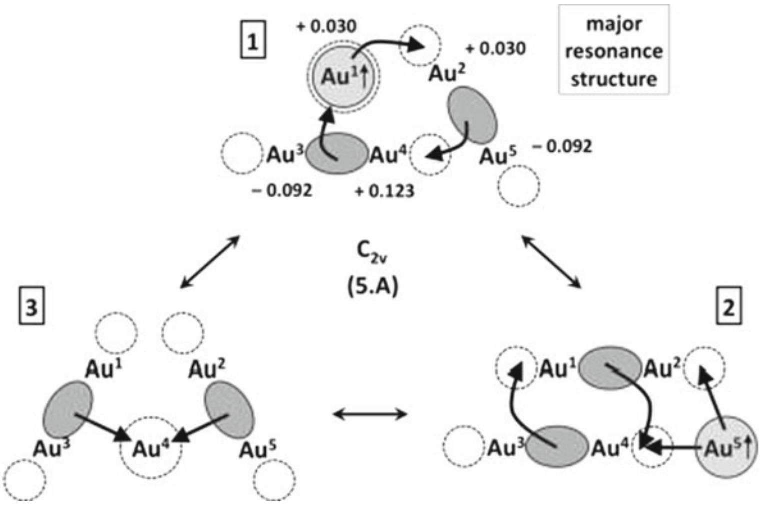

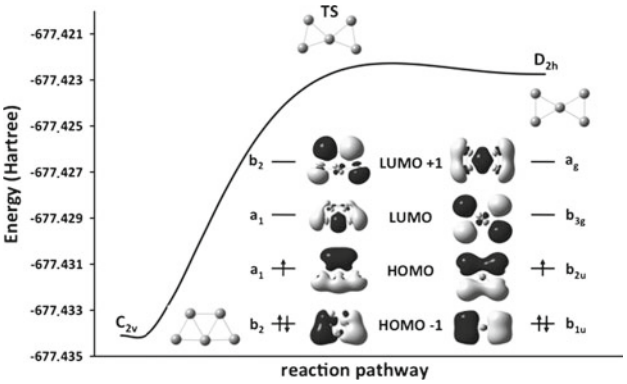

Fig. 9 Potential energy surface of Au_5 showing the two lowest minima with their frontier orbitals

A weighting of these three resonance structures is necessary to predict the structural and electronic properties of the cluster. For this purpose, only an inventory of all interactions present in each of the resonance structure may lead to a hierarchization and bring information on the dominant structure. According to the diagram, only structure 1 allows for a cyclic flow on the entire cluster. Moreover, unlike structures 2 and 3, the resonance structure 1 is the only one where the isolated atom plays both the role of donor and acceptor. At first glance, it appears to be the preponderant structure. An interesting feature of the NBO analysis supports this hypothesis. Indeed, the NBO analysis is able to perform, on the basis of chosen resonance structures, a counting of the number of Lewis and non-Lewis electrons within the computed electron density. In this way, resonance structures may be sorted following the number of Lewis electrons. Structure 1 presents indeed the lowest number on non-Lewis electrons (1.45), while structures 2 and 3 have higher and almost similar values (1.83 e^- and 1.81 e^-, respectively). This major resonance structure can also be justified looking at the spin density or at the inter-atomic distances. Firstly, the spin density in Fig. 10a identifies a major distribution of the unpaired electron on the small side of the trapezoid, which is consistent with resonance structure 1 being dominant. This side can also accommodate an additional gold atom to give the very stable Au_6 isomer. Secondly, bond lengths given in Fig. 2 reflect the weighted superposition of the three distinct resonance structures. Indeed, the internal distances Au^{1-4} and Au^{2-4} are the longest (2.87 Å) as they do not relate to any dimeric unit, whatever the resonance structure being considered. As 1 is predominant, the Au^{1-2} distance (2.78 Å) is slightly longer than other external distances Au^{1-3}, Au^{2-5} (2.75 Å) and Au $^{3-4}$, Au^{4-5} (2.70 Å) since the couple Au^1–Au^2 is not involved in a dimeric unit.

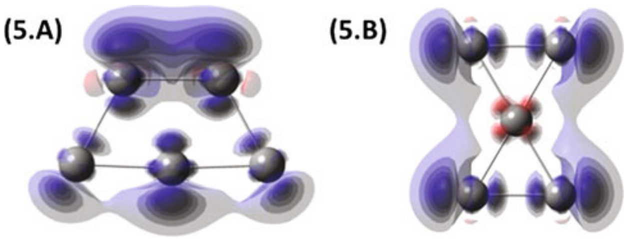

Fig. 10 Spin density of (5.A) and (5.B) isomers of Au_5 (5.10^{-3} e^-/$bohr^3$)

Similar conclusions can be obtained for the (5.B) isomer, which may be represented by two distinct resonance structures schematically given below:

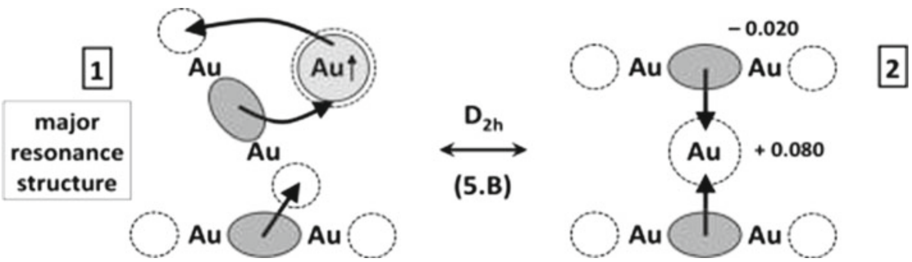

Resonance structure 1 is proposed to be the major structure as its non-Lewis population (1.55 e$^-$) is smaller than structure 2 (1.68 e$^-$). The link can once more be done with the spin density of Fig. 10b and the structural parameters (Fig. 2). The lower stability of this isomer finds its origin in the absence of a cyclic flow in resonance structures, a condition satisfied only for a trapezoidal geometry.

Fig. 11 Spin densities of (7.A) and (9.A) stable states (5.10^{-3} e$^-$/bohr^3) with a schematic representation of the predominant resonance structures

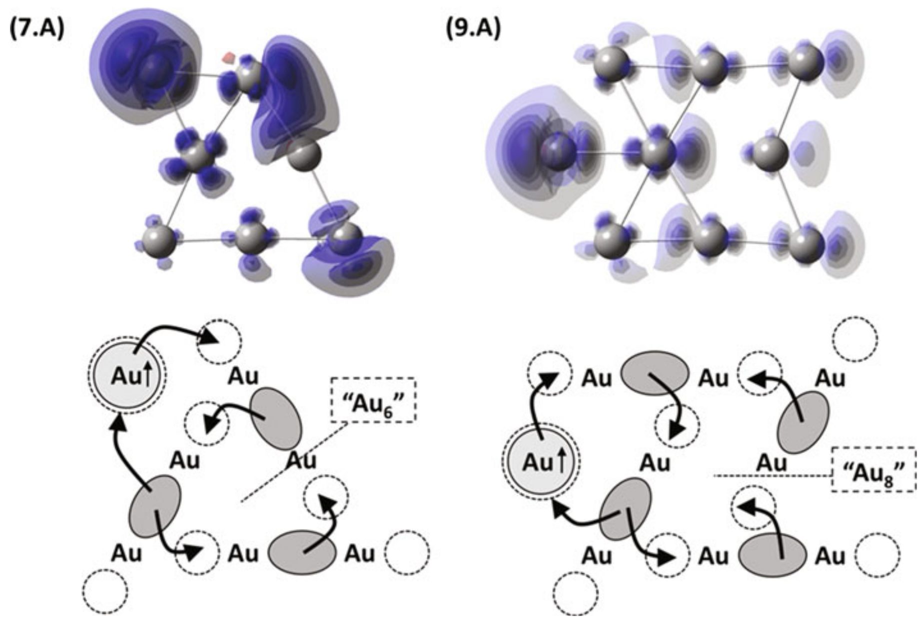

Fig. 12 Predominant resonance structures and spin densities of (7.B) and (9.B) clusters

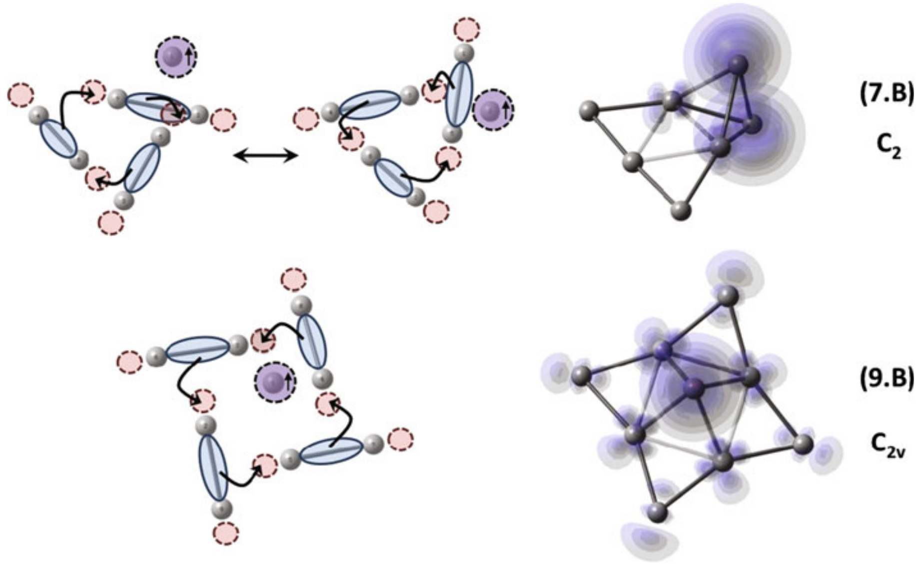

3.3.3 Higher nuclearities

The higher nuclearities are consistent with previous results but the large number of possible dimeric units makes it difficult to define intuitively the predominant resonance structure. For example, Au_7 and Au_9 clusters present both planar ground states (7.A) and (9.A) [25–28] where the major resonance structure corresponds to the addition of one gold atom on the very stable Au_6 and Au_8 templates. For the two clusters, the spin densities reveal the location of the unpaired electron, that is, the most atomic-like center (Fig. 11). In both cases, the major resonance structure corresponds to the addition of a gold atom to the very stable Au_6 and Au_8 templates. This maintains a good electron flow over the entire structure. However, the large number of resonance structures renders a detailed analysis a bit more laborious.

Three-dimensional minima (7.B) and (9.B), respectively, at 5.5 and 2.0 kcal mol^{-1} could be identified. These correspond to the adsorption of an additional gold atom on a face of the very stable Au_6 and Au_8 clusters. Their structure will be slightly deformed adjusting the orbitals overlap by a "push–pull" effect while maintaining a good σ-aromaticity. The unpaired electron becomes easy to locate since the dominant resonance structure, as for (7.A) and (9.A), corresponds to those minima keeping a cyclic flow of electrons in Au_6 and Au_8 templates (Fig. 12). Although these two structures satisfy the condition of an electronic flow, they are less stable than their planar counterparts. This is explained by a weakening of σ–σ* overlaps due to the deformation of the Au_6 and Au_8 templates, and therefore, a decrease in aromaticity. A similar discussion could be carried out for successive nuclearities.

4 Conclusions

It has been shown in this work that the electronic structure of Au_m clusters can be described in an original way through resonance structures, which may be drawn by expressing the considered structure in Au_2 dimeric subunits. It appears that Au_2 is a stable unit presenting a strong coherent electronic structure. This, which at first glance may seem surprising, may be understood if one notes its isoelectronicity to the well-known Hg_2^{2+} cation. This gold dimer constitutes the basic unit that allows interpreting the electronic and geometric structure of more elaborate clusters. The presented analysis, based on the concepts well known by chemists, highlights the rules governing the electronic description of such compounds. Their predictive capability explains geometries but also provides direct information on structural parameters and relative stabilities. Moreover, in the case of open-shell systems, the rules have shown their usefulness in evaluating the distribution of the unpaired electron. Therefore, a good understanding of these rules can restrict the exploration of potential energy surfaces to the most reasonable candidate structures, which can be strategic as we know that the number of conceivable isomers becomes important when the systems size increases. To summarize, the most stable structures ensure:

1. A maximization of σ–σ* overlaps between Au_2 dimeric units.
2. A promotion of cyclic flows of valence electrons on the entire structure (σ–aromaticity).

These conditions are ideally fulfilled for the Au_8 cluster, and to a lesser extent, the Au_6 cluster. Such templates are found in the most stable structures of higher nuclearities. Finally, the rules provide guidelines to the structural transition of small planar gold clusters to three-dimensional structures. It seems that this transition is favored starting from five dimeric units, i.e., Au_{10}.

The discussion presented in this paper leads to a model, which seems consistent with most observed structures. Nevertheless, it remains a theoretical model, which is obtained at a well-defined level of theory that does not extensively introduce all effects, such as relativistic and many body corrections. Even though the authors are confident in the quality of their analysis, one may not exclude such effects to be significant in the case of gold.

Acknowledgments This work was supported by FRIA-F.N.R.S. (*Fonds pour la Formation à la Recherche dans l'Industrie et dans l'Agriculture*-Belgium, fellowship to G.Z.), and F.R.S.-FNRS by its support to access computational facilities (Project FRFC N°2.4502.05 "Simulation numérique. Application en physique de l'état solide, océanographie et dynamique des fluides").

References

1. Moskovits M (1991) Annu Rev Phys Chem 42:465–469
2. Pyykkö P (2004) Angew Chem Int Ed 43:4412–4456
3. Pyykkö P (2005) Inorg Chim Acta 358:4113–4130
4. Schwerdtfeger P (2003) Angew Chem Int Ed 42:1892–1895
5. Mirkin CA, Letsinger RL, Mucic RC, Storhoff JJ (1996) Nature 382:607–608
6. Alivisatos AP, Johnsson KP, Peng X, Wilson TE, Loweth CJ, Bruchez MP Jr, Schultz PG (1996) Nature 382:609–611
7. Haruta M (2002) CATTECH 6:102–115
8. Haruta M (2004) Gold Bull 37:27–36
9. Haruta M, Yamada N, Kobayashi T, Iijima S (1989) J Catal 115:301–309
10. Haruta M (2003) Chem Lett 3:75–87
11. Haruta M (2007) T. Ishida. Angew Chem Int Ed 46:7154–7156
12. Meyer M, Lemire C, Shaikhutdinov S, Freud HJ (2004) Gold Bull 37:72–124
13. Lemire C, Meyer R, Shaikhutdinov S, Freud HJ (2004) Angew Chem Int Ed 43:118–121
14. Lemire C, Meyer R, Shaikhutdinov S, Freud HJ (2004) Surf Sci 552:27–34

15. Jortner J, Phys Z (1992) D At Mol Clusters 24:247–275
16. Arenz M, Gil S, Heinz U (2007) Chem Phys Solid Surf 12:1–47
17. Heiz U, Sanchez A, Abbet S, Schneider WD (1999) Eur Phys J D 9:35–39
18. Sanchez A, Abbet S, Heiz U, Schneider WD, Häkkinen H, Barnett RN, Landman U (1999) J Phys Chem A 103:9573–9578
19. Häkkinen H, Landman U (2000) Phys Rev B 62:2287–2290
20. Wang J, Wang G, Zhao J (2002) Phys Rev B 66:035418-1–035418-6
21. Sierralta N, Rincon L, Almeida R (2003) Mater Condens 49:164–167
22. Xiao L, Wang L (2004) Chem Phys Lett 392:452–455
23. Remacle F, Kryachko ES (2005) J Chem Phys 122:044304-1–0443041-4
24. Koskine P, Häkkinen H, Seifert G, Sanna S, Frauenheim T, Moseler M (2006) New J Phys 8:9
25. Walker AV (2005) J Chem Phys 122:094310-1–094310-12
26. Xiao L, Tollberg B, Hu X, Wang L (2006) J Chem Phys 124:114309-1–114309-10
27. Li XB, Wang HY, Yang XD, Zhu ZH, Tang YJ (2007) J Chem Phys 126:084505-1–084505-8
28. Assadollahzadeh B, Schwerdtfeger P (2009) J Chem Phys 131:064306-1–064306-11
29. Bulusu S, Zeng XC (2006) J Chem Phys 125:154303-1–154303-5
30. Phala NS, Klatt G, van Steen E (2004) Chem Phys Lett 395:33–37
31. Olson RM, Varganov S, Gordon MS, Metiu H, Chretien S, Piecuch P, Kowalski K, Kucharski SA, Musial M (2005) J Am Chem Soc 127:1049–1052
32. Becke AD (1993) J Chem Phys 98:5648–5652
33. Hay PJ, Wadt WR (1985) J Chem Phys 82:270–283
34. Hay PJ, Wadt WR (1985) J Chem Phys 82:284–298
35. Hay PJ, Wadt WR (1985) J Chem Phys 82:299–310
36. Zanti G, Peeters D (2010) J Phys Chem A 114:10345–10456
37. Frisch MJ, Trucks GW, Schlegel HB, Scuseria GE, Robb MA, Cheeseman JR, Montgomery JA Jr, Vreven T, Kudin KN, Burant JC, Millam JM, Iyengar SS, Tomasi J, Barone V, Mennucci B, Cossi M, Scalmani G, Rega N, Petersson GA, Nakatsuji H, Hada M, Ehara M, Toyota K, Fukuda R, Hasegawa J, Ishida M, Nakajima T, Honda Y, Kitao O, Nakai H, Klene M, Li X, Knox JE, Hratchian HP, Cross JB, Bakken V, Adamo C, Jaramillo J, Gomperts R, Stratmann RE, Yazyev O, Austin AJ, Cammi R, Pomelli C, Ochterski JW, Ayala PY, Morokuma K, Voth GA, Salvador P, Dannenberg JJ, Zakrzewski VG, Dapprich S, Daniels AD, Strain MC, Farkas O, Malick DK, Rabuck AD, Raghavachari K, Foresman JB, Ortiz JV, Cui Q, Baboul AG, Clifford S, Cioslowski J, Stefanov BB, Liu G, Liashenko A, Piskorz P, Komaromi I, Martin RL, Fox DJ, Keith T, Al-Laham MA, Peng CY, Nanayakkara A, Challacombe M, Gill PMW, Johnson B, Chen W, Wong MW, Gonzalez C, Pople JA (2004) Gaussian 03, ReVision C.02. Gaussian, Inc., Wallingford, CT
38. Olson RM, Varganov S, Gordon MS, Metiu H, Chretien S, Piechuch P, Kowalski K, Kucharski SA, Musial M (2005) J Am Chem Soc 127:1049–1052
39. Häkkinen H, Yoon B, Landman U, Li X, Zhai H-J, Wang L-S (2003) J Phys Chem A 107:6168
40. Reed AE, Weinhold F (1983) J Chem Phys 78:4066–4073
41. Reed AE, Weinstock RB, Weinhold F (1985) J Chem Phys 83:735–746
42. Reed AE, Curtiss LA, Weinhold F (1988) Chem Rev 88:899–926
43. Jules JL, Lombardi JR (2003) J Phys Chem A 107:1268–1273
44. Berlin T (1951) J Chem Phys 19:208
45. Zubarev DY, Averkiev BB, Zhai H-J, Wang L-S, Boldyrev AI (2008) Phys Chem Chem Phys 10:257–267
46. Howard JA, Sutcliffe R, Mile B (1983) J Chem Soc Chem Commun 1449–1450

Theor Chem Acc (2013) 132:1320
DOI 10.1007/s00214-012-1320-x

REGULAR ARTICLE

Combining molecular dynamics with Monte Carlo simulations: implementations and applications

Erik C. Neyts · Annemie Bogaerts

Received: 16 July 2012 / Accepted: 6 December 2012 / Published online: 20 December 2012

Abstract In this contribution, we present an overview of the various techniques for combining atomistic molecular dynamics with Monte Carlo simulations, mainly in the context of condensed matter systems, as well as a brief summary of the main accelerated dynamics techniques. Special attention is given to the force bias Monte Carlo technique and its combination with molecular dynamics, in view of promising recent developments, including a definable timescale. Various examples of the application of combined molecular dynamics / Monte Carlo simulations are given, in order to demonstrate the enhanced simulation efficiency with respect to either pure molecular dynamics or Monte Carlo.

Keywords Molecular dynamics · Monte Carlo · Long time scale dynamics

1 Introduction

In order to gain control over properties of and processes in materials, an atomic scale understanding is of primary importance. To this end, two main techniques are commonly used, viz. molecular dynamics (MD) and Monte Carlo (MC) simulations [1].

Molecular dynamics (MD) simulations have been shown to be an invaluable tool to investigate both static and dynamic properties of systems at the atomic scale. Consequently, they have been applied to a countless number of systems and processes, ranging from the calculation of structural and morphological properties of materials [2, 3], transport properties [4], growth of thin films and other nanomaterials [5, 6], protein folding [7], etching [8, 9], sputtering [10], chemical reactions [11], friction [12], fraction [13], phase changes [14, 15] and so forth.

Classical MD simulations are based on solving the equations of motion for all particles in the system to obtain the trajectory of the particles in phase space. Thus, essentially, the integration of these equations yields the positions and velocities of the particles, as well as the forces acting on them. The forces are derived from some suitable interatomic potential. This has two immediate implications. First, classical MD simulations are approximative, due to the inexact nature of the calculated forces and energies. Second, exactly because of this approximative nature, they are computationally cheap, making calculations of systems containing millions of atoms feasible, in contrast to more exact approaches such as Car-Parrinello MD. Also, the timescale that can be handled is orders of magnitude longer than what is possible with more exact approaches.

On the other hand, MD simulations are limited in two main respects. First, while the system may contain up to millions of atoms, this still only constitutes a material on the nanometer to sub-micrometer scale at typical solid-state and liquid densities. This makes it difficult to study, for instance, grain boundaries in a polycrystallite [16]. A second, more severe restriction, is the timescale that can be reached. Here, the typical limit is in the nanosecond–microsecond timescale, although in exceptional cases the (sub-)millisecond range may be reached [17]. This makes it difficult to simulate, for instance, the growth of a material, which typically occurs on timescales well beyond this limit.

Published as part of the special collection of articles celebrating theoretical and computational chemistry in Belgium.

E. C. Neyts (✉) · A. Bogaerts
Department of Chemistry, University of Antwerp,
PLASMANT Research Group, Universiteitsplein 1,
Antwerp 2610, Belgium
e-mail: erik.neyts@ua.ac.be

A number of so-called accelerated molecular dynamics techniques have been developed to extend the timescale of MD simulations, as will be discussed in Sect. 2.

An alternative to MD for studying atomic scale processes and calculating material properties is the use of Monte Carlo methods [1]. In a Monte Carlo (MC) simulation, atoms are displaced based on random numbers. Thus, in contrast to MD, the MC technique is not deterministic. The most famous MC technique is undoubtedly Metropolis MC (MMC) [18]. The MMC algorithm leads to a system in equilibrium, corresponding to the Boltzmann distribution. Note, however, that the path toward this equilibrium is not necessarily physical (and usually it is indeed not). Indeed, whereas a MD simulation typically generates a single long trajectory of the system through phase space, MC typically samples configuration space.

Kikuchi et al. demonstrated, however, that MMC is not restricted to the calculation of equilibrium properties, but can also be used to study dynamic properties. Specifically, they applied the MMC method to the study of Brownian motion of a harmonically bound particle [19]. The same authors further extended the method to study interacting Brownian particles including the effects of hydrodynamic interactions [20].

An different kind of Monte Carlo method is the so-called Kinetic Monte Carlo method (sometimes also called Dynamic Monte Carlo) [21], in which the system is allowed to evolve dynamically from state to state, based on a catalog of transitions and associated rates. Each transition is accepted with a probability proportional to its rate. This, however, assumes that a complete catalog of possible transitions is known in advance (see [22] for an example of the importance of this). Alternatively, a catalog may be built on-the-fly, as proposed by Henkelman et al. [23]. Similar to this technique is the transition state theory (TST)-based MC technique of Liu et al. [24].

In contrast to the processes observed in MD, KMC is not self-consistent, that is, it must be assumed that all possible escape paths from the system's current state can be found. Indeed, if one or several paths are systematically missed, this will corrupt the dynamics of the system [25].

Moreover, often we wish to retain the actual trajectories of the atoms, which is not possible with pure MC techniques. However, in many cases, this is of primordial importance, for instance in the study of particles impinging on a surface. At the same time, it may be desirable to include the effect of long timescale events which bring the system toward equilibrium. For this purpose, MD simulations may be combined with MC simulations.

This paper deals with combining MC with MD simulations. However, it is worth to mention also various other techniques, not based on combining MD with MC, for extending the effective timescale or taking into account relaxation phenomena [25]. In the following section, we will, therefore, briefly summarize the most prominent techniques that were specifically designed to simulate the dynamical evolution of the system on a longer timescale (i.e., accelerated molecular dynamics). Subsequently, we will present the various possible combinations of coupling MC to MD. Finally, a number of examples of combined MD/MC simulations will be given.

2 Accelerated molecular dynamics techniques

A large number of techniques have been developed for finding saddle points, exploring the free energy landscape of the system and for exploring the potential energy landscape. In the context of accelerating dynamical processes and taking into account long timescale events in the dynamical evolution of a system, we shall here first describe the most prominent techniques for accessing these dynamics. Techniques specifically designed for identifying saddle points and/or reaction paths (such as nudged elastic band [26], the dimer method [27], transition path sampling [28], the activation relaxation technique (ART) [29], forward flux sampling [30], finite temperature string method [31] and milestoning [32], and techniques aimed at sampling the free energy landscape (including thermodynamic integration [33], metadynamics [34], free energy perturbation [35], umbrella sampling [36], adaptive force bias [37] and steered MD [38]), fall outside the scope of this paper.

Prominent among the methods for exploring the atomic scale dynamics of a system, including relaxation and rare events, are temperature-accelerated dynamics (TAD) [39], hyperdynamics [40] and parallel replica [41], all developed by Voter and coworkers. These techniques build on statistical mechanics principles for infrequent event systems, and as such do not make any prior assumptions regarding the atomistic mechanisms. They are designed to simply allow the system to evolve more quickly from state to state than they would in normal MD, provided that the barriers are relatively high compared to kT.

Note that these techniques are not sampling methods, in contrast to (most of) the methods mentioned above. Similar to combined MD/MC simulations in the context of condensed matter systems, they generate a single long state-to-state trajectory.

2.1 Temperature-accelerated dynamics

In TAD, which assumes that harmonic transition state theory (HTST) holds, the simulation is carried out at elevated temperature in order to collect a sequence of escape times from the local energy minimum in which the system resides. Subsequently, each escape time can be extrapolated to the (lower) temperature of interest, based on the escape time and activation energy as determined from the high temperature simulation. Finally, the transition corresponding to the shortest escape time at the lower temperature is effectively carried out.

Employing this technique, Voter et al. [25] reached a dramatic speed-up factors of 10^7 in the simulation of vapor-deposited growth of a Cu(100) surface at a temperature of 77 K. The simulation conditions corresponded exactly with the experimental conditions of Egelhoff and Jacob [42]. Note, however, that as the boost factor depends on the ratio between the elevated temperature and the lower temperature of interest, much lower factors appear when simulating systems at higher temperatures. Nevertheless, Georgieva et al. [43] recently applied TAD simulations at 500 K to simulate the magnetron sputter deposition of complex oxide Mg–Al–O thin films, extending the typical nanosecond MD timescale to the millisecond range.

2.2 Hyperdynamics

In hyperdynamics, the potential energy surface (PES) of the system is modified by adding a suitable bias potential ΔV. On this modified PES, the system will escape more rapidly from its local state than it would on the original PES. The timescale can be extracted from the value of the bias potential and the MD time required to escape from the state on the modified PES. In contrast to TAD, it only requires TST to hold (instead of HTST), although correlated events are assumed not to occur. In the original hyperdynamics formulation, a Hessian-based bias potential was used [40]. While this approach satisfies the necessary conditions, that is, $\Delta V > 0$ at the potential minimum and $\Delta V = 0$ at the dividing hypersurfaces, it quickly becomes prohibitively expensive with increasing system size as the full $3N$ Hessian needs to be diagonalized in every step.

The main difficulty, therefore, lies in the construction of a suitable and cheap bias potential. Fichthorn et al. [44] developed a so-called bond-boost method, in which the boost potential is derived from the concept of bond breaking events in a solid. Thus, the boost potential in this approach is a function of all nearest-neighbor bond lengths associated with the atoms of interest. Using this technique, these authors studied the diffusion of Cu adatoms, dimers and vacancies on a Cu(001) surface [44]. In these simulations, average boost factors in the range 10^6–10^1 were obtained in the temperature range 230–600 K.

Another very promising way to handle the boost potential problem was proposed by Hamelberg et al. [45]. Their boost potential is defined by functions filling up the energy minima, such that the underlying shape of the unmodified potential energy landscape is retained. At some threshold energy value, the modified potential merges smoothly with the original potential. Combining this boost potential with MC-based system thermalization, Tiwary et al. reached a boost factor of 10^5 for iron lattice diffusion at 285 K.

2.3 Parallel replica

In parallel replica, which is the most exact of the three techniques, a dephased version of the system is replicated on a number of processors. On each of these, the system is allowed to evolve, until a transition is detected on one of the processors. The time accumulated on all processors then corresponds to the advance in simulation time. Parallel replica does not even assume TST to hold. The only requirement is that the infrequent events obey first-order kinetics. Besides this requirement, it is also necessary to dephase the systems on all processors, which typically requires a simulation time of a few ps.

Very recently, Uberuaga employed both TAD and parallel replica simulations to study the formation of fullerene and graphene from carbon nanotube fragments [46]. Using 39 processors, they obtained a boost factor of 28 in the parallel replica simulations, whereas the TAD simulations resulted in boost factors in the range 10–1400 (depending on the exact structure simulated). While the boost factor of parallel replica is typically the lowest of the three methods, it is important to realize that the boost can be trivially increased by increasing the number of processors.

3 Combining MD and MC simulations

3.1 Setting the scene: Monte Carlo simulations

In order to understand Monte Carlo simulations in general and force bias Monte Carlo in particular, it is useful to recall the crucially important condition of detailed balance. This condition can be expressed as

$$W(\mathbf{r}'|\mathbf{r})P(\mathbf{r}) = W(\mathbf{r}|\mathbf{r}')P(\mathbf{r}') \tag{1}$$

where $P(\mathbf{r})$ is the probability of finding a particle at position $\mathbf{r}$, and $W(\mathbf{r}'|\mathbf{r})$ is the transition probability of the particle to go from position $\mathbf{r}$ to position $\mathbf{r}'$. If P follows a Boltzmann distribution, then

$$\frac{W(\mathbf{r}'|\mathbf{r})}{W(\mathbf{r}|\mathbf{r}')} = \exp(-\beta\Delta U) \qquad \text{with } \beta = \frac{1}{\mathrm{k_B T}} \tag{2}$$

where ΔU is the change in potential energy of the system due to the displacement. W can be rewritten as:

$$W(\mathbf{r}'|\mathbf{r}) = A(\mathbf{r}'|\mathbf{r})T_c(\mathbf{r}'|\mathbf{r}) \tag{3}$$

where T_c $(\mathbf{r}'|\mathbf{r})$ represents the probability distribution of selecting a new position $\mathbf{r}'$ from the old position $\mathbf{r}$, and $A(\mathbf{r}'|\mathbf{r})$ is the probability of accepting this new position. Now, we can define a quantity q as follows:

$$q(\mathbf{r}'|\mathbf{r}) = \frac{T_c(\mathbf{r}|\mathbf{r}')}{T_c(\mathbf{r}'|\mathbf{r})}\exp(-\beta\Delta U) = \frac{T_c'}{T_c}\exp(-\beta\Delta U) \tag{4}$$

Using this quantity q, the condition of detailed balance can now be formulated as

$$A(\mathbf{r}'|\mathbf{r}) = \min[1, q(\mathbf{r}'|\mathbf{r})] \tag{5}$$

Thus, the acceptance of the displacement of a particle from $\mathbf{r}$ to $\mathbf{r}'$ is determined by the associated value of q.

In Metropolis Monte Carlo, T_c is defined as

$$T_c = \begin{cases} c \text{ if } \mathbf{r}' & \in D(\mathbf{r}) \\ 0 \text{ if } \mathbf{r}' & \notin D(\mathbf{r})D(\mathbf{r}) \end{cases} \tag{6}$$

in which $D(\mathbf{r})$ is the displacement domain, and c is a constant. From this, it follows that

$$q = \exp(-\beta\Delta U) \tag{7}$$

From Eqs. 5 and 7, it is immediately clear that when the energy of the system is lowered due to the chosen displacement (i.e., $\Delta U < 0$), this displacement is always accepted, while if the energy increases due to the chosen displacement (i.e., $\Delta U > 0$), the probability of accepting the displacement is equal to $\exp(-\beta\Delta U)$.

3.2 Combined MD/MC algorithms

Various approaches have been proposed to combine MD and MC simulations. Three classes can essentially be distinguished:

1. Mixed MD/MC algorithms, in which some atoms are moved by MD and some by MC;
2. Hybrid MD/MC algorithms, in which the algorithm itself is a combination of MD and MC;
3. Sequential algorithms, in which MD and MC cycles alternate.

Note that most of these algorithms are used to generate a single trajectory, similar to the accelerated molecular dynamics techniques. However, the stochastic MC component does not allow to assign a timescale to the simulation, except in the case of so-called time stamped force bias Monte Carlo (tfMC, see below) [47]. Thus, a comparison in terms of a boost factor with the accelerated dynamics techniques cannot be made.

3.2.1 Mixed MD/MC algorithm

In mixed MD/MC simulations, some of the atoms are moved by the MD method and some of the atoms are moved by the MC method. LaBerge et al. [48] demonstrated that this method rigorously converges to the same equilibrium state as either MC or canonical MD alone. Thus, it was shown that the interruption of the forces produced by the application of the MC moves does not incorrectly bias the evolution of the MD particles. This technique was applied by the above authors to a Lennard-Jones fluid. It was anticipated that this model would be superior to either MD or MC on its own, in systems where some particles are more efficiently sampled by MD (for instance solvent motions), while others are more efficiently sampled by MC (for instance highly correlated motions).

Ribeiro et al. [49] recently used mixed MD/MC simulations of polyalanine systems in water. The MC trials, employing the so-called concerted rotations and angles (CRA) approach of Ulmschneider and Jorgensen [50], were applied to a subset of the peptide atoms; the remaining peptide atoms and the solvent molecules were displaced using MD. It was demonstrated that the mixed MD/MC approach led to a faster formation of the secondary structure, and that the α-helix was formed earlier than in pure MD simulations. It should be noted, however, that both the study of LaBerge et al. and Ribeiro et al. use the mixed MD/MC approach for enhanced sampling of configuration space.

3.2.2 Hybrid algorithms

Whereas in mixed MD/MC simulations, some of the atoms are moved by "pure" MD, and other particles are moved by "pure" MC, it is also possible to construct algorithms in which the displacement itself is determined in part by a deterministic factor and in part by a stochastic factor. In this class, we can further distinguish essentially three techniques: Langevin or stochastic dynamics, hybrid Monte Carlo, and force bias Monte Carlo and related techniques.

Langevin dynamics or stochastic dynamics Langevin dynamics or stochastic dynamics [51] is typically employed for simulating systems in which certain degrees of freedom are omitted. A typical example is the simulation of solvent effects. In this case, one wishes to include the average effect of the solvent on the solute, without explicitly adding all solvent molecules. Stochastic dynamics are based on solving the Langevin equation, in which the total force acting on a particle originates from three contributions: the interaction between the particle and the other particles in the systems (*the systematic force*), a frictional drag component on the particle due to the solvent (*the frictional force*), and a random force acting on the particle due to random fluctuations which result from interactions with the solvent (*the stochastic force*). Thus, the equation to be solved, the Langevin equation, is:

$$m_i \frac{d^2\mathbf{r}_i(t)}{dt^2} = \mathbf{F}_i(\mathbf{r}_i(t)) - \gamma_i \frac{d\mathbf{r}_i(t)}{dt} m_i + \mathbf{R}_i(t) \tag{8}$$

where $\mathbf{F}_i$ is the systematic force, γ_i is the friction coefficient divided by the mass m of the particle (but it is often simply called the friction coefficient), and $\mathbf{R}_i$ is the stochastic force. Application of Langevin dynamics leads to a canonical distribution.

Langevin dynamics often allow a significant reduction in computation time, due to the fact that there are considerably less particles to be simulated, and also because often longer time steps can be taken relative to MD. Note, however, that Langevin dynamics do not fully simulate the effect of the solvent. Specifically, this method does not account for electrostatic screening, nor for hydrophilic/hydrophobic effects. Furthermore, there is no conservation of energy, and unless the friction coefficient is small, the generated trajectories are not physical [52].

Langevin dynamics are very often used to study biophysical and biochemical systems. For instance, Forray et al. [53] used Langevin dynamics simulations to study the genome packing in bacteriophage. As an all-atom approach is not feasible for such a system, a coarse-graining approach was used, in which the DNA is represented by a wormlike chain of identical beads. Thus, the chemical structure of the DNA double helix is lost. Each Langevin dynamics step corresponded to a time $\Delta t = 12.9$ ps. The structure of the packaged DNA condensate was found to evolve qualitatively according to experimental data. Thus, Langevin dynamics allows to study systems on a larger length scale and on longer timescales than is possible with standard MD, albeit more approximatively.

Hybrid Monte Carlo In MD, all atoms are displaced simultaneously. In MC, however, typically only one or a few particles are displaced at a time, in order to retain a sufficiently high acceptance rate. The moves in MD are limited by the time step, which needs to be sufficiently small in order to conserve the total energy. The moves in MC, on the other hand, are allowed to be large and unphysical. Hybrid Monte Carlo, or Hamiltonian Monte Carlo, was developed by Duane et al. [54] to combine the advantages of both. The idea is to use MD to generate MC trial displacements. Provided that a time-reversible and symplectic algorithm is used, the collective moves thus generated in MD can be accepted or rejected using the standard MMC criterion. The end result is that trials move across the sample space in larger steps, and because of the Hamiltonian evolution of the system between states, the correlation between successive states is reduced. However, as pointed out by Frenkel and Smit [1], the performance of hybrid MC is not always dramatically better than that of the corresponding MD, although hybrid MC might be advantageous for systems that are not too large.

This technique is most often used in lattice quantum chromodynamics (QCD) simulations. Mehlig et al. [55] demonstrated its use by simulating Lennard-Jonesium as an example of a condensed matter system. Similarly, Clamp et al. [56] simulated a 2D Lennard-Jones fluid using both MD and hybrid MC and found that hybrid MC is more ergodic and samples phase space more efficiently than MD. A more realistic system was studied by Brotz et al. [57], employed hybrid MC to calculate the phase diagram of silicon.

Force bias Monte Carlo and related techniques Several variants of force bias Monte Carlo (fbMC) simulations have been presented in the literature. Essentially, the goal of these algorithms is to have a higher acceptance probability of the atomic displacements relative to MMC, and thus to allow the system to evolve to equilibrium more quickly. The original fbMC method was introduced by Pangali et al. [59, 58]. In the original version, an acceptance criterion was used to accept or reject a new configuration. In later versions by Dereli [60], Mezei [61] and Timonova [62], a uniform acceptance was employed. Recently, detailed balance in these uniform acceptance algorithms was formally demonstrated by Neyts et al. [63].

In fbMC, the possible displacements are *not* chosen randomly in the domain $D(\mathbf{r})$, but are dependent on the force acting on the particle, in contrast to the MMC method. The transition matrix is now written as (in the x-coordinate):

$$T_{c,x} = \begin{cases} K_x^{-1} \exp(\lambda\beta F_x \delta_x) & \text{if } x' \in D(x) \\ 0 & \text{if } x' \notin D(x) \end{cases} \tag{9}$$

In this expression, the displacement δ_x is given by $\delta_x = x' - x$, F_x is the x-component of the force at position x, K_x^{-1} is a normalization constant, and λ is a (in principle) arbitrary parameter. Analogous expressions appear for the components in the other directions.

Thus, from Eq. 9, it is clear that displacements in the direction of the force are more probable than displacements against the force. As a result, considerably less displacements need to be rejected compared to the Metropolis algorithm. The obvious downside is that the force needs to be calculated.

If the domain $D(\mathbf{r})$ corresponds to a cube centered around $\mathbf{r} = (x, y, z)$ and sides $2\Delta \times 2\Delta \times 2\Delta$, then each displacement in a direction v is limited as:

$$-\Delta \leq \delta_v \leq \Delta \tag{10}$$

and the displacement can be written as

$$\mathbf{r}' = \mathbf{r} + \boldsymbol{\xi} \cdot \boldsymbol{\Delta} \tag{11}$$

Each component $\xi_v \in [-1, 1]$ from the vector $\boldsymbol{\xi} = \{\xi_x, \xi_y, \xi_z\}$ can be computed based on a random number $\eta \in [0, 1]$ as

$$\xi_v = \frac{1}{\gamma_v} \ln\left[\eta\left(\mathrm{e}^{|\gamma_v|} - \mathrm{e}^{-|\gamma_v|}\right) + \mathrm{e}^{-|\gamma_v|}\right] \tag{12}$$

in which

$$\gamma_v = \lambda\beta F_v \Delta \tag{13}$$

Just as in the case of MMC, all displacements need to be accepted or rejected, based on the value of q and thus of A. Mezei et al. [61] used this technique to simulate a DNA-octamer duplex and Na^+ions solvated by water molecules employing the AMBER force field.

Dereli [60] proposed to use $\lambda = 1/2$ and accept all displacements, instead of using q to accept or reject displacements. Somewhat confusingly, Dereli termed this technique *Dynamic Monte Carlo*. Recently, Timonova et al. thoroughly reviewed the method and termed it *uniform acceptance force bias Monte Carlo* [62]. These authors performed a number of tests to investigate under which conditions reliable results can be expected. The authors recommended to use a realistic value for the temperature parameter, although it should be treated carefully, especially when using large maximum displacements. From their simulations, it seems that a value for the maximum allowed displacement in the range $\Delta/2 = 0.06R_{\mathrm{eq}} - 0.15R_{\mathrm{eq}}$, where R_{eq} is the equilibrium bond length, is appropriate for temperatures at or above room temperature for silicon. The exact value is dependent on the desired accuracy and speed of the simulation.

Very recently, a formal proof was presented by Neyts et al. [63] that this uniform acceptance formulation using $\lambda = 1/2$ complies with detailed balance, provided that the domain D, and thus the maximum allowed displacement, is chosen sufficiently small. Note that this value is dependent on both the exact potential, as well as on the temperature. The higher the temperature, the larger the maximum displacement can be chosen without violating detailed balance.

A novel version of the uniform acceptance algorithm was recently published by Mees et al. [47]. In this version, which was termed *time stamped force bias Monte Carlo* (tfMC), the conditional probability for a displacement in the x-direction is given by:

$$P_{c,x}(\xi_x) = \begin{cases} \frac{e^{\gamma_x(2\xi_x+1)} - e^{-\gamma_x}}{e^{\gamma_x} - e^{-\gamma_x}} & \xi_x \in [-1, 0[\\ \frac{e^{\gamma_x} - e^{\gamma_x(2\xi_x-1)}}{e^{\gamma_x} - e^{-\gamma_x}} & \xi_x \in]0, 1] \end{cases}. \tag{14}$$

Again, analogous expressions appear for the other directions. In practice, a pair of random numbers (ξ_v, P_v) is generated for each direction v, with $\xi_v \in [-1, 1]$ and $P_v \in [0, 1]$ for all atoms. If $P_{c,v}(\xi_v) > P_v$, the displacement of the atom is accepted and its new position is $r_{v,new} = r_{v,old} + \Delta\xi_v$. Else, if $P_{c,v}(\xi_v) < P_v$, a new random pair (ξ_v, P_v) is generated and its acceptance is reevaluated.

From Eq. 12, it is clear that in fbMC, the displacement of the particles is based on both a deterministic component, that is, the force, and a stochastic component, that is, a random number(s). At low temperature, the deterministic component dominates, and all displacements are essentially in the direction of the force. At high temperature, on the other hand, all displacements will be essentially fully random.

Importantly, an expression for the statistical time per MC step was derived from this algorithm:

$$\langle \Delta t \rangle = \frac{\Delta}{3} \cdot \sqrt{\frac{\pi m_{\min}}{2k_B T}} \tag{15}$$

in which $m_{\min}$ is the mass of the lightest element present in the simulation. In contrast to MMC, this allows to assign a timescale to the MC simulation. From their tests, the authors concluded that time steps between about 2 fs and 50 fs per tfMC step can be obtained. This represents a speed-up relative to MD by a factor of about 2–50 [47]. While this value may seem low compared to the very high boost factors that may be obtained in accelerated dynamics as described above, it should be realized that tfMC in contrast to accelerated dynamics is not limited to infrequent event systems, and it does not require (H)TST to hold. Thus, while the speedup is indeed limited, the method can be considered to have a wider applicability.

Very similar to these force bias Monte Carlo algorithms is the *Smart Monte Carlo* technique by Rossky et al. [64]. This technique also requires the forces acting on the moving atom to be calculated. Also, the displacement is determined by two components, that is, the force, which acts as the deterministic component, and a random vector $\delta\mathbf{r}_i^R$. The displacement is then written as

$$\delta\mathbf{r}_i = \frac{A\mathbf{F}_i}{k_B T} + \delta\mathbf{r}_i^R \tag{16}$$

where $\mathbf{F}_i$ is the force acting on particle i and A is a parameter. The random vector $\delta\mathbf{r}_i^R$ is chosen from a normal distribution with zero mean and variance $2A$.

In contrast to the fbMC methods, the smart Monte Carlo method does not impose a limit on the maximum displacement of the particles. This obviously implies that in this case, acceptance or rejectance must be verified by calculating q (cfr. Eq. 4 above).

3.2.3 *Sequential algorithms: alternating MD and MC*

Many authors have combined MD and MC by simply allowing one technique to alternate with the other technique. In most cases, one technique is applied to all atoms for a predetermined number of steps. The resulting output is subsequently used as input to the other technique, which is also run for a predetermined number of steps. Again, the resulting output is then used as input to the first technique and the cycle repeats.

The underlying idea is that MD can be used to simulate fast processes, for instance the impingement of reactive species on a surface and the chemical bonding to the surface, while the subsequent MC steps take into account the longer timescale thermal relaxation processes, as schematically depicted in Fig. 1. This technique has for instance been applied to the fast equilibration of complex systems such as lipid-cholesterol lipid bilayers and fully hydrated dioleyl and palmitoyl-oleyl phosphatidylcholine lipid bilayers [65, 66], but it is equally suited for simulating for instance deposition processes. Indeed, while in some cases deposition and growth may be successfully simulated using MD alone (see for instance [6, 67], longer timescale processes are very often a critical factor in determining the final thin film properties.

Taguchi et al. [68, 69] applied this technique to model the reactive sputter deposition of thin SiO_2 films and the effect of Ar bombardment on the SiO_2 deposition process. In this particular case, it was found that simulating the deposition process by MD alone resulted in films with a much lower density that those typically obtained from experiments under similar conditions. Applying the sequential MD/MC approach, amorphous SiO_2 films with properties consistent with experiments were obtained.

A somewhat different version of this idea was presented by Tavazza et al. [70]. In their approach, collective moves are added to the standard single-atom moves in the MC method. When an atom or several atoms are displaced by MC, the local environment is first relaxed using a small number of MD steps at constant temperature. Only after this relaxation process the displacement is evaluated and accepted or rejected using the standard Boltzmann criterion. Thus, in their approach, the MD displacements are effectively used as trial displacements for the MC simulation, and as such this idea corresponds to the hybrid MC concept (see above, Sect. 3.2.2)

Yet another version of the same idea was presented by Tiwary and van de Walle [71]. In their approach, the system evolves according to standard MD when the potential energy is above some threshold, whereas it evolves according to MMC when the potential energy falls below this threshold. The MC part takes care of the relaxation of the system, whereas the MD part allows the system to explore the high energy region of phase space in which the infrequent events occur. As there are no velocities in the MC part, the atomic velocities in the MD part are initiated from a truncated Maxwell-Boltzmann distribution at the temperature of interest such that $\mathbf{v}_i \cdot \mathbf{f}_i > 0$ where $\mathbf{v}_i$ is the chosen atomic velocity, and $\mathbf{f}_i$ is the force acting on the atom. In parallel to the MC run intended to relax the system, a second MC run is launched to estimate the time the system should have spent in the potential well.

Fig. 1 Schematic representation of the alternating MD/MC approach

Tiwary et al. [71] applied this algorithm to the vacancy-mediated diffusion in iron and the plasticity and deformation of Au nanopillars at realistic strain rates. In both cases, good agreement with the literature is found, and for the diffusion studies, an impressive boost factor of 10^5 was obtained, demonstrating the usefulness of their technique in the field of condensed matter simulations.

3.2.4 Sequential algorithms: alternating hybrid algorithms

It is of course also possible to combine MD with fbMC, or fbMC with MMC, etc. Various examples can be found in the literature.

Timonova et al. [62] explored two rather similar versions of combining MD and fbMC, which they termed "UFMC+" and "UFMC++," both aiming at bringing the system back to thermal equilibrium and reduce the unphysical spread in atomic potential energies produced by the fbMC algorithm. As pointed out by these authors, this starts by assigning velocities to the atoms, which are absent in the fbMC algorithm. In their UFMC+ simulations, zero velocities were attributed to all atoms, followed by a short NVT MD run at the temperature corresponding to the fbMC temperature. In the UFMC++ version, all atoms were again given zero velocities, and followed by a short constant temperature MD run, but this time with the thermostat set to 0 K. This effectively results in a system quenched to 0 K. The authors found that in both cases, equilibrium was reached in about 1.5 ps. The UFMC+ simulations were used to study the solid–liquid phase transition of Si.

Grein et al. [72] employed a fbMC/MMC technique for simulation of a deposition process. Similar to Taguchi et al. (who used a MD/MMC approach instead of fbMC/MMC [68, 69], these authors used fbMC to follow the actual deposition process and MMC for the subsequent equilibration. The goal was to describe the initial nucleation and growth of Ge epitaxially depositing on Si(001) surfaces. Interestingly, they used a maximum displacement length of 0.5 Å in their fbMC simulations while accepting all displacements. This displacement length is a factor of 100 or more larger than a typical displacement in MD.

While such a large step size must certainly violate detailed balance (see [63]), the authors nevertheless obtained results which seem physically reasonable. It should be noted that such large displacements can be used successfully if an acceptance criterion is used, as was done in the original formulation by Pangali et al. [58, 59].

4 Examples of combined MD/MC

In this section, we will review three representative examples of the techniques described above in the context of reactive condensed matter simulations, taken from our own research efforts: Cu surface diffusion by fbMC, (ultra) nanocrystalline diamond (UNCD) growth using sequential MD/MMC and carbon nanotube (CNT) growth using sequential MD/fbMC.

4.1 Hybrid algorithms: Cu surface diffusion by tfMC

As a first basic example, we consider the diffusion of a Cu adatom on a solid Cu (001) surface, as simulated by tfMC [47]. The Cu–Cu interaction was described by the standard embedded atom method potential. The diffusion coefficient was determined directly from the calculated trajectories, and the rate constant was calculated from the Arrhenius equation. The tfMC simulations were carried out using $\Delta = 0.10$ Å, corresponding to an average MC time step between 7.8 and 10 fs, in the temperature range 550–900 K, and compared with both MD simulations as well as with the literature. The dynamics of the adatom diffusion process as determined from the tfMC algorithm are shown in Fig. 2. It was found that tfMC correctly reproduces the different diffusion mechanisms as observed in the MD simulations. Also, the activation barrier as determined from tfMC, 0.48 eV, is in close agreement with the literature values (0.43–0.51 eV). Interestingly, however, the frequency factor found from the tfMC simulations, 14.7 THz, is in much closer agreement with the literature values (7.5–35.8 THz) than the MD value (52.5 THz). This demonstrates that tfMC is indeed capable of correctly reproducing the atomic dynamics of the system while significantly increasing the timescale that can be reached.

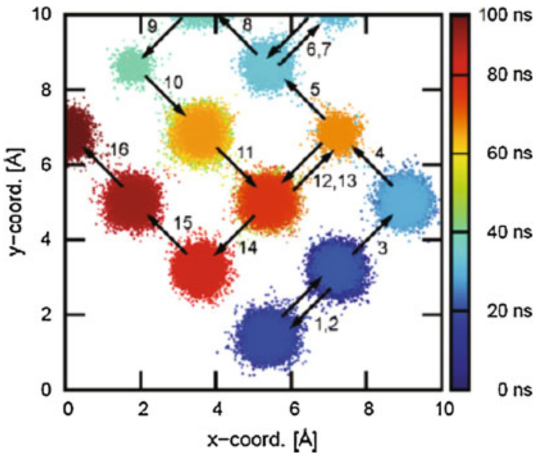

Fig. 2 Illustration of the Cu adatom diffusion dynamics as observed in tfMC simulations. Reproduced with permission by the American Physical Society from [47]

4.2 Alternating MD and MC: (U)NCD growth by MD/MMC

As mentioned in the previous sections, the combination of MC with MD may provide a means to take into account events that occur on timescales that are beyond the reach of pure MD simulations. Thus, we performed a number of hybrid MD/MMC simulations relevant for NCD and UNCD growth, based on the Brenner potential [73, 74, 75]. In an attempt to minimize the computational effort, we combined MD with MMC, introducing two additional criteria, in addition to the standard Metropolis acceptance criterion [74]. In this implementation, a criterion is used to select which atoms are displaced in the MMC (in contrast to moving all the atoms), as well as a criterion deciding after how many steps the MMC is stopped. We found that the MD/MMC algorithm predicts the same processes to occur as pure MD while allowing a speedup of typically one order of magnitude. As a simple example of the application of this technique, Fig. 3 shows the formation of a new diamond 6-ring starting from a previously adsorbed C-atom and C_2H_2 molecule.

These kind of simulations again provide atomic scale insights into the mechanisms, while the resulting structures correspond to the experiment. For instance, the effect of the prolonged application of a bias on the nucleation was investigated by both MD/MMC simulations and experiments [73]. In agreement with the experiment, an exponential increase in the growth rate was observed at high bias voltages. Complementary to the experimental data, it was found that this is caused by the increased flux of reactive particles toward the substrate. Furthermore, it was found that the growing film is activated by the formation of reactive sites when a sufficiently high bias is applied. Also in agreement with the literature, an enhanced formation of long-range order in the films was obtained by the application of a bias up to 100 V. Applying bias voltages above 100 V, diamond crystallites could not be formed, again in agreement with experimental findings.

4.3 Alternating hybrid algorithms: CNT growth by MD/fbMC

Carbon nanotubes continue to attract a lot of research attention because of their extraordinary mechanical, optical

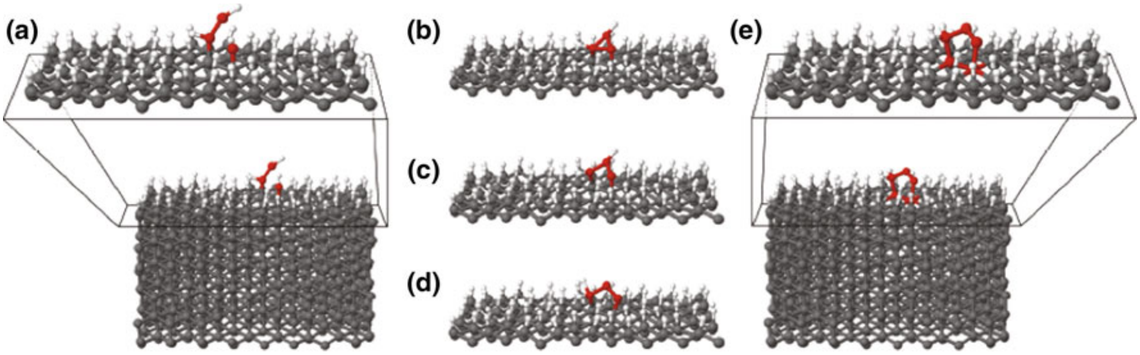

Fig. 3 Formation of a new diamond 6-ring from an adsorbed C-atom and adsorbed C_2H_2 molecule as observed in a MD/MMC simulation. **a** The initial configuration, **b–d** intermediate states and **e** the final state. The *red* atoms indicate the carbon atoms involved in the formation of the new diamond 6-ring. Reproduced from [74] with permission from the Royal Society of Chemistry

and electronic properties. However, these properties are directly determined by their precise structure, thus necessitating very accurate control over the growth process. In this case, atomistic simulations may provide the atomic scale insight needed to understand how the growth process might be controlled, and why specific structures are formed for a given growth condition.

One very important factor during the growth is the phase state of the nanocatalyst. Thus, we performed MD/fbMC simulations, employing the Shibuta potential, to determine the phase state of various Ni-nanoparticles as a function of size and temperature [76]. In this work, the thermalization was carried out using combined MD/fbMC simulations. Analysis of the radial distribution of the atomic Lindemann index revealed that that for the smallest clusters, a dynamic coexistence process occurs. As illustrated in Fig. 4, surface melting is observed for the larger particles. In all cases, a significant depression of the melting temperature relative to the bulk was observed, due to the Gibbs–Thomson effect, in agreement with the literature [77–79].

Subsequently, a number of combined MD/fbMC simulations were performed to study the growth of carbon nanotubes based on the ReaxFF potential to gain an atomic scale understanding in the actual growth process [80–82]. In these simulations, rather conservative values for $\Delta/2 = 0.085R_{\mathrm{eq}}$ [80] and $\Delta/2 = 0.07R_{\mathrm{eq}}$ [81, 82] in the fbMC were chosen. The temperature was set to 1,000 K, corresponding to a typical experimental growth temperature. After each MC cycle, new random velocities were assigned to all atoms, and the simulation was continued with constant temperature MD. Similar to Grein et al., the impact and deposition of atoms (in this case C-atoms) on the substrate (in this case a Ni-nanocluster) were followed by MD, and the subsequent relaxation by fbMC. It was found that the fbMC method results in healing of the carbon network that is formed by the continuous addition of carbon atoms—a process in which high barriers must be overcome. An example of this healing mechanism as observed in the fbMC is shown in Fig. 5. This then finally leads to CNTs with very few defects, as illustrated in Fig. 6, in contrast to what is typically observed in pure MD growth simulations. Both metallic tubes [81] as well as semi-conducting tubes [80] could be obtained. Furthermore, we also observed that the chirality of the tube may change in the initial nucleation stage. It was found that this is due to the incorporation of asymmetric defects, such as so-called 5–7 defects [81]. Thus, these MD/fbMC simulations allow to gain an understanding of how the longer timescale events may influence the growth process.

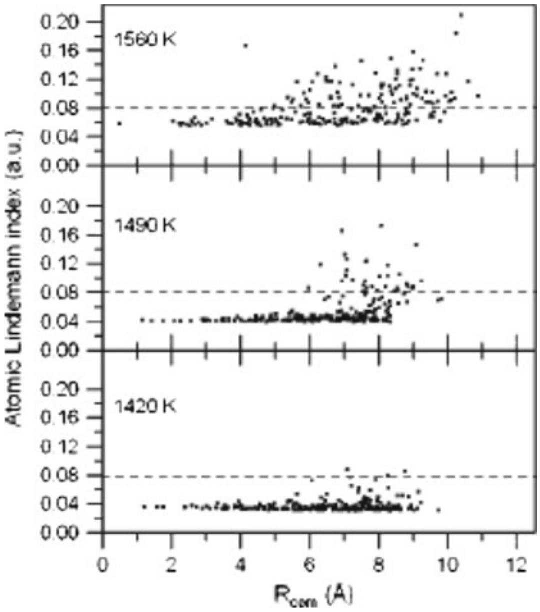

Fig. 4 Calculated radial distribution of the atomic Lindemann index for a Ni_{244} cluster, for various temperatures, revealing a surface melting mechanism. Reproduced from [15] with permission from the American Chemical Society

In another study, we used MD/fbMC simulations to investigate how an electric field may influence the growth process. In agreement with the experiment [83, 84], SWNT

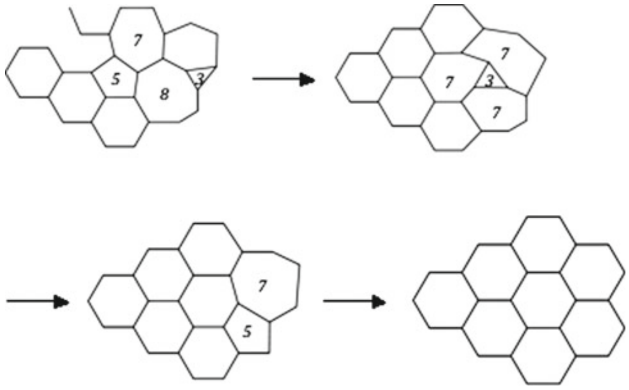

Fig. 5 Observed healing mechanism of the growing carbon network during CNT growth. Reproduced from [81] with the permission of the American Chemical Society

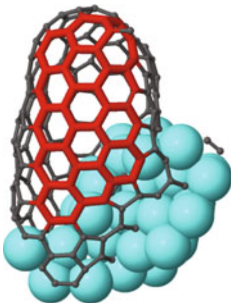

Fig. 6 Simulated SWNT growth based on the MD/fbMC technique, resulting in a SWNT with (7, 7) chirality. Reproduced from [81] with permission from the American Chemical Society

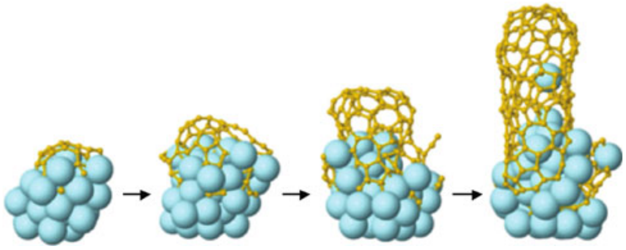

Fig. 7 MD/fbMC simulation of vertically aligned SWNT growth by applying an electric field of 700 kV/cm [82]

alignment was observed if a (sufficiently strong) electric field was applied. This is shown in Fig. 7 for an electric field value of 700 kV/cm. These simulations shed a new light on the underlying mechanism: we found that the electric field is primarily acting on the polar Ni–C bonds, at the interface between the nickel nanocluster and the growing SWNT. Thus, as at this interface the C-atoms are slightly negative, while the Ni-atoms are slightly positive, the carbon atoms experience both an oriented force, pulling them toward the tip of the cluster, but are also subject to random thermal diffusion. If the electric field is sufficiently strong, the directed migration dominates the random diffusion, an a vertically aligned SWNT emerges. Thus, these simulations directly provide information about the relevant processes complementary to the experiment.

5 Conclusion

In this contribution, we have presented a brief summary of the main accelerated molecular dynamics techniques as well as more a elaborate description of the various techniques for combining MD simulations with MC simulations, as an alternative to accelerated molecular dynamics simulations for generating long system trajectories. Using examples from the literature, it is shown that combined MD/MC simulations may provide a dynamic picture of a reactive system, including relaxation events which take place on timescales typically beyond the reach of pure MD. Essentially, we can distinguish between algorithms in which some atoms are moved by MD and some by MC (*combined MD/MC method*), algorithms in which the atomic displacement prescription is in part deterministic and in part stochastic (*hybrid MD/MC method*), and algorithm in which MD cycles alternate with MC cycles (*sequential MD/MC method*).

Three representative examples from our own research efforts were shown to demonstrate the applicability of MD/MC simulations, viz. Cu adatom diffusion, UNCD growth and CNT growth.

In addition to their ease of implementation and their general applicability make these methods very attractive for studying systems in which processes beyond the reach of standard MD are important.

References

1. Frenkel D, Smit B (2001) Understanding molecular simulation: from algorithms to applications. Academic Press, London
2. Cooke DJ, Elliott JA (2007) Atomistic simulations of calcite nanoparticles and their interaction with water. J Chem Phys 127(10). Art no 104706
3. Khalilov U, Pourtois G, van Duin ACT, Neyts EC (2012) self-limiting oxidation in small-diameter Si nanowires. Chem Mater 24(11):2141–2147
4. Lu Y, Cheng H, Chen M (2012) A molecular dynamics examination of the relationship between self-diffusion and viscosity in liquid metals. J Chem Phys 136(21). Art no 214505
5. Matsukuma M, Hamaguchi S (2008) Molecular dynamics simulation of microcrystalline Si deposition processes by silane plasmas. Thin Solid Films 516(11):3443–3448
6. Neyts E, Bogaerts A, Gijbels R, Benedikt J, Van De Sanden M (2004) Molecular dynamics simulations for the growth of diamond-like carbon films from low kinetic energy species. Diam Relat Mater13(10):1873–1881
7. Faccioli P, Lonardi A, Orland H (2010) Dominant reaction pathways in protein folding: a direct validation against molecular dynamics simulations. J Chem Phys 133(4). Art no 045104

8. Rauf S, Sparks T, Ventzek PLG, Smirnov VV, Stengach AV, Gaynullin KG, Pavlovsky VA (2007) A molecular dynamics investigation of fluorocarbon based layer-by-layer etching of silicon and SiO2. J Appl Phys 101(3). Art no 033308
9. Gou F, Neyts E, Eckert M, Tinck S, Bogaerts A (2010) Molecular dynamics simulations of Cl+ etching on a Si(100) surface. J Appl Phys 107(11):113305
10. Postawa Z, Czerwinski B, Szewczyk M, Smiley E, Winograd N, Garrison B (2003) Enhancement of sputtering yields due to C-60 versus Ga bombardment of Ag{111} as explored by molecular dynamics simulations. Anal Chem 75(17):4402–4407
11. Shen XJ, Xiao Y, Dong W, Yan XH, Busnengo HF (2012) Molecular dynamics simulations based on reactive force-fields for surface chemical reactions. Comput Theor Chem 990: 152–158
12. Servantie J, Gaspard P (2003) Methods of calculation of a friction coefficient: application to nanotubes. Phys Rev Lett 91(18). Art no 185503
13. Thaulow C, Sen D, Buehler MJ (2011) Atomistic study of the effect of crack tip ledges on the nucleation of dislocations in silicon single crystals at elevated temperature. Mater Sci Eng A Struct Mater Prop Microstruct Process 528(13–14):4357–4364
14. Shibuta Y (2012) Phase transition of metal nanowires confined in a low-dimensional nanospace. Chem Phys Lett 532:84–89
15. Neyts EC, Bogaerts A (2009) Numerical study of the size-dependent melting mechanisms of nickel nanoclusters. J Phys Chem C 113(7):2771–2776
16. Dongare AM, Rajendran AM, LaMattina B, Zikry MA, Brenner DW (2009) Atomic scale studies of spall behavior in nanocrystalline Cu. J Appl Phys 108(11):113518
17. Shaw DE, Maragakis P, Lindorff-Larsen K, Piana S, Dror RO, Eastwood MP, Bank JA, Jumper JM, Salmon JK, Shan Y, Wriggers W (2010) Atomic-level characterization of the structural dynamics of proteins. Science 330(6002):341–346
18. Metropolis N, Rosenbluth AW, Rosenbluth MN, Teller AH, Teller E (1953) Equation of state calculations by fast computing machines. J Chem Phys 21(6):1087
19. Kikuchi K, Yoshida M, Maekawa T, Watanabe H (1991) Metropolis Monte–Carlo method as a numerical technique to solve the Fokker-Planck equation. Chem Phys Lett 185(3–4): 335–338
20. Kikuchi K, Yoshida M, Maekawa T, Watanabe H (1992) Metropolis Monte-Carlo method for Brownian dynamics simulation generalized to include hydrodynamic interactions. Chem Phys Lett 196(1–2):57–61
21. Bortz AB, Kalos MH, Leibowitz JL (1975) A new algorithm for Monte Carlo simulation of Ising spin systems. J Comput Phys 17:10–18
22. Netto A, Frenklach M (2005) Kinetic Monte Carlo simulations of CVD diamond growth—interlay among growth, etching, and migration. Diam Relat Mater 14(10):1630–1646
23. Henkelman G, Jonsson H (2001) Long time scale kinetic Monte Carlo simulations without lattice approximation and predefined event table. J Chem Phys 115(21):9657–9666
24. Liu YH, Neyts E, Bogaerts A (2006) Monte Carlo method for simulations of adsorbed atom diffusion on a surface. Diam Relat Mater 15(10):1629–1635
25. Voter A, Montalenti F, Germann T (2002) Extending the time scale in atomistic simulation of materials. Ann Rev Mater Res 32:321–346
26. Jonsson H, Mills G, Jacobsen KW (1998) Nudged elastic band method for finding minimum energy paths of transitions. In: Berne BJ, Ciccotti G, Coker DF (ed) Classical and quantum dynamics in condensed phase simulations. World Scientific, Singapore
27. Henkelman G, Jonsson H (1999) A dimer method for finding saddle points on high dimensional potential surfaces using only first derivatives. J Chem Phys 111:7010–7022
28. Dellago C, Bolhuis PG, Csajka FS, Chandler D (1998) Transition path sampling and the calculation of rate constants. J Chem Phys 108(5):1964–1977
29. Barkema GT, Mousseau N (1996) Event-based relaxation of continuous disordered systems. Phys Rev Lett 77(21): 4358–4361
30. Allen RJ, Warren PB, ten Wolde PR (2005) Sampling rare switching events in biochemical networks. Phys Rev Lett 94: 018104
31. Ren WE, Vanden-Eijnden E (2005) Finite temperature string method for the study of rare events. J Phys Chem B 109:6668
32. Faradijan AK, Elber R (2004) Computing time scales from reaction coordinates by milestoning. J Chem Phys 120:10880–10889
33. Tironi IG, van Gunsteren WF (1994) A molecular-dynamics simulation study of chloroform. Mol Phys 83(2): 381–403
34. Laio A, Parrinello M (2002) Escaping free-energy minima. Proc Natl Acad Sci USA 99(20):12562–12566
35. Zwanzig RW (1954) High temperature equation of state by a perturbation method. I. Nonpolar gases. J Chem Phys 22:1420–1426
36. Torrie GM, Valleau JP (1977) Nonphysical sampling distributions in Monte Carlo free-energy estimation: umbrella sampling. J Comput Phys 22(2):187–199
37. Darve E, Pohorille A (2001) Calculating free energies using average force. J Chem Phys 115: 9169–9183
38. Leech J, Prins J, Hermans J (1996) SMD: Visual steering of molecular dynamics for protein design. IEEE Comput Sci Eng 3:38–45
39. Sorensen M, Voter A (2000) Temperature-accelerated dynamics for simulation of infrequent events. J Chem Phys 112(21): 9599–9606
40. Voter A (1997) Hyperdynamics: accelerated molecular dynamics of infrequent events. Phys Rev Lett 78(20):3908–3911
41. Voter A (1998) Parallel replica method for dynamics of infrequent events. Phys Rev B Condens Matter 57(22): 13985–13988
42. Egelhoff WF, Jacob I (1998) Reflection high-energy electron-diffraction (RHEED) oscillations at 77 K. Phys Rev Lett 62(8): 921–924
43. Georgieva V, Voter AF, Bogaerts A (2011) Understanding the surface diffusion processes during magnetron sputter-deposition of complex oxide Mg-Al-O thin films. Cryst Growth Des 11(6): 2553–2558
44. Fichthorn KA, Miron RA, Wang YS, Tiwary Y (2009) Accelerated molecular dynamics simulation of thin-film growth with the bond-boost method. J Phys Condens Matter 21(8):084212
45. Hamelberg D, Mongan J, McCammon JA (2004) Accelerated molecular dynamics: a promising and efficient simulation method for biomolecules. J Chem Phys 120(24): 11919–11929
46. Uberuaga BP, Stuart SJ, Windl W, Masquelier MP, Voter AF (2012) Fullerene and graphene formation from carbon nanotube fragments. Comput Theor Chem 987(SI):115–121
47. Mees MJ, Pourtois G, Neyts EC, Thijsse BJ, Stesmans A (2012) Uniform-acceptance force-bias Monte Carlo method with time scale to study solid-state diffusion. Phys Rev B 85(13):134301
48. Laberge L, Tully J (2000) A rigorous procedure for combining molecular dynamics and Monte Carlo simulation algorithms. Chem Phys 260(1-2):183–191
49. Ribeiro AAST, de Alencastro RB (2012) Mixed Monte Carlo/molecular dynamics simulations in explicit solvent. J Comput Chem 33(8):901–905
50. Ulmschneider JP, Jorgensen WL (2003) Monte Carlo backbone sampling for polypeptides with variable bond angles and dihedral angles using concerted rotations and a Gaussian bias. J Chem Phys 118(9):4261–4271
51. Leach AR (2001) Molecular modelling: principles and applications. Prentice Hall, Essex

52. Bussi G, Donadio D, Parrinello M (2007) Canonical sampling through velocity rescaling. J Chem Phys 126(1):014101
53. Forray C, Muthukumar M (2006) Langevin dynamics simulations of genome packing in bacteriophage. Biophys J 91:25–41
54. Duane S, Kennedy A, Pendleton B, Roweth D (1987) Hybrid Monte-Carlo. Phys Lett B 195(2):216–222
55. Mehlig B, Heermann D, Forrest B (1992) Hybrid Monte-Carlo method for condensed-matter systems. Phys Rev B 45(2): 679–685
56. Clamp ME, Baker PG, Stirling CJ, Brass A (1994) Hybrid Monte-Carlo—an efficient algorithm for condensed matter simulation. J Comput Chem 15(8):838–846
57. Brotz FA, Depablo JJ (1994) Hybrid Monte-Carlo simulation of silica. Chem Eng Sci 49(17):3015–3031
58. Pangali C, Rao M, Berne B (1978) Novel Monte-Carlo scheme for simulating water and aqueous-solutions. Chem Phys Lett 55(3):413–417
59. Rao M, Pangali C, Berne B (1979) Force bias Monte-Carlo simulation of water—methodology, optimization and comparison with molecular-dynamics. Mol Phys 37(6):1773–1798
60. Dereli G (1992) Stillinger-Weber type potentials in Monte-Carlo simulation of amorphous-silicon. Mol Simul 8(6):351–360
61. Mezei M (1991) Distance-scaled force biased Monte Carlo simulation for solutions containing a strongly interacting solute. Mol Simul 5:405–408
62. Timonova M, Groenewegen J, Thijsse BJ (2010) Modeling diffusion and phase transitions by a uniform-acceptance force-bias Monte Carlo method. Phys Rev B 81(14):144107
63. Neyts EC, Thijsse BJ, Mees MJ, Bal KM, Pourtois G (2012) Establishing uniform acceptance in force biased Monte Carlo simulations. J Chem Theory Comput 8: 1865–1869
64. Rossky P, Doll J, Friedman H (1978) Brownian dynamics as smart Monte-Carlo simulation. J Chem Phys 69(10): 4628–4633
65. Chiu S, Jakobsson E, Scott H (2001) Combined Monte Carlo and molecular dynamics simulation of hydrated lipid-cholesterol lipid bilayers at low cholesterol concentration. Biophys J 80(3): 1104–1114
66. Chiu S, Jakobsson E, Subramaniam S, Scott H (1999) Combined Monte Carlo and molecular dynamics simulation of fully hydrated dioleyl and palmitoyl-oleyl phosphatidylcholine lipid bilayers. Biophys J 77(5):2462–2469
67. Jager HU, Belov AY (2003) ta-C deposition simulations: film properties and time-resolved dynamics of film formation. Phys Rev B 68(2):024201
68. Taguchi M, Hamaguchi S (2006) Molecular dynamics study on Ar ion bombardment effects in amorphous Sio2 deposition processes. J Appl Phys 100(12):123305
69. Taguchi M, Hamaguchi S (2007) Md simulations of amorphous Sio2 thin film formation in reactive sputtering deposition processes. Thin Solid Films 515(12):4879–4882
70. Tavazza F, Nurminen L, Landau D, Kuronen A, Kaski K (2004) Hybrid Monte Carlo-molecular dynamics algorithm for the study of islands and step edges on semiconductor surfaces: application to Si/Si(001). Phys Rev E 70(3, Part 2): 036701
71. Tiwary P, van de Walle A (2011) Hybrid deterministic and stochastic approach for efficient atomistic simulations at long time scales. Phys Rev B 84(10):100301
72. Grein C, Benedek R, Delarubia T (1996) Epitaxial growth simulation employing a combined molecular dynamics and Monte Carlo approach. Comput Mater Sci 6(2):123–126
73. Eckert M, Mortet V, Zhang L, Neyts E, Verbeeck J, Haenen K, Bogaerts A (2011) Theoretical investigation of grain size tuning during prolonged bias-enhanced nucleation. Chem Mater 23(6): 1414–1423
74. Eckert M, Neyts E, Bogaerts A (2009) Modeling adatom surface processes during crystal growth: a new implementation of the metropolis Monte Carlo algorithm. CrystEngComm 11(8):1597–1608
75. Eckert M, Neyts E, Bogaerts A (2010) Insights into the growth of (ultra) nanocrystalline diamond by combined molecular dynamics and Monte Carlo simulations. Cryst Growth Design 10(7): 3005–3021
76. Neyts EC, Khalilov U, Pourtois G, Van Duin ACT (2011) Hyperthermal oxygen interacting with silicon surfaces: adsorption, implantation, and damage creation. J Phys Chem C 115(11): 4818–4823
77. Buffat P, Borel J (1976) Size effect on melting temperature of gold particles. Phys Rev A 13(6):2287–2298
78. Jiang A, Awasthi N, Kolmogorov AN, Setyawan W, Borjesson A, Bolton K, Harutyunyan AR, Curtarolo S (2007) Theoretical study of the thermal behavior of free and alumina-supported Fe-C nanoparticles. Phys Rev B 75(20):205426
79. Shibuta Y, Suzuki T (2010) Melting and solidification point of fcc-metal nanoparticles with respect to particle size: a molecular dynamics study. Chem Phys Lett 498(4–6): 323–327
80. Neyts EC, Shibuta Y, Van Duin ACT, Bogaerts A (2010) Catalyzed growth of carbon nanotube with definable chirality by hybrid molecular dynamics-force biased Monte Carlo simulations. ACS Nano 4(11): 6665–6672
81. Neyts EC, Van Duin ACT, Bogaerts A (2011) Changing chirality during single-walled carbon nanotube growth: a reactive molecular dynamics/Monte Carlo study. J Am Chem Soc 133(43): 17225–17231
82. Neyts EC, Van Duin ACT, Bogaerts A (2012) Insights in the plasma-assisted growth of carbon nanotubes through atomic scale simulations: effect of electric field. J Am Chem Soc 134(2): 1256–1260
83. Hatakeyama R, Kaneko T, Kato T, Li YF (2011) Plasma-synthesized single-walled carbon nanotubes and their applications. J Phys D Appl Phys 44(17):174004
84. Kato T, Hatakeyama R (2006) Formation of freestanding single-walled carbon nanotubes by plasma-enhanced CVD. Chem Vap Depos 12(6):345–352